

Nuclear Safety

ISBN 978-92-64-99091-3

# **Nuclear Fuel Behaviour in Loss-of-coolant Accident (LOCA) Conditions**

**State-of-the-art Report**

© OECD 2009  
NEA No. 6846

NUCLEAR ENERGY AGENCY  
ORGANISATION FOR ECONOMIC CO-OPERATION AND DEVELOPMENT

## **ORGANISATION FOR ECONOMIC CO-OPERATION AND DEVELOPMENT**

The OECD is a unique forum where the governments of 30 democracies work together to address the economic, social and environmental challenges of globalisation. The OECD is also at the forefront of efforts to understand and to help governments respond to new developments and concerns, such as corporate governance, the information economy and the challenges of an ageing population. The Organisation provides a setting where governments can compare policy experiences, seek answers to common problems, identify good practice and work to co-ordinate domestic and international policies.

The OECD member countries are: Australia, Austria, Belgium, Canada, the Czech Republic, Denmark, Finland, France, Germany, Greece, Hungary, Iceland, Ireland, Italy, Japan, Korea, Luxembourg, Mexico, the Netherlands, New Zealand, Norway, Poland, Portugal, the Slovak Republic, Spain, Sweden, Switzerland, Turkey, the United Kingdom and the United States. The Commission of the European Communities takes part in the work of the OECD.

OECD Publishing disseminates widely the results of the Organisation's statistics gathering and research on economic, social and environmental issues, as well as the conventions, guidelines and standards agreed by its members.

*This work is published on the responsibility of the Secretary-General of the OECD. The opinions expressed and arguments employed herein do not necessarily reflect the official views of the Organisation or of the governments of its member countries.*

## **NUCLEAR ENERGY AGENCY**

The OECD Nuclear Energy Agency (NEA) was established on 1st February 1958 under the name of the OEEC European Nuclear Energy Agency. It received its present designation on 20<sup>th</sup> April 1972, when Japan became its first non-European full member. NEA membership today consists of 28 OECD member countries: Australia, Austria, Belgium, Canada, the Czech Republic, Denmark, Finland, France, Germany, Greece, Hungary, Iceland, Ireland, Italy, Japan, Luxembourg, Mexico, the Netherlands, Norway, Portugal, Republic of Korea, the Slovak Republic, Spain, Sweden, Switzerland, Turkey, the United Kingdom and the United States. The Commission of the European Communities also takes part in the work of the Agency.

The mission of the NEA is:

- to assist its member countries in maintaining and further developing, through international co-operation, the scientific, technological and legal bases required for a safe, environmentally friendly and economical use of nuclear energy for peaceful purposes, as well as
- to provide authoritative assessments and to forge common understandings on key issues, as input to government decisions on nuclear energy policy and to broader OECD policy analyses in areas such as energy and sustainable development.

Specific areas of competence of the NEA include safety and regulation of nuclear activities, radioactive waste management, radiological protection, nuclear science, economic and technical analyses of the nuclear fuel cycle, nuclear law and liability, and public information.

The NEA Data Bank provides nuclear data and computer program services for participating countries. In these and related tasks, the NEA works in close collaboration with the International Atomic Energy Agency in Vienna, with which it has a Co-operation Agreement, as well as with other international organisations in the nuclear field.

Corrigenda to OECD publications may be found on line at: [www.oecd.org/publishing/corrigenda](http://www.oecd.org/publishing/corrigenda).  
© OECD 2009

You can copy, download or print OECD content for your own use, and you can include excerpts from OECD publications, databases and multimedia products in your own documents, presentations, blogs, websites and teaching materials, provided that suitable acknowledgment of OECD as source and copyright owner is given. All requests for public or commercial use and translation rights should be submitted to [rights@oecd.org](mailto:rights@oecd.org). Requests for permission to photocopy portions of this material for public or commercial use shall be addressed directly to the Copyright Clearance Center (CCC) at [info@copyright.com](mailto:info@copyright.com) or the Centre français d'exploitation du droit de copie (CFC) [contact@cfcopies.com](mailto:contact@cfcopies.com).

## **FOREWORD**

The NEA Working Group on Fuel Safety (WGFS) is tasked with advancing the current understanding of fuel safety issues by assessing the technical basis for current safety criteria and their applicability to high burn-up and to new fuel designs and materials. The group aims at facilitating international convergence in this area, including as regards experimental approaches and interpretation and the use of experimental data relevant for safety.

In 1986, a working group of the NEA Committee on the Safety of Nuclear Installations (CSNI) issued a state-of-the-art report on water reactor fuel behaviour in design-basis accident (DBA) conditions. The 1986 report was limited to the oxidation, embrittlement and deformation of pressurised water reactor (PWR) fuel in a loss-of-coolant accident (LOCA).

Since then, considerable experimental and analytical work has been performed, which has led to a broader and deeper understanding of LOCA-related phenomena. Further, new cladding alloys have been produced, which might behave differently than the previously used Zircaloy-4, both under normal operating conditions and during transients. Compared with 20 years ago, fuel burn-up has been significantly increased, which requires extending the LOCA database in order to cover the high burn-up range. There was also a clear need to address LOCA performance for reactor types other than PWRs.

The present report has been prepared by the WGFS and covers the following technical aspects:

- Description of different LOCA scenarios for major types of reactors: BWRs, PWRs, VVERs and to a lesser extent CANDUs.
- LOCA phenomena: ballooning, burst, oxidation, fuel relocation and possible fracture at quench.
- Details of high-temperature oxidation behaviour of various cladding materials.
- Metallurgical phase change, effect of hydrogen and oxygen on residual cladding ductility.
- Methods for LOCA testing, for example two-sided oxidation and ring compression for ductility, and integral quench test for strength.
- Predictive computer codes.

The WGFS is currently preparing a similar state-of-the-art report on reactivity-initiated accident (RIA) phenomena, which is expected to be issued in December 2009.

## **Acknowledgements**

The NEA Secretariat wishes to express its gratitude to Dr. Kjell Pettersson (MATSAFE AB) for his efforts in drafting the report, to the Swedish Radiation Safety Authority (SSM) for supporting the work, as well as to Dr. Hajung Chung for reviewing the draft.

The following WGFS members and other experts from the industry also provided valuable input to various chapters of the report:

Michael Billone, ANL, United States  
Toyoshi Fuketa, JAEA, Japan  
Claude Grandjean, IRSN, France  
George Hache, IRSN, France  
Lothar Heins, Areva NP, Germany  
Zoltan Hozer, KFKI, Hungary  
Jan In de Betou, SSM, Sweden  
Seppo Kelppe, VTT, Finland  
Ralph Mayer, USNRC, United States  
Fumihisa Nagase, JAEA, Japan  
Joelle Papin, IRSN, France  
Harold Scott, USNRC, United States  
Heinz Sonnenburg, GRS, Germany  
Sham Sunder, AECL, Canada  
Mojmir Valach, NRI Rez, Czech Republic  
John Voglewede, USNRC, United States  
Vera Vrtlikova, UJP, Czech Republic  
Nicolas Waeckel, EdF, France  
Wolfgang Wiesenack, HRP, Norway  
Martin Zimmermann, PSI, Switzerland

## TABLE OF CONTENTS

<b>Foreword .....</b>	3
<b>Executive Summary.....</b>	21
<b>1. Introduction.....</b>	25
1.1 General overview and introduction to the LOCA safety issue.....	25
1.2 Current safety criteria and their background.....	26
1.2.1 Current safety criteria in the United States .....	27
1.2.2 Background to the safety criteria .....	30
1.2.2.1 Metallurgy of cladding embrittlement.....	31
1.2.2.2 The 17%-oxidation criterion and the Baker-Just oxidation law .....	33
1.2.2.3 The 2 200°F criterion.....	36
1.2.3 LOCA safety criteria in other countries .....	39
1.3 References .....	40
<b>2. Description of LOCA accident scenarios for major types of reactors .....</b>	43
2.1 The pressurised water reactor.....	43
2.1.1 PWR large break LOCA .....	43
2.1.2 PWR small break LOCA.....	44
2.2 Boiling water reactor LOCA .....	45
2.3 Risk-informed changes to NRC LOCA technical requirements .....	48
2.4 CANDU reactor LOCA.....	49
2.4.1 Large break LOCA .....	51
2.4.2 Small break LOCA .....	51
2.5 VVER reactor LOCA .....	52
2.5.1 Large break LOCA .....	53
2.5.2 Small break LOCA .....	54
2.6 References .....	54
<b>3. State of fuel and cladding at various burn-up levels .....</b>	55
3.1 State of fuel at various burn-up levels.....	55
3.1.1 UO <sub>2</sub> fuel .....	55
3.1.2 MOX fuel and high burn-up UO <sub>2</sub> fuel .....	56
3.2 State of cladding.....	58
3.2.1 PWR cladding .....	58
3.2.2 BWR cladding.....	61
3.3 High burn-up CANDU fuel.....	63
3.4 References .....	64
<b>4. Phenomena that need to be addressed by experiments and modelling.....</b>	65
4.1 Types of damage to fuel and cladding.....	65
4.2 Changes of temperature and geometry with influence core coolability .....	67

4.2.1	The FEBA and SEFLEX programmes.....	67
4.2.1.1	FEBA test results.....	68
4.2.1.2	SEFLEX test results.....	69
4.2.2	THETIS programme .....	71
4.2.3	FLECHT SEASET programme .....	72
4.2.4	Conclusions from the programmes on cooling of deformed bundles .....	75
4.2.4.1	Main results from the experimental programmes .....	75
4.2.4.2	Pending questions .....	75
4.3	Radiological consequences.....	76
4.3.1	Harmonisation efforts in Europe.....	77
4.3.1.1	List of nuclides to consider in the calculation of the radiological consequences .....	78
4.3.1.2	The failed fuel fraction .....	80
4.3.1.3	The release from failed fuel.....	80
4.3.1.4	The retention in the reactor coolant system and the initial release of fission products to the containment atmosphere .....	81
4.3.1.5	Retention in the containment .....	81
4.3.1.6	Conclusions of the European harmonisation effort .....	83
4.4	References .....	83
<b>5.</b>	<b>Overview of LOCA testing methodology.....</b>	85
5.1	Separate effect tests .....	85
5.1.1	Creep tests.....	85
5.1.2	Determination of diffusion constants.....	93
5.1.3	Determination of the $\alpha$ to $\alpha+\beta$ and $\alpha+\beta$ to $\beta$ transformation temperatures .....	93
5.1.4	Ductility tests .....	96
5.1.4.1	The ring compression test.....	96
5.1.4.2	Ring tensile tests.....	99
5.1.4.3	Tube bending tests .....	100
5.1.4.4	Impact tests .....	101
5.1.5	Oxidation tests .....	103
5.2	Tests with moderate integration .....	107
5.2.1	Steam oxidation tests followed by quenching.....	108
5.2.2	Deformation or ballooning tests in steam .....	110
5.2.3	Constrained deformation or ballooning tests in steam with or without quench.....	113
5.3	Fully integrated tests .....	114
5.3.1	In-reactor tests.....	114
5.3.1.1	The FR2 facility.....	114
5.3.1.2	LOC tests in the power burst facility.....	117
5.3.1.3	PHEBUS test .....	117
5.3.1.4	LOCA tests in the Halden reactor.....	120
5.3.1.5	BTF test .....	123
5.3.2	Out-of-reactor integral tests .....	124
5.3.2.1	The REBEKA programme at Kernforschungszentrum Karlsruhe .....	124
5.3.2.2	Single and multi-rod tests at the Japanese Atomic Energy Research Institute (JAERI).....	126
5.3.2.3	Single and multi-rod burst test (MRBT) at Oak Ridge National Laboratory (ORNL), USA .....	129
5.3.2.4	The Russian PARAMETR-M and TEFSAI-19 facilities .....	131
5.4	References .....	134

<b>6. Preservation of integrity of cladding during oxidation and embrittlement .....</b>	141
6.1 The kinetics of the zirconium alloy steam reaction.....	141
6.1.1 Isothermal oxidation of Zircaloy in steam .....	142
6.1.2 Isothermal oxidation of other zirconium alloys in steam.....	149
6.1.3 Breakaway oxidation of zirconium alloys.....	154
6.1.4 Effect of irradiation on high-temperature zirconium alloy oxidation .....	157
6.1.5 Effect of specimen geometry .....	157
6.1.6 The behaviour of alloying elements during oxidation .....	158
6.1.6.1 Zircaloy-4 .....	158
6.1.6.2 Zr-1Nb .....	159
6.1.7 High-temperature oxidation of pre-oxidized zirconium alloys .....	159
6.1.8 Oxidation of zirconium alloys in impure steam.....	165
6.1.9 Influence of hydrogen in steam on zirconium alloy oxidation.....	166
6.1.10 High-temperature oxidation of zirconium alloys in high pressure steam .....	173
6.1.11 Effect of deformation on zirconium alloy oxidation.....	173
6.1.12 Stress and dimensional changes in oxidized zirconium alloys .....	175
6.2 Embrittlement of zirconium alloy fuel cladding .....	176
6.2.1 Current embrittlement criteria.....	177
6.2.2 Embrittlement and distribution of oxygen in the cladding wall.....	179
6.2.3 Embrittlement below thermal shock temperatures.....	182
6.2.4 Comparison of embrittlement in-reactor and out-of-reactor.....	187
6.2.5 The effect of constraint during quenching .....	188
6.2.6 Quench embrittlement of pre-hydrided or high burn-up Zircaloy cladding.....	190
6.2.7 Recent post-quench ductility tests of Zircaloy, ZIRLO and M5 cladding .....	195
6.2.8 The post-quench embrittlement of E110 cladding .....	205
6.3 Calculation of transient oxidation, hydrogen generation and embrittlement .....	210
6.3.1 Calculation of hydrogen generation .....	210
6.3.2 Calculation of oxygen distribution.....	212
6.4 Discussions on embrittlement criteria .....	214
6.4.1 Regulatory analysis .....	214
6.4.1.1 Beta-layer embrittlement by oxygen .....	214
6.4.1.2 Beta-layer thinning .....	214
6.4.1.3 Localised hydrogen-induced embrittlement in the balloon .....	215
6.4.1.4 Hydrogen-enhanced $\beta$ -layer embrittlement by oxygen .....	215
6.4.1.5 General hydrogen-induced embrittlement from breakaway oxidation .....	215
6.4.1.6 Oxygen pickup from the cladding inside diameter (ID) .....	216
6.4.1.7 Embrittlement criteria.....	216
6.4.1.8 Summary of U.S. regulatory analysis .....	217
6.4.2 Discussions on impact of recent results on criteria .....	217
6.4.2.1 Billone's proposal.....	217
6.4.2.2 Vrtliková's criterion .....	218
6.4.2.3 The proposal by Vitanza and Hrehor.....	219
6.4.2.4 Criteria proposed by Chung.....	221
6.5 Conclusions .....	223
6.5.1 General conclusions on oxidation and hydrogen generation .....	223
6.5.2 General conclusions on embrittlement.....	224
6.6 References .....	224
<b>7. Plastic deformation of cladding .....</b>	235
7.1 The problem .....	235
7.1.1 Internal pressures of fuel rods.....	235

7.2	Factors controlling deformation and rupture of cladding.....	235
7.2.1	Measurement of blockage .....	237
7.3	Experimental data.....	239
7.3.1	In-reactor tests.....	240
7.3.1.1	Single rod tests in the FR2 reactor.....	240
7.3.1.2	Single rod tests in the PBF .....	244
7.3.1.3	Single rod tests in the ESSOR reactor .....	247
7.3.1.4	Single rod tests in the SILOE reactor .....	250
7.3.1.5	Multi-rod tests in the NRU reactor .....	251
7.3.1.6	Multi-rod tests in the PHEBUS loop .....	253
7.3.1.7	LOCA tests in the Halden reactor.....	261
7.3.2	Out-of-reactor tests .....	269
7.3.2.1	The REBEKA programme at Kernforschungszentrum Karlsruhe .....	269
7.3.2.2	Single and multi-rod testing at KWU, Erlangen.....	277
7.3.2.3	Single and multi-rod testing at the Japanese Atomic Energy Research Institute (JAERI).....	284
7.3.2.4	The single and multi-rod burst test (MRBT) programme at Oak Ridge National Laboratory (ORNL) .....	293
7.3.2.5	Single and multi-rod testing at Westinghouse Electric Corporation .....	306
7.3.2.6	Single rod testing at Saclay – CEA.....	307
7.3.2.7	Single and multiple rod testing in the United Kingdom .....	318
7.3.2.8	Experiments in the PARAMETR-M and TEFSAI-19 facilities in Russia.....	322
7.3.2.9	Ballooning of E110 cladding in comparison with Zircaloy-4 .....	326
7.4	References .....	328
<b>8.</b>	<b>Predictive computer codes .....</b>	<b>335</b>
8.1	Some general comments on computer codes .....	335
8.1.1	Types of computer codes .....	335
8.1.2	Documentation .....	336
8.1.3	Code verification.....	337
8.1.4	Code validation .....	337
8.1.5	The accuracy of codes.....	338
8.2	Single rod codes .....	339
8.2.1	Steady-state codes.....	339
8.2.2	Transient codes .....	340
8.3	Assembly/channel codes .....	341
8.4	System codes .....	343
8.5	References .....	343
<b>9.</b>	<b>Energy and core damage distribution assessment: methodologies and results.....</b>	<b>345</b>
9.1	A review of core damage assessment practices in Europe .....	345
9.2	Damage assessments for a Westinghouse PWR.....	349
9.3	A German example of core damage extent analysis .....	350
9.4	References .....	352
<b>10.</b>	<b>Conclusions.....</b>	<b>353</b>
<b>Appendices</b>		
A.	Taking account of anisotropy in creep calculations.....	365
B.	List of abbreviations .....	371

## LIST OF FIGURES

Figure 1.1 Schematic illustration of microstructure (top) and oxygen distribution (bottom) in oxide, stabilised alpha and prior-beta (transformed beta) layers in Zircaloy cladding after oxidation near 1 200°C .....	32
Figure 1.2 Ductility of two-side-oxidized Zircaloy rings as function of slow- or fast-compression temperature and fraction of transformed-beta-layer (from Hobson).....	34
Figure 1.3 Summary of multistep procedure used to establish 17% oxidation criterion during 1973 Rule-Making Hearing (from Docket RM-50-1, April 16, 1973). Note equivalent cladding oxidized was calculated per Baker-Just correlation. For comparison, time to reach threshold fraction of combined oxide and alpha layers of 0.44 is shown as determined per Hobson and Rittenhouse and Pawel .....	35
Figure 1.4 The zirconium rich corner of the Zr-O phase diagram. The thin vertical line shows 0.7 wt % O.....	38
Figure 2.1 PWR primary system arrangement .....	43
Figure 2.2 Double ended cold leg break, pressure difference across the cladding and cladding temperature at the hot spot .....	45
Figure 2.3 Steam and recirculation water flow paths in the BWR .....	46
Figure 2.4 A schematic of a CANDU primary heat transport system (Legend: 1. Steam line leading to electric turbines, 2. Pressuriser, 3. Steam generator, 4. Pumps, 5. Inlet headers, 6. Calandria vessel, 7. Fuel channel, 8. Moderator recirculation pump, 9. Heat exchanger, and 10. Online refueling machines) .....	50
Figure 3.1 Grain boundary gas versus pellet burn-up in UO <sub>2</sub> and MOX fuel (left: ratio from created gas, right: concentration) .....	58
Figure 3.2 PWR fuel state at high burn-up. BWR fuel has a similar state with the exception of the oxide layer which is thinner and with less total pickup of hydrogen in the metal	59
Figure 4.1 FEBA 5×5 bundle with 90% blockage, left and SEFLEX 5×5 bundle with 90% blockage, right .....	68
Figure 4.2 FEBA 5×5 bundle geometries of test series I through VIII .....	69
Figure 4.3 Temperatures measured in the midplane of a 90% blockage and in the blockage by-pass of FEBA and SEFLEX rod bundles .....	70
Figure 4.4 Bundle-wide blockage and axial distributions for FLECHT-SEASET configurations C, D, E and F.....	73
Figure 4.5 Rod temperatures for unblocked and coplanar configurations. a) Central rod b) Peripheral rod .....	74
Figure 4.6 Best estimate failure thresholds for PWR fuel in a large break LOCA.....	80
Figure 5.1 Creep properties of Zircaloy-2 in the temperature range 650-800°C .....	87
Figure 5.2 Heating arrangement in the experiments by Fiveland <i>et al.</i> .....	88
Figure 5.3 The 15.2 cm long specimen used by Chung and Kassner .....	88

Figure 5.4	Maximum circumferential strain at rupture versus burst temperature for axially constrained and unconstrained Zircaloy-4 cladding at a heating rate of 115 K/s. The axial strain of unconstrained tubes also is shown .....	89
Figure 5.5	A pseudobinary phase diagram for the Zircaloy-oxygen system .....	90
Figure 5.6	Schematic of Rosinger's high temperature creep apparatus.....	91
Figure 5.7	Typical creep test results from Rosinger's investigation at 1 573 K.....	92
Figure 5.8	The effect of initial condition on creep properties at 600°C The lowest yield strengths correspond to fully recrystallized material while the other pointr represent various degrees of recrystallization .....	92
Figure 5.9	Oxygen-rich-side Zircaloy-4-oxygen phase diagram determined from metallography of quenched samples, from Chung and Kassner.....	94
Figure 5.10	Comparison between transformation models and experiments on cooling of Zircaloy-4.....	95
Figure 5.11	Plot of $T_{\alpha/\alpha+\beta}$ and $T_{\beta/\alpha+\beta}$ temperatures measured upon heating and cooling at 10°C/min as a function of hydrogen content. The straight lines (average between heating and cooling) are assumed to be representative of equilibrium temperatures....	96
Figure 5.12	The arrangement for a ring compression test .....	97
Figure 5.13	Load-displacement record from a ring compression test on an oxidized Zirlo specimen .....	97
Figure 5.14	Residual ductility (defined as offset displacement at failure divided by ring diameter) plotted against ECR for E110 alloy .....	98
Figure 5.15	Components of a ring tensile test, D grip to the left and specimen to the right .....	99
Figure 5.16	Three-point bending test apparatus .....	100
Figure 5.17	Load-displacement records from three-point bend tests of oxidized Zircaloy-4.....	100
Figure 5.18	Schematic description of a four-point bend test.....	101
Figure 5.19	Dynamic fracture toughness of oxygen-alloyed Zircaloy-4 .....	102
Figure 5.20	Notched impact specimen fabricated from oxidized cladding. Results of tests with this specimen type .....	103
Figure 5.21	The steam oxidation apparatus MiniZWOK .....	104
Figure 5.22	Apparatus for Zircaloy oxidation in hydrogen-steam mixtures. The test specimen, with welded thermocouples, is placed in the centre of the bell jar facing a pyrometer through a quartz glass .....	106
Figure 5.23	High-temperature oxidation apparatus .....	106
Figure 5.24	The UNOPRO facility for continuous recording of weight gain during oxidation.....	107
Figure 5.25	Facility for continuous recording of specimen weight gain during oxidation used by Baek <i>et al.</i> .....	107
Figure 5.26	Weight gain vs time record for Zircaloy-4 oxidized at 900°C in the facility shown in Figure 5.25 .....	107
Figure 5.27	The DEZIROX oxidation and quench facility .....	108
Figure 5.28	Apparatus for oxidation tests of cladding followed by quench in water.....	109
Figure 5.29	UVS, the universal rig for testing overheated core materials.....	110
Figure 5.30	The PROPAT facility for study of cladding deformation in a steam atmosphere.....	110
Figure 5.31	Schematic diagram of ballooning test apparatus used at Chalk River .....	111
Figure 5.32	Schematic view of the EDGAR-2 test facility .....	112
Figure 5.33	Test apparatus for constrained ballooning tests in steam .....	113
Figure 5.34	Schematic illustration of the LOCA simulation facility used at the Korean Atomic Energy Research Institute .....	114
Figure 5.35	Simplified flow scheme of the DK loop, operated with superheated steam, in the FR2 reactor .....	115
Figure 5.36	In-pile test section of the DK loop in the FR2 reactor (simplified).....	115
Figure 5.37	Test fuel rod design for the FR2 experiments .....	115

Figure 5.38	Electrically heated fuel rod simulator design, heated section (not to scale) .....	116
Figure 5.39	Cross section of the PBF-LOC experiment.....	117
Figure 5.40	Schematic design of the PHEBUS test loop.....	118
Figure 5.41	Test train instrumentation.....	119
Figure 5.42	Sketch of the flow starvation facility. 1, main circulation pump; 2, flow regulating valve; 3, electric heater; 4, main circuit cooler; 5, regenerative cooler; 6, purification circuit cooler; 7, cooler; 8, ion exchanger; 9, helium pressurizing tank; 10, water supply pump; 11, graphite seal unit; 12, seal; 13, heat exchanger; 14, central tube for cabling; 15, pressure flask; 16, shroud; 17, triangular tube for cabling; 18, tube for water downflow; 19, fuel rods.....	120
Figure 5.43	Cross section of the IFA-54X assembly and pressure flask.....	121
Figure 5.44	Simplified drawing of the loop used for the IFA-650 experiments.....	122
Figure 5.45	The test rig used in the IFA-650 tests (left) and a cross section of the test rig with outer shroud (right) .....	123
Figure 5.46	Fuel rod cladding loading in a 2F-cold leg break LOCA.....	125
Figure 5.47	The REBEKA fuel rod simulator .....	125
Figure 5.48	Test loop for ballooning experiments. Bundle tests (REBEKA) .....	126
Figure 5.49	Schematic diagram of the facility for burst test of a fuel assembly at JAERI.....	127
Figure 5.50	Schematic drawing of the fuel rods and the heating system of the JAERI tests .....	127
Figure 5.51	Locations of the thermocouples in the JAERI tests .....	128
Figure 5.52	Sequence of the post burst examinations of an assembly in the JAERI tests.....	128
Figure 5.53	MRBT fuel pin simulator also used in the single-rod tests.] .....	129
Figure 5.54	Schematic of the B1 4×4 multi-rod test assembly.....	130
Figure 5.55	Typical simulator response in the B-3 test .....	130
Figure 5.56	Schematic view of the 37-rod assembly in the PARAMETR-M facility.....	132
Figure 5.57	Schematic view of the fuel rod simulators used in PARAMETR-M and TEFSAI facilities .....	133
Figure 6.1	Zircaloy-2 oxidized in steam at 1 200°C for 1 200 s. 80× .....	141
Figure 6.2	The parabolic rate constant as a function of inverse temperature as determined by different researcher. The unit for the parabolic rate constant is $(\text{g O}_2/\text{cm}^2)^2 \text{ s}^{-1}$ .....	145
Figure 6.3	The parabolic rate constant as a function of inverse temperature as determined by different researcher. The unit for the parabolic rate constant is $(\text{g O}_2/\text{cm}^2)^2 \text{ s}^{-1}$ .....	146
Figure 6.4	Parabolic oxide layer growth rate constants obtained for pure steam environments vs inverse temperature.....	148
Figure 6.5	High temperature steam oxidation of Zircaloy-4 cladding. Kinetics of of $\text{ZrO}_2$ scale growth and $\alpha\text{-Zr(O)}$ layer growth. Note the slower kinetics for oxide growth before transition to linear kinetics after long time exposure. at low temperature .....	148
Figure 6.6	Weight gains of VVER-type claddings oxidized in steam at atmospheric pressure .....	149
Figure 6.7	Temperature dependence of the reaction rate constant $K_p$ for zirconium alloys .....	150
Figure 6.8	Oxidation results on $\text{ZrNb}$ at different laboratories. Note that the original figure has been edited to remove incorrect data and to conform with reference numbering of the present report .....	150
Figure 6.9	The kinetics of the steam oxidation reaction of E110 in the temperature range 800-1 200°C. The black line is calculated with the Cathcart-Pawel equation .....	151
Figure 6.10	Results of transient test modes converted to equivalent time at constant temperature for E110.....	152
Figure 6.11	Kinetics of the sponge based E110 claddings compared to standard E110 .....	152
Figure 6.12	The oxidation of M5 and Zircaloy-4 at 1 000, 1 100, and 1 200°C .....	153
Figure 6.13	Oxidation of E635 at 1 100°C compared to other zirconium alloys .....	153

Figure 6.14	Suggested mechanism for high temperature breakaway oxidation in Zircaloy by Leistikow and co-workers .....	155
Figure 6.15	The hydrogen pickup in E110 and Zircaloy-4 during steam oxidation.....	156
Figure 6.16	The appearance of E110 cladding tubes oxidized in steam at 1100°C to different ECR levels.....	156
Figure 6.17	Nb X-ray map obtained by electron microprobe of the $\alpha(O) + \beta(Nb)$ layer below the oxide in M5 alloy oxidized to ECR ~17% at 1100 °C.....	160
Figure 6.18	Examples of corrosion of Zircaloy-4 in different PWRs .....	160
Figure 6.19	Oxidation results for cladding pre-oxidized with a 10 $\mu\text{m}$ oxide.....	161
Figure 6.20	Normalised values of high temperature oxidation of spent fuel cladding as a function of initial oxide thickness, Ozawa <i>et al.</i> .....	162
Figure 6.21	Cross sections of pre-oxidized samples oxidized at 1 100°C for various times. White arrows indicate initiation of high temperature oxidation.....	163
Figure 6.22	High temperature oxidation below an oxide nodule formed during pre-oxidation. 80x .....	164
Figure 6.23	Weight gains recorded in isothermal tests in different gases on Zircaloy-4 .....	165
Figure 6.24	The effect of air on the oxidation of the E110 alloy .....	166
Figure 6.25	Total weight gain of oxidized specimen as function of hydrogen-to-steam volume ratio .....	167
Figure 6.26	Hydrogen content absorbed by specimen in a steam-hydrogen mixture.....	168
Figure 6.27	Ratio of parabolic oxide layer growth rate constant obtained in hydrogen steam mixtures to that obtained in unlimited flux of pure steam as a function of Zircaloy-4 temperatures and steam supply rate.....	169
Figure 6.28	Ratio of parabolic oxide layer growth rate constant obtained in flowing hydrogen steam mixtures to that obtained in unlimited flux of pure steam as a function of Zircaloy-4 temperatures and average hydrogen mole fraction in the inlet mixtures.....	170
Figure 6.29	Fraction of hydrogen atoms dissolved in Zircaloy-4 cladding tube out of total hydrogen atoms produced as a result of Zircaloy steam reaction at isothermal oxidation temperatures .....	171
Figure 6.30	The effect of prehydriding on the high temperature oxidation of low Sn Zircaloy-4 ....	172
Figure 6.31	Effect of hydrogen content on M5 and Zircaloy oxidation kinetics at 1 200°C.....	172
Figure 6.32	Effect of steam pressure on the oxidation of Zircaloy-4 and Zr1%Nb at 850°C .....	173
Figure 6.33	Time dependence of oxidation induced strains at 1 350°C .....	176
Figure 6.34	Clad embrittlement data from USA and UK compiled by Parsons.....	178
Figure 6.35	Thermal-shock failure map for Zircaloy-4 cladding (bottom flooded with water at the oxidation temperature) relative to the ECR parameter and maximum oxidation temperature after rupture in steam. The best-estimate failure boundary for cladding that was slow cooled through the $\beta \rightarrow \alpha'$ before flooding with water and the data of Hesson <i>et al.</i> and Scatena are shown for comparison .....	180
Figure 6.36	Failure map for Zircaloy-4 cladding by thermal shock relative to fractional thickness of previous $\beta$ -phase layer and oxidation temperature after rupture in steam and flooding with water at oxidation temperature. Cooling rate through the $\beta \rightarrow \alpha'$ transformation was ~100 K/s.....	180
Figure 6.37	Failure map for Zircaloy-4 cladding by thermal shock relative to fractional saturation of $\beta$ -phase and oxidation temperature after rupture in steam and flooding with water at oxidation temperature. The failure boundary for cladding that was slow cooled (~5 K/s) through the phase transformation is shown for comparison .....	180
Figure 6.38	Failure map fo Zircaloy-4 cladding by thermal shock relative to the wall thickness with $\leq 0.9$ wt % oxygen after isothermal oxidation and flooding with water at the oxidation temperature. Cooling rate through the $\beta \rightarrow \alpha'$ transformation was ~100 K/s.....	181

Figure 6.39	Capability of Zircaloy-4 cladding to withstand an impact energy of 0.3 J at 300 K relative to the thickness of $\beta$ -phase layer containing <0.7 wt % oxygen and the hydrogen content of the cladding. The above criteria are applicable irrespective of the oxidation temperature, the initial cladding wall thickness and the wall thickness that results from ballooning and deformation .....	184
Figure 6.40	Correlation between distributions of inner surface oxide layer thickness, ring-compression deflection, and absorbed hydrogen content.....	185
Figure 6.41	Iso-deflection curves obtained on segments of burst cladding and tubes oxidized in steam as functions of oxidation temperature and time.....	186
Figure 6.42	Time-temperature oxidation conditions resulting in integrated energies to maximum load above and below 0.3 J from load-vs-deflection curves during slow diametral compression of tube and ring specimens at 300 and 373 K respectively.....	186
Figure 6.43	Failure map for Zircaloy-4 cladding due to handling relative to wall thickness with < 0.7 wt % oxygen .....	188
Figure 6.44	Results from quenching experiments on burst fuel rods. The results to the left are from unconstrained specimens and the results to the right are from constrained specimens .....	189
Figure 6.45	Load histories during quench under various conditions of constraint.....	190
Figure 6.46	Typical post-failure appearances of failed cladding.....	191
Figure 6.47	Failure maps of cladding tubes tested under fully restrained conditions (a) as-received, (b) pre-hydrided tubes (c) pre-hydrided with reduced wall thickness.....	191
Figure 6.48	Failure maps in terms of ECR and hydrogen content for the four restrained.....	192
Figure 6.49	Fracture map in terms of oxidation and initial hydrogen concentration for irradiated and unirradiated cladding with a restraint force of 540 N.....	192
Figure 6.50	Fracture/no-fracture conditions, relevant to ECR value and initial hydrogen concentration .....	194
Figure 6.51	Quench survival/failure of isothermally oxidized Zircaloy-4. Diamonds = unrestrained tests, Squares = partially restrained tests, Triangles = fully restrained tests. Filled symbols represent failures .....	194
Figure 6.52	Embrittlement threshold at 135°C as a function of hydrogen content for prehydrided unirradiated Zircaloy-4 oxidized at 1 200°C and either quenched at 800°C or cooled without quench.....	197
Figure 6.53	Ductility at 135°C after oxidation in steam at 1200°C and cooled slowly for irradiated and unirradiated Zircaloy-4 cladding .....	197
Figure 6.54	High-oxygen alpha layer on the ID resulting from oxygen diffusion from the ZrO <sub>2</sub> fuel-to-cladding bond following OD steam oxidation at 1 200°C.....	198
Figure 6.55	Measured hydrogen and oxygen content in in-cell (ICL) tests on high-burn-up BWR Zircaloy-2 fuel rods.....	198
Figure 6.56	Residual ductility parameter derived from the ring compression test as a function of weight gain at 1 100°C .....	199
Figure 6.57	Room temperature ring compression tests on as-received and pre-hydrided M5 and low-tin Zircaloy-4 after oxidation and quench at 1 200°C .....	200
Figure 6.58	Typical fractographs of the internal prior $\beta$ -phase layer of Charpy impact tested as-received and pre-hydrided material.....	201
Figure 6.59	Impact energy vs the correlation parameter K defined in Equation 6.6.....	202
Figure 6.60	Evolution of prior $\beta$ phase oxygen content (mean value) of as-received and prehydrided Zircaloy-4 (a) and M5 (b) alloys vs the weight gain after oxidation at 1 200°C .....	203
Figure 6.61	Full correlation between the impact energy, the oxygen and hydrogen contents, and the correlation parameter K' .....	204
Figure 6.62	Results of ring compression tests at 135°C after various cooling scenarios .....	204

Figure 6.63	Relative displacement at failure in ring compression tests as a function of ECR for E110 and Zircaloy-4 .....	205
Figure 6.64	The impact behaviour of oxidized cladding vs oxidation ECR.....	206
Figure 6.65	Deformation vs ECR in 20°C ring compression tests of E110 alloy .....	206
Figure 6.66	Relative deformation to failure (first crack) of E110 and Zircaloy samples as a function of oxidation ratio (ECR) and hydrogen content.....	208
Figure 6.67	Relative deformation as function of hydrogen content for E110 and Zircaloy-4 samples oxidized in steam.....	208
Figure 6.68	Hybrid E110 sample following oxidation at 1 000°C for 290 seconds. Machined-and-polished section is lustrous black, while as-fabricated E110 section is in breakaway oxidation .....	209
Figure 6.69	Ductility as a function of calculated oxidation at 1 473 K (1 200°C) for irradiated and unirradiated Zircaloy-4 (rough surface), tested at 408 K (135°C).....	215
Figure 6.70	Specimen of E110 cladding that exhibited severe breakaway oxidation after 1 400 seconds at 1 000°C.....	216
Figure 6.71	Diffusion couple character of oxygen sources and cladding metal.....	216
Figure 6.72	Post-quench ductility results at RT for isothermally exposed E110 specimens. Ac is the residual ductility.....	219
Figure 6.73	Results of Hungarian ring compression tests of specimens subjected to isothermal high temperature steam oxidation .....	220
Figure 6.74	Maximum calculated cladding temperatures in a simulated 200% cold-leg LBLOCA in the PAKS NPP .....	220
Figure 6.75	The burn-up dependence of T <sub>300s</sub> Zircaloy-4, E110 and M5 .....	221
Figure 7.1	Schematic representation of strain anisotropy in zirconium alloy tubing resulting in the “hot side straight” effect.....	236
Figure 7.2	General definition of coolant channel blockage.....	237
Figure 7.3	Examples of blockage .....	237
Figure 7.4	Mask method for measurement of blockage .....	238
Figure 7.5	Deficiencies of the total area method .....	238
Figure 7.6	Definition of sub-channel blockage (left) and sub-channel perimeters and rod gaps (right) .....	239
Figure 7.7	Proposals for dealing with the various types of sub-channels and burst openings.....	239
Figure 7.8	Typical temperature and pressure histories for the FR-2 tests. Measured data of test B3.1 .....	214
Figure 7.9	Relative increase of total void volume versus maximum circumferential elongation (a) and deformation profiles for tests below the average (b), above the average (c), and tests F1 through F5 representing the average (d) .....	242
Figure 7.10	Post test neutron radiograph of test E5 fuel rod .....	243
Figure 7.11	Maximum circumferential strain vs burst temperature .....	243
Figure 7.12	Fuel mass per unit volume of deformed cladding tube after relocation during LOCA burst test .....	244
Figure 7.13	Comparisons of the axial profiles of cladding circumferential strain in the high pressure fresh and irradiated rods, rods 11 and 12, which burst in the alpha phase. (LOC tests in PBF) .....	245
Figure 7.14	Comparisons of the axial profiles of cladding circumferential strain in the high pressure fresh and irradiated rods, rods 3 and 4, which burst in the alpha-plus-beta transition. (LOC tests in PBF) .....	246
Figure 7.15	Comparisons of the axial profiles of cladding circumferential strain on the unirradiated high pressure rods, rods 7A and 7B with initially undeformed and collapsed cladding. (LOC tests in PBF).....	247

Figure 7.16	Test procedure for EOLO tests.....	248
Figure 7.17	Post-irradiation diametral metrology of the five burst claddings in the EOLO experiments.....	249
Figure 7.18	EOLO-2 evolution of the cladding temperature at the level 0.65 m, coolant flow and rod fill gas pressure during the test.....	249
Figure 7.19	EOLO-2 clad temperature and neutron flux axial profiles during the test .....	250
Figure 7.20	Appearance of fuel at rupture plane in the FLASH-5 experiment .....	251
Figure 7.21	Axial distribution of strain in NRU MT-1 test.....	252
Figure 7.22	Axial distribution of strain in the NRU MT-2 test .....	252
Figure 7.23	Axial distribution of strain in the NRU MT-3 test .....	252
Figure 7.24	Axial distribution of strain in the NRU MT-4 test .....	252
Figure 7.25	PHEBUS test 215P. History of clad temperatures measured between two grid spacers .....	253
Figure 7.26	PHEBUS test 215P. Axial deformation profile between interior spacer grids and flow area restriction versus distance from bottom of fuel stack.....	254
Figure 7.27	PHEBUS test 215-P. Comparison of maximum burst strains with radial position. (Low pressure in rods 2, 4 and 6).....	254
Figure 7.28	PHEBUS test 215-P. Metallographic coss sections at elevations 285 and 252 mm from fuel bottom .....	255
Figure 7.29	PHEBUS test 215-R. Histories of clad and fuel temperatures on Rod 6 .....	255
Figure 7.30	PHEBUS test 218. View of burst strains of rods as projected in a same plane.....	257
Figure 7.31	PHEBUS test 219. Burst strain versus average azimuthal temperature difference in the 22-25 s time interval of the transient.....	259
Figure 7.32	Temperature histories in the PHEBUS LOCA tests.....	259
Figure 7.33	Temperature transient a cladding level 4 in the IFA-543 ballooning test .....	263
Figure 7.34	Comparison of predictions of rupture strain as a function of pellet eccentricity for MT-3 and IFA-54X .....	264
Figure 7.35	Measured clad (TTC1-4) and heater (TCH1-2) temperatures, linear heat rate of heater (QH) and readings of Co neutron detector (Cobalt ND5) during the LOCA test run.....	266
Figure 7.36	Ballooned region with relocated fuel in the Halden IFA-650.2 test.....	267
Figure 7.37	Through wall cracks with brittle appearance. Halden IFA-650.2 test.....	267
Figure 7.38	REBEKA test philosophy and test objectives .....	270
Figure 7.39	Burst strain vs azimuthal temperature difference in REBEKA out-of-pile tests.....	271
Figure 7.40	Burst strain vs burst temperature of Zircaloy claddings.....	271
Figure 7.41	First bundle test REBEKA, Test data and test procedure. Starting temperature was 520°C.....	272
Figure 7.42	Circumferential strain of the 9 Zircaloy claddings and fuel blockage in the REBEKA 1 experiment.....	272
Figure 7.43	The temperature history at two axial locations in REBEKA 2 .....	273
Figure 7.44	Circumferential strain of the 9 Zircaloy claddings and fuel blockage in the REBEKA 2 experiment.....	273
Figure 7.45	Circumferential strain of the 9 Zircaloy claddings and fuel blockage in the REBEKA 3 and REBEKA 4 experiments.....	274
Figure 7.46	REBEKA-5. Circumferential cladding strain and flow blockage under reversed flow .....	276
Figure 7.47	REBEKA-6. Circumferential cladding strain and flow blockage under unidirectional flow .....	277
Figure 7.48	Controlled temperature transient test (left) and creep rupture test (simulation of 2 <sup>nd</sup> peak, right) in the KWU programme.....	278

Figure 7.49	Burst temperature vs pressure from single rod tests under idealised conditions Comparison of different initial cladding conditions.....	278
Figure 7.50	Burst strain vs burst temperature from single rod tests under idealised conditions. Comparison of different cladding materials .....	279
Figure 7.51	Burst strain vs wall thickness variation from single rod creep rupture tests under idealised conditions.....	279
Figure 7.52	Burst strain vs mean normalised azimuthal temperature difference from single rod creep rupture tests under idealised conditions .....	280
Figure 7.53	Tube bending vs normalised azimuthal temperature difference in single rod creep rupture test in air .....	280
Figure 7.54	Local axial strain vs tangential strain in the plane of maximum deformation .....	281
Figure 7.55	Axial strain vs tangential strain for creep rupture tests with non-homogeneous temperature distribution on the circumference.....	281
Figure 7.56	Bow vs azimuthal temperature difference.....	282
Figure 7.57	Axial profile of circumferential strain for transient test (5 K/s, 50 bar) in air and flowing steam.....	282
Figure 7.58	Indirectly heated multirod test (3×4) with one isobarically pressurised sample (65 bar) .....	283
Figure 7.59	Indirectly heated multirod test (3×4) with one isobarically pressurised sample (65 bar) .....	283
Figure 7.60	Axial temperature and strain profile from KWU multirod test with forced air cooling .....	284
Figure 7.61	Burst strain vs burst temperature from single rod and multi rod tests (schematically) .....	285
Figure 7.62	Histories of cladding temperatures and internal pressure in JAERI test 7805 .....	285
Figure 7.63	Axial distribution of ballooning in the JAERI 7×7 multirod tests .....	286
Figure 7.64	Axial locations of burst position and ballooned region in assembly No. 7805 .....	287
Figure 7.65	Axial locations of burst position and ballooned region in assembly No. 7910 .....	287
Figure 7.66	Axial locations of burst position and ballooned region in assembly No. 7911 .....	288
Figure 7.67	Portions of tubes with greater than 34% strain in assembly 7912.....	289
Figure 7.68	Illustrated deformation mechanism of a rod surrounded by external heater .....	290
Figure 7.69	Axial locations of burst position and ballooned region in tests Nos. 20 and 21 .....	291
Figure 7.70	Axial locations of channel blockage in tests Nos. 19 and 21, 20 and 23 .....	291
Figure 7.71	Cross-section of maximum blockage in test No. 24.....	292
Figure 7.72	Average rupture strain from single-rod tests heated at 28 K/s .....	294
Figure 7.73	Change in Zircaloy heated length in single-rod tests.....	294
Figure 7.74	Comparison of burst strain in creep rupture and low heating rate tests with data for 28 K/s tests .....	295
Figure 7.75	Comparison of tube volume increase (qualitatively equivalent to average tube strain) in creep rupture and low heating rate tests with data for 28 K/s tests .....	295
Figure 7.76	Comparison of burst strains in B-1, B-2 and B-3 tests with single rod tests data .....	296
Figure 7.77	Comparison of B-3 bundle burst data with ORNL and KfK single-rod data for heating rate of ~10 K/s .....	297
Figure 7.78	Portions of tubes with greater than 32% strain in B-3 test .....	297
Figure 7.79	Axial distribution of bursts in multi-rod burst tests B-1 and B-3.....	298
Figure 7.80	Burst location can be displaced by change in steam flow .....	299
Figure 7.81	Deformation agrees with axial temperature distribution.....	299
Figure 7.82	Comparison of B-1 and B-2 bundle data with ORNL and KfK single-rod data for heating rate of ~28 K/s .....	300
Figure 7.83	Radial temperature distribution base on row- and column-averaged data 43 s after power-on for B-5 rods.....	301

Figure 7.84 Simulator average temperature 43 s after power-on in B-5 test.....	302
Figure 7.85 Approximate orientation of bursts in the B-5 test. The figure shows a predominance of bursts towards the flow channel and the N.E. corner .....	302
Figure 7.86 Sections from highly deformed regions of B5 and B3 bundles showing effects of confinement. Small unconstrained bundles do not produce the same deformation pattern as large constrained bundles for same test conditions.....	303
Figure 7.87 Tube dilatation greater in B-5 interior simulators than in exterior simulators and greater than in comparable B-3 (4×4) test.....	304
Figure 7.88 Subdivision of B-5 data show interior subarrays have greater coolant flow area restriction.....	304
Figure 7.89 Preliminary B-5 data show inner 4×4 array has greater flow restriction than B-3 (4×4) array.....	305
Figure 7.90 ORNL-MRBT. Burst strains of B5 tubes. B3 (4×4) data are shown for comparison with inner 4×4 array of B-5.....	305
Figure 7.91 Burst strain vs internal pressure in Westinghouse single rod burst tests.....	307
Figure 7.92 Westinghouse multi-rod burst test results.....	307
Figure 7.93 Effect of previous heat treatment of the cladding in the two phase domain on reduced creep rates.....	308
Figure 7.94 Uniform elongation versus modified burst temperature in EDGAR tests.....	309
Figure 7.95 Total elongation versus modified burst temperature in EDGAR tests.....	309
Figure 7.96 Time-to-rupture versus stress for EDGAR creep tests of Zircaloy-4, M4 and M5.....	310
Figure 7.97 Total elongation as a function of test temperature for the alloys M4, M5 and Zircaloy-4 .....	311
Figure 7.98 Influence of heating rate on total elongation in EDGAR thermal ramp tests for the M5 alloy.....	312
Figure 7.99 (a) Deformation of as-received and hydrided Zircaloy-4 in a thermal ramp test (b) Calculated phase fraction in as-received and hydrided Zircaloy-4 .....	313
Figure 7.100 Time-to-rupture versus stress for EDGAR creep tests performed on as-received and hydrided Zircaloy-4 cladding tube .....	313
Figure 7.101 Time-to-rupture versus stress for EDGAR creep tests performed on as-received and M5 cladding tubes .....	314
Figure 7.102 Total elongation measured after EDGAR creep tests versus test temperature for as-received and hydrided (~600 and ~1 000 ppm) Zircaloy-4 cladding tubes .....	315
Figure 7.103 Comparison between the burst criterion for as-received and hydride (at 600 ppm) Zircaloy-4 cladding tubes .....	316
Figure 7.104 Comparison between experimental and simulated time to rupture of Zircaloy-4 hydride to 600 ppm using two different models: (a) a model based on experiments with as-received Zircaloy-4 [76], dashed line, and (b) a new model based on experiments with hydrided Zircaloy-4 and taking into account the effect of hydrogen on the $\alpha/\beta$ phase transformation .....	316
Figure 7.105 Evolution of a sample during a thermal ramp test under uniaxial stress loading.....	317
Figure 7.106 Influence of irradiation and hydrogen content on the axial strain of Zircaloy-4 samples during a thermal ramp test under uniaxial loading (80 MPa) upon heating with 100 K/s .....	318
Figure 7.107 Results of stylised transient testing of Zircaloy-4 PWR cladding with mainly convective cooling .....	319
Figure 7.108 Processes controlling strain and its stabilization.....	319
Figure 7.109 Variation of tube rupture strain with rupture temperature during isothermal tests at Springfields Nuclear Laboratories .....	320

Figure 7.110	Mechanical restraint by deformable neighbours. CANSWEL-2 idealization (a) compared with (b) Springfields 4×4 cladding deformation rig cross sections.....	321
Figure 7.111	Cladding temperature (A) and pressure records (B) for test No. 1 (Zr1%Nb alloy).....	323
Figure 7.112	Axial cladding strain distributions in tests Nos. 1, 2 and 3.....	324
Figure 7.113	Microhardness distribution along the simulator 2.1 of test No. 1.....	325
Figure 7.114	Post-test appearance of E635 and Zr1%Nb alloy.....	325
Figure 7.115	Burst pressure versus burst temperature of E110 and Zircaloy-4 claddings tested under similar conditions.....	326
Figure 7.116	Burst pressure an maximum deformation versus oxide layer thickness of E110 cladding.....	327
Figure 7.117	Burst pressure versus pressurization rate for E110 alloy .....	327
Figure 8.1.	Flowchart for the code FRAPTRAN-1.3 .....	340
Figure 8.2.	Deformation pattern at level 15 of the MT-1 experiment as calculated by FRETA-B ..	342
Figure 8.3	Example of DRACCAR calculation in a bundle geometry with rod deformation as the result of a LOCA type transient .....	343
Figure 9.1	Determination of fuel failure rate after LOCA with deterministic method.....	347
Figure 9.2	Probability for fuel rod failure as a function of rod power at different burn-ups.....	347
Figure 9.3	Power and burn-up distribution in a core with failure threshold. Each number gives the number of fuel rods at the particular power-burn-up combination (Siemens) .....	348
Figure 9.4	Peak cladding temperature response for deterministic assessment of extent of rupture	349
Figure 9.5	Flow chart over statistical damage assessment for German PWRs.....	351
Figure 9.6	Map over core damage extent in German PWR after a large break LOCA (Text is visible in magnified view) .....	351
Figure 9.7	Number of failed fuel rods / failure rate during LOCA .....	352

## LIST OF TABLES

Table 4.1	Blockage shapes and configurations tested in the FLECHT SEASET 21-Rod bundle..	73
Table 4.2	BWR Core Inventory Fraction Released Into Containment.....	77
Table 4.3	LOCA Release Phases.....	77
Table 4.4	Computation of the iodine release.....	78
Table 4.5	The release from the gap and fuel for radiologically significant nuclides .....	81
Table 6.1	Temperature dependence of published isothermal parabolic rate equations.....	144
Table 6.2	Temperature dependence of parabolic growth constants for oxide and $\alpha$ -phase.....	144
Table 6.3	Summary of cladding oxidation parameters and performance limits for the ECCs in two PWRs for a double-ended guillotine break in the pump discharge leg.	
	Evaluation of ECCS margin of performance .....	183
Table 6.4	List of the cladding specimens .....	193
Table 6.5	List of LOCA-simulated experiments .....	193
Table 6.6	Variation of embrittlement threshold (percent equivalent cladding reacted) for unirradiated zirconium-alloy cladding materials oxidized in steam at 1 200°C.....	196
Table 6.7	$H_2$ generation from the Zr/ $H_2O$ reaction .....	211
Table 7.1	FR-2 in-pile tests of fuel behaviour, test matrix.....	241
Table 7.2	Summary of cladding deformation data from Tests LOC-3, LOC-5 and LOC-9 .....	246
Table 7.3	Summary of the main measurements in the EOLO tests.....	248
Table 7.4	Thermomechanics of the PHEBUS LOCA tests.....	260
Table 7.5	Summary of the rod burst strains in IFA-54X.....	262
Table 7.6	Summary of the test programme in the REBEKA rig.....	275
Table 7.7	Test parameters of single and multirod investigations by KWU .....	278
Table 7.8	JAERI test matrix of bundle burst tests using W-Re wire heaters and a close fitting unheated shroud.....	286
Table 7.9	The main test parameters and results of VVER type assemblies under LOCA conditions in electroheated facility.....	324
Table 9.1	Best estimate analyses of percentage of fuel rod failures .....	348
Table 9.2	Cases of peak clad temperature (PCT) above 925°C .....	350



## **EXECUTIVE SUMMARY**

In 1986, a Working Group of the Committee on the Safety of Nuclear Installations (CSNI) issued a State-of-the-Art Report (SOAR) on pressurised water reactor fuel behaviour in design basis accident (DBA) conditions. The current State-of-the-Art Report on fuel behaviour in LOCA conditions is an updated version that describes phenomena of importance in the loss-of-coolant-accident (LOCA). New information has been produced concerning these phenomena. Older cladding materials have been replaced by newer alloys that may behave differently under postulated accident conditions. There is also a clear need to include discussions on accident issues for other water cooled reactor types. This is especially important now when the Eastern European countries have joined the discussion on nuclear safety issues.

In the design of nuclear power plants, the consequences of hypothetical accidents are analysed so that suitable mitigating systems can be devised. For design basis accidents, a fundamental acceptance criterion is that there should be no or very limited radiological consequences to the public. In order to fulfill this criterion, derivative acceptance criteria have been formulated for the safety systems of the reactor.

For example the pressurised water reactor design basis loss-of-coolant-accident involves the break of one of the large coolant pipes between the reactor vessel and the main circulation pump. In order to mitigate the consequences of this break, it is necessary to design the emergency core cooling systems so that the fuel is cooled efficiently during all phases of the accident. This requirement naturally leads to a criterion that the fuel must maintain its coolable geometry throughout the whole LOCA sequence and that the structural integrity of the fuel rods is maintained.

The requirement of coolable geometry and structural integrity has turned out to be a very complex issue due to the particular properties of the zirconium alloys used as cladding for the fuel. During the event, the cladding heats up to temperatures over 1 000°C. When the temperature reaches about 800°C, zirconium starts to transform from alpha to the beta phase. Oxygen dissolves in the metal and embrittles the alpha phase. Therefore, there must be a limit on the oxygen-stabilised alpha phase, since the load bearing prior beta layer may be too thin to ensure structural integrity of the fuel during the quench phase of the LOCA.

There are many other issues which must be taken into account. When the fuel rods heat up during the LOCA and the external pressure is lost, the rod internal pressure is large enough to cause plastic deformation of the cladding which leads to ballooning and burst. The ballooning can potentially be detrimental to cooling of the fuel assemblies, and the burst of a rod also leads to cladding oxidation from the inside. In addition, a significant amount of hydrogen is picked up by the cladding. Hydrogen pickup exacerbates cladding embrittlement, especially after the quenching phase. Finally, at elevated temperatures, the rate of steam-cladding oxidation may become so high that the heat can no longer be adequately dissipated by cooling, and may eventually lead to autocatalytic oxidation. If not arrested, cladding metal and reactor core can melt.

Most fuel safety criteria are based on the criteria applied by the United States Nuclear Regulatory Commission (USNRC). The exceptions include Japan, which has adopted a lower maximum oxidation value. The Japanese criteria on cladding embrittlement are not based on the concept of zero ductility of cladding, but on the failure threshold value determined in the integral thermal shock tests under restrained conditions.

Other countries have also made changes. In Germany, for example, an additional requirement is imposed that the fraction of burst fuel rods shall not exceed 10% of the total rods in the core. The purpose of this requirement is to limit fission gas release due to cladding burst.

The different phenomena involved in the heat-up, cool down and quench during a LOCA are more complex. This complexity results from the changes of properties of the zirconium cladding alloys that occur during the transient.

High temperature oxidation tests have been conducted to determine oxidation kinetics of the cladding since early 1970s. Tests are necessary for determining cladding embrittlement after a LOCA simulation, which is very important to safety. The ring compression test technique has been the most widely used ductility test because it is very straightforward to perform, requires a minimum of specimen preparation and is appropriate when there is a limited amount of material to be tested. However, there seems to be no common definition of an acceptable level of ductility in ring compression tests.

Tests with moderate integration have been performed in Canada, France, Japan, Korea, Russia and the United Kingdom to examine steam oxidation, cladding deformation or ballooning in steam, and constrained deformation or ballooning in steam with or without quench. Some of the tests are still used to investigate high burnup effect on the cladding deformation and fracture during a LOCA.

Fully integrated tests were performed at FR-2 (Germany), PBF (US), PHEBUS (France). Those tests provided valuable data base for understanding fuel behaviour in the bundle geometry under more realistic LOCA conditions and validation of computer codes in this category. The test series recently performed at the Halden reactor is a very unique program, where the primary objective is to assess the extent and effect of axial relocation of fuel fragments into the ballooning volume of single rod experiments. These tests were performed with high burnup fuels, taking advantage of various in-pile measurement techniques at the Halden reactor.

In the recent years there has been considerable testing of the post-quench ductility of current cladding alloys in Hungary, France, Russia and the United States. In the case of Zircaloy, the objective has been to determine the effects of the changes in fuel rods associated with high burnup operation, such as due to thick corrosion layer, high hydrogen concentration in the cladding, and pellet-cladding bonding. Results show that unirradiated zirconium alloy cladding types exhibit different embrittlement thresholds. The variations in embrittlement threshold appear to result mainly from manufacturing differences rather than from specific alloy composition. Tests with the so-called pre-hydrided specimens showed a strong effect of hydrogen concentration for some cladding. A cooling-rate effect was also seen that was absent in fresh cladding that contained no hydrogen.

The effect of hydrogen on oxygen solubility in the  $\beta$ -phase has a significant impact on the post-quench ductility of high burnup cladding and on post-quench ductility of ballooned cladding which have absorbed hydrogen in the oxidation reaction on the inside surface of the cladding. Similar effects may also arise in long term transients at about 1 000°C when breakaway oxidation leads to significant hydrogen pickup. These effects are not addressed by the present regulatory criteria and hence there is a need to revise criteria.

WGFS concludes that CSNI and CNRA should consider the following future activities to further refine the nuclear community's understanding of the key aspects of the water reactor fuel behaviour in LOCA conditions:

- To update the CSNI State-of-the-Art Report on water reactor fuel behaviour in LOCA conditions in suitable intervals, to provide a useful reference for workers in this area.
- Ductility-based LOCA criteria derived from ring compression tests of double-side oxidized specimens, and fracture-based LOCA criteria derived from integral rod testing result in quite different burn-up effect on the derived safety limit. There are thus a number of open questions about the different results and the two different methodologies, which have to be further discussed and assessed.
- The breakaway oxidation, which occurs in specific temperature ranges, has been identified as a major problem for the cladding LOCA performance since it is associated with a significant hydrogen pickup which degrades post-quench properties. Therefore, careful examinations are required also for advanced high corrosion-resistance cladding alloys to examine the temperature-time range where the breakaway oxidation occurs.
- As-fabricated cladding was used in the most performed oxidation tests. Data have been accumulated to a certain extent on effects of irradiation, alloying elements, pre-oxidizing and pre-hydriding of the cladding, steam purity (addition of nitrogen or air), and high atmospheric pressure. However, more investigations may be required to better understand the oxidation behaviour of the high burnup fuel cladding.

## **1. INTRODUCTION**

Dated December 1986, the Task Group on Fuel Behaviour of the Committee on the Safety of Nuclear Installations (CSNI) Working Group No. 2 issued the report “The deformation, oxidation and embrittlement of PWR cladding in a loss-of-coolant accident” as a state-of-the-art report on pressurised water reactor (PWR) fuel behaviour in design basis accident conditions [1]. Now more than twenty years later the time has come for making an updated report on the phenomena of importance to the design basis accidents. The reasons for an update are several. New information of importance has been produced concerning the phenomena in the previous report. More importantly, the cladding alloys used then have now largely been replaced by new cladding alloys which behave differently both during normal operation and under postulated accident conditions. There is also a clear need to include discussions on the loss-of-coolant-accident (LOCA) issue for other reactor types than the PWR. This is especially important now when the Eastern European countries have joined the discussion on nuclear safety issues and when the OECD countries in various forms give economic and technical support for improving the safety of the VVER and RBMK reactors.

Compared to the situation twenty years ago the burn-up of the fuel rods before they are taken out of service has increased considerably. This has led to increased oxide thickness and relatively more hydrogen uptake in the fuel cladding, phenomena which influence the behaviour also under loss of coolant conditions. New phenomena have also been identified in the fuel pellets with increasing burn-up. New experiments which take these developments into account must be included in the updated report.

Another safety issue which has been given increased attention during the twenty years since the last state-of-the-art report is the Reactivity Initiated Accident (RIA). This accident scenario is quite different from the LOCA scenarios as are the relevant degradation phenomena of the fuel. Fuel behaviour under RIA conditions will therefore be the subject of a separate state-of-the-art report.

### **1.1 General overview and introduction to the LOCA safety issue**

In the design of nuclear power plants, it is required that various operational occurrences are considered and that the consequences of such occurrences are analysed so that suitable mitigating systems can be designed [2]. Normal operation of the plant can be defined as operation within specified operational limits and conditions. Anticipated operational occurrences (AOOs) are operational processes deviating from normal operation which are expected to occur at least once during the lifetime of a facility but which, in view of appropriate design provision, do not cause any significant damage to items important to safety or lead to accident conditions. The latter condition may be simply defined as deviations from normal operation more severe than anticipated operational occurrences. Accident conditions can be divided into design basis accidents (DBAs) and severe accidents. For the accident conditions, there are acceptance criteria which must be fulfilled. For the design basis accidents, the most fundamental acceptance criterion is typically that there should be no or at most very limited radiological consequences to the public. However, in order to fulfil this criterion, there will be a number of other acceptance criteria related to the different safety systems of the reactor. How these criteria are formulated will depend on the general design of the reactor and the various physical phenomena of importance to the occurrence of a particular design basis accident.

One of the design basis accidents for water cooled reactors is the loss of coolant caused by the failure of a large coolant pipe. More specifically, for the pressurised water reactor the initiating event of the design basis accident is the double-ended guillotine break of one of the large coolant pipes between the reactor vessel and the main circulation pump. In order to mitigate the consequences of this break, it is necessary that the reactor has several emergency core cooling systems. At the time of definition of this design basis accident in late sixties to early seventies, it was generally accepted that in order to minimise radiological consequences to the public it is necessary to prevent the fuel melting and avoid excessive fuel dispersal. It was thus necessary to design the emergency core cooling systems so that the fuel could be cooled efficiently during all phases of the DBA. This requirement naturally led to a criterion that the fuel must maintain a coolable geometry through the whole LOCA sequence and that the structural but not necessarily the hermetical integrity of the fuel rods should be maintained.

The requirement of coolable geometry and structural integrity turned out to be a very complex issue due to the particular properties of the zirconium alloys used as cladding tubes for the fuel. During normal operation, the zirconium alloy oxidizes slowly in the reactor water by the growth of a thin oxide scale on the surface. Inside the oxide the metal is hexagonally close packed  $\alpha$ -phase zirconium with a more or less fine dispersion of second phase particles. During a LOCA, the metal heats up to temperatures over 1 000°C. When the temperature reaches about 800°C the  $\alpha$ -phase zirconium starts to transform to the body centred cubic  $\beta$  phase. At the same time, the oxidation reaction starts to accelerate and the growth of the oxide scale becomes significant. At the same time, oxygen dissolved in the metal stabilises the  $\alpha$  phase. Therefore, a layer of  $\alpha$  phase with a high content of oxygen starts to grow on the  $\beta$  phase underneath the oxide scale. The problem is that oxygen also embrittles the  $\alpha$  phase and that the oxide itself is very brittle when the hot fuel rod is quenched back to low temperature. It is therefore clear that there must be a limit on the amount of growth of brittle oxide and oxygen-stabilised  $\alpha$  phase, since the load bearing prior  $\beta$  layer must not be too thin in order to ensure structural integrity of the fuel during the quench phase of the LOCA, when the fuel rods are subjected to various types of stresses (e.g. thermal stress, thermal-hydraulic stress associated with the violent quenching, and residual mechanical stress associated with rod ballooning and burst).

There are also many detail issues which must be taken into account. When the fuel rods heat up and the external pressure is lost the rod internal pressure is large enough to cause plastic deformation of the cladding which leads to ballooning and burst. The ballooning can potentially be detrimental to cooling of the fuel assemblies and the burst of a rod leads to cladding oxidation also from the inside. It is also possible that the zirconium reacts with Fe- and Ni-based alloys in other core components to form low-melting eutectic mixtures. Significant amount of hydrogen is picked up by the cladding both during low-temperature oxidation under normal operation and during the high-temperature oxidation in the LOCA sequence. Pickup of hydrogen in the cladding significantly exacerbates cladding embrittlement, especially after the quenching phase. Last but not least, important is the large exothermic heat generated during oxidation of the cladding. At high enough temperatures, the rate of steam-cladding oxidation is so high that the heat can no longer be adequately dissipated by cooling, eventually leading to run-away oxidation. If run-away or autocatalytic oxidation is not arrested, cladding metal and reactor core could melt. Although this temperature is well above any temperature expected in a design basis loss-of-coolant-accident, such events occurred in the accident of Three Mile Island PWR.

In the following sections, these phenomena will be described in considerable detail based on the extensive research efforts spent on the LOCA problem over a period of almost forty years.

## 1.2 Current safety criteria and their background

The detailed safety criteria vary from country to country but it is probably fair to say that most of these criteria are modelled or copied from the criteria applied by the United States Nuclear Regulatory

Commission (NRC). Therefore, the NRC criteria will be described in this section with much of the section being devoted to review the background and history of how the criteria were established.

### **1.2.1 Current safety criteria in the United States**

The NRC Regulations, contained in Title 10, Code of Federal Regulations, come in parts numbered between 1 and 171 and can be found on the NRC web site. The relevant part for the LOCA issue is Part 50 “Domestic licensing of production and utilisation facilities”. Part 50 also contains an Appendix A, “General Design Criteria for Nuclear Power Plants”. For the purpose of the present report, it may be relevant to quote the following definition from Appendix A:

*Loss of coolant accidents.* Loss of coolant accidents mean those postulated accidents that result from the loss of reactor coolant at a rate in excess of the capability of the reactor coolant makeup system from breaks in the reactor coolant pressure boundary, up to and including a break equivalent in size to the double-ended rupture of the largest pipe of the reactor coolant system.

This definition forms the basis for General Design Criterion 35:

*Criterion 35 – Emergency core cooling.* A system to provide abundant emergency core cooling shall be provided. The system safety function shall be to transfer heat from the reactor core following any loss of reactor coolant at a rate such that (1) fuel and clad damage that could interfere with continued effective core cooling is prevented and (2) clad metal-water reaction is limited to negligible amounts. [additional text has been omitted]

In the main text of Part 50, we find § 50.46 “**Acceptance criteria for emergency core cooling systems for light-water nuclear power reactors**”. It is these criteria that are often referred to as the LOCA criteria. An abbreviated version of § 50.46 is as follows:

- (a) (1)(i) Each boiling or pressurised light-water nuclear power reactor fueled with uranium oxide pellets within cylindrical Zircaloy or ZIRLO<sup>1</sup> cladding must be provided with an emergency core cooling system (ECCS) that must be designed so that its calculated cooling performance following postulated loss-of-coolant accidents conforms to the criteria set forth in paragraph (b) of this section. ECCS cooling performance must be calculated in accordance with an acceptable evaluation model and must be calculated for a number of postulated loss-of-coolant accidents of different sizes, locations, and other properties sufficient to provide assurance that the most severe postulated loss-of-coolant accidents are calculated.
- (b) (1) Peak cladding temperature. The calculated maximum fuel element cladding temperature shall not exceed 2 200°F [1 204°C].  
(2) Maximum cladding oxidation. The calculated total oxidation of the cladding shall nowhere exceed 0.17 times the total cladding thickness before oxidation. As used in this subparagraph total oxidation means the total thickness of cladding metal that would be locally converted to oxide if all the oxygen absorbed by and reacted with the cladding locally were converted to stoichiometric zirconium dioxide. If cladding rupture is calculated to occur, the inside surfaces of the cladding shall be included in the oxidation, beginning at the calculated time of rupture. Cladding thickness before oxidation means the radial distance from inside to outside the cladding, after any calculated rupture or swelling has occurred but before significant oxidation. Where the calculated conditions of transient pressure and temperature lead to a prediction of cladding swelling, with or without cladding rupture, the unoxidized cladding thickness shall be defined as the cladding cross-sectional area, taken at a horizontal plane at the elevation of the rupture, if it occurs, or at

---

1. Other alloys of zirconium may be used by exemption from the regulation.

the elevation of the highest cladding temperature if no rupture is calculated to occur, divided by the average circumference at that elevation. For ruptured cladding the circumference does not include the rupture opening.

- (3) Maximum hydrogen generation. The calculated total amount of hydrogen generated from the chemical reaction of the cladding with water or steam shall not exceed 0.01 times the hypothetical amount that would be generated if all of the metal in the cladding cylinders surrounding the fuel, excluding the cladding surrounding the plenum volume, were to react.
  - (4) Coolable geometry. Calculated changes in core geometry shall be such that the core remains amenable to cooling.
  - (5) Long-term cooling. After any calculated successful initial operation of the ECCS, the calculated core temperature shall be maintained at an acceptably low value and decay heat shall be removed for the extended period of time required by the long-lived radioactivity remaining in the core.
- (c) As used in this section: (1) Loss-of-coolant accidents (LOCAs) are hypothetical accidents that would result from the loss of reactor coolant, at a rate in excess of the capability of the reactor coolant makeup system, from breaks in pipes in the reactor coolant pressure boundary up to and including a break equivalent in size to the double-ended rupture of the largest pipe in the reactor coolant system.
  - (d) The requirements of this section are in addition to any other requirements applicable to ECCS set forth in this part. The criteria set forth in paragraph (b), with cooling performance calculated in accordance with an acceptable evaluation model, are in implementation of the general requirements with respect to ECCS cooling performance design set forth in this part, including in particular Criterion 35 of Appendix A.

Finally we have Appendix K to Part 50, “ECCS Evaluation Models” which regulates how the calculations used to demonstrate that the criteria are fulfilled shall be performed. It is shown in a strongly abbreviated version below:

“I. Required and acceptable features of the evaluation models

- A. Sources of heat during the LOCA. For the heat sources listed in paragraphs I.A.1 to 4 of this appendix it must be assumed that the reactor has been operating continuously at a power level at least 1.02 times the licensed power level (to allow for instrumentation error), with the maximum peaking factor allowed by the technical specifications. A range of power distribution shapes and peaking factors representing power distributions that may occur over the core lifetime must be studied. The selected combination of power distribution shape and peaking factor should be the one that results in the most severe calculated consequences for the spectrum of postulated breaks and single failures that are analysed.
  - 1. The initial stored energy in the fuel. The steady-state temperature distribution and stored energy in the fuel before the hypothetical accident shall be calculated for the burn-up that yields the highest calculated cladding temperature.
  - 2. Fission heat. Fission heat shall be calculated using reactivity and reactor kinetics.
  - 3. Decay of actinides. The heat from the radioactive decay of actinides, including neptunium and plutonium generated during operation, as well as isotopes of uranium, shall be calculated.
  - 4. Fission product decay. The heat generation rates from radioactive decay of fission products shall be assumed to be equal to 1.2 times the values for infinite operating time in the ANS Standard (Proposed American Nuclear Society Standards – “Decay Energy Release Rates Following Shutdown of Uranium-Fueled Thermal Reactors”).

Approved by Subcommittee ANS-5, ANS Standards Committee, October 1971).

5. Metal-water reaction rate. The rate of energy release, hydrogen generation, and cladding oxidation from the metal/water reaction shall be calculated using the Baker-Just equation (Baker, L., Just, L.C., "Studies of Metal Water Reactions at High Temperatures, III. Experimental and Theoretical Studies of the Zirconium-Water Reaction," ANL-6548, page 7, May 1962). For rods whose cladding is calculated to rupture during the LOCA, the inside of the cladding shall be assumed to react after the rupture.
- B. Swelling and rupture of the cladding and fuel rod thermal parameters  
Each evaluation model shall include a provision for predicting cladding swelling and rupture from consideration of the axial temperature distribution of the cladding and from the difference in pressure between the inside and outside of the cladding, both as functions of time.
- C. Blowdown phenomena  
Omitted here."

In September 1988, the NRC staff amended the requirements of Paragraph 50.46 and Appendix K, so that these regulations reflect the improved understanding of ECCS performance during reactor transients that was obtained through the extensive research performed since the promulgation of the original requirements in January 1974. Paragraph 50.46(a)(1) now permits licensees or applicants to use either Appendix K features or a realistic evaluation model. These realistic evaluation models must include sufficient supporting justification to demonstrate that the analytic techniques employed realistically describe the behaviour of the reactor system during a postulated loss-of-coolant accident. Paragraph 50.46(a)(1) also requires that the uncertainty in the realistic evaluation model be quantified and considered when comparing the results of the calculations with the applicable limits in Paragraph 50.46(b) so that there is a high probability that the criteria will not be exceeded.

Regulatory Guide 1.157, "Best-Estimate Calculations of Emergency Core Cooling System Performance," (May 1989) describes models, correlations, data, model evaluation procedures, and methods that are acceptable-to the NRC staff for meeting the requirements for a realistic or best-estimate calculation of ECCS performance during a loss-of-coolant accident and for estimating the uncertainty in that calculation. Of particular interest to the SOAR on LOCA are use of a more recent version of the standard on decay heat [3] and an improved model for metal-water reaction [4].

There are three specific points that are the focus of the current NRC criteria and Appendix K:

- The calculated maximum fuel element cladding temperature shall not exceed 2 200°F.
- The calculated total oxidation of the cladding shall nowhere exceed 0.17 times the total cladding thickness before oxidation.
- The rate of energy release, hydrogen generation, and cladding oxidation from the metal/water reaction shall be calculated using the Baker-Just equation

The purpose of the first two criteria, regarding maximum cladding temperature and total oxidation, was to ensure that the cladding shall remain sufficiently ductile so that it does not shatter into pieces during and after the quench phase of the LOCA transient. Another important purpose of the 2 200°F (1 204°C) limit was to ensure that fuel cladding does not enter the regime of runaway oxidation and uncontrollable core heatup. As is well-known, both criteria were violated in the case of the Three Mile Island accident in 1979. The debate or controversy with regard to the use of the Baker-Just oxidation correlation is that it results in significant conservatism in comparison with more recent oxidation correlations of zirconium alloys applicable to LOCA.

### ***1.2.2 Background to the safety criteria***

The following account is based largely on a paper by G. Hache and H. M. Chung entitled “The history of LOCA embrittlement criteria” [5]. The Hache-Chung paper covers considerably more than just the background to the current criteria; it also discusses alternative criteria in the light of later findings concerning the behaviour of zirconium alloys under LOCA conditions. Those questions will be the subject of later parts of the present report. The same subjects along with LOCA-specific issues associated with high burn-up and the use of Nb-modified cladding were also reviewed by Chung [6].

In 1967, an Advisory Task Force on Power Reactor Emergency Cooling [7], appointed to provide “additional assurance that substantial meltdown is prevented” by core cooling systems, concluded that:

“The analysis of (a LOCA) requires that the core be maintained in place and essentially intact to preserve the heat-transfer area and coolant-flow geometry. Without preservation of heat-transfer area and coolant-flow geometry, fuel-element melting and core disassembly would be expected... Continuity of emergency core cooling must be maintained after termination of the temperature transient for an indefinite period until the heat generation decays to an insignificant level, or until disposition of the core is made.”

This rationale makes it plainly clear that it is most important to preserve the heat transfer area and the coolant flow geometry not only during the short-term portion of the core temperature transient but also for long term.

Consistent with the conclusions of the Task Force, the U.S. Atomic Energy Commission (AEC) promulgated Criterion 35 of the General Design Criteria which states that: “... fuel and clad damage that could interfere with continued effective core cooling is prevented.” It also promulgated Criterion 3 of the Interim Acceptance Criteria for ECCS for LWR [8] which states that: “The clad temperature transient is terminated at a time when the core geometry is still amenable to cooling, and before the cladding is so embrittled as to fail during or after quenching.”

These criteria were subjected to a Rule-Making Hearing in 1973, which was extensively documented in the Journal of Nuclear Safety in 1974 [9-10]. During the hearing process, the last part of the Criterion 3 was replaced by the modified Criterion 1 and the new Criterion 2 of the Code of Federal Regulations, Title 10, Part 50.46, Article (b), commonly referred to as 10 CFR 50.46 [11]. Thus, the AEC Commissioners wrote:

“In view of the fundamental and historical importance of maintaining core coolability, we retain this criterion as a basic objective, in a more general form than it appeared in the Interim Acceptance Criteria. It is not controversial as a criterion... Although most of the attention of the ECCS hearings has been focused on the events of the first few minutes after a postulated major cooling line break, up to the time that the cladding would be cooled to a temperature of 300°F or less, the long-term maintenance of cooling would be equally important [12].”

There are two key factors to consider to evaluate the change in coolable geometry of the core. One is related to cladding ballooning, burst, and coolant channel blockage. This mode was not treated in the Hache-Chung paper but will be treated later in the present report. The focus in the Hache-Chung paper is on the second factor, the change in coolable geometry due to cladding embrittlement and failure, because that is also the main concern addressed by the criteria. An understanding of the criteria requires an understanding of zirconium properties and behaviour.

Beginning only in the early 1970s, it has been understood, that embrittlement of Zr-alloy cladding such as Zircaloys is caused by the diffusion of oxygen into the metal underneath the surface oxide rather than by the surface oxide itself. That is, while the best measure of the heat generation from Zr

metal-water reaction (hence, core heat-up) is total oxidation (more than about 85% of oxygen pickup being in the oxide layer), cladding structural integrity is really controlled by the small fraction of oxygen atoms (less than about 7%) that are dissolved in the remaining  $\beta$  Zr layer. In retrospect, it appears that out of simplicity and in absence of a good method of calculating oxygen distribution in the metallic layers at that time, the NRC regulations used the time required to accumulate 17% oxidation as a surrogate measure of the time required to diffuse enough oxygen into the underlying metal to embrittle it. In doing so, 10 CFR 50.46 also imposed a parallel limit in maximum cladding temperature of 2 200°F. Both processes of oxide growth and oxygen diffusion in the metal obey exponential kinetics laws, which is discussed in detail in the following section.

#### 1.2.2.1 Metallurgy of cladding embrittlement

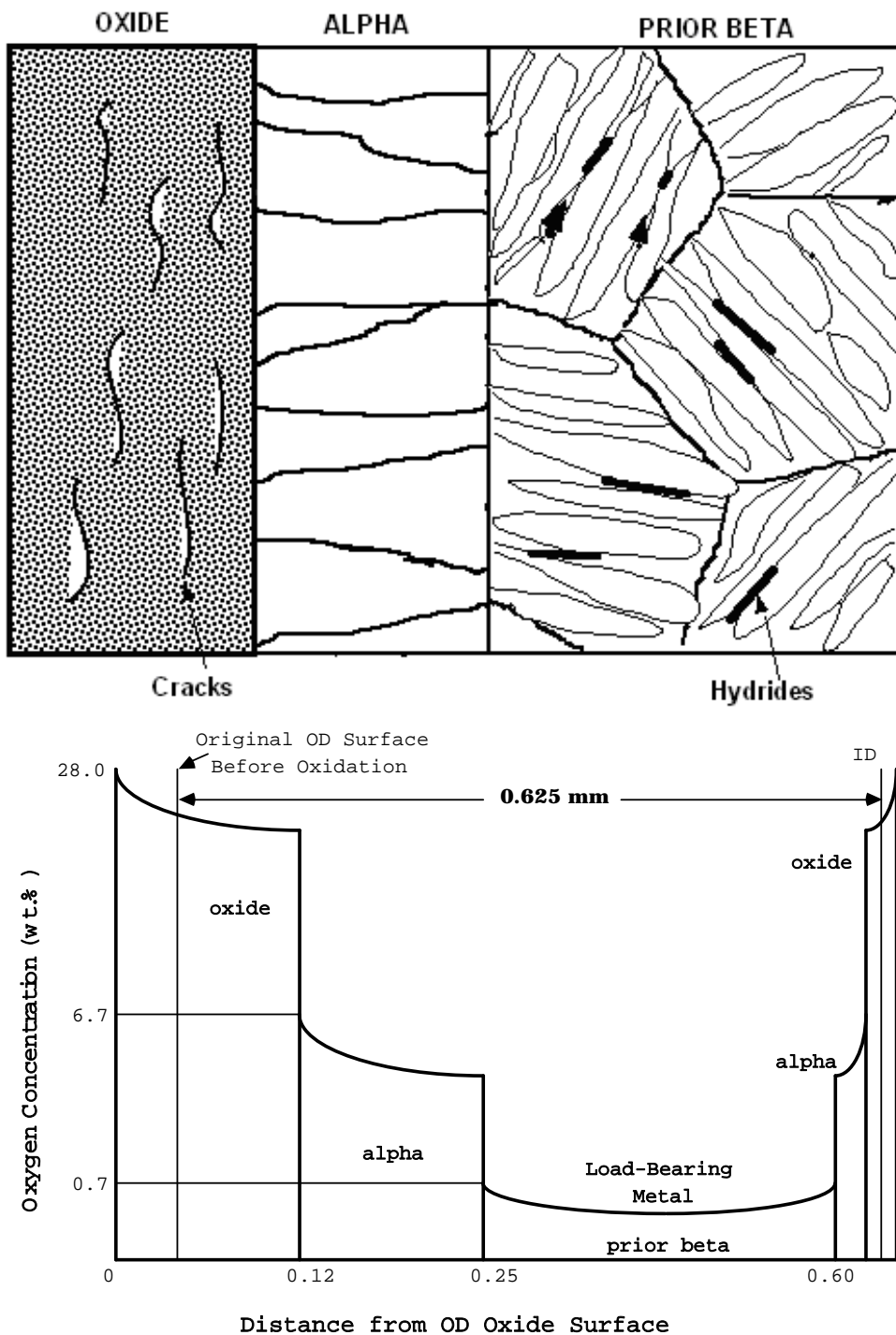
In 1960s, Wilson and Barnes performed laboratory tests simulating steam reactions with Zircaloy-clad fuel rods at high temperatures. They observed embrittlement of oxidized cladding well below the melting temperature of Zircaloy, either during the test itself or during removal of the specimen from the oxidizing furnace. The results were reported in Argonne National Laboratory (ANL) progress reports and synthesised later in [13]. At the same period, investigators in Oak Ridge National Laboratory (ORNL) conducted TREAT Test No. 6 with Zircaloy cladding in steam and observed that the specimen was severely embrittled by oxidation [14]. Also at about the same period, many tests were conducted that simulated reactivity-initiated accident (RIA) in SPERT-CDC and TREAT reactors. Results of metallurgical examination in these tests showed that embrittlement was caused by severe microstructural modification of the cladding. Brittle cladding cross sections exhibited oxide layer, oxygen-stabilised  $\alpha$ -phase layer and a region of acicular prior  $\beta$ -phase. The results were later reported by Fujishiro *et al.* [15].

As a result of these observations, the scientific community was alerted to the fact that oxidation of Zircaloys above the  $\alpha$ -to- $\beta$  transformation temperature results in the formation of inherently brittle phases, i.e., Zr oxide, oxygen stabilised  $\alpha$ -Zr (hcp structure), and diffusion of oxygen into the underlying  $\beta$  phase (bcc structure). This is shown schematically in Figure 1. Ductility of cladding could be severely degraded if the degree of oxidation is high. It was also realised that, if the embrittled cladding fragments into small pieces, the coolability of the core could be seriously impaired during the quench phase as well as during the more long-term cooling after the quench.

The sequence of events in the formation of the microstructure seen in Figure 1.1 would normally be that the  $\alpha$ -phase zirconium present at operating temperature is transformed to  $\beta$  at around 815°C when the cladding is heated. At the same time, the oxide starts to grow. Some of the oxygen in the oxide is dissolved in the metal matrix which is then re-transformed to  $\alpha$  which is referred to as oxygen-stabilised  $\alpha$ . The growth of the oxide and  $\alpha$  layers is controlled by diffusion of oxygen through the layers. The columnar structure of the  $\alpha$  layer is the result of this diffusion controlled growth. Inside the  $\alpha$  layer a large-grained structure of  $\beta$  is formed. When we can observe the  $\beta$  layer it has retransformed to  $\alpha$  during cooling. Since the transformation of  $\beta$  zirconium to  $\alpha$  almost invariably takes place by formation of Widmanstätten plates of  $\alpha$  it is very easy to identify the previous  $\beta$  by its acicular structure as shown in Figure 1.1. Occasionally, some of the  $\beta$  is retransformed to  $\alpha$  by growth into the  $\beta$  layer of a columnar crystal of  $\alpha$  from the  $\alpha$  layer, a so called  $\alpha$  incursion.

Whereas oxygen is an  $\alpha$  stabiliser, hydrogen is a  $\beta$  stabiliser. In other words, the solubility of oxygen is higher in  $\alpha$  and the solubility of hydrogen is higher in  $\beta$ . Therefore, during transformation of  $\beta$  to  $\alpha$ , oxygen and hydrogen solutes in the  $\beta$  layer redistribute themselves during cooling, i.e., oxygen towards and hydrogen away from the growing Widmanstätten plates. This is pronounced only during slow cooling, sometimes leading to precipitation of small hydrides at the periphery of the Widmanstätten plates.

Figure 1.1 Schematic illustration of microstructure (top) and oxygen distribution (bottom) in oxide, stabilised  $\alpha$  and prior- $\beta$  (transformed  $\beta$ ) layers in Zircaloy cladding after oxidation near  $1200^{\circ}\text{C}$



Significantly embrittled cladding can break into two pieces or fragment during the quenching phase of a LOCA. Cladding fragmentation is conducive to significant fuel dispersal. The action of rewetting by ECCS water involves the collapse of the vapour film that covers the cladding outer-diameter (OD) surface prior to subsequent transition to nucleate boiling. This event takes place at a

more or less constant temperature, i.e., the Leidenfrost temperature. For oxidized Zircaloy-4 cladding rewetted by bottom-flooding water, ANL investigators reported that rewetting occurs in the range of 475-600°C [16]. The abrupt change in the heat transfer conditions induces large thermal-shock stresses, which can break or fragment the cladding, if it is sufficiently embrittled by oxidation.

Below the Leidenfrost temperature, there is continued risk of clad failure or fragmentation after quenching, which will influence long-term coolability of the core. The post-LOCA forces, which need to be taken into account, are the hydraulic, seismic, handling, and transport forces.

There are two primary factors that exacerbate the susceptibility of oxidized cladding to post-quench embrittlement in comparison with susceptibility to fragmentation during quenching: i.e., (1) more pronounced effect of oxygen dissolved in prior  $\beta$  phase at lower temperature of loading (i.e., more pronounced after quench than during quench) and (2) more pronounced effect of hydrogen uptake at post-quench temperature. Note that significant hydrogen uptake can occur during irradiation (e.g., in high-burn-up Zircaloy-4) or during transient oxidation in steam (e.g., from cladding inner surface in contact with stagnant steam near a ballooned and burst region). For cooling rates typical of bottom flooding of core (i.e., 1-5 K/s), most hydrogen atoms remain in solution in the prior  $\beta$  phase at Leidenfrost temperature, and in such state, hydrogen has little effect on the fracture resistance of an oxidized Zircaloy. However, a higher level of hydrogen dissolved in  $\beta$  increases the solubility of oxygen in the  $\beta$ , thereby in effect exacerbating the embrittling effect of oxygen. It should be noted however that hydrogen effects were not a great concern in the initial discussions on the criteria established in 1973.

#### *1.2.2.2 The 17%-oxidation criterion and the Baker-Just oxidation law*

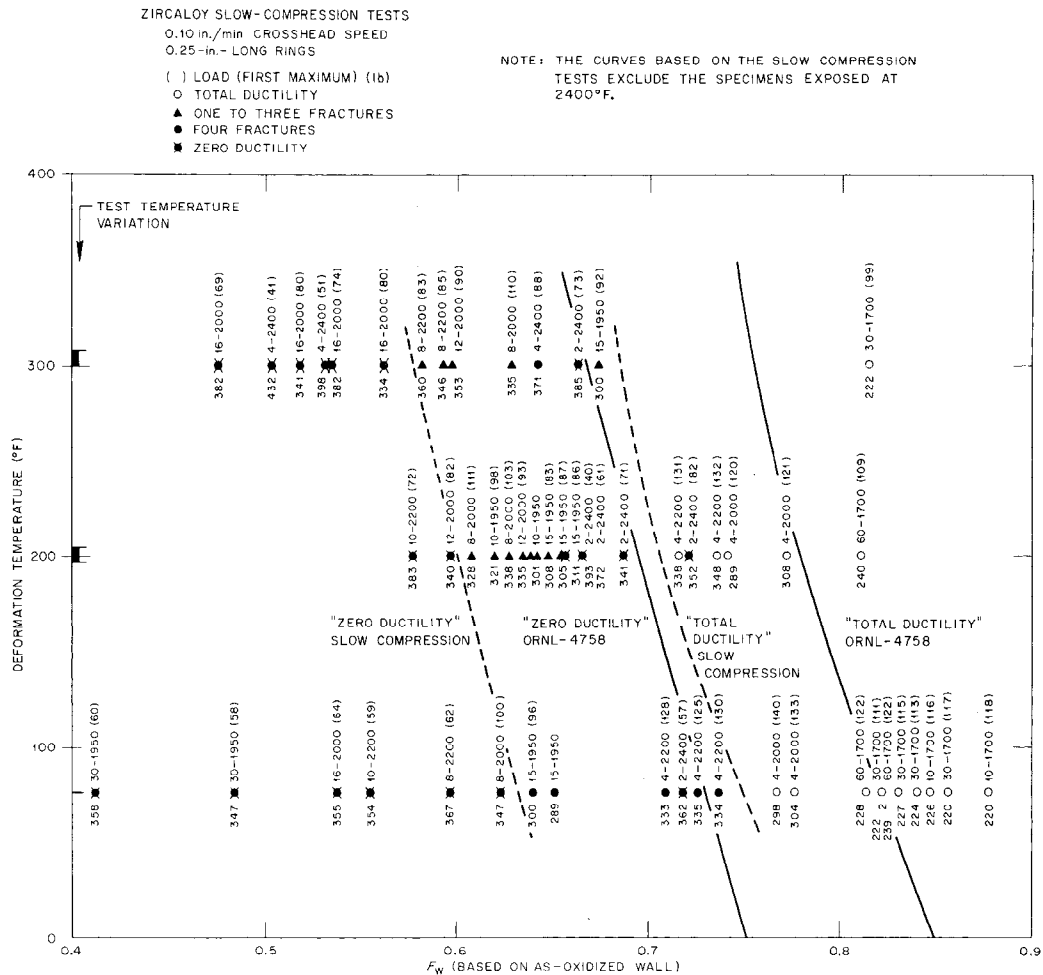
The rationale for the 17% oxidation criterion and the regulated use of the Baker-Just oxidation equation is described in this section. The following description is basically a direct quote from the Hache-Chung paper [5].

As indicated in a few reports [1,16] that reviewed the results of the LOCA-related tests performed before and after the 1973 Hearing, the 17% ECR and 1 204°C criteria were primarily based on the results of post-quench ductility tests and metallographic analysis conducted by Hobson [17,18] and additional metallographic analysis by Pawel [19].

Figure 1.2 summarises the results of Hobson's ring compression tests performed at 23-150°C. Zircaloy-4 cladding tubes were oxidized in steam in a high temperature furnace. The tubes were oxidized on two sides, followed by direct quenching into water. Then, short ring specimens cut from the oxidized tube were either compressed slowly to a total deflection of 3.8 mm or squashed by impact loading. After the test, all broken pieces of the ring were assembled back to determine the degree of brittleness. Zero ductility was defined on the basis of the macroscopic geometry of the broken pieces and the morphology of the fracture surface on microscopic scale. Each data point in Figure 1.2 indicates failure type, test identification number, oxidation time in min., oxidation temperature in °F, and first maximum load in pound.

The dashed line on the left side of Figure 1.2 denotes the zero ductility domain for slow-compression rate. This domain is valid only for oxidation temperatures of <2 200°F or <1 204°C. During the 1973 Hearing, ORNL investigators suggested to consider a zero-ductility temperature (ZDT) no higher than the saturation temperature during reflood, i.e., ≈135°C. Zero-ductility threshold at this temperature is equivalent to a prior  $\beta$ -layer fraction of ≈0.58, or a fraction of combined oxide layer plus  $\alpha$ -layer thickness (defined as  $X_T$ ) of ≈0.42 (based on as-oxidized cladding wall). The latter fraction corresponds to ≈0.44 if it is calculated based on fresh nonoxidized cladding wall (defined as  $W_0$ ).

Figure 1.2 Ductility of two-side-oxidized Zircaloy rings as function of slow- or fast-compression temperature and fraction of transformed- $\beta$ -layer (from Hobson, [14, 15].



The threshold fractional thickness of the combined oxide and  $\alpha$  layer ( $X_T/W_o$ , defined as  $X_{\alpha}$  in Figure 1.3) of 0.44, which corresponds to zero ductility threshold for slow compression at 135°C, was the key number in the establishment of 17% oxidation criterion in the 1973 Hearing. During the hearing, the AEC Regulatory Staff wrote:

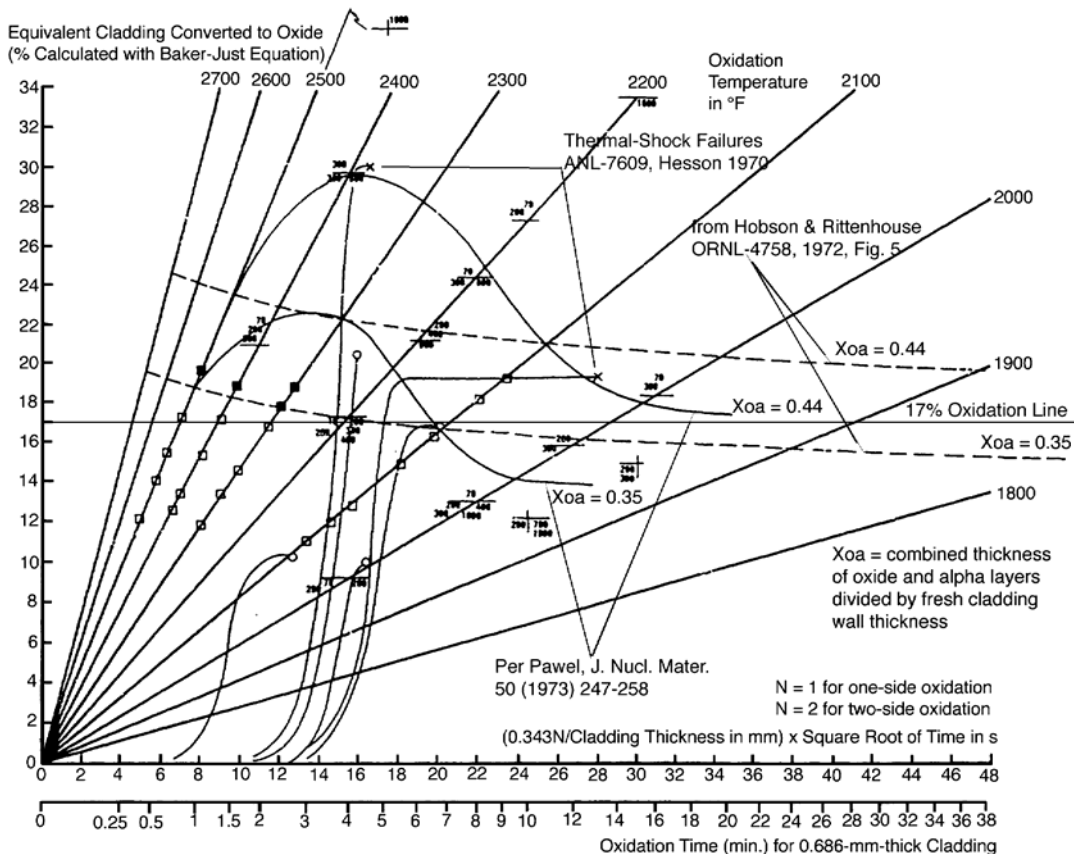
"Giving due credit to the numerous quench experiments and the ORNL zero ductility experimental data points for both impact and slow compression, the staff suggests that an embrittlement criterion be based on a calculated  $X_T/W_o$  that shall not exceed 0.44. This is equivalent to a zero ductility temperature of about 275°F based on the slow compression tests [20]."

Then, it was concluded:

"To preclude clad fragmentation and to account for effects noted in the tests described above, a limit of  $X_T/W_o \leq 0.44$  was earlier suggested by the Regulatory staff as an embrittlement criterion (Exhibit 1113). This limit was inferred from quench tests and mechanical tests. Criterion (b)(2) is now proposed as a better method of specifying a similar limit on the extent of cladding oxidation. The bases for proposing this method are described below: (The) use (of the 17 percent reaction limit) with the Baker-Just equation is conservative when compared to the previously suggested limits of  $X_T/W_o \leq 0.44$ . This is shown in Figure 1.3 (of the present report) for isothermal

conditions. Four lines of constant calculated  $X_T/W_0$  (two for 0.44 and two for 0.35) are constructed on the plot of percent reaction versus a parameter proportional to the square root of exposure time. The solid  $X_T/W_0$  lines are based on Pawel's equation (Exhibit 1133) [19], and the dashed lines are based on Exhibit 09, Figure 5 [17]. As can be seen, the  $X_T/W_0 = 0.44$  lines are both above the 17 percent reaction line..."

**Figure 1.3 Summary of multistep procedure used to establish 17% oxidation criterion during 1973 Rule-Making Hearing\*** (from Docket RM-50-1, April 16, 1973)



- \* Note equivalent cladding oxidized was calculated per Baker-Just correlation. For comparison, time to reach threshold fraction of combined oxide and  $\alpha$  layers of 0.44 is shown as determined per Hobson and Rittenhouse [17] and Pawel [19].

Results of a total of five key tests and calculations are summarised in Figure 1.3, a complex but the most important step used to reach the 17% oxidation limit. They are:

1. Equivalent cladding reacted (ECR) calculated as function of oxidation temperature and square root of time based on the Baker-Just correlation.
2. Two broken curves which define the time and temperature to reach the threshold fractional thickness of the combined oxide and  $\alpha$  layer (denoted as  $X_{\alpha\alpha}$ ) of 0.44 and 0.35, as determined based on the data given in [17] (Figure 5).
3. Two solid curves that define the time and temperature to reach the threshold fractional thickness of the combined oxide and  $\alpha$  layer of 0.44 and 0.35, as determined based on the method of Pawel [19].
4. Six ECR-(time)<sup>0.5</sup> curves from the thermal-shock tests of Hesson *et al.* [13].
5. Results from Combustion Engineering (CE) ring compression tests after one-sided oxidation.

By definition, ECR parameter varies depending on cladding wall thickness, either due to differences in fuel design or due to ballooning and burst during the heat-up phase in a LOCA. Figure 1.3 shows how to take account of the effects of variations in wall thickness and one- vs. two-sided oxidation.

Two of Hesson's thermal-shock experiments resulted in cladding fragmentation at calculated ECR values of  $\approx 19$  and  $\approx 30\%$ , as indicated in the figure. The other four did not fail at ECR values of  $\approx 21$ ,  $\approx 16.5$ ,  $\approx 10$ , and  $\approx 9.5\%$ . The time-temperature transients in Hesson's tests were integrated also by using the Baker-Just equation.

The CE data, discussed in the Hearing, are represented by squares on the oxidation isotherms of 2 500, 2 400, 2 300, and 2 100°F. If the sample fractured on compression by CE's load standard, it was considered to have failed and is denoted with a filled square. Open squares denote CE's non-failed specimens. By the CE's load standard, only those samples with calculated ECR values  $> 17\%$  failed.

Based on the results given in Figure 1.2 and the five sets of information shown in Figure 1.3, one can conclude that no samples tested by slow compression at  $> 135^\circ\text{C}$  failed with zero ductility if equivalent cladding reacted (ECR), calculated on the basis of Baker-Just correlation, was less than 17%. Furthermore, all samples oxidized to  $< 17\%$  ECR (again calculated with Baker-Just correlation) survived direct quenching.

In summary, the AEC Commissioners concluded that the very good consistency between the 17% limit, if calculated with the Baker-Just equation, and a wide variety of experiments supports adoption of this procedure [21], and it was further stated:

"There is relatively good agreement among the industrial participants as to what the limit on total oxidation should be... The regulatory staff in their concluding statement compared various measures of oxidation and concluded that a 17% total oxidation limit is satisfactory, if calculated by the Baker-Just equation... As argued by the regulatory staff, it appears that the 17% oxidation limit is within the Rittenhouse criteria. Thus a remarkable uniformity of opinion seems to exist with regard to the 17% oxidation limit [12]."

It is clear that the primary rationale of the 17% criterion is retention of cladding ductility at temperatures higher than 275°F ( $135^\circ\text{C}$ , i.e., the saturation temperature during reflood). Of major importance in this proceeding is that the threshold ECR value of 17% is tied with the use of Baker-Just correlation. That is, the 17% ECR criterion is specific to the Baker-Just correlation that must be used to determine the degree of total oxidation. If an oxidation correlation other than the Baker-Just equation (e.g., Cathcart-Pawel correlation) were used, the threshold ECR would have been less than 17%. This means that use of a best-estimate correlation may not necessarily be conservative in evaluating post-quench cladding ductility.

Also note that the 17% ECR limit was derived on the basis of zero ductility data obtained from the slow compression test only, that is, excluding similar data obtained from impact-type ring-crushing test. If the latter type of data were used, the ECR limit would have been  $\approx 14\%$  (Figure 1.3). No rationale for this exclusion was given in the 1973 Hearing.

#### 1.2.2.3 The 2 200°F criterion

From the results of posttest metallographic analysis of the slow-ring-compression specimens, Hobson [18] observed a good correlation between zero ductility temperature (ZDT) and fractional thickness of transformed- $\beta$  layer (or the sum of oxide plus  $\alpha$  layer thickness) as long as the specimen was oxidized at  $\leq 2 200^\circ\text{F}$  ( $1 204^\circ\text{C}$ ) (Figure 1.2). However, in spite of comparable thickness of transformed  $\beta$  layer, specimens oxidized at 2 400°F ( $1 315^\circ\text{C}$ ) were far more brittle. This observation was explained on the basis of excessive solid-solution hardening of transformed- $\beta$  phase at high oxygen concentrations.

For mechanical properties near room temperature the critical concentration of oxygen in the transformed- $\beta$  was estimated to be  $\approx 0.7$  wt%. Above this concentration, transformed  $\beta$  phase becomes brittle near room temperature. Because of the solubility limit of oxygen in the  $\beta$  phase, this high O concentration cannot be reached at 2 200°F (1 204°C) but can be reached at 2 400°F (1 315°C). Hobson concluded that: “embrittlement is not simply a function of the extent of oxidation alone, but is related in yet another way to the exposure temperature.”

The NRC understood that a criterion based solely on the extent of total oxidation is not enough, and that some additional criterion is needed to assure that the metal under the oxide layer is not too brittle. Thus during the 1973 Rule-Making Hearing, AEC Staff endorsed Hobson’s conclusion and wrote: “The staff recognises the importance of oxygen concentration in the  $\beta$  phase in determining the load bearing ability of Zircaloy cladding, and the implication from the recent compression tests that this may not be satisfactorily characterised above 2 200°F by a ZDT as a function of remaining  $\beta$  fraction only. We therefore believe that peak cladding temperatures should be limited to 2 200°F [20].”

Subsequently, it was also concluded that:

“Additional metallurgical and slow compression mechanical tests on other quenched samples from the ORNL experiments indicated that an important consideration was the amount and distribution of oxygen in the nominally ductile prior- $\beta$  phase. However, these factors could not be correlated as functions of time and temperature in the same manner as the (combined oxide and  $\alpha$  layer) penetration. In particular, the slow compression tests indicated a greater degradation in cladding ductility at higher temperatures than would be expected from considerations of (combined oxide and  $\alpha$  layer) penetration alone. It was on this basis that **the staff previously suggested a 2 200°F maximum cladding temperature**... What was observed in the slow compression tests was that 6 samples exposed at 2 400°F for only two minutes and with relatively high values of  $F_w$  ( $F_w$  being fractional thickness of prior  $\beta$ , all greater than 0.65) all fractured with nil ductility... Only when brittle failure was detected at high  $F_w$  in the slow compression tests did the suspicion arise that ductility was a function of both  $F_w$  and the exposure temperature... As the temperature rises above 2 200-2 300°F, solid solution hardening in the  $\beta$  phase appears to contribute significantly to formation of a brittle structure. That is, brittle failure occurs even though  $\alpha$  incursions are not observed, and the fraction of remaining  $\beta$  is greater than that observed in lower temperature tests. This is confirmed by examination of the six samples from the ORNL exposed at 2 400°F for two minutes (Exhibit 1126)... From the foregoing, there is ample evidence that load bearing ability and ductility decrease with increasing exposure temperatures, even for transients with comparable  $F_w$ . Increased solubility of oxygen in the prior- $\beta$  phase has been discussed as a contributing factor... The staff believes that because of high-temperature degradation... phenomena (... strongly suggested by the experimental evidence cited), the suggested 2 200°F limit should be imposed [21].”

Then it was added:

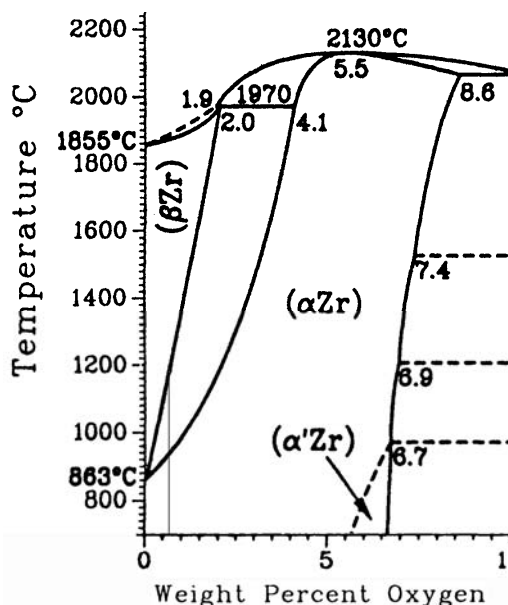
“The situation is complicated by the fact that not all of the prior  $\beta$  phase is equally strong or ductile, since these properties depend on the amount of dissolved oxygen. This fact has been suspected for some time... From the phase diagram, given by both Scatena and Westinghouse, it is obvious that it is possible for the  $\beta$ -phase zirconium to take on a higher oxygen content at 2 600°F than at 2 000°F. Furthermore, since the diffusion rate depends exponentially upon temperature, one might expect a greater incursion of oxygen into the  $\beta$  phase for a given thickness of oxide and stabilised  $\alpha$  phase at higher temperatures... Others (than Hobson) have also observed that the resistance to rupture depends upon the temperature at which oxidation occurs as well as the extent of oxidation... To recapitulate, measures of Zircaloy oxidation, whether by percent,  $X_T$ , or  $F_w$ , are largely or wholly determined from the brittle layers of zirconium oxide or stabilised  $\alpha$  phase, while the ductility and

strength of oxidized zirconium depend upon the condition and the thickness of the prior  $\beta$  phase... Thus a criterion based **solely on the extent of total oxidation is not enough, and some additional criterion is needed** to assure that the prior  $\beta$  phase is not too brittle. The specification of a maximum temperature of 2 200°F will accomplish this **adequately. The data cited in exhibit 1113 would not support a choice of a less conservative limit [12].**"

Subsequent work has deduced that an oxygen content of 0.7 wt% in the  $\beta$  phase is a critical limit for ductility of the prior  $\beta$  layer at room temperature [19,22]. Although somewhat different from the phase diagram of Zircaloy-oxygen [23], the partial phase diagram of the Zr-oxygen binary shown in Figure 1. 4 serves as a guide to show how this limit was reached at the  $\alpha/\beta$  interface at about 1 200°C. At temperatures higher than that the oxygen content will soon be well above the 0.7% limit in the  $\beta$  since oxygen diffusion in  $\beta$  is quite fast at these temperatures. In 30 s,  $(2Dt)^{0.5}$  is about 125  $\mu\text{m}$  at 1 250°C. Both Pawel and Sawatsky proposed alternative criteria based on the 0.7 wt% limit. The drawback with both these criteria is that they require diffusion calculations which are certainly more complicated than the simple 1 204°C temperature limit. On the other hand, any LOCA analysis requires extensive calculations and calculating the 0.7 wt%  $\beta$  content only adds marginally to this hardship.

Figure 1.4 The zirconium rich corner of the Zr-O phase diagram

*The thin vertical line shows 0.7 wt% O*



It is important to realise that in the early experiments of oxidation of Zircaloys at high temperatures [13,17-18], specimen temperatures were not measured directly, e.g., by using spot-welded thermocouples. Likewise, specimen temperatures in the experiment of Baker-Just [24] were determined indirectly. Before mid-1970s, it appears that the effect of the large exothermic heat of oxidation of Zr was not well recognised by the investigators. In Hobson's experiments [17-18], the temperature of Zircaloy tube being oxidized was assumed to be the same as the temperature of the uniform central zone of the high-temperature furnace. This assumption would be reasonable for low temperatures, e.g., <800°C. However, at higher temperatures – e.g. >1 100°C – high rate of self heat generation from oxidation causes actual specimen temperature significantly higher than that of the furnace temperature. In this respect, actual oxidation temperature of a Zircaloy tube reported in Hobson's experiment is believed to be significantly higher, e.g., 1 200°C vs. 1 260°C.

At about  $>1\ 100^{\circ}\text{C}$ , a relatively small difference in isothermal oxidation temperature can cause a significant difference in actual or calculated values of ECR, which depends on oxidation time at temperature. At about  $>1\ 200^{\circ}\text{C}$ , it also influence significantly the distribution of oxygen in the  $\beta$  layer, hence, the degree of cladding embrittlement.

Note also that the Zircaloy-oxygen pseudobinary diagram was reported only after the 1973 Hearing [23]. It is considerably different from the Zr-oxygen binary diagram shown in Figure 1.4. Oxygen solubility in  $\beta$  phase is also influenced by the hydrogen concentration.

Because of the above-mentioned uncertainties (in actual specimen temperature, threshold ECR, and threshold oxygen concentration in  $\beta$  phase), a lingering question remained after the 1973 Hearing whether indeed post-quench ductility is assured for the limiting condition of  $2\ 200^{\circ}\text{F}$  PCT and 17% ECR. Only in 1980, it was demonstrated for Zircaloy-4 (wall thickness the same as that of Hobson's study) that a sufficient level of post-quench ductility was retained after exposure to this limiting condition in the study of [16]. In this study, several improved techniques were used; that is, specimen temperature was measured directly using spot-welded thermocouples, load-elongation behavior was measured, and accurate ECR value was determined on the basis of measured thicknesses of oxide,  $\alpha$ , and prior  $\beta$  layers.

### **1.2.3 LOCA safety criteria in other countries**

The similarity of LOCA safety criteria between different countries was demonstrated in a recent compilation of safety criteria in NEA member countries performed by NEA/CSNI [25]. With few exceptions the different countries have adopted the NRC criteria. In the cases when there are exceptions, they must in most cases be regarded as fairly small. Thus Japan has adopted an ECR-value of 15% instead of the usual 17% while the Czech Republic uses a value of 18% for VVER 440 reactors but retains the 17% value for VVER 1 000 reactors. This is related to the different cladding materials in the two types of reactor, Zr1Nb and Zircaloy-4 respectively. The 18% ECR-value is also applied in Russia [26]. However this value is based on quench test results rather than on ring compression tests as the American criteria [27]. As will be discussed in later sections, an E110 criterion based on ring compression tests would probably be much more restrictive than the 17% ECR criterion. Hache has estimated that an application of the same methodology as in the 1973 Rule-making hearing would have led to a limit of 6% ECR [27].

With regard to peak cladding temperature (PCT) most countries have chosen to round down the NRC limit of  $1\ 204^{\circ}\text{C}$  to  $1\ 200^{\circ}\text{C}$ . In the application of the ECR criterion some countries include the pre-LOCA oxidation and some do not.

The Japanese LOCA criteria on cladding embrittlement, 15% ECR and  $1\ 200^{\circ}\text{C}$  peak cladding temperature, were established in 1975 and were based on the concept of zero ductility of cladding as in the U.S. The oxidation criterion was reduced by 2% taking account of uncertainty for the effect of cooling rate on cladding embrittlement, which was pointed out after the establishment of the criteria in the U.S. After their establishment, Uetsuka *et al.* found that inner surface oxidation after rod burst is accompanied by significant hydrogen absorption [28]. Ring compression tests were performed by Uetsuka and coworkers [28-30] on the cladding specimens that experienced rod burst and double sided oxidation to examine the embrittlement of the cladding due to oxidation and hydrogen absorption. The ductility of ring specimens fell down to the zero ductility range when the cladding was oxidized to several percent ECR, indicating that significant hydrogen absorption enhances cladding embrittlement [29]. Accordingly, they conducted "integral thermal shock tests" to evaluate the failure bearing capability of oxidized cladding under simulated LOCA conditions [30]. In the test, a short test rod was heated up, burst, oxidized in steam and quenched by flooding water. Obtained results confirmed that the criterion of 15% ECR still had safety margin when the Baker-Just correlation was used, and the

results were referred when the LOCA criteria were reassessed in 1981. Therefore, the current Japanese LOCA criteria on fuel safety are not based on the concept of zero ductility of cladding, but on the failure threshold value determined in the integral thermal shock tests under restrained conditions.

An exception to the rule of using specified temperature and oxidation criteria is Canada. Canadian reactor safety analysis is based on ensuring that the radiological dose to the public resulting from a design basis accident remains below a given amount. The regulator does not prescribe how this is to be achieved, but makes it the responsibility of the industry to demonstrate compliance. To do this, the Canadians use a suite of qualified computer codes to analyse the consequences of the postulated design basis accidents to determine: the fission product inventory in the fuel, the probable number of fuel-sheath failures, the transport of fission products through the heat transport system to containment, the release of fission products from containment, the dispersion of fission products into the atmosphere, and finally the dose to the public. Thus, there are no formalised PCT or ECR limits in Canada.

In addition to the maximum temperature and oxidation limits, safety criteria in Germany contain an additional requirement that the fraction of burst fuel rod shall be no more than 10% of the total rods in the core. The purpose of this requirement is to limit fission gas release due to cladding burst.

### 1.3 References

1. Parsons, P.D., Hindle, E.D., and Mann, C.A., "PWR fuel behaviour in design basis accident conditions. A State-of-the-Art Report by the Task Group on Fuel Behaviour of CSNI Principal Working Group No 2", Committee on the Safety of Nuclear Installations, OECD Nuclear Energy Agency, CSNI Report 129.
2. IAEA (2001), *Safety Assessment and Verification for Nuclear Power Plants*, IAEA, Vienna.
3. ANSI/ANS-5.1-1994: Decay Heat Power in Light Water Reactors. 1994, American Nuclear Society.
4. Cathcart, J.V., *et al.*, "Zirconium metal-water reaction kinetics. IV. Reaction rate studies", ORNL/NUREG-17.
5. NEA (2001), Hache, G. and Chung, H.M., "The History of the LOCA embrittlement criteria" (pp. 37-64), Topical Meeting on LOCA Fuel Safety Criteria held in Aix-en-Provence, OECD.
6. Chung, H.M., "Fuel behavior under loss-of-coolant-accident situations", Nuclear Engineering and Technology, 37(2005), pp. 327.
7. Report of Advisory Task Force on Emergency Cooling, TID-24226.
8. "Interim Acceptance Criteria for Emergency-Core-Cooling Systems for Light-Water Power Reactors", U.S. Federal Register 36 (125). 1971. p. 12247-12250.
9. Cottrell, W.B., "ECCS rulemaking hearings", Nuclear Safety, 15(1974), pp. 30-55.
10. New acceptance criteria for emergency core-cooling systems of light-water-cooled nuclear power reactors, Nuclear Safety, 15(1974), pp. 173-184.
11. Acceptance Criteria for Emergency Core Cooling Systems for Light-Water Nuclear Power Reactors, U.S. Code of Federal Regulations, Title 10, Part 50, Section 46. 1974.
12. Atomic Energy Commission Rule-Making Hearing, Opinion of the Commission, Docket RM-50-1, 28 December, 1973.
13. Hesson, J.C., *et al.*, "Laboratory Simulations of Cladding-Steam Reactions Following Loss-of-Coolant Accidents in Water-Cooled Power Reactors", Argonne National Laboratory, ANL-7609, January 1970.
14. Parker, J.W., *et al.*, "Release of fission products from reactor fuels during transient accidents simulated in TREAT", International Symposium on Fission Product Release and Transport under Accident Conditions., 1965, Oak Ridge.

15. Fujishiro, T., *et al.*, "Light water reactor fuel response during reactivity initiated accident experiments", NUREG/CR-0269., August 1978.
16. Chung, H.M. and Kassner, T.F., "Embrittlement Criteria for Zircaloy Fuel Cladding Applicable to Accident Situations in Light-Water Reactors. Summary Report", NUREG/CR-1344, January 1980.
17. Hobson, D.O. and Rittenhouse, P.L., "Embrittlement of Zircaloy Clad Fuel Rods by Steam During LOCA Transients", Oak Ridge National Laboratory, ORNL-4758, January 1972.
18. Hobson, D.O., "Ductile-brittle behavior of Zircaloy fuel cladding", ANS Topical Meeting on Water Reactor Safety, 1973, Salt Lake City, pp. 274-288.
19. Pawel, R.E., "Oxygen diffusion in  $\beta$  Zircaloy during steam oxidation", Journal of Nuclear Materials, 50(1974), pp. 247-258.
20. Atomic Energy Commission Rule-Making Hearing, Supplemental Testimony of the Regulatory Staff, Docket RM-50-1, 26 October, 1972.
21. Atomic Energy Commission Rule-Making Hearing, Concluding Statement of the Regulatory Staff, Docket RM-50-1, 16 April, 1973.
22. Sawatsky, A., "Proposed criterion for the oxygen embrittlement of Zircaloy-4 fuel cladding", 4<sup>th</sup> Symposium on Zirconium in the Nuclear Industry, 1978, Stratford-on-Avon, ASTM STP-681, ASTM, pp. 479-496.
23. Chung, H.M. and Kassner, T.F., "Pseudobinary Zircaloy-oxygen phase diagram", Journal of Nuclear Materials, 84(1979), pp. 327-339.
24. Baker, L. and Just, L.C., "Studies of metal-water reactions at high temperatures. III. Experimental and theoretical studies of the zirconium-water reaction", Argonne National Laboratory, ANL 6548, May 1962.
25. Fuel safety criteria in NEA member countries. Compilation of responses received from member countries, NEA Committee on the Safety of Nuclear Installations, NEA/CSNI/R(2003)10, March 2003.
26. Bibilashvili, Y.K., *et al.*, "Thermomechanical properties of zirconium-based alloys oxidized claddings in LOCA simulating conditions", IAEA Technical Committee Meeting on Fuel behaviour under transient and LOCA conditions., 2001, Halden, Norway, IAEA, pp. 186-208.
27. Hache, G., "Rationale of the LOCA 10 CFR 50.46b criteria and comparison with the E 110 alloy", Topical Meeting on LOCA Fuel Safety Criteria., 2001, Aix-en-Provence, Nuclear Energy Agency, pp. 17-36.
28. Uetsuka, H., *et al.*, "Zircaloy-4 cladding embrittlement due to inner surface oxidation under simulated loss of coolant conditions", Journal of Nuclear Science and Technology, 18(1981), pp. 705-717.
29. Furuta, T., Uetsuka, H., and Kawasaki, S., "Estimation of conservatism of present embrittlement criteria for Zircaloy fuel cladding under LOCA", Zirconium in the Nuclear Industry: Sixth International Symposium, 1982, Vancouver, Canada, ASTM STP 824, ASTM, pp. 734-746.
30. Uetsuka, H., Furuta, T., and Kawasaki, S., "Failure-bearing capability of oxidized Zircaloy-4 cladding under simulated loss-of-coolant conditions", Journal of Nuclear Science and Technology, 20(1983), pp. 941-950.

## 2. DESCRIPTION OF LOCA ACCIDENT SCENARIOS FOR MAJOR TYPES OF REACTORS

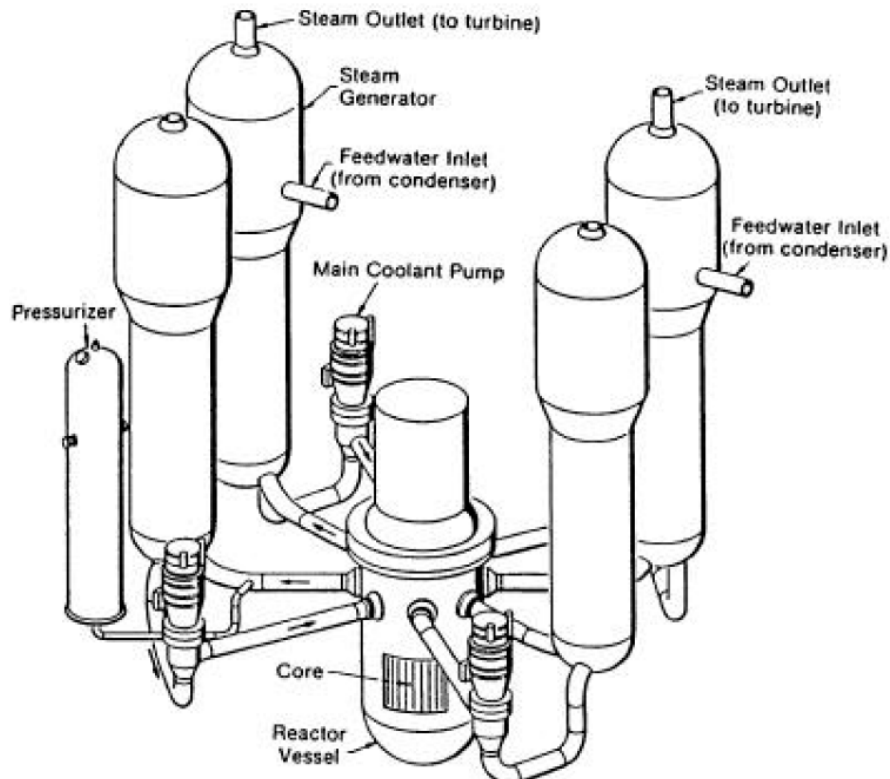
The following descriptions come mainly from a USNRC PIRT (Phenomenon Identification and Ranking Tables) study of LOCAs in PWRs and BWRs with high burn-up fuel [1]. The description thus applies to American types of reactors. It is expected that conditions will be similar for other types of PWRs while the variations in behaviour will be greater in different types of BWRs around the world. For instance, for BWRs with internal recirculation pumps the large break LOCA is more or less non-existent. For other main types of reactors, the CANDU and the VVER reactors separate descriptions are given.

### 2.1 The pressurised water reactor

#### 2.1.1 PWR large break LOCA

A PWR primary system is shown in Figure 2.1. The design basis accident in the PWR is a double-ended guillotine break in a cold leg between the reactor coolant pump and the reactor vessel.

Figure 2.1 PWR primary system arrangement



The blowdown period (0-30 s) occurs as a result of a break in the coolant system through which the primary coolant is rapidly expelled. Within a fraction of a second after the break, the core voids

and goes through departure from nuclear boiling. The negative void reactivity rapidly shuts down the core. With the diminished cooling and the redistribution of stored energy in the fuel, the cladding heats up. Interactions between the pump and the break dynamics cause intermittent flow reversals. The primary system pressure rapidly decreases and the high-pressure safety injection begins, but most of this flow is lost out of the break. Injection from the cold-leg accumulators begins but much of the injected flow is swept around the downcomer, into the broken-loop cold leg and out the break. As the blowdown progresses, an increasing amount of the accumulator-injected coolant stays in the downcomer and some water begins to enter the lower plenum. The average peak cladding temperature (PCT) during the blowdown phase of a large-break LOCA is approximately 1 500°F (815°C) and the PCT at 95% confidence level is about 1 750°F (954°C), assuming a loss-of-offsite power and the worst single failure assumption for the emergency core cooling system.

The refill period occurs between 30 and 40 s following the start of the LOCA. The primary pressure has decreased to a level at which the low-pressure injection system activates and begins to inject water into the system. The lower plenum begins to fill with accumulator water as coolant bypass diminishes. While refilling of the lower plenum is underway, however, the core heats up in a near adiabatic mode due to decay heat. Some fuel rods balloon and burst, causing blockage of some of the flow channels during refill.

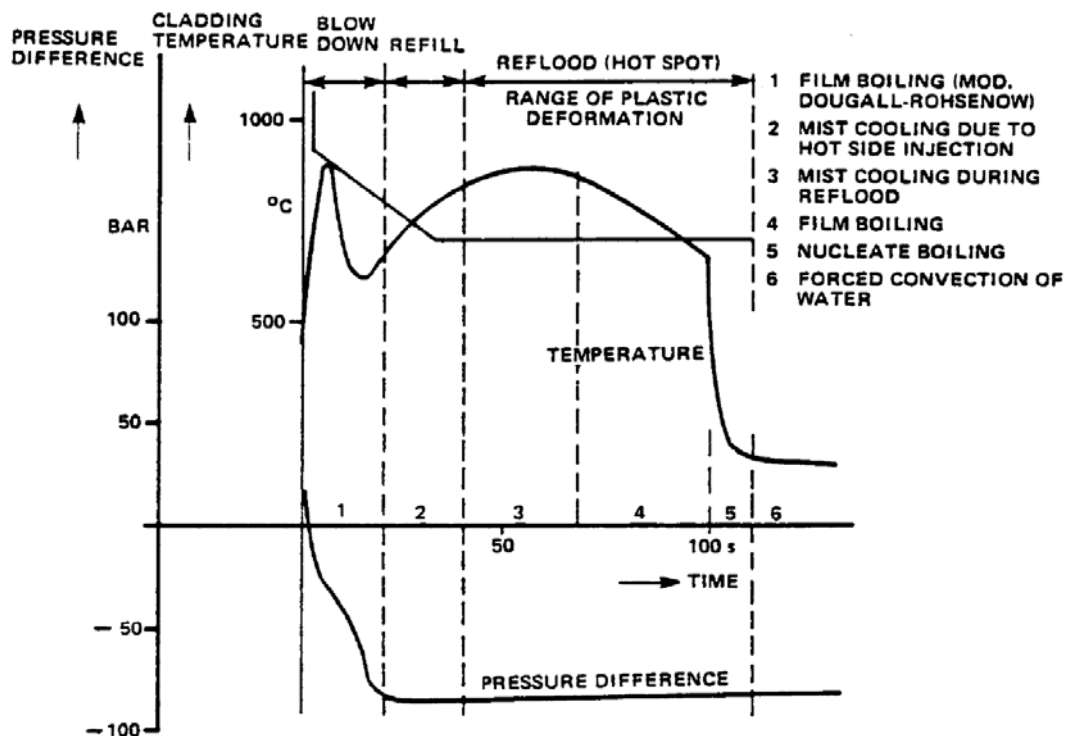
The reflood period occurs between 40 and 200 s; it begins at the time when the lower plenum has filled and the core begins to refill. Water injected by the accumulators fills the downcomer and creates the driving head for refilling the core. The lower elevations of the core quench, generating a two-phase mixture that provides some cooling to the upper elevations of the core. However, the fuel rods continue to heat up until the quench front begins to move upward through the core. Some additional number of fuel rods may burst during the reflood period. Zirconium-water reactions can occur for high temperature regions of the core. As the quench front continues to advance, the fuel rod upper elevations are cooled by a dispersed non-equilibrium two-phase mixture of superheated steam and entrained droplets. Eventually, there is sufficient cooling in advance of the quench front to terminate the increase in cladding temperature and the PCT is reached. The average reflood PCT during this period is approximately 1 680°F (915°C) and the PCT at 95% confidence is about 1 975°F (1 080°C). The maximum amount of cladding oxidized at a given location during this phase of the LOCA is about 10% for beginning-of-life (BOL) UO<sub>2</sub> fuel and the total oxidation is less than 1%.

An example of the complete pressure and temperature history for a fuel rod is shown in Figure 2.2 [2]. Note that the figure demonstrates principle rather than detail. The exact history will depend on fuel rod location and type of PWR as can be seen for instance in Figures 6.68 and 9.4.

### **2.1.2 PWR small break LOCA**

Breaks with flow areas typically less than 1-ft<sup>2</sup> and greater than 3/8 in. in diameter span the category of small breaks. A small break is sufficiently large that the primary system depressurises to the high-pressure safety injection set point and a safety injection or “S” signal is generated, automatically starting the High-Pressure Safety Injection (HPSI) system. Breaks smaller than 3/8-inch in diameter do not depressurise the reactor coolant system because the reactor charging flow can replace the lost inventory. The control rods shut down the reactor such that only decay heat is generated in the core. The limiting small-break LOCA is determined by the inter-play between core power level, the axial power shape, break size, the high-head safety injection performance, and the pressure at which the accumulator begins to inject. The limiting break is one that is large enough that the high-pressure safety injection system cannot make-up the mass loss from the reactor system but small enough that the reactor system does not quickly depressurise to the accumulator set point. This combination of circumstances leads to a core uncover.

Figure 2.2 Double ended cold leg break, pressure difference across the cladding and cladding temperature at the hot spot [2]



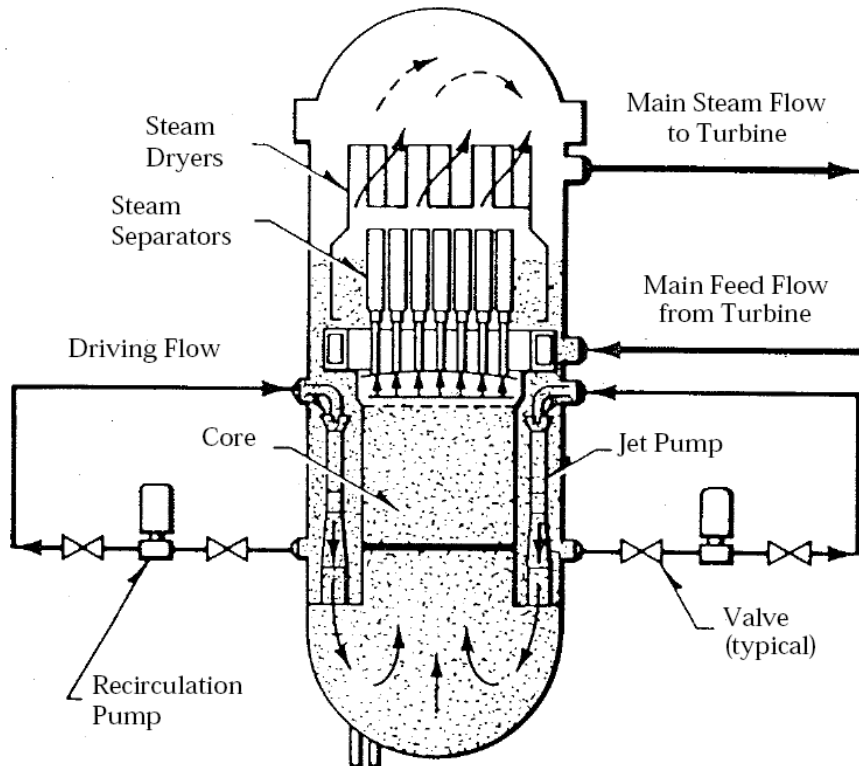
For Westinghouse plants, the limiting breaks are typically in the 2-4 inch range. A spectrum of break sizes has been calculated for a Westinghouse three-loop plant. Calculations were performed assuming both fresh fuel and fuel with burn-up between 30 and 54 GWd/t. These calculations are thought to accurately display the effect of burn-up on fuel performance. As an example, with fresh fuel, a three-inch break was found to produce the highest PCTs for breaks in the range of 2 to 6 inches. The PCT of 1 830°F (1 000°C) occurred at approximately 1 480 s. The core average cladding oxidation was 0.5%. No bursting of the fuel is predicted for fresh fuel.

The available calculated results for fuel that has been in the reactor indicate that as burn-up increases, some of the fuel will burst and experience double-sided cladding reactions. However, the burn-up reduces the linear heat rate such that the calculated PCTs are below those for fresh fuel and are, therefore, less limiting. At 54 GWd/t, the hot rod PCT is predicted to be approximately 1 500°F (815°C).

## 2.2 Boiling water reactor LOCA

The steam and recirculation water flow paths in a General Electric type BWR-6 are shown in Figure 2.3. The steam-water mixture first enters steam separators after exiting the core. After subsequent passage through steam dryers located in the upper portion of the reactor vessel, the steam flows directly to the turbine system. The water, which is separated from the steam, flows downward in the periphery of the reactor vessel and mixes with the incoming main feed flow from the turbine. This combined flow stream is pumped into the lower plenum through jet pumps mounted around the inside periphery of the reactor vessel. The jet pumps are driven by flow from recirculation pumps located in relatively small-diameter external recirculation loops, which draw flow from the plenum just above the jet pump discharge location.

Figure 2.3 Steam and recirculation water flow paths in the BWR



The fuel is uranium dioxide ( $\text{UO}_2$ ) and the cladding is Zircaloy-2 with a zirconium-based inner liner. Each fuel assembly has several fuel rods with a burnable poison, gadolinia ( $\text{Gd}_2\text{O}_3$ ) mixed in solid solution with  $\text{UO}_2$ .

The design basis accident for a BWR-6 is a double-ended break in the suction-side of the recirculation line. Shortly after the break, the reactor scrams, typically on drive flow pressure. Because of the large flow reductions immediately following the LOCA caused by the depressurisation, there is a rapid increase in the core average void fraction. The negative void reactivity rapidly shuts down the core. The flow reverses in the broken loop jet pump. With the flow reversal all the drive flow to that jet pump is lost and one-half the drive flow that is supporting the core flow is lost.

A loss of offsite power is also assumed. Thus, there is no power to the recirculation pump, which means that the intact loop pump also starts to coast down. The coastdown time of the pump is on the order of 10-15 seconds. With the loss of pumped flow, there is an almost instantaneous and large reduction in the core flow, which causes an early boiling transition in the core, typically within one second after the break.

The cladding temperature rapidly increases; the resulting blowdown peak cladding temperature is dominated by the stored energy in the fuel.

Valves are closed to isolate the system, typically within four seconds after the LOCA. System depressurisation and loss of liquid inventory continue. As a result of the loss of inventory, the water level in the downcomer decreases and as the water level eventually drops down to the top of the jet pump. This opens a flow path through which steam can flow to the break. The rate of depressurisation increases following jet pump uncoverage.

During normal operation, the inlet subcooling at the bottom of the core is 20°F (11 K). With the rapid depressurisation, there is a large amount of flashing of the fluid in the lower plenum, this occurring at approximately 10 s. This causes a large increase in the coolant flow through the core, quenching the fuel, and returning the cladding temperature to the saturation temperature.

As the LOCA and depressurisation continue, the level inside the core region decreases, as well as forming a level in the lower plenum region. The flow into the core is limited and the core uncovering leads to a second boiling transition. That typically happens at approximately 20 secs into the transient.

Within 35-40 s following the LOCA, the high pressure core spray system begins to deliver coolant to the top of the core, the time being determined by the time to start the diesel generator that drives the high pressure core spray system. The low-pressure injection begins when the system pressure drops below the shutoff head for the pumps, typically on the order of about 200 psi.

A second transition and core heatup begins in the period 20-35 s. This heatup is terminated by the operation of the BWR-6 safety systems.

The BWR-6 has one high-pressure coolant system, one low-pressure core spray system, and three low-pressure coolant injection (LPCI) systems injecting into the bypass region. The worst single failure for the BWR-6 is the failure of one of the diesel generators that will drive two of the LPCI systems. The outcome of this failure is that the system behaviour is based on the availability of the high-pressure core spray, the low-pressure core spray and one LPCI system that injects into the bypass region.

Given the operation of these systems, the core refills before the lower plenum. The refilling and reflooding processes restores the liquid inventory in the core and quenches the core in the period 100-150 s following the LOCA. Throughout the transient, the best-estimate peak cladding temperature for nominal conditions is approximately 800°F (427°C). The upper bound estimate for a 95%-95% upper bound is approximately 1 200-1 300°F (590-700°C).

For the BWR/4, the ECC configuration is slightly different. However, the early part of the transient is very similar to the BWR-6. These differences cause the core reflood during the refilling and reflooding phase of the LOCA to take somewhat longer than in a BWR-6. This results in a somewhat higher peak cladding temperature for the BWR/4, with the peak cladding temperature for nominal conditions being approximately 1 000°F (540°C) and the upper bound estimate approximately 1 400-1 500°F (760-815°C).

The BWR/2 is the older-generation BWR without jet pumps. The core cannot be reflooded. The peak cladding temperature is controlled by a balance between decay heat and the core spray heat transfer. Typically, the peak cladding temperature occurs late in the transient, perhaps 600-800 s following the LOCA. Quenching of the fuel rods is also very slow. The upper bound peak cladding temperature for the BWR/2 is approximately 1 700°F. For these plants, cladding oxidation, rather than PCT, may be limiting.

For the purposes of the PIRT [1], the panel did not differentiate between BWR small-break and large-break LOCAs. The BWR is designed to automatically convert postulated small-breaks that would uncover the core into a large-break through the activation of an Automatic Depressurisation System (ADS). The ADS opens several of the standard safety relief valves, causing a controlled depressurisation with system response quite similar to that for a postulated large break in the reactor steam line.

## **2.3 Risk-informed changes to NRC LOCA technical requirements**

In June 1999, the NRC decided to implement risk-informed changes to the LOCA technical requirements. As a result, the requirements for large-break loss of coolant accident were re-examined. A number of possible changes were considered. These included changes to General Design Criterion (GDC) 35 and changes to Paragraph 50.46 acceptance criteria, evaluation models, and functional reliability requirements. The NRC also proposed to refine previous estimates of LOCA frequency for various sizes of LOCAs to more accurately reflect the current state of knowledge of the mechanisms and likelihood of primary coolant system rupture.

Industry interest in a redefined LOCA was shown by the Nuclear Energy Institute (NEI) filing of Petition for Rulemaking in February 2002. The petition requested that the NRC amend § 50.46 and Appendices A and K to allow – as an option to the double-ended rupture of the largest pipe in the reactor system – the maximum LOCA break size to be “up to and including an alternate maximum break size that is approved by the NRC.

NRC received 17 sets of comments. Most were from the power reactor industry in favour of the petition. A few other stakeholders were concerned about potential impacts on defence-in-depth or safety margins if significant changes were made to reactor designs based upon use of a smaller break size. The NRC staff considered the technical issues raised by the petitioner and stakeholders in this proposed rulemaking.

During public meetings, industry representatives expressed interest in a number of possible changes to licensed power reactors as a result of redefining the large-break LOCA. These include lengthening diesel generator start times, optimizing containment spray system setpoints, increasing power, improving fuel management, and other changes.

July 2004, the Commission stated that the NRC staff should determine an appropriate risk-informed alternative break size and that breaks larger than this size should be removed from the design basis event category. The proposed rule should be structured to allow operational as well as design changes and should include requirements for licensees to maintain the capability to mitigate the full spectrum of LOCAs up to the double-ended guillotine break of the largest reactor coolant system pipe. To maintain the core in a coolable geometry, the Commission stated that a high-level criterion in the rule should include the requirement for the licensee to provide effective mitigation capabilities, including effective severe accident mitigation strategies directed at break sizes larger than the alternative maximum break size permitted by the rule.

The Commission also stated that the mitigation capabilities for beyond-design-basis events should be controlled by NRC requirements commensurate with the safety significance of these capabilities. Finally, the Commission stated that LOCA frequencies should be periodically reevaluated and if increases in frequency required licensees to restore the facility to its original design basis or make other compensating changes,

Based on the above Commission guidance, the staff has prepared a proposed rule which contained alternative emergency core cooling system (ECCS) evaluation requirements [“Proposed Rulemaking for “Risk-Informed Changes to Loss-of-Coolant Accident Technical Requirements”, SECY-05-052 (March 2005)]. These alternative requirements would be codified in a new regulation, Paragraph 50.46a, and could be used in lieu of the requirements in the current Paragraph 50.46. The rule could be adopted by current nuclear power reactor licensees. The proposed rule would divide the current spectrum of LOCA break sizes into two regions. The division between the two regions is determined by a “transition break size” (TBS). The first region includes small breaks up to and including the TBS. The second region includes breaks larger than the TBS up to and including the

double-ended guillotine break of the largest reactor coolant system pipe. The term “break” in the TBS does not mean a double-ended guillotine break; rather it refers to an equivalent opening in the reactor coolant system boundary.

The staff determined that an appropriate TBS would be the cross-sectional area of the largest pipe attached to the reactor coolant system. Thus, the TBS will vary from plant to plant depending on the specific piping system design. For pressurised water reactors (PWRs), the largest attached pipe would be the pressuriser surge line whose diameter varies from about 8 inches to 14 inches. For boiling water reactors (BWRs), the area of the TBS break is the cross-sectional flow area of the larger of either the feedwater or the residual heat removal piping inside primary containment. The BWR TBS corresponds to a pipe diameter of approximately 20 inches.

Pipe breaks in the smaller break size region are considered much more likely than pipe breaks in the larger break size region. Consequently, each region will be subject to ECCS requirements commensurate with the relative likelihood of breaks in that region. LOCAs in the smaller break size region would continue to be “design basis accidents” and would continue to be analyzed by current methods, assumptions, and criteria.

In the design basis accident region, licensees must perform analyses under current ECCS requirements to determine the limiting size and location for breaks up to and including the TBS. Pipe breaks larger than the TBS, because of their lower likelihood, can be analyzed by the more realistic and less stringent analysis methods established in the new Paragraph 50.46a. Although LOCAs for break sizes larger than the transition break will become “beyond-design-basis accidents,” the proposed rule includes requirements ensuring that licensees maintain the ability to mitigate all LOCAs up to and including the double-ended guillotine break of the largest reactor coolant system pipe. Although these breaks must be mitigated, the methods and initial and boundary conditions used for the mitigation analysis may be more realistic. The analysis results must show that the core remains amenable to cooling. Licensees would be allowed to take credit for reliable non-safety related systems without assuming other independent failures. The specific metrics for demonstrating “coolable core geometry” are not necessarily limited to a peak cladding temperature of 2 200°F and less than 17% local cladding oxidation, as required for breaks smaller than the TBS. Licensees could use other metrics and acceptance criteria for demonstrating coolable core geometry if an adequate technical basis is provided to support the licensee’s proposal.

Licensees who perform LOCA analyses using the risk-informed alternative requirements may find that their plant designs are no longer limited by certain parameters from previous largebreak analyses. The new analyses could enable licensees to propose a wide range of design or operational changes. The intent of the proposed rule is that licensees use the revised Paragraph 50.46a to optimise safety system design and setpoints, and that overall implementation would result in a net reduction in risk to public health and safety. Nevertheless, the proposed rule would require that any increases in core damage frequency (CDF) and large early release frequency are themselves small and that plant baseline risk remains relatively small.

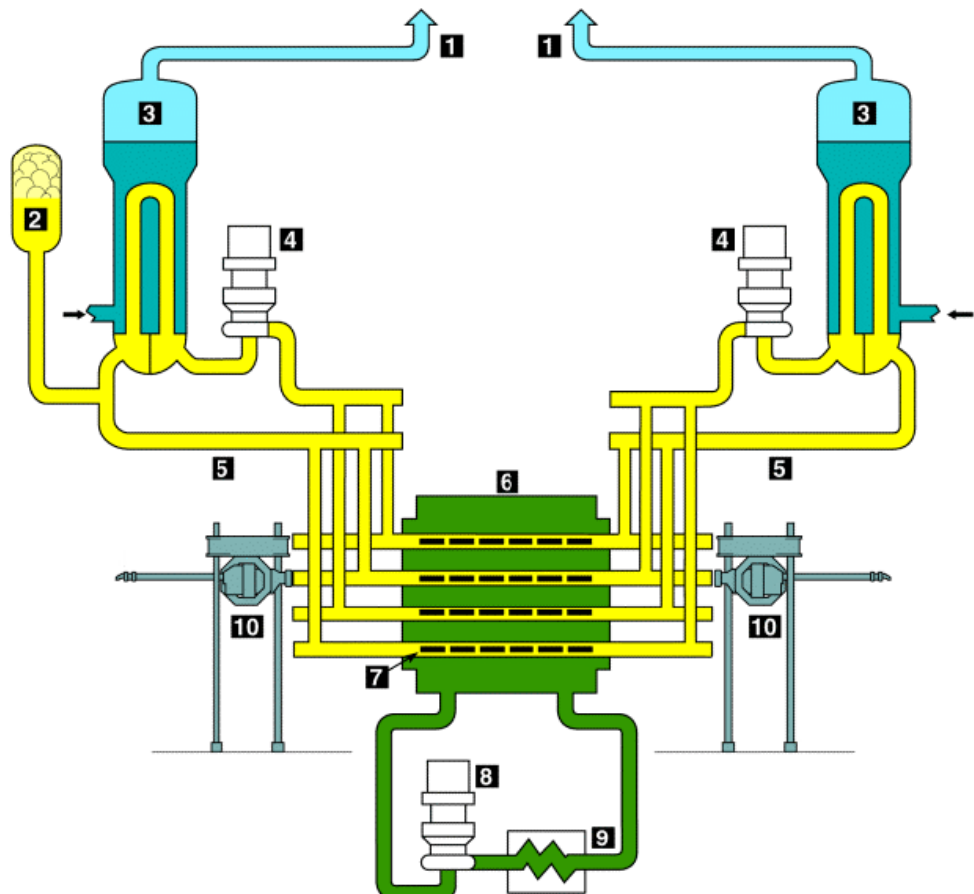
The NRC continues to pursue this regulatory development in this area. The current status may be found in “Rulemaking to Make Risk-Informed Changes to Loss-of-Coolant Accident Technical Requirements,” SECY-07-082 (May 2007).

## 2.4 CANDU reactor LOCA

The information in this section was provided by A.F. Williams and S. Sunder. In a CANDU reactor, the fuel is loaded into horizontal pressure tubes, and is cooled by the flow of pressurised

heavy water [3], Figure 2.4. The moderator is also heavy water contained in a calandria vessel. The pressure tubes pass through the calandria vessel and are separated from the moderator by a calandria tube and a CO<sub>2</sub> filled annulus. Coolant is supplied to the pressure tubes via a system of large headers and smaller feeder pipes. The moisture content of the CO<sub>2</sub> is continuously monitored and it provides early warning of any potential leak in the system.

Figure 2.4 A schematic of a CANDU primary heat transport system



**Legend:**

- |   |                                  |
|---|----------------------------------|
| 1. Steam line leading to electric turbines. | 6. Calandria vessel.             |
| 2. Pressuriser.                             | 7. Fuel channel.                 |
| 3. Steam generator.                         | 8. Moderator recirculation pump. |
| 4. Pumps.                                   | 9. Heat exchanger.               |
| 5. Inlet headers.                           | 10. Online refueling machines.   |

In broad terms, a LOCA in a CANDU follows a similar sequence to that described for a PWR. A break in the heat transport system initiates reactor shut down. There is an initial period of blowdown as the pressurised coolant vents from the system. As the coolant pressure drops, cooling is degraded and the fuel under goes a temperature transient. During this period, there is the possibility of fuel damage and the release of fission products to containment. Initiation of the emergency core cooling (ECC) system re-floods the reactor core, cooling the fuel and terminating the accident.

Despite these similarities with the PWR LOCA sequence, the horizontal pressure tube design and heavy water moderator mean that the details of the accident progression are quite different. In the CANDU-6 design, the coolant void reactivity is positive but the coolant void reactivity is negative in

the advanced CANDU reactor (ACR) design. The presence of the moderator around the fuel channels also plays an important role as a heat sink during the accident. Hence the determination of the pressure tube behaviour plays an important role in CANDU safety analysis.

LOCA type accidents are divided into two categories, according to the size of the break in the heat transport system.

#### **2.4.1 Large break LOCA**

A large break LOCA involves a break in the heat transport system pressure boundary of sufficient magnitude that the reactor regulating system (RRS) is incapable of maintaining reactivity balance. As the pressure tubes and feeder pipes are of relatively small diameter this type of LOCA can only be due to a break in the larger headers above the reactor core.

The initial phase of the accident (0-5 s) is characterised by a short power transient, which is terminated by either a neutron or process trip. The main safety concern for this short period prior to reactor trip is that the fuel temperature might rise sufficiently high for the formation of molten UO<sub>2</sub>, which could potentially cause pressure tube rupture. In turn the resulting hot spots in the pressure tube could result in localised straining and possible failure of the pressure tube. In practice, this safety concern is not realised as the fuel is cooled by the flow of coolant resulting from the blowdown.

The second phase of the accident (5-30 s) is characterised by the blowdown and depressurisation of the fuel channel prior to ECC injection. Despite the reactor shutdown, fuel temperatures may remain high due to the degradation in cooling, decay heat and oxidation of the fuel sheath. The fuel sheath may undergo significant deformation and may fail releasing fission products to the fuel channel and subsequently to containment. During this phase, the temperature of the pressure tube also rises and the pressure tube deforms into contact with the calandria. Once the pressure tube is in contact with the calandria tube, the moderator acts as a heat sink, cooling the pressure tube and preventing failure of the fuel channel.

The third phase of the accident (30-200 s) is characterised by the initiation of ECC. During this period, ECC is being injected into the primary heat transport system, but has not yet reached sufficient levels to effectively cool the fuel. Depressurisation of the heat transport system continues and stored heat and decay heat from the fuel is radially removed to the moderator through the pressure tube and calandria tube. Fuel failures are likely during this stage of the accident.

During the fourth and final phase of the accident (>200 s) the injection of ECC has reached a level where it can effectively cool the fuel. The heat transport system pumps have tripped, refill of the channels in the core proceeds and a quasi-steady state is attained.

#### **2.4.2 Small break LOCA**

A small break LOCA refers to a break where the reactor regulating system is capable of preventing a significant power excursion. A small LOCA may occur due to a break in a header or other heat transport pipes such as feeders and steam generator tubes. Because the range of possible locations of a small break LOCA is far wider than that of a large break LOCA, the safety analysis is more complex. Small break LOCAs are divided into categories depending on the location and type of break.

A special class of small LOCA events are single channel events involving breaks in the primary heat transport system up to the size of the largest feeder. Breaks may occur spontaneously or may be a consequence of flow blockages within a fuel channel. Single channel events may occur outside of the core or within the core. Breaks within the core fall into two categories. In one category, only the

pressure tube fails, leading to steam discharge to containment via the annulus between the pressure tube and calandria. In the other category both the pressure tube and calandria may fail in which case the discharge is ultimately to containment via the moderator.

The following general features characterise a single channel event or small break LOCA:

1. A modest power excursion to approximately 105% of full power is possible, driven by rapid coolant voiding in the affected channel. Reactor shut down systems may not detect the failure immediately so that the reactor continues to operate at or slightly above full power.
2. A low rate of coolant discharge from the break into containment, moderator and other reactor subsystems, such as the steam generator secondary side, occurs, depending on the break location.
3. There is limited potential for pressure tube deformation from early impairment of fuel cooling.
4. Fuel failures occur in the affected channel in the case of flow blockages or flow stagnation.
5. Significant increases in heat load to the moderator via the coolant discharge are possible in the event of channel failure.
6. For very small breaks, the reactor could be shutdown manually and the heat transport system cooled in a controlled manner to avoid the necessity for ECC injection.
7. An over pressure period in containment develops during which there can be a pressure driven release outside of containment. Maximum pressure tends to be lower than for large break LOCA due to the lower discharge rate.

## 2.5 VVER reactor LOCA

The VVER reactors are a type of pressurised water reactors. However they differ from the PWRs discussed in Section 2.1 in a few respects [4]. For instance, the VVER-440 reactors differ from the PWR in the following respects:

- Six loops of primary circuit.
- Loop seals in hot legs.
- Horizontal steam generator with two headers.
- Elevation of the top of steam generators tubes related to the top of the active (about 4 m, PWR about 10 m).
- Shrouded fuel assemblies with hexagonal fuel rod arrangement.
- ECCS injection points.
- Secondary side water volume in steam generators compared with nominal thermal core power is larger.
- Two isolation valves in each main loop.
- Special pressure suppression system (bubble condenser).
- Each control rod consists of two parts: lower fuel assembly and upper absorber.
- Lower plenum volume larger and different internal structures.

The VVER-1000 plants are equipped with ECCS (emergency core cooling system) and containment spray systems that have a similar design basis and basic configuration as in western PWRs. These systems have 3×100% redundancy with the exception of the ECCS water storage tank, which is common to all subsystems. The same tank serves as a containment sump. The tank is located under the containment and has open connections to the containment through the bottom plate:

- Four loops of primary circuit.
- Horizontal steam generators with 2 headers.

- ECCS injection points.
- Secondary side water volume of the steam generators compared with the nominal thermal core power is larger.
- Lower plenum internal structures.
- Fuel assemblies with hexagonal fuel rod arrangements.

### **2.5.1 Large break LOCA**

A guillotine break of the VVER-1000 reactor main circulation pipeline (diameter 850 mm) at the reactor inlet is considered an initiating event of a LB LOCA.

It is conservatively assumed that simultaneously with the main circulation pipeline break occur also: loss of unit power supply, loss of steam removal to turbine and tripping of the main circulation pumps. Steam pressure in steam generator rises.

A break of the large diameter primary pipeline resulting in the blow-out of large quantities of coolant leads to a pressure drop in the primary circuit and core dewatering. Consequently, the heat removal from the core worsens and temperature of the fuel cladding rises sharply with the rate of approximately  $10^2$  K/s (due to the heat accumulated in the core).

When the primary circuit parameters reach the corresponding setting points (in 0.01 s after the accident started) the emergency protection signal is actuated. As a result of decreased coolant density in the core and the emergency protection system response, the reactor power decreases up to the residual heat level.

The boric acid solutions needed for emergency core cooling are supplied by the emergency core cooling system (SAOZ) – ECCS, which includes:

- High-pressure safety injection system (HPSI).
- ECCS passive part (pressurised accumulator tanks).
- Low-pressure safety injection system.

When the primary circuit pressure becomes lower than the gas pressure in accumulator tanks (in 7-9 s after the accident started), the non-return valves (check valves) on the connecting pipelines open, and boron solution is fed into the reactor. It results in a partial core flooding; the temperature rise on fuel cladding stops (for the fuel assembly with the maximum calculated power the first peak is approx. 1 000°C, for a group of fuel elements (assemblies) with higher heat flux density – approx. 900°C). (Group of fuel elements resp. assemblies with higher heat flux density is composed of assemblies with the relative power 1.2-1.4 and burn-up up to approx. 37 MWd/tU.) The coolant pressure at the approximately same time becomes lower than the inner pressure in fuel elements (in 3-9 s after the accident started, depending on burn-up). Thus, depending on combination of the temperature-loading conditions during the accident first phase, is possible both – cladding collapse to the fuel column and its swelling/ballooning up to rupture.

After lapse of time needed for the safety systems actuation and preparation for action (not more than 40 s after the accident started), the pumps of high- and low-pressure injection systems start to feed boron solution into the primary circuit.

When the boron solution volume in accumulator tanks drops below acceptable level (after 53-58 s after accident started), the shut-off valves are triggered, the boron solution supply from the tanks is cut – to preclude gas getting into the primary circuit; further cooling is ensured by emergency injection systems. During such regime the cladding temperature of fuel elements with high heat rate/linear

power may rise with the rates of 1-5 K/s (due to residual heat). The temperature maximum can be reached in 100-200 s after the accident started, and its value can be approx. 1 100°C for the fuel assembly with the maximum calculated power and approx. 950°C for a group of fuel elements (assemblies) with higher heat rate/linear power. When cladding temperature becomes higher than 800°C, the cladding balloons and high heat rated fuel rods burst.

Cladding oxidation kinetics is complex due to non-stationary temperature regime, cladding deformation and loss-of-tightness, etc. According to conservative computations, ECR of fuel elements/assembly with maximum calculated power can reach  $\approx$  5%. In a group of fuel elements with higher heat rates, ECR can reach 1%.

According to computational assessments the share of oxidized zirconium in the core is not higher than 0.1-0.2% of its total mass in fuel claddings usually.

Core re-flooding is finished in 200-400 s after the accident started (depending on the calculation scenario). Estimates of cladding oxidation state allow to say with confidence that fuel elements will withstand thermo-mechanical loads during reflooding.

A guillotine break of the VVER-440 reactor main circulation pipeline (diameter 500 mm) at the reactor inlet is considered an initiating event of a LB LOCA.

Since the linear heat rates in VVER-440 are significantly lower than in VVER-1000, the main thermo-mechanical and corrosion/oxidation characteristics/damage levels of fuel elements during an VVER-440 accident are much lower than for VVER-1000.

Computational assessments of PCT for the fuel assembly with the maximum calculated power are not higher than 900°C, ECR – not higher than 1%. For a group of fuel elements (assemblies) with high heat linear rating, computational assessments of PCT are not higher than 700°C, ECR – not higher than 0.1%; under these circumstances **ballooning and cladding failure are not expected**.

### **2.5.2 Small break LOCA**

A small leak break of the VVER-1000 primary pipeline of a small diameter or the main circulation pipeline rupture (equivalent diameter  $\leq$  100) is considered an initiating event of a Small Break LOCA.

According to the SB LOCA thermohydraulic calculations, the departure from nucleate boiling can occur only on the fuel elements with the highest heat flux density/linear heat rates, its duration and PCT level are significantly smaller than in LB LOCA. Consequently ECR is also significantly lower; **ballooning and cladding failure are not expected**.

## **2.6 References**

1. Boyack, B.E., *et al.*, "Phenomenon Identification and Ranking Tables (PIRTs) for Loss-of-Coolant Accidents in Pressurised and Boiling Water Reactors Containing High Burn-up Fuel", Los Alamos National Laboratory, U.S. Nuclear Regulatory Commission, NUREG/CR-6744,LA-UR-00-5079, December 2001.
2. Rininsland, H., *et al.*, "Stand der Reaktorsicherheitsforschung in Projekt Nukleare Sicherheit", KfK Jahreskolloquium, 1982.
3. Hart, R.S., "CANDU Technical Summary", Atomic Energy of Canada Limited, October 1997.
4. Valach, M., Private communication. 2006.

### **3. STATE OF FUEL AND CLADDING AT VARIOUS BURN-UP LEVELS**

This section is basically cut and pasted from Appendices G and H of the PIRT report [1], separate contributions on CANDU fuel and MOX fuel. Some editing was done since the PWR fuel description addressed fuel behaviour during RIA transients while the BWR fuel description addressed fuel behaviour during power oscillations. It may be assumed that fuel behaviour in other types of water-cooled reactors with UO<sub>2</sub> fuel and zirconium base alloy cladding is sufficiently similar to these two types so that further descriptions are unnecessary. However, a section on MOX fuel has been added

The extended operational exposure that accompanies high burn-up causes changes to the fuel and cladding that may affect the fuel rod's ability to withstand the accident without losing its integrity (Figure 3.2). These changes, which occur gradually over the life of the fuel rod, can be considered as initial conditions for the accident.

There are many changes that occur to the fuel and cladding as a result of prolonged exposure to the irradiation field present in a reactor core, and to the corroding environment and high temperature. The combination of high temperature, radiation damage, transmutations, mechanical stresses and chemical reactions causes the microstructure of cladding and fuel to evolve considerably during reactor exposure. These changes in microstructure, microchemistry, and macroscopic characteristics of pellet and cladding are responsible for the changes in material behaviour observed at high burn-up. These changes are very complex and difficult to predict in a mechanistic fashion. Of the many changes to the fuel and cladding, it is important to discern which are of greatest importance to determining fuel rod behaviour during LOCA. Some of the more important material degradation phenomena are listed below, recognising that the list may not be inclusive. The changes to the fuel and cladding are important to both pressurised water reactor (PWR) and boiling water reactor (BWR) fuel types. While the state of fuel is more or less identical for PWR and BWR fuel and can thus be treated together, there are significant differences for the claddings which make it necessary to treat them in separate sections.

#### **3.1 State of fuel at various burn-up levels**

##### **3.1.1 UO<sub>2</sub> fuel**

###### *Fission Products*

During normal operation, solid and gaseous fission products are generated within the UO<sub>2</sub> fuel pellet. Whereas the solid fission products generally remain at the birthsite, the gaseous fission products are more mobile and distribute largely into five separate inventories: (i) gas dissolved in the UO<sub>2</sub> matrix, (ii) gas in intragranular (matrix) bubbles, (iii) gas in intergranular (on grain boundaries) bubbles (iv) gas released to the fuel rod void volume and (v) gas in fuel porosity. The amount of gas dissolved in the UO<sub>2</sub> matrix is limited by the solubility in UO<sub>2</sub>. Solid fission products result in a progressive swelling of the fuel material with irradiation exposure. Gaseous fission product inventories (iii), and to a lesser extent (ii) and (v), under high temperature low restraint conditions, can also result in fuel swelling with consequent pellet-cladding contact. Ramp experiments on high burn-up fuel have demonstrated that in connection with a temperature increase a transient swelling may occur which can deform the cladding. Inventory (iv) is referred to as fission gas release (FGR) and

produces an increase in the fuel rod internal pressure and corresponding cladding loading. The exact partitioning of the fission gases among the identified inventories is dependent primarily on the fuel pellet microstructure and thermal operating history.

#### *Rim formation*

Because of U-238 resonance neutron capture near the  $\text{UO}_2$  pellet surface, the amount of Pu formed in the fuel is greater at the edge of the pellet than in the centre. This causes the fission rate near the pellet surface to slowly increase with burn-up while the fission rate in the bulk of the pellet decreases. The ratio of fission at the edge of the pellet to the centre may be as high as 3 at high burn-ups. Such a region is called the **rim region** and its thickness is approximately 100 to 300 microns. The rim region is formed when the local burn-up at the rim exceeds approximately 60 GWd/t (40-45 GWd/t radial averaged). The **rim region** has a characteristic microstructure that consists of sub-micron size grains with bubbles under high gas pressures and has high porosity (20-30%). Some of these bubbles may be in non-equilibrium with the matrix because there are large strain fields around the smaller bubbles and there is further evidence that they exist within the interior of the pellet as well as on the rim if the irradiation temperatures are low.

The main concern with the formation of the rim region concerns its effects on the amount of fission gas loading, and the relocation or dispersal of fuel during a LOCA.

#### *Fuel restructuring and macrocracking*

During the initial rise to power, the thermal stresses caused by the pellet radial temperature gradient cause the pellet to crack (primarily radially). With the release of strain energy, the cracked pellet segments relocate outwards toward the cladding (called fuel relocation or restructuring). With continued irradiation, additional outward movement of the pellet segments can occur. At ~mid-life exposures, the combined effects of pellet relocation, fuel irradiation swelling, and cladding creepdown result in a closed pellet-cladding gap. From this point, (1) a reduction in the fuel pellet expansion (such as caused by a power decrease) can result in partial gap opening, and (2) additional fuel expansion (by progressive fuel swelling or as a result of a power increase) can cause pellet radial cracks to (partially) close, thereby increasing the effective pellet stiffness, and imposing loading and deformation of the cladding. No particular change in this behaviour is expected at elevated exposures.

#### *Pellet-Cladding Interface*

With the onset of pellet-cladding contact, a bond layer develops between the fuel pellet and the cladding. Pellet-cladding bonding is thought to progress as oxygen atoms inter-diffuse between cubic  $(\text{U},\text{Pu})\text{O}_2$  and cubic  $\text{ZrO}_2$  which is formed under irradiation. At elevated exposure, the magnitude (bond layer thickness) and extent (circumferential and axial surface coverage) increases. The development of this bond layer inhibits the ability of the pellet and cladding to move independently, and thereby affects load transfer from the pellet to the cladding and the subsequent cladding stress state. Pellet-cladding bonding is conducive to a smaller clad ballooning strain under otherwise similar conditions. The bond layer can fracture during cooldown or power reductions, leading to an intermediate state.

One important fuel property with regard to LOCA is obviously the fission gas release since it directly affects the internal pressure and consequently the ballooning behaviour of the fuel. Another is the fuel-cladding bonding layer as a source of oxygen during a high temperature accident.

#### **3.1.2 MOX fuel and high burn-up $\text{UO}_2$ fuel (Contributed by J. Papin)**

The high burn-up fuel is characterised by a quasi-closed gap, with a more or less pronounced bonding between fuel and internal zirconia layer, and a high fission gas retention; this high fission gas

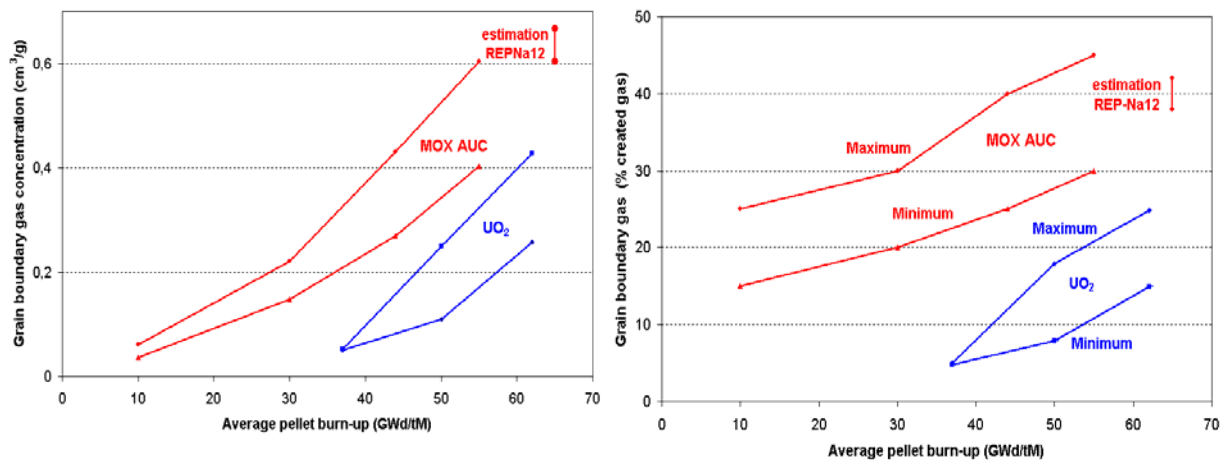
content results from a low gas release under normal operating conditions and increases quasi-linearly with burn-up. Furthermore, in irradiated fuel, a significant increase of the gas volume located inside pores and bubbles at the grain boundaries (called “grain boundary – GB gases”) occurs with the formation of the typical High Burn-up Structure (HBS), in the rim zone of high burn-up UO<sub>2</sub> fuel and in the (U,Pu)O<sub>2</sub> clusters of the MOX MIMAS fuel, which initially concentrate almost all the fissile material. This MOX heterogeneous structure results from its fabrication process that blends 25-30% enrichment Pu particles (mixture of UO<sub>2</sub> and PuO<sub>2</sub> powders with average particle sizes ranging up to several tens of micro-meters) into a depleted UO<sub>2</sub> matrix. That leads to two phases in the fresh fuel microstructure of the MIMAS/AUC (Ammonium Urano-Carbonate) type MOX: the (U,Pu)O<sub>2</sub> agglomerates with a Pu content of about 27% and the UO<sub>2</sub> matrix that contains some residual Pu.

The formation of high burn-up fuel structures starts at a local burn-up of about 70-80 GWd/tM, and is fully developed at a local burn-up of about 120 GWd/tM. It is characterised by the subdivision of the original grains, the depletion of intra-granular gas inventory, and the development of a high porosity (up to approximately 20%) in the form of over-pressurised micrometer size pores that contain a major portion of the created gases. In UO<sub>2</sub> fuels, this microstructure change appears in the outer cold zones of the high burn-up UO<sub>2</sub> fuels above an average pellet burn-up of about 40 GWd/tM, and is well established on a peripheral layer of 100 µm width at an average pellet burn-up of approximately 60-65 GWd/tM. In MOX fuels, the “rim structure” or HBS is clearly observed earlier, above a mean pellet burn-up of about 30 GWd/tM, with a measured local burn-up in the (U,Pu)O<sub>2</sub> agglomerates of 100-160 GWd/tM, depending on the initial enrichment. However, only the agglomerates of a significant size (higher than the recoil distance of fission gas atoms – 7 to 9 µm) are involved; the others contribute to the increase of gas retention in the MOX fuel matrix and probably to some accumulation of fission gases at inter-granular sites.

There is substantial experimental evidence from RIA tests and also during heating ramps in out-of-pile annealing tests simulating LOCA transients [2-4] that the grain boundary gas can be easily available for release during heat-up transients. The grain boundary gas contribution to transient fuel swelling is obvious in the case of no or low external constraint (NSRR tests [5] and annealing tests [2-3]), in relation with the fission gas release that may influence the rod internal pressure under LOCA transients. The grain boundary gas inventory is probably one of the more relevant parameters to predict the high burn-up fuel behaviour during accidental events, either in RIAs and LOCA since it may contribute significantly to transient fuel swelling and gas release.

Some estimates of the GB gas content in irradiated UO<sub>2</sub> and MOX fuel can be obtained from the few microprobe measurements presently available that have been performed on various samples coming from rods irradiated in French commercial reactors up to 60-65 GWd/tM. In microprobe analysis, only Xenon in solution or precipitated in micro-bubbles ( $\leq 100$  nm) within the fuel matrix can be detected. Microprobe results show that the difference between the detected gas and the calculated formation increases with burn-up, and is higher than the gas released during the irradiation. Therefore, the surplus corresponds to the gas accumulated in porosities (as-fabricated pores or pores resulting from irradiation) and to the gas precipitated into inter and intra-granular micro-bubbles of a large size. This last part can be neglected, as examinations by optical microscopy (OM) and scanning electronic microscopy (SEM) do not show significant intra-granular precipitation inside the grains of the fuel matrix in the range of examined burn-up. Finally, an upper bound of the grain boundary (GB) gas content (averaged on the pellet) in irradiated fuel can be deduced from the microprobe results, taking into account the local gas release. Typical results are plotted in Figure 3.1 in fraction of creation, and in cm<sup>3</sup> (Xe+Kr) STP/g versus burn-up.

Figure 3.1 Grain boundary gas versus pellet burn-up in  $\text{UO}_2$  and MOX fuel  
(left: ratio from created gas, right: concentration)



In spite of the large scatter observed in the results, it appears clear that, at similar burn-up levels, the GB gas concentration is much higher in MOX fuel than in  $\text{UO}_2$  fuel, mainly in the range of low and medium burn-up. This relative difference decreases in the high burn-up range, due to the decreasing influence of clusters in MOX fuel, and to the increasing rim formation in the  $\text{UO}_2$  fuel. The major part of this GB gas content is contained in the large pores of the irradiated fuel (as-fabricated pores or pores resulting from irradiation with a strong contribution from the HBS zones). In high burn-up  $\text{UO}_2$  fuel (60-65 GWd/tM), the contribution of the rim zone to the total GB gas quantity is about 50% (mainly located in large pores under high pressure – 50 to 100 MPa), and represents approximately 8-10% of the pellet total retention. In MOX fuel, the major part of GB gas is located in the large over-pressurised pores inside the  $(\text{U},\text{Pu})\text{O}_2$  agglomerates. Furthermore, from both “experimental” and “theoretical” estimations [5], it has been concluded that the GB gas fraction increased with initial Pu enrichment, as soon as the agglomerates have reached the full restructuration threshold.

### 3.2 State of cladding

The difference in operating temperature between PWR and BWR has a significant effect on the state of cladding in the two types of reactors. It is therefore appropriate to treat PWR and BWR cladding separately.

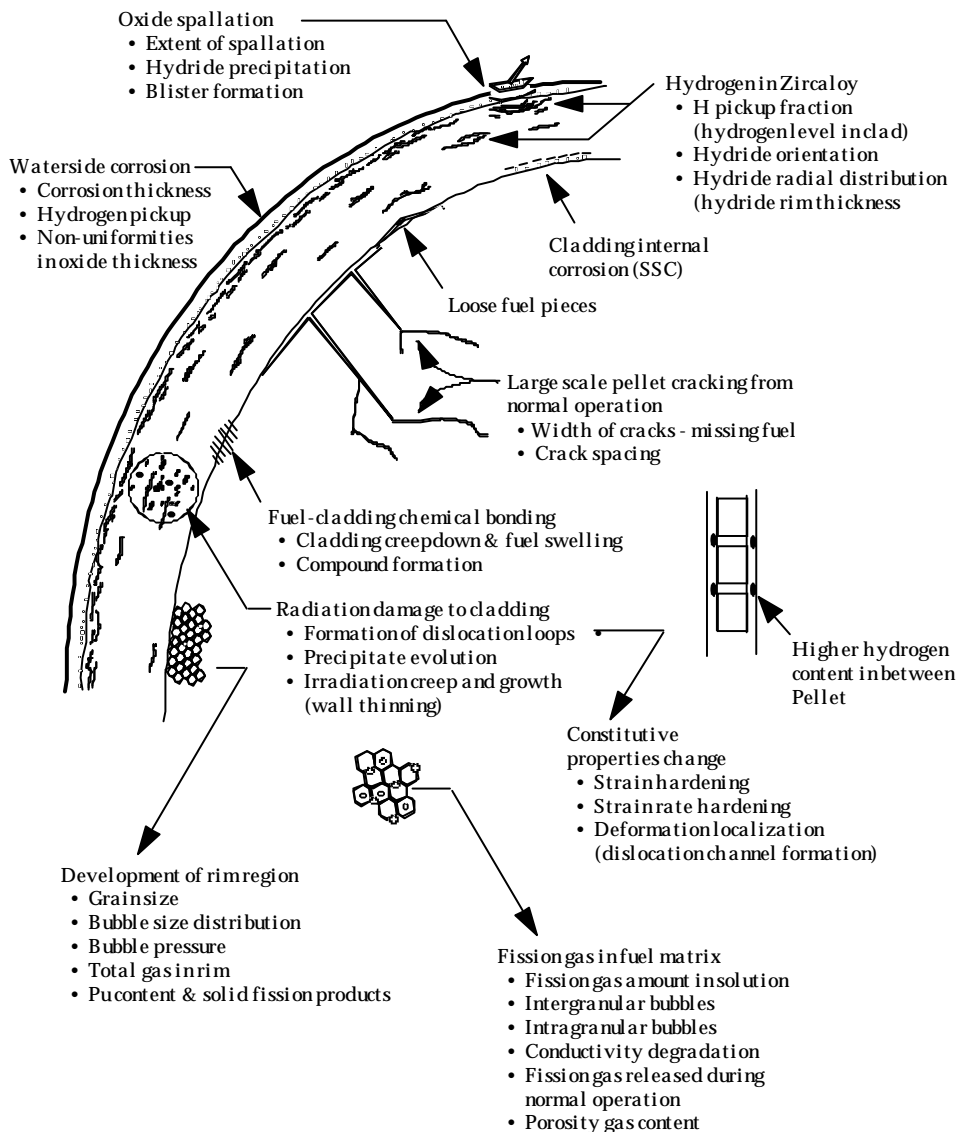
#### 3.2.1 PWR cladding

In early years PWR cladding was almost exclusively fabricated from Zircaloy-4. Recently however Zircaloy-4 has largely been replaced by Zr-Nb-Sn (Zirlo) and Zr-Nb (M5) alloys. In VVER reactors similar Russian alloys (E635 and E110) are also used. The Nb alloyed claddings are characterised by significantly lower corrosion rates than Zircaloy-4 and consequently also lower hydrogen pickup rates. The main degradation mechanisms to PWR cladding include uniform waterside corrosion, hydriding, and radiation damage.

**Uniform waterside corrosion** occurs throughout the reactor exposure. Uniform corrosion in the present context means primarily that the waterside oxide layer is more or less uniform with respect to circumferential direction; the oxide layer varies in fact strongly with respect to grid span (axial direction). The corrosion rates depend on many factors including alloy chemistry and thermomechanical treatment, coolant chemistry, radiation-induced changes to cladding microchemistry, and irradiation temperature. For cladding with burn-ups in excess of 50 GWd/t, the oxide thickness can exceed 100  $\mu\text{m}$  depending on fuel duty, i.e., power and temperature versus time and burn-up.

**Figure 3.2 PWR fuel state at high burn-up**

BWR fuel has a similar state with the exception of the oxide layer which is thinner and with less total pickup of hydrogen in the metal



The burn-up level at which any given oxide thickness is reached for a given alloy is dependent on the fuel duty. The more modern alloys such as ZIRLO and M5, can have lower corrosion rates than standard Zr-4 and low-Sn Zr-4 at similar burn-up. All of the zirconium alloys examined to date show a transition in corrosion rate when the oxide exceeds a certain thickness (20 to 30  $\mu\text{m}$  in thickness), which indicates a change in corrosion regime, termed **breakaway corrosion**. Therefore, it is likely that even the new modern alloys such as ZIRLO will eventually experience breakaway corrosion. The question with the new modern alloys is the burn-up level at which breakaway corrosion will occur.

A fuel rod that experiences a high fuel duty will experience breakaway corrosion at a lower burn-up level than a fuel rod with a lower fuel duty. One of the concerns with large oxide thicknesses is the higher probability of **oxide delamination**, whereby portions of the oxide layer are detached from the adherent oxide creating an oxide region with worse heat conduction characteristics. Ultimately the detached oxide can break off (**oxide spalling**) creating a thinner oxide. The associated temperature gradients created by

spalling have been shown to influence hydride blister formation in the spalled region [6]. The hydride blister is brittle, and its presence has been shown to affect overall cladding ductility.

The main concerns associated with excessive uniform corrosion are: (a) potential for oxide spalling resulting in hydride blisters, which affect the overall cladding ductility, (b) loss of thermal conductivity, (c) non-uniform wall thinning (non-uniform oxide), (d) overall wall thinning, and (e) excessive hydrogen uptake and hydriding in general. Excessive levels of oxide layer thickness and hydriding in PWR fuels play major roles in high-burn-up LOCA situations.

Local variations in the degree of oxide thickness, oxide spalling, hydride blisters, metal wall thinning, and a hydride rim are conducive to a greater circumferential temperature variations during cladding ballooning under LOCA conditions, which is conducive to a smaller ballooning and smaller burst opening.

**Hydriding** occurs as hydrogen is absorbed into the cladding as a result of the cladding uniform corrosion (roughly 15 to 20% of the hydrogen generated by the corrosion reaction is absorbed into the alloy). Clad H/D pickup is influenced by coolant chemistry (e.g., H concentration), neutron fluence, coolant/clad temperatures and clad properties [7]. The hydrogen precipitates as hydrides throughout the cladding thickness at corrosion thicknesses greater than 50 microns. When the overall hydrogen level is high enough (>2 000 ppm), the cladding is brittle when tested at operating temperatures. Lower levels of hydrogen (600-800 ppm) affect cladding ductility at low temperature.

However, lower levels of hydrogen, can also degrade the overall cladding ductility depending on the hydride distribution. The mobility of hydrogen is high, and its solubility in Zircaloy is very low, so hydrogen will tend to precipitate out in any cold spot formed in the material. For example, there is a much greater hydride concentration near the surface of the cladding creating a **hydride rim** with local hydrogen levels higher than about 1 000 ppm. In addition to being radially localised, the axial distribution of hydrogen is also non-homogeneous, with greater concentration in the region in-between the fuel pellets due to the slightly lower heat fluxes and lower temperatures at pellet interfaces.

The main concerns associated with hydriding are: (a) lower ductility and/or embrittlement resulting from an overall change in constitutive properties, (b) creation of weak spots in cladding resulting from the formation of a hydride rim, and/or hydride blisters, and (c) a sub-critical crack growth phenomenon due to precipitation and cracking of hydrides at a loaded crack tip, delayed hydride cracking (DHC) [8], observed in connection with power ramps.

**Radiation damage.** When irradiated to 30 GWd/t (corresponding to a fast fluence of  $\sim 10^{22}$  n/cm<sup>2</sup>, E>1 MeV) the cladding suffers an amount of radiation damage calculated at about 20 dpa (displacements per atom) [9]. The dpa level is roughly proportional to the fluence or burn-up, so that 60 GWd/t corresponds to about 40 dpa and 75 GWd/t to 50 dpa. This very high level of displacements is translated mostly into radiation-induced dislocation loops, both <a> and <c> type that form from the agglomeration of point defects. Although the overall <a> dislocation density saturates after about one month of reactor irradiation, the <c> type dislocations evolve over a more extended period of time. In addition there are microchemical changes in the alloy related to irradiation-induced amorphisation and dissolution of intermetallic precipitate, which can **change normal corrosion resistance** and hydrogen pickup. However these latter changes are more important at BWR operating temperatures.

The **constitutive response** of the cladding is also affected by the radiation damage, in particular by the dislocation loops formed under irradiation. The yield stress increases, and the uniform strain decreases, i.e. the material undergoes **hardening** and ductility decrease. The increase in dislocation loop density decreases the strain hardening coefficient of the material. At the microscopic level, these loops can also influence deformation localisation (dislocation channeling); the effects of these

microscopic processes on macroscopic deformation and failure are not clear at the moment. There is also **cladding creepdown**, which can cause the gap to be closed, creating the conditions for fuel-clad chemical bonding to develop. Another phenomenon related to irradiation creep is bundle bowing due to excessive compressive forces on the bundle structure.

The main concerns relating to radiation damage are (a) radiation hardening and possible embrittlement, (b) change of corrosion resistance through microchemical changes, (c) mechanical property changes and (d) deformation localisation (e.g dislocation channeling, possibly leading to easier axial crack propagation).

However, the impact of these phenomena on the LOCA behaviour is varied. The most important phenomenon with regard to LOCA is probably hydrogen uptake. Hydrides are rarely observed in the prior beta layer after LOCA-typical slow cool-down and quenching. But redistributed hydrogen atoms in the beta layer from dissolved hydrides at  $>100^{\circ}\text{C}$  leads to significantly increased oxygen level in the prior beta, thereby significantly exacerbating post-quench embrittlement of the cladding. The presence of a thick oxide itself is probably less of a problem as will be clear later in the present report. The importance of radiation damage is minimal since most of the damage will have been annealed out well before the cladding reaches  $800^{\circ}\text{C}$ . Irradiation creep as it affects bundle bowing may have some impact on clad ballooning and burst behaviour during LOCA, since it changes both the geometry of the core and the power distribution in the core.

### 3.2.2 BWR cladding

The cladding material applied in BWRs is Zircaloy-2, mostly in annealed and fully recrystallized condition with a zirconium-based inner liner, although cold-worked stress relieved material and non-liner applications also exist. The zirconium liner can contain varying amounts of alloy additions, which is intended for post-defect corrosion resistance. Similar to PWR fuel cladding, primary effects of BWR operation are waterside corrosion, hydriding, and radiation damage.

**Cladding corrosion** occurs through direct exposure of the cladding outer surface to a high temperature, highly oxidizing environment enhanced by the radiation field. The effects of cladding corrosion are wall thinning, increased heat transfer resistance, and cladding hydrogen absorption. In general, the BWR suppliers have progressively refined the cladding fabrication process to minimise the occurrence of nodular corrosion, thereby resulting in a more uniform corrosion these days. Whereas large cladding corrosion occurs typically at higher grid span elevations in PWRs, the corrosion distributions are generally flatter along the fuel rod length in a BWR, with possible peaking at the lower elevations. Circumferential variations in cladding oxide layer thickness are observed in BWRs, but are generally minor in magnitude. Whereas cladding corrosion thicknesses of up to or greater than  $100\ \mu\text{m}$  has been observed in PWRs, BWR cladding corrosion is significantly less, typically less than  $50\ \mu\text{m}$  at exposures up to  $\sim 62\ \text{GWd/MtU}$  peak rod average exposure.

An important consideration is oxide layer cracking, delamination, and spalling. Oxide layer cracking and delamination can lead to an acceleration in the oxide layer growth rate. Spalled oxide regions result in a cooler cladding metal temperature during operation than exists under the adjacent unspalled oxide regions. The presence of such “cold spots” can promote redistribution of any hydrogen absorbed from the cladding outer surface corrosion process, thereby leading to hydride localisations and even bulk hydride formation (observable as bulges or blisters) in the outer region of the cladding. Such bulk hydride formation regions are highly embrittled and are often accompanied with partial cladding cracks even in the absence of applied loading by the fuel pellets. This is caused by the volume expansion associated with the conversion of zirconium to zirconium hydride. Whereas significantly accelerated corrosion and oxide layer spalling have been observed in PWRs, similar conditions are rarely observed in BWR fuels with modern cladding materials.

Corrosion localisations have been observed near fuel assembly spacer locations, adjacent to Inconel components (typically referred to as “shadow corrosion”). Accelerated localised corrosion, leading to fuel rod failure, has occurred at one BWR with an earlier cladding material type. This type of corrosion localisation develops relatively quickly, but then remains relatively stable for modern BWR claddings, at least to exposure levels up to ~62 GWd/MtU

BWRs operate with several water chemistry options: Hydrogen Water Chemistry, Zinc Injection, and Nobel Metal Chemical Addition. To date, unacceptable changes in the cladding corrosion performance have not been observed under these water chemistry options.

In summary, for modern BWR cladding, the primary corrosion-related effects are: (1) wall thinning, (2) decreased heat transfer, and (3) hydrogen pickup.

**Hydring** occurs as hydrogen, liberated by the cladding outer surface corrosion process, is absorbed into the cladding. For a typical BWR cladding, less than 20% of the hydrogen generated by the corrosion reaction is absorbed by the cladding. This absorbed hydrogen precipitates mostly as circumferential hydride stringers when the amount of absorbed hydrogen exceeds the solubility level. Available testing has demonstrated no adverse influence of hydrogen on elevated temperature irradiated Zircaloy ductility (total elongation) for hydrogen contents up to at least 850 wppm [10]. At higher hydrogen levels, e. g. in excess of 1 000 ppm, the cladding ductility can be reduced at operating temperatures. Typically, modern BWR cladding contains <200 wppm hydrogen at ~50 GWd/MtU rod average exposure. Although higher levels (up to ~600 wppm) have been observed in older cladding types at elevated exposures (up to ~65 GWd/MtU rod average exposure), even this level is below that required to significantly affect the cladding mechanical properties.

With the generally lower hydrogen concentration observed in BWR fuel cladding, PWR-like dense hydride rims or extreme localisations at pellet-pellet interfaces are not typically observed, although the tendency of hydride accumulations toward the cladding outer surface or near pellet-pellet interfaces has been observed.

Another consideration, although not typically observed in either PWR or BWR applications is the development of radially oriented hydrides, which, in significant concentration, could affect the cladding ductility near operating temperatures.

In summary, for BWR fuel, the primary concerns related with cladding hydring are: (1) the impact on cladding mechanical properties, and (2) hydride localisations conducive to producing weak, damage-susceptible regions. However, these effects have not been found to be significant for the hydrogen contents observed in modern BWR cladding to date. Sub-critical crack growth due to the DHC phenomenon has been observed in BWR cladding in connection with power ramping.

**Radiation damage** to the cladding material occurs as a direct consequence of exposure to fast neutrons. Radiation damage is manifested as radiation-induced dislocation loops, both  $\langle a \rangle$  and  $\langle c \rangle$  type that form from the agglomeration of point defects. Although the overall  $\langle a \rangle$  dislocation density saturates very early in life, the  $\langle c \rangle$  type dislocations evolve over a more extended period of time. The effect of this damage is a strengthening of the material, with a corresponding reduction in ductility, and increased irradiation-induced stress-free growth (which occurs in the absence of an applied stress). Additionally, microchemical changes occur as irradiation induces amorphisation and dissolution of intermetallic precipitates, which can alter the mechanical properties, corrosion resistance and possibly also the hydrogen pickup of the cladding material.

In addition to irradiation-induced growth of the cladding material, irradiation also induces cladding creep in response to the applied fuel rod internal-external pressure difference and pellet expansion loadings.

In summary, the primary considerations relative to cladding radiation damage are (1) radiation hardening and the corresponding impact on mechanical properties, and (2) deformation caused by irradiation-induced growth and creep.

Out of these factors, only hydriding and hydrogen in solution are expected to have any significance for the LOCA behaviour of BWR cladding. In an unlikely case that fresh or low-burn-up BWR fuel is heated to a sufficiently high temperature so that cladding ballooning and burst occur, the Zr liner may exacerbate breakaway corrosion and hydrogen absorption from the inner surface near the burst opening.

### 3.3 High burn-up CANDU fuel (contributed by M. Floyd and S. Sunder)

A brief description of the design of CANDU reactors is given in Section 2.4 of this report. CANDU reactors use UO<sub>2</sub>, containing natural abundance of uranium isotopes, as fuel. Although normal nominal burn-up in CANDU reactors is lower than that in light water reactors (e.g., the burn-up of *reference CANDU fuel* for the Canadian nuclear fuel waste management program is ~190 MWh/kg U, i.e., ~8 GWd/t U<sup>1</sup> [11]), considerable work has been carried out to study the behaviour of CANDU fuel at higher burn-ups. Significant experience exists with CANDU fuel irradiated to extended burn-ups up to 1200 MWh/kg HE<sup>2</sup> (i.e., 50 GWd/t HE) including natural UO<sub>2</sub> power reactor fuel and experimental fuel containing UO<sub>2</sub>, MOX and thoria pellets. Results of the studies on high burn-up CANDU fuel have been documented by Floyd [7] and the following summary of studies on CANDU fuel at extended burn-ups is based on his paper.

It was observed that the fission-gas release (FGR) from the pellets to the free void of the fuel element is a key performance parameter at extended burn-up. Stress-corrosion cracking related defects may be observed due to overpressurisation when FGR exceeds 100 mL in standard 37-element fuel. Other fuel parameters such as endcap closure-weld geometry may also influence defect thresholds. The means to avoid gas overpressurisation at a given burn-up include increasing element internal void space (e.g., plenums and/or modified pellet geometry), and lowering element linear powers (through greater subdivision of the bundle; i.e., CANFLEX [12]).

UO<sub>2</sub> microstructural changes follow a similar trend to that of FGR. An apparently benign rim structure may begin to develop in CANDU fuels irradiated to >500 MWh/kg HE.

CANLUB<sup>3</sup> retention is typically higher at <350 MWh/kg HE, but typically declines above this burn-up, especially at >500 MWh/kg HE. As such, diminished CANLUB retention does not appear to be an issue for fuel that experiences power ramps up to 350 MWh/kg HE. The waterside sheath (fuel cladding) corrosion rate above 450 MWh/kg HE is approximately twice that observed below 450 MWh/kg HE. Nevertheless, corrosion layers up to 30 µm appear to be benign. Internal sheath corrosion is inhibited by the presence of the CANLUB interlayer.

Large variations are observed in sheath (fuel cladding) H/D concentrations, suggesting that parameters in addition to burn-up (irradiation time) have a dominant effect on H/D pickup. The H/D levels observed in extended-burn-up fuel are not, of themselves, detrimental to fuel performance, although they may influence stress-corrosion cracking (SCC) thresholds.

Sheath strain is primarily influenced by fuel power, but also increases with increasing burn-up due to pellet fission-product swelling. Midpellet residual sheath strains are typically limited to 1.0%, but may increase beyond this value when internal gas volumes exceed 100 mL (in standard 37-element fuel). Pellet geometry/density and as-fabricated pellet-sheath diametral clearance also influence sheath strain.

- 
1. 24 MWh/kg HE = 1 GWd/t HE.
  2. HE stands for Heavy Element, e.g., U, Pu, Th.
  3. CANLUB is a “graphite-based” coating on the inner bore of the fuel sheath.

Extended-burn-up fuel cycles will require power ramps at burn-ups >150 MWh/kg HE, where failure margins are smaller than at <150 MWh/kg HE. Tests are underway to better define power-ramp defect thresholds at burn-ups >150 MWh/kg HE, and to confirm the effectiveness of advanced coatings and optimised fuel element designs.

In summary, AECL has significant experience with CANDU fuel behaviour at extended burn-up. By understanding the parameters that affect fuel behaviour at extended burn-up, confidence exists in designing fuel that will achieve the same excellent performance experienced with natural uranium fuel presently operating in CANDU reactors. AECL has a number of fuel irradiation tests underway that will further elucidate extended burn-up fuel behaviour, and confirm both individual and integrated design features for extended burn-up application.

### 3.4 References

1. Boyack, B.E., *et al.*, "Phenomenon Identification and Ranking Tables (PIRTs) for Loss-of-Coolant Accidents in Pressurised and Boiling Water Reactors Containing High Burn-up Fuel", Los Alamos National Laboratory, U.S. Nuclear Regulatory Commission, NUREG/CR-6744, LA-UR-00-5079, December 2001
2. Guèrin, Y., "In pile and out-of-pile burst release of fission gases", EHPG Meeting, 2002, Storefjell, Norway, OECD Halden Reactor Project.
3. Pontillon, Y., *et al.*, "Experimental and theoretical investigation of fission gas release from UO<sub>2</sub> up to 70 GWd/t under simulated LOCA type conditions: the GASPARD program", 2004 International Meeting on Light Water Reactor Fuel Performance, 2004, Orlando, Florida, American Nuclear Society, pp. 490-499.
4. Une, K., Kashibe, S., and Takagi, A., "Fission gas release behavior from high burn-up UO<sub>2</sub> fuels at rapid heating conditions", ANS-Water Reactor Fuel Performance Meeting, 2005, Kyoto, Japan, American Nuclear Society.
5. Lemoine, F., *et al.*, "The role of grain boundary gases in high burn-up fuel under reactivity initiated accident", International Topical Meeting on Fission Gas Behaviour in Water Reactor Fuel, 2000, Cadarache, France.
6. Garde, A.M., Smith, G.P., and Pirtek, R.C., "Effects of Hydride Precipitate Localization and Neutron Fluence on the Ductility of Irradiated Zircaloy-4", 11th International Symposium on Zr in the Nuclear Industry, 1995, Garmisch-Partenkirchen, ASTM STP-1295, ASTM, pp. 407-430.
7. Floyd, M.R., "Extended-burn-up CANDU fuel performance", 7<sup>th</sup> CANDU Fuel Conference, 2001, Kingston, Ontario, Canada, pp. 5A-1 to 5A-20.
8. Pettersson, K., Efsing, P., and Kese, K., "Studies of delayed hydride cracking of Zircaloy cladding", 9<sup>th</sup> International Symposium on Environmental Degradation of Materials in Nuclear Power Systems-Water Reactors, 1999, Newport Beach, Minerals, Metals and Materials Society/AIME, pp. 1201-1210.
9. "Standard Practice for Neutron Radiation Damage Simulation by Charged-Particle Irradiation", Standard Practice E521-96. 1996, American Society for Testing and Materials.
10. Wisner, S.B. and Adamson, R.B., "Combined Effects of Radiation Damage and Hydrides on the Ductility of Zircaloy-2", Nuclear Engineering and Design, 185(1998), pp. 33-49.
11. Sunder, S., "Calculation of radiation dose rates in water layer in contact with used CANDU UO<sub>2</sub> fuel", Nuclear Technology, 122(1998), pp. 211-221.
12. Floyd, M.R. and Harrison, N.F., "Recent irradiations and PIE supporting the development of advanced CANDU UO<sub>2</sub> fuel technology", 9<sup>th</sup> CANDU Fuel Conference, 2005, Belleville, Ontario, Canada.

## **4. PHENOMENA THAT NEED TO BE ADDRESSED BY EXPERIMENTS AND MODELLING**

As should be clear from the previous sections the different phenomena involved in the heat-up, cooldown and quench during a LOCA transient are much more complex than one might first think. This complexity comes from the changes of properties of the zirconium cladding alloys which take place during the transient. In the following description of the types of damage to fuel and cladding which must be addressed by experiment and modelling, they are most easily followed as they take place during the transient.

### **4.1 Types of damage to fuel and cladding**

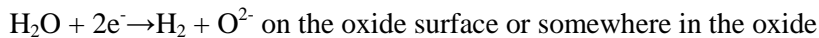
Typically a LOCA transient will start with the fuel under normal operating conditions. The cladding then has a temperature slightly above 300°C. At the pellet cladding interface the temperature is about 400°C with an approximately parabolic temperature distribution in the pellet. The centre temperature in the pellet is perhaps 1 200-2 000°C depending on the local power level. At the start of the LOCA, the fissions quickly cease due to the loss of moderator and insertion of control rods. With the loss of coolant, the cladding will start to heat up. The stored energy in the pellet redistributes towards a more flat radial temperature profile but heatup still will occur due the decay heat of the fuel. The initial heat-up of the cladding is mainly due to the redistribution of heat, the stored energy of the pellet, but in the longer term, it is the decay heat which is responsible for the heating of the cladding.

During the heat-up the pressure in the cladding will increase due to heatup of the mixture of the fill gas and the fission gases. At the same time the strength of the cladding is reduced and eventually the cladding will start to deform plastically, it will start to creep. It is thus necessary to have a good knowledge of the strength and creep properties of zirconium alloys and how they depend on alloy composition and other factors. There are however several complications along the way and these make both analytical modelling and interpretations of experimental results difficult. The first complication is that zirconium alloys generally are very anisotropic when they are in the hexagonal  $\alpha$  phase condition. The typical anisotropy of a cladding tube is such that, when the diameter is increased, the material shrinks in the axial direction. For an isotropic material, the diametral expansion by plastic deformation has no effect on other dimensions of a tube. The importance of the shortening comes when there is a non-uniform temperature distribution around a tube. It will deform more on the hotter side and thus shorten more on that side which of course leads to bending of the tube. This phenomenon will be discussed in more detail later but obviously, a good understanding of the phenomenon is central to a successful modelling of a LOCA event.

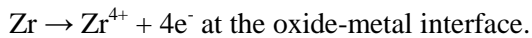
The second complication is the phase transformation which takes place at temperatures around 800°C and above. Pure zirconium transforms from the hexagonal closed packed phase  $\alpha$  to the body centred cubic  $\beta$  phase at ~860°C. However, commercial zirconium alloys generally contain  $\beta$  stabilizing elements which means that the transformation temperature is reduced. It also means that the transformation takes place over a temperature interval rather than at a fixed temperature. In the temperature interval, the volume fraction of  $\beta$  increases from zero to 100%. Since  $\beta$  has different creep properties from  $\alpha$ , the creep during the transformation must be estimated by some law of mixtures. In

fact, things may be even more complicated. It has been shown that in the  $\alpha+\beta$  field zirconium alloys have displayed superplastic behaviour [1], an indication that a deformation mode unique to the mixture may be at work rather than a combination of the creep mechanisms of the two phases. Somewhat paradoxically though experiments on cladding tubes result in a ductility minimum in the  $\alpha$  to  $\beta$  transformation range [2]. The type of damage which primarily results from the creep is rupture of the cladding. Quite clearly a number of different phenomena must be mastered in order to predict the instance of rupture.

In about the same temperature range as when the material starts to transform to  $\beta$ , oxidation starts to become important. The oxidation reactions are:



and



The oxide is understoichiometric and the oxidation rate is controlled by oxygen diffusion into the oxide. The hydrogen is released into the outer environment and it is this hydrogen which may lead to hydrogen explosions if it is not taken care of by recombination equipment. Some of the hydrogen may be absorbed into the cladding where it will contribute to embrittlement of the cladding at low temperatures.

The main source of embrittlement however is the absorption of oxygen into the cladding. As can be seen in Figure 1.4, oxygen stabilises the  $\alpha$  phase. This means that the  $\beta$  phase adjacent to the oxide will retransform to  $\alpha$  and an  $\alpha$  layer will start to grow on the  $\beta$  as can be seen in Figure 1.1. The dissolved oxygen embrittles the  $\alpha$  phase and the ductility goes down to zero above a certain level of oxygen content. The thickness of the oxygen-stabilised  $\alpha$  layer is controlled by the diffusion rate of oxygen in the  $\alpha$  layer. As can be seen in Figure 1.4, the  $\beta$  phase also dissolves some oxygen. This oxygen is also important to the ductility of the cladding since the  $\beta$  retransforms to  $\alpha$  during cooling and if the oxygen content in the  $\beta$  is too high the retransformed  $\beta$  will also have zero ductility. Another contributor to the embrittlement of the cladding are the cracks in the oxide which serve as crack initiators for the underlying  $\alpha$  phase. In case hydrogen has been absorbed, it will also affect ductility both through an intrinsic effect and through an increase of oxygen solubility in the  $\beta$  phase.

Another important effect of oxidation is that it strengthens the cladding so that the creep rate slows down in cases where the cladding tubes have not yet ruptured. For some slow LOCA transients this can lead to a new type of low ductile clad rupture. Cracks in the oxide may lead to a concentration of strain to the underlying  $\alpha + \beta$  layers so that these layers will deform faster than the oxide can reform at the bottom of the crack. The final result is that the metal is drawn out to a chisel point and a crack has formed in the cladding.

In the analysis of what happens to the cladding in a LOCA transient it is also important to consider the state of the cladding at the start of the transient. A cladding with a thick oxide layer can potentially behave differently from a cladding with a thin oxide layer. With a thick layer the initial high temperature oxidation may be slower. However, the reason why the oxide layer can become thick during normal operation is that the outer layers of the oxide are fairly permeable for water molecules so it is doubtful whether this protective effect is significant. Perhaps the most important effect of a thick initial layer is the reduced metal thickness and the hydrogen absorbed in association with the formation of the thick oxide layer. Cracks in a thick initial oxide layer may also influence the rupture behaviour during the LOCA transient.

When zirconium oxidizes significant heat is released. At high temperatures, when oxidation is fast the heat from oxidation can be significant in comparison with the decay heat in the fuel. At 1 200°C the heat generation from a 75 µm thick oxide is about 2 W/cm which is comparable to the decay heat at the time the oxide has reached this thickness. If higher temperatures were to be reached a runaway oxidation might start as the result of the heat generation from oxidation.

The behaviour and possible damage modes of the fuel are much less complex than for the cladding. During normal operation the fuel cracks so that a pellet is actually a conglomerate of several mm-sized fragments. If the cladding balloons, it is obvious that there is a possibility that these fragments move and for instance fill the additional space in a balloon. At high burn-up however several new phenomena are encountered which may or may not have an effect on the LOCA behaviour. Quite frequently, the pellet will bond with the cladding, a phenomenon which gives some limitation to the movement of pellet fragments, but it may also affect the ballooning behaviour. Another high burn-up effect is the increasing amount of fission gases in the fuel which might result in bubble swelling of the fuel if it reaches high temperatures. The last burn-up effect which might have an effect on LOCA behaviour is the so-called rim effect. Due to the resonance capture of neutrons in  $^{238}\text{U}$  large amounts of fissile, Pu is formed in the rim of the pellet which therefore receives a locally very high burn-up. This gives the fuel material special properties. Whether or not those properties have an impact on the LOCA behaviour is still uncertain.

## 4.2 Changes of temperature and geometry with influence on core coolability

A LOCA will lead to a global temperature increase in the core of the reactor, which is later terminated by a cool down phase. This might lead to temperature gradients which in turn lead to bending of fuel bundles and thermal stresses due to differences in thermal expansion between for instance control rod guide tubes and fuel rods. A recent analysis of such cases can be found in [3].

Impaired coolability could result from plastic deformation of the cladding, leading to constriction of the sub-channels between rods, or from fragmentation of the cladding through oxidation and embrittlement. The coolability of a deformed assembly is a key question for the post-LOCA phase of a pipe rupture accident and has thus been subject to extensive research. Parts of this research are described in the following sections based on a recent review by C. Grandjean [4-5].

### 4.2.1 The FEBA and SEFLEX programmes

The FEBA (Flooding Experiments with Blocked Arrays) programme [6] involved performing separate effects tests under different reflood conditions (reflood rate, system pressure and feedwater temperature) with the specific aim of quantifying the effects of:

- A partial blockage in a group of fuel rods, with the presence of a by-pass region or not (non-deformed fuel rods at the blockage periphery) and
- The presence of spacer grids, upon cladding/ coolant heat exchanges in the vicinity of the blockage.

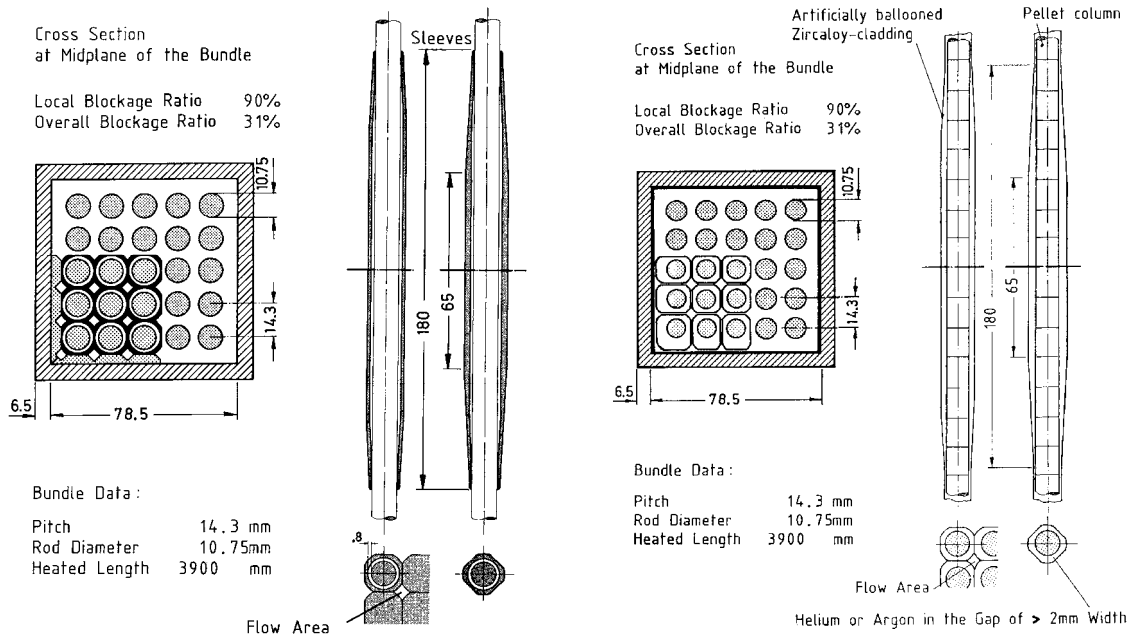
upon cladding/coolant heat exchanges in the vicinity of the blockage.

The SEFLEX (fuel rod Simulator Effects in Flooding Experiments) programme [7-8] was designed to evaluate the sensitivity of FEBA-type reflood test results on fuel rod and blockage simulation technologies. This analysis was based on a limited number of tests performed under conditions identical to those in corresponding FEBA tests, thus enabling the immediate comparison of results.

The FEBA and SEFLEX tests were performed in the same facility at the KFZ Karlsruhe, Germany. Both experiments used 5×5 rod arrays enclosed in a stainless steel shroud with a large heat

capacity to simulate the thermal environment of surrounding fuel rods. The rods were 3.9 m long and held by 7 spacer grids. The rod internal heaters in the FEBA bundle tests were “solid-type” simulators, each composed of a spiral heating element embedded in a magnesium oxide insulator, itself tightly encased in 1 mm thick stainless steel cladding. The heater rods used in the SEFLEX tests were the more representative fuel rod electric simulators used in the REBEKA programme described in Section 5.3.2.1. Figure 4.1 illustrates the main features of the fuel bundles in the two experiments.

**Figure 4.1 FEBA 5×5 bundle with 90% blockage, left and SEFLEX 5×5 bundle with 90% blockage, right**



The blockage in the FEBA bundles was simulated with hollow stainless steel sleeves with a relatively large wall thickness, 1 mm for 62% blockage and 1 to 2.35 mm for 90% blockage. In the SEFLEX tests on the other hand the blockage was simulated by deforming the Zircaloy tubes in a suitable mould. Thus the wall thickness in the balloons was representative of that of real balloons.

#### 4.2.1.1 FEBA test results

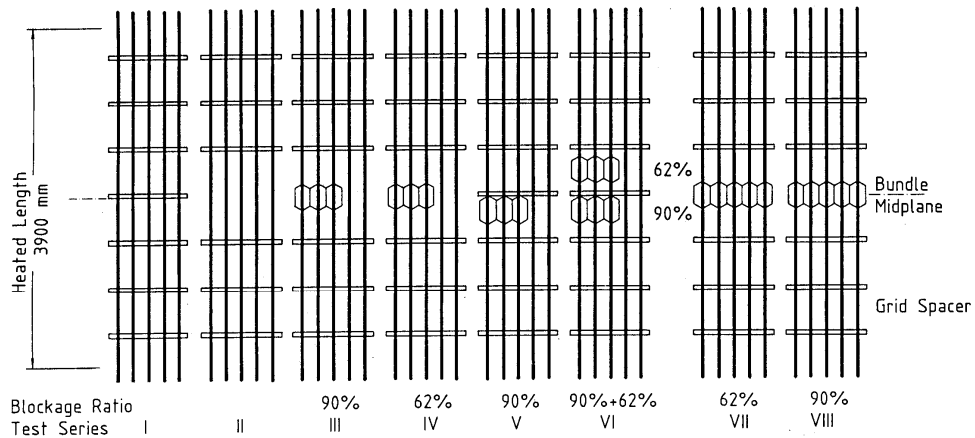
The FEBA test matrix is shown in Figure 4.2 where each of the 8 test series correspond to a specific blockage scenario. Tests were performed using the same experimental procedure:

- Reaching initial steady-state operating conditions in stagnant steam with the required power to obtain the desired temperature at the bundle mid-plane, between 600 and 800°C.
- Establishing reflood at a constant forced rate with a power history defined according to the decay law ANS71 +20%, 40 seconds after reactor shutdown.

Within the same series, the test parameters included: reflood rate, coolant inlet temperature and system outlet pressure. A pressure of 4 bar and a reflood rate of 3.8 cm/s were chosen as reference conditions.

The main FEBA test result was that temperature in the blockage generally was lower than in the by-pass even with 90% blockage. This observation also applied to the cases of double blockage. In cases without a by-pass, the coolability was significantly increased.

**Figure 4.2 FEBA 5×5 bundle geometries of test series I through VIII**



Even though the FEBA test results did not reveal any alarming behaviour impairing the coolability of a blocked fuel assembly under reflood conditions (no detrimental behaviour with a 62% blockage ratio and only a 40°C penalty upon the maximum temperature downstream from a 90% blockage), the programme could be criticised for the poor representativity of tests in comparison to fuel rods subjected to realistic PWR conditions, in which clad ballooning, proportionally reduces the cladding thickness, hence thermal inertia. It was also pointed out that superimposing sleeves on heater rods induces a delay in rewetting immediately downstream from the blockage due to the axial thermal conduction on rod cladding from the hot region located under the sleeve. These issues led to the carrying out of the SEFLEX tests with realistic blockage design.

#### 4.2.1.2 SEFLEX test results

The SEFLEX tests were divided into four series:

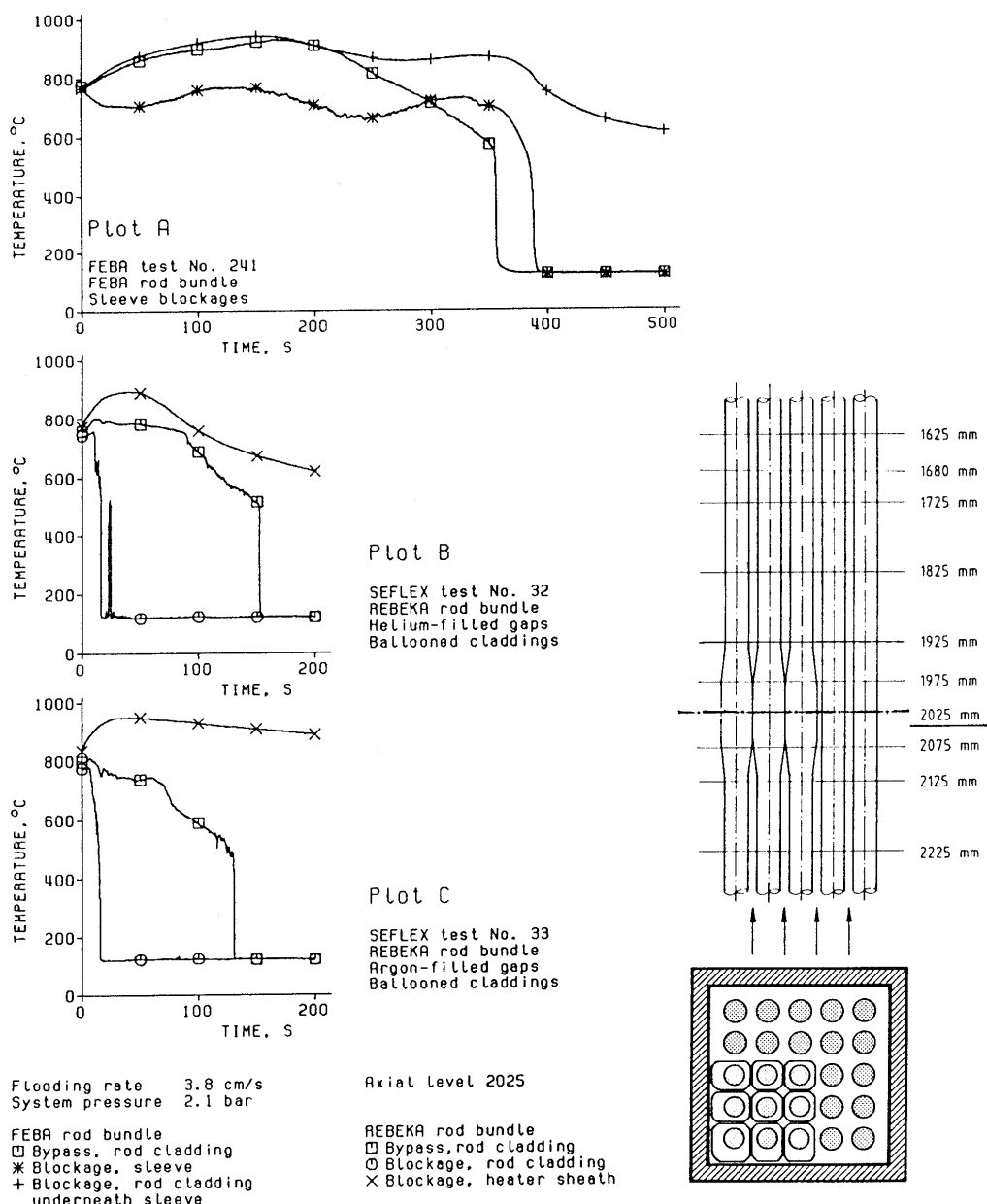
- Series 1 was performed on a blockage-free bundle containing 7 spacer grids; rods were pressurised with helium. This series of reference tests is to be compared with the FEBA series I.
- Series 2 is a variation of series 1 using argon-pressurised fuel rods.
- Series 3 involves a 90% blockage ratio near the mid-plane elevation in a 3×3 cluster in the corner of the 5×5 array, with the mid-plane spacer grid having been removed. Fuel rods were pressurised with helium. This series is to be compared with series III of the FEBA programme.
- Series 4 is a variation of series 3 using argon-pressurised fuel rods.

Fuel rods were pressurised with helium or argon in order to study the effect of the gap thermal conductivity on the reflood behaviour: helium is the filling gas for fresh fuel rods whereas argon thermal conductivity roughly simulates that of the fission gases mixed with helium found in high burn-up fuel rods. The internal pressure of rods was set at 1 bar above test pressure conditions.

Figure 4.3 compares temperature variations measured at the mid-plane of the 90% blockage for a FEBA test (Plot A) and two SEFLEX tests, with helium-pressurised (Plot B) and argon-pressurised (Plot C) rods. All three tests were performed under the same reflood conditions (3.8 cm/s, 2.1 bar). Concerning the FEBA test, the sleeve temperature is lower than the cladding temperature on a by-pass

rod at the same level for a period of 300 s, after which it becomes higher until rewetting that occurs at 385 s, approximately 30 s after that on the by-pass rod. As for the SEFLEX tests, ballooned cladding temperatures are always lower than those of the by-pass rod and moreover, cladding rewetting occurs at a considerably earlier stage – around 15 s – than it does for a by-pass rod, occurring between 130 to 150 s. This difference in behaviour can be explained by the much lower thermal capacity of the SEFLEX balloons in comparison to the FEBA sleeves, as well as greater thermal decoupling from the heater rod due to a larger gap. After balloon rewetting, the temperature of the heater sheath underneath the balloon remains high, particularly for the argon-pressurised rod, due to the high thermal resistance in the 2.3 mm wide gap; this had already been observed on the FEBA test rod (Plot A), with however a narrower steam-filled gap (~0.8 mm).

**Figure 4.3 Temperatures measured in the midplane of a 90% blockage and in the blockage by-pass of FEBA and SEFLEX rod bundles**



The SEFLEX programme results illustrate that – within the limited range of the selected test conditions – better cooldown and significantly earlier cladding rewetting occur within and downstream from the blockage in comparison to the by-pass or during a blockage-free test.

However, it would have been beneficial that the SEFLEX test matrix had included blockage tests performed under severe reflood conditions: 2 cm/s reflood rate, 2 bar pressure and inlet temperature of about 100°C. Such tests would have made it possible to evaluate the effect of favourable elements (low thermal inertia of the cladding or balloon, low conductance with the heater rod) under the most adverse thermohydraulic conditions, particularly taking into account the trends observed in FEBA and THETIS tests which partially met these conditions.

Concerning the simulation of a blockage for which the heater elements remain unchanged in the balloons and non-deformed regions, SEFLEX test results tend to highlight the marked conservatism of FEBA test results. In contrast, the marked difference between comparable test results from the two programmes seems to indicate that a high coupling between the heat source and the ballooned cladding – such as what can be found in a reactor situation for a balloon filled with relocated fuel fragments – might significantly impair the coolability of a blockage formed by such balloons in comparison to a scenario without fuel relocation. This question cannot be correctly investigated by extrapolating FEBA or SEFLEX test results and therefore requires performing specific tests.

#### **4.2.2 THETIS programme**

The THETIS programme was carried out by the United Kingdom Atomic Energy Authority (UKAEA) at the Atomic Energy Establishment in Winfrith. This programme involved conducting a set of thermohydraulic tests on an assembly containing 49 full-length fuel rod simulators with a severe blockage of 90% [9] or 80% [10-11] over a length of 20 cm.

Four different types of experiments were performed:

- 1) Single-phase (nitrogen) flow heat transfer tests.
- 2) Forced reflood tests.
- 3) Gravity reflood tests.
- 4) Level swell tests.

Forced reflood test results, being the greatest in number and providing analytical information on the cooling of a partially blocked assembly, only are discussed by Grandjean in [5]. Gravity reflood test results are reviewed in [2] and show similar results in terms of blockage coolability, to forced reflood test results conducted under comparable initial conditions, which justifies the choice of forced reflood tests for the study of partially blocked assembly cooling.

The THETIS test assembly consisted of a 7×7 rod array with a 4×4 group of rods containing the blockage region. The assembly was enclosed in a square shroud tube with an inside width of 115.5 mm and a thickness of 6.5 mm. The fuel rod simulators, of SGHWR-size (12.2 mm in diameter), had a heated length of 3.58 m and were held in a set of 7 spacer grids. These fuel rod simulators were solid-type electric simulators similar to FEBA test rods.

Ballooning of the rod cladding was simulated by superimposing a pre-shaped Inconel sleeve. The maximum blocked region extended over 200 mm, with entry and exit tapers, 200 mm and 50 mm long respectively, connecting the circular rod section with the sleeve square section. The cladding balloons therefore occupied almost a complete grid interval. The sleeve thickness in the maximum deformed region was 0.3 mm, which is comparable to that of a real cladding balloon.

The most important results of the THETIS experiments can be summarised as follows:

The series of forced reflood tests simulating a 90% blockage with a pressure of 2 bar and an inlet temperature of 90°C produced the following observations:

- With a 3 cm/s reflood rate, the blockage was found to be coolable, with the peak blockage temperature not exceeding the peak by-pass temperature by more than 60°C.
- With a 2 cm/s reflood rate, the maximum blockage temperature rose above the facility operating limit, which made it necessary to reduce power before the complete cooling of the blockage was achieved. It may therefore be believed that these test conditions do not permit suitable blockage cooling.

THETIS test results seem to imply that a long 90% blockage may no longer be coolable at a constant reflood rate below 2 to 3 cm/s.

When comparing results of tests performed with 90% and 80% blockages under similar conditions, it became apparent that an 80% blockage is more efficiently cooled at high reflood rates. However, differences tended to be minor, sometimes proving to be even better for the 90% blockage with intermediate reflood rates that are most relevant to reactor safety analysis. These results therefore reveal that the blockage ratio of 90% – considered as an upper bound value of the flow blockage ratio possibly obtained under a LOCA with a fresh fuel assembly – does not necessarily represent the most penalising case in terms of coolability for extended axial deformations such as those simulated in the THETIS experiments.

#### **4.2.3 FLECHT SEASET programme**

The FLECHT SEASET programme (Full Length Emergency Cooling Heat Transfer – Separate Effects and System Effects Tests) [12] was an extensive programme that was launched in 1977 in cooperation between USNRC, EPRI and Westinghouse. The programme's main objective was to improve understanding of the complex thermohydraulic phenomena occurring during a hypothetical LOCA scenario. In the short term, programme results were to be used to identify excessive conservatisms in licensing requirements.

The FLECHT SEASET programme part dealing with blocked assembly cooling involved three main tasks:

- Performing tests on a 21-rod array to determine the effects of different blockage configurations and geometries upon reflood heat transfer.
- Performing tests on a 163-rod array to evaluate the effect of a large flow by-pass under the most severe heat transfer conditions observed in the 21-rod bundle test series.
- Analysing results and developing associated models with the COBRA-TF code.

The average blockage ratios used were no higher than 62% in the most detrimental coplanar configuration which had particularly short balloons, 60 mm in length with a cosine profile. Therefore, results of these tests cannot be compared to test results with high blockage ratios from previously discussed programmes. In [5] Grandjean limits the discussion mainly to the tests with 21-rod assemblies; results of 163-rod tests are discussed in the extended review [2]. Table 4.1 shows the 6 blockage configurations used in the 21-rod tests with appropriate comments.

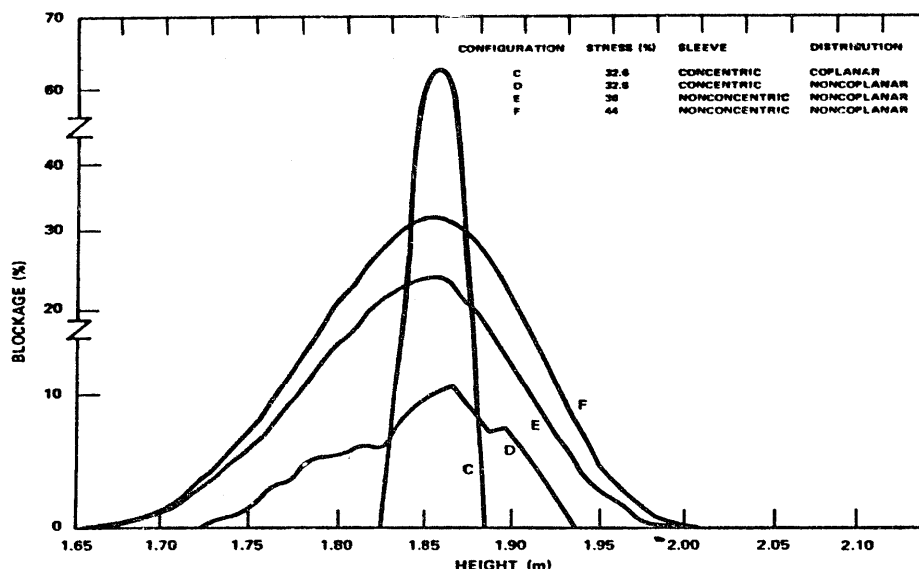
The test assembly was composed of 21 full-length heater rods, with a diameter of 9.5 mm and a heated length of 3.05 m, held in 8 spacer grids and including 4 triangular solid fillers. The assembly was housed in a stainless steel cylindrical shroud, with an inside diameter of 6.82 mm and a thickness of 4 mm.

Table 4.1 Blockage shapes and configurations tested in the FLECHT SEASET 21-Rod bundle

Test Series	Configuration Description	Comments
A	No blockage on the rods	This configuration served as a reference.
B	Short concentric sleeve, coplanar blockage on 9 centre rods. Maximum strain = 32.6%	This series provided for both blockage effect and some by-pass effects.
C	Short concentric sleeve, coplanar blockage on all 21 rods. Maximum strain = 32.6%	This series was the easiest to analyze since it provided no flow by-pass effects with maximum flow blockage effect at one axial plane.
D	Short concentric sleeve, non-coplanar blockage on all 21 rods. Maximum strain = 32.6%	This test series examined a non-coplanar blockage distribution and was comparable to series C.
E	Long non-concentric sleeve, non-coplanar blockage on all 21 rods. Maximum strain = 36%	This test series permitted a one-to-one comparison with series D in which all rods were blocked. Comparison of series D and E with unblocked data indicated the worst shape.
F	Test series E with increased sleeve strain, non-coplanar blockage on all 21 rods. Maximum strain = 44%	This test series increased the blockage effect relative to series E.

The choice of 36% strain as the most representative value for the non-concentric sleeves was based on results from ORNL and REBEKA burst tests. The orientation of bulges for non-concentric sleeves was based on known effects of temperature variations in a bundle. Figure 4.4 illustrates the axial distributions of bundle-wide blockage ratio for configurations C, D, E and F, all with a sleeve on all 21 fuel rods. As expected, configuration C (coplanar concentric) produces the highest blockage ratio (62%), whereas the non-coplanar configurations barely reach a maximum bundle blockage ratio of 30%, even if the local blockage in a specific sub-channel can reach much higher values (90%).

Figure 4.4 Bundle-wide blockage and axial distributions for FLECHT-SEASET configurations C, D, E and F



In total, 87 forced reflood tests and 10 gravity reflood tests were conducted. Forced reflood tests were used to study the separate effects of variations upon the different test parameters:

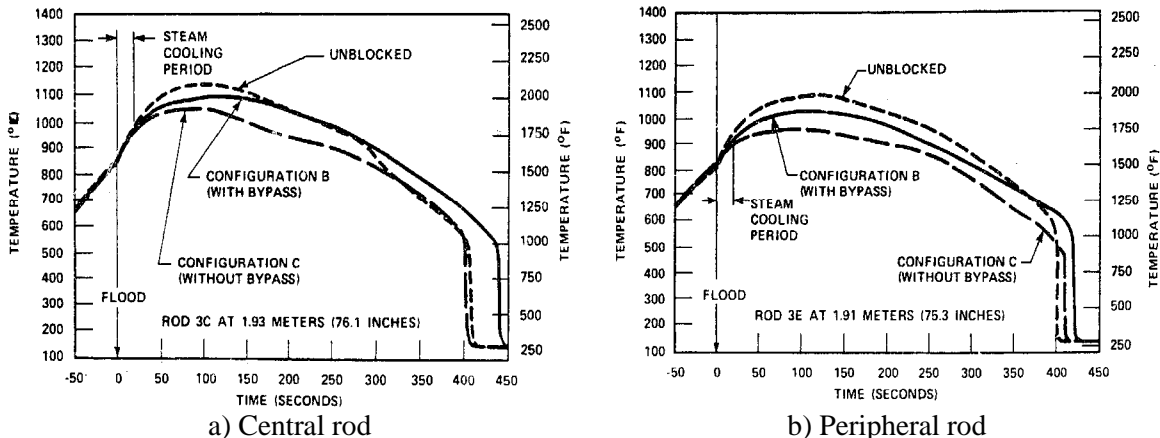
- Reflood rate: from 1.27 cm/s (0.5 in./s) to 15.2 cm/s (6 in./s).

- Pressure: from 1.4 bar to 2.8 bar.
- Inlet fluid temperature sub-cooling: 22°C (40°F) and 78°C (140°F).
- Initial peak linear power: from 0.89 kW/m to 2.57 kW/m.

The same set of test conditions were used for each configuration.

Figure 4.5 a and b compares the temperature variations for a central and a peripheral rod, respectively, in the three configurations: no-blockage, co-planar blockage with and without by-pass.

**Figure 4.5 Rod temperatures for unblocked and coplanar configurations**



Following a short period of about 15 s after flood during which temperature variations appear indistinguishable – corresponding to the start of boiling at the assembly bottom – the temperature rise slows down in blockage configurations, particularly in the configuration without by-pass. This decrease in the temperature rise results from cooling generated by liquid droplets carried in the steam flow, which is even more pronounced when this flow is deprived of a by-pass. For the central rod, the difference in maximum temperatures approaches 100°C between the blockage-free configuration and the blockage configuration without by-pass, and about half that value between the blockage-free configuration and the blockage configuration with by-pass.

For the non coplanar blockages the temperatures were generally lower in the blocked region compared to the unblocked configuration, with the exception of the short balloons for which there was little difference between the temperatures.

The main conclusion derived from the 163-rod array test results was that the beneficial effect of the blockage upon the increase in heat transfer remains sufficiently dominant, at least at the beginning of the transient. This compensates for the detrimental effect of the flow by-pass and produces lower maximum temperatures in comparison to those obtained in a blockage-free configuration.

The FLECHT SEASET 21-rod array test results – backed up by FEBA 25-rod array test results – highlighted the importance of considering the two-phase nature of the flow and the considerable influence of the liquid droplets field via:

- The entrainment of droplets in the steam flux even at low reflood rates (2.5 cm/s), which are swept into the blockage region when they have sufficient inertia.
- The shattering of these droplets on balloon surfaces, creating finer droplets, more easily evaporated, hence increasing steam de-superheating and surface heat transfer both in and downstream from the blockage.

#### **4.2.4 Conclusions from the programmes on cooling of deformed bundles**

The following conclusions, with associated pending questions, were drawn by C. Grandjean in [5].

Vast experimental programmes have been devoted to answering the question of coolability under postulated LOCA conditions of an assembly containing a partial blockage. All of these programmes have focused on large break LOCA scenarios and more particularly on blockage cooling under reflood conditions. Examination of these main programmes has helped establish a more global understanding of the physical processes involved in such a situation.

##### *4.2.4.1 Main results from the experimental programmes*

Temperature variations in and downstream from a blockage region in a fuel rod assembly resulting from cladding deformation during a LOCA transient are generally conditioned by heat transfers taking place at the beginning of the reflood phase with two-phase mist flow conditions. A blockage induces antagonistic effects whose relative significance depends on the geometrical conditions of the blockage and its by-pass, as well as the thermohydraulic conditions of the reflood. These effects result from the following physical phenomena:

- Reduction of the flow passage in the blockage leads to flow diversion towards the by-pass, therefore reducing the mass flow in blockage sub-channels. For sufficiently long blockages ( $\geq 200$  mm), the reduction in the steam flow is approximately proportional to the reduction in the cross section area. This reduction in coolant flow therefore tends to restrict blockage coolability.
- However, in a two-phase flow, the inertia of droplets favours their penetration of the blockage, particularly if the quench front is sufficiently far off to have permitted their acceleration in the steam flow. Inside the blockage, the liquid droplets are dispersed due to their impact on the blockage surfaces, fragmented and re-entrained in the form of finer droplets, which significantly increases heat transfer with steam. This de-superheating of steam, associated with the increase in turbulence, improves the coolability of the blockage surfaces.
- At the blockage outlet, the deceleration of the steam flow in the widening section can cause bigger droplets to fall under gravity onto the hot blockage surfaces, thereby leading to dispersion and evaporation in steam jets, which once again leads to an accentuated cooling in the region.

It must be noted however that though it seems that blockages of significant ratios (90%) but of moderate lengths (<10 cm) do not create any particular problems in terms of coolability, it should not be assumed, as one might be tempted to do considering FEBA and SEFLEX test results, that a 90% blockage is always coolable. It has also been demonstrated that the maximum blockage ratio of 90% does not necessarily represent the most penalising case in terms of coolability for axially extended deformations.

##### *4.2.4.2 Pending questions*

In conclusion, it is important to underline the fact that all results and trends discussed in Grandjean's review were drawn from out-of-pile tests performed on assemblies containing electric fuel rod simulators. The fixed heated elements in these simulators cannot be used to simulate a possible accumulation of fuel in the balloons (fuel relocation) as was demonstrated in in-pile tests performed on irradiated fuel rods. Furthermore, the significant difference between comparable FEBA and SEFLEX test results seems to indicate that significant thermal coupling between the heat source and the

ballooned cladding – as may exist in a clad balloon full of relocated fuel fragments – is susceptible of significantly hindering the coolability of a blockage with such balloons, in comparison to a case where fuel relocation does not occur. This question cannot be correctly investigated by extrapolating FEBA or SEFLEX test results. The effect of fuel relocation (leading to a local accumulation of power and quasi-closure of the gap in the blockage) upon the blockage coolability was not explored in any existing tests and therefore remains to be investigated in specific tests. Such tests should be conducted preferentially, as in those discussed above, on rod arrays bearing pre-shaped deformed regions, but with taking account of a local increase in power density and a reduction in gap width to simulate the relocation of fuel in the balloons.

### 4.3 Radiological consequences

Even after a successfully terminated large break LOCA transient, where all safeguard systems have worked as planned, a large number of fuel rods will have failed. Large amounts of radioactivity will have reached the containment in the form of gases or particulate aerosols. From a regulatory point of view some of this radioactivity will leak out of the containment and reach the environment outside the nuclear plant where it will cause a dose burden to the public. For calculation of the doses it has to be assumed that the containment leak rate is the highest permissible rate stated in the technical specifications of the plant [13-16]. Other pathways out of the containment must also be considered like the systems for recirculation of sump water outside the containment and the main steam isolation valves for BWRs. That leaks do occur in connection with radioactive releases to the containment was demonstrated at the Three Mile Island incident although releases of iodine were significantly lower than expected from assumed maximum leak rates for the containment [17]. In calculations of external radiological consequences the basis always is the so-called “in-containment source term” which is the object of the present section.

When a break of the reactor coolant system occurs at operating conditions, approximately 50% of the primary coolant mass will flash leading to steam discharged into the containment which then condenses in the atmosphere or on the surfaces of primary containment. From the atmosphere condensation droplets or from some small water droplets discharged from the break, an aerosol water phase is present in the containment atmosphere. Following a LOCA, in the cold leg, the fission products released by the fuel are transferred to the containment in different steps [18]. During the dry phase (up to 250 s), noble gases and a fraction of iodine and caesium (CsI) are transferred by the steam to the containment. At this time, only a small fraction of iodine is released as molecular iodine. During the wet phase (after reflooding), molecular iodine is generated by water radiolysis in the vessel and released through the break. In the long term, all the fission product inventory in the water vessel is transferred by the water to the containment sump. The concentration of fission products in the containment atmosphere (noble gases, iodine, caesium and other species released by the fuel) depends on the release rate from the break and the depletion mechanisms. For designs not provided with a spray system, the aerosol behaviour is affected only by natural process, such as agglomeration and steam condensation, and aerosols will be removed from the containment atmosphere by gravity and phoretic effects [18]. For the volatile species (molecular iodine), the depletion in the containment atmosphere is governed by the gas/liquid mass transfer and adsorption on painted surfaces. In designs provided with a spray system, this system provides an additional mechanism for airborne aerosols or molecular iodine depletion from the containment atmosphere. In the evaluation of radiological consequences of a LOCA, licensing approaches may consider a global removal rate coefficient for the evaluation of fission product depletion from the containment atmosphere. This coefficient depends on the physical and chemical nature of the species. Different practices consider a constant value of removal rate coefficient up to a maximum decontamination factor (from 100 to 1 000) or consider different values for this coefficient for different time periods.

It is in principle possible to include corrosion products dissolved in the primary water in the in-containment source term since they will spread in the containment in connection with the LOCA. However it has been shown that they give a negligible contribution to the external dose [19]. The same argument applies to fission products and actinides released to the coolant before large scale fuel failures in connection with the LOCA [19]. The main contributor to the in-containment source term thus is the release of the core inventory of fission products. This inventory can be calculated with appropriate isotope generation and depletion computer codes such as ORIGEN- 2, ORIGEN-ARP [13-14] or FISPIN [19]. The inventory of fission products is distributed unevenly in the fuel rods and not all of them are available for release. The distribution is also strongly burn-up dependent. The part of the inventory most readily released is the gap inventory consisting noble gases and volatile iodine compounds. In the gap there may also be water soluble fission products like caesium species. The fission products less readily available for release are slowly leached out from the fuel matrix. The rates of release will depend on the fragmentation of the fuel which may be highly burn-up dependent. With knowledge of fission product distributions and reliable estimates of the number of failed fuel rods it would in principle be possible to reach reasonably realistic numbers for the in-containment source term.

However, from a regulatory point of view, it is in the United States for instance assumed that there is a core melt and that the containment nonetheless should retain most of the fission products. Therefore, conservative core-melt release fractions are provided in Regulatory Guides 1.3 and 1.4. More realistic alternative source terms for a core-melt are provided in Regulatory Guide 1.183 and these release fractions are given by the following table [13-16]:

Table 4.2 BWR core inventory fraction released into containment

<b>Group</b>	<b>Gap release phase</b>	<b>Early in-vessel phase</b>	<b>Total</b>
Noble gases	0.05	0.95	1.0
Halogens	0.05	0.25	0.3
Alkali metals	0.05	0.20	0.25
Tellurium metals	0.00	0.05	0.05
Ba, Sr	0.00	0.02	0.02
Noble metals	0.00	0.0025	0.0025
Cerium group	0.00	0.0025	0.0005
Lanthanides	0.00	0.0002	0.0002

A corresponding table for PWR is almost identical. As can be seen in the table, two release phases are identified: gap release and early in-vessel. The timing of these phases varies according to reactor type.

Table 4.3 LOCA release phases

<b>Phase</b>	<b>PWRs</b>		<b>BRWs</b>	
	<b>Onset</b>	<b>Duration</b>	<b>Onset</b>	<b>Duration</b>
Gap release	30 s	0.5 hr	2 min	0.5 hr
Early in-vessel	0.5 hr	1.3 hr	0.5 hr	1.5 hr

#### 4.3.1 Harmonisation efforts in Europe

Regulatory practice in Europe has been more varied as demonstrated by a questionnaire within a recent project aimed at increasing the harmonisation in the area of the safety of nuclear installations [19]. Examples of the variation of approach can be seen in Table 4.4 which shows how iodine release has been calculated in different countries.

Table 4.4 Computation of the iodine release

Country	ECCCS injection	Failed fuel fraction	Gap inventory	Additional release	I131 released fraction of the gap B, E, HU, SI= fraction of the CI	Iodine forms of the release (initially in the atm., unless otherwise specified)		
						Mol.	Part.	Org.
B	C	100%	N	–	25% atm 50% sumps	91%	5%	4%
F [3.1]	C	100%	Y		100% (atm)	90%	0%	10%
F – updated hypothesis under discussion		≤33%	Y		10% dry phase (atm) 90% wet phase to the sump	1% 2% atm	99% 97.8% water	0% 0.2% atm
D	CH	10%	Values based on an old calcul.	Y	100% (10% atm)	No assumptions explicitly made.		
E	C	100%	N	–	50% atm/ 50% sumps	95.5%	2.5%	2%
UK	C	100%	Y	Y	100% (atm) (10% dry phase 90% wet phase)	2% of the total release will be I <sub>2</sub>	99.8%	Formation: 0.2%
CZ	VVER	100%	Y	–				
FIN	CH	100%	Y	Y	Dry phase: 10% Wet phase: 90%	Wet phase 55%	100% init.	
HU	VVER	100%	Y	N				Formation
I	C	100%	Y	N	100%	49.5%	49.5%	1%
NL	CH	10%	N	N	75% atm 25% sumps	50%	0%	50%
SI	C	100%	N	–	25% atm 50% sumps	91%	5%	4%
CH	CH	10%	cf D			1.7%		1%

One reason for the differences in approach is that there is a difference between the German PWRs and other PWRs. The German plants have simultaneous injection of ECC water in both the hot and cold leg while the other plants have ECC injection in the cold leg only. Another difference is that the former do not have a containment spray while the latter have such a spray. Hot and cold leg injection leads to lower fuel temperatures and fewer failed fuel rods in connection with a large break LOCA. The absence of containment spray on the other hand leads to a slower removal rate of fission products from the containment atmosphere.

As a basis for the harmonisation effort reported in [19] a previous attempt at calculating realistic values for releases and consequences of a large break LOCA was used [18]. The report on harmonisation lists a number of proposals for a common position on the various issues of importance to the analysis of the radiological consequences of a large break LOCA.

#### 4.3.1.1 List of nuclides to consider in the calculation of the radiological consequences

It is noted that the dose of the successfully terminated LBLOCA is mainly due to a small number of nuclides (iodine, caesium and noble gases). Iodine and noble gases are always considered in the licensing studies. With the present computers, it is possible to consider all fission products and to compute the source term for each of them. The main problem is the lack of data, especially for the

**Table 4.4 Computation of the iodine release**

Spray	Additive element	(Init./ Recirc.)	Removal rate of iodine ( /h – i=immediate) (max. decontamination factor)			Radioactive decay	Daughter products	Country
			Mol.	Part.	Org.			
Y	NaOH	R	10 after 20 min (100)	0.8 (100)	0	Y	Y	B
Y	NaOH	I+5min	I (1000)	0	0	Y	Y	F [3.1]
Y	NaOH	I	20 ×	4 xx	0			F – updated hypothesis under discussion
N			7h to reach equilibrium value: $I_{\text{water}}/I_{\text{gas}} = 10^4$					D
Y	Na <sub>3</sub> PO <sub>4</sub>	R	20+3.13 (100)	5.46 (50) 0.55	0	Y	Y	E
Y	Na <sub>3</sub> PO <sub>4</sub>	R	0	1.3 (<0.6h) - 0.5 (>0.6h) (10000)	0	Y	N	UK
Y								CZ
Y	N <sub>2</sub> H <sub>4</sub> -KOH	I				Y	Y	FIN
Y	(severe acc: N <sub>2</sub> H <sub>4</sub> -KOH)					Y	Y	HU
Y	NaOH		12 (200)	3.1 (200)	0	Y	N	I
N			–	–	–	Y	Y	NL
Y	NaOH	I	10 (100)	3.8 (100)	0	Y	Y	SI
Y	–		Elem. Iodine: 0.5% after 4h			Y	Y	CH

release fractions of involatile fission products and actinides. Corrosion products and actinides may be considered to be negligible contributors to the dose and do not need necessarily to be taken into account. Moreover, the computation of their consequences will be subject to a large uncertainty. However, it is very important for public acceptance that actinides are considered. Thus even if they are negligible, it should be explicitly justified if they are not taken into account for the dose calculations. Given that some countries already consider an extended list of radionuclides (except very short half-life nuclides):

- Accounting for an extended list of radionuclides in the calculation of radiological consequences is possible and easy with the available computers.
- It is important for public acceptance to demonstrate that all radionuclides are considered, even if they are negligible for the dose assessment.

It is proposed, for future licensing studies, that:

- All fission products should be considered. If some fission products are not considered, a justification must be presented.
- Actinides should be considered. They may be screened out, based on qualitative arguments.
- It is not necessary to consider the corrosion products for this accident.

#### 4.3.1.2 The failed fuel fraction

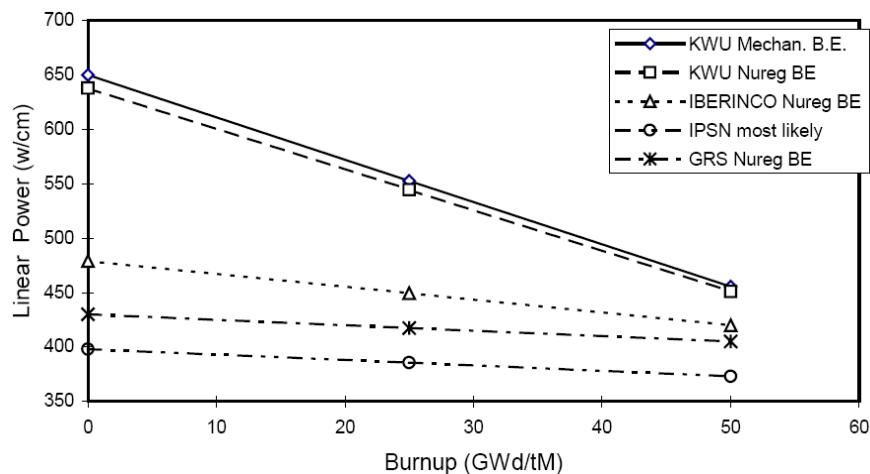
For the fraction of failed fuel, the results from another joint European study were used [20]. The objectives of that study were to:

- Review the existing clad failure criteria and licensing approaches in each participant's country.
- Form a consensus view on clad failure criteria.
- Determine the impact of the clad failure criteria on the extent and form of clad failure for a reference design in each of the participants' country.

Mechanistic and non-mechanistic clad failure criteria were considered. Mechanistic models have been developed by EdF, GRS, Siemens and NNC. A non-mechanistic (empirical) model for cladding failure has been produced in NUREG-0630 [21] as part of a methodology for clad swelling and rupture for use in LOCA analysis. More recent experimental data have been compared to the NUREG-0630 clad rupture temperature correlation and revised best estimate and conservative correlations have been proposed.

On the basis of the mechanistic analyses participants in the project determined failure thresholds for the fuel. The best estimate failure threshold is shown in Figure 4.6 [20]. A similarly estimated conservative failure lie about 50-150 W/cm lower depending on participant. Based on the failure thresholds, the failed fuel fraction could be calculated. In the best estimate analyses only one of the participants arrived at a non-zero value. In the more conservative analyses, failed fuel fractions between 0 and 16.6% were obtained. These values were significantly below the 100% normally applied by the different countries. Therefore, it was suggested as a common position that in licensing calculations a failed fuel fraction of 33% should be applied for reactor designs with cold leg injection only. For reactors with injection into both hot and cold legs, a failed fuel fraction of 10% was supported which is the same as that adopted in the German licensing methodology.

Figure 4.6 Best estimate failure thresholds for PWR fuel in a large break LOCA



#### 4.3.1.3 The release from failed fuel

For the common position on release from the fuel the recommendation is based on the study of realistic releases. The recommendations are summarised in Table 4.5. The table gives both the gap release and a contribution from the fragmentation of the fuel. The recommendations are valid for fuel with a burn-up up to 50 GWd/te. With regard to the release of fuel particulates from fuel, especially at high burn-up the study did not result in any recommendation. It was noted however that experimental data is available but needs to be reviewed before any recommendation can be given.

Table 4.5 The release from the gap and fuel for radiologically significant nuclides

Nuclide	Best estimate			Conservative
	Gap release (G %)	Fuel release (F %)	Total release (%)	Total release (%)
Kr-85	1.0	6.5	7.5	9.5
Xe-133	0.2	1.95	2.15	4.2
I-131	0.25	0.4	0.65	2.5
Cs-134	1.0	0.86	1.86	3.1
Cs-137	1.0	1.0	2.0	3.3

#### 4.3.1.4 The retention in the reactor coolant system and the initial release of fission products to the containment atmosphere

In a successfully terminated large break LOCA some of the fission products may be retained in the reactor coolant system (RCS). Based among other things on calculation with the severe accident code MELCOR the joint European study arrived at the following proposal for retention of fission products and timing of the release [19]:

All the noble gases are released directly to the containment atmosphere during the dry phase. The releases of the other radionuclides (I, Cs) are divided into the dry phase (10%) and the wet phase (90%).

For the design with injection only into the cold leg, the molecular iodine (2% of the total iodine release – the same applies for bromine) and all the dry phase are entirely released to the containment atmosphere.

For the design with injection into both hot and cold legs, the molecular iodine (2% of the total iodine release – the same applies for bromine), 10% of the rest of the iodine (and bromine) release occurring during the dry phase, 10% of the dry phase release of the alkalines and 1% of the dry phase release of the other nuclides enter to the containment atmosphere.

Some part of this release may be retained in the RCS itself but this retention is a matter submitted to a great number of uncertainties. Therefore, it is concluded that radionuclide retention in the RCS should not be credited for licensing DBA source term analyses.

The rest of the release transfers into the reactor coolant. The release occurring into the water is assumed to be transferred to the sumps.

#### 4.3.1.5 Retention in the containment

The most complex part of the containment source term problem is the retention in the containment since it also determines the time dependence of the source term. In the European harmonisation project the problem was divided into a number of subproblems. Proposals for plants with cold and hot leg injections are only relevant to Germany.

##### 4.3.1.5.1 Iodine behaviour and chemistry

Design with cold leg and hot leg injection without spray

In future licensing calculations the retention of iodine in the containment and the effect of pH in the sump water should be considered. The iodine behaviour (especially the effect of pH in the sump)

should be calculated e.g. with an iodine code. In this calculation the initial release form of iodine should be CsI (100 %). The release should be supposed to occur instantaneously.

The following phenomena should be considered in the calculation: aerosol CsI removal, radiolysis in the water phase, other reactions in the water phase, reactions in the gas phase, mass transfer from sump to the gas phase, deposition on wall surfaces in the gas phase and formation of organic iodine.

#### Cold leg injection with containment spray

For this case, performed studies show that dominant effects concerning the concentration of iodine species in the containment atmosphere are:

- Release of molecular iodine following in vessel radiolysis during the wet phase.
- pH condition on spray droplets and sump water, leading to retention or release of iodine dissolved in the water.
- Adsorption of molecular iodine on the non-submerged containment surfaces, leading to molecular iodine retention and organic iodine formation and release.

Then, it is recommended to use a specific iodine code taking into account a realistic iodine release kinetic model during the dry and wet phase, and iodine removal by spray and adsorption on the containment wall. In this case there is no need to assume a maximum decontamination factor.

When a validated iodine code is not available, in addition to the atmosphere containment release as recommended in Section 4.3.1.4, 60% of the wet phase release of iodine (bromine) is supposed to be converted into I<sub>2</sub> (Br<sub>2</sub>) and also directly released to the containment atmosphere (recommendation of [18]). Iodine removal could be evaluated by removal constants associated to a maximum decontamination factor (depending on pH conditions). New values (compared to [18]) for molecular iodine spray removal constant are proposed depending on pH conditions of the spray water:  $\lambda_{\text{spray}} = 0.2 \text{ h}^{-1}$  for acidic spray droplet water,  $\lambda_{\text{spray}} = 2.7 \text{ h}^{-1}$  in the case of alkaline spray droplet water. The removal constants associated to iodine adsorption on nonsubmerged painted surface are still very uncertain.

#### Organic iodine

A value of 0.2% of the iodine released in the dry phase is assumed to be converted into organic iodine, instantaneously present in the containment atmosphere. There is no other removal than by radioactive decay. This value of 0.2 % is of the same order of magnitude as the value recommended in the 1992 study [18].

#### 4.3.1.5.2 Aerosol removal (including iodine aerosols)

In the case of LOCA, aerosols are released during the first 250 seconds of the accident when the containment reactor pressure is highest (at least in the case with spray actuation) leading to the highest leak rates. In order to evaluate realistic fission products release from the containment, it could be advisable to use a detailed mechanistic aerosol collection model taking into account different removal mechanisms models as function of the aerosol size and considering an aerosol size distribution. This should lead to higher removal rate effectiveness at the beginning of the accident. In this case, a maximum decontamination factor should not be considered. If this model is not available, for a conservative approach, a total removal coefficient should be used (as proposed in [18]), associated to a maximum decontamination factor.

#### *4.3.1.6 Conclusions of the European harmonisation effort*

The work has resulted in progression towards harmonisation of the licensing methodology for the successfully terminated LBLOCA (calculation of the source term inside the containment). It was proposed that the list of nuclides used to compute the radiological consequences should be extended to include more fission products than iodine and noble gases which are normally considered. This is more from the aspect of meeting public acceptability in demonstrating that the safety calculations are complete and does not imply that there were shortcomings in earlier assessments. General assumptions regarding the sequence definition were agreed between the partners. There exists an agreement concerning the percentage of failed fuel which could be used in future licensing assessments (however this subject is still under discussion in France, a lower value is thinkable).

For the release from damaged fuel, the agreement was not complete: AVN (Belgium) wished to maintain its present approach. IPSN (France), GRS (Germany) and NNC (UK) prefer to use their own methodologies that result in slightly different values to the proposed values for a common position. There are currently no recommendations for the release of fuel particulates. An agreement was reached on the fact that no retention in the RCS is to be accounted for, and on the release part going to the containment atmosphere.

For the retention in the containment (chemistry of iodine and spray/natural removal of iodine and aerosols), the partners agreed for the recommendation to use a code allowing an accurate modelling of the phenomena. However, such codes may not be available for everybody or are still subject to some validation problems. In that case, simple conservative models are proposed.

The problem of organic iodine formation is still a controversial subject but a value of 0.2% of the release to the containment atmosphere seems to be acceptable.

## **4.4 References**

1. Kearns, J.J., McCauley, J.E., and Nichols, F.A., "Effect of  $\alpha/\beta$  phase constitution on superplasticity and strength of Zircaloy-4", *Journal of Nuclear Materials*, 61(1976), pp. 169-184.
2. Grandjean, C., "A state-of-the-art review of past programs devoted to fuel behaviour under LOCA conditions: 1st Part: Clad swelling and rupture, assembly flow blockage", IRSN, Technical Report DPAM/SEMCA 2005/313, December 2005.
3. Waeckel, N., *et al.*, "Evaluation of fuel rod axial forces during LOCA quench", Topical Meeting on LOCA Fuel Safety Criteria., 2001, Aix-en-Provence, France, Nuclear Energy Agency.
4. Grandjean, C., "A state-of-the-art review of past programs devoted to fuel behaviour under LOCA conditions: Part 2. Impact of clad swelling on assembly cooling", IRSN, Technical Report SEMCA 2006-183, July 2006.
5. Grandjean, C., "Coolability of blocked regions in a rod bundle after ballooning under LOCA conditions", *Nuclear Engineering and Design*, 237(2007), pp. 1872-1886.
6. Ihle, P. and Rust, K., "FEBA. Flooding experiments with blocked arrays. Evaluation Report", KfK 3657, March 1984.
7. Ihle, P. and Rust, K., "SEFLEX. Fuel rod simulator effects in flooding experiments. Part 1: Evaluation Report", KfK 4024, March 1986.
8. Ihle, P. and Rust, K., "PWR reflood experiments using full length bundles of rods with Zircaloy cladding and alumina pellets", *Nuclear Engineering and Design*, 99(1987), pp. 223-237.

9. Pearson, K.G., *et al.*, "Reflooding experiments on a 49-rod cluster containing a long 90% blockage", UKAEA Report AEEW-R 1591, September 1983.
10. Cooper, C.A., Pearson, K.G., and Jowitt, D., "The THETIS 80% blocked cluster experiment. Part 3: Forced reflood experiments", UKAEA Report AEEW-R 1765, September 1984.
11. Pearson, K.G., Cooper, C.A., and Jowitt, D., "The THETIS 80% blocked cluster experiment. Part 4: Gravity reflood experiments", UKAEA Report AEEW-R 1766, September 1984.
12. Hochreiter, L.E., "FLECHT SEASET program final report", NUREG/CR-4167; EPRI NP-4112; WCAP-10926, November 1985.
13. U.S. Nuclear Regulatory Commission Regulatory Guide 1.195, "Methods and Assumptions for Evaluating Radiological Consequences of Design Basis Accidents at Light-Water Nuclear Power Reactors (ML0314906401113 – May 2003).
14. U.S. Nuclear Regulatory Commission Regulatory Guide 1.183, "Alternative Radiological Source Terms for Evaluating Design Basis Accidents at Nuclear Power Reactors" (ML003716792 – July 2000).
15. U.S. Nuclear Regulatory Commission Regulatory Guide 1.3, "Assumptions Used for Evaluating the Potential Radiological Consequences of a Loss of Coolant Accident for Boiling Water Reactors" (Rev. 2, ML003739601) – June 1974).
16. U.S. Nuclear Regulatory Commission Regulatory Guide 1.4, "Assumptions Used for Evaluating the Potential Radiological Consequences of a Loss of Coolant Accident for Pressurized Water Reactors" (Rev. 2, ML003739614) – June 1974).
17. Soffer, L., *et al.*, "Accident source terms for light-water nuclear power plants", Nuclear Regulatory Commission, NUREG-1465, February 1995.
18. Stephenson, W., *et al.*, "Realistic methods for calculating the releases and consequences of a large LOCA", Commission of the European Communities, EUR14179EN, 1992.
19. "Determination of the in-containment source term for a large-break loss of coolant accident", European Commission, April 2001.
20. "Fuel cladding failure criteria", European Commission, EUR 19256EN, September 1999.
21. Powers, D.A. and Meyer, R.O., "Cladding swelling and rupture models for LOCA analysis", NUREG-0630, April 1980.

## 5. OVERVIEW OF LOCA TESTING METHODOLOGY

LOCA testing methodology comprises a large number of different techniques. One reason for this variety of techniques is that the objectives of the different experiments vary. Because it is simply impossible to accurately simulate a LOCA, one must incorporate simulations of important factors as best as possible and as much as the test scope and cost allow. The objective can vary from determining the effect of a LOCA transient on a complete fuel bundle, irradiated or non-irradiated, to determining the effect of alloy elements on phase transformation behaviour. The former types of experiment are obviously quite complicated, expensive, and require extensive instrumentation and post-test metallographic evaluation. The latter experiment can be performed on small amounts of material with equipment on a laboratory workbench. However, it is still part of LOCA testing methodology because it is performed for the sole purpose of providing knowledge necessary for understanding and modelling LOCA phenomena and it may also require particular attention to experimental details unique to the LOCA question.

A somewhat arbitrary classification of various types of test could be the following:

- Separate effects tests aimed at elucidating one phenomenon.
- Tests with moderate integration, tests in which the interaction between two or more phenomena is studied.
- Integrated tests – tests on single real or simulated fuel rods or fuel bundles in or out of reactor.

For the separate effects test many of the main results will be presented in this section of the report while the results of latter types of tests are given in Sections 6 and 7.

### 5.1 Separate effects tests

#### 5.1.1 Creep tests

The creep properties of cladding alloys are central to modelling the deformation and failure of cladding tubes during a LOCA. Therefore, creep tests have been performed in the absence of an oxidizing steam atmosphere. Hardy [1] and Hunt and Foote [2] studied the high-temperature deformation behaviour of Zry-4 and Zry-2.5 Nb cladding tubes of the dimension typical of CANDU reactor fuel. The test technique was heating of 0.5 m long sections of cladding tubes in vacuum by passing an electrical current through the tubes. A heating rate of 25 K/s was used and the pressure was held constant. At a predetermined temperature, the electrical power was switched off and the internal pressure vented. After cooling in vacuum the diametral expansion was measured at room temperature. The procedure was repeated until specimen burst after which a curve of strain versus temperature could be evaluated. No axial constraint was used in these tests and it was observed that the specimens contracted while the temperature was in the  $\alpha$ -phase range [1]. Zry-2.5Nb is a stronger alloy than Zry-4. However, since it transforms to soft  $\beta$  at a lower temperature than Zry-4 it deforms at a higher rate than Zry-4 until all  $\alpha$  has been transformed to  $\beta$  because of the low strength of the two phase mixture of  $\alpha$  and  $\beta$ . As soon as the transformation was complete, a discontinuous decrease in creep rate was observed for both alloys.

This decrease is explained as an effect of solution hardening since all alloying elements are dissolved in the  $\beta$  phase. The same equipment has later been used in a study of LOCA transients on  $\beta$  heat treated material [3].

There are a couple of technical details worth commenting on since they apply to the methodology used by many of the experimenters. The use of self-resistance heating of cladding tubes which are expanded by an internal pressure leads to a relatively uniform temperature distribution in the tubes. The reason is that the power density in the material is  $\rho i^2$  where  $\rho$  is the resistivity of the material and  $i$  the current density. To a first approximation then the current density remains constant when the tube expands since the cross sectional area remains constant. Even if a local bulge starts to develop, it does not lead to any locally increased power density which would lead to a thermal instability. This behaviour is in contrast to the behaviour of a uniaxially stressed specimen with electrical heating for which any tendency to non-uniform deformation is exacerbated by the locally increased heating.

The other point to note is the change in stress with diametral expansion when the test is performed with constant internal pressure. An exact treatment of the deformation of cladding tubes requires that they are treated as thick-walled tubes. However, in the present context we will simplify the treatment by regarding them as thin-walled tubes. If the initial diameter is  $D_0$  and the initial wall thickness is  $h_0$ , volume constance during deformation leads to:

$$D_0 h_0 = D h \quad (5-1)$$

We can define engineering diametral strain  $e$  as

$$e = D / D_0 - 1 \quad (5-2)$$

The stress under the internal pressure  $p$  is given by:

$$\sigma = \frac{pD}{2h} = \frac{pD_0}{2h_0} (1+e)^2 = \sigma_0 (1+e)^2 \quad (5-3)$$

where  $\sigma_0$  is the nominal stress or initial stress of the test. In terms of true stresses and strains the relationship is:

$$\sigma = \sigma_0 \exp(2\epsilon) \quad (5-4)$$

The exponential in (5-4) perhaps better than (5-3) demonstrates that the stress increases sharply with diametral expansion. Under creep conditions there is no strain hardening of the material. If a bulge starts to develop, it will be unstable and lead to a local failure. Hunt and Foote, in agreement with most other workers in the field, assumed a strain rate equation of the form:

$$\dot{\epsilon} = A \exp\left(-\frac{Q}{RT}\right) \bar{\sigma}^n \quad (5-5)$$

where  $A$  is a constant,  $Q$  the activation energy, and  $\bar{\sigma}$  the effective stress evaluated with regard to the anisotropy of the tubes. In an isothermal test, the time  $t$  to reach the strain  $\epsilon$  is given by:

$$t = \frac{1}{2n\dot{\epsilon}_0} (1 - \exp(-2n\epsilon)) \quad (5-6)$$

where  $\dot{\epsilon}_0$  is the strain rate at time 0. In particular, the time  $t_f$  to reach infinite strain is given by:

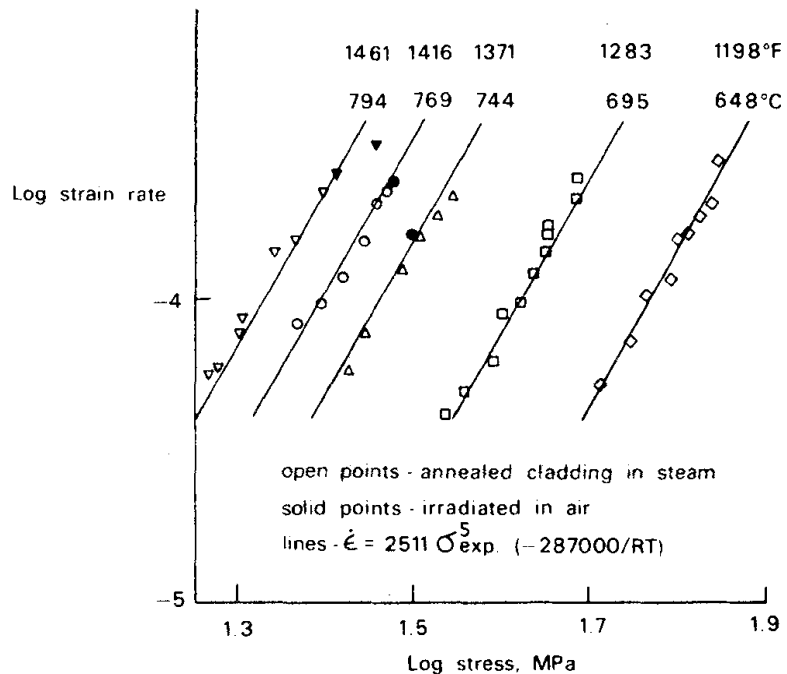
$$t_f = \frac{1}{2n\dot{\epsilon}_0} \quad (5-7)$$

Often  $n$  has a value of 4-5. Then this failure time deviates little from the time to failure if the tube would fail at say 50% strain. With  $n=5$  the time to reach 50% strain is 99.3% of  $t_f$ . Another point to note is that if there is a small irregularity in the wall thickness this will lead to the formation of a bulge or balloon on the specimen but again the effect on time to failure will be small.

The discussion above implicitly assumed that the material was isotropic. However, as mentioned before,  $\alpha$ -zirconium is anisotropic. If a tube is expanded under internal pressure, it becomes shorter. Therefore, the relation (5-1) is not strictly true. How it is modified for zirconium alloys and other aspects of the anisotropy are discussed further in Appendix A.

Rose and Hindle used a similar technique with electrical heating when they studied the deformation and fracture of Steam Generating Heavy Water Reactor cladding [4]. However, in contrast to Hunt and Foote, they performed isothermal tests and used photography to record strains in tests on unirradiated cladding. On irradiated cladding, the deformation was tracked with a telescope. Some of their results are summarised in Figure 5.1.

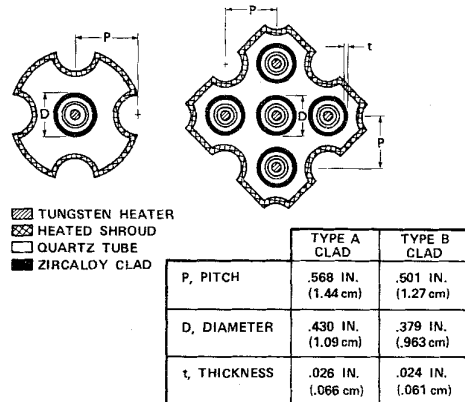
Figure 5.1 Creep properties of Zircaloy-2 in the temperature range 650-800°C



Fiveland *et al.* used a different arrangement for heating the cladding in a tube burst test [5] (Figure 5.2). They used a tungsten rod as an internal radiation heater. Its primary advantage is its quick response. To simulate the surrounding environment in a reactor core, the test rod or rods were surrounded by a heated stainless steel shroud. The temperature during testing was monitored by up to 12 Type K thermocouples. Specimen pressure was monitored continuously by calibrated pressure transducers. The tests were carried out in an argon atmosphere and argon was also used for the internal pressurisation of the tubes. A test started at a constant temperature of 315°C until steady state was reached, then the temperature was increased at a constant rate until all tubes had ruptured. The pressure remained nearly constant during the test. A main result of the test series was a relation between rupture temperature and hoop stress:

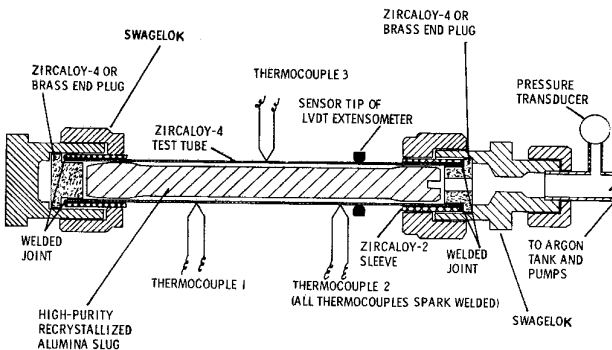
$$T_R(\text{°C}) = 1008 - 3.17 \sigma (\text{MPa}) \quad (5-8)$$

Figure 5.2 Heating arrangement in the experiments by Fiveland *et al.* [5]



Chung and Kassner reported tests in vacuum and steam of Zircaloy cladding heated with alternating current [6]. Their specimen design is shown in Figure 5.3.

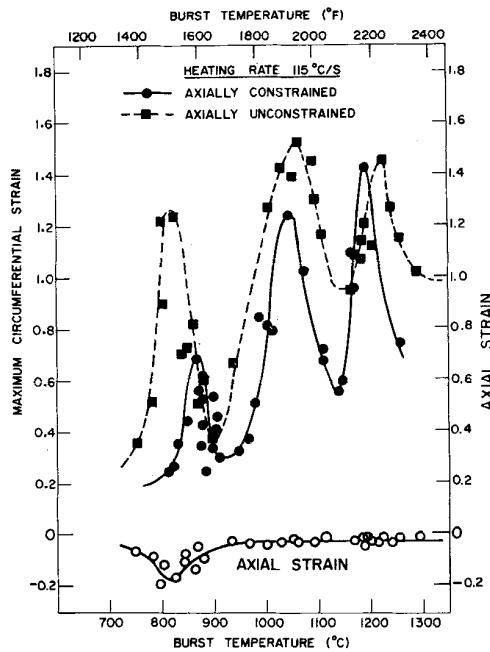
Figure 5.3 The 15.2 cm long specimen used by Chung and Kassner



In addition to the extensometer seen in the figure for monitoring of diametral expansion, the specimen was also photographed with a high-speed camera during the test for post-test evaluation of diametral expansion and axial deformation. The gap between end plugs and  $\text{Al}_2\text{O}_3$  mandrel could be varied in order to produce various degrees of axial constraint. The experiments were carried out in a bell jar vacuum chamber with or without steam flow. Several different heating rates were used, from 5 K/s to 115 K/s. For the analysis of the onset of ballooning, Chung and Kassner used a theory developed by Franklin [7]. However, this theory probably does not apply to this type of test. It is more probable that ballooning is started as a combined effect of temperature maxima and wall thickness minima. Figure 5.4 shows the rupture strain of unconstrained tubes tested in vacuum as a function of burst temperature, which provides baseline burst behaviour for unoxidized cladding.

Tube axial strain (shrinkage in length) can also be seen in Figure 5.4. The axial shrinkage, hence, the effect of axial constraint, should be greatest when the material is at the highest temperature yet when the material is still in anisotropic  $\alpha$  phase. This temperature is about 812–815°C. Once the material starts to transform to  $\alpha+\beta$ , it becomes more or less isotropic because the softer  $\beta$  controls the overall deformation. Then, the effect of constraint should disappear, because multiple slip systems in the softer  $\beta$  control the overall deformation, rather than the limiting prism slip in the hard  $\alpha$  material. Axial shrinkage, hence, the effect of axial constraint, is still observed for higher burst temperatures because pre-balloonning uniform deformation still occurs in  $\alpha$ -phase range, i.e., at <815°C. This pre-balloonning axial contraction is, therefore, more or less independent of burst temperature.

**Figure 5.4 Maximum circumferential strain at rupture vs burst temperature for axially constrained and unconstrained Zircaloy-4 cladding at a heating rate of 115 K/s.**  
**The axial strain of unconstrained tubes also is shown.**



Although the authors did not discuss the three ductility maxima in great detail, they attributed the first maximum to the superplasticity observed near the  $\alpha/\beta$ -boundary temperature from isothermal uniaxial tensile tests [8-9]. The first strain maximum in Figure 5.4 was very sensitive to the magnitude of azimuthal temperature variation that was produced by the variation in heat transfer between the cladding and the internal mandrel or alumina pellets that simulated fuel pellets. The second and the third strain maxima were strongly suppressed by the high-temperature steam oxidation, the latter being almost invisible at slow heating rate.

In summary, ballooning and burst behaviour is strongly influenced by and a complex function of maximum cladding temperature, azimuthal temperature variation in the ballooning region, axial constraint, heating rate, and steam oxidation.

The strong effect of azimuthal temperature variation in the ballooning region is one of the most important factors that determine fuel rod burst behaviour near 800°C and fuel assembly flow channel blockage under LOCA. Axially extended uniform ballooning accompanied by large burst strain is conducive to serious flow channel blockage in the core. This concern was once a serious LOCA issue in late 1970s and early 1980s, and numerous experimental programmes were devoted to address the issue in the early years. On single-rod basis, Chung and Kassner showed that such extended uniform ballooning with large burst strain is very difficult to occur because of azimuthal and axial temperature non-uniformity of various origins [6].

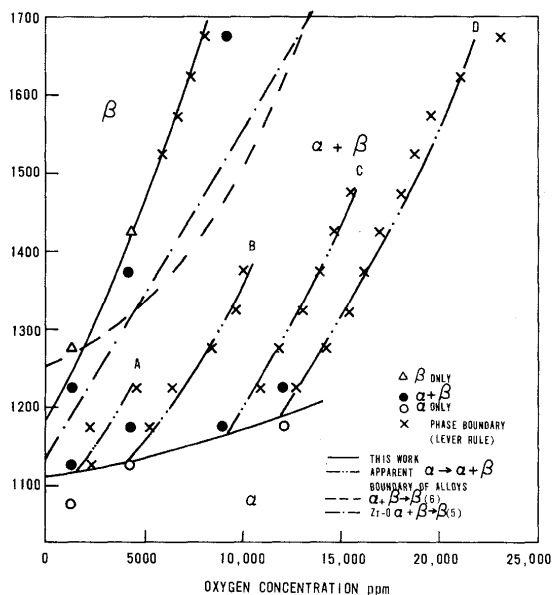
Rizkalla *et al.* studied the effect of oxygen concentration on the high temperature deformation of Zircaloy-2 [10]. The four alloys used were made by consumable arc melting of Zircaloy-2 and zirconium oxide to produce nominal oxygen concentrations of 1 200, 4 000, 8 000, and 12 000 ppm by weight. The alloys were prepared in the form of 12.7 mm diameter rods by extrusion and grinding.

The tests were carried out in an Instron testing machine modified for constant true-strain-rate hot compression. Specimens 13.8 mm long and 8.2 mm in diameter were machined from the rods. Tests

were carried out at 1 273, 1 373, and 1 473 K under a vacuum of  $10^{-4}$  Pa. The flow behaviour at different strain rates and temperatures was too complicated to be described in the present context. One of the conclusions of the work was that the effect of oxygen on strength is twofold in the  $\alpha + \beta$  region: the oxygen contributes to solid solution strengthening and it also increases the volume fraction of  $\alpha$ .

The authors also evaluated by metallography the effect of oxygen on the fractions of  $\alpha$  and  $\beta$  at different temperatures to produce the pseudobinary Zircaloy-2 – oxygen phase diagram shown in Figure 5.5. Great caution must be exercised in this technique, because unless such a metallographic specimen is rapidly quenched from the equilibrating high temperature, significant fraction of  $\beta$ -phase periphery transforms and is absorbed into equiaxed  $\alpha$  grains during cooling. Because of these unique characteristics, the phase boundary in Figure 5.5 needs careful scrutiny. This topic is discussed later in more detail.

Figure 5.5 A pseudobinary phase diagram for the Zircaloy-oxygen system



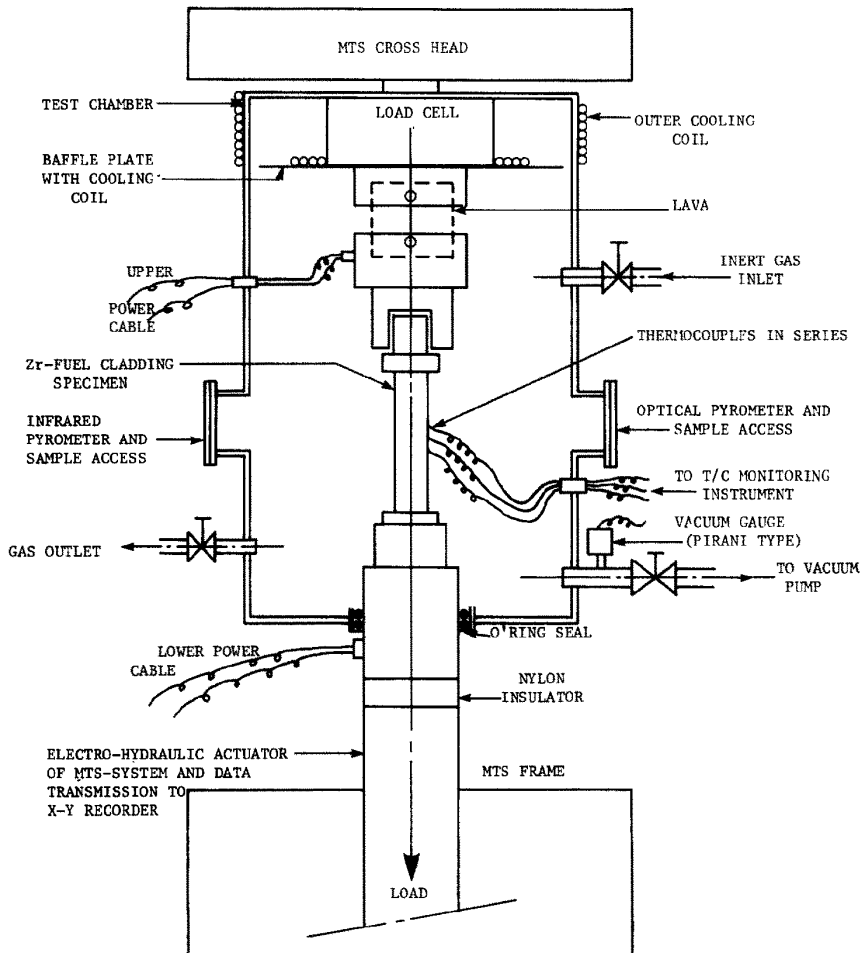
Hindle has performed stress rupture tests of Zircaloy-4 PWR tubes of the 17×17 type [11]. The results showed that their rupture life can be predicted approximately using the simple relationship  $\dot{\varepsilon}_i \cdot t_R = 1/2n$  where  $\dot{\varepsilon}_i$  is the initial secondary creep rate and n the stress exponent according to eq. 5-5. This prediction is a consequence of eq. 5-7.

It is important, however, to note that some simulation techniques lead to unrealistically uniform and large tube deformation that is not applicable to LOCA situations. Such simulation techniques are usually simpler, and the results are academically easier to model, e.g., isothermal creep or slow-strain-rate test using uniform heating method. Deformation behaviour under LOCA is, however, far more complex, and great caution is needed in the interpretation of such results relative to LOCA situations.

Rosinger [12] and Rosinger *et al.* [13] have performed an extensive study of the creep of Zircaloy-4 fuel cladding from 940 to 1 873 K. As can be seen in Figure 5.6, the specimens were tested in uniaxial tension.

The specimens were heated by ac current at a rate of 50 to 100 K/s. A constant load during testing could be maintained through the load control mode of the MTS system. The creep tests were terminated after either 10 min or 0.15 strain. Figure 5.7 shows some typical results from the tests.

Figure 5.6 Schematic of Rosinger's high temperature creep apparatus



Rosinger *et al.* summarised their results with some results from the literature and found the following equation for the steady-state creep of Zircaloy-4  $\alpha$ -phase at  $940\text{K} \leq T \leq 1095\text{ K}$ :

$$\dot{\epsilon}_{ss} = 2000\sigma^{(5.32 \pm 0.14)} \exp(-284000/RT) \quad (5-9)$$

A corresponding relation for the  $\beta$ -phase is:

$$\dot{\epsilon}_{ss} = 8.1\sigma^{(3.79 \pm 0.02)} \exp(-142300/RT) \quad (5-10)$$

In the two phase region,  $1095 < T < 1245$  the strain rate dependence of stress is creep rate dependent. For strain rates over  $3 \times 10^{-3} \text{ s}^{-1}$

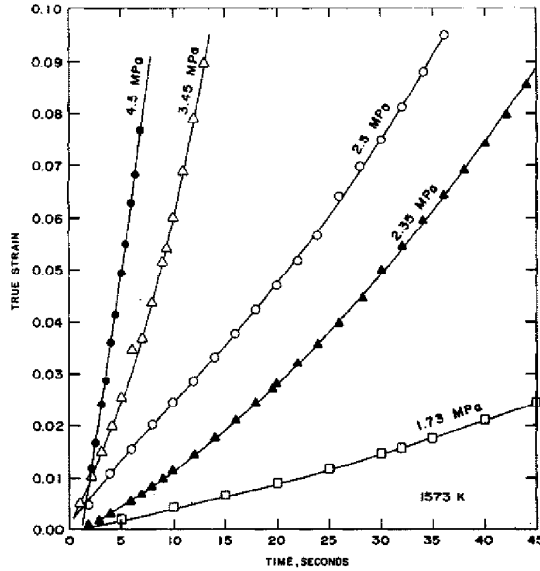
$$\dot{\epsilon}_{ss} = 84\sigma^{(2.28 \pm 0.06)} \exp(-155100/RT) \quad (5-11)$$

and for strain rates less than  $3 \times 10^{-3} \text{ s}^{-1}$

$$\dot{\epsilon}_{ss} = 6.8\sigma^{1.8} \exp(-56600/RT) \quad (5-12)$$

The latter equation indicates that grain boundary sliding is an important deformation mode in the two phase region and it is also this mechanism which leads to the superplastic behaviour observed in this region.

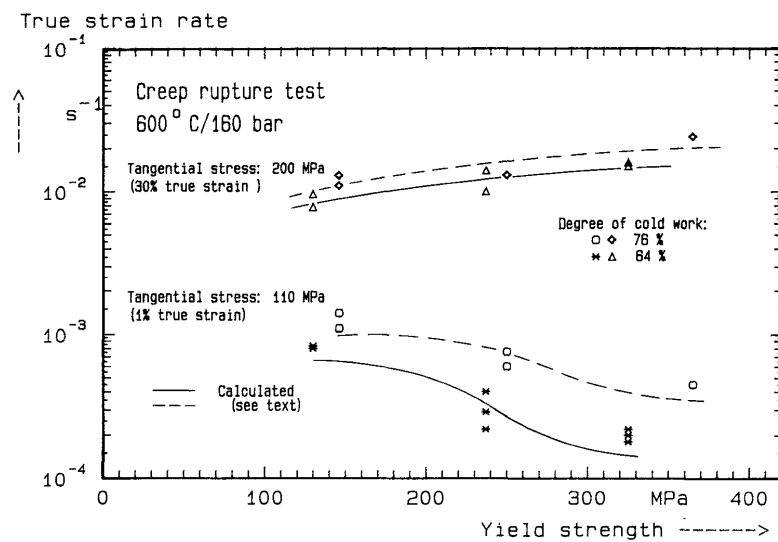
Figure 5.7 Typical creep test results from Rosinger's investigation at 1 573 K [13]



The creep experiments performed by Ortlieb et al were performed on tubes heated by resistance heating in order to obtain a very uniform temperature [14]. The object of the experiments was to determine if there was any influence of initial material condition on the deformation of Zircaloy-4 cladding tubes at 600 and 800°C. The cladding tube deformation was recorded by an automatic camera. The pressurizing medium was helium and the outer environment air. The specimens contained a fixed volume of gas which leads to a decreasing pressure with increased strain but still a monotonically increasing circumferential stress. For creep tests, the temperature was increased by 50 K/s and then held constant until specimen rupture. In creep rupture tests, different heating rates were used until the specimen ruptured. The main result of the investigation was that the initial condition played little role at 800°C while at 600°C effects of initial condition were observed as plotted in Figure 5.8.

Figure 5.8 The effect of initial condition on creep properties at 600°C

The lowest yield strengths correspond to fully recrystallized material while the other point represent various degrees of recrystallization [14]



### 5.1.2 Determination of diffusion constants

Modelling of the growth of the oxide layer and the oxygen stabilised  $\alpha$  layer requires knowledge of the diffusion coefficients of oxygen in the two phases. In addition, it is necessary to know the diffusion coefficient in the  $\beta$  layer in order to calculate how fast the  $\alpha$  grows into the  $\beta$ . It is, in principle, possible to infer from observed growth rates what magnitude and temperature dependence the diffusion constants should have provided that one also has reliable information on the compositions at the phase boundaries. This is also what many investigators have tried to do. However, there is a considerable advantage with directly determined diffusion constants since they provide independent confirmation of the values determined in a less direct manner.

Early examples of direct determination of oxygen diffusion in  $\alpha$ -phase,  $\beta$ -phase and oxide can be found in the review by Douglass [15]. The only example of a direct determination related to the LOCA issue can be found in a paper by Pawel *et al.* [16]. They determined the diffusion coefficient in  $\beta$  phase by studying the diffusion of the  $^{18}\text{O}$  isotope. For determination of the tracer diffusion coefficient, a 2  $\mu\text{m}$  thick oxide layer was grown from  $\text{H}_2^{18}\text{O}$  at 800°C which was subsequently dissolved in the metal. The chemical diffusion coefficient was determined by studying a diffusion couple with 0.1 wt% O on one side and 0.6 wt % O on the other side with the oxygen enriched in  $^{18}\text{O}$  by an oxidation annealing process. The tracer diffusion samples and diffusion couples were heat treated in a vacuum furnace for different times at different temperatures. After heat treatment, the specimens were sectioned in the direction of diffusion and prepared metallographically. Concentration gradients were determined by radiographic techniques that involved either proton bombardment radioactivation of  $^{18}\text{O}$  or by Auger electron spectroscopy. The observed concentration was correlated to known solutions to the respective diffusion problems. It turned out that observed values of the tracer diffusion coefficient and the chemical diffusion coefficient belonged to the same data set. A best fit to the data set after correction for the mass difference between  $^{18}\text{O}$  and  $^{16}\text{O}$  is:

$$D_\beta = 0.063 \exp(-14192/T) \quad (5-13)$$

This value differs somewhat from values given in Douglass [15].

### 5.1.3 Determination of the $\alpha$ to $\alpha + \beta$ and $\alpha + \beta$ to $\beta$ transformation temperatures

The temperatures, when  $\alpha$  starts to transform to  $\beta$  and when the transformation to  $\beta$  is complete, depend on the alloying elements in zirconium. The pure Zr metal transforms at 862°C but the addition of an alloying element will change this transformation temperature. It also changes the character of the transformation so that it occurs in a temperature interval over which the volume fraction of  $\beta$  grows at the expense of the volume fraction of  $\alpha$ . The beginning of the temperature interval will be denoted  $T_{\alpha/\alpha+\beta}$  and the end  $T_{\alpha+\beta/\beta}$ . The addition of an alloying element either increases or decreases the transformation temperature. If it increases the temperature the element is called an  $\alpha$  stabiliser. Examples are O which is a strong  $\alpha$  stabiliser and Sn. Examples of  $\beta$  stabilisers are most other elements including common alloying elements like Nb, Fe, Cr and Ni and inadvertently added elements like H.

In several earlier works [10,17] the transformation interval for Zircaloy has been charted by metallographic evaluation of the volume fraction of  $\beta$  after fast cooling from a known temperature. The former  $\beta$ , which at room temperature of course also is  $\alpha$ , is easily distinguished from the high temperature  $\alpha$  phase by the transformation structure in the former  $\beta$  grains which consists of fine Widmanstätten plates. At a temperature slightly above the  $\alpha$ - $\beta$  equilibrium boundary, only a small amount of the  $\beta$  phase is present at grain boundary triple points and as thin films surrounding the  $\alpha$  grains. This type of  $\beta$  can be detected only through direct quenching of the equilibrated specimen into a cold bath of oil or water [17]. Under usual cooling conditions without direct quenching from the

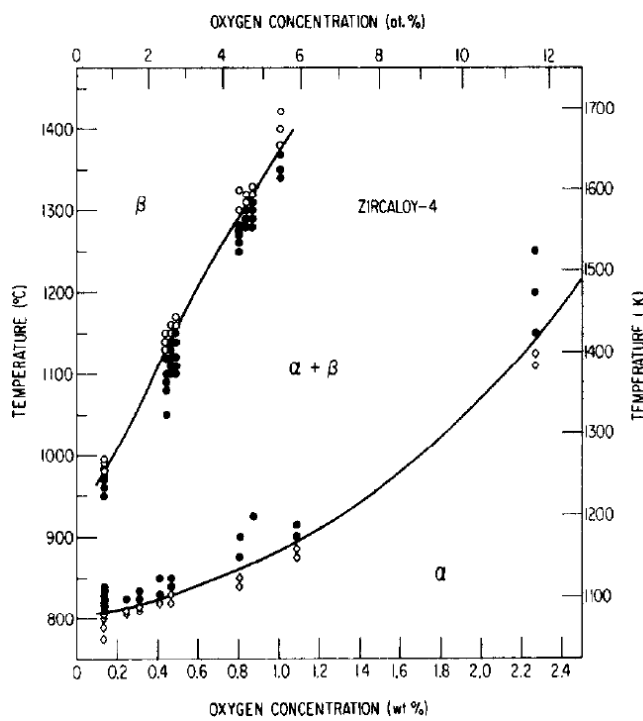
equilibration temperature, this type of  $\beta$  cannot be detected, because such thin  $\beta$  is quickly absorbed into the equiaxed  $\alpha$  grains during cooling. Thus, at room temperature the sample contains only equiaxed  $\alpha$ , misleading the true structure present at equilibration temperature. Because of this difficulty characteristic of a Zr-based alloy, early investigations commonly led to  $\alpha$ - $\beta$  phase-boundary temperatures significantly higher than true boundary temperatures, e.g., the boundaries deduced from metallography of non-quenched sample shown in Figure 5.5.

Figure 5.9 shows equilibrium phase boundaries reported by Chung and Kassner from examination of quenched metallographic specimens of Zircaloy-4 [17]. Note that for as-received Zircaloy-4 that contains oxygen concentration of  $\approx 0.12$  wt %,  $\alpha$ - $\beta$  boundary temperature is  $\approx 812^\circ\text{C}$ . This temperature is close to the temperature at which the first superplastic strain peak and maximum axial contraction occur during ballooning (Figure 5.4). Based on the result of Figure 5.9, Chung and Kassner developed a correlation for solubility of oxygen in  $\beta$  phase ( $C_s$ ) as function of absolute temperature ( $T$ ) for as-fabricated Zircaloy-4 (hydrogen content  $< 50$  wppm):

$$C_s = \exp(5.02 - 8220.0/T) \quad \text{for } T \geq 1373.16^\circ\text{K}$$

$$C_s = -2.505 + 0.00211T \quad \text{for } T < 1373.16^\circ\text{K}$$

Figure 5.9 Oxygen-rich-side Zircaloy-4-oxygen phase diagram determined from metallography of quenched samples, from Chung and Kassner [17]



As described in Chapter 1, pages 1-19, Pawel deduced 0.7 wt % as the threshold oxygen concentration in  $\beta$  below which post-quench ductility was retained in the Zircaloy-4 specimens that were oxidized on two sides and tested by Hobson in 1973 [18,19]. It is interesting to note that this threshold concentration corresponds to true specimen temperature of  $\approx 1\ 256^\circ\text{C}$  rather than Hobson's furnace temperature of  $1\ 204^\circ\text{C}$  ( $2\ 200^\circ\text{F}$ ).

More recently the interest in the  $\alpha$  to  $\beta$  transformation has grown because of the increased use of Nb containing alloys and the expected high hydrogen concentrations in high burn-up fuel. Of particular importance is the effect of increased concentration of H (a  $\beta$  stabiliser) on the solubility limit of O (an  $\alpha$  stabiliser) in  $\beta$  phase.

Forgeron *et al.* studied the transformation temperatures for Zircaloy-4, M4, and M5 alloys [20]. Their methods were calorimetry, dilatometry, and image analysis on elemental X-ray maps. A high temperature high-sensitivity calorimeter was used with slow heating-cooling rates for determining quasi-equilibrium values. For studies of the  $\alpha \rightarrow \beta$  kinetics a dilatometer was used on 12 mm long pieces of cladding. The point of using cladding pieces instead of other forms of the alloys is that initial metallurgical conditions were found to have a large effect on the  $\alpha \rightarrow \beta$  kinetics upon heating. On the other hand, compensation for texture and the resulting anisotropy of thermal expansion had to be made.

Volume fractions of  $\alpha$  and  $\beta$  were also evaluated by image analysis on samples which had been heat treated 2 hours at the equilibrium temperature. The microstructures used for image analysis were Sn X-ray maps. Since Sn accumulates in  $\alpha$  at the equilibration temperature and is a slow diffuser, the X-ray maps should give a relatively accurate picture of the amount of  $\alpha$  phase at temperature even though the samples were not quenched rapidly. The result of the image analysis compared to the calorimetric results was that full equilibrium is not achieved by the 2-hour heat treatment.

The experimental results were compared to two analytical models. One model due to Holt *et al.* on a mechanistic basis could be made to fit well to data from heatup but did not work well on data from cooling. Therefore the authors developed a more empirical model based on the sigmoidal shape of the transformed volume fraction versus temperature curves. If  $y$  is the transformed volume fraction the following equation leads to a sigmoidally shaped curve:

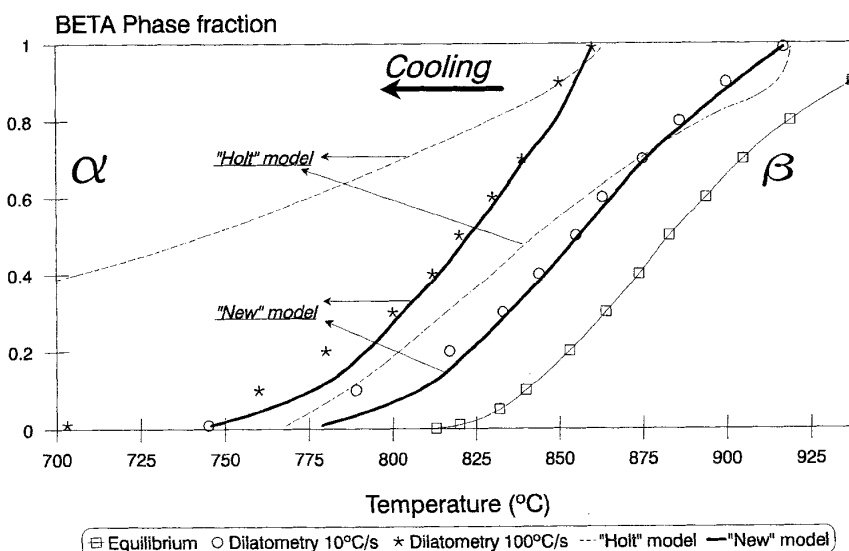
$$dy/dt = K(T) \cdot y \cdot (1-y) \quad (5-14)$$

where  $K(T)$  is an empirical function of temperature:

$$K = \pm |T - T_{eq}| \cdot \exp(c_1 + c_2 \cdot |T - T_{eq}|) \quad (5-15)$$

The constants  $c_1$  and  $c_2$  are to be fitted to experimental data. Figure 5.10 shows how the model works on two different cooling rates from 1 020°C.

Figure 5.10 Comparison between transformation models and experiments on cooling of Zircaloy-4

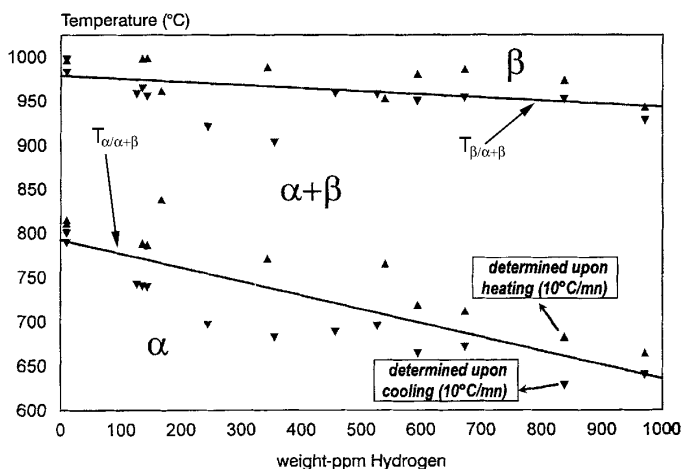


The same techniques were used in a study by Brachet *et al.* on the effect of hydrogen on the phase transformation of the same three alloys [21]. Figure 5.11 shows the effect of hydrogen on the transformation temperatures of Zircaloy-4.

In the calorimetric measurements, they performed several cycles and noted that hydrogen was lost by desorption in each cycle. It was also possible to determine the hydrogen content after each cycle by noting when hydride precipitation started. In a separate run with specimens with known hydrogen content, it had been established that the onset of hydride precipitation agreed well with literature values. Thus a curve like Figure 5.11 required fewer specimens than the number of data points suggests. Data from dilatometric measurements were used to determine transformation temperatures at different heating rates. The observations were used to calibrate a model for the transformation kinetics described in detail in their paper [21].

**Figure 5.11 Plot of  $T_{\alpha/\alpha+\beta}$  and  $T_{\beta/\alpha+\beta}$  temperatures measured upon heating and cooling at 10°C/min as a function of hydrogen content**

The straight lines (average between heating and cooling) are assumed to be representative of equilibrium temperatures [21]



Note that in Figure 5.11, the  $\beta$ -to- $\alpha$  transformation in as-received Zircaloy-4 (hydrogen content  $\approx 15$  wppm) starts at about 812–815°C, virtually the same as the equilibrium temperature shown in Figure 5.11. This indicates that virtual equilibrium was maintained for the slow cooling rate of 10 K/s.

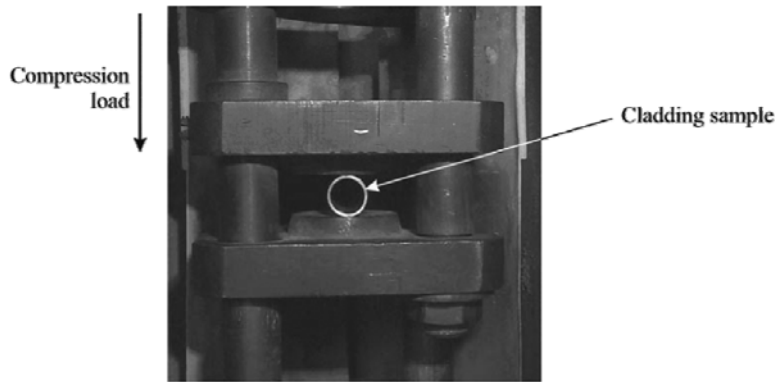
As part of a study on the creep rupture behaviour of Zircaloy-4 Sell and Ortlieb determined the phase fraction  $\beta$  with the aid of synchrotron radiation [22]. The measurements were done on electrically heated tubes which were prevented from oxidation by an argon atmosphere. The synchrotron radiation was monochromatised at a photon energy of 70 keV corresponding to 0.18 Å with a spot size of  $2 \times 1$  mm<sup>2</sup>. A horizontal slice of the diffraction cone was recorded moving an image plate detector continuously behind a slit. This permitted a quasi continuous evaluation of the kinetics of the transformation. In one test series, the diffraction pattern as a function of the time was determined at different temperatures. In another test series, the diffraction pattern as a function of the time was determined at two different heat-up rates, 1 and 10 K/s. The evaluated phase fractions from the diffraction patterns agreed well with but did not exactly correspond to the data by Forgeron *et al.* [20].

### 5.1.4 Ductility tests

#### 5.1.4.1 The ring compression test

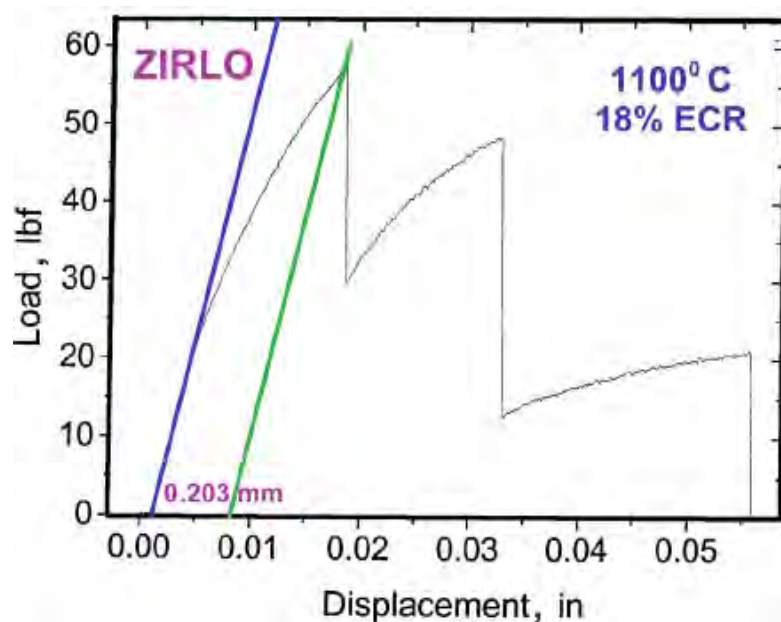
Ever since the original work by Hobson and Rittenhouse [18-19] the ring compression test has been the most widely used ductility test for determining cladding embrittlement after a LOCA simulation. Its main advantage is that it is very simple to perform, requires a minimum of specimen preparation and requires only a limited amount of material. Figure 5.12 shows an example of the arrangement for a ring compression test [23].

Figure 5.12 The arrangement for a ring compression test [23]



The experiment is typically performed with a displacement rate of the order of 1 mm/min and to a predetermined displacement, or until it is clear that the specimen has fractured. When the specimen has been oxidized on the outside diameter only fracture occurs at the 3 and 9 o'clock positions while with two-sided oxidation it is also possible to have fracture in the 6 and 12 o'clock positions. An interesting question which seems to be rarely discussed in connection with the tests is whether or not these positions are equivalent. A simple stress analysis based on the theory of the bending of beams with constant curvature shows that there is a significant difference in the magnitude of the bending moments between the 3 and 9 o'clock locations and the 6 and 12 o'clock locations. The bending moment is in fact about 75% higher in the loading positions than in the horizontal diameter positions. Since there is in the latter positions also a compressive stress due to the vertical load, the tensile stress in the horizontal positions is only about half of the tensile stress in the loading positions. These statements are based on an analysis of the ring as a homogeneous isotropic material. The real case of an oxidized ring is much more complex with outer layers of oxide and oxygen stabilised  $\alpha$  which crack easily and a more or less brittle inner layer of prior  $\beta$ -phase. Figure 5.13 shows a representative load versus displacement record from a ring compression test on a Zirlo ring.

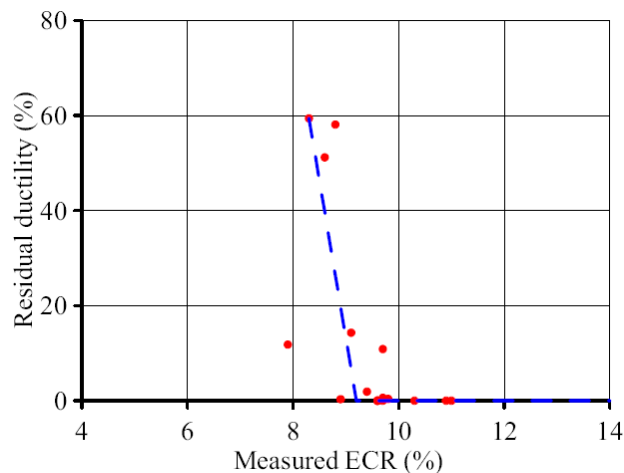
Figure 5.13 Load-displacement record from a ring compression test on an oxidized Zirlo specimen [25]



The record shows three large load drops which correspond to fracture of the ring in one of the critical locations. Quite frequently a load-displacement record will contain some minor load drops corresponding to fracture of the oxide and/or  $\alpha$  layer but the large load drops seen in the figure are typical of all through cracks. The line drawn from the first load drop parallel to the elastic loading line defines the offset displacement at fracture. If the offset displacement is divided by the specimen diameter, a nominal plastic hoop strain at failure can be defined. According to Billone *et al.* [24], for small offset displacement, it is recommended to unload the specimen at the first load drop and measure the difference between the diameter at the load point before and after testing. For some reason, this is not equal to offset displacement evaluated from the load displacement record. The displacement divided by the diameter is sometimes also called the “relative displacement” [23].

There seems to be no clear definition on what is an acceptable ductility from the ring compression test. However, in most cases, when the ring compression test is used, tests are performed at several different levels of oxidation. Then, if the offset displacement at failure or the “residual ductility” as defined by Yegorova *et al.* [23] is plotted against ECR there is usually a relatively narrow ECR interval when the residual ductility decreases rapidly with ECR (Figure 5.14).

**Figure 5.14 Residual ductility  
(defined as offset displacement at failure divided by ring diameter)  
plotted against ECR for E110 alloy [23]**



Then it is natural to define the critical ECR as that obtained by extrapolating the fall in residual ductility to zero.

Another definition of unacceptable brittleness has been proposed by Hózer and Györy [26], and an example of its application can be found in a paper by Hózer *et al.* [27]. Hózer and Györy proposed to use strain energy per mm of specimen length spent during the compression test up to the formation of the first through crack as a brittleness criterion. If the strain energy is <50 mJ/mm, the specimen is defined as brittle. They note that any one of relative deformation, residual ductility or energy will work as a fracture criterion but prefer the latter because of the similarity with the standard for reactor vessel embrittlement. As another advantage they note that by using mJ/mm, it is possible to compare specimens of different lengths. This is obviously also true for relative displacement at failure as well as residual ductility unless length has some unexpected effect on the results of the ring compression tests. That such unexpected effects are in fact absent has been verified by Yegorova *et al.* [23] in a series of ring compression tests on specimens of different lengths, 8 mm, 15 mm and 25 mm. However, they warn that in case short specimens that were oxidized in their final dimension are tested, then the oxides present on the ends of the specimen may have an adverse effect on ductility.

Quite clearly all the proposed criteria or test results will to some extent be dependent on cladding dimension. This should be clear from the fact that results of calculations of the stresses for a homogeneous material vary somewhat with cladding dimension. However, there are currently relatively small differences between the dimensions of different types of tested cladding tubes. Therefore, in view of the variations in results inherent in a complex process such as steam oxidation followed by a ductility test, it seems reasonable to assume that these attempts to standardise the brittleness criteria can be quite successful.

#### 5.1.4.2 Ring tensile tests

The ring tensile test can be almost as simple to perform as a ring compression test. In a study of oxygen embrittlement criteria Sawatsky [28] used rings of cladding tube in which D grips were inserted to provide tangential load on the specimen. The D grips were attached to the pull rods of the tensile machine. The specimen circumference was taken as gage length. Friction between the specimen and grips resulted in scattered and consistently low elongation values.

A bit more elaborate arrangement for a ring tensile test is shown in Figure 5.15 with the D grip in the upper left corner of the Figure.

Figure 5.15 Components of a ring tensile test, D grip to the left and specimen to the right [29]



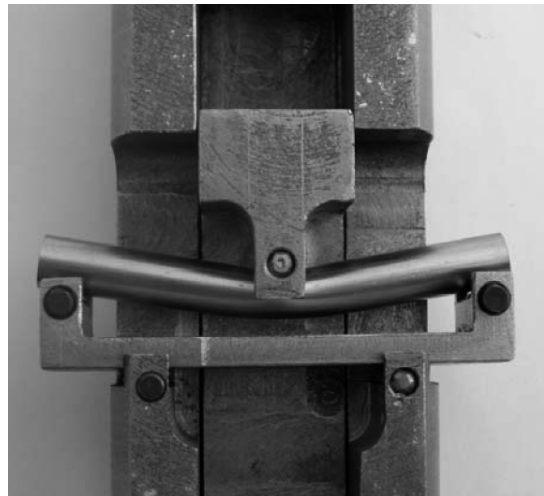
Here the ring has been milled so that two parallel-sided gage lengths have been formed. The gage length is loaded by the D grip which is connected to the tensile machine pull rods. It is necessary to lubricate the surface between D grip and specimen in order to get a uniform value for the stress along the gage length. Kim and Lee have shown that lubricating with vacuum grease or teflon tape results in almost identical stress-strain curves [29]. An alternative way of performing the ring tensile test is to orient the gage lengths so that they are parallel with the loading direction. In this orientation lubrication is less critical but with increasing deformation the specimen will tend to straighten in the gap between the D grips. This disadvantage can be remedied to some extent by adjusting the shape of the D grips so that supporting pieces with the same curvature as the inner surface of the cladding can be placed at the gap.

The main difference between the ring compression test and the ring tensile test is the stress distribution over the specimen wall thickness. In the compression test, it is a typical bending stress which goes from compression to tension. In the ring tensile stress, the stress distribution is approximately a uniform tensile stress. In view of that difference, it seems possible that results of the two types of tests will not give comparable results. However, Yegorova *et al.* have performed a comparison between the ring compression test and ring tensile test. In tests performed on E110 alloy oxidized at 1 100°C, both types of test resulted in the same value of the zero ductility threshold [23].

#### 5.1.4.3 Tube bending tests

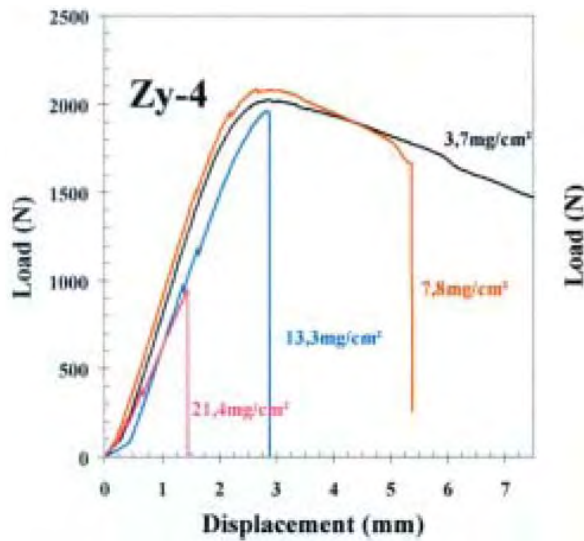
A typical three-point bending test is shown in Figure 5.16.

Figure 5.16 Three-point bending test apparatus, from [23]



In the work reported in [23], the sample length was 80 mm and the distance between the outer supports was 70 mm. Both the supports and the loading point were cylindrical rollers with 5 mm diameter. This minimises friction effects during the bending of the tube. The specimen is typically loaded with 1 mm/min and the relation between displacement and load is recorded during the test. Typical records are shown in Figure 5.17.

Figure 5.17 Load-displacement records from three-point bend tests of oxidized Zircaloy-4 [30]

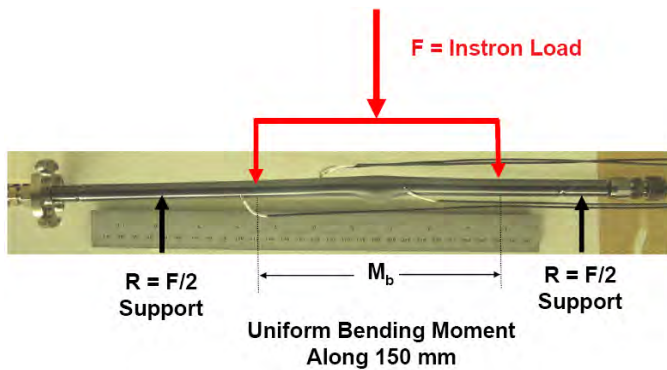


In the three-point bend tests, the stress distribution is nominally uniform over the specimen thickness while its magnitude and sign varies around the circumference. The word nominally is used because in a test of LOCA-oxidized material, the differences in properties between the different layers will lead to non-uniformity of the stress distribution during a test. It can be also noted that, in the three-point bend test, the material is stressed axially which is perhaps a more realistic loading situation in relation to real LOCA loads. Yegorova *et al.* have also compared the three-point bend test with the ring compression test with

regard to the critical ECR for clad embrittlement [23]. For E110 cladding tubes oxidized at 1 100°C, the zero ductility threshold determined by the three-point bend test was ECR=11.8% whereas the ring compression test gave ECR=8.3%. In comparison with the ring compression test, Portier *et al.* have noted that it is easier to detect complete failure through the cladding wall in the three-point bend test [31].

Occasionally four-point bend tests are performed. One such test is described schematically in Figure 5.18. As shown in the figure, there is a constant bending moment between the two inner supports. Therefore, the four-point bend test can be used to find the weakest point along the tube in case there are axial variations in brittleness or some other property of interest. In the case shown in Figure 5.18, the burst location has been oriented so that it is subjected to a tensile stress. In cases where tubes have burst, it is not necessarily the burst location which is the most brittle since inner surface oxidation after the burst may lead to extensive hydrogen pickup a few cm from the hole [32]. This effect makes it interesting to identify the weakest point axially on a tube after specimen burst.

Figure 5.18 Schematic description of a four-point bend test [33]



#### 5.1.4.4 Impact tests

An impact test reveals sensitivity to embrittlement at high strain rates. The reason why high strain rate is conducive to more pronounced embrittlement is that the high strain rate results in a higher stress level for plastic deformation than a low strain rate. Some materials exhibit a brittle-to-ductile transition behaviour in a narrow range of test temperature. Such materials have an intrinsic fracture stress which when it is exceeded results in brittle fracture. Ductile behaviour starts when the in general temperature dependent yield strength falls below this fracture stress. In most impact tests, a notched specimen is used. Just under the notched surface, a triaxial stress state is obtained which raises the general stress level before yield. Thus, a brittle behaviour of materials with a brittle-to-ductile transition will be obtained at a significantly higher temperature than under uniaxial loading.

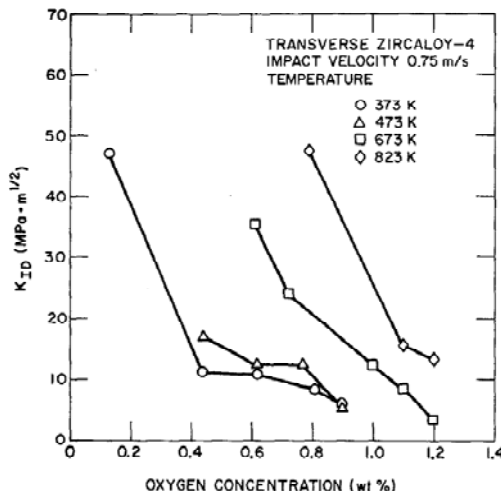
Zircaloy or other zirconium alloys do not in themselves have a brittle-to-ductile transition. However, when zirconium alloys contain a certain amount of hydrides a ductile-to-brittle transition is observed in the temperature range 100-200°C, depending on alloy composition, hydrogen content and strain rate [34]. Although it has not been investigated systematically until recently by Stern *et al.* [35], it is reasonable to assume that a ductile-to-brittle transition may also occur in zirconium alloys with an oxygen content above a certain level as was in fact confirmed in the work by Stern *et al.* It is, however, well established that there is no ductile-to-brittle transition even at extremely low temperatures at the oxygen levels typical of commercial cladding, i.e. 0.10-0.14 wt %.

A more practical reason to perform impact tests in the LOCA context is that some of the loads of concern may be in the form of impact, for instance rod-to-rod impact in ballooned regions during quenching or post-quench handling. In fact the first ring compression tests performed by Hobson and Rittenhouse were impact tests in which 10.7 mm diameter rings were compressed 3.81 mm by impact

loading [19]. Later Hobson reported slower strain rate compression tests on the same material [18]. The results of these later tests are plotted in Figure 1.2 in which the zero ductility temperature (ZDT) observed in the impact tests are shown as full lines while the ZDT estimated from the slow tests are shown as dashed lines. The difference in the zero ductility temperatures for the two types of test for a given value of  $F_w$  can be calculated to be about 185 K from formulae given by Hobson [18].

Chung *et al.* attempted to determine basic information on fracture of Zircaloy-4 with different oxygen contents with impact tests [36]. The material was sheet fabricated into  $5 \times 5 \text{ mm}^2$  and 55 mm long Charpy V-notch specimens. The specimens were oxidized in steam to produce oxygen contents between 0.2 and 1.2 wt %. After oxidation, the specimens were heat treated at  $1400^\circ\text{C}$  for a sufficient time to homogenise the oxygen. The success of the homogenisation was checked by microhardness testing over the thickness. The impact tests were conducted in a dropweight machine. Instrumentation on the tup permitted recording of load- and energy-time data during a test. From the maximum load during a test a dynamic fracture toughness could be evaluated as shown in Figure 5.19.

Figure 5.19 Dynamic fracture toughness of oxygen-alloyed Zircaloy-4



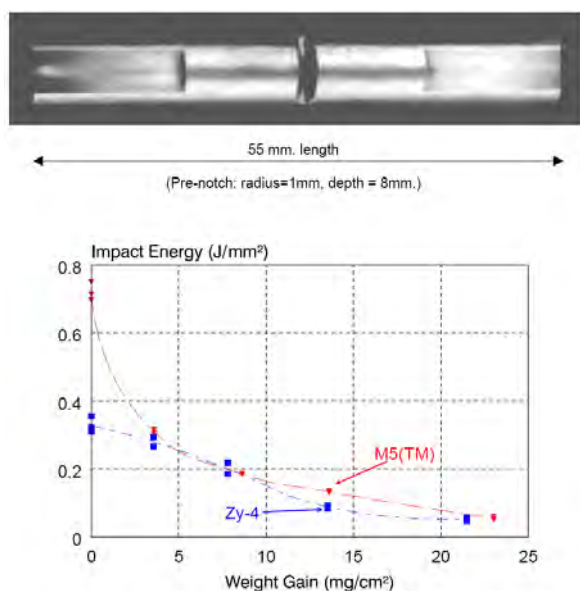
Chung *et al.* also impact tested Zircaloy-4 tubing after it had been subjected to steam oxidation transients [36-37]. In one type of test, 152-mm-long undefor med two-side-oxidized tubes which had survived a quench after steam oxidation were subjected to pendulum impact in a three-point bend configuration with relatively small loads and a low tup velocity. Impact energies of 0.03, 0.15, and 0.3 J were used. The results were later plotted together with failure data from quench tests to provide maps of various degrees of embrittlement as a function of oxidation temperature and time at temperature and the degree of oxidation.

In another type of test, 152-mm-long tube specimens were internally pressurised, ballooned, burst, steam oxidized, slow-cooled, and quenched. After cooling to the test temperature, impact testing was performed in-situ on tubes that survived the quenching thermal shock with both ends of the tubes in fixed position. An 11-mm-wide impact tup with a tup radius of 1 mm was used. The bottom and the top ends of the tube specimen were tightly fixed using a Sawgelok and a three-finger gripping device, respectively. The load was increased in 10 g steps until the tube failed. The energy was calculated as  $E=mgh$  where  $m$  is the mass of the weight with tup,  $h$  the elevation before drop and  $g$  the gravitational acceleration. Chung and Kassner [37] found that an impact failure energy of 0.03 J corresponds to the tube threshold oxidation state which separated failure and survival of the tube during bottom-flooding and quenching. Therefore, the toughness of a test specimen that withstands 0.3-J impact is approximately 10 times greater than the toughness required to survive the quenching thermal shock.

A more recent use of impact tests has been reported by Brachet *et al.* [30]. After an oxidation transient one of the many experiments performed in the French programme to characterise post-LOCA properties is an impact test on a notched specimen as shown in Figure 5.20. The notch serves mainly to localise the fracture location. The wall thickness of the cladding is too small to produce any significant triaxiality of the stress state below the notch surface. The impact energies seen in Figure 5.20 can be compared to the tests performed by Chung and Kassner [36], with 0.03 J and 0.3 J which translate to  $0.15 \text{ J/cm}^2$  and  $1.5 \text{ J/cm}^2$ , respectively, for the cladding dimensions used by them.

Caution must be exercised, however, when one interprets a plot like Figure 5.20 in terms of degree of oxidation, because the combined effect of oxygen distribution in and the thickness of  $\beta$  layer controls failure impact energy rather than the total weight gain from oxidation.

**Figure 5.20 Notched impact specimen fabricated from oxidized cladding**  
Results of tests with this specimen type



### 5.1.5 Oxidation tests

In early 1970s, cladding tube oxidation tests seem to have been regarded as fairly simple tests and in many cases only very sketchy descriptions are given. Hobson and Rittenhouse [19] describe oxidation of 0.45 m long cladding specimens in a ceramic muffle tube inserted in a furnace. Steam was supplied from below in amounts so that the reaction was not steam limited. Exposure temperatures were from 926 to 1 370°C with exposure times from 2 to 60 minutes.

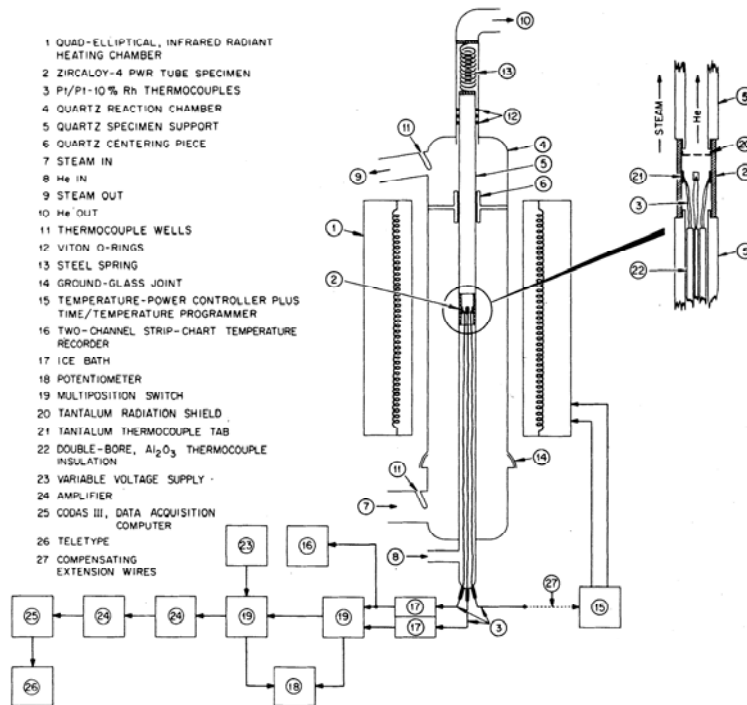
A very important aspect of the early experiments of Hobson and Rittenhouse [19] and Hobson [18] in early 1970s is that apparently specimen temperature was not measured but was assumed to be the same as the measured furnace temperature. This assumption may be reasonably accurate for low temperatures, e.g., for  $<800^\circ\text{C}$ . However, for high temperatures, e.g.,  $>100^\circ\text{C}$ , self heat generation from large exothermic heat of Zr oxidation is significant, and true specimen temperature must have been measured directly, e.g., by use of spot-welded thermocouples. Their papers do not mention this, and only describes the temperature variation of  $6^\circ\text{C}$  over a distance of 7.5 cm at the centre of the furnace heat zone.

In view of this and similar lack of direct measurement of specimen temperatures in the oxidation experiment of Baker-Just, ORNL investigators in late 1970s embarked on a series of oxidation

experiments, in which accurate specimen temperature measurement was one of the primary efforts. Pawel *et al.* discuss the importance of accurate temperature measurement and control in order to achieve success in an experimental oxidation programme [16]. They devoted a substantial effort to that problem, which was described as difficult, not only because of the high temperatures involved but also because of the environment in the steam oxidation experiments. Their experimental apparatuses and procedures were designed to minimise errors in temperature measurements. This goal required numerous tests and equipment modifications before the final version of their primary oxidation apparatus was decided.

Figure 5.21 shows the apparatus used for most of their experiments. The MiniZWOK is a low thermal inertia system in which the temperature of the specimen is controlled to a programmed temperature-time excursion. The specimen is a 3 cm length of Zircaloy-4 PWR tubing supported between two machined quartz tubes as shown in the insert. During an experiment steam flows past the outside surface of the specimen while a slightly positive pressure of helium is maintained inside the support tube to prevent leakage of steam. Each specimen was instrumented at its midpoint on the inner surface with three carefully calibrated Pt/Pt-10Rh thermocouples. The thermocouples were welded on the specimen using an iridium pad and positioned at 12, 1, and 6 o'clock. The diametrically positioned couples were used for data acquisition while the 1 o'clock thermocouple was used for control of temperature. Although this arrangement permitted arbitrary temperature excursions most experiments were run as isothermal exposures. For each temperature investigated at least ten specimens were oxidized. The apparatus has also been used in other studies [38].

Figure 5.21 The steam oxidation apparatus MiniZWOK



The ORNL investigators relied on heating from the outside in furnaces although with different thermal inertias. From late 1970s and on, many other investigators commonly used welded thermocouples to measure specimen temperature directly. Sawatsky also used a furnace for heating and oxidizing 1 cm long specimens [39]. The specimens were pushed in and out of the furnace with a ceramic push rod. The heating time for a specimen was about 10 s. In another facility Sawatsky used a 20-kW induction heating unit for heating the specimen which was placed on a zirconia pedestal inside

a vertical quartz tube. The temperature was varied manually from 850°C to above the melting point of zirconium. The steam was supplied by a 6 000 W steam generator at a rate of up to 1 g/s. The steam was preheated to 660°C before entering the quartz tube. Sawatsky did not report any differences caused by the two heating methods.

Dobson *et al.* used a commercial specimen heating system, a Gleeble, which originally is a weld simulation system [40]. In the Gleeble, the specimen is heated by a current. In addition, the test facility comprised a steam generator and superheating supply, a reaction chamber, a condensing system, and a vacuum system. A control circuit within the Gleeble monitors temperature and compares measured temperature to programmed temperatures. If there is any deviation, the system will correct it.

An interesting variant of induction heating was used by Urbanic [41]. Instead of tubes he used cylindrical specimens about 2.54 cm in length and 1.27 cm in diameter. The specimen was supported inside a graduated glass column by a recrystallised alumina tube closed at one end. The temperature was measured with a thermocouple inside the alumina tube. The specimens were heated inductively with a 30 kW induction heating unit. The surface temperature of the specimens was measured with an optical pyrometer which had been calibrated against known melting points of various metals. Before testing, the glass column was filled with water. The specimen was heated rapidly producing a steam blanket around the specimen. The rate of hydrogen production from the reaction was determined by measuring the times it took to displace successive volumes of water from the top of the column. After converting the gas volumes to standard temperature and pressure, the quantities of collected hydrogen were converted to equivalent amounts of reacted Zry-2.5Nb. This was checked by weighing the specimens after each exposure.

Leistikow and co-workers have performed extensive investigations of the oxidation of Zircaloy tubing in steam using an atmospheric pressure steam loop with heating of 3 cm long segments of cladding tube in a resistance furnace and the extent of oxidation estimated by both gravimetry and oxidized phase width measurements [42]. They also in one case compared oxidation behaviour of Zircaloy with stainless steel [43].

The Three Mile Island accident in 1979 resulted in an increased interest in zirconium alloy oxidation at temperatures in excess of 1 200°C and in presence of hydrogen-steam mixtures. Figure 5.22 shows one arrangement for study of Zircaloy oxidation in a steam-hydrogen mixture used by Chung and Thomas [44]. The bottom end of the specimen was tightly sealed to prevent access for the hydrogen steam mixture. The top end was left partially open to simulate fuel cladding rupture thus exposing the specimen inner surface to a hydrogen-rich environment containing a limited amount of steam. The specimen was heated by a-c power self-resistance. Specimen temperature was controlled by a feedback circuit of the power supply driven by the amplified signal from a spot-welded thermocouple at the centre. The pyrometer, calibrated against thermocouples, was used as an auxiliary temperature measurement. Specimen temperatures from thermocouples were recorded as function of time under isothermal oxidation conditions.

Figure 5.23 shows a low-thermal-inertia equipment which also was used by Prater and Courtwright for measurement of oxidation kinetics at very high temperatures, higher than normal LOCA temperatures although still of course of interest to the LOCA problem [45]. The specimen is only 3.8 mm in diameter and 0.9 mm thick. The heating is accomplished from one side with a defocussed CO<sub>2</sub> laser beam. The temperature measurements by a pyrometer were considered to be accurate to within 15°C. Oxidation was measured metallographically. The heating from one side resulted in temperature gradients through the specimen which altered the cubic-to-tetragonal thickness ratio at high temperature and which possibly may have an effect on the oxidation kinetics.

**Figure 5.22 Apparatus for Zircaloy oxidation in hydrogen-steam mixtures**

The test specimen, with welded thermocouples, is placed in the centre of the bell jar facing a pyrometer through a quartz glass.

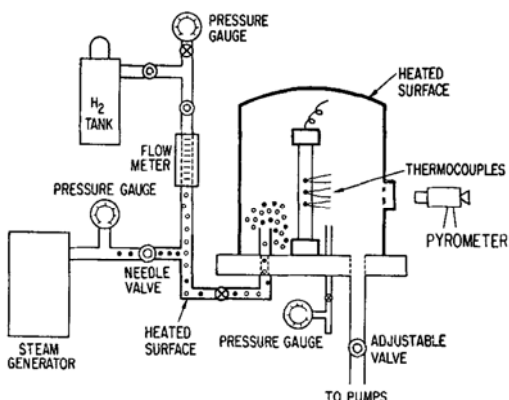
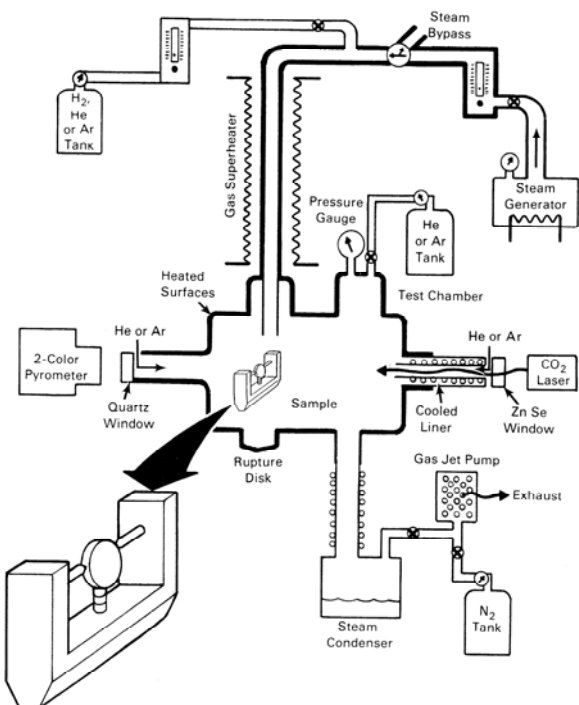


**Figure 5.23 High-temperature oxidation apparatus**



A heating method not represented among the separate effects test of oxidation but widely used in more integral experiments is the use of internal heating elements. This heating method is the one most similar to the real case and a question arises whether or not the method of heating has any effect on the oxidation behaviour. This question has been discussed rather extensively in a paper by Ocken *et al.* [46]. They distinguish between experiments with external heating, using radiant furnaces and what they call internal heating, either resistance heating or inductive heating. They show that the oxidation parameters evaluated from the different experiments agree fairly well but that there are statistically significant differences between parameters from different types of experiments. They also note that the method of determining the amount of oxidation does not play any role for the differences observed in the oxidation parameters. The most important difference is that the experiments with external heating have a slightly higher activation energy.

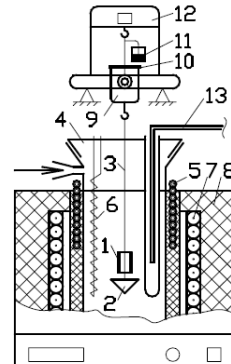
The method of heating also affects the relative thicknesses of the oxide and oxygen stabilised  $\alpha$  layers. This is a result of the sign and magnitude of the thermal gradient through the cladding during oxidation. In an externally heated experiment the outside is hottest while in an internally heated experiment the inside tends to be hotter. This implies that in experiments in which specimens are externally heated the oxide layer forms at a higher temperature than the stabilised  $\alpha$  layer, with the converse holding for experiments in which specimens are heated internally. Consequently, higher oxide-stabilised  $\alpha$  thickness ratios would be expected in those experiments in which specimens are externally heated, since the range of oxygen concentrations in the  $\alpha$  is greater when the temperature is lower (see the phase diagram, Figure 5.9).

Some of the oxidation experiments have been conducted with continuous recording of the weight gain. One example is the Russian UNOPRO facility [47-48] shown in Figure 5.24.

The cladding samples used in the facility were typically 30 or 60 mm in length.

Figure 5.24 The UNOPRO facility for continuous recording of weight gain during oxidation

- |      |                                |
|------|--------------------------------|
| 1    | specimen                       |
| 2    | Pt bowl for $ZrO_2$ collecting |
| 3    | Pt suspender                   |
| 4    | working zone                   |
| 5    | Pt heater                      |
| 6, 7 | compensating heater            |
| 8    | furnace shaft                  |
| 9    | frame                          |
| 10   | balance pan                    |
| 11   | liquid damper                  |
| 12   | scale-beam                     |
| 13   | Pt-Pt/Rh thermocouple          |



Another example of continuous recording of specimen weight gain has been reported by Baek *et al.* [49]. The apparatus used is a modified Shimadzu TGA (Thermogravimetric Analyzer) (Figure 5.25).

The test specimen hangs freely from a Pt wire connected to the TGA apparatus. The steam generator can supply steam continuously to the furnace. The steam flow rate was 0.5-0.6 mm/min so as not to affect the weighing accuracy due to buoyancy effects. The weight change could be determined within  $\pm 0.001$  mg. The heating rate used was 50 K/min and the temperature was controlled to within  $\pm 0.1^\circ\text{C}$  by a computer system. The specimens were 8 mm in length and both ends of the specimens were ground carefully by SiC 1200 emery paper to minimise the error during oxidation. A typical weight gain versus time record is shown in Figure 5.26.

Figure 5.25 Facility for continuous recording of specimen weight gain during oxidation used by Baek *et al.* [49]

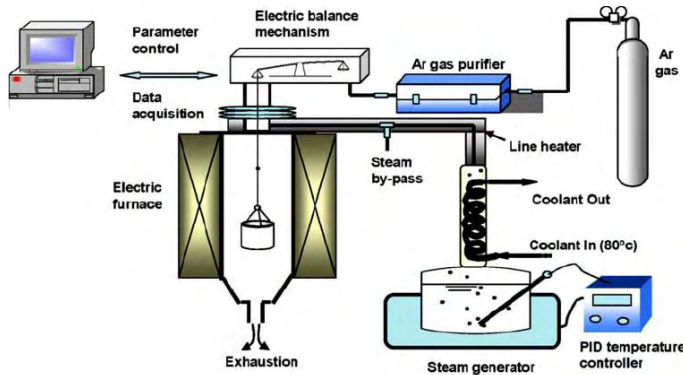
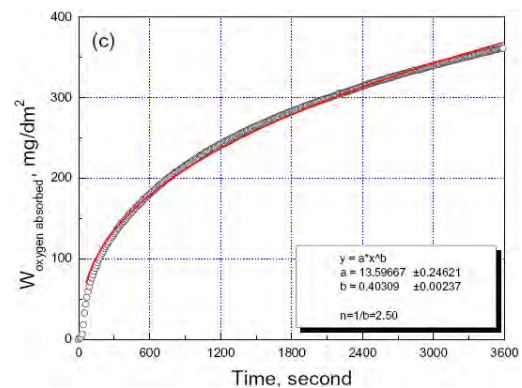


Figure 5.26 Weight gain vs time record for Zircaloy-4 oxidized at  $900^\circ\text{C}$  in the facility shown in Figure 5.25



## 5.2 Tests with moderate integration

A possible classification of tests with moderate integration used in the present report is the following:

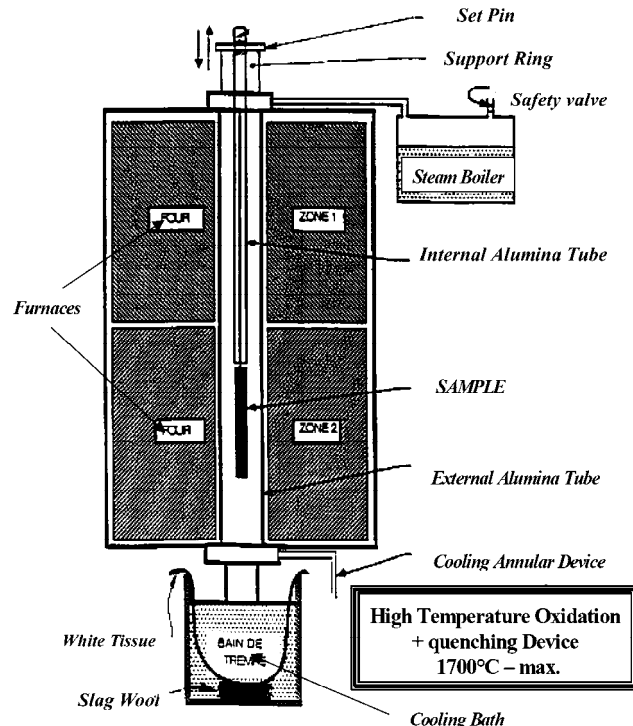
- Steam oxidation tests followed by quenching.
- Deformation or ballooning tests in steam.
- Constrained deformation or ballooning tests in steam with or without quench.

It should be noted that this overview is incomplete. Tests similar to those described subsequently have been done at other laboratories. The purpose of the overview is rather to describe typical features of the various test techniques.

### 5.2.1 Steam oxidation tests followed by quenching

The DEZIROX facility shown in Figure 5.27 is basically an oxidation test facility but qualifies as an integrated test because it is possible to release the oxidizing specimen so that it falls down in a cold water bath [30].

Figure 5.27 The DEZIROX oxidation and quench facility



As shown in Figure 5.27 the maximum temperature is 1 700°C. The purpose of the white tissue in the water bath is to collect spalled oxide which can be weighed together with the oxidized specimen to determine the total weight gain and the fraction of delaminated oxide. The length of the sample is normally 150 mm and the temperature gradient along the tube is less than 20 K.

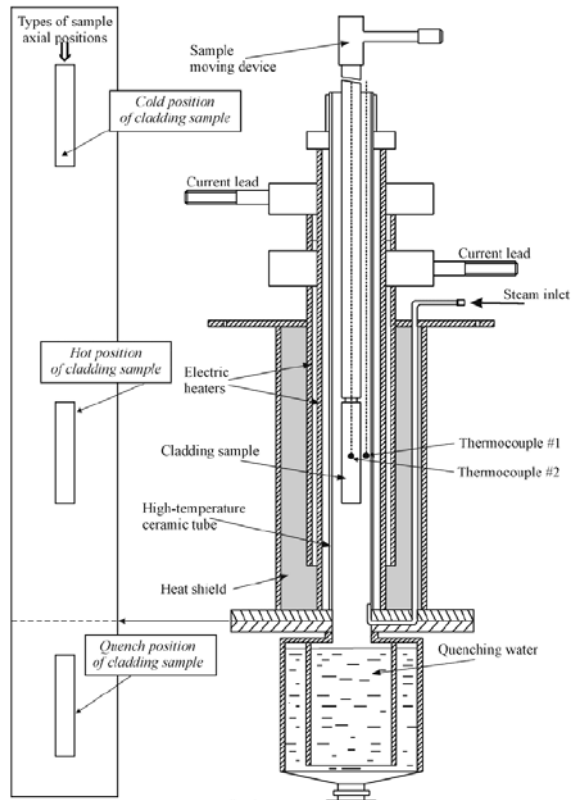
A similar facility used by Yegorova *et al.* is shown in Figure 5.28 [23].

The oxidation facility consists of the following basic elements:

- Electric furnace.
- Device for the movement of E110 sample in the several given positions (cold position, hot position, and quench position).
- Steam generator.
- System to supply argon gas to the oxidation facility.
- Measurement apparatus (measurement of temperature inside and outside of E110 sample, temperature of water in the steam generator).
- Tank with water in the low part of facility.

The electric furnace provides the radiant heating and cooling of cladding sample with various heating rates. In the experiments, various types of temperature cycles were simulated, fast heating/fast cooling (FF), fast heating/slow cooling (FS), slow heating/fast cooling (SF) and slow heating/slow cooling (SS) [23].

Figure 5.28 Apparatus for oxidation tests of cladding followed by quench in water [23]



The steam generator provides the generation of water steam with the following parameters:

- Temperature: 150°C.
- Mass flow rate: 0.01–0.04 g/s (mass flow rate is a function of electric power).
- Atmospheric pressure.

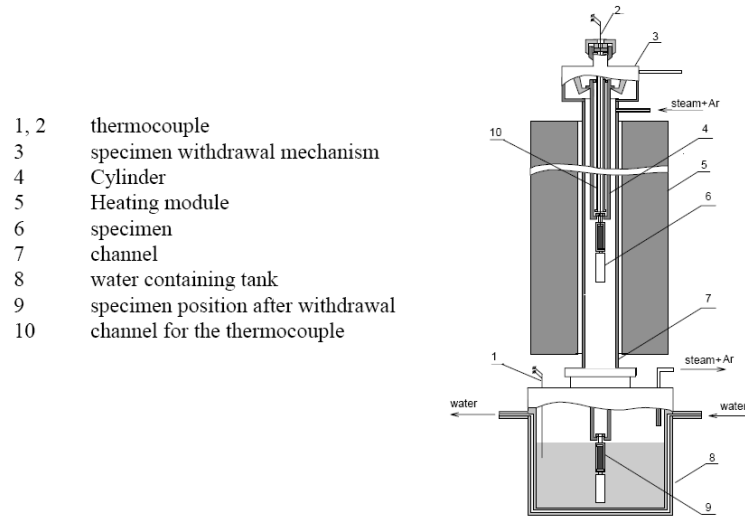
The system to supply argon gas to the oxidation facility was used at the beginning of each test mode. The gas-supply system flushed the inner atmosphere of the test facility.

The temperature limit was used to change the type of coolant. The Ar flow was stopped at the temperature about of 300°C and after that the heating was continued with the water steam. The cladding samples used in the facility were empty cladding samples with a useful length of 100 mm. The test specimens could be either open or closed. The specimen temperature was measured with a thermocouple located inside the specimen. In a separate test series, it was determined that this thermocouple registered the same temperature as a thermocouple spot welded to the outside of the specimen except during the transient heating and cooling cycles termed F.

Another similar Russian facility described as a universal rig to investigate the behaviour of core materials to overheated above the operating temperature in inert gas, air or steam gas environment, UVS, is shown in Figure 5.29 [47].

Different fuel rod simulators were used in the rig in order to include the effect of pellets inside the tubes on the possible embrittlement during the quench and subsequent disassembly and handling of the specimen. Segments of fuel cladding irradiated to burn-ups from 46 to 50 MWd/kg have been tested in the facility.

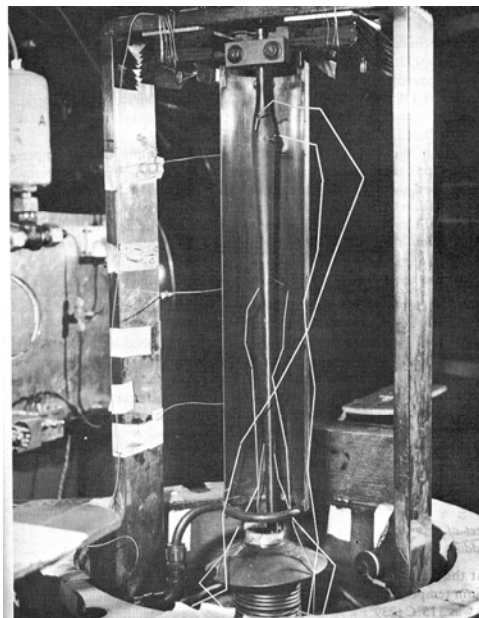
Figure 5.29 UVS, the universal rig for testing overheated core materials



### 5.2.2 Deformation or ballooning tests in steam

Figure 5.30 shows a photograph of the PROPAT rig used at the Springfields laboratory in the United Kingdom to study deformation of zirconium alloys cladding tubes in steam [50]. In the facility, conditions could be arranged so that the heat loss is mainly by convective cooling with a heat transfer coefficient of about  $80 \text{ W/m}^2\text{K}$  which is typical of those that are calculated to occur during a LOCA. This required a steam flow of 80 litres/min in the arrangement shown in Figure 5.30. Radiative heat loss was minimised by surrounding the specimen with a cylindrical copper shroud, a half of which can be seen behind the specimen in Figure 5.30. The choice of copper was dictated by its high reflectivity in the wave length band of the spectrum typical of black body radiation at about 1 000 K. It was estimated that 96% of the heat was reflected back so the specimen received about as much radiative heat as if it had been surrounded by similar bodies at a temperature of  $(0.96)^{1/4}\text{T}$ . With  $\text{T}=1 023 \text{ K}$  that gives an effective temperature of 740°C.

Figure 5.30 The PROPAT facility for study of cladding deformation in a steam atmosphere

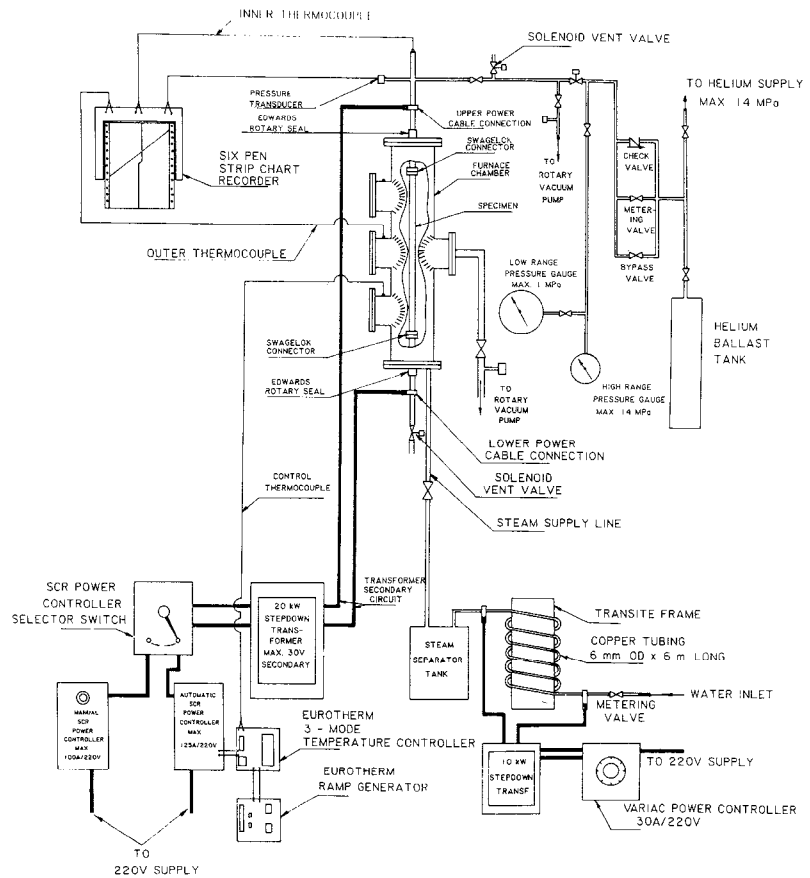


The specimen contained alumina pellets and an internal free volume of about 20 ml. The method of heating was direct electric heating. The specimen was heated to about 600°C, held for about 60 s while the internal pressure was applied, and then ramped at 10 K/s as measured by the centrally placed thermocouple. The temperature at that point was maintained until the specimen failed.

An important purpose of the test arrangement described here was to determine the effect of convective cooling. The result is the carrot shaped specimen seen in Figure 5.30.

The arrangement used by Sagat *et al.* [51] in Chalk River Nuclear Laboratories for the study of cladding deformation in a steam atmosphere is shown in Figure 5.31. The furnace chamber houses the specimen which can be either vacuum at about 1.3 Pa or steam. The specimen is electrically heated by its own resistance (Joule heating). Temperature was measured by tungsten-rhenium thermocouples which were spot-welded directly to the surface of the specimens. Prior to each test in steam, steam was admitted into the test chamber at a flow of 2 g/s to provide an oxidizing environment on the specimen outside diameter. The apparatus was allowed to stabilise for 600 s and after the specimen was internally pressurised with helium to the test pressure after which the temperature was ramped until a predetermined strain was reached or until burst occurred. During the tests, the specimens were axially unconstrained and could freely expand or contract via an Edwards rotary seal.

Figure 5.31 Schematic diagram of ballooning test apparatus used at Chalk River



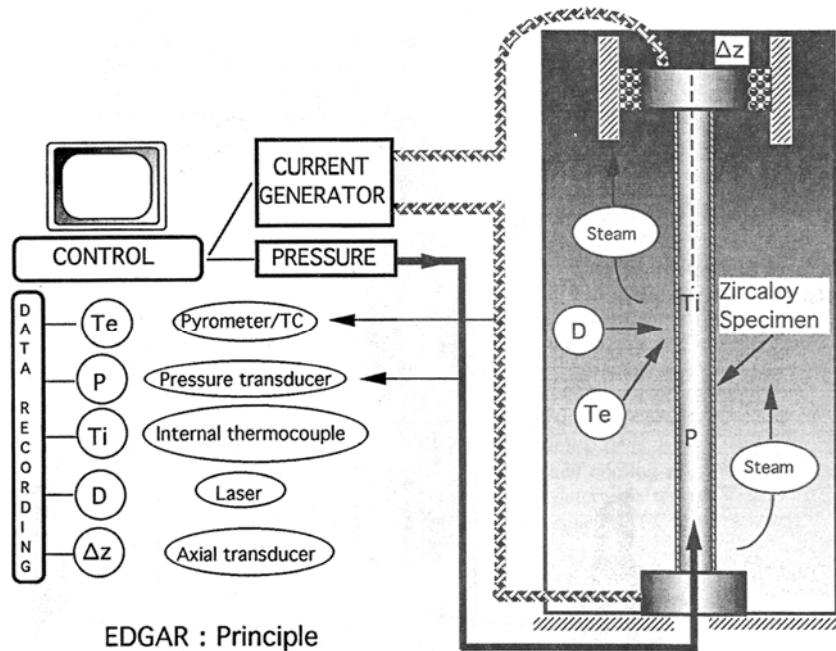
At CEA, in France, the EDGAR facility has been used for biaxial creep testing in a steam atmosphere. The first EDGAR facility was used from the 1970s to determine the LOCA properties of Zircaloy-4 [52]. The EDGAR-2 facility shown in Figure 5.32 was built in 1993 to similar specifications as the original EDGAR facility [20].

The facility allows testing of any kind of simultaneous and independent thermal and pressure transients on 490 mm length cladding specimens. To obtain rapid heating a low voltage alternating electric current is passed through the specimen. It is regulated by a thyristor device controlled by feedback from the external clad temperature,  $T_e$ , via a microcomputer that controls the whole test and also performs data recording in real time. The specimen is internally pressurised by argon gas through a servo-controlled device managed by the microcomputer. The tests are performed inside a containment vessel in a flowing steam environment. To preserve the biaxial stress state of a closed-end tube, the upper grip of the specimen is free to move and its weight is compensated mechanically.

The EDGAR-2 facility operates in the temperature range 350 to 1 400°C in steady-state or transient conditions. The heating rates can be controlled between 0.1 and 250 K/s. The maximum internal pressure is limited to 200 bars. Pressure rates can be controlled between -10 to +10 bar/s in transient conditions.

The temperatures and the diametral deformation are measured at the same axial location of the specimen, around the middle of the useful part of the specimen which is about 300 mm. The temperature gradient in the useful part is less than 5 K. The external clad temperature is measured by optical pyrometers or by spot-welded Pt-PtRh type thermocouples. The internal gas temperature is measured by an internal K type thermocouple. The change in the cladding diameter during the test is continuously measured by a laser device that operates, like the pyrometers, through a quartz window fitted in the vessel. The displacement of the top grip is measured by an inductive transducer. The real time recording of the measurements was achieved by the microcomputer with an adjustable frequency in the 0.5 to 5 Hz range.

Figure 5.32 Schematic view of the EDGAR-2 test facility [20]



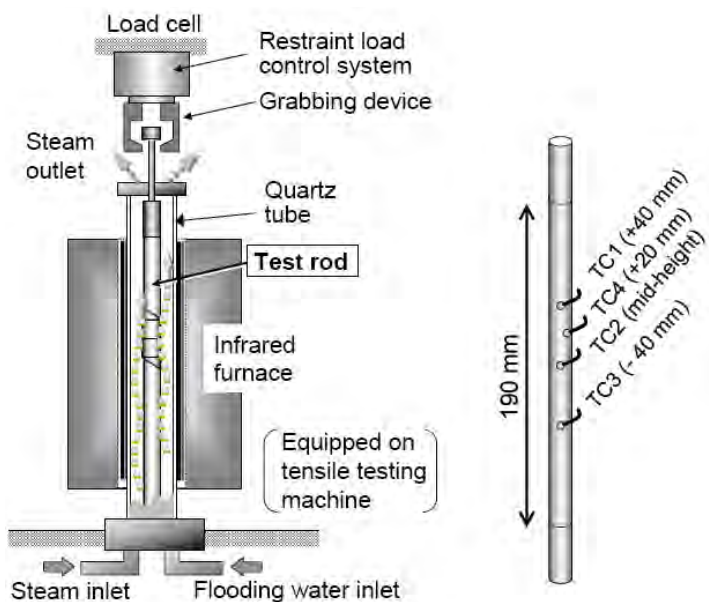
The tests are normally performed until cladding burst. Postmortem measurements, made with thin paper ribbons, are made of three cladding circumferences, one at the largest diameter in the ballooned section and one each on the two diameters located 20 mm above and below the edges of the burst opening. The largest of these diameters defines the uniform elongation as the circumferential strain at that section. The total elongation is defined as the circumferential strain at the largest diameter.

### 5.2.3 Constrained deformation or ballooning tests in steam with or without quench

In the late 1970s and early 1980s, Furuta and co-workers [53-55] performed ballooning experiments in steam in which the cladding was axially constrained. More recently Nagase and coworkers have performed similar experiments on hydrided, preoxidized and irradiated cladding [56-64]. Figure 5.33 shows a schematic view of the test equipment. The appearance of the equipment vary somewhat from publication to publication, the one chosen here is from [58].

The cladding tube is filled with alumina pellets to simulate the heat capacity of UO<sub>2</sub> pellets. After welding Zircaloy end caps to the cladding, the rods are pressurised to about 5 MPa with Ar gas at room temperature and sealed. For non-irradiated cladding, the length used has been 580 mm while the irradiated cladding has been tested in lengths of 190 mm.

Figure 5.33 Test apparatus for constrained ballooning tests in steam [58]



As can be seen in Figure 5.33, the furnace with the various connections is placed in the frame of a tensile test machine in which one part of the cladding tube is fixed to the mobile cross-head while the other end is fixed to the frame. With the use of a servo-controlled machine, it is in principle possible to control any parameter relevant for the cladding tubes. Tests have been run with a fully constrained tube and with the axial load fixed at a constant value.

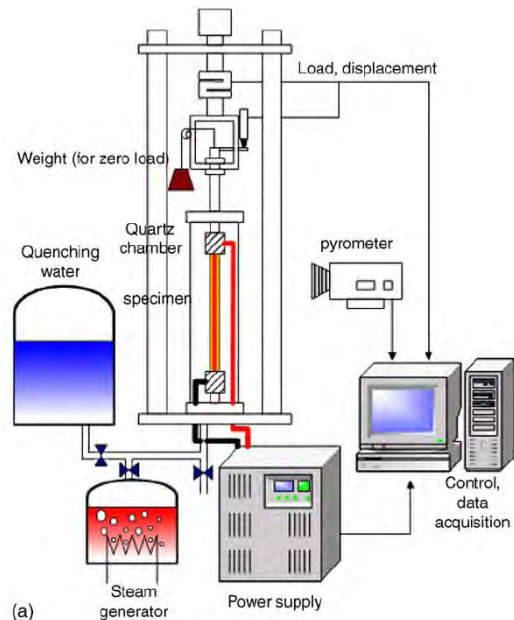
In a typical test, the cladding would be heated with a rate of 10 K/s. Steam is introduced prior the heat-up at a rate of about 36 mg/s, sufficient to oxidize the cladding without steam starvation. During the heating up to the temperature for isothermal oxidation, the specimen normally ruptures. Typically the isothermal oxidation is run for 120 to 500 s.

At the end of isothermal oxidation, the axial restraint is initiated and the cladding is allowed to cool down in the steam flow to about 700°C when quenching starts by flooding the specimen with water. The average cooling rate is about 20 K/s from the oxidation temperature to 900°C and about 5 K/s from 900 to 700°C. The water for the quench rises with a rate of 30 to 40 mm/s.

The test rod is quenched under non-restrained or restrained condition. The rod can be fully restrained or fixed at a certain axial load in simulation of the frictional forces that occur between cladding and spacer grids during a real LOCA.

Another apparatus for quench testing of ballooned cladding tubes under axial restraint used at Korea Atomic Energy Research Institute is shown in Figure 5.34 [65-66]. The cladding tube length is 330 mm, 200 mm of which is considered the actual heating length. Direct heating by the specimen ohmic resistance allows heating up to temperatures between 1 000 and 1 250°C. The specimen temperature is measured by a pyrometer. To simulate the cooling during the ECCS phase of a LOCA, the specimen is cooled to an intermediate temperature of 700°C for 100 s after oxidation and then quenched.

**Figure 5.34 Schematic illustration of the LOCA simulation facility used at the Korean Atomic Energy Research Institute [65-66]**



During the test, the specimen may be subjected to unnecessary loads due to an attached electrode, wire and connecting rod etc. In order to compensate for such a load, the same weight is applied with a reverse direction to balance the net force in the test specimen to zero. A crosshead is installed in the upper part of the specimen to control the axial stress. A load cell and a linear variable differential transducer is used to measure the change of specimen thermal stress and length during the oxidation and thermal shock All the data and procedures are collected and controlled by a computer.

### 5.3 Fully integrated tests

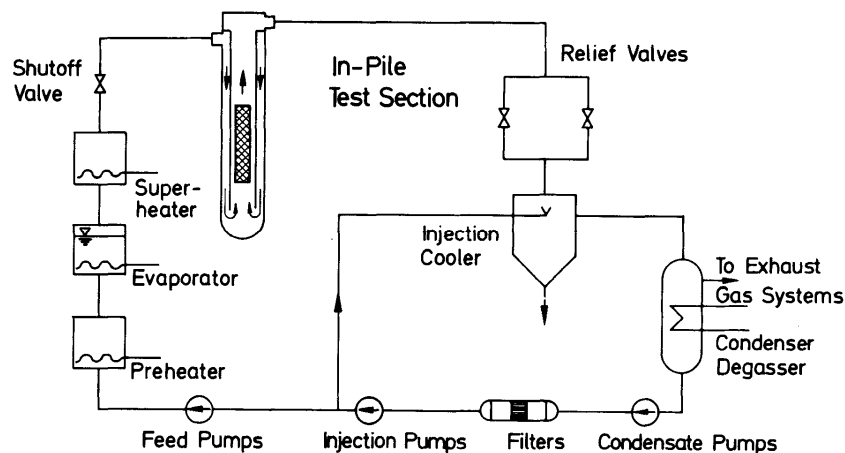
#### 5.3.1 In-reactor tests

##### 5.3.1.1 The FR2 facility

The FR2 research reactor a heavy water cooled and moderated tank reactor located at KfK was shut down in 1981. The LOCA experiments were performed in the DK loop of the reactor which could provide the desired thermal hydraulic conditions for the tests [67]. A simplified scheme of the DK loop is shown in Figure 5.35.

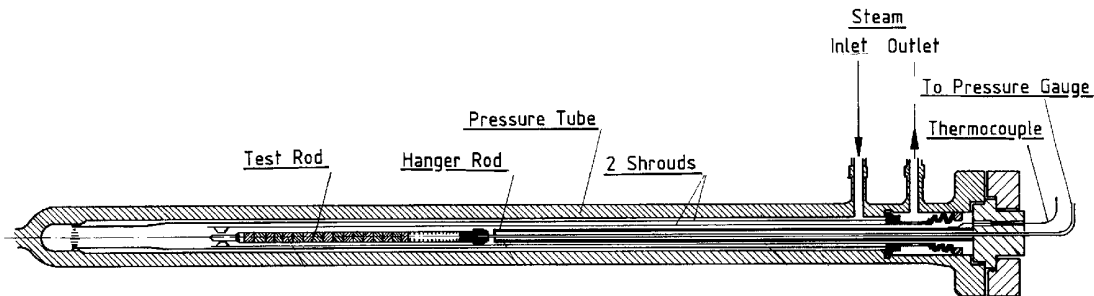
During the steady state phase of the test the loop was operated at a pressure of 60 bar at a steam temperature of about 300°C and a coolant mass flow of 120 kg/h. The loop was particularly suitable for experiments on fuel rod failure because it was equipped with condensation and filter systems for retaining fission products and retarding noble gases.

**Figure 5.35 Simplified flow scheme of the DK loop, operated with superheated steam, in the FR2 reactor**



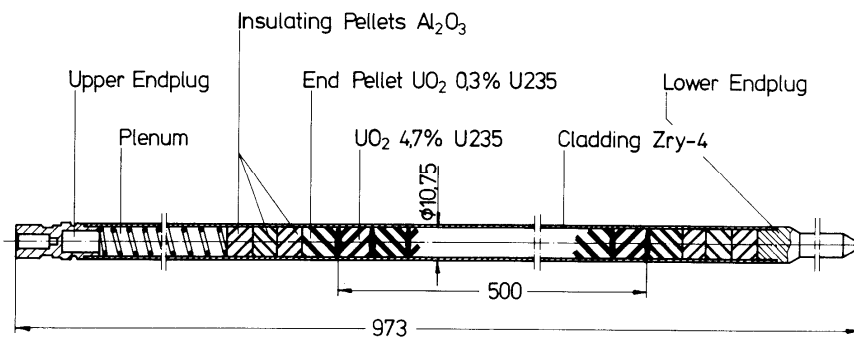
The test specimens were contained in the in-pile test section shown in Figure 5.36.

**Figure 5.36 In-pile test section of the DK loop in the FR2 reactor (simplified)**



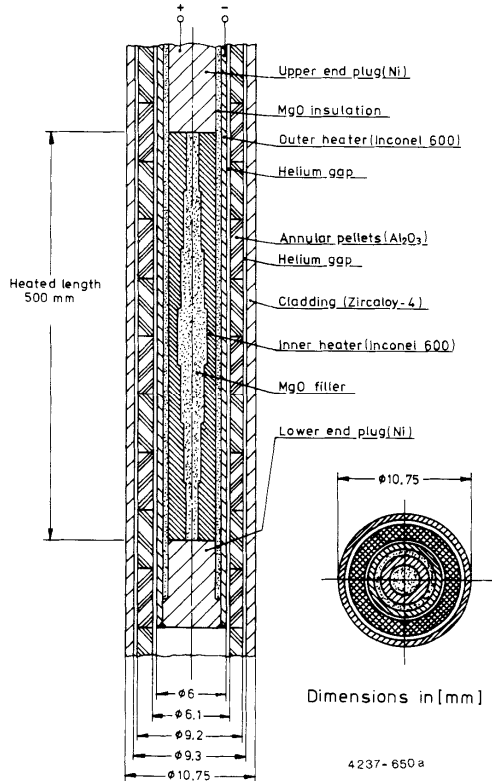
The fuel rod design is shown in Figure 5.37. Its radial dimensions were identical to those of a fuel rod of a German 1 300 MWe PWR with an active fuel length of 50 cm. The test rod had only an upper plenum compared with the two plenums of a German PWR fuel rod. The size of plenum volume including the internal volume of the pressure measuring system was chosen to equal the void volume of the two plenums in a PWR rod.

**Figure 5.37 Test fuel rod design for the FR2 experiments**



For comparison some unfueled test rods with internal electrical heaters were used in some of the experiments. The design of the fuel rod simulators is shown in Figure 5.38.

Figure 5.38 Electrically heated fuel rod simulator design, heated section (not to scale)



Both the fuel rods and the electrically heated fuel rod simulators were instrumented with thermocouples and a pressure sensor. The pressure sensor was of strain-gauge type which was connected to the plenum by a tube approximately 5 m long with an inside diameter of 1.6 mm. During pre-irradiation, the diaphragm through which the pressure sensor capillary tube would eventually penetrate was protected by a specially designed end cap.

The nuclear test rods were initially filled with 0.3 MPa He at room temperature and pre-irradiated in bundles of six rods in fuel element positions of the FR2 reactor. The coolant pressure was 2.5 bar and the coolant temperature was 60°C.

Each test began with a steady state phase during which the rod was pressurised to the desired level at steady state temperature by adding helium to the fission gas generated during pre-irradiation. Also during this phase instrumentation calibration, rod power determination and axial flux profile measurements were performed. The test rod was then exposed to a standard temperature history derived from licensing calculations for a PWR fuel rods in a LB-LOCA. The transient in the test loop was initiated by interruption of the loop coolant flow and system depressurisation. This was done by rapidly closing the coolant shutoff valve and simultaneously opening a relief valve with a large cross-section downstream of the test section (Figure 5.35).

The coolant flow past the test rod decreased to zero and the system pressure to approx. 0.1 bar within 8 to 10 s. During the subsequent heatup phase, the test rod power was kept constant until the target cladding temperature of approximately 930°C was reached. At that temperature, the rod power was rapidly reduced by reactor scram. After the turnaround point as the result of the reactor scram, when the cladding temperature had decreased to about 730°C, the coolant mass flow reactivated and a quenching effect took place. Results of the tests can be found in Section 7.3.1.1.

### 5.3.1.2 LOC tests in the power burst facility

The power burst facility (PBF) at INEL in Idaho was a water-cooled and -moderated tank type research reactor used for various reactor transient tests. One of the test series performed was the PBF-LOC tests which simulated a large break LOCA. Four tests were performed with four fuel rods in each test. The rods were 15×15 PWR rods with a 0.91 m active length, each contained in a separate unheated shroud. The rods were subjected to the same thermal-hydraulic conditions existing in the test section (Figure 5.39).

The test transient starts from a steady-state regime under water at nominal condition: 320°C, 15.2 MPa, 45 kW/m linear heat rate. After isolation of the test section from the PBF circuit, a valve opening leads to blowdown representative of a cold leg break large LOCA. The axial profile of the nuclear power has been flattened to simulate the mid height of a PWR. During the test the power is monitored in order to reach and maintain the target temperature of the test.

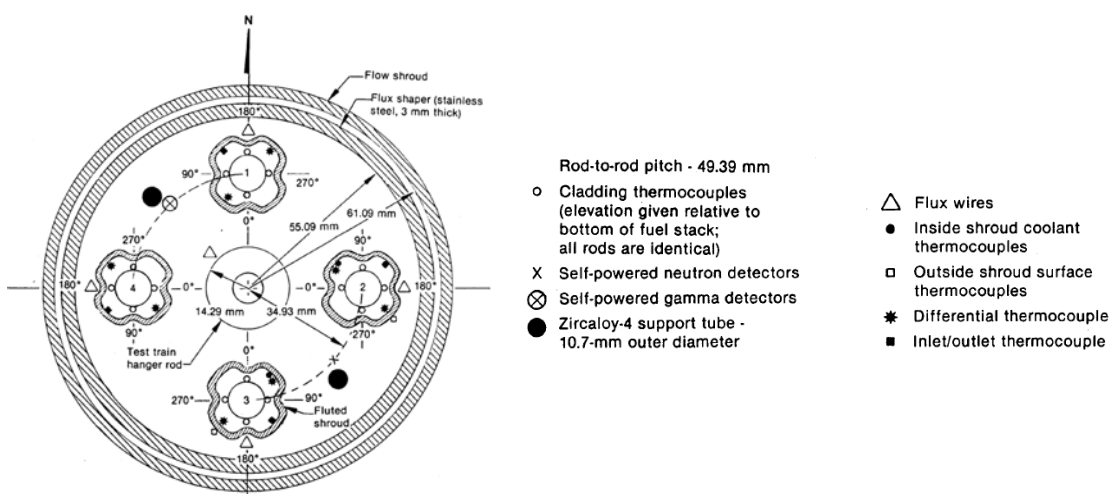
The heating rate of the different rods in a test will vary between rods, depending on initial stored energy and the fuel/clad heat transfer. After having maintained the plateau temperature for a sufficient duration so as to reach rod rupture, the test is terminated by quenching. Results and details of the PBF-LOC tests are presented in Section 7.3.1.2.

### 5.3.1.3 PHEBUS test

The PHEBUS experiments are in-pile experiments which allow simulation of real fuel behaviour in bundle configuration involving all the potential phenomena in a plant [52,68]. The programme at PHEBUS has been performed to fulfil the following general objectives:

- To assess the phenomenology of the fuel rod behaviour under LOCA conservative conditions, including rod rupture and a subsequent temperature plateau for clad oxidation up to the acceptance limit, before a final representative quenching.
- To assess the adequacy of safety criteria with respect to the coolability of fuel rods and the clad embrittlement, so as to allow an assessment of safety margins.
- To provide an experimental data base for the validation of computer codes used in the simulation of the thermohydraulics and mostly the thermomechanics in LB LOCA, particularly the CATHACOMB module of the CATHARE system code.

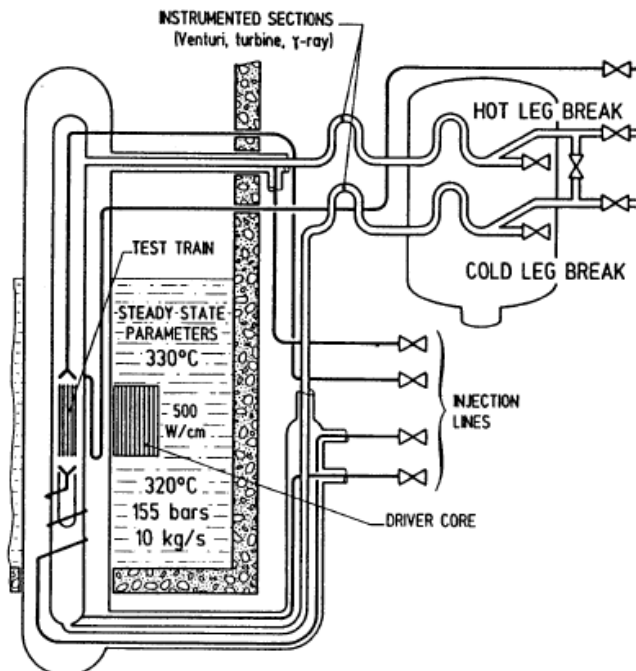
Figure 5.39 Cross-section of the PBF-LOC experiment



The central component of the experimental facility is the test train. It consists of a bundle of 25 rods of fresh UO<sub>2</sub> fuel of PWR type on a 5×5 pattern, maintained by 4 Inconel spacer grids. The fuel pins are 1 m long (0.8 m active length) and can be internally pressurised. The fuel bundle is surrounded by a massive Zircaloy-2 shroud that links the square section of the bundle to the circular section of the concentric outer structures: a zirconia insulation layer and the Zircaloy-2 test tube 114 mm in O.D. The test tube is itself placed in successive concentric outer tubes (pressure tube and safety tube) to insure the confinement of the test train and the circulation of coolant around it.

The test device is thus included in a loop inserted in the PHEBUS driver core that provides the neutronic flux for the nuclear heating of the test rods. The test loop (Figure 5.40) allows reproducing the initial steady state conditions of the power plant, before transient initiation. The transient is initiated by isolating the test section of the loop containing the fuel bundle, then rapid opening of valves on the upstream and downstream pipes to simulate breaks on the cold and hot legs. Simultaneously, the power of the driver core is decreased to simulate the nuclear power transient following plant shutdown.

Figure 5.40 Schematic design of the PHEBUS test loop



The area of the breaks was adjusted in order to provide the desired system pressure history as well as the flow rates in the hot and cold legs, that allows to control the position of the stagnation point (zero flow). Four injection lines, upstream and downstream of the test train, allowed the refill of the loop and the bundle reflooding after the blowdown phase.

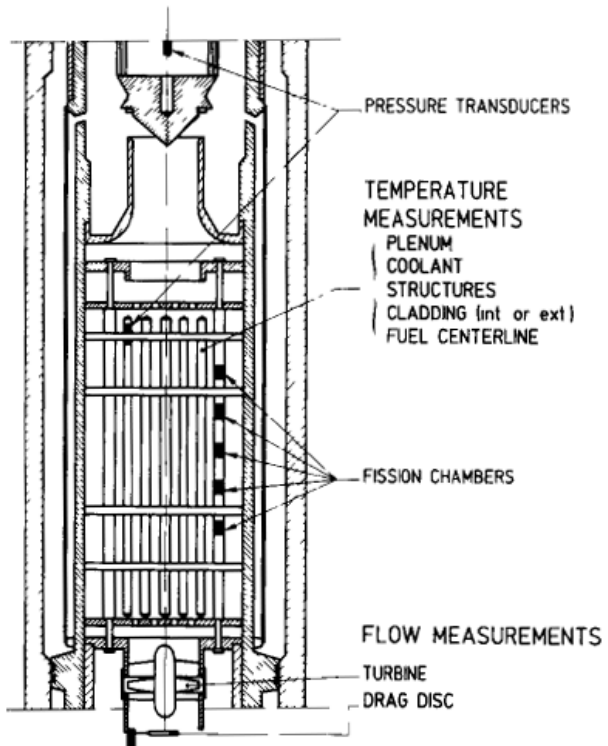
The instrumentation is designed for two kinds of measurements, flow measurements and rod bundle measurements.

For flows, the usual measurements were made of coolant temperatures in several places, of system pressures, structure temperature and injection flow rates. In addition, two instrumental pipe sections were installed in the hot and cold legs including gamma-ray, turbine and venturi, in order to obtain the best possible information on two-phase flows (Figure 5.40). A drag disk was also inserted at the bottom of the test train (Figure 5.41), and gave valuable information on the flow at the bundle inlet. For the last tests the flow at the bundle inlet was also measured with a turbine.

For the fuel bundle, the instrumentation shown in Figure 5.41 enables measurement of:

- The cladding temperature.
- The fuel centreline temperatures which enable along with cladding temperatures determination of the thermal behaviour of the rods.
- The gas plenum temperatures which, besides temperature transient measurements, give accurate determination of rod rupture times.
- The rod internal pressure, which along with system pressure, give an indication of the load on the cladding and of rupture time.
- The nuclear power in the bundle by using fission chambers.

Figure 5.41 Test train instrumentation



An evaluation of the accuracy of the different measurements has been carried out, especially for the cladding temperatures in transient conditions that were measured with thermocouples on the outer side. A detailed specific study of the rod thermal behaviour has provided an estimate of the temperature difference between clad and thermocouple, allowing an assessment of the influence of the thermocouples on the rod thermal behaviour:

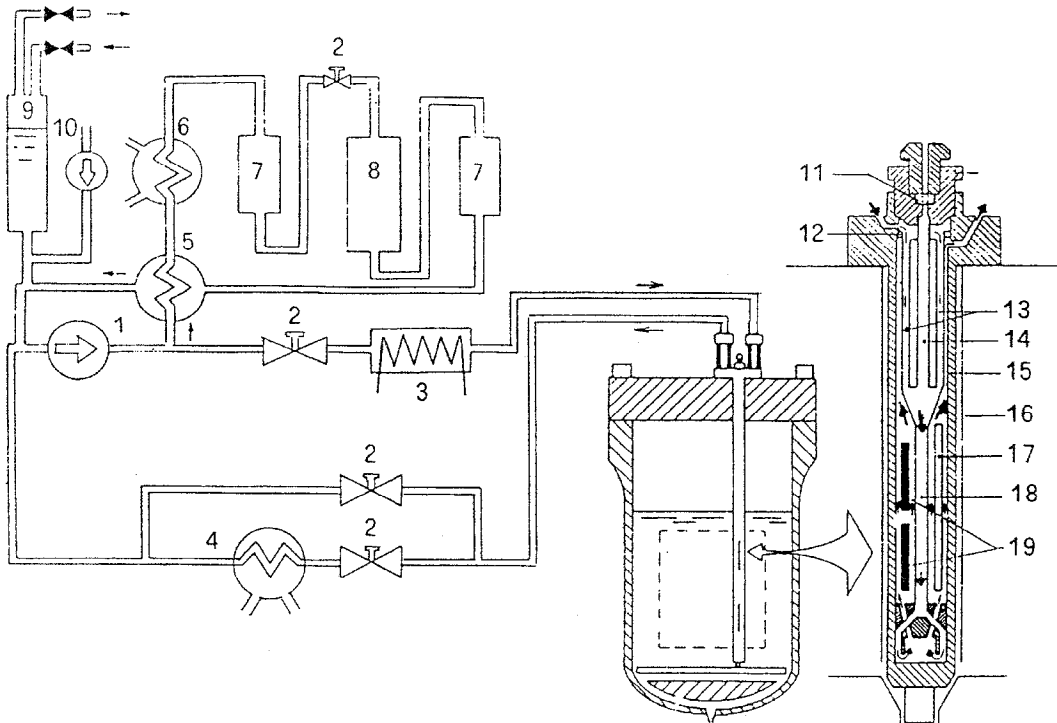
- The small size of the thermocouples and the way they were implemented on the claddings allows to limit the deviations induced by these sensors.
- During the 1<sup>st</sup> temperature peak and the subsequent pseudo-adiabatic phase of the transient, the TC induce a low temperature difference (around 10°C) in the circumferential temperature distribution.
- The difference between the “true” temperature and the measured one strongly depends on the heat flux exchanged on the clad surface: it remains <20°C for low heat fluxes but can reach 50°C for the more elevated heat flux in the cooling phase.

### 5.3.1.4 LOCA tests in the Halden reactor

#### 5.3.1.4.1 The IFA-511.X and IFA-54X experiments

The IFA-511.X and IFA-54X experiments were performed in one of the four flow starvation facilities of the Halden reactor. A sketch of the facility is shown in Figure 5.42 [69].

Figure 5.42 Sketch of the flow starvation facility



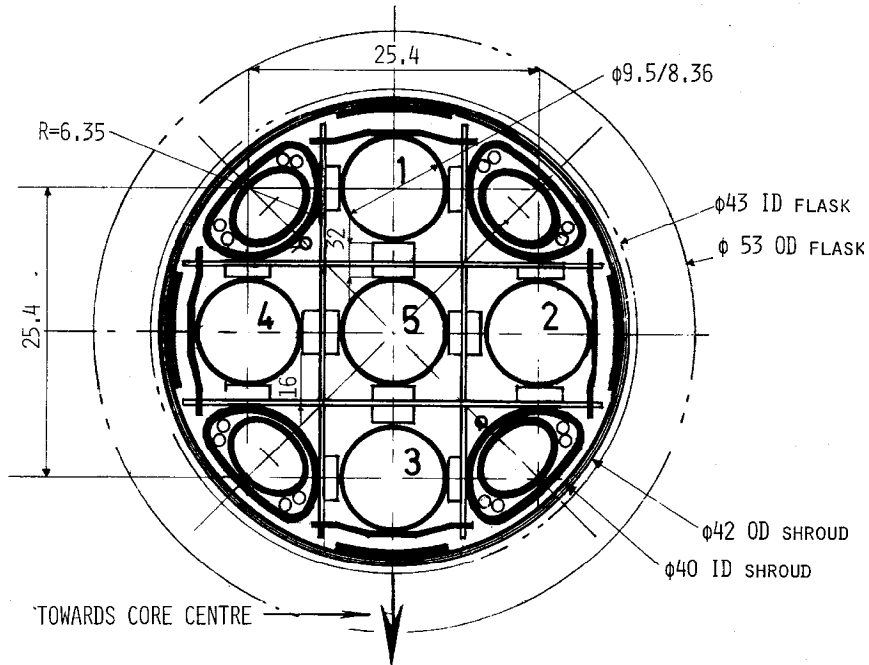
- |                                 |                              |                                  |
|---------------------------------|------------------------------|----------------------------------|
| 1. Main circulation pump.       | 7. Cooler.                   | 13. Heat exchanger.              |
| 2. Flow regulating valve.       | 8. Ion exchanger.            | 14. Central tube for cabling.    |
| 3. Electric heater.             | 9. Helium pressurising tank. | 15. Pressure flask.              |
| 4. Main circuit cooler.         | 10. Water supply pump.       | 16. Shroud.                      |
| 5. Regenerative cooler.         | 11. Graphite seal unit.      | 17. Triangular tube for cabling. |
| 6. Purification circuit cooler. | 12. Seal.                    | 18. Tube for water downflow.     |
|                                 |                              | 19. Fuel rods.                   |

The IFA-511X experiments were pure thermohydraulic experiments and were performed with a bundle with 7 rods in a circular configuration. In the ballooning tests IFA 54X the 5 rod bundle was in the form of a cross (Figure 5.43). Four downcomer tubes were placed in the corners of the cross to complete a 3×3 square array. The unheated downcomers presented to the other rods curved surfaces corresponding to cladding at a strain of 33%.

One of the objectives of the IFA-511.X and IFA-54X experiments was to determine if there were any differences between nuclear heating with fuel pellets and internal electric heating used in many out-of-pile experiments. Therefore about half of the experiments were performed with nuclear heating and half with internal electric heating using either REBEKA heaters (Figure 5.47) or a heater called the Semiscale heater. The experiments were monitored by several thermocouples at critical locations. The cladding was Zircaloy-2 with 9.5 mm diameter and a fuelled length of 1 482 mm. The rods had a cold fill pressure of 5 MPa with He. The free volume was 25.5 cm<sup>3</sup> [70].

The transients of the test series were initiated by a blow-down phase, usually a hot leg blow down, opening an electric valve connected with an ambient pressure tank. When local dry-out conditions were achieved, the heat-up phase started. At a predetermined time, the reflood coolant was injected into the assembly, controlled by the proper flow restriction valves.

Figure 5.43 Cross-section of the IFA-54X assembly and pressure flask



#### 5.3.1.4.2 The IFA-650.X test series

The test conditions in the IFA-650.X series are planned to meet the following primary objectives:

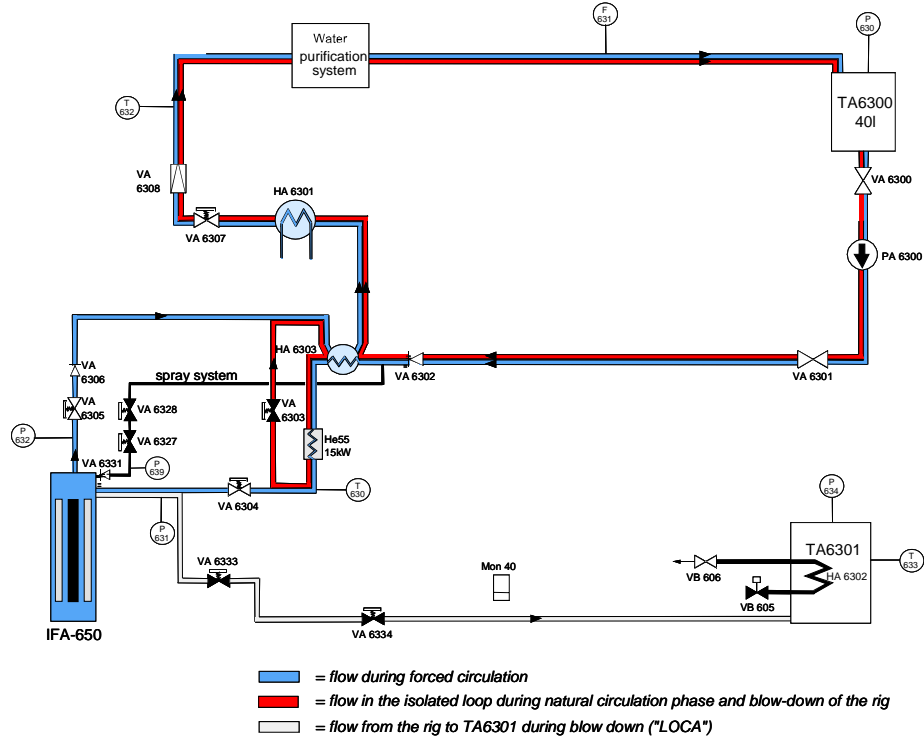
- To maximise the ballooning size to promote fuel relocation and to evaluate its possible effect on the cladding temperature and oxidation.
- To investigate the extent (if any) of “secondary transient hydriding” on the inner side of the cladding around the burst region.

Tests are planned to be carried out on pre-irradiated fuel rods with high burn-up. The rods are filled with a gas mixture of 5% helium and 95% argon at typically 40 bar. Argon is used to simulate fission gases whereas a small amount of helium is required for leak test of the rod.

The fuel rod is located in a standard high-pressure flask in the IFA-650 test rig, which is connected to a high-pressure heavy water loop and a blow-down system. A simplified layout of the loop is presented in Figure 5.44. During normal operation prior to the test, the rig is connected to the loop. Shortly before the test start the outer loop is bypassed, and after a few minutes with natural circulation in the rig the LOCA is initiated by opening the valves leading to a 110-litre shielded blow-down tank. The initial pressure in the loop is ~70 bar and the counter pressure in the blow-down tank is ~2 bar. A gamma monitor is placed on the blow-down line to measure total transported activity.

The rod is located in the centre of the rig and surrounded by an electrical heater inside the flask. The heater is part of a flow separator, which divides the space into a central channel surrounding the fuel rod and an outer annulus. The heater length is slightly longer than the fuel length, ~518 mm.

Figure 5.44 Simplified drawing of the loop used for the IFA-650 experiments [71]



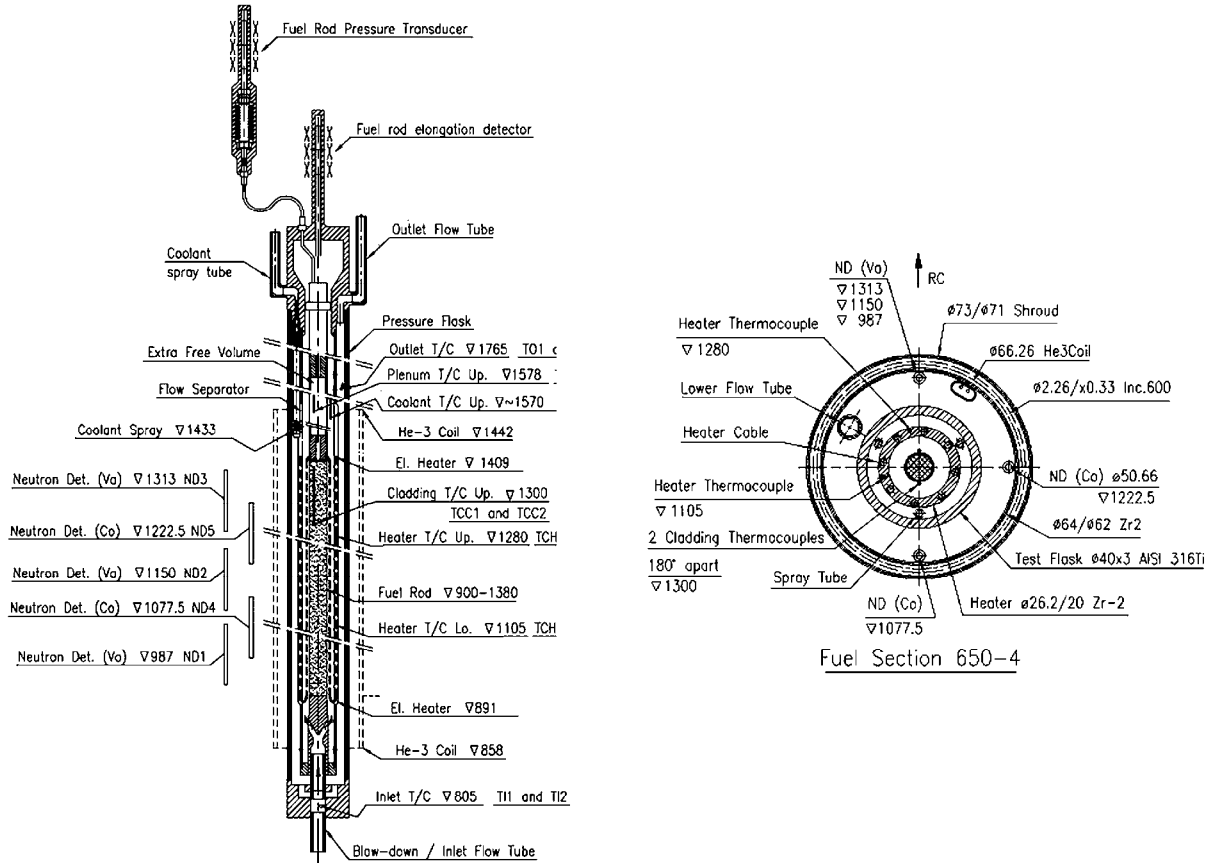
The pressure flask is inserted inside a shroud with a He<sup>3</sup>-coil incorporated. Neutron detectors are attached inside the He<sup>3</sup>-coil. The heater is used to simulate the isothermal boundary conditions, i.e. heat from adjacent fuel rods during a LOCA. Cladding temperature is influenced by both rod and heater power. The rod power can be controlled by changing the reactor power and by the He<sup>3</sup>-coil. However, the He<sup>3</sup>-coil is not used in every test.

A schematic of the test rig with its instrumentation is shown in Figure 5.45 together with the cross-section of the test rig. The rig instrumentation consists of three cladding surface thermocouples (TCC), a cladding extensometer (EC), a fuel pressure sensor (PF), two fast response cobalt neutron detectors and three vanadium neutron flux detectors at three elevations, two heater surface thermocouples (TCH) and thermocouples at the inlet (TI) and outlet (TO) of the rig. Two cladding thermocouples are located 8 cm below the fuel top and one 10 cm above the fuel bottom. The fourth cladding thermocouple, TCC3, is placed “hanging” in the inner flow channel ~9 cm above the fuel top. The temperature of the heater is measured by two embedded thermocouples, one 10 cm below the fuel top and the other 3.5 cm below the fuel mid plane. The axial power distribution can be observed by three self-powered vanadium neutron detectors (ND). Rapid power changes can be monitored using two fast responding cobalt NDs.

In the preparatory phase of a test the rod is at a predetermined LHGR with the outer loop connected and forced circulation flow. Then the LHGR is reduced to ~0.1 kW/m by decreasing reactor power. At this stage the heater is turned on to a preset value. The power levels are based on previous tests and calculations to achieve the desired peak cladding temperature.

When the correct power level has been reached the rig is disconnected from the loop. At this stage, there is natural convection flow in the rig and still full pressure. The temperatures in the rig are allowed to stabilise before blow-down which is started opening the valve to the dump tank. The rig is practically emptied of water in a few tens of seconds.

**Figure 5.45 The test rig used in the IFA-650 tests (left) and a cross section of the test rig with outer shroud (right)**



Stagnant superheated steam around the test rod provides inadequate cooling and the fuel cladding temperature increases rapidly. The heater power is turned down stepwise when target temperature is approached. Ballooning and rupture will usually take place during the heat up phase and is detected by the pressure drop in the rod. Depending on the desired character of the transient spray injection can be started as appropriate. After the test, the outer loop is not reconnected in order to avoid contamination. The rig is filled with helium to secure dry storage.

### 5.3.1.5 BTF test

#### 5.3.1.5.1 Introduction

Integrated tests on CANDU fuel elements were carried out in a specially designed facility called Blowdown Test Facility (BTF) in Canada. The BTF experiments were performed in the NRU reactor at the Chalk River Laboratories of AECL. The CANDU Owners Group (COG) sponsored the BTF experiments under joint funding from Ontario Power Generation (OPG), Hydro Québec, New Brunswick Power, and AECL.

Four BTF in-reactor experiments were performed in order to improve the understanding of CANDU fuel and fission-product behaviour under accident conditions, and to provide data for use in reactor safety code validation [72]. All four BTF tests have been completed.

### 5.3.1.5.2 Description of facility and test results

BTF tests were conducted in the NRU reactor at the AECL Chalk River Laboratories [72]. The insulated test section was oriented vertically in a Zircaloy re-entry flow tube, which fit inside a thick-walled stainless-steel pressure tube located in the reactor core. The BTF test section and the NRU reactor core had separate heat transport systems. Test assemblies in the BTF were cooled with pressurised water or saturated steam. An accident sequence was initiated by isolating the in-reactor test section from the rest of the loop, and voiding the coolant through an instrumented blow-down line and a wire-mesh filter into a sealed tank in the basement of the reactor building. Steam, inert gas and cold water were available for post-blow-down cooling in the BTF. The blow-down line was instrumented to measure coolant thermalhydraulic parameters and fission-product  $\gamma$  emissions.

In the BTF-107 experiment, a three-element cluster of CANDU-sized fuel elements was subjected to severely degraded cooling conditions resulting in a high-temperature ( $\geq 2\ 770$  K) transient [73-74]. A partial flow blockage developed during the test due to relocation of a molten U-Zr-O alloy and the high-temperature transient was terminated with a cold-water quench. The results of the BTF-107 test were used in development and validation of safety thermalhydraulics and fuel behaviour codes [73,75].

The other three experiments in the BTF programme, BTF-104, BTF-105A and BTF-105B, were conducted with single CANDU-sized fuel elements at maximum temperatures of 1 800-2 200 K in steam-rich environments. The tests were performed to evaluate the behaviour of a CANDU fuel element and the resultant fission-product release and transport in a LOCA/LOECC scenario.

- The BTF-104 experiment, provided data on fuel behaviour and volatile fission-product release and transport (Kr, Xe, I, Cs, Te and Ba) from a previously irradiated fuel element at a volume-averaged fuel temperature of about 1800 K [76-79].
- The BTF-105A experiment used an internally instrumented fresh fuel element [80-83]. The BTF-105A test provided data for validation of transient fuel performance codes and tested instrumentation for the BTF-105B experiment.
- The BTF-105B experiment investigated fission-product release and transport from a previously irradiated fuel element at an average fuel temperature of 2 100 K [84-85]. The thermalhydraulic boundary conditions for the BTF-105B test were better quantified than for previous BTF tests due to improved measurements of fuel-cladding temperature, flow and neutron flux, and better control of steam condensation in the test section.

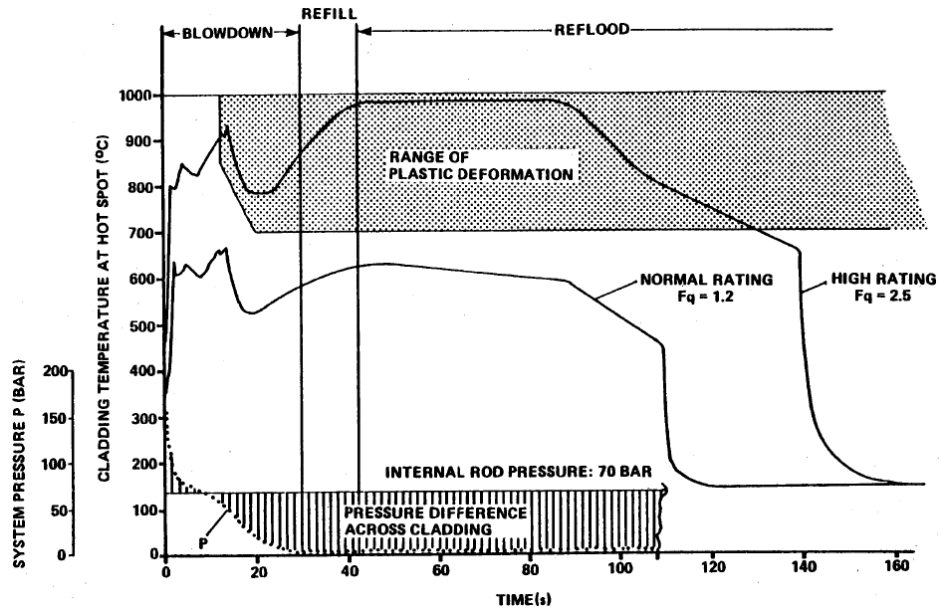
Data from BTF-107, BTF-104 and BTF105A experiments were used to qualify the transient fuel code ELOCA [86], used in CANDU safety analysis. Data from BTF-105A experiment was also used by OPG to qualify the fuel and fuel channel safety analysis code FACTAR [87]. The fission-product release, deposition and aerosol measurements from the BTF-104 and BTF-105B tests are being used to validate the fission product fraction release code SOURCE [88] and the fission product transport code SOPHAEROS [89].

### 5.3.2 Out-of-reactor integral tests

#### 5.3.2.1 The REBEKA programme at Kernforschungszentrum Karlsruhe (KfK)

This programme [90] uses single and multi-rod geometries to investigate the deformation of Zircaloy fuel cladding during the refilling and reflooding phases of a LOCA (Figure 5.46).

Figure 5.46 Fuel rod cladding loading in a 2F-cold leg break LOCA



There is particular emphasis on the conditions relating to the KWU design of PWR which includes hot leg injection of cooling water in addition to the cold leg injection used in US-designed PWRs. The fuel rod has a plenum at both top and bottom instead of one at the top as in US designs. There is thus more than double the internal volume in the German rod, i.e.~40 cm<sup>3</sup> [91].

The source of heat in REBEKA is an internal electrically heated fuel simulator shown in Figure 5.47 [92]. The multi-rod tests use full-length rods (heated length 3 900 mm) with spacer grids at positions corresponding to those in a fuel assembly. The test loop can provide steam cooling from the top to simulate hot leg injection effects, and steam or reflooding water from the bottom. These facilities enable the rig to simulate the adiabatic heating of a “blown-down” core followed by emergency cooling (Figure 5.48).

Figure 5.47 The REBEKA fuel rod simulator

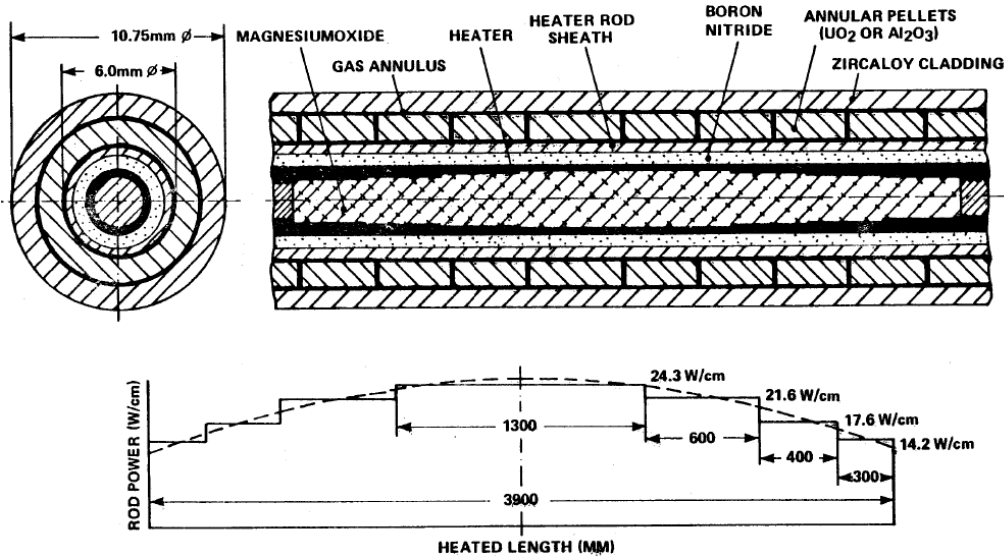
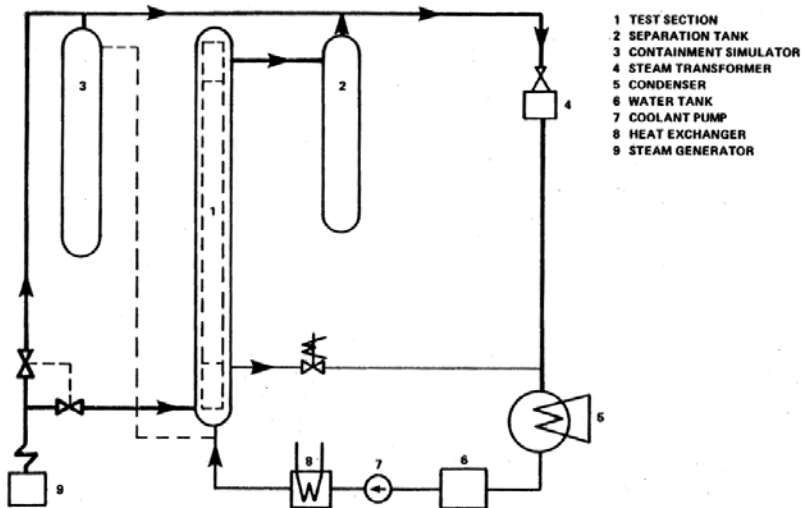


Figure 5.48 Test loop for ballooning experiments. Bundle tests (REBEKA) [92]



The test procedure is firstly to circulate water around the lower part of the loop and steam down the test section; both exit via the same valve. Meanwhile the test bundle is heated to about 800K and the rods are pressurised. Then they are fed with 8.57 kW each which causes them to ramp in the downward flowing steam at about 7 K/s. Reflooding is initiated by shutting the exit valve which forces the circulating water to flow up the test section. This firstly reverses the flow of steam and then, as the water contacts the hot rods, produces an upward flow of steam with entrained water droplets i.e. two-phase cooling. During reflooding, the power is reduced to  $6.6 \text{ kW} \pm 3\%$  to give  $20 \text{ W/cm}$ , equivalent to decay heat, in the central region of the fuel rod simulators. The reason for the extra power during heat-up is that the rods have about 20% greater heat capacity than an actual fuel rod and thus require the extra power ramp at the rate calculated for actual fuel rods.

### 5.3.2.2 Single and multi-rod tests at the Japanese Atomic Energy Research Institute (JAERI)

The rod size used in the JAERI tests, which have  $7 \times 7$  arrays, represents those used in a  $15 \times 15$  type of PWR fuel assembly. Figures 5.49 and 5.50 are schematic representations of the test rig and heating systems whilst Figure 5.51 shows the location of the thermocouples [93].

The heat source for the cladding in the more recent tests, i.e. number 5 onwards, was six W-3% Re wires, running through holes in a stack of alumina pellets. The minimum distance between the outer edge of the pellet and the surface of the wires was 0.05 in. The W-3% Re wire has a higher positive temperature coefficient of resistivity than either the Kanthal used in the ORNL heaters or Inconel used in the Kf K heaters. Because of this a hot spot tends to cause an increase in local heat generation i.e. at  $1000^\circ$  a  $50^\circ\text{C}$  local increase in the temperature of the wire results in a 5% increase in local heat generation [94].

The tests are conducted in a steam atmosphere but the flow rate was so low in most of the tests reported in Section 7, that flow effects can be discounted. A higher steam flow,  $5.79 \text{ g/cm min}$ , has been used in later work; however, this is still lower than that used in the ORNL test series [94].

The system for destructive examination of the test assemblies is unique; they are disassembled first into vertical rows and photographed, then into individual rods, and measured, then all the rods are reassembled into a  $7 \times 7$  array set in resin and finally sectioned horizontally (Figure 5.52).

Figure 5.49 Schematic diagram of the facility for burst test of a fuel assembly at JAERI

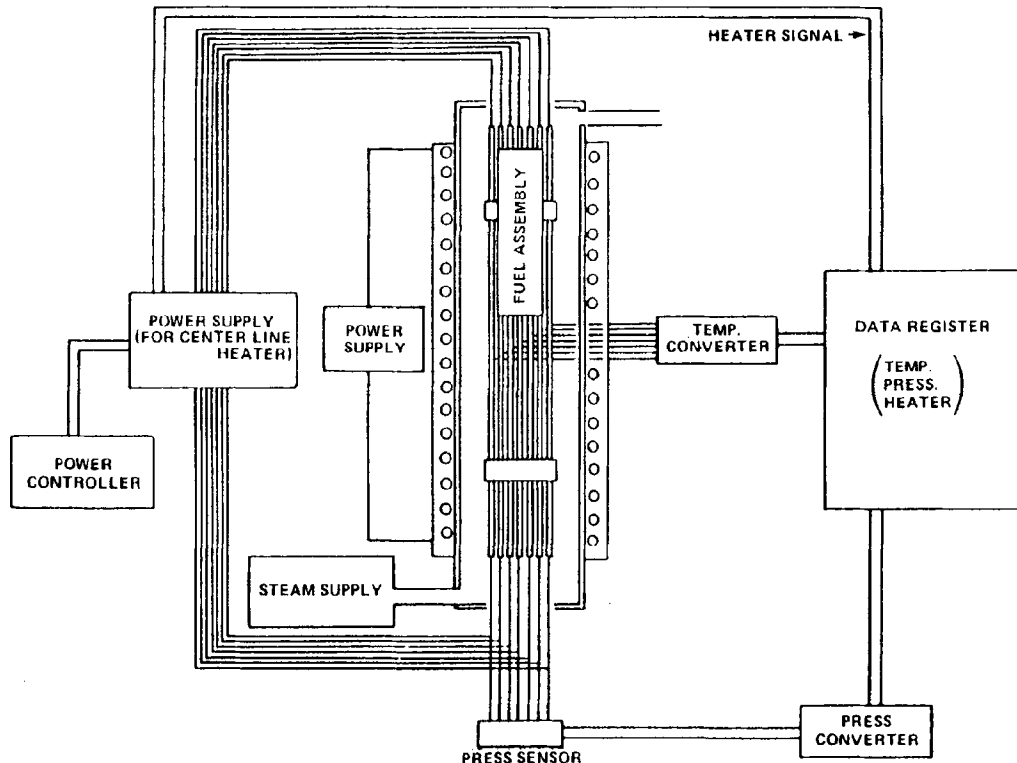


Figure 5.50 Schematic drawing of the fuel rods and the heating system of the JAERI tests

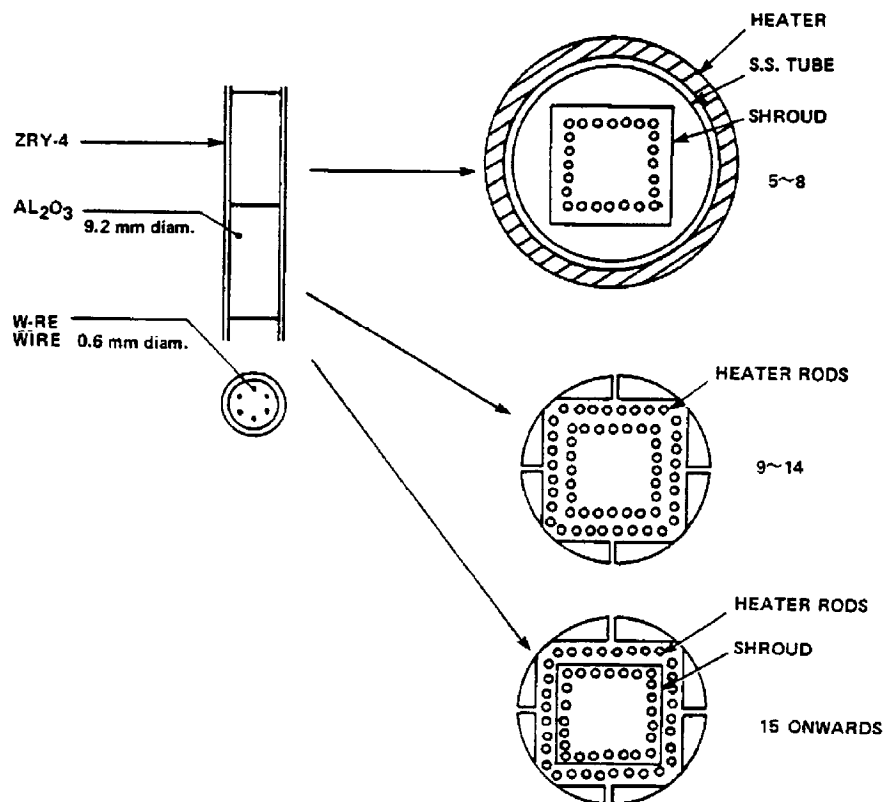


Figure 5.51 Locations of the thermocouples in the JAERI tests

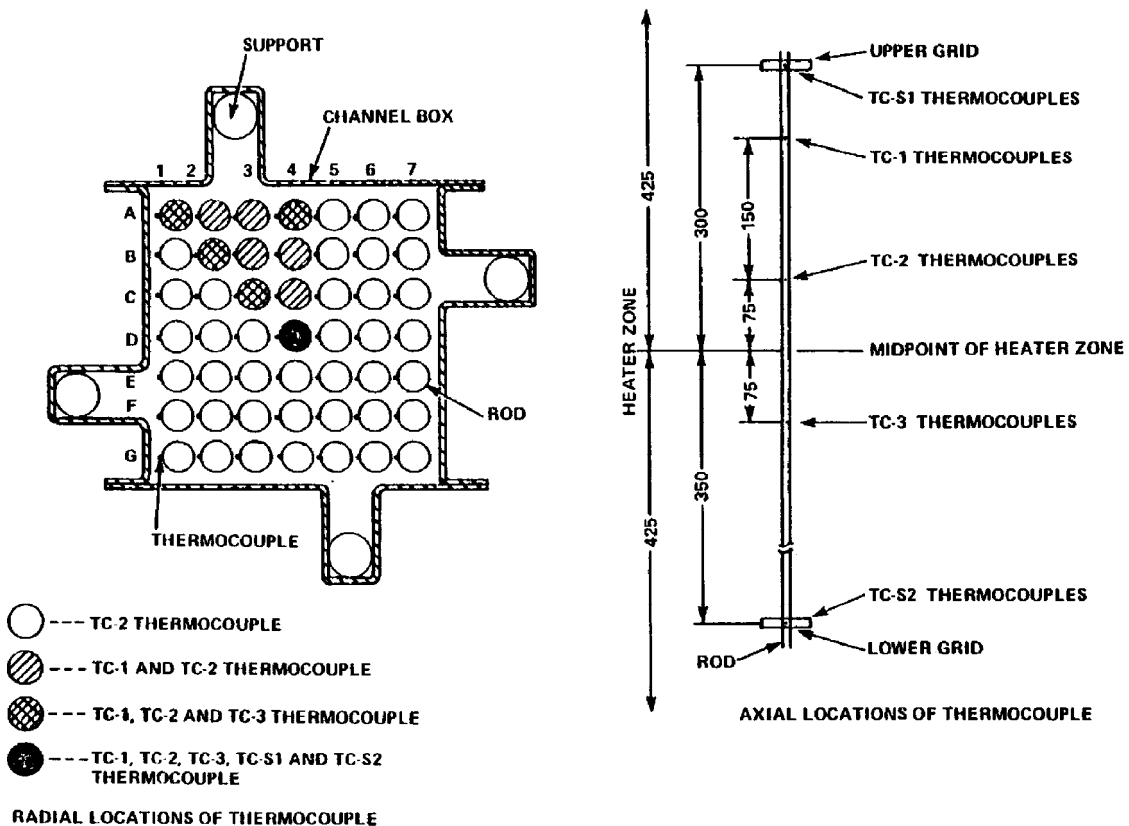
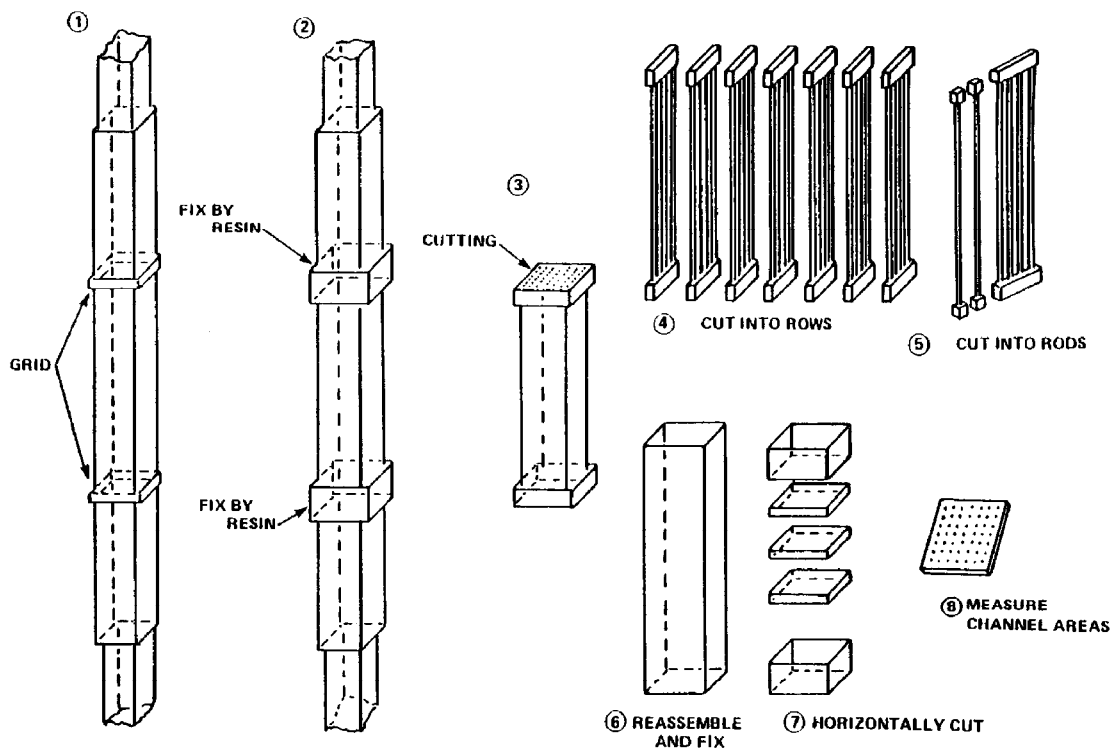


Figure 5.52 Sequence of the post burst examinations of an assembly in the JAERI tests

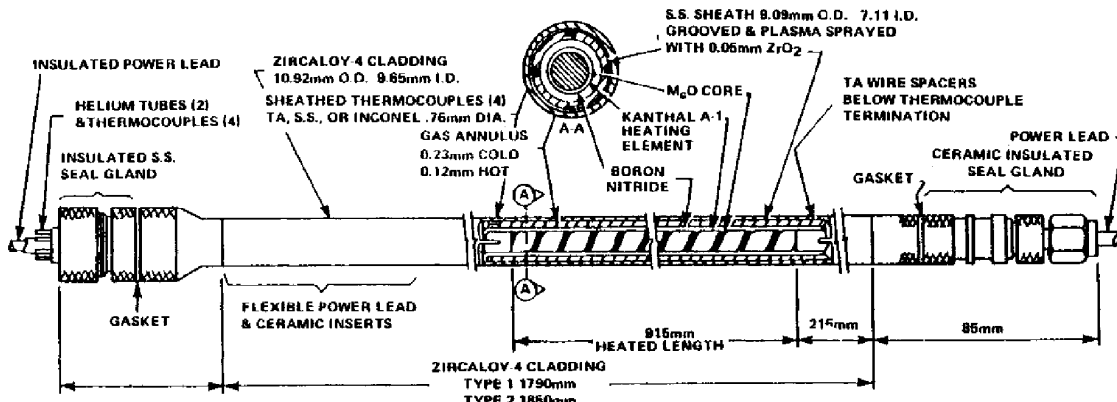


### 5.3.2.3 Single and multi-rod burst test (MRBT) at Oak Ridge National Laboratory (ORNL), USA

A series of tests at ORNL sponsored by the USNRC started in 1975 and had the following objectives: effects of rod to rod interaction on failure behaviour, magnitude and geometry of resulting blockage patterns, rupture temperature-pressure inter-relationships, flow resistance coefficients as a function of flow blockage and to provide an internally consistent data set that is amenable to statistical analysis.

The Zircaloy-4 tubing used was from the master lot purchased specifically for use in all the NRC cladding research programmes [95]. The dimensions (10.92 mm o.d. wall thickness 0.635 mm) were intermediate between then current PWR and BWR designs. The electric heater rod used to simulate the fuel had a spiral wound Kanthal heating element and a uniform heat flux profile [96]. In the outer stainless steel sheath, there were four grooves spaced at 90° in which lie thermocouples attached at their ends to the inner cladding surface (Figure 5.53). The test specimens had a heated length of 915 mm and an internal gas volume of 49-51.5 cm<sup>3</sup>, which is the minimum that is attainable with this particular design. Of this volume, 13% is in the heated portion of the annulus between the heater and cladding and 10% in the unheated portion, 33% in the pressure transducer and piping, and 44% in the end regions (mainly the upper) of the test specimen. This volume is about the same as used in the REBEKA fuel simulators but over twice that used in the then current U.S. PWR fuel (~17 cm<sup>3</sup>).

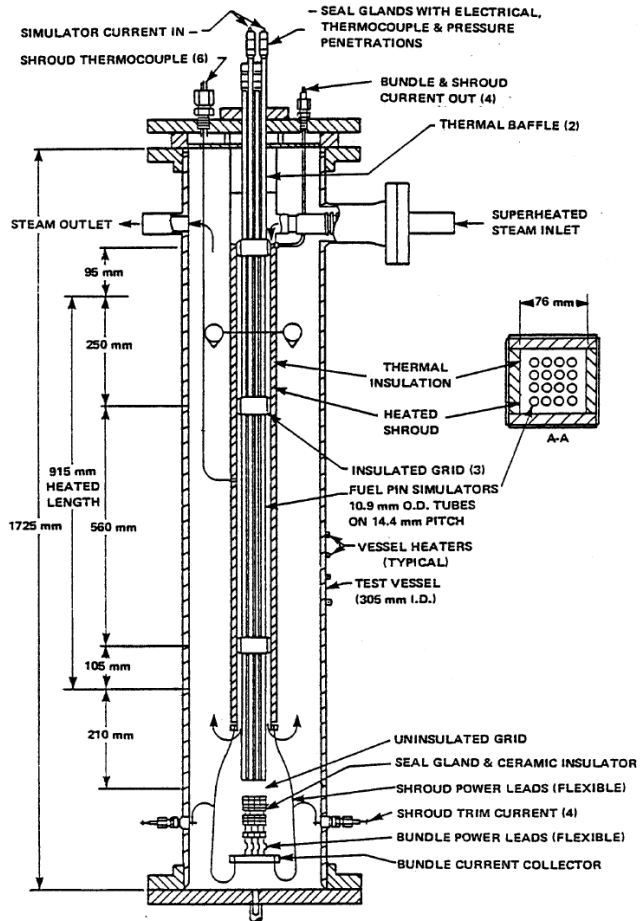
Figure 5.53 MRBT fuel pin simulator also used in the single-rod tests [97]



In the multi-rod burst tests, the test vessel shown in Figure 5.54 was used [98]. The fuel pin arrays were suspended from the vessel cover flange to allow free axial movement. A thin shroud surrounded the test arrays to provide well-defined flow boundaries. The arrangement shown in the Figure is for the 4×4 tests when an electrically heated shroud located 13 mm from the rod grid was used. Heating of the shroud at a temperature close to that of the test array has provided a good radial temperature boundary. However, the large spacing between shroud and outer rod rows has allowed non restrained deformation and bowing of these outer rods without contact.

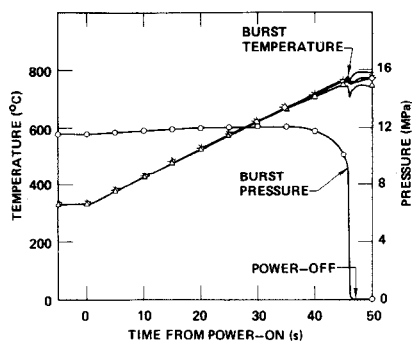
The tests carried out on a 8×8 rod array used an unheated shroud spaced 1.8 mm from the outer surface of the outer rods row (that is nearly one half of the gap thickness between two adjacent rods). This low spacing did not allow a direct resistance heating of the shroud as in the 4×4 and 6×6 tests. Therefore, the shroud was made of a thin (0.1 mm) stainless steel layer, with a highly polished gold-plated inner surface to minimise thermal capacity and radiative losses. The stainless steel sheet was backed on the outside with an isolating and strong support structure.

Figure 5.54 Schematic of the B1 4×4 multi-rod test assembly



Preparations for a test included equilibration at initial temperature conditions using electric heaters external to the test vessel and a small downward flow ( $288 \text{ g/s/m}^2$ ) of low-pressure superheated steam. Power was not applied to the simulators during equilibration. Immediately prior to the transient, the helium pressure inside the simulators was adjusted to a value that would cause fracture in the high  $\alpha$  range. Then the simulators were individually isolated from the gas supply system to ensure testing under conditions of constant gas inventory. The tests were conducted under essentially constant heating rate conditions by applying d-c voltage at a constant value. Figure 5.55 shows typical data recorded by the computer-controlled data acquisition system during the B-3 test. The data system also counted the tube bursts as they occurred and generated a signal to terminate the power input after the final tube burst.

Figure 5.55 Typical simulator response in the B-3 test [99]



Post-test examination included casting each array in an epoxy matrix and sectioning it at 10- to 20-mm intervals. Enlarged photographs of the sections were digitised to facilitate computer analysis of the deformation data. These data were processed to obtain strain profiles of the individual tubes, deformed tube areas and centroids, and flow area restriction as a function of bundle axial position.

#### *5.3.2.4 The Russian PARAMETR-M and TEFSAI-19 facilities*

In Russia, fully integrated tests are carried out on 19 and 37 rod VVER type assemblies in the electroheated facilities PARAMETR-M and TEFSAI-19 [100]. The PARAMETR-M facility is located at the Science Industrial Association, “LUCH”, while the TEFSAI-19 facility is located at the A.A. Bochvar All-Russia Research Institute of Inorganic Materials, VNIINM.

Variables studied in the experiments are heating rate, max fuel rod cladding temperature, steam flow rate, quench conditions and fuel rod cladding material.

The objectives of the experiments and post-test examinations are:

- Investigation of the temperature-force loading parameters, corresponding to different thermohydraulic LB-LOCA scenarios, influence on the assemblies damage characteristics.
- Research of deformation behaviour of the fuel rod simulator claddings gathered in an assembly and their depressurisation parameters (temperature, pressure, deformations and coordinates of places of rupture).
- Definition of the FA cross-section blockage and cladding balloonings distribution along the assembly height.

Verification of the codes used to design VVER-type reactors is an important goal of the integral experiments. The results of the experiments presented are used for verification of the RAPTA-5 code.

The 37-rod VVER fuel assembly used in the PARAMETR-M tests is shown in Figure 5.56 and the electroheated and passive rods used in the assembly is shown in Figure 5.57. The fuel assembly is placed in a hexagonal Zr1%Nb shroud with thermal insulation of porous ZrO<sub>2</sub>.

In the 37-element assembly the central simulator and 12 simulators of the second row are passive, while 6 simulators of the first row and 18 of the fourth are electro-heated by means of the central tungsten electrode.

The 19-element assemblies tested on the PARAMETR and TEFSAI-19 facilities have a similar design. All the fuel rod simulators of the 19-element assembly are electro-heated.

Cladding thermocouples and the internal pressure transducers are used to record pressure and temperature during the experiments. After the experiments the FAs are dismantled and the claddings cross-section perimeters are measured.

The calculated estimated cross section blockage for the hexagonal cell of one fuel rod is determined using the equation:

$$B_{\sin gl} = \pi(R^2 - R_0^2) / \left( \frac{\sqrt{3}}{2} H_{gr} - \pi R_0^2 \right) \times 100\% \quad (5-16)$$

where  $R_0$  is the initial radius of the rod,  $R$  the post-test radius taking crack width into account, and  $H_{gr}$  the pitch of the hexagonal grid.

Figure 5.56 Schematic view of the 37-rod assembly in the PARAMETR-M facility

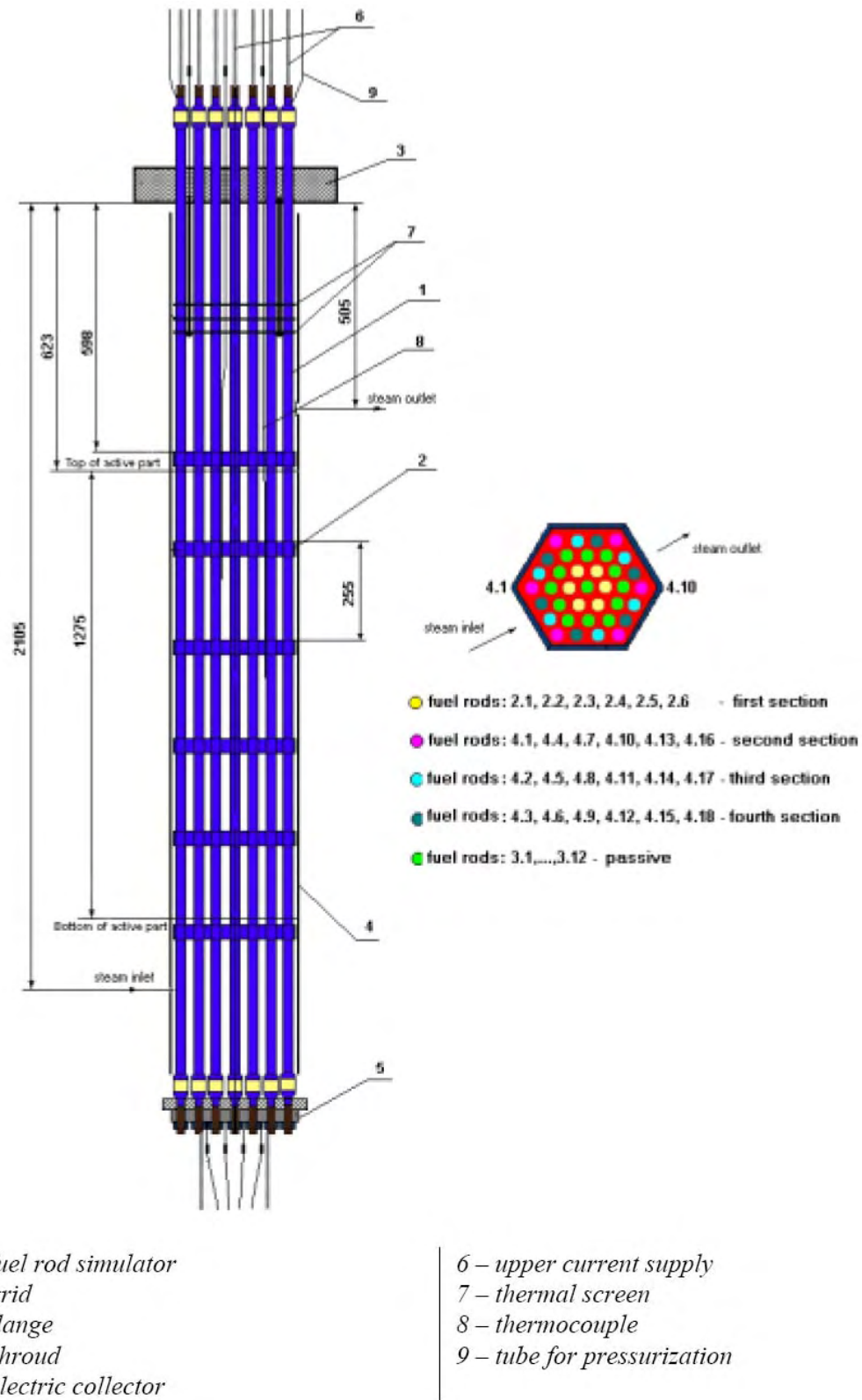
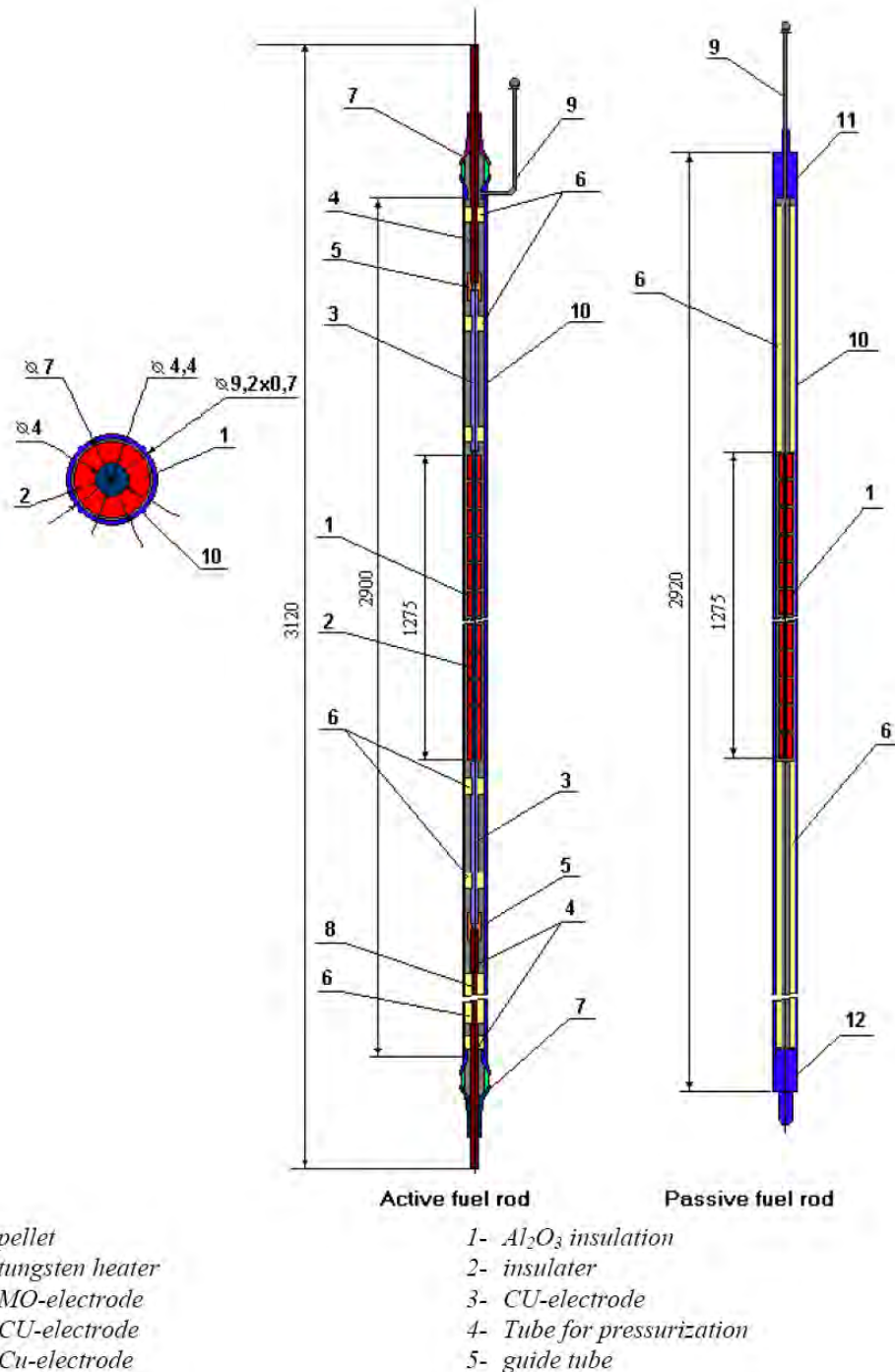


Figure 5.57 Schematic view of the fuel rod simulators used in PARAMETR-M and TEFSAI facilities



The assembly cross section is calculated as an arithmetic mean of the blockages  $B_{\text{singl}}$  as a function of axial location z:

$$B(z) = \sum B_i(z) / N \quad (5-17)$$

where N is the number of fuel rods in an assembly and  $B_i(z)$  the cross section blockage for the i:th simulator as a function of the axial coordinate z.

## 5.4 References

1. Hardy, D.G., "High temperature expansion and rupture behaviour of Zircaloy tubing", Topical Meeting on Water Reactor Safety, 1973, Salt Lake City, USA, pp. 254-273.
2. Hunt, C.E.L. and Foote, D.E., "High temperature strain behaviour of Zircaloy-4 and Zr-2.5Nb fuel sheaths", Zirconium in the Nuclear Industry, 1976, Quebec, Canada, ASTM STP 633, ASTM, pp. 50-65.
3. Hunt, C.E.L. and Newell, W.G., "Effect of B-phase heat treatment on the subsequent  $\alpha$ -phase ballooning behavior of Zircaloy-4 fuel sheaths", Zirconium in the Nuclear Industry: (Fourth Conference), 1978, ASTM STP 681, ASTM, pp. 447-464.
4. Rose, K.M. and Hindle, E.D., "Diameter increases in Steam Generating Heavy Water Reactor fuel cans under loss-of-coolant conditions", Zirconium in the Nuclear Industry, 1976, Quebec, Canada, ASTM STP 633, ASTM, pp. 24-35.
5. Fiveland, W.A., Barber, A.R., and Lowe, J., A.L., "Rupture characteristics of Zircaloy-4 cladding with internal and external simulation of reactor heating", Zirconium in the Nuclear Industry, 1976, Quebec, Canada, ASTM STP 633, ASTM, pp. 36-49.
6. Chung, H.M., Garde, A.N., and Kassner, T.F., "Deformation and rupture behavior of Zircaloy cladding under simulated loss-of-coolant conditions", Zirconium in the Nuclear Industry, 1976, Quebec, Canada, ASTM STP 633, ASTM, pp. 82-97.
7. Franklin, D., "Theory of plastic instability in thin-wall tubes", Acta Metallurgica, 20(1972), pp. 839-843.
8. Garde, A.N., Chung, H.M., and Kassner, T.F., "Micrograin superplasticity in Zircaloy at 850 C", Acta Metallurgica, 26(1978), pp. 153-166.
9. Kearns, J.J., McCauley, J.E., and Nichols, F.A., "Effect of  $\alpha/\beta$  phase constitution on superplasticity and strength of Zircaloy-4", Journal of Nuclear Materials, 61(1976), pp. 169-184.
10. Rizkalla, A., Holt, R.A., and Jonas, J.J., "Deformation of oxygen enriched Zircaloy-4 at elevated temperatures", Zirconium in the Nuclear Industry (Fourth Conference), 1978, Stratford-on-Avon, UK, ASTM STP 681, ASTM, pp. 497-513.
11. Hindle, E.D., "Stress rupture and creep of Zircaloy-4 fuel cladding in the temperature range 875 to 915 K", UKAEA Report ND-R-191(S), September 1978.
12. Rosinger, H.E., *et al.*, "The steady-state creep of Zircaloy-4 fuel cladding from 940 to 1873 K", AECL-6193, Nov. 1978.
13. Rosinger, H.E., Bera, P.C., and Clendinning, W.R., "Steady-state creep of Zircaloy-4 fuel cladding from 940 to 1873 K", Journal of Nuclear Materials, 82(1979), pp. 286-297.
14. Ortlieb, E., Cheliotis, G., and Weidinger, H.W., "Influence of the initial material condition on the deformation behavior of Zircaloy cladding tubes in the high- $\alpha$ -phase region", Zirconium in the Nuclear Industry: Seventh International Symposium, 1985, Strasbourg, France, ASTM STP 939, ASTM, pp. 539-554.
15. Douglass, D.L., "The metallurgy of zirconium. Atomic Energy Review, Supplement. 1971, Vienna: IAEA.
16. Pawel, R.E., *et al.*, "Diffusion of oxygen in  $\beta$ -Zircaloy and the high temperature Zircaloy-steam reaction", Zirconium in the Nuclear Industry, 1976, Quebec, Canada, ASTM STP 633, ASTM, pp. 119-133.

17. Chung, H.M. and Kassner, T.F., "Pseudobinary Zircaloy-oxygen phase diagram", Journal of Nuclear Materials, 84(1979), pp. 327-339.
18. Hobson, D.O., "Ductile-brittle behavior of Zircaloy fuel cladding", ANS Topical Meeting on Water Reactor Safety, 1973, Salt Lake City, pp. 274-288.
19. Hobson, D.O. and Rittenhouse, P.L., "Embrittlement of Zircaloy Clad Fuel Rods by Steam During LOCA Transients", Oak Ridge National Laboratory, ORNL-4758, January 1972.
20. Forgeron, T., *et al.*, "Experiment and modeling of advanced fuel rod cladding behavior under LOCA conditions: A-B phase transformation kinetics and EDGAR methodology", Zirconium in the Nuclear Industry: Twelfth International Symposium, 1998, Toronto, ASTM STP 1354, ASTM, pp. 256-278.
21. Brachet, J.-C., *et al.*, "Influence of hydrogen content on the  $\alpha/\beta$  phase transformation temperatures and the thermal-mechanical behavior of Zy-4, M4 (ZrSnFeV), and M5 (ZrNbO) alloys during the first phase of a LOCA transient", Zirconium in the Nuclear Industry: Thirteenth International Symposium, 2001, Annecy, ASTM STP 1423, ASTM, pp. 673-701.
22. Sell, H.-J. and Ortlib, E., "Effects of  $\alpha\text{-}\beta$  transformation on high temperature (LOCA) creep behavior in Zr-alloys", Zirconium in the Nuclear Industry: Thirteenth International Symposium, 2001, Annecy, ASTM STP 1423, ASTM, pp. 658-672.
23. Yegorova, L., *et al.*, "Experimental study of embrittlement of Zr-1%Nb VVER cladding under LOCA-relevant conditions", NUREG/IA-0211, IRSN 2005-194, NSI RRC KI 3188, March 2005.
24. Billone, M., Yan, Y., and Burtseva, T.A., "Post-quench ductility of Zircaloy, E110, Zirlo and M5", SEGFSM Topical Meeting on LOCA Issues, 2004, Argonne, USA.
25. Yan, Y., Burtseva, T., and Billone, M.C., "Post-quench ductility results for Zry-4 and ZIRLO oxidized at 1000 C and 1100 C", Argonne National Laboratory, (available at [www.nrc.gov](http://www.nrc.gov) in NRC's public document system, ADAMS, as ML041420178).
26. Hózer, Z. and Györy, C., "Derivation of a LOCA ductility limit from AEKI ring compression tests", SEGFSM Topical Meeting on LOCA Issues, 2004, Argonne, USA.
27. Hózer, Z., *et al.*, "Ductile-to-brittle transition of oxidised Zircaloy-4 and E110 claddings", Journal of Nuclear Materials, 373(2008), pp. 415-423.
28. Sawatsky, A., "Proposed criterion for the oxygen embrittlement of Zircaloy-4 fuel cladding", 4<sup>th</sup> Symposium on Zirconium in the Nuclear Industry, 1978, Stratford-on-Avon, ASTM STP-681, ASTM, pp. 479-496.
29. Kim, S. and Lee, C., "Mechanical tests based on ring tensile tests of high burn-up nuclear fuel cladding in hot cell", SEGFSM Topical Meeting on LOCA Issues, 2004, Argonne, USA.
30. Brachet, J.-C., *et al.*, "Mechanical behaviour at room temperature and metallurgical study of low tin Zy-4 and M5 (Zr-Nb) alloys after oxidation at 1100 C and quenching", IAEA Technical Committee Meeting on Fuel behaviour under transient and LOCA conditions., 2001, Halden, Norway, IAEA, pp. 139-158.
31. Portier, L., *et al.*, "Influence of long service exposures on the thermal-mechanical behavior of Zy-4 and M5 alloys in LOCA conditions", Zirconium in the Nuclear Industry: Fourteenth International Symposium, 2004, Stockholm, ASTM STP 1467, ASTM, pp. 896-920.
32. Uetsuka, H. *et al.*, "Zircaloy-4 cladding embrittlement due to inner surface oxidation under simulated loss of coolant conditions", Journal of Nuclear Science and Technology, 18(1981), pp. 707-717.

33. Yan, Y., Billone, M., and Burtseva, T.A., "LOCA test results for high-burn-up BWR fuel and cladding", SEGFSM Topical Meeting on LOCA Issues, 2004, Argonne, USA.
34. Northwood, D.O. and Kosasih, U., "Hydrides and delayed hydrogen cracking in zirconium and its alloys", International metals reviews, 28(1983), pp. 92-121.
35. Stern, A., *et al.*, "Investigations of the microstructure and mechanical properties of prior  $\beta$ -structure as a function of the oxygen content in two zirconium alloys", Zirconium in the Nuclear Industry: 15<sup>th</sup> International Symposium, 2007, Sun River, USA, ASTM.
36. Chung, H.M., Garde, A.N., and Kassner, T.F., "Development of an oxygen embrittlement criterion for Zircaloy cladding applicable to loss-of-coolant accident conditions in light-water reactors", Zirconium in the Nuclear Industry (Fourth Conference), 1978, Stratford-upon-Avon, UK, ASTM STP 681, ASTM, pp. 600-627.
37. Chung, H.M. and Kassner, T.F., "Embrittlement Criteria for Zircaloy Fuel Cladding Applicable to Accident Situations in Light-Water Reactors. Summary Report", NUREG/CR-1344, January 1980.
38. Pawel, R.E. and Campbell, J.J., "A comparison of the high-temperature oxidation behavior of Zircaloy-4 and pure zirconium", Zirconium in the Nuclear Industry; Fifth Conference, 1980, Boston, USA, ASTM STP 754, ASTM, pp. 370-389.
39. Sawatsky, A., Ledoux, G.A., and Jones, S., "Oxidation of zirconium during a high-temperature transient", Zirconium in the Nuclear Industry, 1976, Quebec, Canada, ASTM STP 633, ASTM, pp. 134-149.
40. Dobson, W.G., Biederman, R.R., and Ballinger, R.G., "Zircaloy-4 oxidation in steam under transient oxidizing conditions", Zirconium in the Nuclear Industry, 1976, Quebec, Canada, ASTM STP 633, ASTM, pp. 150-167.
41. Urbanic, V.F., "Oxidation of zirconium alloys in steam at 1000 to 1850 C", Zirconium in the Nuclear Industry, 1976, Quebec, Canada, ASTM STP 633, ASTM, pp. 168-181.
42. Leistikow, S., Schantz, G., and Berg, H.V., "Kinetics and morphology of isothermal steam oxidation of Zircaloy-4 at 700-1300 C", KFK 2587, Mar. 1978.
43. Leistikow, S., "Comparison of high-temperature steam oxidation kinetics under LWR accident conditions: Zircaloy-4 versus austenitic stainless steel 1.4970", Zirconium in the Nuclear Industry: Sixth International Symposium, 1982, Vancouver, Canada, ASTM STP 824, ASTM, pp. 763-779.
44. Chung, H.M. and Thomas, G.R., "High temperature oxidation of Zircaloy in hydrogen steam mixtures", Sixth International Symposium on Zirconium in the Nuclear Industry, 1982, Vancouver, Canada, ASTM STP 824, ASTM, pp. 793-809.
45. Prater, J.T. and Courtwright, E., "Oxidation of Zircaloy-4 in steam at 1300-2400 C", 7<sup>th</sup> International Symposium on Zirconium in the Nuclear Industry, 1985, Strasbourg, ASTM STP 939, ASTM, pp. 489-503.
46. Ocken, H., *et al.*, "Evaluation models of Zircaloy oxidation in light of recent experiments", Fourth International Symposium on Zirconium in the Nuclear Industry, 1978, Stratford-on-Avon, ASTM STP 681, ASTM, pp. 514-536.
47. Bibilashvili, Y.K., *et al.*, "Thermomechanical properties of zirconium-based alloys oxidized claddings in LOCA simulating conditions", IAEA Technical Committee Meeting on Fuel behaviour under transient and LOCA conditions., 2001, Halden, Norway, IAEA, pp. 186-208.

48. Sokolov, N.B., *et al.*, "Thermomechanical behaviour of zirconium-based alloys claddings under LOCA conditions", Fontevraud 5 International Symposium, 2002, Fontevraud, France, pp. Paper 93.
49. Baek, J.H., Park, K.B., and Jeong, Y.H., "Oxidation kinetics of Zircaloy-4 and Zr-1Nb-1Sn-0.1Fe at temperatures of 700-1200°C", Journal of Nuclear Materials, 335(2004), pp. 443-456.
50. Hindle, E.D. and Mann, C.A., "An experimental study of the deformation of Zircaloy PWR fuel rod cladding under mainly convective cooling", Zirconium in the Nuclear Industry; Fifth Conference, 1980, Boston, USA, ASTM STP 754, ASTM, pp. 284-302.
51. Sagat, S., Sills, H.E., and Walsworth, J.A., "Deformation and failure of Zircaloy fuel sheaths under LOCA conditions", Zirconium in the Nuclear Industry: Sixth International Symposium, 1982, Vancouver, Canada, ASTM STP 824, ASTM, pp. 709-733.
52. Greandjean, C., "A state-of-the-art review of past programs devoted to fuel behaviour under LOCA conditions: 1st Part: Clad swelling and rupture, assembly flow blockage", IRSN, Technical Report DPAM/SEMCA 2005/XX.
53. Furuta, T., *et al.*, "Zircaloy clad fuel rod burst behaviour under simulated loss of coolant conditions in PWRs", Journal of Nuclear Science and Technology, 15(1978), pp. 736-744.
54. Furuta, T., *et al.*, "Ductility loss of Zircaloy cladding by inner surface oxidation during high temperature transients", Journal of Nuclear Science and Technology, 18(1981), pp. 802-810.
55. Furuta, T., Uetsuka, H., and Kawasaki, S., "Estimation of conservatism of present embrittlement criteria for Zircaloy fuel cladding under LOCA", Zirconium in the Nuclear Industry: Sixth International Symposium, 1982, Vancouver, Canada, ASTM STP 824, ASTM, pp. 734-746.
56. Nagase, F. and Fuketa, T., "Effect of Pre-Hydriding on Thermal Shock Resistance of Zircaloy-4 Cladding under Simulated Loss-of-Coolant Accident Conditions", Journal of Nuclear Science and Technology, 41(2004), pp. 723-730.
57. Nagase, F. and Fuketa, T., "Behavior of Pre-Hydrided Zircaloy-4 Cladding under Simulated Loss-of-Coolant Accident Conditions", Journal of Nuclear Science and Technology, 42(2005), pp. 209-218.
58. Nagase, F. and Fuketa, T., "Results from Simulated LOCA Experiments with High Burn-up PWR Fuel Claddings", 2004 International Meeting on Light Water Reactor Fuel Performance, 2004, Orlando, Florida, American Nuclear Society.
59. Nagase, F. and Fuketa, T., "Study of high burn-up fuel behaviour under a LOCA conditions at JAERI: Hydrogen effects on the failure-bearing capability of cladding tubes", 29<sup>th</sup> Nuclear Safety Research Conference, 2001, Washington, USA, NRC.
60. Nagase, F. and Fuketa, T., "Recent results from LOCA study at JAERI", 2003 Nuclear Safety Research Conference, 2003, Washington, USA, NRC.
61. Nagase, F. and Fuketa, T., "Results from studies on high burn-up fuel behavior under LOCA conditions", 2004 Nuclear Safety Research Conference, 2004, Washington DC, NRC, pp. 224-230.
62. Nagase, F., *et al.*, "Experiments on high burn-up fuel behavior under LOCA conditions at JAERI", 2000 International Topical Meeting on Light Water Reactor Fuel Performance, 2000, Park City, Utah, American Nuclear Society.
63. Nagase, F., Otomo, T., and Uetsuka, H., "Oxidation kinetics of low-Sn Zircaloy-4 at the temperature range from 773 to 1573 K", Journal of Nuclear Science and Technology, 40(2003), pp. 213-219.

64. Nagase, F., Tanimoto, M., and Fuketa, T., “Study on high burn-up fuel behaviour under a LOCA condition at JAERI”, IAEA Technical Committee Meeting on Fuel behaviour under transient and LOCA conditions., 2001, Halden, Norway, IAEA,
65. Kim, J.H., *et al.*, “Embrittlement behavior of Zircaloy-4 cladding during oxidation and water quench”, Nuclear Engineering and Design, 235(2005), pp. 67-75.
66. Kim, J.H., *et al.*, “Deformation of Zircaloy-4 cladding during a LOCA transient up to 1 200°X”, Nuclear Engineering and Design, 234(2004), pp. 157-164.
67. Karb, E.H., *et al.*, “LWR fuel rod behaviour in the FR2 in-pile tests simulating the heatup phase of a LOCA”, KfK 3346, March 1983.
68. Réocreux, M. and Scott de Martinville, E.F., “A study of fuel behavior in PWR design basis accident: an analysis of results from the PHEBUS and EDGAR experiments”, Nuclear Engineering and Design, 124(1990), pp. 363-378.
69. Svanholm, K., *et al.*, “Halden Reactors IFA-511.2 and IFA-54X: Experimental series under adverse cooling conditions”, Experimental Thermal and Fluid Science, 11(1995).
70. Vitanza, C., Johnsen, T., and Höglberg, N.W., “In-pile data report on the first cladding ballooning experiment in the Halden reactor (IFA-543)”, OECD Halden Reactor Project, HPR 291, December 1983.
71. Ek, M., “LOCA testing at Halden, the third experiment IFA-650.3”, OECD Halden Reactor Project, HWR-785, October 2005.
72. Walsworth, J.A., *et al.*, “The Canadian in-reactor blowdown test facility (BTF)”, IAEA Specialists Meeting on Program in Support of Reactor Safety, 1989, IAEA, IAEA-SM-310/102.
73. DeVaal, J.W., *et al.*, “Post-test simulations of BTF-107: An in-reactor loss-of-coolant test with flow blockage and rewet”, Third International Conference on CANDU fuel, 1992, Pembroke, Ontario.
74. MacDonald, R.D., *et al.*, “An in-reactor loss-of-coolant test with flow blockage and rewet”, Thermal Reactor Safety Meeting, 1991, Portland, Oregon.
75. Popov, N.K., *et al.*, “Post-test analysis of the BTF-107 severe-fuel-damage experiment using the CATHENA thermohydraulic code”, International Conference on New Trends in Nuclear System Thermohydraulics, 1994, Pisa, Italy.
76. Dickson, L.W., *et al.*, “Preliminary results of the BTF-104 experiment: An in-reactor test of fuel behaviour and fission-product release and transport under LOCA/LOECC conditions”, 16<sup>th</sup> Annual Conference Canadian Nuclear Society, 1995, Saskatoon, Saskatchewan, Canada.
77. Dickson, L.W., *et al.*, “The BTF-104 experiment: An in-reactor test of fuel behaviour and fission-product release and transport under LOCA/LOECC conditions”, Fourth International Conference on CANDU Fuel., 1995, Pembroke, Ontario, Canada.
78. Dickson, R.S., *et al.*, “Post-test analysis of the BTF-104 severe fuel damage experiment using the VICTORIA fission product transport code”, Third OECD Specialist Meeting on Nuclear Aerosols in Reactor Safety, 1998, Köln, Germany.
79. Popov, N.K., *et al.*, “Post-test analysis of the BTF-104 severe-fuel-damage experiment using the CATHENA thermalhydraulics code”, ASME-JSME Fourth International Conference on Nuclear Engineering (ICON-E-4), 1996, New Orleans, Louisiana, USA, pp. 205-213.

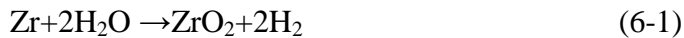
80. DeVaal, J.W., *et al.*, "Preliminary results of the BTF-105 test: An in-reactor instrument development and fuel behaviour test", Fifth International Conference on CANDU Fuel, 1997, Toronto, Canada.
81. Popov, N.K., *et al.*, "Post-Test Analysis of the BTF-105A Severe-Fuel-Damage Test Using the CATHENA Thermalhydraulics Code", Sixth International Conference on Nuclear Engineering (ICONE-6), 1998, San Diego, California, USA.
82. Valliant, P.J., Irish, J.D., and Craig, S.T., "Post-irradiation results from the BTF-105A LOCA/LOECC test", Sixth International Conference on CANDU Fuel, 1999, Niagara Falls, Canada.
83. Walters, L.C., *et al.*, "Development of a model for calculating sheath thermocouple finning losses for application in the in-reactor severe fuel damage tests", Canadian Nuclear Society Simulation Symposium, 1997, Niagara-on-the-Lake, Ontario, Canada.
84. Irish, J.D., Craig, S.T., and Valliant, P.J., "Preliminary fission product and post-irradiation examination results from the BTF-105A LOCA/LOECC test", Sixth International Conference on CANDU Fuel, 1999, Niagara Falls, Canada.
85. Irish, J.D., *et al.*, "Preliminary results of the BTF 105B experiment: An in-reactor test of fuel behaviour and fission-product release and transport under LOCA/LOECC conditions", 19<sup>th</sup> Annual Conference of the Canadian Nuclear Society, 1998, Toronto, Canada.
86. Williams, A.F., "The ELOCA fuel modelling code: Past, present and future", 9<sup>th</sup> International Conference on CANDU Fuel, 2005, Belleville, Ontario, Canada.
87. Middleton, P.B., Rock, R.C.K., and Wadsworth, S.L., "FACTAR 2.0 code validation", Fifth International Conference on CANDU Fuel, 1997, Toronto, Canada.
88. Barber, H., *et al.*, "SOURCE IST: Fission product release code", 9<sup>th</sup> International Conference on CANDU Fuel, 2005, Belleville, Ontario, Canada.
89. Dickson, L.W., *et al.*, SOPHAEROS-IST 2.0 Validation: An update on the current status, CNS 6<sup>th</sup> International Conference on Simulation Methods in Nuclear Engineering, 2004, Montreal, Québec, Canada.
90. Erbacher, F.J., "LWR fuel cladding deformation in a LOCA and its interaction with the emergency core cooling", ANS/ENS Topical Meeting on Reactor Safety Aspects of Fuel Behaviour, 1981, Sun Valley, USA,
91. Karwat, H., "Specification of international standard problem 14: Behaviour of a fuel bundle simulator during a heat-up and flooding period (REBEKA experiment)", GRD Technische Universität, FRG, March 1983.
92. Erbacher, F.J., Neitzel, H.J., and Wiehr, K., "Interactions between thermohydraulics and fuel clad ballooning in a LOCA - results of REBEKA multi-rod burst tests with flooding", 6<sup>th</sup> Water Reactor Safety Information Meeting, 1978, Gaithersburg, USA, NRC.
93. Parsons, P.D., Hindle, E.D., and Mann, C.A., "PWR fuel behaviour in design basis accident conditions. A State-of-the-Art Report by the Task Group on Fuel Behaviour of CSNI Principal Working Group No 2", Committee on the Safety of Nuclear Installations, OECD Nuclear Energy Agency, CSNI Report 129.
94. Longest, A.W., "Multi-rod burst test program. Progress report Jan-June 1981", NUREG/CR-2366 Vol. 1 ORNL/NUREG/TM-8058, December 1981.

95. Chapman, R.H., "Characterization of Zircaloy-4 tubing procured for fuel cladding research programs", ORNL/NUREG/TM-29, June 1976.
96. McCulloch, R.W., Jacobs, P.T., and Clark, D.L., "Development of a fabrication procedure for the MRBT fuel simulator based on the use of cold-pressed boron nitride performs, NUREG/CR-1111, March 1980.
97. Chapman, R.H., "Multi-rod burst test program: progress report", July-September 1977, ORNL/NUREG/TM-200, June 1978
98. Chapman, R.H., Crowley, J.L., and Longest, A.W., "Effect of bundle size on cladding deformation in LOCA simulation tests", Zirconium in the Nuclear Industry: Sixth International Symposium, 1982, Vancouver, Canada, ASTM STP 824, ASTM, pp. 693-708
99. Chapman, R.H., *et al.*, "Zirconium cladding deformation in a steam environment with transient heating", Zirconium in the Nuclear Industry: (Fourth Conference), 1978, ASTM STP 681, ASTM, pp. 393-408.
100. Bibilashvili, Y.K., *et al.*, "WWER-1000 type fuel assembly tests on electroheated facilities in LOCA simulating conditions", IAEA Technical Committee Meeting on Fuel behaviour under transient and LOCA conditions., 2001, Halden, Norway, IAEA, pp. 169-185.

## **6. PRESERVATION OF INTEGRITY OF CLADDING DURING OXIDATION AND EMBRITTLEMENT**

### **6.1 The kinetics of the zirconium alloy steam reaction**

As discussed previously in this report zirconium alloy fuel cladding is reactive in steam. The following description refers to Zircaloy but also applies to other Zr-base alloys with the exception of some details. The products of the reaction can be represented in a simple form by an elementary molecular equation:

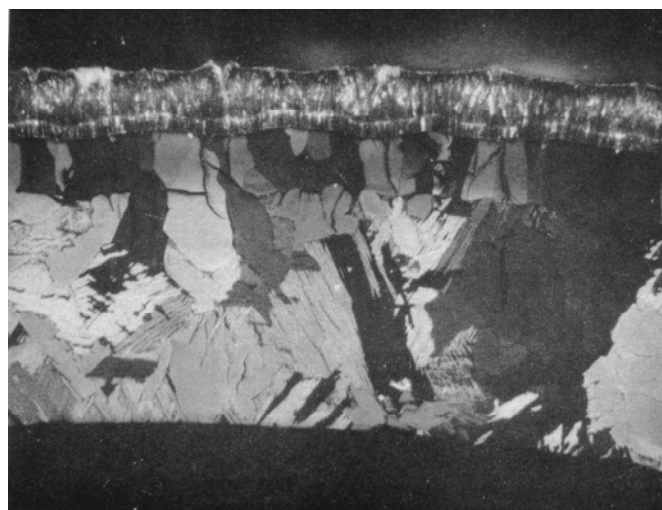


The rate of reaction is dependent on temperature and at temperatures above  $\sim 950^\circ\text{C}$  in conditions where the availability of steam is unlimited and the integrity of the oxide film is maintained, is generally believed to be controlled by the rate of diffusion of oxygen anions in the anion deficient zirconia film.

The reaction products are also dependent on temperature. At temperatures below the  $\alpha \rightarrow (\alpha + \beta)$  transus,  $812^\circ\text{C}$  for Zry-4, the oxidation of Zircaloy results in the formation of a zirconia film and the diffusion of some oxygen into the underlying  $\alpha$ -Zircaloy metal.

At higher temperatures, hexagonal close packed  $\alpha$ -Zircaloy is unstable and transforms to body centred cubic  $\beta$ -Zircaloy. Hence, Zircaloy oxidized at temperatures above the transformation temperature consists of an outer layer of zirconia, a layer of high oxygen Zircaloy metal which is stabilised in the  $\alpha$ -Zircaloy form by the high oxygen content, and beneath this a  $\beta$ -Zircaloy layer. The resulting structure is illustrated in Figure 6.1 which shows a section of Zircaloy-2 cladding tube oxidized in a Swedish BWR LOCA transient corresponding to 800 s at  $1200^\circ\text{C}$  [1].

Figure 6.1 Zircaloy-2 oxidized in steam at  $1200^\circ\text{C}$  for 800 s 80 $\times$



Diffusion controlled solid state processes are characterised by a parabolic rate law. If w represents the amount of reactant used or product formed then:

$$\frac{dw}{dt} = \frac{1}{2} \frac{\delta^2}{w} \quad (6-2)$$

The constant of proportionality is the parabolic rate constant and is generally given the nomenclature  $\delta^2/2$  such that on integration, equation 6-2 becomes:

$$w^2 = \delta^2 t + c \quad (6-3)$$

where t is the time of oxidation and c is zero in fresh cladding (other systems of notation define the parabolic rate constant K<sub>p</sub> as the constant of proportionality in equation 6-2 such that  $w^2 = 2Kpt$ ).

The parabolic rate of reaction constant,  $\delta^2/2$  or K<sub>p</sub>, is dependent on temperature according to an Arrhenius expression:

$$\delta^2 / 2 \text{ or } K_p = A \exp - Q / RT \quad (6-4)$$

Where: A = pre-exponential factor. Q = activation energy, J/mol.  
T = temperature, K. R = gas constant, 8.314 J/mol/K.

In the present report,  $\delta^2/2$  will be used for the rate constants. However, in some of the sources from which figures have been reproduced, K<sub>p</sub> has been used. Typical units for the parabolic rate constant are g<sup>2</sup> O<sub>2</sub> cm<sup>-4</sup>s<sup>-1</sup> if the reaction is monitored by total oxygen uptake, i.e. weight gain, or g<sup>2</sup> H<sub>2</sub> cm<sup>-4</sup>s<sup>-1</sup> if hydrogen production is monitored. The growth of the oxide and stabilised  $\alpha$ -Zircaloy layers are also found to obey a parabolic rate law over a wide range of temperature and respective parabolic rate constants have been measured for the growth of these layers.

Other rates of reaction have also been observed in Zircaloy steam reactions. At lower temperatures e.g. below ~950°C, the formation of zirconia is observed to conform to a cubic rate law whilst stabilised  $\alpha$ -Zr[O] continues to grow according to a parabolic rate law. Additionally at generally lower temperatures i.e. <1 050°C and longer times, the Zircaloy-steam oxidation reaction transforms to a linear rate i.e. breakaway oxidation is observed.

### **6.1.1 Isothermal oxidation of Zircaloy in steam**

Since the 1950s, many measurements of the rate of reaction of Zircaloy in steam have been made and in 1973 the US AEC adopted the isothermal parabolic rate constants published by Baker and Just [2] in 1962 for calculation of total oxygen uptake in cladding exposed to steam in thermal transients. Starting in 1974 more detailed and accurate measurements have been made in laboratories in the US, the United Kingdom, Japan, W. Germany and Canada. A review of all the available data in 1977 [3] showed the Baker-Just data to be conservative. Likewise recently completed programmes of oxidation measurements also confirmed that the Baker-Just correlation overpredicts the reaction rate. This conservatism was recognised by the NRC with issuance of Regulatory Guide 1.157, “Best-Estimate Calculations of Emergency Core Cooling System Performance,” (May 1989) which permits use of an improved model for metal-water reaction.

In the temperature range of interest in LWR conservative accident analyses, the Zircaloy is highly reactive with steam and the high temperatures and exothermicity of the reaction introduce considerable experimental difficulties in determining the kinetics of the reaction. The major sets of data are, however, in general agreement although there are many differences in detail and in the following section the main conclusions from the available data are briefly reviewed.

The reaction rate constants for Zircaloy-4 in steam were measured in the temperature range 871-1 482°C by Biederman *et al.* [4]. Steam had access to both o.d. and i.d. of a Zircaloy fuel tube which was resistance-heated in a Gleeble testing machine. The extent of reaction was measured by weight gain and by metallographic measurements of oxidized phase thickness. No effect of steam superheat temperature or flow rate was detected unless the steam flow rate dropped to a value such that steam availability was limited or hydrogen was not removed efficiently. A tin-rich phase which became coarser with increasing oxidation time and temperature was observed to precipitate near the middle of the oxide film. Other investigators have also observed this phenomenon and Biederman suggested that the phase was responsible for the loss of uniformity of the oxide/α-phase boundary at lower temperatures due to the pinning action of the tin-rich precipitates. Above 1 482°C, the oxide phase also contains stabilised α-phase and a fine unidentified lenticular phase.

The reaction was found to follow a parabolic rate law above the  $\alpha/\alpha+\beta$  transus and the temperature dependence of the parabolic rate constant for oxygen uptake is shown in Figure 6.2 and listed in Table 6.1. The temperature dependences of the growth of the oxide and combined oxide and α phases are listed in Table 6.2.

The Zircaloy-steam reaction was also investigated by Biederman *et al.* [5] in a lower temperature range of 650-980°C. The growth of the oxidized phases was measured at temperatures below the  $\alpha/\beta$  transus, i.e. ~871°C and also in the  $\alpha + \beta$  range i.e. ~871-980°C. Below the  $\alpha$  transus the oxidation rate, although remaining parabolic, deviated from extrapolation of data obtained at higher temperatures. The temperature dependence did not conform to an Arrhenius relationship over the range 871-980°C i.e. the  $\alpha + \beta$  region. At temperatures above and below the  $\alpha + \beta$  range of coexistence in equilibrium, the parabolic rate constants obeyed an Arrhenius relationship, the activation energy being much lower in the lower temperature range 650-820°C.

The measured rate constants are shown as a function of reciprocal temperature in Figure 6.2 and the Arrhenius temperature dependence of the parabolic rate constant for the lower temperature range is listed in Table 6.1. The temperature dependence of the growth rate constants for the oxidized layers are listed in Table 6.2.

The parabolic rates of reaction over the temperature range 973-1 251°C have been measured by Westerman and Hesson [6] in 7.5 g min<sup>-1</sup> flowing steam in an induction furnace. The extent of reaction was measured by metallographic measurement of oxidized phase layer thicknesses and by measurement of the product hydrogen evolved. The temperature dependence of the parabolic rate constants derived from this work are also shown in Figure 6.2, where the results are compared to several other works. The temperature dependence of the parabolic rate constants is also listed in Table 6.1. Westerman and Hesson also measured the hydrogen uptake in the oxidized samples and reported 220-250 ppm hydrogen which is in excess of that reported by other workers [4,8] typically 20-30 ppm.

Kawasaki *et al.* [9] used gravimetry and phase thickness measurements to determine the rates of reaction of Zircaloy-4 exposed to 0.4 g cm<sup>-2</sup> min<sup>-1</sup> flowing steam in a resistance furnace over the temperature range 1 000-1 330°C. Steam flow was found not to be rate limiting above 0.18 g cm<sup>-2</sup> min<sup>-1</sup> and the oxidation followed a parabolic rate law at temperatures of 1 000°C and above, deviating from a parabolic law at 900 and 950°C. The temperature dependence of the rate constant describing oxygen uptake is plotted in Figure 6.2 and listed in Table 6.1. The temperature of the rate constants describing the growth of the oxide and α-layers are listed in Table 6.2.

Table 6.1 Temperature dependence of published isothermal parabolic rate constants

Source	Temperature range °C	I	
		$\left(\frac{\delta^2}{2}\right)O_2/2$ (gm/cm <sup>2</sup> ) <sup>2</sup> / s	A Q in J/mol
Leistikow <i>et al.</i> [7] KfK	1 000-1 300	0.262	174 360
Pawel <i>et al.</i> [8] ORNL	1 000-1 500	0.1811	167 190
Kawasaki <i>et al.</i> [9] JAERI	900-1 300	0.234	170 410
Brown <i>et al.</i> [10] BNL	1 000-1 200 single oxide	0.1028	163 190
	1 000-1 400 double	0.2238	174 250
Biederman <i>et al.</i> [4]	980-1 480	0.0191	139 690
WPI [5]	650-816	$5.73 \cdot 10^{-4}$	114 445
Westerman <i>et al.</i> [6] BNWL	970-1 250	0.0321	145 255
Urbanic <i>et al.</i> [11] AECL	1 050-1 580	0.0182	139 900
	1 580-1 850	0.0541	138 155
Baker-Just [2]	...-1 852	2.049	190 465

Table 6.2 Temperature dependence of parabolic growth constants for oxide and  $\alpha$ -phase

Authors	Oxide $\delta^2$ cm/s		$\alpha$ -phase $\delta^2/2$ cm/s	
	A	Q	A	Q
Leistikow <i>et al.</i> [7]	$3.91 \times 10^{-2}$	168 127	0.254	182 347
Pawel <i>et al.</i> [8]	$1.126 \times 10^{-2}$	150 236	0.7615	201 515
Biederman <i>et al.</i> [4-5]	$9.392 \times 10^{-4}$	122 734	0.0189	154 422
Kawasaki <i>et al.</i> [9]	$1.07 \times 10^{-2}$	150 110	-	-
Urbanic and Heidrick [11]	$6.48 \times 10^{-4}$	169 978	0.0765	164 937
Sagat <i>et al.</i> [12-13]	$4.2 \times 10^{-2}$	169 978	0.303	183 561

A detailed and comprehensive study of the oxidation of Zircaloy-4 in steam at temperatures between 900-1 500°C was performed by Pawel *et al.* [8,14]. Very fast heating and cooling of small sections was achieved in a radiant infra-red furnace. The most important task of accurate temperature measurements was performed meticulously with a great degree of precision. Steam flowed up the reaction tube at 1 m s<sup>-1</sup> and measurements were made of phase widths and weight gain. The oxide and  $\alpha$ -phase layers grew parabolically at temperatures above 1 000°C, below this temperature the oxide phase deviated from parabolic behaviour and tended towards a cubic growth rate, thought to be a feature of the tetragonal to monoclinic phase transformation. The parabolic rate constants derived from this work are reproduced in Tables 6.1 and 6.2 and compared to other data in Figure 6.2.

The weight gain of Zircaloy-2 specimens exposed to steam in the temperature range 1 000-1 200°C was measured by Brown and Healey [10]. The specimens were heated in a tube furnace and cooled rapidly by quenching. Different oxidation behaviour was observed above and below 1 200°C. Above this temperature the oxide film was duplex whereas only occasionally was a duplex film formed below 1 200°C. In common with many other workers the authors report the occurrence of a tin-rich layer of precipitate particles at the interface of the two types of oxide layer above 1 200°C. The weight gain data was analysed as conforming to a parabolic rate law of oxidation and the rate constants for single layer and double layer oxide growth are listed in Table 6.1. Although this data set belongs to the same category as the data in Figure 6.2, for clarity it is included among the high-temperature data in Figure 6.3.

**Temperature dependence of published isothermal parabolic rate constants Table 6.1**

II		III	
$\left(\frac{\delta^2}{2}\right) H_2/2 \text{ (STP gm/cm}^2\text{)}^2/\text{s}$		$K_p \text{ (mgZr/cm}^2\text{)}^2/\text{s}$	
A	Q	A	Q
$5.14 \cdot 10^5$	As column I	$42.58 \cdot 10^5$	As column I
$3.55 \cdot 10^5$	As column I	$29.32 \cdot 10^5$	As column I
$4.59 \cdot 10^5$	As column I	$38.03 \cdot 10^5$	As column I
$2.02 \cdot 10^5$	As column I	$16.71 \cdot 10^5$	As column I
$4.39 \cdot 10^5$	As column I	$36.37 \cdot 10^5$	As column I
$3.74 \cdot 10^4$	As column I	$3.10 \cdot 10^5$	As column I
$1.12 \cdot 10^4$	As column I	$9.32 \cdot 10^3$	As column I
$6.30 \cdot 10^4$	As column I	$5.22 \cdot 10^5$	As column I
$3.57 \cdot 10^4$	As column I	$2.96 \cdot 10^5$	As column I
$1.06 \cdot 10^5$	As column I	$8.79 \cdot 10^5$	As column I
$4.02 \cdot 10^6$	As column I	$333 \cdot 10^5$	As column I

**Figure 6.2 The parabolic rate constant as a function of inverse temperature as determined by different researcher.** The unit for the parabolic rate constant is  $(\text{g O}_2/\text{cm}^2)^2 \text{ s}^{-1}$

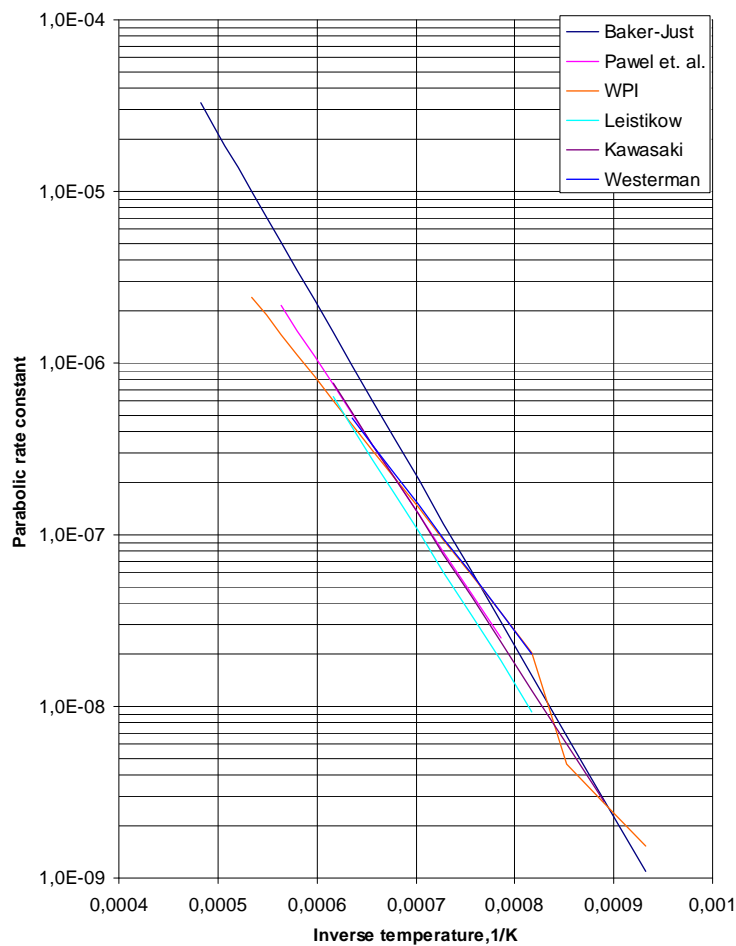
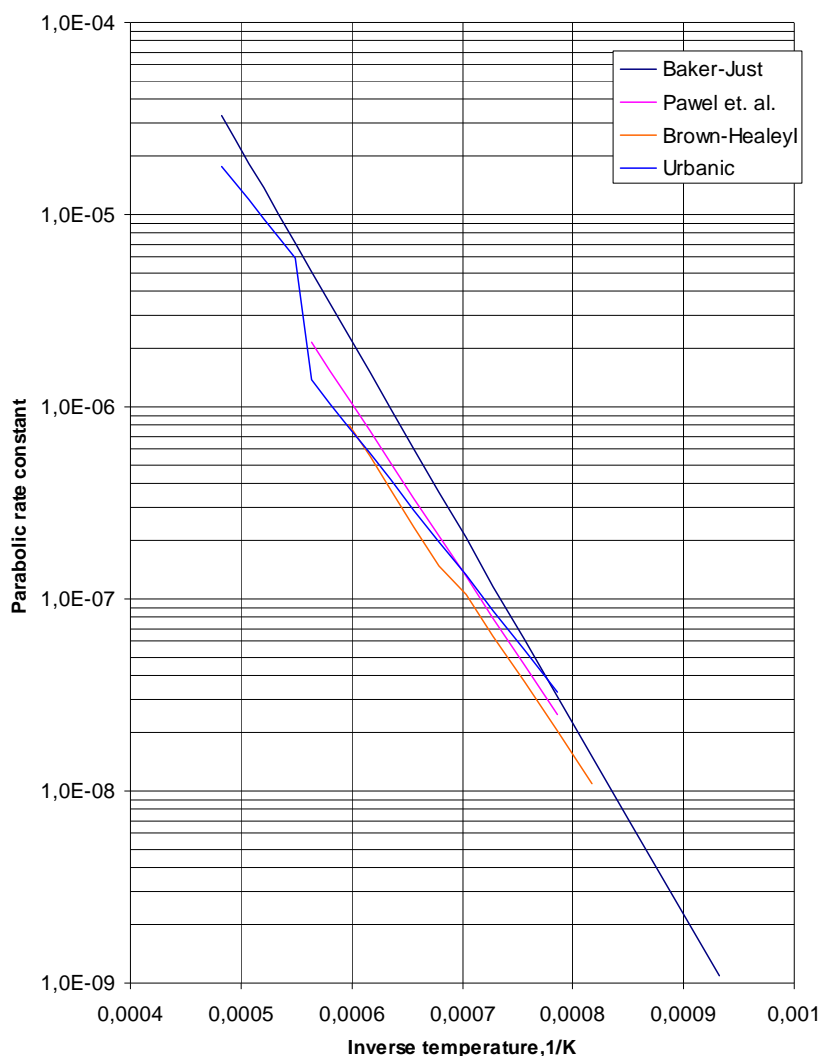


**Figure 6.3 The parabolic rate constant as a function of inverse temperature as determined by different researcher.** The unit for the parabolic rate constant is  $(\text{g O}_2/\text{cm}^2)^2 \text{ s}^{-1}$



The kinetics of both Zircaloy-2 and Zircaloy-4 oxidized in unlimited steam were measured by Urbanic and Heidrick [11] in the temperature range 1 150-1 850°C using an induction furnace. Phase boundary movement, hydrogen evolution and weight gain were measured and yielded parabolic oxidation rates over the whole temperature range. However, at ~1 580°C, the parabolic rate constant increases sharply with only a small change in activation energy.

The increase is due to a change in the kinetics of the formation of the oxide phase associated with the tetragonal to cubic phase transformation in zirconia. The rate of growth of the  $\alpha$ -phase remained at that which would be extrapolated from the lower temperature region. The temperature dependences of the oxidation rate constants are listed in Table 6.1 and compared to other data in Figure 6.3.

A number of measurements of oxide and  $\alpha$ -layer formation during transient heating have been performed by Sagat *et al.* [12-13] at Chalk River. The parabolic rate constants determined during transient heating agree closely with those of Leistikow [7] for isothermal conditions (Table 6.2).

Perhaps the most extensive investigation of the kinetics of the Zircaloy-steam reaction has been performed 1978-1982 by Leistikow, Schanz and co-workers at KfK. Initially, the rates of reaction were measured for short exposure times, up to 15 mins, in the temperature range 700-1 300°C [7]. Zircaloy-4 samples were heated in a flow of steam, 1 m/s in a resistance furnace and the extent of oxidation was determined by both gravimetry and oxidized phase width measurements. The reaction obeyed a parabolic rate law at and above 900°C but below 900°C, it tended to exhibit a cubic rate law. Limited observations of oxidation at longer times at 1 000°C showed an accelerated rate of reaction associated with fissuring of the oxide film. Isothermal parabolic rate constants for total reaction derived from this work are compared with other data in Figure 6.2 and listed in Table 6.1. The growth constants for oxide and  $\alpha$ -layer are also listed in Table 6.2. The published oxidation rate constants were established from the data in the temperature range 1 000-1 300°C but they are reported to be a good approximation over the temperature range 800-1 500°C.

Oxidation rate has also been investigated at temperatures up to 1 600°C [15-16]. Zircaloy-4 cladding tube sections were exposed isothermally in flowing steam at 50°C intervals between 1 300 and 1 600°C. A dense protective columnar grained oxide scale was formed in all tests which varied in time/temperature from 60 min at 1 300°C to about 6 min at 1 600°C and in all tests a parabolic rate law was obeyed. However, at 1 550 and 1 600°C the parabolic reaction rates were considerably higher than the extrapolation from lower temperatures. The microstructure of Zircaloy oxidized at 1 550 and 1 600°C exhibited a dual layered appearance, the inner layer of zirconia containing stringers and precipitates of  $\alpha$ -Zr[O] along crystallographic directions and grain boundaries. The inner oxide is thought to have been cubic zirconia at the isothermal oxidation temperature but later transformed on cooling by a eutectoid decomposition to the stable monoclinic  $ZrO_2$  and  $\alpha$ -Zr[O].

The parabolic rates of reaction for oxygen uptake at 1 300 to 1 600°C are plotted in Figure 6.3 and compared with the measurements of Baker-Just [2] and Urbanic and Heidrick [11].

Chung and Thomas [17] also measured the zirconia scale growth at temperatures above and below the nominal temperature of the tetragonal to cubic zirconia phase transformation and observed a stepwise increase in the parabolic rate constant at ~1 580°C with a similar activation energy in both temperature regimes. Figure 6.4 shows the zirconia scale growth rate constants of Urbanic and Heidrick [11], Leistikow *et al.* [16] and Chung and Thomas [17] at temperatures above 1 580°C in comparison with the Baker-Just [2] correlation converted to equivalent  $ZrO_2$ . The difference between the former and the latter (Baker-Just) rates is significantly smaller for >1 580°C than for <1 580°C.

The parabolic rates of reaction for oxygen uptake at 1 300 to 1 600°C are plotted in Figure 6.3 and compared with the measurements of Baker-Just [2] and Urbanic and Heidrick [11]. Chung [17] also measured the zirconia scale growth at temperatures above and below the nominal temperature of the tetragonal to cubic zirconia phase transformation and observed an increase in the parabolic rate constant at ~1 580°C with a similar activation energy in both temperature regimes. Figure 6.4 compares the zirconia scale growth kinetics of Urbanic and Heidrick [11], Leistikow *et al.* [16] and Chung and Thomas [17] at temperatures above 1 580°C with the Baker-Just [2] correlation converted to equivalent  $ZrO_2$ .

Leistikow and co-workers have also investigated the kinetics of Zircaloy-steam reactions after times much greater than previously reported, i.e. for times up to 25 hours. The temperature range of investigation was from 700°C up to 1 600°C and since the Zircaloy test pieces were from cladding tube the times at higher temperatures were limited to those at which complete consumption of the tube wall occurred, e.g. ~6 min at 1 600°C and ~40 min at 1 500°C. The zirconia scale and the  $\alpha$ -layer growth are shown in Figure 6.5 as functions of time and temperature along with earlier data up to 15 min exposure time.

Figure 6.4 Parabolic oxide layer growth rate constants obtained for pure steam environments vs inverse temperature

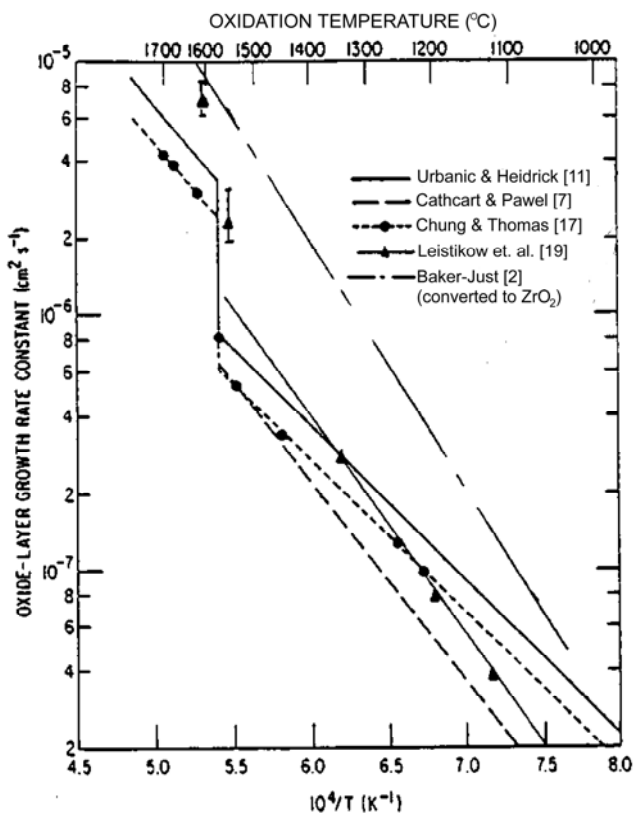
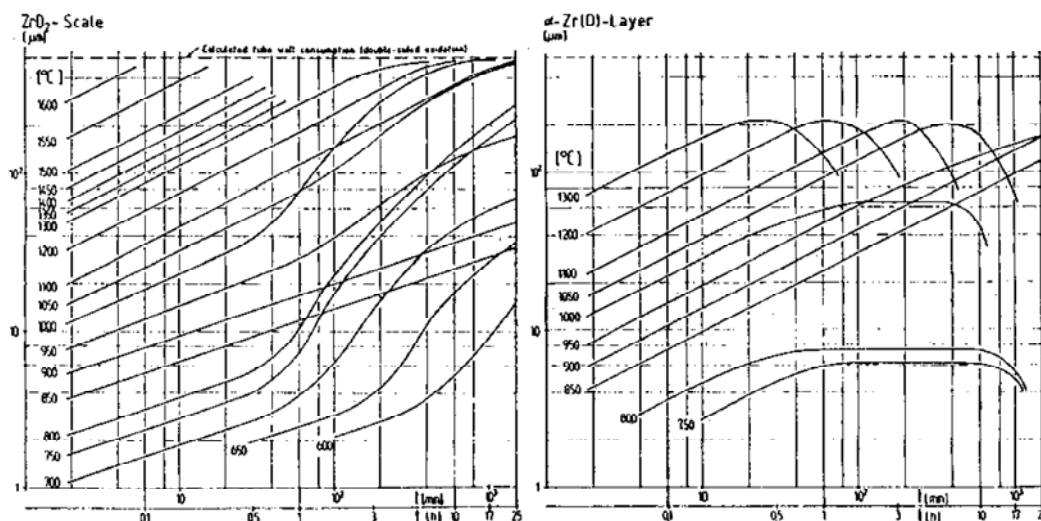


Figure 6.5 High-temperature steam oxidation of Zircaloy-4 cladding  
Kinetics of  $\text{ZrO}_2$  scale growth and  $\alpha\text{-Zr(O)}$  layer growth. Note the slower kinetics for oxide growth before transition to linear kinetics after long time exposure at low temperature.



Above  $\sim 1050^\circ\text{C}$ , the oxide scales remain protective and the kinetics remain parabolic, however at lower temperature there is significant acceleration of oxidation rate at longer times. The kinetics of  $\alpha$ -layer growth remain constant until consumption by conversion to zirconia.

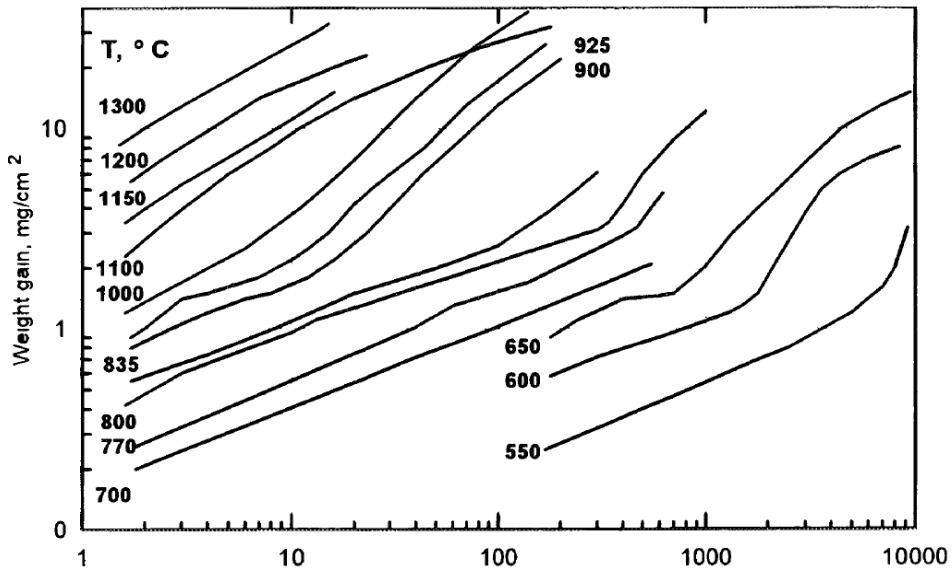
### 6.1.2 Isothermal oxidation of other zirconium alloys in steam

The E110 alloy, Zr1%Nb, has been used extensively in the Soviet designed VVER reactors built in Russia and other countries in Eastern Europe. Work to determine the steam oxidation properties of the alloy performed up to about 1995 has been reviewed by Bibilashvili *et al.* [18]. The bulk of the data has been obtained in experimental rigs with well-thermostated work-sections. A significant amount of this data has been recorded in rigs with continuous measurement of weight gain during the steam/zirconium reaction. Short lengths of cladding tubes were used typically 10, 30 or 60 mm in length. The temperature was measured by Pt-PtRh thermocouples in immediate proximity of the specimens.

As a measure of the reaction W, the specimen weight gain, was used. Thicknesses of the different layers formed were measured metallographically. However, weight gain was the preferred measure due to possible spalling of oxide film and the intrinsic inaccuracy of thickness measurements in metallographic cross sections.

Oxidation behaviour under a wide range of temperatures from 700°C upwards and times from several seconds to 10 hours was investigated. Figure 6.6 summarises the results for different temperatures and times. It is interesting to note the similarities with Figure 6.5, i.e. (1) a higher parabolic rate exponent at higher temperatures than at lower temperatures and (2) that at lower temperatures there is a transition to faster kinetics after a certain time.

Figure 6.6 Weight gains of VVER-type claddings oxidized in steam at atmospheric pressure



The weight gain data was analysed according to Eq. 6-2 and the temperature dependence of the K<sub>p</sub> parameter was determined. It was found that a bounding relation for the oxidation to be used in design estimates is  $K_p = 84640 \exp(-20820/T)$  mg<sup>2</sup>cm<sup>-4</sup>s<sup>-1</sup> in the temperature range 550 to 1 200°C. Expressed in the terms of Table 6.1 this means  $A = 0.423$  g<sup>2</sup>cm<sup>-4</sup>s<sup>-1</sup> and  $Q = 173\ 100$  J/mol. These values are close to the Baker-Just relation as can be seen in Figure 6.7. A more realistic estimate also shown in Figure 6.7 lies slightly below Urbanics data for Zr2.5Nb [19] which in turn are almost coincident with his data for Zircaloy. Thus Bibilashvili's reported values for Zr-1Nb seems to indicate that E110 oxidizes slower than Zircaloy in the range of parabolic growth.

More recently an extensive investigation of the LOCA properties of E110 alloy has been performed by Yegorova *et al.* under international sponsorship [20]. The object of the investigation was to resolve various issues with regard to the behaviour of the E110 alloy raised from tests in several

laboratories. Another issue was the observed differences in behaviour between E110 and the French alloy M5 which is also a Zr1%Nb alloy often denoted Zr1Nb(O) to emphasise that it is produced from sponge Zr with a higher concentration of oxygen than that used in the production of E110.

Figure 6.7 Temperature dependence of the reaction rate constant  $K_p$  for zirconium alloys

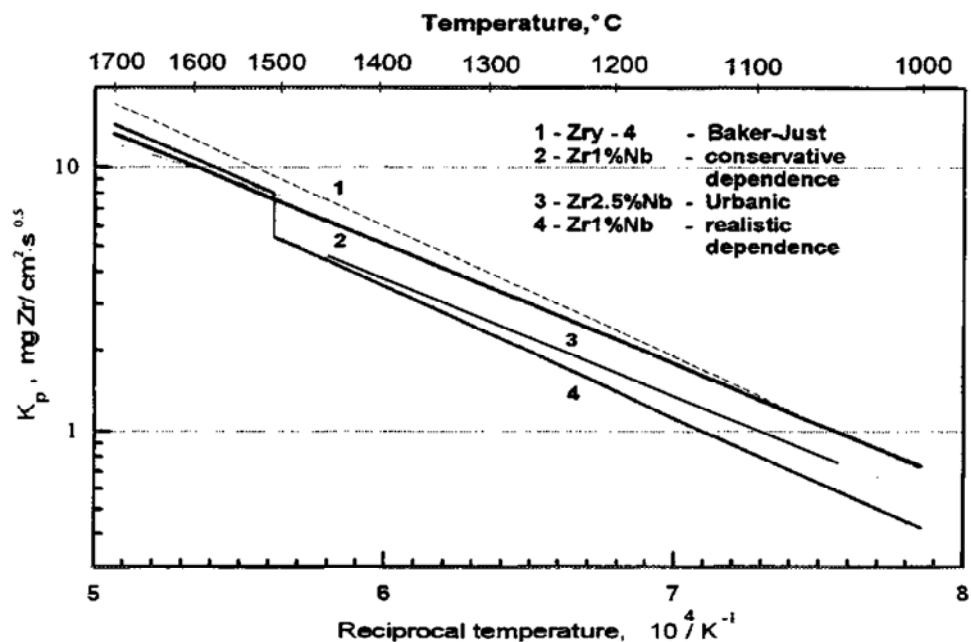
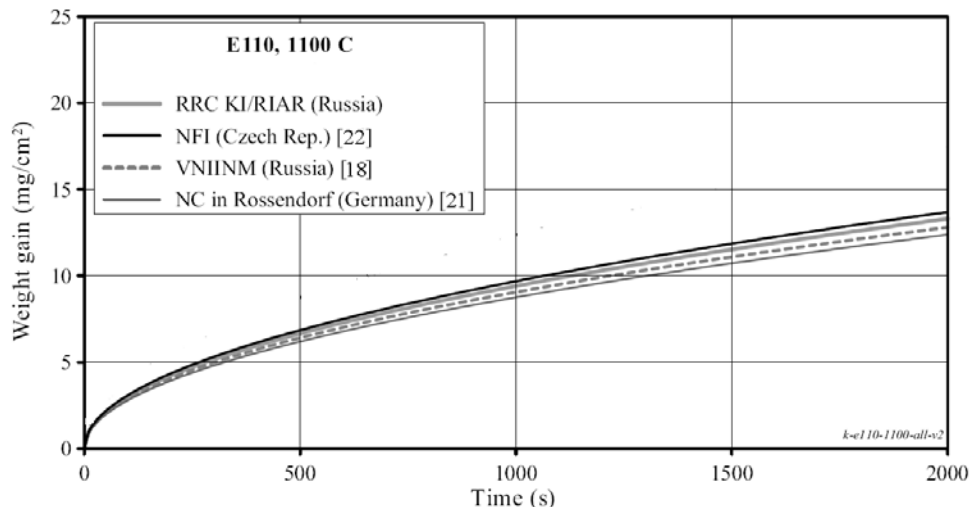


Figure 6.8 Oxidation results on Zr1Nb at different laboratories

Note that the original Figure [20] has been edited to remove incorrect data and to conform with reference numbering of the present report.

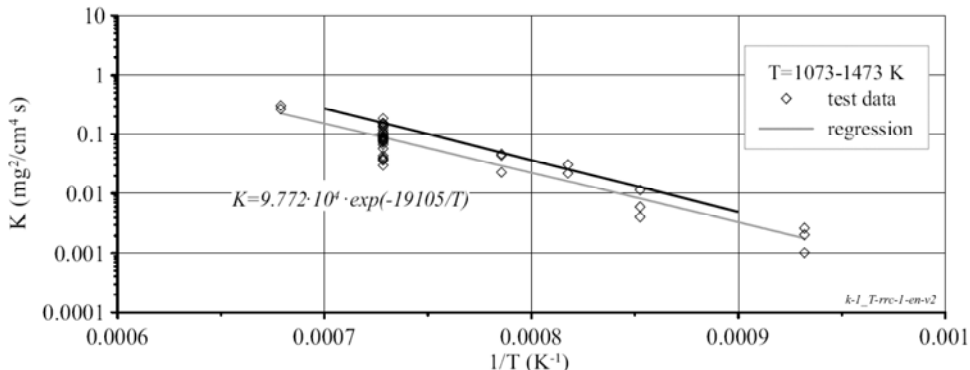


The equipment used by Yegorova *et al.* is shown in Section 5.2.1. Tests performed on Zircaloy-4 showed results quite similar to other published data which allows a confidence in the subsequently produced results of theirs on E110. Figure 6.8 shows the results obtained on E110 at 1100°C in comparison with results from other laboratories.

Figure 6.9 shows the result of their evaluation of the kinetics of the reaction.

Figure 6.9 The kinetics of the steam oxidation reaction of E110  
in the temperature range 800-1 200°C

The black line is calculated with the Cathcart-Pawel equation.



The results show that E110 oxidizes slightly slower than Zircaloy-4 under conditions of steady scale growth. However as will be discussed in the next section E110 is prone to oxide spalling and transition to linear growth kinetics. Therefore, it is not generally true that it oxidizes slower than Zircaloy-4.

Another factor is the contribution from the oxidation during heating and cooling. The oxidation experiments by Yegorova *et al.* were carried out under isothermal conditions. However, the approach to the peak oxidation temperature as well as the post-oxidation cooling were done with different rates, ranging from direct quenching to very slow cooling or heating which were of significant duration compared to the time at constant temperature. The results which form the basis for Figure 6.9 are all from fast cooling and heating. For slower cooling and heating, it is necessary to calculate an equivalent time at temperature. This was done according to the relation:

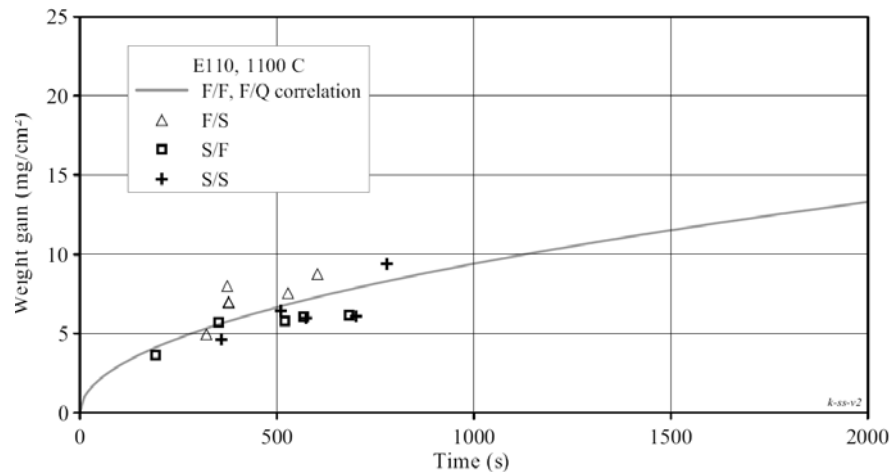
$$t_{eq} = \frac{\int_0^{t_{ox}} \exp\left(-\frac{Q}{RT(t)}\right) dt}{\exp\left(-\frac{Q}{RT_{eq}}\right)} \quad (6-5)$$

where   
 $t_{ox}$  = time for the complete oxidation  
 $Q$  = the activation energy  
 $R$  = the gas constant  
 $T(t)$  = the oxidation temperature as a function of time  
 $T_{eq}$  = the assigned steady temperature.

The success of the approach can be seen in Figure 6.10 where the transient data converted to equivalent time at constant temperature has been plotted with the parabolic law for isothermal tests.

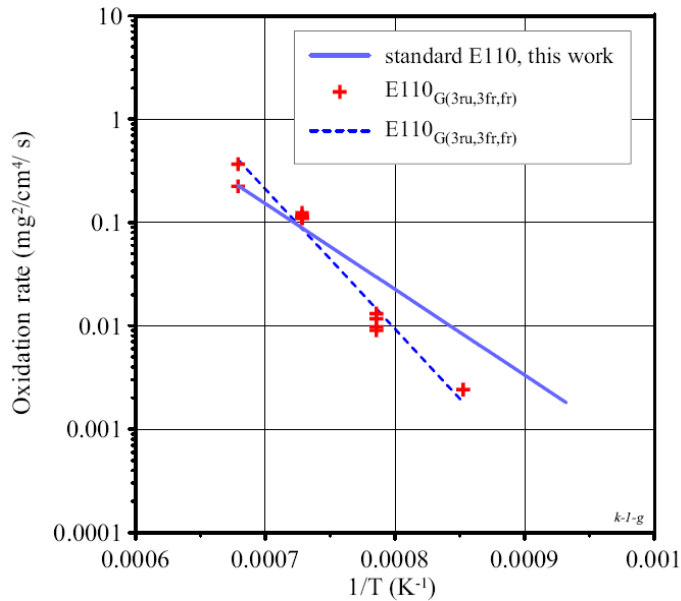
To compare oxidation behaviour with M5, Yegorova *et al.* tested modified E110 cladding tubes that were fabricated from sponge Zr instead of the mixture of iodide and electrolytic Zr normally used in Russia (see [21] for a comparison of fabrication processes of M5 and E110). These materials differ not only in oxygen content but also in the various impurities present in the materials [20]. Somewhat surprisingly, the sponge-Zr-based modified E110 exhibited a different kinetics than most other zirconium alloys, as can be seen in Figure 6.11. Note in the figure significant difference in weight gain rate constant vs. inverse temperature.

**Figure 6.10 Results of transient test modes converted to equivalent time at constant temperature for E110**



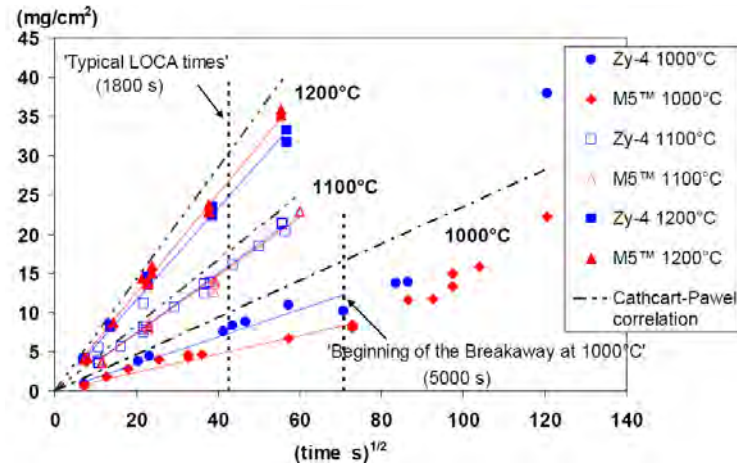
Metallography revealed that the relative amounts of  $\text{ZrO}_2$  layer growth compared to  $\alpha\text{-Zr(O)}$  layer growth differs between the two materials and this is the reason for the difference in kinetics. It is believed that the underlying cause for this difference is the differences in impurity elements between the materials. It is not caused by the difference in oxygen content since M5 with high oxygen follows the kinetics of standard E110.

**Figure 6.11 Kinetics of the sponge based E110 claddings compared to standard E110**



The isothermal oxidation kinetics of the M5 alloy,  $\text{Zr1\%Nb(O)}$ , has been reported by Mardon and coworkers [22-23] and by Portier *et al.* [24]. Figure 6.12 shows parabolic oxidation curves for M5 compared to Zircaloy-4 and the Cathcart-Pawel correlation [24]. Note that the data points for weight gain vs. square root of oxidation time follow well a straight line for 1100°C and 1200°C, which indicates a good control of isothermal oxidation temperature.

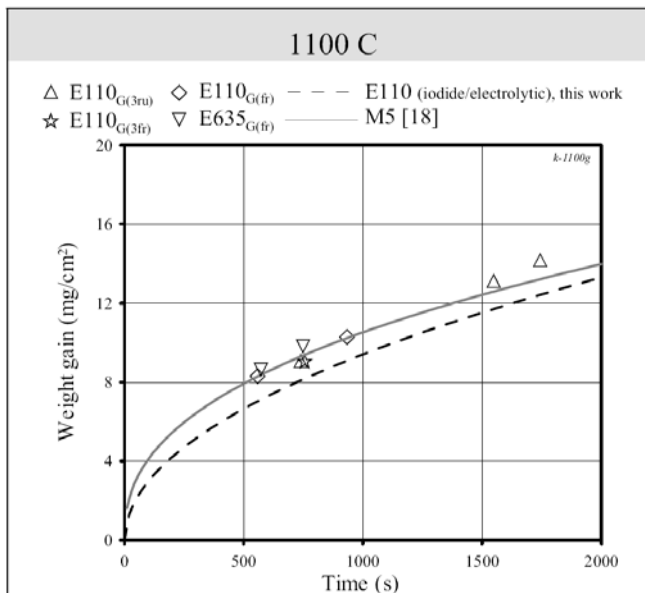
Figure 6.12 The oxidation of M5 and Zircaloy-4 at 1 000, 1 100, and 1 200°C



It is clear that the oxidation kinetics of M5 is very similar to the kinetics of the Zircaloy-4 used in the same investigation and slightly slower than the Cathcart-Pawel correlation which is based on older data on Zircaloy-4.

There is only limited data on the Russian alloy E635 (Zr-1%Nb-1.2%Sn-0.35%Fe). According to Bibilashvili *et al.* [25], its oxidation properties are similar to those of E110. This is also illustrated by Figure 6.13 from the report by Yegorova *et al.* [20].

Figure 6.13 Oxidation of E635 at 1 100°C compared to other zirconium alloys



Another relatively new alloy is ZIRLO™ (Zr-1%Nb-1%Sn-0.1%Fe-1200ppmO). Leech has reported oxidation data for ZIRLO in comparison with Zircaloy-4 oxidized under identical conditions [26]. The test samples were 32 mm long open ended tubing which were exposed to steam at temperatures between 980 and 1 200°C for times ranging from 5 to 30 minutes. When weight gains of identically exposed samples of the two alloys were plotted as function of the square root of time all points fell close to a straight line indicating that ZIRLO oxidized about 10% faster than Zircaloy-4. For both alloys the oxide layers were black shiny, adherent and with no sign of delaminations.

### **6.1.3 Breakaway oxidation of zirconium alloys**

Leistikow *et al.* [16] reported that the kinetics of the Zry-4/steam reaction in the temperature range 600-800°C change from cubic to linear with time, before finally exhibiting a decreased rate of reaction due to the finite thickness of the specimen. The weight gain at which accelerated oxidation begins increases with temperature. The microstructure of Zircaloy oxidized for long times between 600-800°C exhibits numerous lateral fissures and penetrating radial cracks. It was postulated that the oxide cracking is the cause of the accelerated oxidation which is analogous to the breakaway oxidation phenomena reported for lower temperature aqueous and gaseous oxidation.

In the interval between 850-950°C, oxide cracking was observed to be much reduced and transition to a breakaway accelerated oxidation rate did not occur although there was an increase in rate to a parabolic rate of oxidation. At 1 000-1 050°C the breakaway type of accelerated oxidation reoccurs. Leistikow *et al.* [16] also report that under transient oxidation conditions, oxide scales showed breakaway above the critical oxide thickness, but recovered at a temperature where the oxide thickness was less than critical and the conclusion was made that the isothermal breakaway data could be incorporated into transient calculations.

Consideration of the mechanism of breakaway oxidation was initially concerned, with breakaway phenomena at lower temperatures in aqueous media or in some cases in gaseous media. Subsequently several studies have been made of a wide range of zirconium based alloys in different oxidizing media and a temperature range up to ~800°C. Cox [27] summarised the conclusions of many investigators and described two alternative mechanisms of breakaway oxidation. One mechanism is based on the hypothesis that cracking of the oxide film, caused by the stresses generated in growing oxide films, is the primary cause of a transition to accelerated corrosion. The alternative mechanism is that the stresses induced in the oxide cause a phase transformation and pore generation in the oxide film, the pores promoting the formation of cracks. However, the precise mechanism of the transition from cubic/parabolic kinetics to linear kinetics has not been established to the general satisfaction of all workers in the field not even today, about 30 years after Cox review.

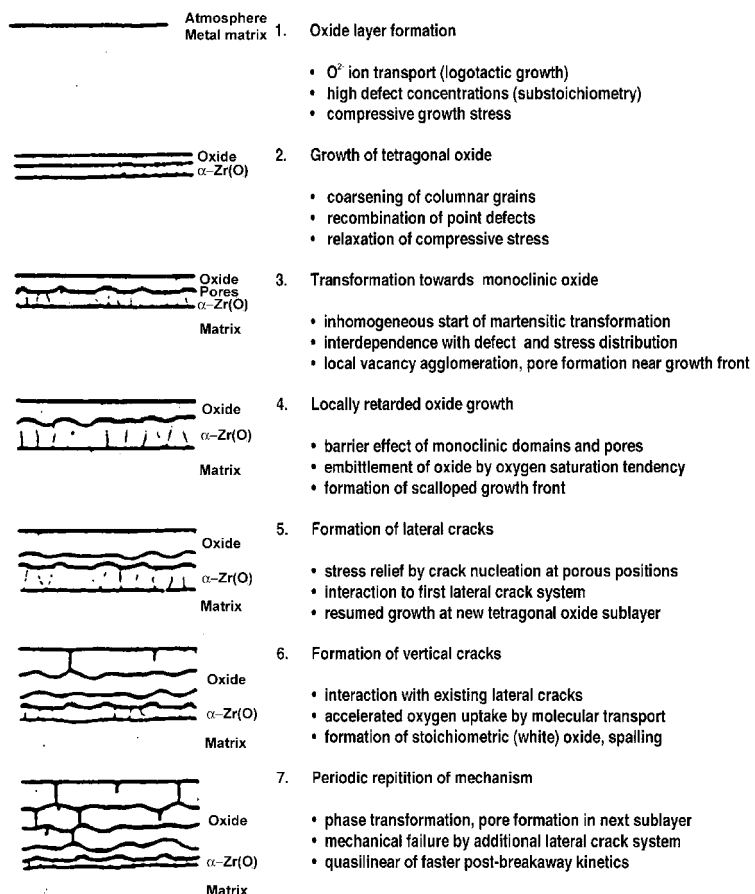
Leistikow and his coworkers [16,28] have considered the mechanism of breakaway oxidation of Zircaloy in steam at temperatures above ~700°C. Their proposed mechanism is illustrated in Figure 6.14.

After the initial growth of the tetragonal polymorph of zirconia, which is stabilised at a lower temperature by stress in the growing oxide film, it is postulated that the tetragonal to monoclinic zirconia phase transformation (martensitic) is initiated by a combination of stress relaxation, columnar grain coarsening and point defect recombination. At this stage of the process, a scalloped oxide/metal interface is observed which is due to the formation of pores at the interface thus locally retarding the oxide growth. The oxide then becomes more brittle as a result of oxygen saturation and lateral cracks form followed by vertical penetrating cracks. The short circuiting of the oxidation path by such cracking leads to the higher rates of oxidation. This cycle is repeated with the initiation of fresh oxide formation and the overall response is a linear kinetics. The oxidation response of Zircaloy in the temperature range 850-900°C does not seem to conform to the above pattern of behaviour. A transition of oxidation rate is observed but it is a less abrupt change to parabolic kinetics. This behaviour is not well understood but other factors may have an influence on the reaction kinetics in the temperature range 850-900°C for instance two phase ( $\alpha+\beta$ ) matrix and hydrogen uptake of the Zircaloy.

The breakaway oxidation has been identified as a major problem for the E110 cladding LOCA performance since it is associated with a significant hydrogen pickup [20,29] which degrade post-quench properties. The hydrogen affects the  $\alpha/\beta$  transformation temperature and therefore indirectly the high-temperature deformation properties of the material. It also increases significantly the

solubility of oxygen in  $\beta$  for given temperature. The most significant effect of hydrogen is that it can result in a post-transient loss of ductility as will be discussed in a later section. Figure 6.15 shows an example of the hydrogen pickup in E110 in connection with steam oxidation [29].

**Figure 6.14 Suggested mechanism for high-temperature breakaway oxidation in Zircaloy by Leistikow and coworkers [16, 28]**



Normally the oxide film serves as a barrier to hydrogen pickup since the decomposition of the water molecules takes place on the outside of the oxide. However, according to the model by Schantz and Leistikow, after the onset of breakaway, the water or steam molecules can penetrate through the cracks in the oxide and then react on the outside of the thin inner protective layer of oxide, which is far less of a diffusion barrier than a thick uncracked compact oxide.

The breakaway in E110 has been described as a form of nodular oxidation, because many nodule-like white-coloured oxide spots are initially observed [30]. Nodular oxidation is different from the breakaway mechanism described by Schantz and Leistikow. At a certain stage in the oxidation process, small lenticular spots of white oxide form in the otherwise uniform black oxide. These nodules grow both in diameter and depth at a much higher rate than the uniform oxide. More familiar nodular oxidation near operating temperatures has been observed both in-pile, in boiling water environment, and in high-temperature autoclave tests. As for the breakaway transition, there is still no generally accepted theory for the mechanism behind nodular oxidation. The appearance of a cladding tube subjected to nodular oxidation is somewhat similar to the appearance of the E110 cladding that was oxidized under LOCA conditions, see Figure 6.16 which is reproduced from the report by Yegorava *et al.* [20].

Figure 6.15 The hydrogen pickup in E110 and Zircaloy-4 during steam oxidation

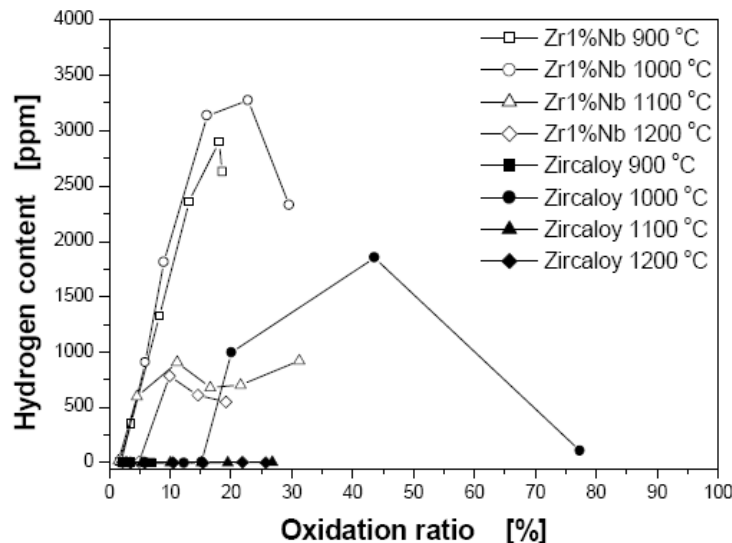
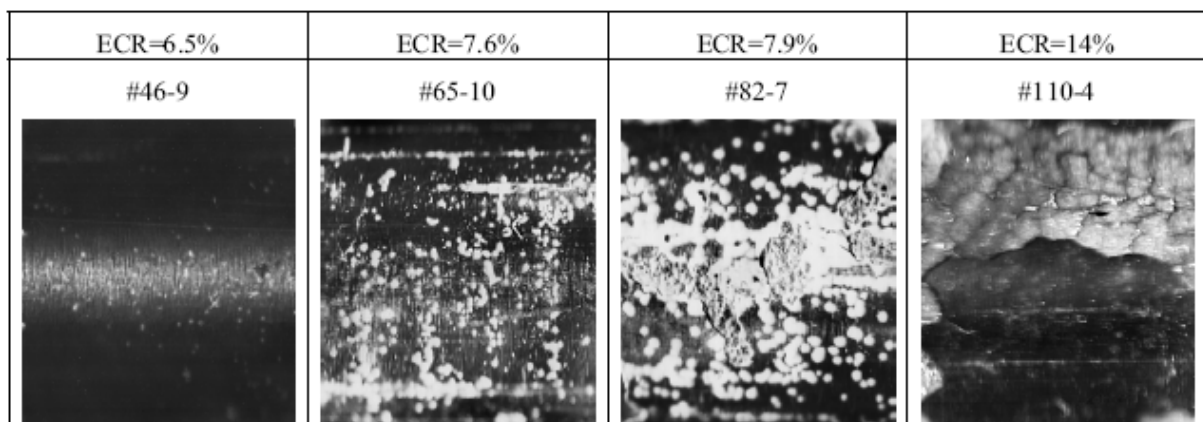


Figure 6.16 The appearance of E110 cladding tubes oxidized in steam at 1100°C to different ECR levels



However Yegorova *et al.* did not consider the breakaway in E110 to be a form of nodular oxidation. In contrast to the metallographic cross sections reported by Chung [30], nodules examined by Yegorova *et al.* [20] was relatively uniform in depth and lacked the depthwise growth characteristic of nodular oxidation. Instead they note that breakaway oxidation starts in small local points on the cladding surface after about 7% ECR. The breakaway spots then grow laterally giving the appearance of growing nodules. The breakaway is in this case probably the formation of a lateral crack in the oxide. Once the cracked area has grown to a certain size, the oxide starts to flake off as has been observed on E110.

Chung has attempted to explain the contrasting susceptibility to breakaway oxidation of E110 and M5 both of which have nominally similar chemical composition [30]. Although he is not referring to actual mechanism of either nodular corrosion or breakaway, his proposed explanation is based on the premise that a stoichiometric oxide (monoclinic) is more susceptible to microcracking than a significantly understoichiometric oxide (tetragonal). He proposed that minor impurities pick-up during fabrication of the E110 or M5 cladding play an important role in determining the oxide stoichiometry during high-temperature oxidation. He thus concentrated on the effects of minor impurity ions associated with nuclear-grade Zr production on the transport properties and phase stability of the oxide.

By examining the differences in the manufacturing routes of E110 and M5, Chung concludes that in M5 manufacturing, Ca and Al are picked-up in association with Hf purification by the process of methylisobutyl ketone and extractive distillation, respectively, and Mg is picked-up in association with the production of sponge Zr by the Kroll process. These strongly undervalent impurities are beneficial, because they keep the oxide more understoichiometric and in relatively tougher tetragonal form, in effect leading to suppression of the susceptibility to breakaway oxidation. Absence of such pickup is predicted to be deleterious, because they are conducive to making the oxide stoichiometric and monoclinic.

In the production of E110 or E635 on the other hand, fluorine is picked-up, because zircon ore is decomposed by the use of potassium fluozirconate, and Hf is purified by the process of fractional-crystallization. Most Zr in E110 is reduced by electrolysis of the F-containing compound of potassium fluozirconate in a molten bath; only minor portion of iodide Zr is used. Such F pickup, combined with the absence of fabrication-related pickup of Ca, Mg, or Al, is predicted to conjointly exacerbate the susceptibility to nodular oxidation.

#### ***6.1.4 Effect of irradiation on high-temperature zirconium alloy oxidation***

The measurements of oxidation kinetics described above have been determined using virgin zirconium alloy samples in unlimited steam, in the absence of radiation. Reactor cladding subject to high-temperature transients in accident situations will begin the transient with a range of in-service histories. Although the neutron flux will be minimal in a LOCA situation a  $\gamma$ -irradiation field will be present. The effects of the deposition of energy from  $\gamma$ -radiation in Zircaloy or in the steam phase on the oxidation rate of Zircaloy in LOCA conditions have not been systematically investigated. However, the effect of irradiation on the oxidation of Zircaloys and other zirconium based alloys in water and steam at near operating temperatures has been extensively investigated by numerous workers and reviewed by Cox [27,31] and Asher [32]. Enhanced corrosion has been observed in water in the presence of a fast neutron flux. In steam, even with added oxygen, the in-reactor enhancement is only very small and is related to the effects of neutron irradiation on the transport properties of the solid oxide/metal rather than the gas phase. It is further concluded that the small effects vanish completely at 400-450°C possibly due to thermally activated recovery processes.

Mixed gaseous environment may reduce available oxidizing species for incorporation into the oxide lattice or the oxygen anion concentration gradient within the oxide. Such a condition may arise from simple steam starvation or by effects produced by high hydrogen concentration (Section 5.2.4). For Zircaloy oxidation in unlimited steam, the rate limiting process is generally believed to be the transport of oxygen anions in the n-type anion deficient oxide film by a process involving point defects. A perturbation of the defect population by the radiation field after a LOCA would be negligible. Thus measureable influence of radiation on Zircaloy oxidation rates is not predicted in LOCA.

In view of this discussion, experience with steam oxidation experiments of spent fuel cladding will be regarded as experiments on pre-oxidized cladding and discussed in that section.

#### ***6.1.5 Effect of specimen geometry***

Pawel and Campbell [33] have pointed out that initial parabolic kinetics only apply whilst the cladding behaves as a semi-infinite sink for oxygen. Experimental work at 1 300°C and calculations for oxidation in the range 1 000-1 500°C have shown that once the  $\beta$ -phase begins filling with oxygen the kinetics of oxide and  $\alpha$  layer growth deviate from the initial parabolic rate and become faster, the effect being much larger on the  $\alpha$ -phase growth kinetics. At 1 300°C one-sided oxidation experiments showed that the initial parabolic rates were maintained for ~500 s but thereafter the rate of boundary movements increased; the cladding original oxygen concentration was 0.12 w% and the wall thickness

was 0.0635 cm. On saturation of the  $\beta$ -phase, growth of the oxide and  $\alpha$ -phase would proceed at a new increased parabolic rate until the  $\alpha$ -phase began to fill with oxygen. However, the total oxygen uptake rate is slightly lower since no additional oxygen is being absorbed by the  $\beta$ -phase. For Zircaloy with saturated  $\alpha$ -phase, growth rate constants for the oxide and  $\alpha$  phases between 1 000-1 500°C were calculated to increase by ~3 to ~17% and ~45 to ~135% respectively. The overall oxygen uptake rate constant decreased by ~3 to ~13%.

A perhaps more trivial effect is the effect of specimen length in cases of cladding oxidation studies. As discussed by for instance Yegorova *et al.* [20] specimen end effects lead to an increased oxidation and in cases of breakaway also to an increased hydrogen pickup. The ends get a higher ECR value and become more embrittled than the main parts of the tubes. The ECR value for the whole specimen becomes too high if the ends are included. Another undesirable aspect is that the end-effects intensify the development of breakaway. These considerations led Yegorova *et al.* to use specimens with a minimum length of 100 mm in their study.

### 6.1.6 The behaviour of alloying elements during oxidation

#### 6.1.6.1 Zircaloy-4

The corrosion resistance of Zircaloy under normal operation is structure dependent and can be optimised by heat treatments to produce certain distributions of second phase particles. The particles are intermetallics that precipitate during fabrication along the edges of the Widmanstätten  $\alpha$ -platelets formed on transformation from  $\beta$  to  $\alpha$  [34]. They are reported to be mostly Zr,Fe,Cr compounds with a C14  $Zr(CrFe)_2$  crystal structure and a composition  $ZrFe_{2-x}Cr_x$ , [35-36] in Zry-4. Zry-4 phase equilibria at high temperatures, 750-1 050°C have been investigated by Miquet and Charquet [34], who determined the number and nature of the phase domains between the  $\alpha$ - and  $\beta$ -solid solution states. Four phase domains were observed,  $\alpha_{ss}+Zr(Fe,Cr)_2$  up to 808°C;  $\alpha_{ss}+Zr(Fe,Cr)_2+\beta_{ss}$  from 808 to 845°C,  $\alpha_{ss}+\beta_{ss}$  from 845 to 1 000°C and  $\beta_{ss}$  above 1 000°C. In the  $\alpha+Zr(Fe,Cr)_2$  domain, Sn is dissolved in the  $\alpha_{ss}$  phase, whilst in the  $\alpha+Zr(Fe,Cr)_2+\beta$  domain Sn is also present in  $\beta$  as well as some Fe,Cr in  $\beta$ . It was previously thought that in the  $\alpha+\beta$  domain, Sn has greater solubility in  $\beta$  [37]. However, recent studies of the phase equilibria Sn-Zr have shown that Sn is an  $\alpha$ -stabiliser [38] and therefore  $\alpha$  must have the higher Sn content in the  $\alpha+\beta$  domain. In the  $\beta$  domain, all the alloying elements are in solid solution.

Subsequent re-distribution of alloying elements during high-temperature oxidation of Zircaloy has been observed by many workers. Yurek *et al.* [39] characterised oxide scales in terms of alloying element distribution in Zry-4 oxidized in steam at 1 000-1 300°C. Prior to oxidation, Sn is homogeneously distributed in  $\alpha$ -Zr and Fe,Cr are present mostly as intermetallic  $Zr(Fe,Cr)_2$  precipitates in the grains. After oxidation the Fe and Cr were observed to have been segregated in the prior  $\beta$ -phase. The oxide scale contained a Sn rich intermetallic which existed as a line of particles at about the mid-depth of the scale. In the scale outer layer there was little Sn except for a thin layer at the oxide/gas surface. The inner oxide contained columnar grains of  $ZrO_2$  with a fine metallic phase at the grain boundaries. During continued oxidation the Sn-rich intermetallics move towards the metal. Biederman *et al.* [4] determined the composition of the intermetallic phase in the oxide as  $Zr_4Sn$  and suggested the grain boundary phase in the inner oxide was  $\alpha$ -Zr(O). Urbanic and Heidrick [11] observed globules and stringers of  $\alpha$ -Zr(O) in the oxide scales of Zry-4 oxidized in steam at 1 050-1 800°C. The volume fraction of  $\alpha$ -Zr(O) in oxides formed below 1 580°C was ~2%. This is consistent with the  $ZrO_2$  (tetragonal)  $\rightarrow$   $ZrO_2 + \alpha$ -Zr(O) eutectoid transformation on cooling at ~1 000°C. In oxides formed at >1 580°C, the volume fraction of  $\alpha$ -Zr(O) was ~10%, which is consistent with the  $ZrO_{2x}$  (cubic)  $\rightarrow$   $ZrO_2$  (tetragonal) +  $\alpha$ -Zr(O) eutectoid transformation on cooling at ~1 577°C.

The behaviour of alloying elements in Zry-4 transiently oxidized in 80%-20% argon-oxygen at higher temperatures (1 600-1 800°C) was reported by Gambini *et al.* [40]. The composition of the intermetallic particles in the oxide scale was determined to be ZrSn<sub>1.1</sub>-ZrSn<sub>1.9</sub>. In the  $\alpha$ -Zr(O) layer, adjacent to the oxide, two metallic phases were observed. The most abundant phase was of composition near Zr<sub>5</sub>Sn<sub>3</sub>, the other being Zr(Fe,Cr)<sub>0.5-0.8</sub>. Both phases contained ~10% oxygen after oxidation at 1 600°C and ~20-25% oxygen at 1 700-1 800°C. Islands of Zr<sub>5</sub>Sn were also observed in the growing ZrO<sub>2</sub> near the oxide/metal interface. The morphology, distribution and composition of the Zr-Sn intermetallics in the oxide scale were found to be strongly dependent upon temperature and the characteristics of the transient. At higher temperature and at longer time, Zr<sub>4</sub>Sn particles observed by previous workers are, are thought to have transformed to Sn rich liquid droplets by progressive oxidation of the zirconium component. The formation and migration of liquid droplets is attributed to general transportation of the alloying elements in liquid form towards the inner surface of cladding. It is interesting to note that a quantitative appraisal of the nature and distribution of the intermetallic phases in high-temperature oxidized Zry-4 may facilitate the estimation of temperature of cladding in high-temperature severe fuel damage experiments.

#### 6.1.6.2 Zr-1Nb

When the layer of oxygen stabilised  $\alpha$ ,  $\alpha$ -Zr(O), starts to grow on the  $\beta$  layer,  $\beta$ -stabilising elements like Fe, Cr, and Nb are rejected from the  $\alpha$  and are forced into the  $\beta$  phase. This is no problem in Zry-4 since the concentrations of Fe and Cr are low and their diffusion coefficients are high enough to permit a sufficient diffusion away from the interface. Thus, in Zry-4 growth of the  $\alpha$ -layer usually results in a sharp and straight interface between the  $\beta$  and  $\alpha$ . In Zr1Nb on the other hand the Nb diffuses relatively slowly. Brachet *et al.* have reported that at 1 100°C the Nb diffuses about 10-20 times slower than Cr and 40-80 times slower than Fe [41]. Since there is no time for the Nb to diffuse away, an eutectoid like structure is formed inside the oxide where thin Nb rich  $\beta$  lamellae lie between coarse  $\alpha$ -phase needles (Figure 6.17). As a result, there is no sharp interface between the oxygen stabilised  $\alpha$  and the underlying  $\beta$  layer in the Zr1Nb alloys.

Brachet *et al.* also measured the oxygen content in the former  $\beta$ -phase in both Zircaloy-4 and M5 by electron microprobe analysis. For oxidation at 1 100°C, the concentration was 5 500-6 000 wppm in Zry-4 while it was between 2 000-4 000 wppm in M5. It is likely that both values are too high due to oxygen contamination on the sample surfaces. However, the relative difference between the oxygen contents of the two alloys is considered to be fairly accurate.

#### 6.1.7 High-temperature oxidation of pre-oxidized zirconium alloys

Zircaloy cladding oxidizes slowly during normal operation of an LWR. Many out-of-reactor studies have been made of oxidation in the temperature range relevant to normal running and some in-reactor measurements of oxidation have also been made [42-43]. The initial oxidation rate in reactor is cubic (for ~100-500 days). When the oxide is a few microns thick (~2-5  $\mu\text{m}$ ), the oxidation rate becomes linear owing to the transition discussed earlier. This transition is normally associated with fissuring of the oxide film. Later in life a second transition to an even higher oxidation rate may occur. The waterside corrosion of Zircaloy-4 in the hydrogen overpressure environment of a PWR was previously not a fuel life or performance limiting factor for reactor operation. However, with current industry-wide burn-up goals an oxide thickness of up to 100  $\mu\text{m}$  may be reached as can be seen in Figure 6.18. There is also an incentive to maintain a high coolant pH to minimise the transport of highly activated corrosion products, and hence, minimise man-rem doses.

Figure 6.17 Nb X-ray map obtained by electron microprobe of the  $\alpha$ (O)+ $\beta$ (Nb) layer below the oxide in M5 alloy oxidized to ECR ~17% at 1 100°C [41]

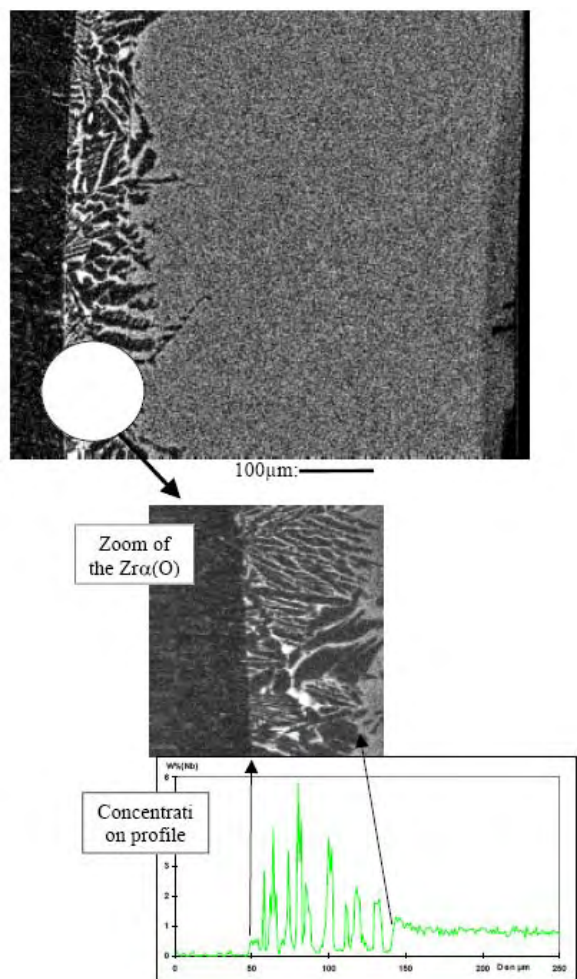
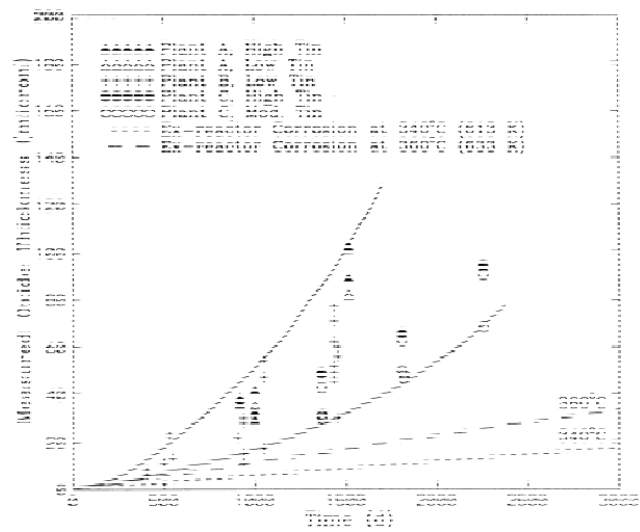


Figure 6.18 Examples of corrosion of Zircaloy-4 in different PWRs



Oxidation of Zircaloy may be enhanced in extended burn-up simply because of increased exposure time. Additionally, a thicker oxide film with associated poor heat transfer characteristics, raises the oxide/metal interface temperature and further increases the oxidation rate. Data are also available that show the enhanced corrosion of Zircaloy in very high pH (high lithia) water. This effect is thought to occur from hide-out and concentration of lithia in porous oxide.

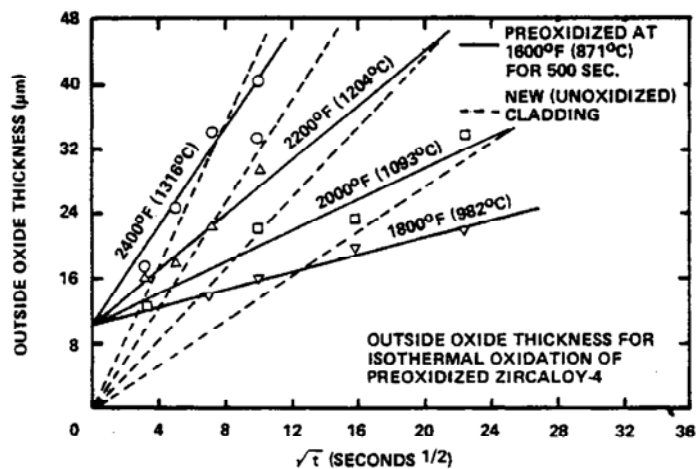
The effect of lithia on oxidation of Zircaloy under LOCA conditions is not reported but the subsequent high-temperature steam oxidation of pre-oxidized Zircaloy (albeit mostly at higher temperatures than reactor operating) has been reported by a number of workers.

High-temperature oxidation of Zircaloy with pre-formed oxide has been studied by Leistikow *et al.* [7] who pre-formed oxide in the range of 350-600°C up to 50 µm in thickness prior to further oxidation at temperatures of 1 000 and 1 200°C. The authors concluded that the pre-formed oxides were generally protective if the temperature of further oxidation did not exceed 1 200°C. Beyond this temperature highly defective tetragonal zirconia formed and the protective action of the pre-formed oxide decreased. Leistikow *et al.* [44] also pre-formed oxides ~30 µm thick in the temperature range of ~400-800°C and exposed the samples to transient high-temperature oxidation. The authors concluded that pre-oxidation in this range did not affect subsequent high-temperature oxidation systematically. Their data did not provide a sufficient basis for an analytical description of the high-temperature transient oxidation of pre-corroded Zircaloy.

Zircaloy specimens pre-oxidized at 871°C for 110 s and 500 s (oxide films 5 µm and 10 µm thick respectively) were oxidized in steam isothermally at 980-1 315°C by Biederman *et al.* [5]. Oxidation at high temperature continued to obey a parabolic rate law although as shown in Figure 6.19 the amount of oxidation became increasingly less than that expected on virgin cladding as the isothermal oxidation time increased. Figure 6.19 shows the results on 10 µm pre-oxidized cladding. The results for 5-µm pre-oxidation are basically similar. Note that the treatment of data in Figure 6.19 is not self-consistent. In parabolic square root representation pre-oxidized material do not give straight lines unless the pre-formed oxide is completely non-protective. On the other hand, the smaller slopes in the figure, which means reduced reaction rate coefficients, are only possible if a moderating influence on the rate limiting mechanism is assumed. Possibly influencing this behaviour are the boundary values or profile of the anion vacancy concentration of the  $\text{ZrO}_2$  scale.

Kawasaki *et al.* [9] also pre-corroded Zircaloy in pressurised water at 300°C to give an oxide film ~1 µm thick. Subsequent oxidation in steam at 900 and 950°C showed a protective effect i.e. less oxidation for up to 50 mins at these temperatures.

Figure 6.19 Oxidation results for cladding pre-oxidized with a 10 µm oxide



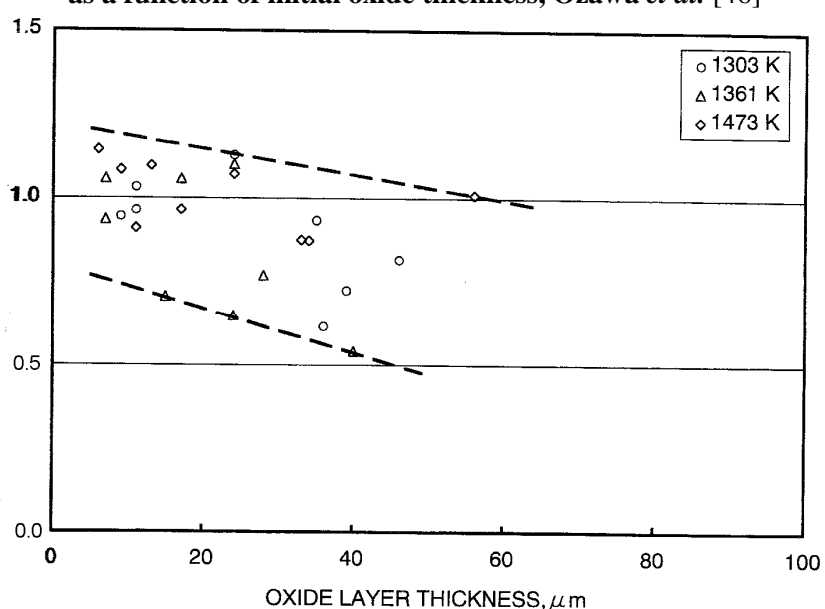
Iglesias [45] has pointed out that tests with pre-oxidized Zircaloy have been interpreted in terms of a premise that a “protective” oxide forms at temperatures below 1 200°C. However only three points in Figure 6.19 (2 000°F and 1 800°F for  $t^{1/2} > 16$ ) support this premise. If specimens are pre-oxidized, the oxygen gradient produced in the stabilised  $\alpha$ -layer dictates the speed of advancement of the oxide/ $\alpha$  interface during further oxidation at different temperature. As the oxygen gradient adjusts itself by diffusion to be aligned with the new oxidation temperature, parabolic kinetics will be re-established. At high temperatures ( $>1 200^\circ\text{C}$ ), oxygen diffusion is so rapid that concentration gradient re-aligns easily and little effect of pre-oxidation is noted. Such an effect cannot be represented using parabolic rate laws but can be accounted by means of moving-boundary diffusion models (see Section 6.3.2).

Ozawa *et al.* [46] reported oxidation tests on both pre-oxidized unirradiated cladding of Zry-4 and spent fuel cladding after four cycles of irradiation to a burn-up of 45.9 MWd/kgU. The unirradiated cladding was tested (1) as-received, (2) hydrogen precharged and (3) hydrogen precharged and pre-oxidized. The irradiated cladding had initial oxide thicknesses of 7 to 56  $\mu\text{m}$  based on measurements on sibling rods. From this oxide thickness its hydrogen content was estimated based on a hydrogen pickup fraction of 12%. The oxidation tests were carried out on 1-cm-long cladding segments and the weight gain was recorded. For the irradiated material spalling off of the oxide occurred frequently during testing, but the spalled oxide was collected in a saucer under the specimen so that it could be included in the weight measurement.

A comparison of results from the hydrogen precharged specimens, 420-840 wppm, with results for as-received specimens tested at 1 060-1 225°C revealed no effect of the hydrogen uptake on the oxidation kinetics. This is in contrast to low-temperature corrosion behaviour in which hydrides can exert a significant effect on corrosion rate [47]. The authors conclude that the hydrogen probably dissolved rapidly in the  $\beta$ -phase and therefore no hydrides were present.

For the irradiated cladding oxidation at high temperature was somewhat slower than for the as-received cladding. In Figure 6.20, the oxidation result for irradiated cladding has been normalised with respect to the result for as-received cladding oxidized under the same conditions. There is a clear trend that the high-temperature oxidation of irradiated cladding is retarded by the presence of the oxide formed during reactor operation.

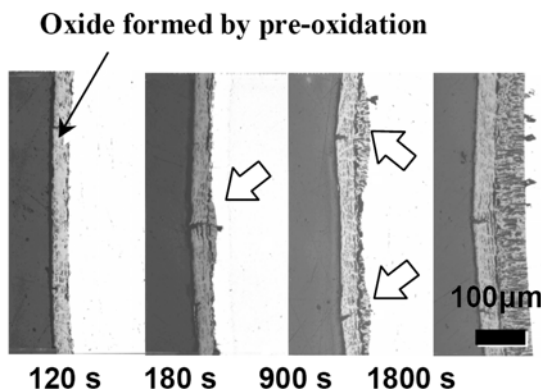
**Figure 6.20 Normalised values of high-temperature oxidation of spent fuel cladding as a function of initial oxide thickness, Ozawa *et al.* [46]**



Basically the same behaviour is observed for unirradiated cladding pre-oxidized before the high-temperature exposure. The presence of a thick oxide retards the high-temperature oxidation. Metallographic observations on the irradiated cladding show that the initial oxide lies more or less unaffected by the high-temperature test on the outside of the oxide layer formed at high temperature. There is no indication that the initial oxide to any extent has dissolved in the  $\alpha$ -phase.

Nagase *et al.* have reported oxidation tests on pre-oxidized low Sn Zircaloy-4 [48]. In isothermal tests at 1 100°C, the weight gain of samples pre-oxidized to 40 to 50  $\mu\text{m}$  thickness were lower than those for as received samples for times shorter than 1 800 s. For longer times, the weight gains were comparable. Metallographic cross sections on samples oxidized for various times revealed the mechanism behind this behaviour (Figure 6.21).

**Figure 6.21 Cross sections of pre-oxidized samples oxidized at 1 100°C for various times**  
White arrows indicate initiation of high-temperature oxidation.



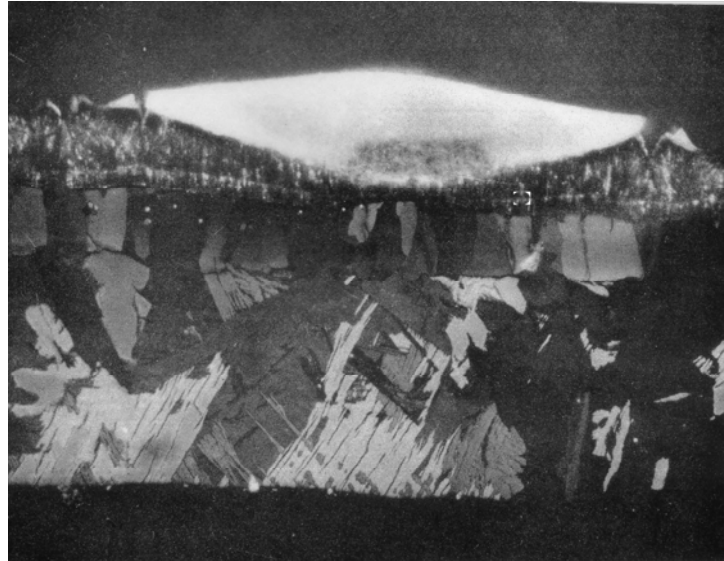
As can be seen in the Figure, no additional oxidation is observed in cladding samples exposed to high-temperature steam for times shorter than 180 s. An additional oxide is locally formed at cracked positions of the pre-formed oxide after 180 and 900 s as indicated with arrows in the figure, and after 1800 s the high-temperature oxide grows uniformly beneath the pre-formed oxide layer. These results show that pre-formed oxide can be a protective layer for the high-temperature oxidation, that high-temperature oxidation initiates at cracks in the pre-formed oxide, and that this retarding effect is maintained until additional oxide layer by high-temperature oxidation is uniformly formed beneath the pre-formed oxide layer.

Recently Brachet *et al.* reported the effect of 5 and 15  $\mu\text{m}$  oxides formed in a hot water loop before LOCA testing [49] for both Zircaloy-4 and M5. The pre-formed oxides reduced the weight gains in the LOCA tests significantly. However, the resulting microstructure beneath the oxide scales were not affected. Thus post-quench ductility was similar for specimens tested with and without the pre-formed oxide.

An interesting example of the pre-formed oxide acting as a barrier to high-temperature oxidation is shown in Figure 6.22 which is from a study by Pettersson and Haag on the effects of nodular preoxidation [1]. The nodule was formed during a 10 MPa steam autoclave treatment at 500°C for 24 hours. One of the explanations to low-temperature nodular oxidation is that the oxide in a nodule is very much non-protective like most post-transition oxides. It is therefore somewhat surprising that the nodules as well as the other pre-oxides seem to have a protective function during LOCA transients. One part of the explanation is that the nodules as well as the post-transition oxides are stoichiometric. Therefore oxygen vacancies in the oxide will be negligible to permit solid state diffusion of oxygen. Then steam has to be transported at high temperature through the pores in the stoichiometric oxide until it reaches the fresh substoichiometric oxide. Under normal oxidation conditions this transport is

very rapid compared to the prevailing corrosion rates, and the oxide is totally non-protective. However, under the fast oxide growth during a LOCA transient the steam transport through the pre-oxide may well be rate limiting. This hypothesis could also explain the change of rate constant for oxide growth after pre-oxidation which was observed in the experiments by Biedermann *et al.* [5]

Figure 6.22 High-temperature oxidation below an oxide nodule formed during pre-oxidation 80×



A metallographic analysis was reported by Chung on a PWR high-burn-up spent-fuel cladding that was oxidized in steam in a LOCA-like transient situation [21]. Fuel burn-up was  $\approx 63$  MWd/kgU, and the spent-fuel cladding, fabricated from standard Zircaloy-4, had a pretransient corrosion layer thickness of  $\approx 70$   $\mu\text{m}$ , remaining metal wall thickness of  $\approx 0.70$ - $0.71$  mm, and a total hydrogen uptake of  $\approx 550$ - $800$  wppm. The fuel-containing cladding segment was heated rapidly to  $\approx 1$  050°C, then slowly heated from  $\approx 1$  050°C to  $\approx 1$  200°C in  $\approx 70$  s, and held at  $\approx 1$  200°C for various periods of time up to  $\approx 300$  s. Post-quench nil-ductility was observed by the time the cladding was exposed to  $\approx 1$  200°C for  $\approx 100$ - $120$  s. For a similar cladding in non-irradiated fresh state under nominally the same time-temperature exposure condition, total oxidation calculated with Cathcart-Pawel correlation was  $\approx 10\%$  ECR.

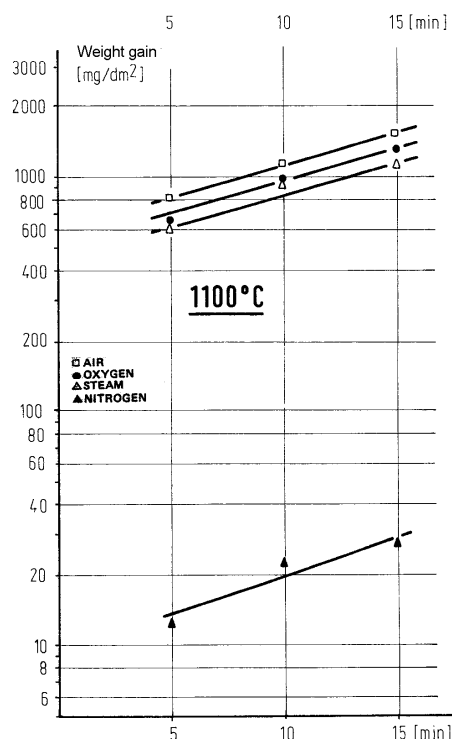
However, metallographic measurements of the oxide and stabilised layer thicknesses in the LOCA-like-oxidized spent-fuel cladding showed that actual ECR was significantly less, indicating a strongly retarding effect of the pretransient corrosion. Compared to optical metallography, scanning electron microscopy allowed more accurate thickness measurement of cauliflower-shaped pretransient corrosion layer, columnar high-temperature-oxide layer, and stabilised  $\alpha$  layer. There were indications that the inner portion of the porous pretransient corrosion layer (predominantly monoclinic oxide) transformed to compact columnar oxide (tetragonal oxide) during the high-temperature exposure. The combined thickness of the two types of oxide was not much different from the thickness of the pretransient corrosion layer, i.e.,  $\approx 70$   $\mu\text{m}$ . Furthermore, the thickness of the stabilised  $\alpha$  layer was also significantly smaller than that predicted by the equation developed by Cathcart-Pawel. Chung suggested that the large amount of hydrogen atoms that are dissolved in the  $\beta$  layer can lead to a relatively thinner layer of stabilised  $\alpha$ , because hydrogen is a strong  $\beta$  stabiliser. The pretansient corrosion layer formed in PWR is most likely a hydroxide rather than an oxide. This may be a factor related to the high-temperature transformation of the inner part of the corrosion layer to columnar tetragonal oxide indicated in this study. At any rate, it seems that oxidation of high-burn-up Zircaloy-4 PWR cladding cannot be predicted well by Cathcart-Pawel correlation, from the standpoint of not only post-quench embrittlement but also oxidation-related heat generation.

### 6.1.8 Oxidation of zirconium alloys in impure steam

The oxidation of Zircaloy at high temperatures in oxidizing media other than pure steam has been investigated for a range of conditions. Cathcart *et al.* [50] added small amounts of impurity ( $N_2$  or  $O_2$ , up to 10 vol.% and  $H_2$  up to 5 vol.%) to steam and oxidized Zircaloy at temperatures of 1 100 and 1 300°C. Yet no significant effects on the oxidation rate were observed.

Zircaloy was exposed to pure  $N_2$ ,  $O_2$  and air by Leistikow *et al.* [7] in the temperature range of 900-1 150°C. The results at 1 100°C are shown in Figure 6.23 which show that the weight gain is slightly higher for oxidation in air or oxygen than in steam. In air, zirconium nitride forms which is itself oxidized, permitting further easier access of oxidant. In oxygen, there are no gaseous reaction products and hence no perturbations to the flux of oxidizing species arriving at the oxidized surface. Results at the other temperatures were similar.

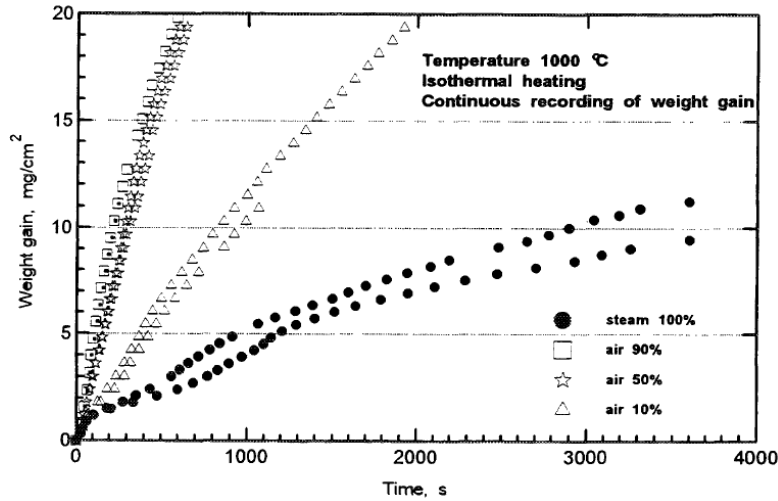
Figure 6.23 Weight gains recorded in isothermal tests in different gases on Zircaloy-4



Leistikow, Kraft and Pott [51] also oxidized Zircaloy tubes in steam and air in comparative stress rupture tests. It was concluded that at temperatures up to ~800°C the oxidation characteristics in air and steam were similar as were the mechanical properties in stress rupture. However, at ~1 000°C, although the oxide formed in steam remained adherent and protective and delayed stress rupture, the oxide formed in air was extensively cracked and conferred no strengthening effect in stress rupture. The mechanism of enhanced corrosion in air at temperature > ~1 000°C was the dissolution of nitrogen and the formation of zirconium nitride which is highly reactive, brittle, and has a high Pilling-Bedworth ratio.

Bibilashvili *et al.* have reported the effect of air-steam mixtures on the oxidation of the E110 alloy at 800, 1 000 and 1 200°C [18]. The mixtures in the study contained 10, 50 and 90% air. The largest effect on the oxidation was observed at 1 000°C (Figure 6.24). At 1 200°C, there was no effect of 10% air. At the higher concentrations of air, the oxididation rate increased significantly similar to the observation at 1 000°C. At the lower temperatures, there was a characteristic inflection in the curves, possibly indicating start of breakaway oxidation.

Figure 6.24 The effect of air on the oxidation of the E110 alloy [18]



They have also reported a study of the effect of nitrogen concentration on oxidation kinetics. The results are similar to the results in air. Both in air and nitrogen mixtures they explain the increase in reaction rate as a result of the “activising” influence of nitrogen. They also note that the transition from parabolic to linear kinetics at low temperatures comes earlier with nitrogen than with pure steam.

### 6.1.9 Influence of hydrogen in steam on zirconium alloy oxidation

All previously published measurements of Zircaloy oxidation have been made with flows of steam such that the reaction never became limited by gas-phase diffusion, a condition that was ensured by experimentally determining the minimum flow rate necessary to supply the oxide/gas phase interface with sufficient oxidizing species.

In some circumstances, notably in some beyond design basis accidents (i.e., severe-fuel-damage accident) it is envisaged that the supply of steam to oxidize the fuel cladding will be from the boil-off of water as the core is uncovered. The steam flows convectively up the fuel channels and the oxidation of fuel cladding produces hydrogen gas which increases in concentration with height above the boiling water. In such circumstances, calculation of the extent of cladding reacted using kinetic data obtained as above, may be unrealistic.

Additionally, in the region of the perforation in ballooned and burst cladding, the steam ingress oxidizes the cladding inner surface. The residual hydrogen gas in this situation results in a high hydrogen-steam ratio adjacent to certain locations of the inner surface. This strongly influences the mode of oxidation, and in some circumstances, the degree of local embrittlement (Section 6.2.3) at these locations.

The effect of hydrogen on the oxidation characteristics of Zircaloy was noted at ~750°C, in earlier years by Westerman [52] who reported lower weight gain in an approximately 80% hydrogen-steam mixture.

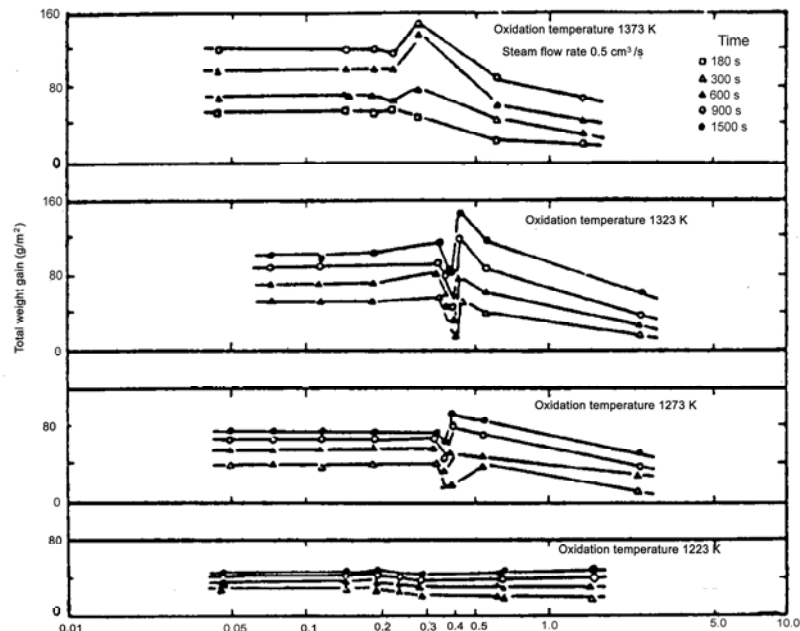
Furuta *et al.* [53] observed different oxidation characteristics on the inner diameter of a dummy fuel rod burst and oxidized in flowing steam. Further work by JAERI on the oxidation of burst dummy fuel rods in steam [54-57] has shown a different morphology of oxide formed on the inner surface and the effects of such oxidation on the mechanical properties of oxidized Zircaloy.

Evaluation of the fuel rods after in-reactor LOCA tests in the FR2 reactor, performed by KfK in Germany, has identified thicker internal oxide compared to the external oxide layers near the rupture

elevation for all high-burn-up fuel rods. Steam consumption, hydrogen enrichment, as well as burn-up influences (growth of defective scales) have been interpreted as contributing to this modified oxidation behaviour [58].

The effects of hydrogen-steam mixtures on the oxidation of non-deformed Zircaloy have been reported by JAERI investigators [56,59,60]. Small sections of Zircaloy-4 cladding were heated isothermally in the temperature range of 950-1 100°C in a flowing mixture of steam and hydrogen. The volume ratio of hydrogen to steam was varied over the range of 0.05-2.0. The total weight gain was found to be a function of flow rate, temperature, time and hydrogen concentration. At a high flow rate of  $18.3 \text{ cm}^3\text{s}^{-1}$  and temperatures of 1 000, 1 100°C there was a slight but definite decrease in the weight gain of specimens oxidized in mixed gas of  $V_{\text{H}_2}/V_{\text{H}_2\text{O}}$  ratio 0.4 as compared to those in steam. At a flow rate of  $0.5 \text{ cm}^3\text{s}^{-1}$ , weight gain as a function of time, temperature and  $\text{H}_2/\text{H}_2\text{O}$  volume ratio is shown in Figure 6.25. For temperatures of 1 000°C and above, there is a critical  $\text{H}_2/\text{H}_2\text{O}$  volume ratio below which the oxidation behaviour is the same as in pure steam, but above which the weight gain exhibits a marked decrease. This critical ratio depends on temperature and flow rate and tends to be lower as the temperature increases from 1 000-1 100°C.

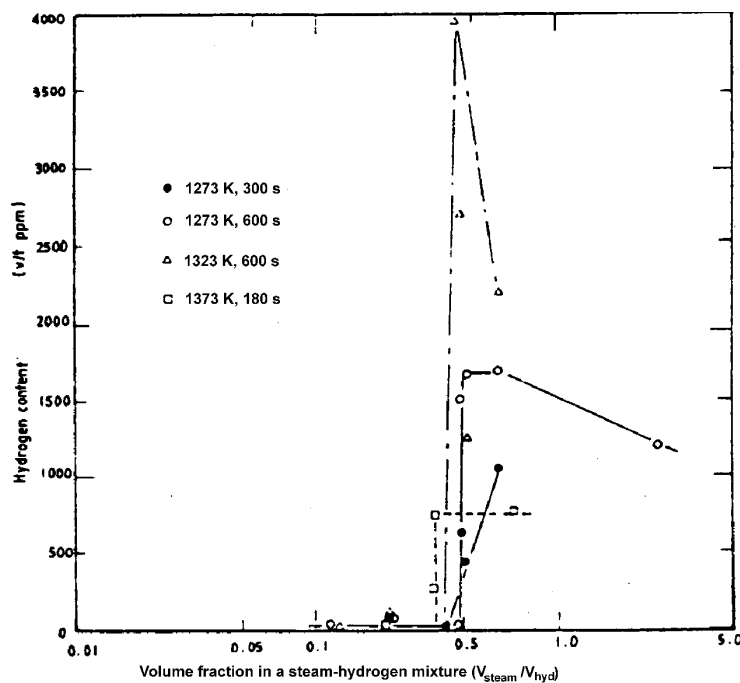
Figure 6.25 Total weight gain of oxidized specimen as function of hydrogen-to-steam volume ratio



The effect of hydrogen concentration in mixed hydrogen/steam gas on the hydrogen uptake in oxidized Zircaloy-4 is shown in Figure 6.26. Below the critical  $\text{H}_2/\text{H}_2\text{O}$  volume ratio, the hydrogen uptake is similar to that observed in pure steam. At the critical ratio the hydrogen uptake increases rapidly.

In hydrogen/steam below the critical ratio the oxide structure and morphology were the same as in pure steam that is the oxide was compact, dense and in room temperature examination, has a monoclinic crystal structure. Above the critical ratio, the increased hydrogen concentration caused the oxide to form as a porous oxide consisting of both the monoclinic and tetragonal polymorphs of  $\text{ZrO}_2$ . Additionally, a measurement of oxygen distribution in the transformed  $\beta$ -phase of specimens oxidized for 1 200 s at 1 000°C showed a lower oxygen concentration in the specimen that was oxidized in a mixed gas of  $\text{H}_2/\text{H}_2\text{O}$  ratio above the critical ratio. This sample contained as much as 3 230 ppm hydrogen.

Figure 6.26 Hydrogen content absorbed by specimen in a steam-hydrogen mixture [59]



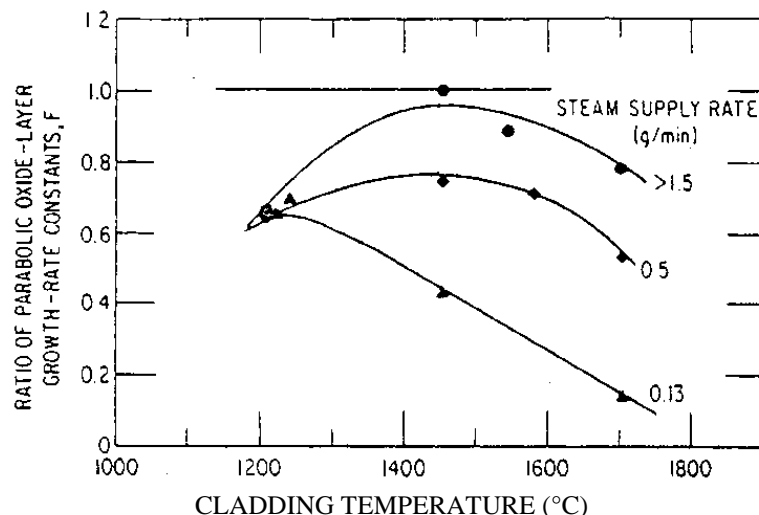
The authors conclude that hydrogen in steam can have a marked effect on the oxidation characteristics of Zircaloy-4 in steam hydrogen mixtures. The weight gain varies with the  $H_2/H_2O$  volume ratio at temperatures of 950–1100°C and the effect is more pronounced as the flow rate decreases. The critical value of the  $H_2/H_2O$  ratio depends on temperature and flowrate. Tetragonal oxide associated with oxidation in gas mixtures above the critical  $H_2/H_2O$  ratio is promoted by the absorbed hydrogen observed in such samples. The oxygen concentration profile in transformed  $\beta$ -Zircaloy can be influenced by hydrogen uptake and the occupancy by the hydrogen of the octahedral sites in  $ZrO_2$ .

Chung and Kassner [61] and Chung and Thomas [17,62–63] have also investigated the effects of hydrogen/steam mixed gas oxidation of Zircaloy mainly to study the implications to core heat up in degraded core type accidents where hydrogen in steam and reaction kinetics above 1200°C are particularly significant. Chung and Kassner [61] observed anomalous oxidation on the inner and outer surfaces of Zircaloy cladding oxidized in steam. Several types of specimens were examined including  $Al_2O_3$ -pelleted, pressurised and ruptured cladding. Tests were performed with pellets of various diameter. Undeformed claddings with various sizes of holes were also tested to admit steam into the cladding inner volume at various rates. Significant variations in oxide and  $\alpha$ -phase thicknesses were frequently observed in ruptured cladding which were not attributable to local temperature fluctuations. Two distinct types of anomalous oxide were observed. An oxide observed only on the outer surface is characterised by white contrast under polarised light and is somewhat similar to that observed in the breakaway oxidation regime at low temperatures (Section 6.1.3). A second type of porous oxide was observed on both inner and outer surfaces and is characterised by small circumferential cracks and a much larger oxide thickness relative to normal dense oxide. This type of oxide was observed in highly localised areas which suggest that temperature or  $H_2/H_2O$  ratios are not particularly influential since they would not vary much over the small distances observed. The authors suggest local stress variations are more likely to have influenced the formation of such oxides. However, in the very narrow capillary-type gap between the pellets and the cladding inner diameter, mixing of stagnant steam and hydrogen gas is difficult. This may lead steep gradients in  $H_2/H_2O$  ratio over a short distance along the gap. Since many interdependent factors combine to determine the precise conditions

of oxidation in such type of tests, e.g. local stress concentrations, size of rupture, steam/hydrogen transport, outside and inside the cladding, distance from the rupture centre, and temperature variations, it was not possible to unequivocally establish the relationship between the various factors such as H<sub>2</sub>/H<sub>2</sub>O ratio on the oxidation characteristics of the Zircaloy cladding.

Chung and Thomas [17,62-63] have also investigated the effects of hydrogen/steam mixture on oxidation of Zircaloy-4 at very high temperatures. The objective was mainly to study the implications to core heat up under severe-fuel-damage-accident situations where hydrogen in steam and reaction kinetics are particularly large. They performed a series of experiments to investigate the influence of hydrogen in steam on the oxidation of the free outer surface of Zircaloy-4 cladding in simulated environments that can occur in a severe-fuel-damage accident. In the first series of experiments, the oxidation rate in hydrogen-steam mixtures was measured in the temperature range 1 200-1 700°C in an overpressure of 33 KPa hydrogen in a total pressure of ~38-45 KPa. Steam-helium mixtures were also used to distinguish between rate limitations in the gas phase and surface reactions. The extent of reaction was measured as oxide thickness. The ratio of the parabolic oxide layer growth constants obtained in steam-hydrogen and in pure steam is plotted as function of cladding temperature and steam supply rate in Figure 6.27. It is evident that the oxidation rate is retarded in steam hydrogen mixtures. The retardation is greater for higher hydrogen-steam ratios and for a given hydrogen-steam ratio, this effect is more pronounced at higher temperatures. In pure steam, the oxidation rate was always parabolic and similar to previously reported data, hence steam starvation was not occurring in these tests. Oxidation in hydrogen-steam mixtures is parabolic or linear depending on the specimen temperature, the pressures of steam and hydrogen at the specimen surface and the time of oxidation i.e. the oxide layer thickness. Initial oxidation kinetics in hydrogen-steam were linear rather than parabolic at the lower steam supply rates and were lower. This indicates that the oxidation was limited by either gas-phase diffusion or some kind of surface reaction (e.g. dissociation of water molecules or subsequent reduction of oxidizing species). Since oxidation in steam-helium mixtures in similar conditions was observed to be parabolic, based on the assumption that steam has similar diffusivities in hydrogen and helium, it was concluded that the rate limiting process in steam-hydrogen is a surface reaction.

**Figure 6.27 Ratio of parabolic oxide layer growth rate constant obtained in hydrogen steam mixtures to that obtained in unlimited flux of pure steam as a function of Zircaloy-4 temperatures and steam supply rate [17]**

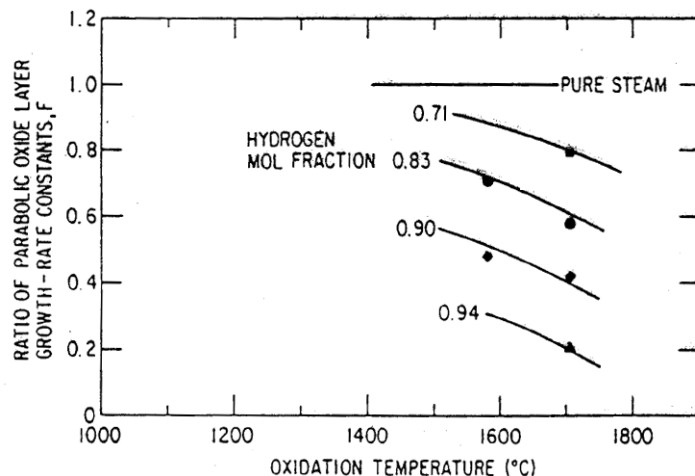


Eventually as the oxide film thickens, the flux of oxidizing species at the oxide/metal interface decreases, solid state diffusion becomes rate limiting and parabolic kinetics are obeyed. In these

circumstances lower oxidation rates than would be achieved in pure steam were observed, and it is postulated that hydrogen dissolved in the cladding is responsible for decreased oxygen diffusion. It is suggested that this is due to interstitial or substitutional  $H^+$  ions producing an increase in the oxygen vacancy concentration in the oxide near the gas/specimen surface thus decreasing the oxygen vacancy concentration gradient across the oxide and hence the oxygen diffusion rate.

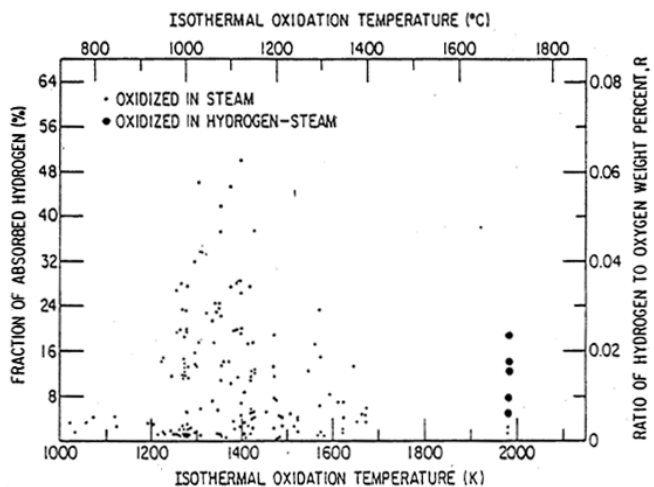
The limitations of the former experiments in adequately quantifying the effects of hydrogen on Zircaloy oxidation in the realistic conditions of flowing steam were subsequently stated by Chung and Thomas [17]. In the above experiments, the steam molecules impinge on the oxide by natural convection in a static overpressure ( $\sim 33$  kPa) of hydrogen. Steam impingement rate varies by virtue of a controlled steam supply rate, a decreased supply rate implying an increased hydrogen molar fraction. Under these conditions the oxidation rate is a function of steam supply rate as well as temperature and it is not possible to quantify the steam and hydrogen partial pressures at the reaction site. Chung and Thomas [17] reported further experiments in which a shroud was placed around the Zircaloy cladding and flowing steam-hydrogen mixtures were passed over the Zircaloy. A flow of hydrogen was maintained at 10 l/min and the steam supply varied between 0.5-3.2 g/min to give hydrogen molar fractions ranging from 0.94 to 0.71. The ratio of the oxide layer growth constants for the hydrogen-steam and pure steam are shown in Figure 6.28 as a function of cladding temperature. The lower parabolic rates observed in steam-hydrogen mixtures are again interpreted as being due to hydrogen entering the zirconia lattice either as interstitial or substitutional  $H^+$  ions. Confirmation that hydrogen was contained in the surface oxide was obtained by powdering the surface layers and chemical analysis. The analysis showed that the oxide formed in hydrogen-steam mixtures contained a significant quantity of hydrogen in the outer layer, having a composition which approximates to  $ZrOH$ . Zircaloy oxidized in pure steam contained little hydrogen ( $\leq 0.03$  w.%) but as the hydrogen-steam ratio increased the hydrogen content of the outer oxide increased and the oxygen content decreased.

**Figure 6.28 Ratio of parabolic oxide layer growth rate constant obtained in flowing hydrogen steam mixtures to that obtained in unlimited flux of pure steam as a function of Zircaloy-4 temperatures and average hydrogen mole fraction in the inlet mixtures [17]**



The fraction of the total hydrogen generated which becomes dissolved in the cladding can be significant as shown by Figure 6.29. The data derives from tests on pressurised ballooned ruptured and oxidized Zircaloy tubes in simulated LOCA situations [61]. Anomalous porous oxidation generally observed on the inner diameter at  $\leq 120^\circ\text{C}$  is responsible for the large dissolved hydrogen fraction at about  $120^\circ\text{C}$ . Chung and Thomas [17] point out that such data demonstrate the importance of Zircaloy cladding as a sink for hydrogen and also point out that further data are required for a satisfactory understanding of all the features associated with hydrogen-steam oxidation of Zircaloy.

**Figure 6.29 Fraction of hydrogen atoms dissolved in Zircaloy-4 cladding tube out of total hydrogen atoms produced as a result of Zircaloy steam reaction at isothermal oxidation temperatures.** Data from [17,61]



Chung and Thomas [64] analysed the implications of high hydrogen concentrations on core heat-up in beyond-design-basis accidents and although more data are required on oxidation rates in high hydrogen/steam ratios before a quantitative analysis is possible, it was concluded that, during prolonged core uncovering, the cladding oxidation rate will be lower and therefore the core-heat-up rate will be lower. Additionally, the lower oxidation rate should not affect embrittlement behaviour since this will be established before the high hydrogen concentrations have an effect. Finally, less liquid UO<sub>2</sub> and debris will be formed than would be predicted using unlimited steam oxidation kinetics.

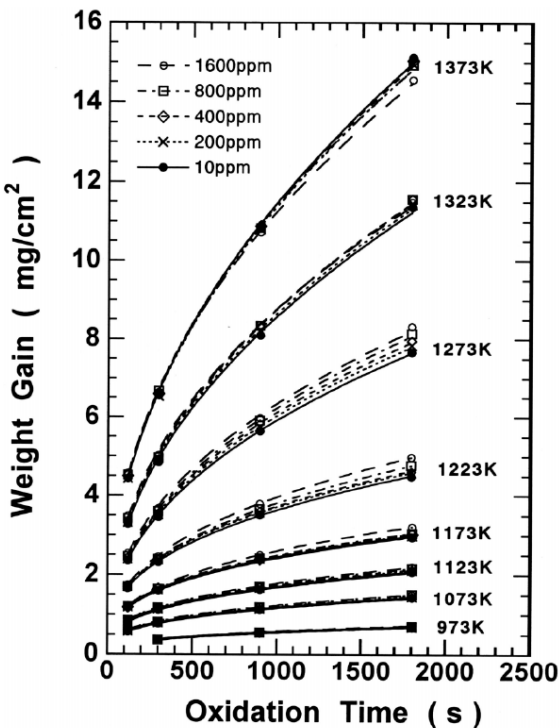
A later investigation by Prater and Courtright [65] conflicts with that reported above in that oxidation in steam-hydrogen mixtures between 1 300°C and 2 400°C has failed to show any influence of hydrogen on the initial parabolic growth rates of the ZrO<sub>2</sub> and  $\alpha$ -Zr(O) phase thicknesses until the hydrogen concentration reaches ~90 mol %. At this high concentration the gas-phase mass-transfer of steam molecules is reduced to a flux less than that required to oxidize Zircaloy at the rate determined by solid-state diffusion.

Results on Zr1%Nb reported by Bibilashvili *et al.* did not reveal any significant influence of hydrogen on the rate of zirconium/steam kinetics at tests done at 1 200°C in which tests in pure steam were compared to tests in 90% hydrogen-steam mixture [18].

At high burn-up, when the oxide layer may reach thicknesses of up to 100  $\mu\text{m}$ , there is also a significant hydrogen pickup in the cladding. For a pickup fraction of 15%, the expected hydrogen content will be about 600 ppm at an oxide thickness of 100  $\mu\text{m}$ . Due to thermal diffusion of hydrogen, much of this hydrogen will be located near the outer surface of the cladding. At low temperatures, it has been observed that the presence of hydrides has an accelerating effect on corrosion [47]. However, as soon as the material has been transformed to the  $\beta$ -phase in a LOCA transient, practically all hydrides become dissolved in the metal. As suggested by Chung and Thomas, hydrogen dissolved in oxide may have a retarding effect on oxide growth [63]. The results of Ozawa *et al.* presented in Section 6.1.7 did not reveal any effect of hydrides formed in the metal [46].

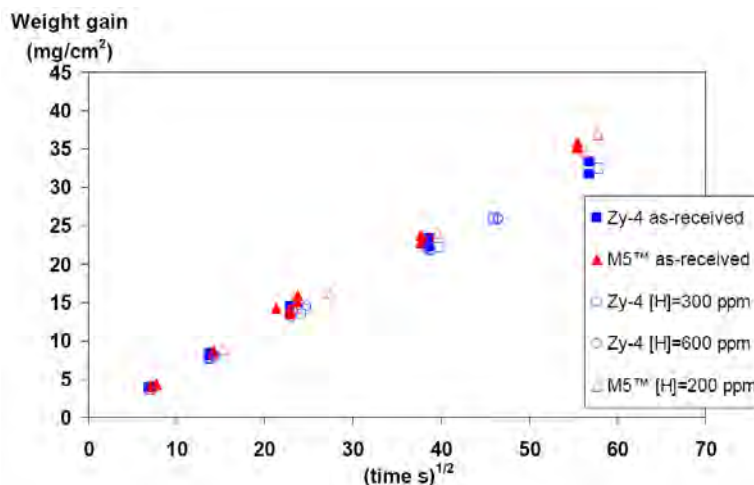
Nagase *et al.* have studied the effect of prehydriding on the high-temperature steam oxidation of low-Sn Zircaloy [48]. As can be seen in Figure 6.30, the effect is very small. However, in all cases except at the highest temperature (1 100°C), the presence of hydrogen in the material serves to accelerate the oxidation.

Figure 6.30 The effect of prehydriding on the high-temperature oxidation of low Sn Zircaloy-4



Portier *et al.* compared M5 with Zircaloy-4 and also included the effect of hydrogen content in the comparison [24]. As can be seen in Figure 6.31 there are small differences between Zircaloy-4 and M5 and the effect of hydrogen content is minimal. The rationale for only testing a low content for M5 was because in-reactor corrosion rate of M5 is much lower than Zircaloy-4. Thus M5 is not expected pick up more hydrogen than 200 ppm at the end-of-life.

Figure 6.31 Effect of hydrogen content on M5 and Zircaloy oxidation kinetics at 1 200°C



More recently E. Perez-Feró *et al.* have reported results on the oxidation of E110 alloy in hydrogen-steam mixtures with 20, 28, and 36 vol.% hydrogen at 900, 1 000, and 1 100°C [66]. The experiments were conducted in a tube furnace with the sample being pushed in and out of the heated zone of the tube at the beginning and end of the experiment respectively. The oxidation was determined from the weight gain of the samples. The figure presented in the paper by E. Perez-Feró *et*

*al.* indicates a relatively large spread in the results and that there was no difference in oxidation behaviour within the range of hydrogen concentrations used. However, the best fit to the results showed that the oxidation rate in the hydrogen-steam mixtures was about 60% of the rate calculated from a best fit of oxidation rates of E110 in steam.

### 6.1.10 High-temperature oxidation of zirconium alloys in high pressure steam

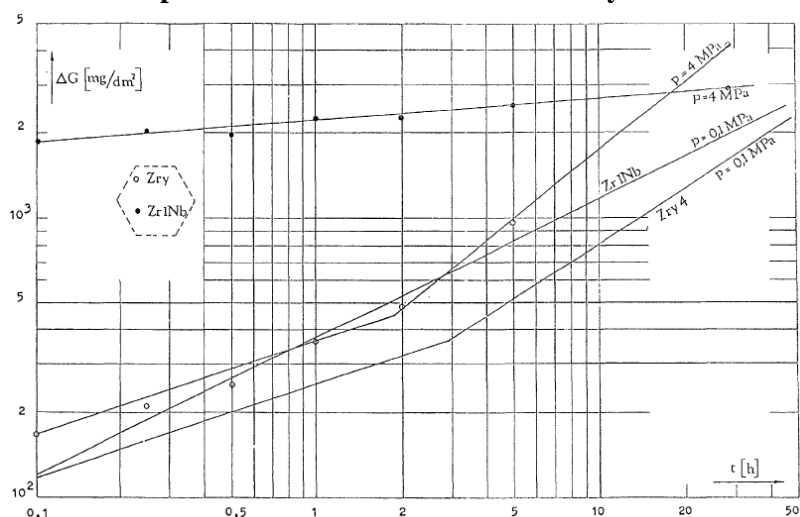
The majority of measurements on the oxidation of Zircaloy in steam have been carried out in ambient pressure steam. For parabolic oxidation, the rate controlling process is diffusion of oxygen anion species. Theories of parabolic oxidation based on diffusion predict rates independent of pressure. Pawel *et al.* [67] have measured the oxidation of Zircaloy in steam at pressures up to 10.34 MPa (1 500 lb/in<sup>2</sup>) and at temperatures of 900 and 1 100°C for times up to 2 500 and 500 s respectively. Measurements of the oxide and  $\alpha$ -phase thickness showed that at 1 100°C there was no effect of pressure, but at 900°C increase in steam pressure tended to increase the thickness of the oxide phase. The authors were unable to postulate a mechanism for the observed effect but suggested that the formation of fine cracks in the outer layer of oxide may enhance oxidation at high pressure.

An alternative explanation of enhanced oxide formation during oxidation at 900°C at high pressure may be the increased transformation of the oxide to the more stable tetragonal oxide in which oxygen transport is greater than in the lower temperature monoclinic form [68].

Other studies have also indicated that there is a reduced influence of steam pressure on oxidation kinetics with an increase in temperature. The effect observed at 900°C is reduced at 1 000°C and at 1 100°C no effect is observed [69-70].

Vrtlikova *et al.* [70] and Bibilashvili *et al.* [18] have reported the effect of steam pressure on the high-temperature steam oxidation of E110 (Zr1%Nb). At 700°C, the oxidation increases with a factor of about 2 when the pressure is increased from ambient to 2-4 MPa [18]. The effect of pressure on the oxidation of both Zircaloy-4 and Zr1%Nb is shown in Figure 6.32 [70].

Figure 6.32 Effect of steam pressure on the oxidation of Zircaloy-4 and Zr1%Nb at 850°C [70]



### 6.1.11 Effect of deformation on zirconium alloy oxidation

Cladding may undergo simultaneous deformation and oxidation during a LOCA until the cladding ruptures. The deformation increases the available surface for oxidation hence increases the volume of oxide formed. Since deformation generally occurs at lower temperatures than at temperatures of

significant oxidation, little work has been done to measure explicitly the enhancement of oxidation in Zircaloy arising from simultaneous deformation and oxidation.

Knights and Perkins [71] reported that under certain conditions i.e. at  $>400^{\circ}\text{C}$  and an oxide film thicker than  $\sim 2 \mu\text{m}$ , an applied tensile stress in the creep range increased the oxidation of Zircaloy-2 in steam and in wet oxygen but not in pure oxygen, up to  $475^{\circ}\text{C}$ . The enhancement of the oxidation rate varied between 1.2 to 2.0 and was attributed to a stress induced inhibition of the parabolic to cubic kinetic transition.

Bradhurst and Heuer [72] compressed Zircaloy rings in flowing steam at  $700\text{-}1\ 300^{\circ}\text{C}$ . It was concluded that deformation imposed during high-temperature oxidation could significantly increase the amount of oxidation. However, in such inhomogeneously strained specimens the effects of deformation were local and overall weight gain was only slightly influenced. The enhanced oxidation takes the form of increased local penetration beneath oxide cracks, and for similar time, temperature exposures the effect was more pronounced at a slow strain rate than at a fast strain rate. The maximum enhancement factor observed was about two.

Simultaneous oxidation and creep at  $900^{\circ}\text{C}$  was investigated by Leistikow and Kraft [73] who pressurised sections of sealed cladding at various pressures and exposed them to either argon or steam for up to 30 min. The strain to failure was found to be dependent on strain rate and was lower for tubes ruptured in steam due to the strengthening effect of the oxide film. A comparison of oxide thickness on strained and unstrained tubes showed that the amount of oxidation increased with increasing stress. The enhancement was attributed to oxide cracking and the provision of new surface for oxidation rather than any influence of deformation on the basic oxygen transport mechanisms through the oxide film.

Furuta and Kawasaki [74] studied the oxidation of axially strained to failure tensile specimens simultaneously oxidized in steam at temperatures between  $700\text{-}1\ 000^{\circ}\text{C}$  and a strain rate of  $\sim 2.8 \times 10^{-2} \text{s}^{-1}$ . An increased oxide thickness was observed in deformed specimens, the enhancement being greater with increasing strain but decreased with increasing temperature. The maximum enhancement factor was  $\sim 1.3$  in the ruptured area at  $700^{\circ}\text{C}$  and after 300 s exposure. No observations on oxide morphology or the nature of the oxidation enhancement were reported.

More recently Parsons and Hand [75] conducted oxidation tests in flowing steam on pressurised Zircaloy-4 cladding at  $\sim 710^{\circ}\text{C}$  and  $\sim 150 \text{ lb/in}^2\text{g}$  and  $\sim 800^{\circ}\text{C}$  and  $\sim 80 \text{ lb/in}^2\text{g}$ . The oxidizing cladding simultaneously deformed (swelled). Tube samples were withdrawn from the furnace at various intervals with diametral strains ranging from  $\sim 5\%$  to  $\sim 30\%$  overall but up to 80% local strain at the perforation. At  $\sim 710^{\circ}\text{C}$ , unpressurised control cladding oxidized initially at a cubic rate before a transition to an approximately linear rate. The deforming cladding very quickly oxidized at a near linear rate with an enhanced weight gain which increased with increasing strain giving a weight gain  $\sim 2\text{-}2.5$  times greater than unpressurised cladding after this exposure. At  $800^{\circ}\text{C}$  unpressurised cladding continued to oxidize at a cubic rate up to 7 hours but pressurised cladding exhibited a transition to a near linear rate after  $\sim 5$  hours after which the weight gain was enhanced by  $\sim 2.5\text{-}3$  times compared to unpressurised controls.

The oxide thickness was also measured and showed the same general enhancement as the weight gain. The oxide was extensively cracked at strains greater than  $\sim 10\%$  at  $\sim 710^{\circ}\text{C}$  and  $\sim 5\%$  at  $\sim 800^{\circ}\text{C}$  and beneath the cracks there was an increased penetration of  $\alpha\text{-Zr(O)}$ . The increase in total oxidation is in part due to the increased surface area on deformed (swollen) cladding but the increase in oxide thickness relative to the undeformed cladding suggests that the enhanced oxidation is also a consequence of increased access of oxidant to the underlying metal by virtue of cracking of normally protective oxide.

### **6.1.12 Stress and dimensional changes in oxidized zirconium alloys**

Since the molar volume of  $\text{ZrO}_2$  is appreciably greater than that of zirconium (i.e. the Pilling-Bedworth ratio is ~1.5-1.6), significant compressive stresses may be generated in the growing oxide scale. These stresses and tensile strains generated in the metal from dilation by oxygen solution can result in significant tensile stresses on the metal substrate. Although various mechanisms may relieve the induced stresses e.g. oxide plasticity, oxide cracking, and metal plasticity the net result will be dimensional changes in the oxide-metal composite Zircaloy material. Oxidation-induced deformation of 0.7 mm thickness Zircaloy-2 sheet has been measured by Donaldson and Evans [76] in Zircaloy oxidized in steam in the range 800-1 210°C. Typical strains were about 1%, the maximum strain being ~3% after 300 mins at 900°C. It was established that the dilation produced by oxygen solution in  $\alpha\text{-Zr}$  has a large effect on stress distribution in the metal substrate and hence influences the average stresses within the oxide. The tensile deformation at high temperatures is attributed to the hydrostatic compressive stresses brought about by dilation due to oxygen solution rather than the stresses produced by oxide growth, the latter being accommodated almost wholly by outward growth.

For short times at lower temperatures, oxygen solution and associated stresses are small, thus net compressive stresses from the oxide (~1 300 MPa) result in deformation of the metal substrate. With increased temperature and time the oxygen-solute-induced stresses grow and eventually dominate the overall stress, exerting a net tensile stress on the oxide of the magnitude of ~200, 300 and 150 MPa at 800, 900, and 1 210°C respectively. Further oxidation allows relaxation and the stress eventually becomes compressive and the metal substrate deforms by creep at lower stress levels, typically 100 and 10 MPa at 900 and 1 210°C. The authors also report that the stress levels generated in the oxide are not sufficient to influence the basic oxygen transport mechanisms in the oxide scale.

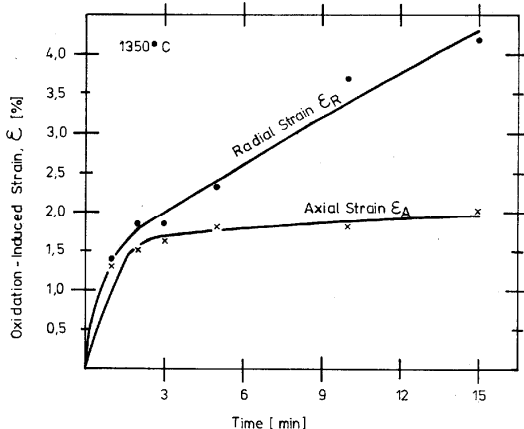
Hammad *et al.* [77] measured the deformation of Zircaloy-4 tubes oxidized in air at temperatures up to 900°C. Hoop and axial stresses are generated in oxidizing tubes and both radial and axial deformation was observed. The time dependence of strain was initially parabolic later becoming linear coincident with the onset of breakaway oxidation. The radial strain varied from ~1.5% after long exposure at 650°C to ~7% after ~10 hours at 750°C. The axial strain tended to follow the same trend as radial strain but was smaller in magnitude.

However oxidation of Zircaloy in air has only limited comparability to that in steam, Leistikow *et al.* [51] showed that the oxidation characteristics of Zircaloy in air and steam were similar at temperatures up to 800°C. However at 1 000°C in air, the formation of brittle zirconium nitride accompanied by a high volume expansion, substantially altered the morphology, kinetics and stresses generated in the oxide film. Thus at temperatures above ~800°C the oxide scales were cracked and the simultaneous reaction of nitriding induced much faster rates of oxidation.

Aly [15] measured the radial and axial strain in Zircaloy-4 cladding tubes oxidized in steam in the range 1 350-1 600°C. The time dependance of radial strain showed an initial non-uniform rate followed by a linear rate. Both the radial and axial strains increased with time and temperature. The time dependence of both strains at 1 350°C is shown in Figure 6.33

Comparative studies of the oxidation behaviour of Zircaloy-4 and austenitic 15 Cr-15 Ni steel by Leistikow [78] have included the measurement of oxidation-induced dimensional changes. Oxidation for 6 h at 1 200 to 1 308°C resulted in an increase of the outer diameter of tube sections of 12% for Zircaloy-4 compared with 10% for the steel. The inner diameter increased by 8% for Zircaloy-4 and decreased by 10% for the steel. The measured increase of wall thickness was 30-60% for Zircaloy-4 compared with 120% for the steel.

Figure 6.33 Time dependence of oxidation induced strains at 1 350°C [15]



## 6.2 Embrittlement of zirconium alloy fuel cladding

A brief description of the fundamental metallurgy of zirconium alloy embrittlement in connection with LOCA type transients can be found in Section 1.2.2 “Background to the safety criteria”. Some of the information will be repeated in this section following the text of the 1986 State-of-the-art report by Parsons *et al.* [37]. In many instances where the word Zircaloy is used the statement also applies to other cladding alloys.

Oxidation of Zircaloy above the  $\alpha/\beta$  transformation temperature results in the formation of inherently brittle phases, zirconia and  $\alpha$ -phase with a high oxygen content. The latter phase comes in two varieties: oxygen stabilised  $\alpha$  and transformed  $\beta$ -phase (or more commonly referred to as prior  $\beta$ ). The former is always brittle while the brittleness at low temperature of the prior  $\beta$  will depend on its oxygen content and how much  $\beta$  there is left. The oxygen content will depend on oxidation temperature and time while the amount of  $\beta$  left primarily depends on oxidation time.

When sufficiently embrittled, fuel cladding may fracture on cooling and break up into pieces thus losing a coolable geometry. The action of re-wetting involves the collapse of the vapour film and nucleate boiling commences. This event takes place at a more or less constant temperature, the Leidenfrost point and for Zircaloy rewetted by water, Chung and Kassner [61] report that rewetting occurs in the range 475-600°C. The change in heat transfer conditions induces large thermal shock stresses which fracture the cladding if sufficiently embrittled by oxidation.

The extent of oxidation necessary to embrittles fuel cladding such that it fragments during rewetting has been determined experimentally by a number of workers for a range of cladding dimensions. Early work resulted in the formulation of criteria defining the onset of embrittlement in terms of total extent of oxidation and maximum temperature of oxidation. Subsequent work has shown that the embrittlement of Zircaloy cladding after transient oxidation in LOCA conditions is more accurately described in terms of the distribution of oxygen in the oxidized cladding.

The external pressure on cladding is reduced to near ambient during a large break loss-of-coolant accident and the cladding initially expands away from the fuel. In pressurised transients the cladding is heated under coolant pressure and contacts the  $\text{UO}_2$  fuel. The  $\text{UO}_2$  is reduced by Zircaloy and the oxygen diffuses into Zircaloy where it forms  $\alpha\text{-Zr(O)}$  and also diffuses into the  $\beta$ -phase. Thus in pressurised transients oxidation of the Zircaloy cladding occurs on both i.d. and o.d. and both contribute to the embrittling of the cladding.

If oxidized cladding remains intact after rewetting, there is the further possibility that seismic forces or the hydraulic forces during reflood and quenching or the forces associated with fuel handling and transport could fragment the cladding. The response of oxidized cladding to such loadings at lower temperatures than that of thermal shock has also been considered and a criterion for predicting failure has been proposed.

### **6.2.1 Current embrittlement criteria**

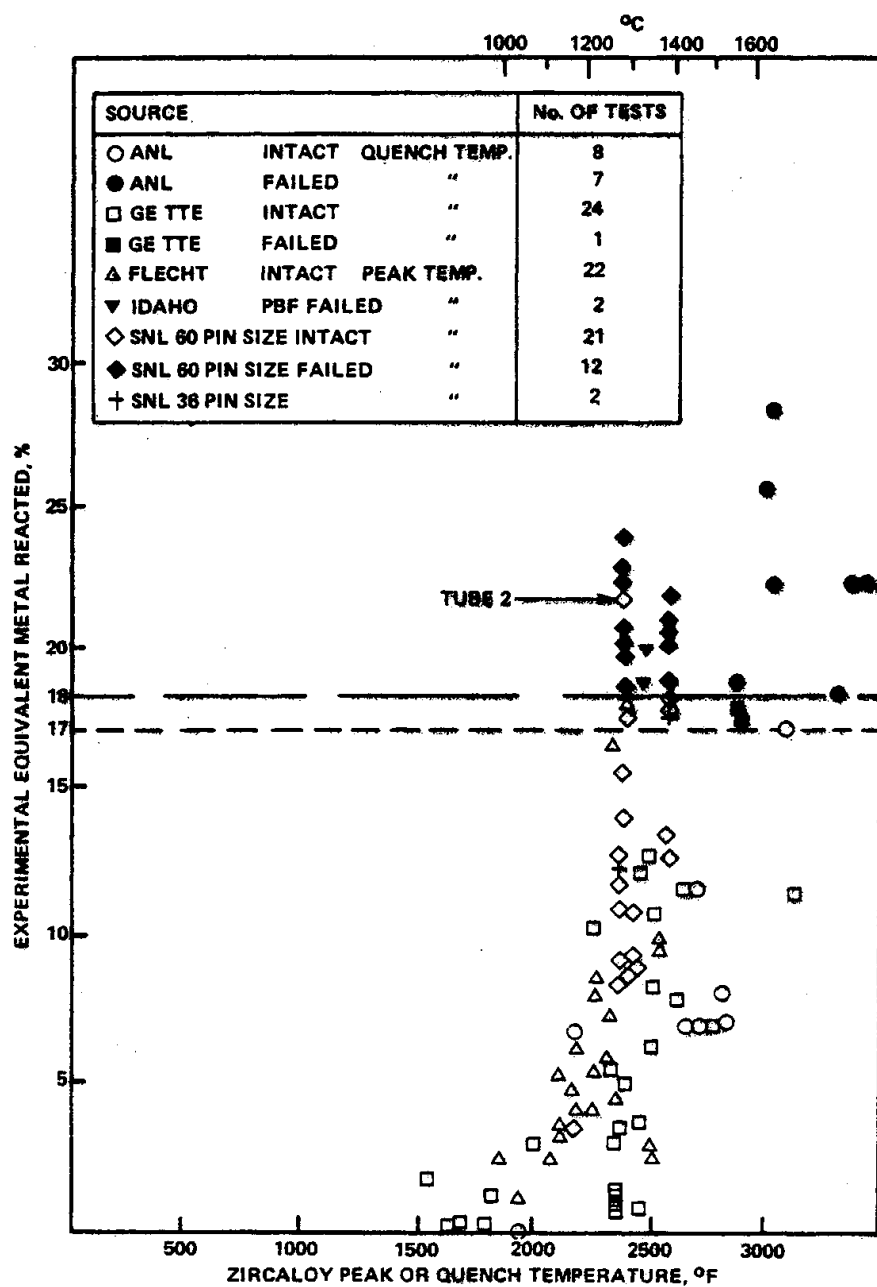
The current criteria and their background have been described in Section 1.2. They are summarised in the following five points:

- Peak cladding temperature – the calculated maximum fuel element cladding temperature shall not exceed 1 204°C.
- Maximum cladding oxidation – the calculated total oxidation of the cladding shall nowhere exceed 0.17 times the total cladding thickness before oxidation. The term equivalent cladding reacted (ECR) including oxygen dissolved in the rest of the cladding is used frequently for this measure of cladding oxidation.
- Maximum hydrogen generation – the calculated total amount of hydrogen generated from the chemical reaction of the cladding with water or steam shall not exceed 0.01 times the hypothetical amount that would be generated if all the metal in the cladding cylinders surrounding the fuel, excluding the cladding surrounding the plenum volume, were to react.
- Coolable geometry – calculated changes in the core geometry shall be such that the core remains amenable to cooling.
- Long-term cooling – after any calculated successful initial operation of the ECCS, the calculated core temperature shall be maintained at an acceptably low value and decay heat removed for the extended period of time required by the long-lived radioactivity remaining in the core.

The experimental work on which these criteria is based, has been reviewed and extended by Parsons [79] and by Chung and Kassner [61]. Typical experiments were to heat Zircaloy tubes in steam either isothermally or through a pre-defined transient and at the appropriate time to quench either by spraying or by bottom flooding with cold water. The extent of oxidation was expressed as the fractional wall thickness of Zircaloy which would be converted to stoichiometric zirconia if all the oxygen taken up were combined with Zircaloy to form  $ZrO_2$  i.e., a measure of the total Zr reacted or total oxygen uptake without regard to the detailed reactions and oxygen distribution in the clad wall. The equivalent metal reacted, as described above for the limited number of tests performed was found to correlate well with survival or failure of the cladding in the thermal shock of rewetting. The correlation is shown in Figure 6.34 which contains both the original US data and data derived at Springfields Nuclear Laboratories on SGHWR sized cladding. The US data shows a clear division between fractured and intact cladding above and below 17% equivalent cladding reacted and hence 17% ECR was adopted as the embrittlement criterion.

An additional criterion was also imposed, that the maximum temperature should not exceed 2 200°F (1 204°C). The condition arose from the work of Hobson and Rittenhouse on the oxidation and embrittlement of standard Zircaloy-4 cladding. Hobson and Rittenhouse [80] showed that the growth of the oxide plus  $\alpha$ -Zr(O) phases,  $\xi$ , (brittle phases) accelerated above 2 200°F (1 204°C). Hobson [81] also investigated the effect of the extent of oxidation expressed as  $F_w$ , the fractional thickness of the prior  $\beta$ -phase layer (i.e., thickness of prior  $\beta$  divided by as-oxized wall thickness), with the deformation response of rings cut from oxidized tubes and tested (flattened) in compression at high (0.25 in/min) and low (0.1 in/min) strain rates. For a given  $F_w$ , the specimens exhibited less

Figure 6.34 Clad embrittlement data from the United States of America and the United Kingdom compiled by Parsons [79]



ductility as the temperature of the deformation test decreased. The temperature at which the specimens broke in brittle fashion (i.e. zero ductility), the temperature of the ductile to brittle transition, was defined as the zero ductility temperature (ZDT). The Zircaloy tubes were oxidized on both sides for various times in the range 1 700-2 500°F (927-1 371°C), and for the specimens tested at the higher strain rate, there was a good correlation between  $F_w$  and ZDT. For specimens tested at the slower strain rate there was a good correlation for specimens previously oxidized up to 2 200°F (1 204°C) but specimens oxidized at 2 400°F (1 316°C) were brittle at all values of  $F_w$ . Hobson concluded that the embrittlement of Zircaloy cladding is determined by the concentration and distribution of oxygen in the  $\beta$ -phase which is influenced to some extent by the degree of formation of  $\alpha$ -incursions.

Further evidence [79] that the embrittlement of Zircaloy is not uniquely dependent on total oxidation was obtained with SGHWR cladding with pre-formed nodular oxidation which survived quenching even though the equivalent cladding reacted was 20%. The oxide and  $\alpha$ -Zr(O) phases are extremely brittle at post-quench temperatures, therefore, the ability of cladding to resist the thermal shock depends on the ability of the prior  $\beta$ -phase to remain intact, which in turn depends on the profile of diffused oxygen in the  $\beta$ -phase.

The particular character of a transient i.e. the parameters of time at temperature during a LOCA, determine the eventual location of the oxide and  $\alpha$ -Zr(O) phase boundaries and also the amount and distribution of oxygen in the  $\beta$ -phase. Hence, the resultant mechanical properties of the cladding depend on the details of the transient i.e. rates of heating and cooling as well as time at maximum temperature. Since the total extent of reaction is a measure of oxidation which does not necessarily reflect the above consideration, it was necessary to determine fracture behaviour in terms of the oxygen distribution.

The above discussion refers to the response of cladding to fracture from the thermal shock forces of re-wetting at the temperature of the Leidenfrost point. The post-quench ability of cladding to remain intact when subject to the forces of seismic, hydraulic and handling loads at ambient temperature, after a LOCA is a separate but related issue.

### ***6.2.2 Embrittlement and distribution of oxygen in the cladding wall***

Pawel [82] used ideal models of diffusion to calculate the oxygen concentration profiles, the fractional saturation and the mean oxygen content in the  $\beta$ -phase of the oxidized specimens used by Hobson [81]. The observed embrittlement was correlated with the calculated oxygen in the  $\beta$ -phase and it was suggested that the critical criteria for the onset of room temperature brittleness was 0.7 wt % average oxygen or 95% saturation in the  $\beta$ -phase.

Sawatzky [83] measured the temperature dependence of the tensile properties of oxidized Zircaloy-4 as a function of oxygen concentration, cooling rate, maximum test temperature and oxygen distribution. It was found that at temperatures up to 800°C, the tensile properties were essentially independent of maximum cladding temperature and cooling rate but were dependent on oxygen distribution through the cladding wall. On the basis of the results obtained, an interim oxygen embrittlement criterion was proposed that the oxygen content should not exceed 0.7 wt % over at least half the cladding thickness. This criterion is consistent with the previously mentioned suggested criteria and applies to all cladding thicknesses.

The relationship between various parameters which can be considered to express the extent of oxidation of Zircaloy and the fracture behaviour of Zircaloy has been comprehensively studied by Chung and Kassner [61]. Lengths of Zircaloy cladding (200 mm) containing alumina pellets and pressurised with helium were heated isothermally in a flow of steam. The cladding was cooled to below the  $\alpha/\beta$  transformation (i.e. to ~800°C) at a controlled cooling rate and then quenched by bottom flooding with water. The widths of the oxide and  $\alpha$ -Zr(O) phases were measured and used along with a model of oxidation as data for a computer code calculation of oxygen profile across the wall of the clad. Several parameters describing oxidation were computed, e.g. equivalent cladding reacted (ECR), fractional saturation of the  $\beta$ -phase ( $F_B$ ), fractional thickness of the  $\beta$ -phase ( $F_w$ ), and thickness of the  $\beta$ -phase containing less than a specified amount of oxygen ( $L_{C\gamma}$ ). The mechanical response of the quenched tubes was correlated with the above parameters and presented as a series of failure maps which are reproduced as Figures 6.35 to 6.38.

Figure 6.35 Thermal-shock failure map for Zircaloy-4 cladding

(bottom flooded with water at the oxidation temperature) relative to the ECR parameter and maximum oxidation temperature after rupture in steam. The best-estimate failure boundary for cladding that was slow cooled through the  $\beta \rightarrow \alpha'$  before flooding with water and the data of Hesson *et al.* [84] and Scatena [85] are shown for comparison [61]

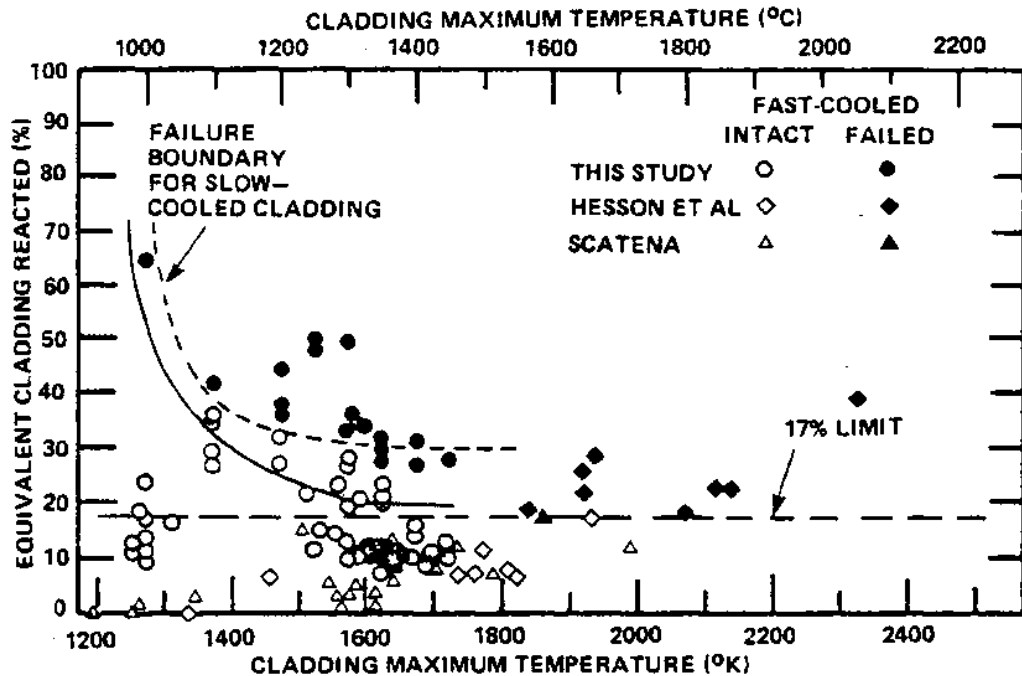


Figure 6.36 Failure map for Zircaloy-4 cladding

by thermal shock relative to fractional thickness of previous  $\beta$ -phase layer and oxidation temperature after rupture in steam and flooding with water at oxidation temperature. Cooling rate through the  $\beta \rightarrow \alpha'$  transformation was  $\sim 100$  K/s [61]

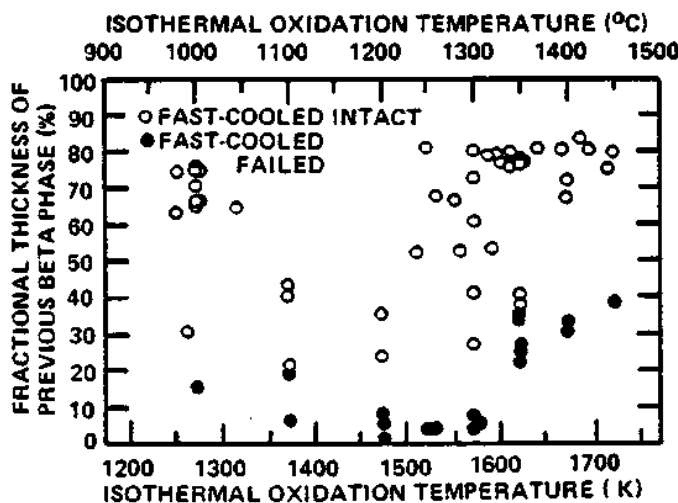


Figure 6.37 Failure map for Zircaloy-4 cladding by thermal shock relative to fractional saturation of  $\beta$ -phase and oxidation temperature after rupture in steam and flooding with water at oxidation temperature. The failure boundary for cladding that was slow cooled ( $\sim 5$  K/s) through the phase transformation is shown for comparison [61]

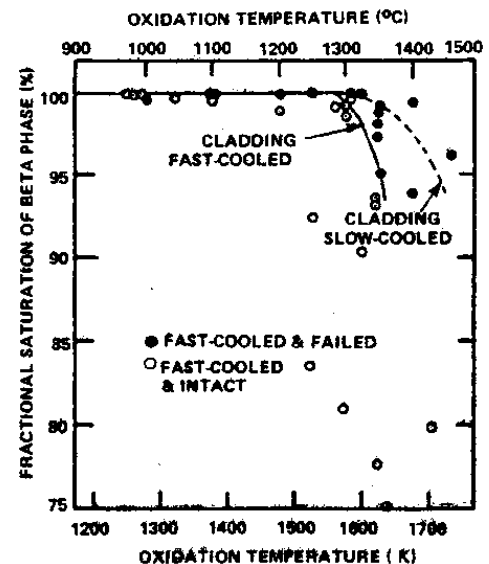
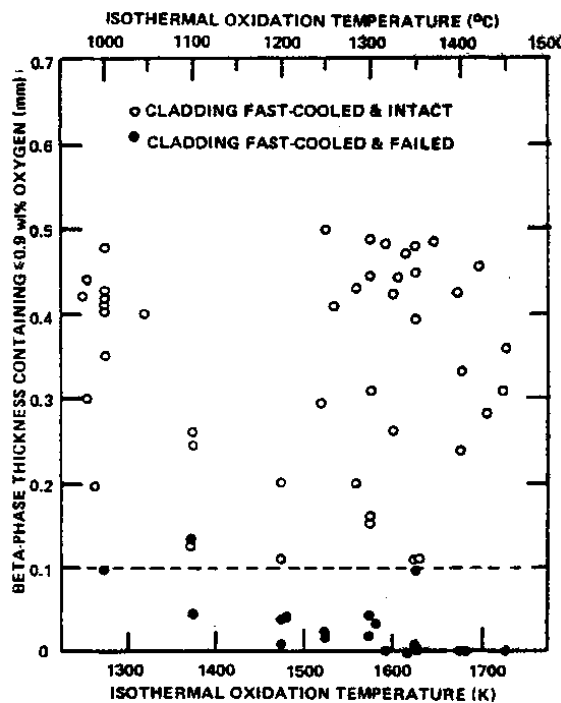


Figure 6.38 Failure map for Zircaloy-4 cladding by thermal shock relative to the wall thickness with  $\leq 0.9$  wt % oxygen after isothermal oxidation and flooding with water at the oxidation temperature. Cooling rate through the  $\beta \rightarrow \alpha'$  transformation was  $\sim 100$  K/s [61]



The cladding was cooled through the  $\alpha/\beta$  transformation temperature either slowly (5 K/s) or quickly ( $\sim 100$  K/s) by direct quenching from the isothermal oxidation temperature and the cooling rate modified the metallurgical structure of the cladding which produced slightly different mechanical behaviour.

The correlation of fracture behaviour and equivalent metal reacted (ECR) in Figure 6.35 shows that fast-cooled cladding is more brittle than slow cooled cladding and that at lower maximum temperatures of oxidation (i.e. at  $< 1400^\circ\text{C}$ ) the 17% ECR criterion is very conservative. A single valued criterion is not apparent from the correlation of the fractional thickness of  $\beta$ -phase ( $F_w$ ) or from the fractional saturation of the  $\beta$ -phase ( $F_B$ ) as shown in Figures 6.36 and 6.37. Chung and Kassner concluded that the best correlation was in terms of a residual width of  $\beta$ -phase containing less than a specified calculated concentration of oxygen ( $L_{C\gamma}$ ) as shown in Figure 6.38. Cladding with less than a calculated 0.1 mm of  $\beta$ -phase with oxygen concentration  $\leq 0.9$  wt % (fast cooled) or  $\leq 1.0$  wt % oxygen (slow cooled) failed on rewetting. This criterion was obeyed irrespective of the wall thickness, overall oxidation or maximum temperature of the oxidation exposure. The authors also report that the location of fracture with respect to the perforation of the fuel tube was temperature dependent. For tubes oxidized above  $\sim 1330^\circ\text{C}$  the fracture occurred in the ballooned region whereas at lower temperature a fin-cooling effect reduced the effective oxidation of this area and fracture occurred away from the perforation.

Kassner and Chung [86] also assessed the margin of performance of ECCS's in LWR against embrittlement criteria based on total oxidation and on oxygen distributions. During blowdown, ballooning and rupture of the clad can occur which results in wall thinning of the clad and the resultant oxidation of the clad will be a function of not only the time at temperature in steam but also the nature of the wall thinning. Hence embrittlement of the cladding will be influenced by wall thinning. They calculated the wall thinning for the peak temperature nodes and rupture nodes from double-ended

guillotine breaks in two PWRs from data on circumferential straining of clad in single pin and multi-rod burst tests. The influence of wall thickness ratio on the embrittlement criteria, equivalent cladding reacted (ECR), thickness of transformed  $\beta$ -phase with <0.9 wt % oxygen ( $L_{C\gamma}$ ) was calculated for the peak temperature and rupture nodes and the two types of transient considered during single- and double-sided oxidation. The results are summarised in Table 6.3 and show significant conservatism in the criterion based on total oxidation in transients not exceeding  $\sim 1200^\circ\text{C}$ . That is for an average circumferential strain of  $\sim 38\%$  and two-sided oxidation of the cladding at the peak temperature node, the ECR parameter is 26% and 22.5% i.e. failure and the  $L_{C\gamma}$  parameters is 0.25 mm and 0.28 mm therefore no failure is predicted in either of the transients. For one-sided oxidation neither criterion indicates failure.

### **6.2.3 Embrittlement below thermal shock temperatures**

During quenching thermal shock, the maximum loading occurs in the range  $475\text{--}600^\circ\text{C}$  [61]. At these temperatures and for the cooling rates associated with quenching, hydrogen is in solution and has little effect on the fracture resistance of oxidized Zircaloy. The ductility necessary to withstand hydraulic, seismic and handling forces, essentially impact forces which may be imposed at lower temperatures e.g.  $100\text{--}200^\circ\text{C}$ , are usually termed the post-quench-ductility (PQD). In this temperature range dissolved hydrogen or precipitated zirconium hydride  $\text{ZrH}_x$  (for the most common hydride, the  $\delta$  hydride,  $\times \sim 1.6$ ) may influence the fracture characteristics of oxidized cladding. The volume fraction of hydride precipitated is strongly influenced by the cooling rate. In consideration of possible fragmentation from such forces, Chung and Kassner [61] measured the impact, diametral tube compression, and tensile properties at ambient temperature of undeformed and deformed and ruptured oxidized cladding which had survived the quenching thermal shock. The combined effects of wall thinning, oxidation and hydrogen uptake are represented in the mechanical property measurements. Within the  $\beta$ -phase, as the Zircaloy cools through the  $\beta \rightarrow \alpha$  and  $\beta \rightarrow \alpha + \text{ZrH}_x$  transformation, oxygen tends to concentrate in the centre of  $\alpha\text{-Zr(O)}$  grains and hydrogen precipitates or diffuses to the oxygen depleted regions of the  $\alpha$ -phase.

It was found that oxygen distribution in the  $\beta$ -phase and hydrogen content of the cladding were the greatest influences on the impact failure properties (note that after exposure to high temperature, practically all hydrogen atoms end up dissolved in the  $\beta$  phase, and after quenching in the prior  $\beta$ ). The resistance to fracture is determined by the amount of low oxygen  $\beta$ -phase and its ductility which in turn is influenced by the hydrogen content. Data on the combined effect of oxygen and hydrogen on the impact properties of Zircaloy was not available, thus Chung and Kassner [61] correlated the susceptibility to impact with the  $\beta$ -phase thickness, the hydrogen content and the calculated centreline oxygen content of the  $\beta$ -layer. The capability of oxidized cladding to withstand an impact energy of 0.3 J at ambient temperature was found to be best correlated in terms of the  $\beta$ -phase thickness containing < 0.7 wt % oxygen as shown in Figure 6.39. The hydrogen concentration in the specimens used for this correlation did not contain  $> 2200$  wppm hydrogen. However the influence of oxygen and hydrogen on the Charpy impact properties of homogeneous Zircaloy containing a range of oxygen and hydrogen contents were measured and these and other data were used to conclude that hydrogen concentration  $> 2000$  wppm along with oxygen would not cause a significant change in ambient impact failure characteristics.

Although the magnitudes of hydraulic, seismic and fuel handling loads have not been accurately estimated, Chung and Kassner consider the magnitude of the 0.3 J impact loading as a reasonable approximation to such post-LOCA low-temperature loadings. Furthermore, the authors showed that all specimens that survived the quenching thermal shock survived at least 0.03-J impact at room temperature. Therefore, the threshold impact energy of 0.3 J was considered to be equivalent to 10 times of the threshold energy that is sufficient to survive the quenching thermal shock.

**Table 6.3 Summary of cladding oxidation parameters and performance limits  
for the ECCCs in two PWRs for a double-ended guillotine break in the pump discharge leg (from [86])**

Evaluation of ECCS margin of performance

		Clad oxidation parameters <sup>a</sup>					Performance limits <sup>b</sup>			
Reactor plant	Design basis accident	Node	17% ECR s	t <sub>f</sub> s	ECR %	L <sub>(0.7)</sub> mm	L <sub>(0.9)</sub> mm	Total oxidation 17% ECR	0.3 Joule Impact L <sub>(0.7)</sub> /0.3	Thermal shock L <sub>(0.9)</sub> /0.1
<b>Two-side oxidation</b>										
OS	0.8 DEGPLD	PCT	275	500	26.0	0.25	0.25	0.65	0.83	2.5
CF	1.0 DECLG	PCT RUP	325 -	475 100	22.5 4.0	0.28 0.30	0.28 0.30	0.75 4.20	0.93 1.00	2.8 3.0
OS	0.8 DEGPLD	PCT	500	13.5	0.34	0.34	1.26	1.10	3.4	
CF	1.0 DECLG	PCT	475	11.5	0.35	0.35	1.48	1-17	3-5	

<sup>a</sup> Values computed from the oxidation model reported in ANL-79-48, NUREG/CR-1344.

<sup>b</sup> Values of  $\geq 1$  indicates performance limit is met.

However, until a sufficiently accurate and quantitative assessment of the lower temperature impact loadings are available and since impact failure data and measured and calculated properties from the diametral compression tests in general are essentially an indication of material toughness or ductility for a given mode of loading, the low-temperature impact criterion is cited as an interim criterion.

In conclusion Chung and Kassner recommend two embrittlement criteria:

1. For cladding to have the capability to withstand thermal shock during reflood – the calculated thickness of the cladding with  $\leq 0.9$  wt % oxygen based on the average wall thickness at any axial location shall be greater than 0.1 mm.
2. For cladding to have the capability to withstand fuel handling transport and storage – the calculated thickness of the cladding with  $\leq 0.7$  wt % oxygen based on average wall thickness of any axial location shall be greater than 0.3 mm.

**Figure 6.39 Capability of Zircaloy-4 cladding to withstand an impact energy of 0.3 J at 300 K relative to the thickness of  $\beta$ -phase layer containing <0.7 wt % oxygen and the hydrogen content of the cladding.** The above criteria are applicable irrespective of the oxidation temperature, the initial cladding wall thickness and the wall thickness that results from ballooning and deformation.

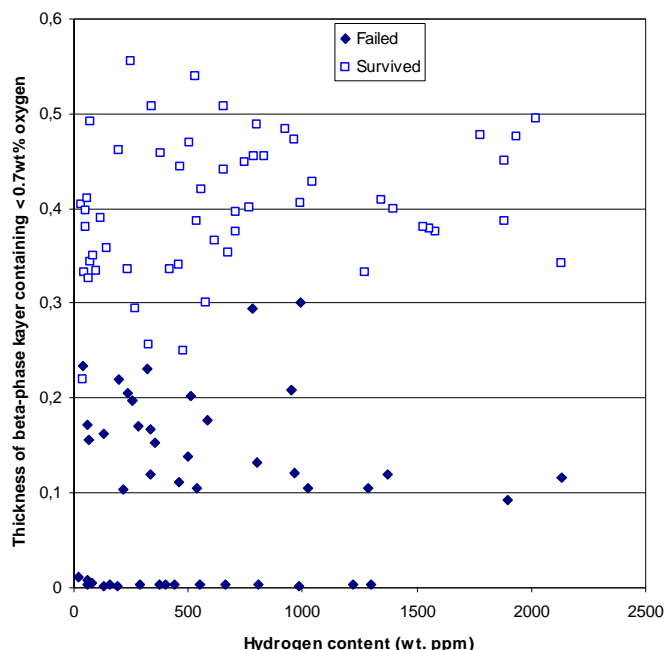
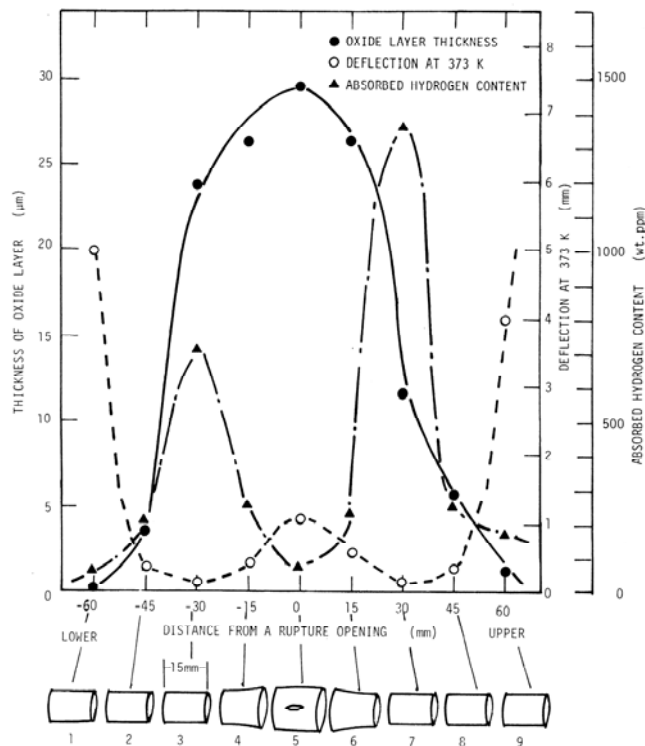


Figure 6.40 shows the distribution of the hydrogen and its effect on the cladding ductility. It is clear that two strong maxima in hydrogen content are formed about 30-40 mm from the rupture opening. At these locations large amounts of hydrogen gas, produced during the rapid oxidation near the opening, are present at the same time as there is little steam present as evidenced by the reduced oxidation at a distance from the opening. Under the heating condition of Kawasaki *et al.*, the axial temperature distribution near the burst is significantly more uniform than in the self-resistance-heating condition of Chung and Kassner [61].

**Figure 6.40 Correlation between distributions of inner surface oxide layer thickness, ring-compression deflection, and absorbed hydrogen content**



The ring compression results show that the hydrogen has a strong embrittling effect on the cladding. Furuta *et al.* also performed ring compression tests on specimens oxidized without any deformation [87]. The results from the two series of tests are compared in Figure 6.41. The samples from the rod-burst tests lie below the 15% oxidation line calculated with the Baker-Just relation. The use of 15% reflects the oxidation limit of the Japanese embrittlement criteria.

Figure 6.42 shows the relationship between the time-temperature parameters of the oxidation and the associated integrated energies obtained from the load-deflection curves to the point of maximum load (i.e. initial cracking) above and below 0.3 J. These were obtained from diametral tube tests at ambient temperature by Chung and Kassner [61] and from ring specimens compressed at 100°C by Kawasaki *et al.* The 100°C-tested ring specimens show a significantly lower failure boundary, in terms of time at temperature to achieve failure, than that of Chung and Kassner. However, Chung and Kassner point out that the different experimental techniques of heating, direct resistance (Chung and Kassner) vs. furnace heating (Kawasaki *et al.*) result in large temperature differences in the ruptured region by fin cooling of resistance heated tubes and such regions have lower oxygen and hydrogen uptake. If the failure characteristics are evaluated in terms of the material parameters i.e. the oxygen distribution and hydrogen uptake instead of time at an apparent temperature, the failure boundaries are similar.

Figure 6.41 Iso-deflection curves obtained on segments of burst cladding and tubes oxidized in steam as functions of oxidation temperature and time

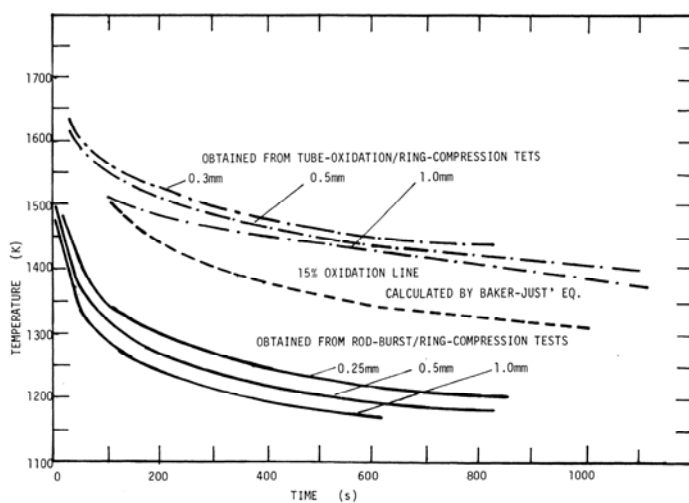
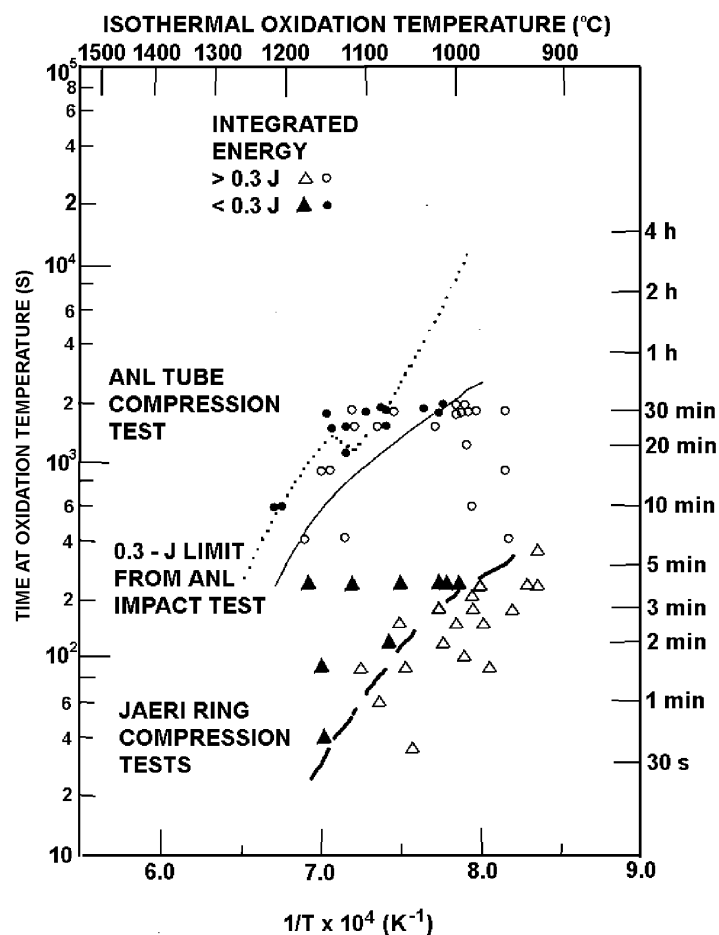


Figure 6.42 Time-temperature oxidation conditions resulting in integrated energies to maximum load above and below 0.3 J from load-vs-deflection curves during slow diametral compression of tube and ring specimens [60] at 300 and 373 K respectively [64]



#### **6.2.4 Comparison of embrittlement in-reactor and out-of-reactor**

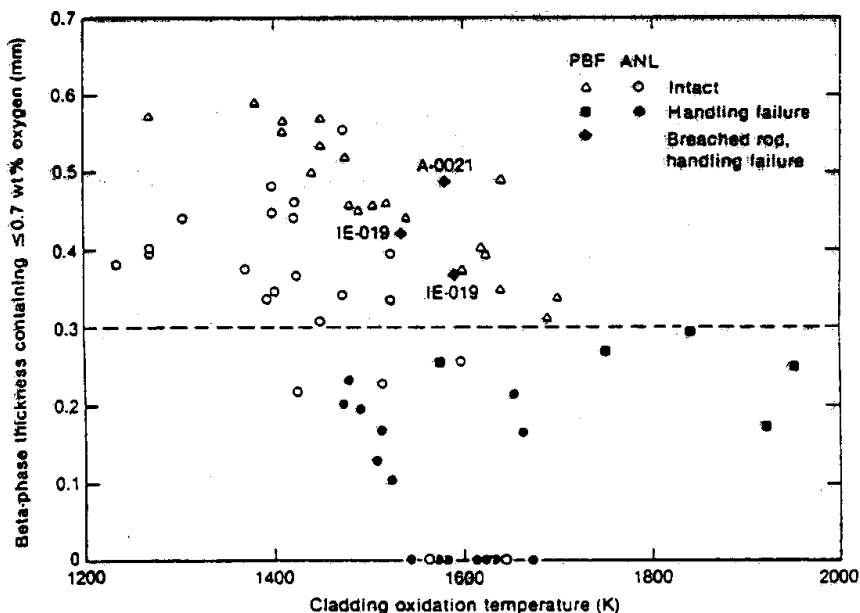
The embrittlement of in-reactor-oxidized and quenched-cladding has been studied in the Irradiation Experiments (IE series) and the Power Coolant Mismatch (PCM series) fuel tests in the PBF reactor at INEL by Hobbins and his coworkers [88-89]. The fuel rods were subject to cycles of film boiling operation at full coolant pressure and subsequent quenching at a cooling rate of ~100 K/s. Some failures were observed after quenching whilst other failures occurred on post-quench handling. The cladding was oxidized on the outer surface by steam and on the inner surface by UO<sub>2</sub>. The nature and kinetics of oxidation of Zircaloy by UO<sub>2</sub> have been investigated by Hofmann *et al.* [90] and Parsons *et al.* [3]. Oxygen embrittlement of the inner surface is considered approximately equivalent to that occurring from steam oxidation on the outer surface. In-reactor equivalent isothermal film boiling temperatures were calculated using observed post-test phase thicknesses and an ideal diffusion oxidation code COBILD (Section 6.3.2). The various oxidation related embrittlement criteria previously considered were determined and Haggag [88] compared the data obtained with the out-of-reactor embrittlement data obtained by Chung and Kassner [61] for cladding quenched at a similar cooling rate i.e. ~100 K/s.

Haggag concluded that the F<sub>w</sub> ≤ 0.5 and the ECR ≤ 17% criteria poorly predict thermal shock failure and do not predict handling failure at all. The in-reactor thermal shock failure was predicted by the Chung and Kassner criterion of 0.1 mm of β-phase with <0.9 wt % oxygen. The handling failures resulting from the in reactor tests were confined to two rods in which the cladding experienced film boiling in the breached condition and the handling failure of these rods was not predicted by any criterion. These rods were considered to be embrittled to a greater extent than intact rods oxidized with similar time temperature parameters. Hydride platelets were observed in the microstructure of these rods and it is suggested [91] that hydrogen influenced the fracture resistance. Chung [92] however pointed out that the calculation of the β-phase oxygen concentration gradient cannot be carried out very accurately for Zircaloy experiencing cycles of non-isothermal film boiling transients and thus comparisons are difficult. It was also noted that Pawel's criteria of 95% saturation and 0.7 wt % oxygen in β-phase accounted for all failures except the PBF handling failure and one ANL handling type failure but did not distinguish between the two phenomena. Haggag finally recommended that the Chung and Kassner criteria should be used for predicting failure either by thermal shock or handling for severe fuel damage experiments i.e. beyond design basis LOCA.

A comparison of the in-reactor and out-of-reactor data for the embrittlement criterion for handling is shown in Figure 6.43. It is seen that it did not work for the rods IE-019 and A-0021. Hobbins *et al.* reported hydrogen contents of 1 000 wppm and 340 wppm respectively for those two rods [89]. This is well above the limit of 50 to 100 wppm necessary to embrittle breached Zircaloy cladding reported by Homma [60].

A different analysis of the failure behaviour of the rods IE-019 and A-0021 has been given recently by Chung [21]. The oxidation temperatures of the four cladding segments, i.e., ≈ 1 262°C (from Rod IE019), ≈ 1 327°C (from Rod IE019), 1 420°C (from Rod IE019), and ≈ 1 307°C (from Rod A0021) were determined by Haggag [88] on the basis of measured thicknesses of the outer-surface oxide layers. These temperatures are, therefore, kind of averaged-out "metallographic foot-print" temperatures. As such, maximum temperatures actually reached by the failed segments were probably somewhat higher. Even if Haggag's estimated temperatures were accurate, Zircaloy-oxygen phase diagram predicts that oxygen concentrations in the β in all four segments were higher than ~0.7 wt %. Furthermore, considering that the large hydrogen content of 340-1 000 wppm increases the solubility of oxygen significantly, it is almost certain that actual oxygen concentrations in all four β layers were higher than ~0.7 wt %. Therefore, the β layer thicknesses containing <0.7 wt % oxygen at such high temperatures of fast diffusion were most likely zero or very small.

Figure 6.43 Failure map for Zircaloy-4 cladding due to handling relative to wall thickness with <0.7 wt % oxygen



Chung also compared the failure-survival behaviour of 33 segments from the PBF tests and from 102 segments from the 0.3-J impact tests performed at room temperature. The failure-survival behaviour was plotted in terms of measured maximum oxidation temperature and equivalent cladding reacted which was determined based on measured thicknesses of phase layers. All of the PBF- and impact-tested segments that had ECR <17% and maximum oxidation temperature of <1 204°C did not fail.

A limited in-pile study has been presented by Katanishi *et al.* [93]. It was performed with test fuel rods in a capsule in the driver core of the NSRR reactor. The test rods were heated by thermal heaters up to about 800°C after which nuclear heating started. The environment was steam. Each test was terminated by bottom flooding. In one of the tests, the cladding surface temperature reached 1 025°C and the rod ruptured after ballooning. The oxidation was about 10% and the rod survived the quenching. In the other test, the maximum temperature was 1 260°C and this rod fragmented at the locations of highest temperature on quenching with 35% of the cladding thickness oxidized. These results are clearly in agreement with current embrittlement criteria. The experiments were analysed with the SCDAP computer code. The SCDAP calculations agreed well with the test results.

### 6.2.5 The effect of constraint during quenching

Kawasaki, Uetsuka, and Fureta have reported results of quenching after rod burst experiments in steam [55-57,87]. The experiment is described in Section 5.2.3. Segments (500 mm long) of pressurised Zircaloy fuel rods were exposed to steam at isothermal temperatures within the range of 900 to 1 300°C. The fuel rods burst during the exposure. The experiment was terminated by bottom flooding at the oxidation temperature or at 500°C. One end of the rod was tightly fixed while the other was connected to the cross head of a tensile test machine. With the cross head fixed the specimen was constrained and the load cell of the test machine could record the resulting load during quench.

The rationale for the experiment is that during a LOCA the rods may be constrained between spacer grids. The design of the PWR fuel bundle is such that the control rod guide tubes are fixed to the spacer grids while the fuel rods are contacting the grid via spacer spring forces. During quenching,

it is expected that the hotter fuel rods will shrink more than the guide tubes so that tensile forces will occur in the fuel rods and compressive forces in the guide tubes. Nagase and Fuketa [94] have performed compressive buckling tests on guide tubes oxidized to ECR values from 13 to 24% according to the Baker-Just correlation. They found that the buckling force is always less than 2000 N. With 11 fuel rods per guide tube, it can be estimated that the maximum tensile force in a fuel rod must be less than 190 N during quenching.

**Figure 6.44 Results from quenching experiments on burst fuel rods**

The results to the left are from unconstrained specimens and the results to the right are from constrained specimens.

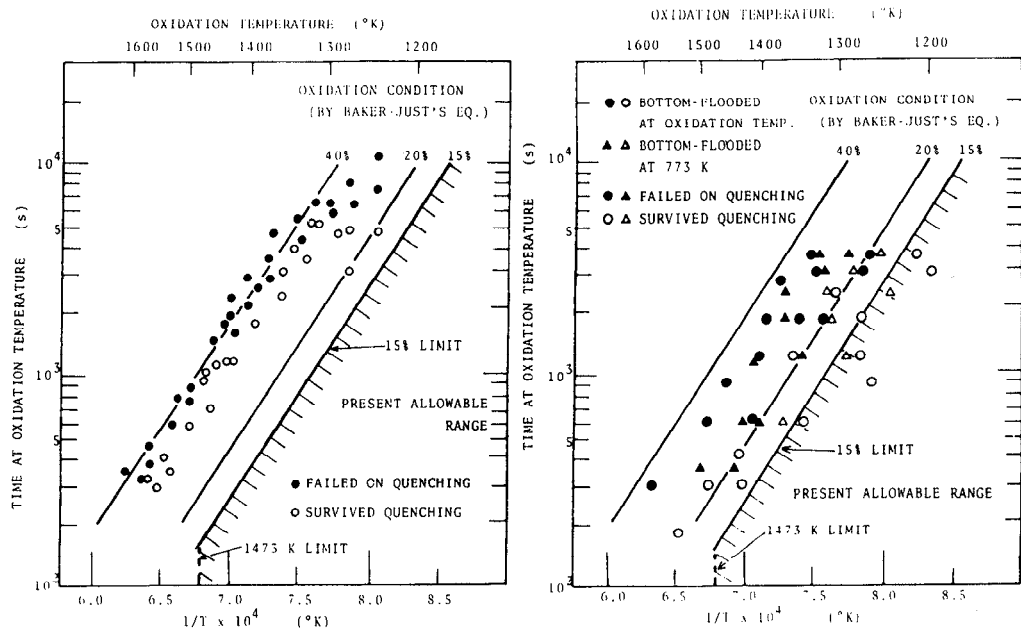


Figure 6.44 shows a comparison between the results from quenching of unconstrained and constrained specimens. The results from unconstrained specimens are in general agreement with the results of Chung and Kassner [61]. The failure boundaries in the maps are calculated as ECR by the Baker-Just equation. At temperature above 1 050°C, the failure boundary is about 38% BJ-ECR while, at lower temperatures, it is about 30%. For constrained specimens, the failure boundary is estimated to be about 20%. As indicated in Figure 6.44, the temperature of start of bottom flooding did not play any significant role for the failure. However, the cooling rates through the  $\beta \rightarrow \alpha$  transformation were very different, about 300 K/s with bottom flooding at the oxidation temperature and 4 K/s with bottom flooding at 500°C. The location of failure was about 50 mm from the rupture location and did not coincide with the maximum hydrogen content. The hydrogen distribution around the rupture was similar to those observed in the rod burst tests with two maxima located at about 60 mm from the burst centre. Evaluation of remaining  $\beta$ -phase showed that it was smaller at the perforation and increased continuously away from the perforation. Therefore, it is speculated that the location of fracture during the quench is a combination of  $\beta$  thickness, oxygen content in  $\beta$  and hydrogen content (note the location of failure did not coincide with maximum hydrogen content). The fracture loads of the specimens that failed on quenching were always below 1.5 kN whereas those that survived quenching and fractured by tension tests always had failure loads exceeding 1.5 kN. Similar experiments have subsequently been performed on pre-hydrided cladding and high burn-up cladding (Section 6.2.6).

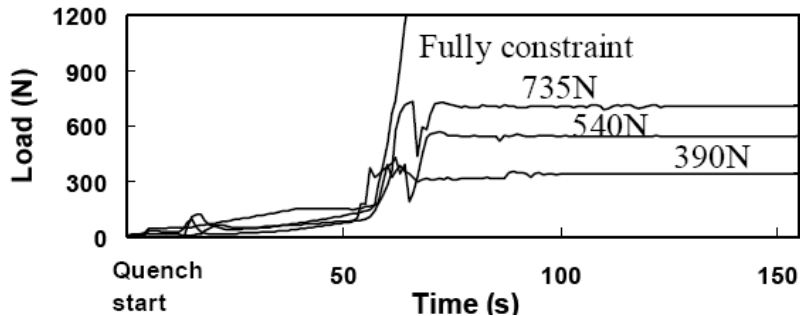
### 6.2.6 Quench embrittlement of pre-hydrided or high burn-up Zircaloy cladding

At high burn-up, especially in a PWR, thick oxide scales are formed. This oxidation is associated with significant hydrogen pickup. An 80 µm thick oxide scale will result in a hydrogen content of about 600 wppm at the hydrogen pickup fraction of 15% which is a representative value. Therefore, it has been considered necessary to perform oxidation and embrittlement tests on pre-hydrided cladding in order to understand LOCA behaviour of high burn-up cladding. To a limited extent it has also been possible to perform confirmatory tests on spent fuel cladding after high burn-up. Nagase and co-workers have reported extensively on quench embrittlement tests on pre-hydrided Zircaloy-4 cladding [48,94-101]. The test equipment was an infrared furnace in which a simulated fuel rod, Zircaloy-4 cladding tube filled with alumina pellets, was enclosed in a quartz tube. In the bottom of the quartz tube, there was a steam inlet for oxidation and a water inlet for bottom flooding. One end of the tube was fixed to the frame of a tensile test machine and in the other end to the mobile cross head of the machine. Testing has been performed in three different modes, totally unrestrained, fixed ends with recording of tensile force during quenching and tests with constant tensile force.

In the tests reported in [94,101], the specimens were filled to a pressure of 5 MPa with Ar. Hydrogen contents studied were 100 to 1200 wppm. Some of the cladding tubes were mechanically thinned 10% to simulate the effect of wall thickness reduction due to oxidation before the transient. The cladding used was low-tin Zircaloy-4 for 17×17 fuel bundles with 9.5 mm outer diameter and 0.57 mm wall thickness or 0.513 mm after the 10% reduction. The whole LOCA sequence with heat-up, rod burst, oxidation in steam and quench by flooding of water was simulated. The heat-up rate was 10 K/s up to the isothermal oxidation temperature of 1 000 to 1 250°C for times between 120 to 5 500 s. Rod burst took place at temperatures from 750 to 800°C during the heat-up. At the end of oxidation, the furnace was turned off and the restraint was applied. The rod was quenched with water from the bottom after slow cooling to about 800°C. The reflooding rate was 30 to 40 mm/s.

Over 200 tests were performed and 95 cladding failures were observed during quenching. Figure 6.45 shows the records of load from four different tests.

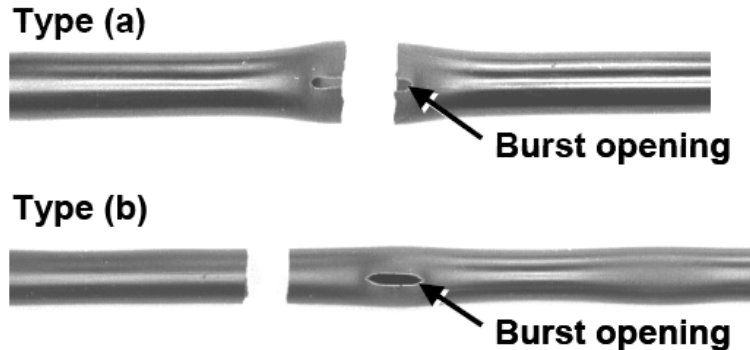
Figure 6.45 Load histories during quench under various conditions of constraint [94,99]



Most failed cladding tubes split into two parts with circumferential cracking, while fragmentation due to severe embrittlement was observed only in tubes oxidized to very high ECR at high temperatures. Typical appearances of failed rods are shown in Figure 6.46.

Type (a) failure occurred in 82 of the 95 failures while type (b) was observed only in a few high ECR tests. This is different from the earlier tests on 14×14 cladding (10.7 mm outer diameter) which tended to fail away from the rupture position as discussed in Section 6.2.5. However, hydrogen analyses showed that also in this thinner cladding the hydrogen distribution had two maxima about 25-50 mm from the burst opening.

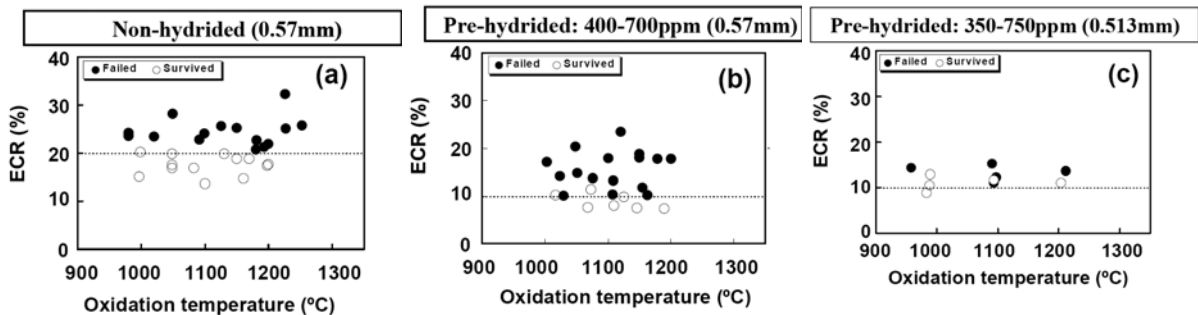
Figure 6.46 Typical post-failure appearances of failed cladding



The amount of oxidation, the ECR value, was calculated with the Baker-Just equation. Both reduction in cladding wall thickness due to ballooning and double-sided oxidation after cladding rupture were taken into account in the calculation. The data in Figure 6.47 (a) agrees very well with previous data on  $14 \times 14$  cladding from ref. [57]. On the other hand, the failure threshold decreases to about 10% ECR-BJ for pre-hydrided cladding tubes as can be seen in (b). The results shown in (c) demonstrate that the failure threshold is unchanged for the thinned cladding simulating loss of wall thickness due to pre-oxidation. If a failure map is plotted in a diagram of oxidation as a function of inverse temperature, the shift of the failure boundary for fully restrained tubes is about 100 K for pre-hydrided tubes in comparison with non-hydrided. For unrestrained tubes, the difference was smaller. The failure boundary for as-received cladding was 46% ECR-BJ while it was 40% for pre-hydrided tubes.

Figure 6.47 Failure maps of cladding tubes tested under fully restrained conditions

- (a) as-received, (b) pre-hydrided tubes
- (c) pre-hydrided with reduced wall thickness



Under full restraint conditions, the pre-hydrided and thinned cladding had fracture loads between 800 and 1800 N. It was judged that realistic restraint conditions probably lies between the non-restrained and fully restrained conditions. Therefore the load levels of 390, 540 and 735 N were chosen for the tests with constant axial loads applied during quenching. Figure 6.48 shows failure maps in terms of ECR-BJ and hydride content for the four different conditions of constraints used in this type of tests.

An important conclusion of the work, illustrated in Figure 6.48, is that when the restraint load is  $<535$  N, the fracture threshold is higher than 20% ECR-BJ, which is sufficiently higher than the 15% ECR-BJ limit in the Japanese ECCS acceptance criteria, irrespective of the hydrogen concentration. This load is also well below the estimated maximum restraint load of 190 N which is estimated based on the buckling load of oxidized guide tubes [94].

Nagase *et al.* have also reported tests on spent high burn-up fuel cladding [95-97,102-104]. The test method is basically the same as for the unirradiated cladding but the length of specimen is reduced to 190 mm. After defueling, the specimens were filled with alumina pellets to simulate the heat capacity of UO<sub>2</sub> pellets. The irradiated cladding segment was tested with a restraint force of about 540 N which corresponds to 30 to 35 MPa based on initial metal cross section. Figure 6.49 shows the results for 6 irradiated specimens from two PWR Zircaloy-4 clad fuel rods irradiated to burn-ups from 39 to 44 MWd/kg compared to unirradiated test results.

**Figure 6.48 Failure maps in terms of ECR and hydrogen content for the four restrained conditions**

(a) 390 N, (b) 535 N, (c) 735 N, and (d) fully restrained [99]

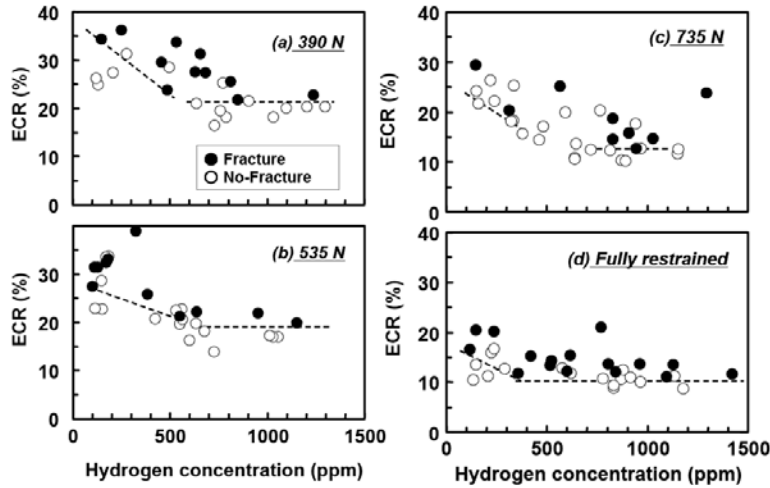


**Figure 6.49 Fracture map in terms of oxidation and initial hydrogen concentration for irradiated and unirradiated cladding with a restraint force of 540 N [95]**

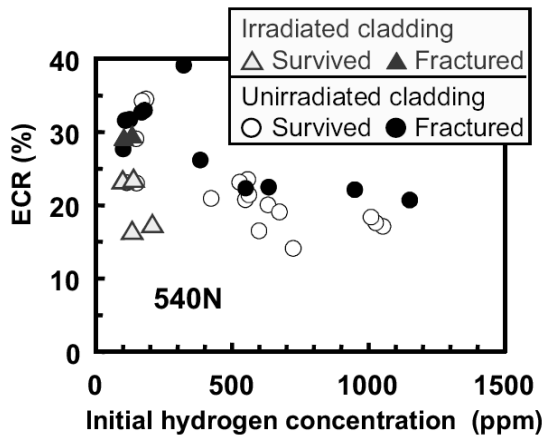


Figure 6.49 shows that there is no significant difference between the irradiated and unirradiated cladding in terms of embrittlement. The irradiated cladding had a relatively low initial hydrogen content, 120-210 wppm estimated from oxide thickness, but picked up a considerable amount after rupture in the LOCA test just like unirradiated cladding.

In a subsequent series of experiments, Nagase *et al.* tested various cladding alloys from fuel rods irradiated to burn-ups from 66 to 77 MWd/kg [102-103]. The tested specimens are summarised in Table 6.4.

Table 6.4 List of the cladding specimens

Sample ID	Reactor	Burn-up (MWd/kg)	Cladding alloy	Corrosion layer (μm)	Hydrogen content (ppm)
MDA-1R	Vandellos 2	76	MDA <sup>a</sup>	51	720
MDA-2R		76		62	838
ZIR-2R	Ringhals	71	ZIRLO <sup>TM</sup>	51	496
ZIR-3R		77		79	764
MFI-1	McGuire / R2	66	M5®	6	73
MFI-2		66		7	69
NDA-1	Leibstadt	69	NDA <sup>b</sup>	33	214
ZRT-1	Zircaloy-2 / LK3 <sup>c</sup>	66		30	297
ZRT-2		73		25	182

a Mitsubishi Developed Alloy (Zr-0.8Sn-0.2Fe-0.1Cr-0.5Nb) developed by Mitsubishi Heavy Industries, Ltd.

b New Developed corrosion resistance Alloy (Zr-1.0Sn-0.27Fe-0.16Cr-0.1Nb-0.01Ni) was developed by Nuclear Fuel Industries, Ltd. and Sumitomo Metal Industries, Ltd.

c Cladding material of Westinghouse Electric Sweden AB [105].

The rod is heated up at a rate of 3 to 10 K/s. Steam introduction is started prior to the heat-up, and the steam flow is maintained at a supply rate of about 40 mg/s during the oxidation. The cladding specimen balloons and ruptures during the heat-up, with both an increase in rod internal pressure and a decrease in cladding strength. The rod is isothermally oxidized after the rupture. After the isothermal oxidation, the rod is cooled in the steam flow to about 970 K and is finally quenched with water flooding from the bottom (Section 5.2.3).

The results of the tests are summarised in Table 6.5. As can be seen in the table, only one specimen failed during the quench after oxidation, MDA-2R. The probable cause of failure is the higher oxidation level in this specimen compared to the others. This leads to a higher hydrogen concentration at the rupture position compared to the other rods with a lower ECR value. Somewhat mysteriously no rupture during the heatup could be observed for the rod

Table 6.5 Summary of LOCA-simulated experiments

Sample ID	Rupture temp. (K)	Circumferential increase (%)	Oxidation temp. (K) <sup>a</sup>	Oxidation time (s)	Oxidation amount ECR (%) <sup>c</sup>	Restraint Load (N)	Fracture / No-fracture
MDA-1R	988	9.9	1 480	131	18.3 (16.4)	<350	N.F.
MDA-2R	-	6.1	1 463 <sup>b</sup>	719	38.0 (35.6)	530	F.
ZIR-2R	945	28.0	1 473	228	27.3 (20.8)	518	N.F.
ZIR-3R	949	20.6	1 459	153	20.2 (16.4)	519	N.F.
MFI-1	1 053	20.1	1 470	151	19.5 (15.9)	<400	N.F.
MFI-2	1 035	19.2	1 469	229	23.6 (19.5)	0 <sup>d</sup>	N.F.
NDA-1	988	8.9	1 467	280	22.5 (20.4)	518	N.F.
ZRT-1	1 036	17.7	1 468	222	21.2 (17.7)	519	N.F.
ZRT-2	1 051	20.6	1 467	232	22.0 (17.9)	0 <sup>e</sup>	N.F.

a. Oxidation temperature at rupture position except for MDA-2R.

b. Oxidation temperature at fracture position.

c. Calculated with the Baker-Just equation with oxidation temperature and time, for reduced metallic thickness after ballooning. The value in parenthesis is ECR for the initial metallic thickness before ballooning.

d. Accidentally not restrained due to failure of specimen fixing.

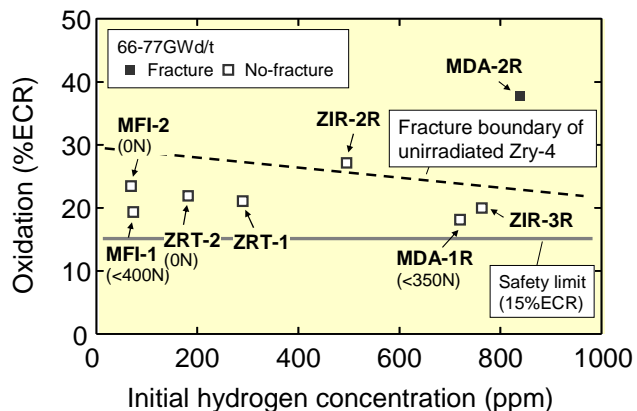
e. Intentionally not restrained considering the construction of the BWR fuel bundle.

MDA-2R. However metallographic examination of the rod showed oxidation on the inside so a small rupture opening must have been present.

Metallographic examination of the oxide layers showed that the preformed oxide has a protective effect on the high-temperature oxidation in steam. However, the preformed oxide cracks during the initial ballooning and steam penetrates through the cracks. Therefore, the extent of high-temperature oxidation is equivalent at the outer and inner surface after a longer period. Hydrogen distributions in the specimens were similar to those observed in unirradiated specimens with maxima located about 20 mm from the rupture openings.

Figure 6.50 shows a fracture/no fracture map over the results. The dashed line for unirradiated material shows how pre-hydriding reduces the fracture boundary for unirradiated cladding. The fracture of the MDA-2R rod is consistent with the fracture criteria of the unirradiated cladding with similar hydrogen concentration. From the results of the other specimens oxidized to 18.2-27.2% ECR, it is concluded that the fracture threshold is not reduced significantly by high burn-up or use of new alloys at this burn-up level, though the restraint load was lower than planned in some of the tests. The most important conclusion from these tests on high burn-up cladding is that the fracture boundary of the high burn-up cladding is sufficiently higher than the 15% limit in the Japanese ECCS acceptance criteria.

**Figure 6.50 Fracture/no-fracture conditions, relevant to ECR value and initial hydrogen concentration**



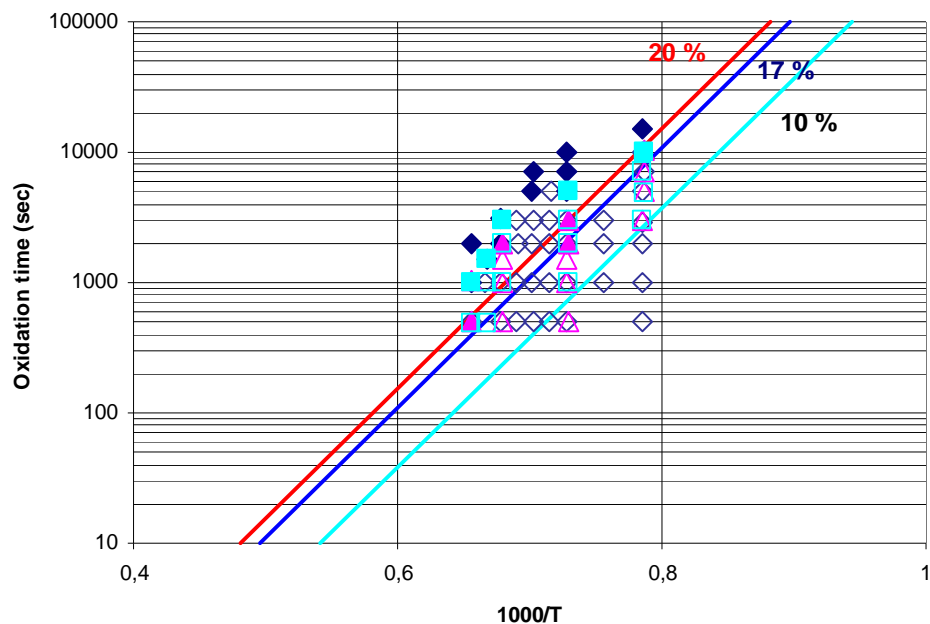
Nagase and Fuketa have discussed the mechanism of embrittlement that causes cladding failure at quenching [99]. As discussed previously, it is the properties of the prior  $\beta$ -phase which controls the ductility. In this part of the microstructure there are no hydride platelets present like those present after irradiation. Uetsuka *et al.* [106] have determined by TEM examination and X-ray analysis that the hydride is present as fine  $\delta$ -zirconium hydrides smaller than 1  $\mu\text{m}$  on the  $\alpha'$  grain boundaries. Nagase and Fuketa therefore conclude that similar fine  $\delta$  hydrides are densely distributed in the prior  $\beta$ -phase region in the pre-hydrided claddings and that the density of hydrides and the extent of embrittlement is higher in the cladding with a higher hydrogen concentration. Another important factor is the effect of hydrogen on the  $\alpha/\alpha+\beta$  and  $(\alpha+\beta)/\beta-\pi\eta\alpha\sigma\epsilon$  boundaries. Observations show that the phase boundaries are shifted to lower temperatures when hydrogen is added to the Zr-O binary system. This would lead to a higher oxygen content in the  $\beta$ -phase and thus increase the embrittlement when the  $\beta$  transforms to  $\alpha$ . Some support for this idea comes from observations of fracture surfaces of embrittled cladding with different levels of hydrogen concentrations. On the cladding with higher hydrogen concentration, there are more glossy surfaces of fractured  $\alpha'$  than on the cladding with much less hydrogen concentration.

Kim *et al.* have also studied the effect of restraint [107]. A cladding tube of 350 mm in length was heated by an electric current and oxidized isothermally in steam. At the end of oxidation the temperature was reduced to 700°C where a hold time of 100 s was applied before the specimen was

quenched by bottom flooding with room temperature water. Experiments were conducted without any restraint and with a full restraint in which the length of the specimen was kept constant throughout the test. In one test series, a partial restraint was applied. The specimens were allowed to deform freely during the isothermal oxidation but a restraint was applied before start of cooling to 700°C and the subsequent quench. Figure 6.51 shows the result of the tests in a failure map where it has been noted whether or not the specimen failed during the quench. The straight lines represent ECR-BJ levels calculated according to the Baker-Just correlation. The results show that both for unrestrained and partially restrained specimens there is a sufficient margin to the 17% limit according to the Baker-Just correlation. For the fully restrained specimens, a few failures have occurred below the 17% limit. The relevance of the fully restrained test is however in some doubt, although the condition could be close to a limiting situation where spacer grids may completely lock up the fuel rod or when oxide build-up near the spacer grids may prevent the rod to elongate, e.g., at high burn-up. During the oxidation phase of a ballooned, burst, and bent PWR cladding in a LOCA, the rod may elongate significantly without further bending. Since elongation was hindered in the test of Kim *et al.*, the specimens bent during oxidation which may have resulted in non-uniform deformations and also extra stresses due to bending moments in the quench phase of the experiment.

**Figure 6.51 Quench survival/failure of isothermally oxidized Zircaloy-4**

Diamonds = unrestrained tests, Squares = partially restrained tests,  
Triangles = fully restrained tests. Filled symbols represent failures [107] [25,108]



### 6.2.7 Recent post-quench ductility tests of Zircaloy, ZIRLO and M5 cladding

In the last several years there has been considerable testing of the post-quench ductility of current cladding alloys. In the case of Zircaloy, the objective has been to determine the effects of the changes in fuel rods associated with high-burn-up operation, such as, thick corrosion layer, high hydrogen concentration, and pellet-cladding bonding. M5 and ZIRLO are relatively new alloys and data on their LOCA behaviour at all levels of burn-up are needed for safety assessment of fuel fabricated from this new class of cladding.

At Argonne National Laboratory, specimens of all three alloys have been tested in the same equipment which makes the results intercomparable with regard to the performance of the different alloys [109-116]. During the course of that work, it was recognised that measured oxidation (weight

gain) is not a good parameter for characterising embrittlement. It is well known that embrittlement is caused by the diffusion of oxygen into the metal underneath the surface oxide rather than by the surface oxide itself. In other words, the time required to accumulate, say 17%, oxidation on the surface is just a measure of time required to diffuse enough oxygen into the underlying metal to embrittle it. Thus a more direct time-related parameter is better than a measured value of oxidation, particularly when the actual oxidation or weight gain is affected by breakaway or spalling that would not affect oxygen diffusion in the metal. Hence in all recent embrittlement work at Argonne, a calculated oxidation value has been used rather than a measured value. The Cathcart-Pawel (CP) correlation [47] was chosen for that calculation, and equivalent-cladding-reacted oxidation values (ECR) are given as CP-ECR.

One of the first discoveries in that research was that the embrittlement threshold for unirradiated Zircaloy (Zr-1.4%Sn) is not fixed at exactly 17% as assumed in U.S. regulations. This can be seen in Table 6.6, which shows test results for a number of cladding materials, including three different manufacturing quantities of Zircaloy-4 that exhibit thresholds from 15.6 to 19%. The cladding types M5 and E110 are also nominally the same alloy (Zr-1%Nb), yet they too exhibit very different embrittlement thresholds (see next section). Although multiple batches of Zircaloy-2 and ZIRLO were not examined, these two different alloys showed embrittlement thresholds (19%) that are very similar to the other modern cladding materials that are manufactured with similar techniques. The variations in embrittlement threshold are thus seen to result mainly from manufacturing differences rather than from specific alloy composition.

**Table 6.6 Variation of embrittlement threshold** (percent equivalent cladding reacted)  
for unirradiated zirconium-alloy cladding materials oxidized in steam at 1 200°C

Alloy and Geometry	Manufacturer	Vintage	Threshold (CP-ECR)
Zircaloy-4, 15×15	Siemens	Old, H. B. Robinson	15.6
Zircaloy-4, 17×17	Westinghouse	Current, low tin	17
Zircaloy-4, 15×15	Areva	Current, low tin	19
Zircaloy-2, 10×10	Global Nuclear Fuel	Current, Zr liner	19
ZIRLO, 17×17	Westinghouse	Current, standard tin	19
M5, 17×17	Areva	Current	20

Additional tests were performed at Argonne with unirradiated samples that had been charged with hydrogen, the so-called prehydrated specimens. Results from these tests show a strong effect of hydrogen concentration as seen in Figure 6.52 for Zircaloy-4 cladding. Although oxygen diffusion into the metal is still responsible for embrittlement, hydrogen accelerates the diffusion rate, increases the solubility of oxygen in the  $\beta$  phase, and speeds up the embrittlement process. A cooling-rate effect was also seen that was absent in fresh cladding that contained no hydrogen.

Similar tests were then performed on irradiated cladding taken from high-burn-up fuel rods with Zircaloy-4, ZIRLO, and M5 cladding. As expected, the embrittlement thresholds in the irradiated materials were also found at substantially lower oxidation levels as seen in Figure 6.53 for the Zircaloy-4 cladding. Because the hydrogen that is absorbed during normal operation comes from the dissociation of water during corrosion, cladding materials that corrode more readily tend to embrittle more readily. Hydrogen pickup fractions vary from one material to another, however, such that the effect is characterised more precisely by hydrogen concentration than by CP-ECR as shown. Testing has also shown that the effectiveness of the hydrogen in irradiated material is also altered by the cooling rate at the end of a LOCA transient.

**Figure 6.52 Embrittlement threshold at 135°C**  
as a function of hydrogen content for prehydrated unirradiated Zircaloy-4 oxidized  
at 1 200°C and either quenched at 800°C or cooled without quench

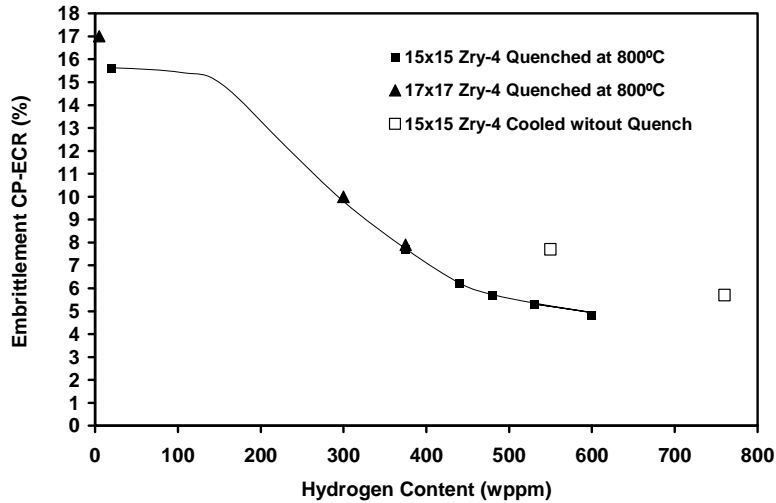
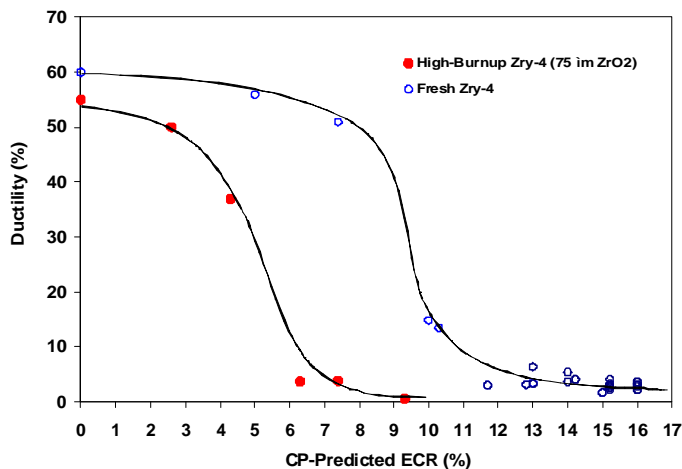
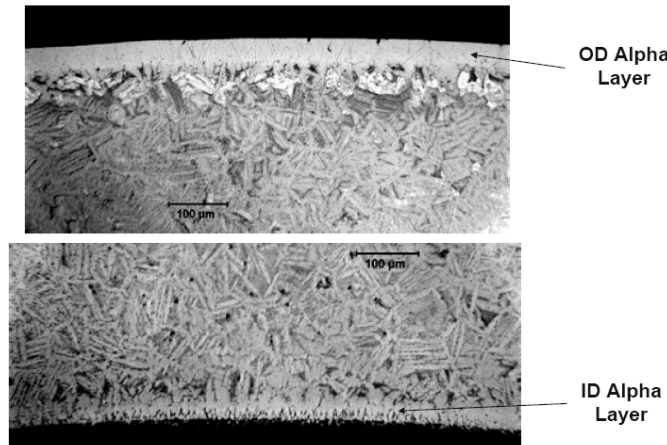


**Figure 6.53 Ductility at 135°C after oxidation in steam at 1 200°C and  
cooled slowly for irradiated and unirradiated Zircaloy-4 cladding**



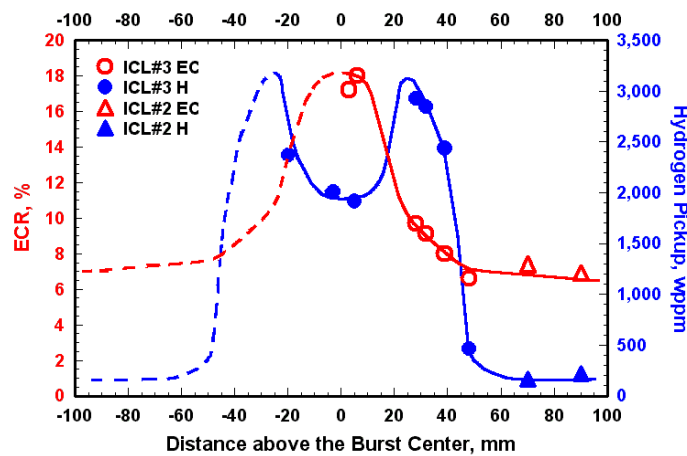
Another conclusion for high-burn-up fuel from the Argonne work was that oxygen can diffuse into the cladding metal from the inside diameter (ID) as well as from the outside diameter (OD), even when no steam oxidation is occurring on the ID. This can be seen in Figure 6.54, where an ID  $\alpha$  layer is clearly visible in a specimen that was oxidized only on the OD. The ID oxygen diffusion phenomenon was discovered in the United States of America in 1977 [89], confirmed by tests in Germany in 1979 [117], and seen in the Argonne results. Oxygen diffusion has always been associated with ID oxidation in the ballooned region where steam enters the rupture opening. In high-burn-up fuel, however, there will usually be a zirconium oxide layer on the cladding ID even far away from the balloon as the result of bonding between the UO<sub>2</sub> fuel pellets and the cladding. This oxygen source can be just as effective as a steam-oxidation layer in providing oxygen for diffusion into the cladding metal. Thus, two-sided oxygen diffusion has to be accounted for in some cases to accurately predict the onset of embrittlement.

**Figure 6.54 High-oxygen  $\alpha$  layer on the ID resulting from oxygen diffusion from the  $\text{ZrO}_2$  fuel-to-cladding bond following OD steam oxidation at 1 200°C**



In other tests at Argonne with high-burn-up fuel rods (cladding and fuel pellets), enhanced hydrogen absorption was observed near the cladding balloon as seen in Figure 6.55. This observation confirms the work of others in the 1980s (Sections 6.2.3 and 6.2.6). Hydrogen from dissociating water is trapped inside the balloon and is then absorbed in the metal. Just as with breakaway oxidation, this hydrogen results in rapid embrittlement, but embrittlement in this case is localised near the balloon. Thus the balloon may not retain ductility even when two-sided oxygen diffusion is limited as, for example, by the U.S. regulations. Although it does not appear that ductility could be assured in a balloon with reasonable criteria, there are extenuating circumstances. Based on the work at ANL, fragmentation has never been observed in the ballooned region in quench tests; fracturing in the ballooned region has not been observed in quench tests without externally applied loads; and the ballooned region is generally only a few inches long such that a fractured rod would still retain most of the  $\text{UO}_2$  fuel pellets (a major objective of safety regulations).

**Figure 6.55 Measured hydrogen and oxygen content in in-cell (ICL) tests on high-burn-up BWR Zircaloy-2 fuel rods**



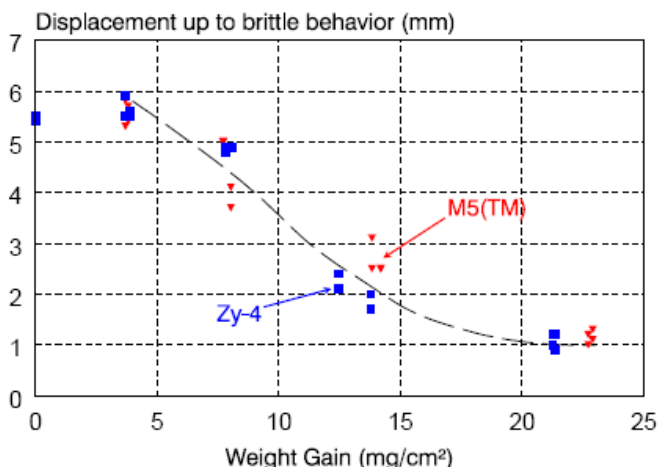
French work on the post-quench ductility of low-tin Zircaloy-4 and M5 alloy and to a lesser extent on the M4 alloy has been reported by Brachet *et al.* [41], Portier *et al.* [24], Mardon and Waeckel [23], Mardon *et al.* [22] and most recently by Mardon and Dunn [118] and Brachet *et al.* [49].

Brachet *et al.* [41] oxidized 150 mm long specimens on the outside in the DEZIROX facility. This is a tube furnace in which the specimen hangs on a wire. The oxidation can be terminated by letting the specimen fall into a bowl of water, a method of direct quenching without simulation of slow cooling. It is arranged so that spalled oxide can be collected and weighed together with the specimen. The oxidation was done in steam at a temperature of 1 100°C to various weight gains up to ~17% ECR. It was noted that no failure occurred in this range of ECR during the quench. After the quench, specimens were prepared for ring compression tests, three-point bend tests, and impact tests. Hydrogen analyses showed that only a small amount of hydrogen pickup had occurred during oxidation.

Figure 6.56 shows the results of ring compression tests. Unfortunately the “residual ductility parameter” is not defined in the paper and does not agree with the definition discussed in Section 5.1.4.1. Since it contains the elastic deflection, the curve is not directly comparable to the corresponding results from Argonne National Laboratory. A comparison would also necessitate translation of the weight gain to ECR. For translation of weight gain (Wg), Billone [109] has given the following formulae where  $h$  is tube wall thickness and  $D$  outer diameter of tube:

- Outer surface oxidation:  $ECR = (0.4385Wg/h)/(1-h/D)$ .
- Double-sided oxidation:  $ECR = 0.8769Wg/h$ .

**Figure 6.56 Residual ductility parameter derived from the ring compression test as a function of weight gain at 1 100°C**



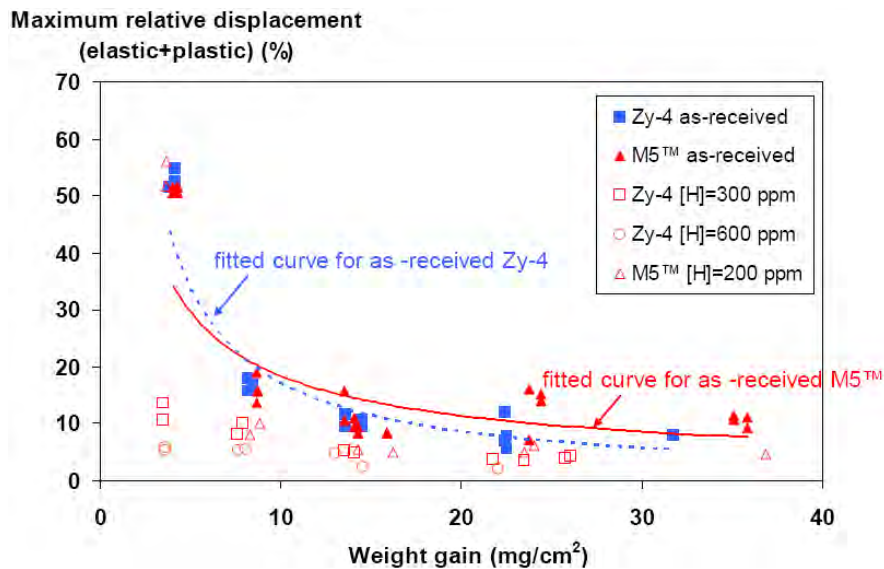
Since M5 and Zircaloy-4 have different wall thicknesses [24], there will be a small relative movement of points if Figure 6.55 is expressed in terms of ECR. Approximately 10 mg/cm<sup>2</sup> corresponds to 8.2% ECR.

The three-point bend tests which results in a sharper defined failure point than the ring compression test (Section 5.1.4.3) did not reveal any differences between M5 and Zircaloy-4. However the impact tests revealed a small difference in ductility between M5 and Zircaloy-4 at a weight gain of about 13 mg/cm<sup>2</sup>. A similar small difference can be seen at the same weight gain in the ring compression test (Figure 6.55) with Zircaloy having the lower ductility. Brachet *et al.* [41] performed a very thorough metallographic examination with microprobe analysis of different microstructural features. In particular they found that the prior  $\beta$ -phase in Zircaloy-4 contained 5 500-6 000 ppm of oxygen and had a hardness of 330-370 HV(50g). M5 oxidized at the same temperature, 1 100°C, and for about the same time, 3 600 s compared to 3 000 s had an oxygen content of 2 000-4 000 ppm and a hardness of 260-300 HV(50g). This can explain the somewhat better ductility of M5 compared to Zircaloy-4 in the room temperature tests. Note that the oxygen concentrations include an unknown amount due to the presence of a thin oxide film on the specimens used for analysis.

Subsequent to the previous work, the electron microprobe technique has been improved and it is estimated that the data obtained for oxygen concentrations in later work have an uncertainty of -500 to +1 000 ppm [49].

The results of Brachet *et al.* [41] was extended to other oxidation temperatures, 1 000 and 1 200°C and to pre-hydrided material by Portier *et al.* [24] using the same techniques. Figure 6.57 shows the results of ring-compression tests at room temperature on specimens oxidized at 1 200°C.

**Figure 6.57 Room temperature ring compression tests on as-received and pre-hydrided M5 and low-tin Zircaloy-4 after oxidation and quench at 1 200°C**



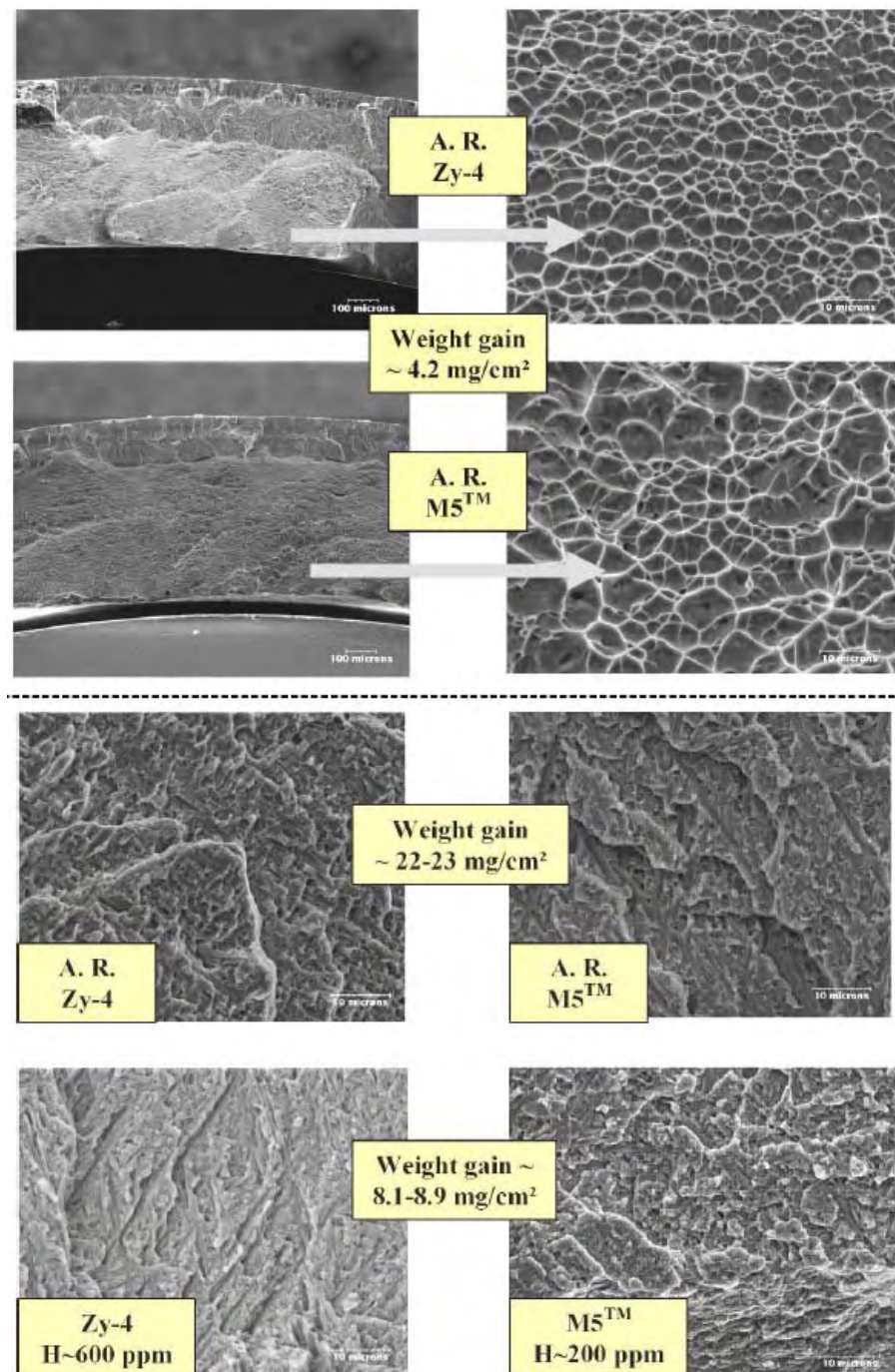
Basically similar results were obtained in the three-point bend test. The effect of pre-hydriding is very clear. The hydrogen levels chosen correspond well with actual hydride contents found in high burn-up cladding used by Portier *et al.* in clad deformation tests [24]. In the case of Zircaloy-4, the hydrogen content was measured to  $433 \pm 120$  ppm after 5 cycles while M5 had a hydrogen content of 58–63 ppm after 6 cycles.

Figure 6.58 shows examples of the fractography of Charpy impact tested materials. The fractography concerns the prior  $\beta$ -phase since both oxide and  $\alpha$ -phase were completely brittle in the experiments. At low weight gains, the oxygen had not had time to diffuse into the  $\beta$  phase and the resultant fracture is a ductile dimple fracture. At higher weight gains, the fracture is quasi-brittle in both the as-received materials and in the pre-hydrided materials. In order to gain a better understanding of the fracture behaviour, Portier *et al.* performed oxygen analyses and hardness testing on the prior  $\beta$ -phase. In order to avoid the problem with oxygen contamination of the surface discussed by Brachet *et al.* [41], Portier *et al.* used nuclear reaction analysis (NRA) with ions accelerated in a Van de Graaf accelerator. Deuteron ions are accelerated into the target where the  $^{16}\text{O}(\text{d},\text{p})^{17}\text{O}$  reaction takes place. The number of detected protons permits calculation of the bulk oxygen content.

Further French work has been aimed at elucidating the effect of dissolved hydrogen as reported recently by Brachet and coworkers [119]. Two other questions have also been studied:

- The influence of a pre-existing OD (and ID) zirconia layer on the transient HT oxidation kinetics (Section 6.1.7) and the post-quench mechanical behaviour.
- The influence of the final cooling scenario and in particular the effect of cooling rate from the high-temperature oxidation phase to the quench temperature.

Figure 6.58 Typical fractographs of the internal prior  $\beta$ -phase layer of Charpy impact tested as-received and pre-hydrided material



In order to obtain basic embrittlement data impact tests (Section 5.1.4.4, Figure 5.20) were performed on Zircaloy-4 and M5 specimens oxidized at  $1250^\circ\text{C}$  for two different times. At the shorter time, 120 s, the fracture surface of the prior  $\beta$  phase was divided in one brittle part and one ductile part. At the longer time, 300 s, the whole fracture surface of the prior  $\beta$  phase was brittle with the exception of a thin layer on the inside surface of the M5 specimen. EPMA analysis of the oxygen concentration over the prior  $\beta$  layer showed that the transition to brittle behaviour occurred at 0.3-0.4 wt % O.

This is in good agreement with results of Stern *et al.* [120] who oxidized sheet specimens of Zircaloy-4 and M5 and subsequently homogenised the material in order to determine the mechanical properties of prior  $\beta$ -phase with different oxygen contents. For oxygen contents of 0.25 wt % and higher the material showed a brittle-ductile transition in tension testing. The transition temperature increased with increasing oxygen content, from -50°C at 0.25 wt % oxygen to 100°C with 0.9 wt % oxygen. For high oxygen contents typical of oxygen stabilised  $\alpha$ -phase,  $\sim>2.4$  wt %, the material was brittle at all tested temperatures. There was no significant difference between Zircaloy-4 and M5 with respect to the influence of oxygen on the mechanical properties of prior  $\beta$ -phase.

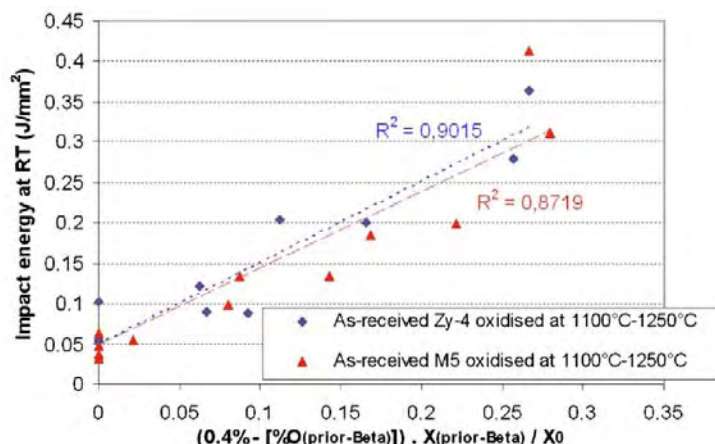
Brachet *et al.* [49] also characterised the prior  $\beta$  phase with regard to microhardness and confirmed the previously known quasi-linear relationship between microhardness and oxygen concentration in the  $\alpha$  phase. These relations can then be used to estimate oxygen content by microhardness measurements. The critical Vickers microhardness for brittle behaviour in the RT impact test was determined to be  $\sim 350 \pm 25$  for Zircaloy-4 and  $\sim 325 \pm 25$  for M5, both values corresponding to  $\sim 0.3$  wt % O.

RT impact test results on materials oxidized at 1 100, 1 200, and 1 250°C to ECR levels ranging from  $\sim 3$  to  $\sim 20\%$  were analysed with regard to thickness of prior  $\beta$  layer as determined by SEM BSE imaging and to the average prior  $\beta$ -πηασε layer average oxygen content as determined by EPMA or microhardness measurements. The result could be expressed as a correlation parameter K given by Eq. 6-6:

$$K = 0.4\% - [O]_{prior-\beta} \cdot X_{prior-\beta} / X_0 \quad (6-6)$$

where  $[O]_{prior-\beta}$  is the average oxygen concentration in the prior  $\beta$  layer,  $X_{prior-\beta}$  its thickness, and  $X_0$  the initial clad wall thickness. Figure 6.59 shows the measured impact energy as a function of the correlation parameter K. An energy of 0.1 J/mm<sup>2</sup> or less is regarded as brittle behaviour.

Figure 6.59 Impact energy vs the correlation parameter K defined in Eq. 6-6



Previous work had shown that hydrogen increased the oxygen solubility in the  $\beta$  phase [24]. The effect was verified by thermodynamic calculations with the Thermo-Calc software [121] using a specially prepared database for zirconium alloys, "Zircobase", [122]. The calculations indicated an oxygen solubility increase at 1 200°C of  $\sim 3\,000$ - $3\,500$  ppm due to hydrogen. The effect of hydrogen on the post-quench ductility of pre-hydrided zirconium alloys is thus two-fold: (1) the direct effect due to embrittling hydride platelets, and (2) the increased oxygen content in the prior  $\beta$ -phase.

Brachet *et al.* [49] determined what they called the intrinsic hydrogen effect by carrying out short oxidation treatments at 1 000°C followed by a quench to room temperature. In that way, the influence

of oxidation, <0.5% ECR, on the impact test result will be negligible and the ductility only dependent on the hydrogen content of the prior  $\beta$  phase. For hydrogen contents up to ~600 ppm they found that the post-quench impact energy, KCV, depended on hydrogen concentration as:

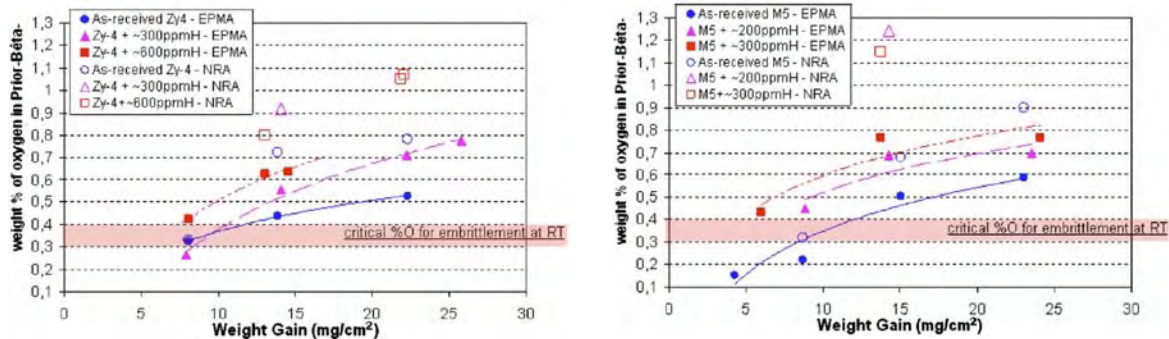
$$KCV \sim 0.4 \exp(-0.003[H]) \quad (6-7)$$

where [H] is the hydrogen concentration in ppm. The mechanism behind the embrittlement is uncertain since the microstructure contains no hydrides visible by LOM or SEM. It is thought that small hydride plates only visible by TEM lie behind the embrittlement, a hypothesis which still has to be confirmed by TEM examinations.

The effect of hydrogen on oxygen solubility has consequences of almost autocatalytic character. The first fact to take into account is that under normal high-temperature steam oxidation conditions little hydrogen is picked up or lost from the cladding material. Due to the  $\beta$  stabilising character of hydrogen, almost all hydrogen will accumulate in the  $\beta$  phase. When the  $\beta$  is consumed by growth of  $\alpha$  phase, the hydrogen concentration increases in the  $\beta$  phase. The increased hydrogen concentration leads to a higher oxygen concentration in the  $\beta$  phase at the  $\alpha/\beta$ -phase boundary and thus to a more rapid diffusion of oxygen into the  $\beta$  phase due to the increased concentration gradient. Figure 6.60 shows how the average oxygen concentration in the prior  $\beta$  phase varies with weight gain at various hydrogen contents [49].

**Figure 6.60 Evolution of prior  $\beta$  phase oxygen content (mean value) of as-received and prehydrided Zircaloy-4**

(a) and M5 (b) alloys vs. the weight gain after oxidation at 1 200°C [49]



On the basis of these results a new correlation parameter for the impact test results on as-received and pre-hydrided cladding was defined. The new parameter  $K'$  which combines the intrinsic hydrogen effect with the hydrogen effect on oxygen solubility is defined as:

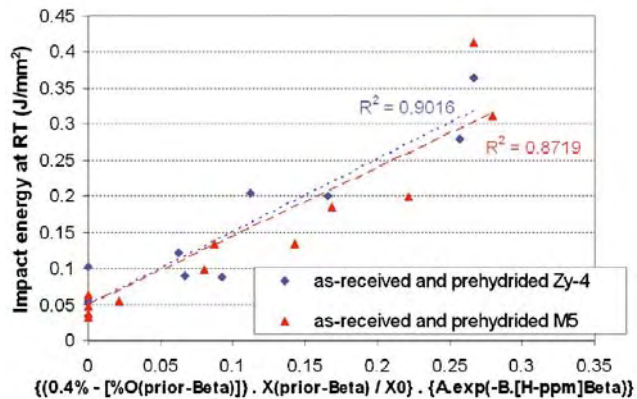
$$K' = K \cdot 0.4 \cdot 0.4 \exp(-0.003[H]_{\beta}) \quad (6-8)$$

where  $K$  is the parameter defined in eq. (6-6) and  $[H]_{\beta}$  is the final hydrogen concentration in the  $\beta$  phase. Taking into account that all initial hydrogen is located in the residual  $\beta$  phase  $[H]_{\beta}$  is given by

$$[H]_{\beta} = [H]_0 - X_0 / (1/2X_{\alpha+\beta} + X_{\beta}) \quad (6-9)$$

where  $[H]_0$  is the initial hydrogen content,  $X_0$  the initial wall thickness,  $X_{\alpha+\beta}$  the thickness of the two-phase layer (small in Zircaloy-4, bigger in M5), and  $X_{\beta}$  the thickness of the residual  $\beta$ -phase layer. Figure 6.61 shows the full correlation between the impact energy and  $K'$  for specimens oxidized at 1 100-1 250°C to a range of ECR from ~3% up to ~17-20%.

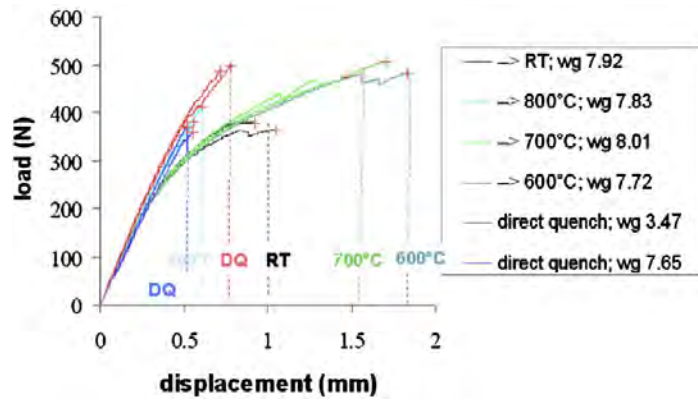
Figure 6.61 Full correlation between the impact energy, the oxygen and hydrogen contents, and the correlation parameter K' [49]



The study of the effect of pre-oxidation to  $\sim 5$  and  $\sim 15 \mu\text{m}$  thickness showed that this pre-oxidation had no effect on the post-quench ductility despite the fact that the weight gain during the transient was reduced considerably compared to as-received cladding. The absence of the effect is relatively easy to understand. It is the oxygen diffusion into the cladding which controls the ductility. What happens is that in the initial stages of the transient the thermodynamically unstable (in relation to oxygen deficient  $\alpha$  phase) pre-oxide dissolves at the oxide/ $\alpha$  interface and works as an oxygen source. Thus the oxygen stabilised  $\alpha$  layer thickness and the consequent diffusion of oxygen into  $\beta$  is more or less unchanged in comparison with as-received cladding with similar hydrogen content.

Brachet *et al.* also performed a study on the post-quench ductility effect of cooling scenario on pre-hydrided cladding from oxidation at  $1200^\circ\text{C}$ . They used a direct quench, and a quench after furnace cooling in the DEZIROX facility to  $800$ ,  $700$ , and  $600^\circ\text{C}$ . They also included a specimen furnace cooled to room temperature. Figure 6.62 shows the results of ring compression tests on specimens subjected to these scenarios.

Figure 6.62 Results of ring compression tests at  $135^\circ\text{C}$  after various cooling scenarios



The figure shows that the cladding has the highest ductility after cooling to  $700$  and  $600^\circ\text{C}$  before quench. Direct quench or quench from  $800^\circ\text{C}$  results in relatively brittle behaviour and furnace cooling to room temperature leads to more brittle behaviour than quench from  $700$  and  $600^\circ\text{C}$ . Microstructural studies have shown that the oxygen concentration in the prior  $\beta$  phase is quite uniform for the directly quenched specimens and that a separation between  $\alpha$  and prior  $\beta$  has occurred in the specimen cooled from  $800^\circ\text{C}$ . In the specimens quenched from  $700$  and  $600^\circ\text{C}$  the oxygen concentration is again more uniform but a precipitation of iron and chromium rich particles has

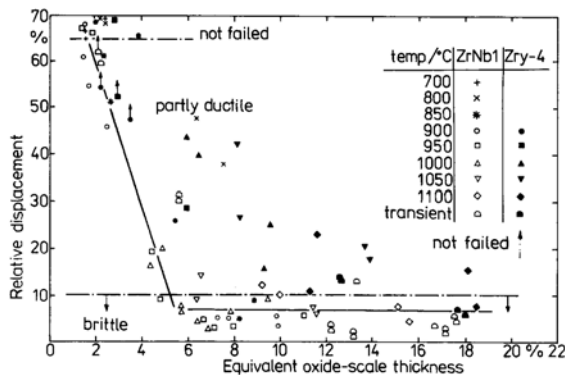
occurred in subgrain boundaries. In the specimen furnace cooled to room temperature relatively large hydride plates have precipitated which probably explains its embrittlement relative to the specimens furnace cooled to 700 and 600°C.

These microstructural observations do not explain the differences in embrittlement with the exception of the RT specimen. However, ~40 randomly located microhardness measurements on the prior  $\beta$  phase in each specimen revealed that in the directly quenched specimen as well as in the specimen quenched from 800°C all values were above 300 HV quite close to the critical limit already discussed. In the other specimens the microhardness values ranged from 160 HV to 460 HV with the majority of the values below 300 HV. Further work is planned in order to gain a better understanding of these phenomena.

### 6.2.8 The post-quench embrittlement of E110 cladding

The results presented in the preceding section showed that the Zr-1%Nb alloy M5 had similar post-quench ductility properties to Zircaloy-4. From a practical point of view M5 is expected to be better than Zircaloy-4 since it has a lower oxidation and less hydrogen pickup at high burn-up. The case is, however, very different for Zr-1%Nb alloy E110. In 1993, Böhmert *et al.* presented a comparative study of high-temperature corrosion in E110 and Zircaloy-4 [123]. They studied double-sided oxidation of short tube segments in flowing steam in a tube furnace. 20-mm long specimens were studied for weight gain, 8-mm long specimens for ring compression tests and 5-mm-long specimens for metallography. The observed oxidation kinetics was very similar for the two alloys and the results for Zircaloy-4 agreed well with other published results. However, the oxide scales on the E110 alloy had a very heterogeneous appearance with a multilayer character which tended to flake. This appearance was also associated with a high hydrogen pickup fraction, 15-70% in the temperature range 900-1 050°C where the corresponding value in Zircaloy-4 was ~2-5%. Ring compression tests showed that the E110 alloy had lost its ductility at about 6% ECR while the ductility of Zircaloy-4 was gradually reduced to zero at about 18% ECR as can be seen in Figure 6.63.

Figure 6.63 Relative displacement at failure in ring compression tests as a function of ECR for E110 and Zircaloy-4



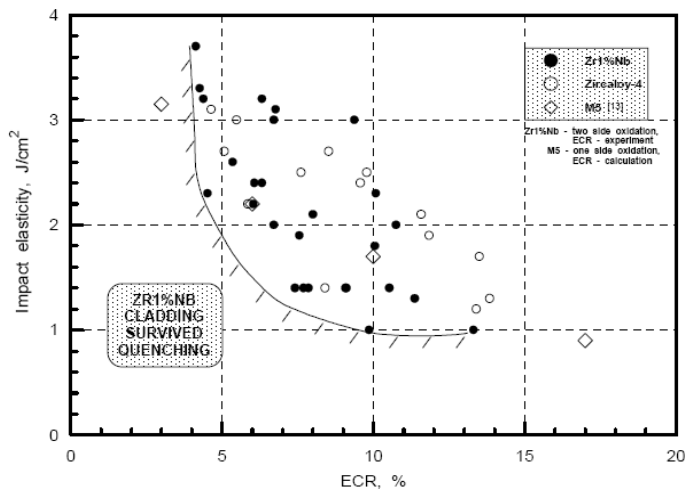
Microhardness measurements on the prior  $\beta$ -phase layer showed that the hardness was generally higher in E110 for equivalent oxidation conditions. As discussed in previous sections there is a direct correlation between hardness and oxygen content. The higher hardness of E110 was thus interpreted as a result of the  $\beta$  stabilising effect of the Nb in E110 which is expected to increase the oxygen solubility in the  $\beta$ -phase.

Another important observation was that the hardness was relatively uniform in the E110 alloy while it varied considerably in Zircaloy-4 with low hardness in the prior  $\beta$ -phase matrix and hardness maxima

in  $\alpha$  inclusions and in  $\alpha$  that precipitated during cooling. The authors suggest that the ductility of Zircaloy-4 is controlled by the low hardness part of the prior  $\beta$ -phase which serve as a crack stopper for cracks formed in the harder and more brittle parts of the material, whereas the low ductility of the E110 alloy is caused by the higher oxygen content in the prior  $\beta$ -phase. No mention was made of any effect of hydrogen uptake on ductility despite the observation of high hydrogen pickups in the E110 alloy.

Bibilashvili *et al.* report that the E110 alloy generally survives a quench from the oxidation temperature to room temperature after oxidation within the Russian criteria, <18% ECR and <1 200°C [25]. In post-quench impact tests they regard the E110 alloy as at least as good as Zircaloy-4 and M5, based on the results from a comparative study shown in Figure 6.64.

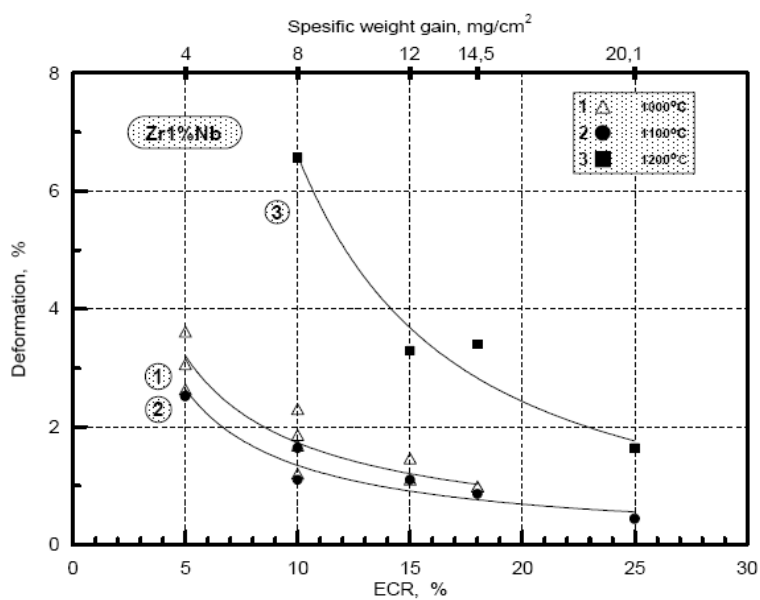
Figure 6.64 The impact behaviour of oxidized cladding vs. oxidation ECR [25]



The impact elasticity in the figure is defined as the absorbed energy divided by the specimen cross sectional area under the 0.5-mm-deep notch.

The results from ring compression tests are shown in Figure 6.65.

Figure 6.65 Deformation vs ECR in 20°C ring compression tests of E110 alloy [25]



The authors define a specimen as brittle if the deformation at failure is <0.1%, as having low ductility if deformation <4.0% and otherwise as having partial ductility. Figure 6.64 shows that specimens oxidized at 1 000 and 1 100°C have low ductility at all values of ECR while specimens oxidized at 1 200°C have low ductility only for ECR>14%. This is a clear indication that the relatively hydrogen uptake plays a major role for the low ductility of E110 alloy since the oxygen content in the prior  $\beta$ -phase is higher for material oxidized at 1 200°C as long as hydrogen concentration is low or insignificant in the beta. Note that breakaway oxidation that leads to a large hydrogen uptake in E110 occurs at 1 000°C and 1 100°C but does not occur at 1 200°C. Similar data have been reported by Sokolov *et al.* with some additional data concerning the E635 alloy [108].

Work by Vrtliková and coworkers at the UJP institute on E110 alloy predates the results reported by Böhmert *et al.* but it was published much later together with results from later work by the same group [124-126]. The UJP work started in 1985 to verify the 17% oxidation criterion for E110-clad fuels. It was soon observed that oxide on the E110 alloy spalled during high-temperature transients with an accompanying high hydrogen pickup. The oxidation kinetics was parabolic and the oxidation rate slightly lower than for Zircaloy-4. However, ductility loss in the ring compression test occurred at ECR as low as 5%. It was also noted that when the oxide was adherent the hydrogen content was low and the ductility comparable to Zircaloy-4.

These results led to the conclusion that hydrogen contained in the alloy has a strong influence on the mechanical properties after transients and that it is, therefore, possible that cladding tubes of other alloys could exhibit similar behaviour due to hydrogen pickup during reactor operation. Vrtliková and coworkers, therefore, performed an extensive program of tests on cladding tubes after pre-oxidation. The pre-oxidations was conducted through long-term corrosion in steam at 425°C or in water at 360°C (with VVER-1000 chemical additions). In this way, they obtained samples with oxide thicknesses of 2, 10, 30 and 50  $\mu\text{m}$  and hydrogen contents up to 1 200 wppm. Preoxidized samples were compared to non-oxidized samples. The samples were subjected to isothermal high-temperature exposure in steam and quenched in ice water at the end of transient. Weight gains, hydrogen contents, thickness of reaction layers, microhardness of prior  $\beta$  phase and residual ductility in 20°C ring compression tests were determined. In this way an extensive data base of E110, ZIRLO and Zircaloy-4 properties was produced which was subsequently used to propose a new LOCA criterion as discussed in Section 6.4.

Hózer *et al.* have reported Hungarian tests on E110 cladding [127]. Ring compression tests on oxidized E110 and Zircaloy-4 cladding produced results very similar to those reported by Böhmert (Figure 6.62). Quench tests confirmed the results by Bibilashvili *et al.* Oxidized E110 tubes survived direct quench (i.e. dropping of 5-cm long specimen into cold water from the oxidation temperature) if the oxidation conditions are within the embrittlement criteria, that is, 18% ECR and 1 200°C.

To better understand the post-quench embrittlement of the E110 alloy, Hózer *et al.* performed a study on the effect of hydrogen content on the embrittlement of zirconium alloys [29]. They studied E110 and Zircaloy-4 oxidized in both steam at 900 to 1 200°C and in an argon-oxygen mixture at 800°C. Hydriding was carried out at 900°C where controlled amounts could be added from a calibrated volume. Figure 6.66 summarises results on materials oxidized in argon-oxygen with well-defined hydrogen contents. It can be seen that at low hydrogen contents, <100 ppm, Zircaloy-4 is slightly more brittle than E110. At higher contents, the behaviour is practically identical. For specimens oxidized in steam, the results of the ring compression tests are very similar to those observed by Böhmert *et al.* (Figure 6.63). Hydrogen analyses of oxidized specimens showed that especially at low temperature 900 to 1 000°C the hydrogen pickup increased rapidly with ECR in E110. At 1 100 and 1 200°C, the hydrogen pickup levelled off at about 800 ppm. In Zircaloy-4, there was no hydrogen pickup except at 900°C where breakaway oxidation occurred.

**Figure 6.66 Relative deformation to failure (first crack) of E110 and Zircaloy samples as a function of oxidation ratio (ECR) and hydrogen content [29]**

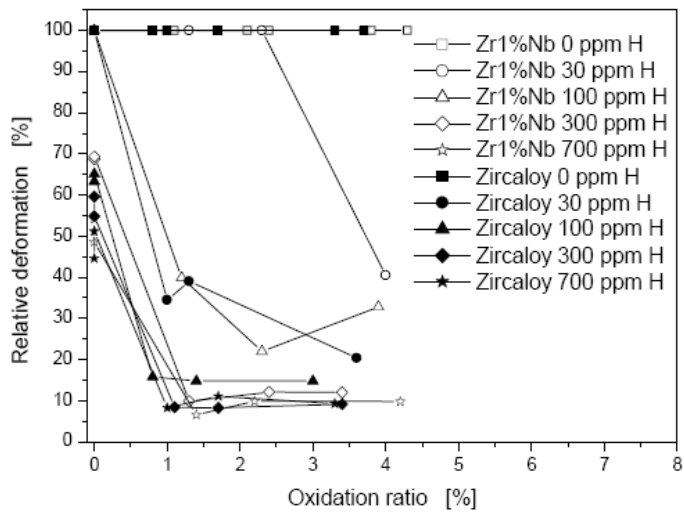
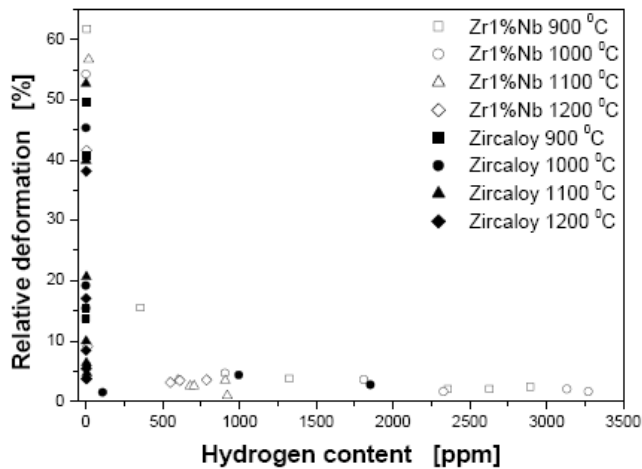


Figure 6.67 shows the effect of hydrogen content on the relative deformation in the ring compression test. The authors conclude that hydrogen seems to play a more important role than oxygen in the post-quench embrittlement of zirconium alloys. They also conclude that the combined effect of high hydrogen and oxygen contents leads to a faster degradation of ductility than the separate effects of hydrogen and oxygen.

**Figure 6.67 Relative deformation as function of hydrogen content for E110 and Zircaloy-4 samples oxidized in steam [29]**



Perhaps, the most extensive investigation of the post-quench embrittlement of E110 alloy and its causes has been performed by Yegorova *et al.* [20,128-129]. They demonstrate rather conclusively that the embrittlement is caused by hydrogen pickup during oxidation of E110 alloy. The hydrogen pickup is in turn caused by the start of breakaway oxidation of the E110 alloy. At 1 100°C for instance breakaway oxidation starts at around ~7% ECR. Cladding ductility disappears at ~8% ECR and hydrogen content is increased from nearly zero to about 1 200 ppm in the range of 7.5 to 9% ECR. The breakaway is associated with lateral cracks in the oxide and subsequent spalling of the oxide. Böhmert *et al.* [123] have suggested that steam gets ingressed in the lateral cracks leading to a situation of steam starvation and high hydrogen concentration in the steam. Japanese experiments have

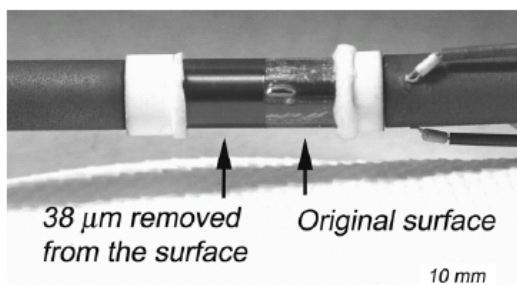
demonstrated that hydrogen pickup will occur under such conditions [54,59,106]. Apart from the oxidation breakaway, the microstructure in E110 and its development with oxide growth are similar to that of M5 described in Section 6.1.6.2.

All these data indicate that the cause behind the post-quench embrittlement of E110 is the breakaway oxidation and the associated hydrogen pickup. E110 is manufactured from a mixture of iodide zirconium and electrolytic zirconium which leads to a lower content of oxygen than in the M5 alloy. M5 is manufactured from sponge zirconium. As a first step in finding the cause of breakaway, Yegorova *et al.* manufactured E110 in which high oxygen scrap had been added so that the oxygen content was similar to that of M5. However, this alloy denoted as E110K behaved similarly to standard E110 with regard to breakaway and had the same zero ductility threshold. The difference between E110 and M5 is thus not simply an effect of the difference in oxygen content.

Yegorova *et al.* also studied the properties of E110 alloy produced from sponge zirconium [20]. This led to a significant improvement in oxidation properties compared to standard E110 and almost identical properties compared to M5. Chung [30] has explained this improvement in terms of important impurities in sponge zirconium as described in Section 6.1.3. However, at 1 200°C despite the absence of visual indications of breakaway oxidation up to 23% ECR, a significant hydrogen pickup was detected already at 8% ECR in the specimens tested by Yegorova.

Oxidation and embrittlement of E110 was also studied at Argonne National Laboratory [110]. Billone *et al.* discovered that surface treatment was very important and that polished surfaces provide a substrate for oxide growth that suppresses breakaway. This is shown graphically in Figure 6.68. This effect was subsequently confirmed by Yegorova *et al.* [20].

**Figure 6.68 Hybrid E110 sample following oxidation at 1 000°C for 290 seconds**  
Machined-and-polished section is lustrous black, while as-fabricated E110 section is in breakaway oxidation



The low ductility of E110 made from sponge zirconium (8% ECR at 1 200°C) as reported by Yegorova can thus be explained. First, the sponge zirconium specimen used by Yegorova did not have polished surfaces and breakaway was thus not suppressed as much as in the M5 specimens which had polished surfaces. Second, this result corresponds to ring-compression tests performed at 20°C rather than at 135°C as for the M5 tests performed at Argonne, and the lower test temperature will give a significantly lower ductility. Third, the material used for these tests (specimen #120) was not made from pure sponge zirconium, but also had iodide zirconium and recycled scrap in the ingot. And fourth, the 8% ECR value was a measured ECR value, and measured values of oxidation are not well suited for characterising embrittlement as described at the beginning of this section. All of these factors led to the low reported ductility of 8% and may be the reasons why the ductility was not comparable to the M5 ductility measured at Argonne.

A recent study by Nikulin *et al.* indicates that the ductility of the E110 alloy is not simply a function of its hydrogen pickup during oxidation but also to some extent dependent on the impurity content [130]. The total impurity contents were 140, 70, and 35 ppm. Fe is not included in the

impurities although the heats contained 80-100, 350-380, and 400-450 wppm Fe, respectively. The alloys were oxidized in steam to ECR levels of 10 and 18% at 1 100°C and to 17% at 1 200°C. The time to reach the ECR values differed between the alloys but did not correlate with impurity content.

The Widmanstätten structures formed when the  $\beta$ -phase transforms to  $\alpha$  can have two morphologies, the parallel plate structure when practically all Widmanstätten plates in the prior  $\beta$  grain have the same orientation, or the basketweave structure when plates of different orientations cross each other in the same prior  $\beta$ -grain [131]. In as-received Zircaloy-4, the latter type forms at a certain range of medium cooling rate. It is thought that the formation of the latter type of structure is promoted by the presence of some particles which facilitate nucleation of the  $\beta$  plates. Nikulin *et al.* found that the volume fraction of basketweave structure increased with impurity content. They also observed a plate-like, still unidentified dark phase which also increased in number with the impurity content. Tests on material oxidized at 1 100°C showed that ductility increased with decreased impurity content. However, for material oxidized at 1 200°C, there were no differences in ductility among the three tested heats.

### 6.3 Calculation of transient oxidation, hydrogen generation and embrittlement

The consequences of high-temperature oxidation of cladding are hydrogen generation, heat of reaction, and embrittlement of cladding. The hydrogen generated in a large break loss-of-coolant accident from the zirconium-steam reaction is, in the first few hours, the most significant quantity of hydrogen produced. In design basis accidents in which steam is unlimited, the hydrogen generated and the heat evolved can be calculated for transient oxidation by application of the isothermal parabolic rate constants for total extent of reaction. In steam limited conditions such as in severe-fuel-damage accident situations, the calculation would be conservative.

The equivalent metal reacted may be calculated similarly to assess the embrittlement of the cladding with respect to the 17% ECR criterion, although transient ECR calculation for some type of high-burn-up fuel (e.g., Zircaloy-4 fuel) is not so straightforward. However, for the calculation of the detailed distribution of the oxygen in the  $\beta$ -phase for the assessment of embrittlement in terms of the Chung and Kassner criteria, it is necessary to use more sophisticated techniques and more fundamental oxygen transport data under moving-phase-boundary conditions. Transient total oxidation may be computed using isothermal oxidation data by approximating the transient to a series of small isothermal steps, the sum of the isothermal oxidations representing the total oxidation of the transient.

#### 6.3.1 Calculation of hydrogen generation

The hydrogen released when Zircaloy is oxidized in steam is directly proportional to the oxygen consumed or Zircaloy reacted. Thus for each mol of zirconium reacted two mols of hydrogen gas are produced, hence for each kilogram of zirconium reacted 0.044 kg or 0.491 m<sup>3</sup> (STP) hydrogen are produced and the amount of hydrogen produced at any time is expressed as:

$$W_{H_2} = 2 \cdot \frac{M_{H_2}}{M_{Zr}} \cdot (Kpt)^{1/2} \quad (6-10)$$

where  $W_{H_2}$  = mass (mg) of H<sub>2</sub> produced per unit (cm<sup>2</sup>) of Zr surface

$M_{H_2}$  = mol.wt of H<sub>2</sub> (2.016) mg/mg mol

$M_{Zr}$  = mol.wt of Zr (91.22) mg/mg mol

$t$  = time seconds

$Kp$  = parabolic rate constant (mg Zr/cm<sup>2</sup>)<sup>2</sup> s<sup>-1</sup>

Thus the calculation of hydrogen generated as a function of time in a transient or the integrated hydrogen may be calculated using parabolic rates of reaction which are available over a very wide range of temperature from  $\sim 700^{\circ}\text{C}$  up to the melting point of Zry-4, as described in Section 6.1. The data are scattered due to difficulties in measuring temperature and different experimental and evaluation methods. Ocken [132] has suggested that external and internal heating of specimens results in parabolic rate constants with different pre-exponential factors and activation energies due to the different temperature gradients across the cladding wall. It is suggested that the correlation for internally heated specimens most closely represents the in-reactor fuel temperature gradients. The ANS Standard for Containment Hydrogen Control [133] suggests use of the above correlation below  $1\ 205^{\circ}\text{C}$  and the Baker-Just correlation above  $1\ 205^{\circ}\text{C}$ . The latter correlation is shown in Figures 6.2 to 6.4 to be the conservative data. Overall, the data promotes an acceptable basis for the calculation of hydrogen generated provided the steam availability is maintained and that the oxidation does not deviate significantly from a parabolic rate.

$$K_p = 3.33 \cdot 10^5 \exp(-140600 / RT) \quad (6-11)$$

The conditions of possible steam limitation have been described previously (Section 6.1.9). The deviation from parabolic oxidation has been observed by some workers at temperatures below  $\sim 1\ 000^{\circ}\text{C}$  but oxidation in this temperature range is low and the deviation is not considered significant for LOCA calculations. Pawel and Campbell [33] have pointed out that significant filling of the  $\beta$ -phase with oxygen influences the kinetics of oxide and  $\alpha$ -phase growth but the overall effect is not significant for design basis LOCA calculations of total oxidation. The time for which the initial parabolic rate constants measured in the temperature range  $750\text{--}1\ 600^{\circ}\text{C}$  for times up to 25 hours are applicable after including specimen geometry and breakaway oxidation effects, has been determined by Leistikow *et al.* [16,28] e.g. Figure 6.5. At very high temperatures, above the melting point of Zircaloy there were no reported data on the oxidation rate of liquid Zircaloy at the time of the previous state-of-the-art report [37] although work on this topic was reported to be in progress [134]. It has not been possible to locate any publication of this work or any other systematic experimental work on oxidation of liquid zirconium alloys. A theoretical study by Olander [135] shows that chemical thinning of the oxide layer by dissolution in the molten metal can be significant if the metal is far from saturation with respect to oxygen when it melts. However, as long as steam is present part of the oxide layer will remain. Olander states that the method of analysing oxidation of liquid Zircaloy is basically no different from the theoretical technique applied to oxidation of the solid metal.

The calculation of oxidation or hydrogen generated using total oxidation parabolic rate constants has been assembled into computer codes examples of which are BILD5 [50] COBILD [88] and TRANS [5], SIMTRAN [136], and ECR-17 [61]. Using the kinetic data of Pawel *et al.* [8] a simple calculation has been performed by Sherman *et al.* [137] to illustrate the rate of hydrogen generation from the oxidation of a Zircaloy surface area such as in the core of TMI-2, the time to generate 100 kg of hydrogen is shown in Table 6.7.

Table 6.7 H<sub>2</sub> generation from the Zr/H<sub>2</sub>O reaction from [137]

Temp (K)	$W_{H_2} / \sqrt{t}$ (kg/s)	Time to produce 100 kg of H <sub>2</sub> (s)
800	0.012	$6.5 \times 10^7$ (2 years)
1 000	0.15	$4.4 \times 10^5$ (5 days)
1 200	0.83	$1.5 \times 10^4$ (4 hours)
1 400	2.8	$1.3 \times 10^3$ (21 mins)
1 600	6.8	216
1 800	13.9	52
2 000	24.1	17
2 200	37.0	7.3

### **6.3.2 Calculation of oxygen distribution**

The calculational techniques generally used to predict the distribution of oxygen in unstressed, isothermally or transiently oxidized cladding can be generalised into two types of computer code that differ in the method of calculating the oxygen distribution in the oxide and  $\alpha$  phases. In the first simpler type, the position of the oxide/ $\alpha$  and  $\alpha/\beta$  boundaries are estimated by application of the experimentally determined parabolic growth rate constants for the oxide and  $\alpha$  phases, and hence, only apply if semi-infinite parabolic oxidation is maintained.

The oxygen concentration profile in the  $\beta$ -phase is calculated by considering the diffusion of oxygen through the  $\beta$ -phase using a finite difference technique. Examples of such codes are BILD5 and COBILD. The latter code is a development of BILD5 and also includes the calculation of oxidation on the inner surface by contact with  $\text{UO}_2$ . For calculation of the critical  $\beta$  thickness to survive thermal shock, it is necessary to use a method in which the effects of saturation of the  $\alpha$  or  $\beta$  phases and deviation from parabolic behaviour are accounted for.

More complex codes are also available which are based on finite-difference solutions to the fundamental oxygen transport process, i.e. diffusion. Such codes also account in principle, for changes in the parabolic rates due to the approach to saturation. Examples of these codes include SIMTRAN/MULTRAN [136,138], ZORO [139] and PRECIP II [140].

The basic data for these calculations are isothermal oxygen diffusion coefficients in each phase and equilibrium interface oxygen concentrations. The diffusion coefficients for oxygen in  $\alpha$  and  $\beta$  Zircaloy have been determined [82,141-142] and for zirconia, which were deduced from oxidation experiments and previously established values of  $D_{\alpha}\text{Ox}$  and  $D_{\beta}\text{Ox}$ . The interface solubilities for oxygen in zirconium [143] and Zircaloy [143,144] have also been published. More recent evaluations of the Zr-O systems can be found in “Zircobase” [122] from which estimates of the effect of alloying elements on the interface concentrations can be calculated with a software like the Thermo-Calc system [121].

Calculations based on ideal models of diffusion assume that the diffusion coefficient is constant in the material with an oxygen concentration gradient and that the concentration of oxygen at the phase boundaries is that of equilibrium conditions even in transient temperature-time oxidation. These assumptions are not strictly valid and their use gives rise to erroneous predictions. Attempts have been made to replace equilibrium oxygen concentrations at phase boundaries by empirically determined oxygen concentrations.

For a limited range of transients the codes predict oxygen concentration distribution with reasonable accuracy but for less simple transients certain aspects of the oxidation process are not accounted for by either a parabolic rate constant or an ideal diffusion model. Examples of departure from the ideal model are the formation of  $\alpha$ -incursions ahead of the  $\alpha$ -boundary [33] and anomalous two-peak oxidation in certain transients with two temperature maxima [4,145]. In such transients the oxide has been observed to be thinner on Zircaloy directly heated to a higher temperature. Pawel [145] postulated that the effect was due to the hysteresis in the monoclinic/tetragonal phase transformation over the temperature range of 900-1 200°C and concluded that insufficient data were available to permit modelling of the phenomenon although the conditions of such anomalous oxidation occurs were well defined.

The SIMTRAN code developed in ORNL and KfK [136] solves simultaneously the diffusion and heat conduction equations in order to determine the oxygen and temperature profiles in the cladding wall. The most recent version of SIMTRAN contains material properties extending to 1800 K [138]; it

models the non-equilibrium concentration at the interfaces during transients and calculates the fuel temperature. The code has a particular application for beyond-design-basis accidents, i.e. severe accidents where the influence of oxidation exothermic heat induces large temperature gradients in the cladding and its influence on fuel behaviour is significant. In most design basis LOAs, the temperature gradients across the cladding are smaller and average temperatures are used for oxidation calculations. The MULTRAN [138] code was derived from SIMTRAN for design-basis-oxidation-calculations by removing the heat transfer calculations. For further simplicity, cylindrical geometry is also replaced by slab geometry. Malang and Neitzel [138] also suggest that the oxygen profile in  $\beta$ -phase after cooldown is best approximated by the profile existing just before fast cooldown. A limited amount of code validation has been published. Cathcart *et al.* [50] concluded that both the early version of SIMTRAN and the BILD5 codes adequately predict the thickness of oxide to within 10% except for the anomalous oxidation observed in certain two peak temperature LOAs. However if equilibrium oxygen solubilities are maintained, the  $\alpha$ -phase thickness is overpredicted during rapid cooling. Malang and Schanz [146] reported good agreement between oxide and  $\alpha$  thicknesses calculated by a later version of SIMTRAN with a non-equilibrium model and experimental transient oxidations. Malang and Neitzel [138] reported the use of the most recent version of SIMTRAN in predicting oxygen distribution in electrically heated fuel rod simulators that were heated in simulations of severe accidents to  $\sim 2\ 000^\circ\text{C}$ . Future development of the code will include modelling of the heat and mass transfer between oxidized cladding and steam. This model will also address the concentration profiles of hydrogen and steam near the cladding surface to allow modelling of steam starvation and hydrogen blanketing.

Suzuki and Kawasaki [140] have used the SIMTRAN code as a basis for improving and extending the prediction of oxidation parameters in LOCA conditions. The code PRECIP-II was developed by improving the treatment of the boundary conditions during the cooling phase. In the code, as the temperature falls, the diffusivity of oxygen in the  $\beta$ -phase is reduced by a factor which is a function of the local supersaturation. Additionally, to obtain good correlation with measured oxidation parameters on transiently exposed samples, the temperature dependence of the oxygen solubility in the  $\alpha$ -phase at the oxide- $\alpha$  boundary was modified, the diffusivity in the oxide and the  $\beta$  phases were also modified slightly with respect to values previously used in the SIMTRAN code. Under these conditions the measured and calculated data for weight gain, oxide and  $\alpha$  phases were within  $\pm 10\%$  for Zircaloy that was exposed to transients similar to those postulated in a LOCA.

Biederman *et al.* [4] also made comparisons for the TRANS and ZORO codes and found reasonable agreement except for the anomalous two peak LOAs.

The various codes and investigations described above refer to oxidation calculation for as-received cladding without pre-existing oxide.

Transient oxidation of virgin and pre-oxidized Zircaloy has also been studied by Leistikow *et al.* [44]. Variables such as blowdown peak temperature, heating and cooling rates were considered. The authors reported that there is a large variation in oxidation response from pre-oxidized Zircaloy that was subsequently oxidized in transients. It is postulated that the detailed reactor operating history determines localised oxidation phenomena, therefore, subsequent high-temperature oxidation must necessarily reflect the varied starting conditions of low temperature pre-corroded oxide. At transient temperatures less than  $1\ 200^\circ\text{C}$  preoxidation was generally protective but above  $1\ 200^\circ\text{C}$  the subsequent oxidation was greater than that measured on initially unoxidized metal. The authors conclude that although high-temperature transient oxidation on virgin metal is amenable to calculation it is difficult to define parameters which would enable acceptable calculations to be made for initially oxidized cladding in a wide range of transients.

A moving boundary model of oxidation named FROM (Full Range Oxidation Model) has also been developed [147] at Chalk River and comparisons with experimental data are reported as satisfactory for both isothermal and transient heating [148].

At KfK, the modelling has been extended to Zircaloy-UO<sub>2</sub> interactions observed during high pressure transients [149]. The model PECLOX predicts the combined external and internal oxidation of the cladding due to the reaction with steam on the outside and with the UO<sub>2</sub> fuel on the inside surfaces. It describes the formation, growth, and disappearance of the various interaction layers and the corresponding oxygen profiles as functions of temperature and time.

Ignat *et al.* have developed a computer code based on the analytical solution to the oxygen diffusion equations in the three phases [150]. Transient oxidation is handled by separating the transient into small isothermal steps. For each step, an equivalent time can be defined so that the transient in effect is converted to a constant temperature. The structure of the resulting computer code OXCON is much simpler than the more common finite-difference codes. A comparison between OXCON and the two finite-difference codes FROM and PRECIP II showed that they give very similar results.

## 6.4 Discussions on embrittlement criteria

High burn-up cladding is expected to contain significant amounts of hydrogen. A vast body of experiments have shown that cladding with hydrogen contents above about 100 ppm does not conform to the current LOCA embrittlement criteria. These observations together with results of work on alloys other than Zircaloy-4 make it necessary to modify and/or complement the current criteria.

### 6.4.1 Regulatory analysis

(Contributed by NRC, extract from conference paper by R.O. Meyer [151])

The U.S. Nuclear Regulatory Commission has recognised that experimental results on fuel behaviour under LOCA conditions have shown strong alloy and burn-up effects, or more precisely strong materials and corrosion effects [20,152]. Zirconium containing niobium oxidizes more slowly than zirconium containing tin under operating and transient conditions. Niobium does not go into complete solution in zirconium metal as tin does, affecting the alloy's microstructure. Under some circumstances, Zr-Nb alloys also seem to be more susceptible to breakaway oxidation. Surface roughness of the cladding also makes the oxide more susceptible to breakaway oxidation. Corrosion, on the other hand, is accompanied by significant hydrogen absorption, and this always enhances oxygen embrittlement of the metal. Several mechanisms, which are related to these effects, are now known to affect cladding embrittlement under LOCA conditions.

#### 6.4.1.1 Beta-layer embrittlement by oxygen

As temperature increases during a LOCA transient, the amount of oxygen that a zirconium alloy's  $\beta$  phase can hold also increases. Above about 1 473 K (1 200°C), oxygen solubility becomes high enough in these cladding alloys that, after cooling, the prior- $\beta$  region will be brittle. This mechanism was understood in 1973. Based on data available at that time, the 1477 K (1 204°C, 2 200°F) temperature limit in NRC regulation was thought to preclude such embrittlement, but the data only covered unirradiated Zircaloy [153].

#### 6.4.1.2 Beta-layer thinning

With time, diffusion of oxygen into the metal will convert more and more of the  $\beta$  phase to an oxygen-rich  $\alpha$  phase, the  $\alpha$  layer grows and the  $\beta$  region shrinks. For long times at high temperature,

the  $\beta$  region becomes so thin that the macroscopic specimen exhibits brittle behaviour when it is cooled. This mechanism was also understood in 1973 and was thought to be accommodated by the 17% oxidation limit in NRC's regulation, but again the data only covered unirradiated Zircaloy [153].

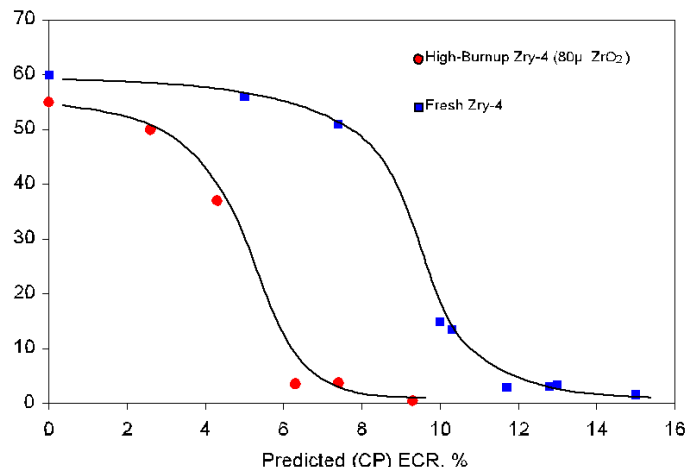
#### 6.4.1.3 Localised hydrogen-induced embrittlement in the balloon

Steam that enters through a rupture in a balloon causes oxidation inside the cladding. Hydrogen that is freed during this reaction is not swept away as it is on the outside of the cladding, but is rapidly absorbed, resulting in enhanced embrittlement near the burst location. This effect, which is neither burn-up nor alloy dependent, was discovered earlier [153] and has been confirmed in the present research programme. The localised nature of this effect and the clean fractures that occur when stressed to failure do not suggest a safety issue.

#### 6.4.1.4 Hydrogen-enhanced $\beta$ -layer embrittlement by oxygen

Some hydrogen from the outside cladding corrosion process is also absorbed in the cladding metal during normal operation. When that cladding is exposed to high-temperature LOCA conditions, the elevated hydrogen levels increase the solubility of oxygen in the  $\beta$  phase. Thus, even for LOCA temperatures below about 1 473 K (1 200°C), embrittlement can occur for times corresponding to less than 17% oxidation, as seen in Figure 6.69. This burn-up effect was discovered in the current research program and can be accounted for by reducing the time permitted for oxidation at high temperatures in proportion to the amount of corrosion.

Figure 6.69 Ductility as a function of calculated oxidation at 1 473 K (1 200°C) for irradiated and unirradiated Zircaloy-4 (rough surface), tested at 408 K (135°C)



#### 6.4.1.5 General hydrogen-induced embrittlement from breakaway oxidation

Zirconium dioxide can exist in several crystallographic forms (allotropes). The normal tetragonal oxide that develops under LOCA conditions is adherent and protective. There are, however, conditions that promote a monoclinic "breakaway" form that is not adherent and permits rapid hydrogen ingress, as seen in a specimen in Figure 6.70. One of the conditions is cladding surface roughness (belt polishing is beneficial) and another is the impurity content of the zirconium starting material (sponge zirconium is beneficial). Hydrogen that enters in this manner during a LOCA transient has the same effect on embrittlement as hydrogen from the normal burn-up process. Although breakaway oxidation was known in 1973, the connection to embrittlement and the factors affecting it were discovered only recently in NRC programmes.

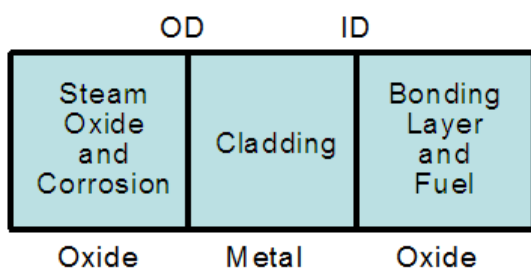
Figure 6.70 Specimen of E110 cladding that exhibited severe breakaway oxidation after 1 400 seconds at 1 000°C



#### 6.4.1.6 Oxygen pickup from the cladding inside diameter (ID)

At high burn-up, there will be a corrosion layer on the outside diameter (OD) and there can be a bonding layer on the inside diameter (ID) between the UO<sub>2</sub> fuel and the cladding. The corrosion layer and the bonding layer are both largely ZrO<sub>2</sub>, and they can provide oxygen for diffusion into the metal. This situation is like a multilayer diffusion couple as illustrated in Figure 6.71. The actual thicknesses of the OD oxygen source and of the ID oxygen source are relatively unimportant because they generally contain much more oxygen than will diffuse into the metal (see Hofmann and Politis [117]).

Figure 6.71 Diffusion couple character of oxygen sources and cladding metal



#### 6.4.1.7 Embrittlement criteria

No change is foreseen in NRC's 1 477 K (2 200°F) temperature limit. For temperatures below that limit, cladding embrittlement, including burn-up and alloy effects, has been characterised with limits on time spent at high temperatures from relatively simple measurements. One time limit was obtained from ring-compression tests on unirradiated cladding, oxidized at about 1 477 K (2 200°F), in combination with the known corrosion thickness for that type of cladding at the burn-up of interest. The amount of oxidation at the onset of embrittlement in the tests was reduced by the corrosion thickness, and that reduced amount of oxidation was related to the time limit by the Cathcart-Pawel equation [50]. The other time limit was obtained from tests on unirradiated cladding specimens that were oxidized at various temperatures to determine the time at which rapid hydrogen absorption began as a consequence of breakaway oxidation. That time was used as the limit when it was less than the

one mentioned above. These oxidation-related time limits are similar in form to the current oxidation limit in the regulations. Although NRC's research has found these criteria to be effective, they have not yet been subjected to public comment or adopted in regulations.

#### *6.4.1.8 Summary of U.S. regulatory analysis*

Based on results of this research, revisions to NRC's regulatory criteria for LOCA are underway. Although current criteria can be non-conservative under certain conditions, the criteria have been applied in an overall conservative way such that U.S. plants operate with adequate safety margins.

#### *6.4.2 Discussions on impact of recent results on criteria*

As discussed in the section on regulatory analysis, recent results on (mostly simulated) high burn-up cladding, new zirconium alloys, and an increased awareness of the consequences of breakaway oxidation in both pre-LOCA and during a LOCA transient has led to the conclusion that current regulation concerning LOCA to some extent is inadequate. As a consequence a number of workers in the field have proposed changes in the LOCA criteria. Four examples of these proposals will be given in the present section.

##### *6.4.2.1 Billone's proposal*

A set of alternative criteria based on the recent experiments at Argonne National Laboratory and CEA have been discussed at length by Billone [109]. An important feature of the alternative criteria is that they are based on the Cathcart-Pawel (CP) oxidation correlation which has proved to be very reliable in predicting oxidation in high-temperature steam tests. Based on their extensive work [110], Billone writes that:

"ANL post-quench ductility data are summarised for: as-fabricated 17×17 Zry-4, ZIRLO and M5 oxidized to Cathcart-Pawel-calculated ECR (CP-ECR) values of  $\leq 20\%$  at 1 000°C, 1 100°C and 1200°C; unirradiated prehydrated 17×17 Zry-4 oxidized at 1 200°C to CP-ECR values of 7.5% and 10% and prehydrated 15×15 Zry-4 oxidized at 1 200°C to CP-ECR values of 5% and 7.5%; and irradiated high-burn-up Zry-4 (800 wppm H) oxidized at  $\approx 1$  200°C to a measured ECR value of  $\approx 5.5\%$ . Also presented are post-oxidation ductility results for high-burn-up Zry-4 (550 wppm H) oxidized at  $\approx 1$  200°C to measured ECR values of  $\approx 5.5\%$  and  $\approx 7.5\%$ . Ductile-to-brittle transition CP-ECR values vs. H-content are determined for Zry-4 oxidized at  $\approx 1$  200°C: 5% CP-ECR and  $\approx 600$  wppm H, 7.5% CP-ECR and  $\approx 400$  wppm H, and 10% CP-ECR and  $\approx 300$  wppm H. These transition ECR values are dependent on the oxidation heating rate. The ECR values would be lower for higher heating rates as oxidation at 1 200°C is more embrittling than oxidation at lower temperatures during the ramp to 1 200°C. The high-burn-up Zry-4 results are consistent with the prehydrated Zry-4 results when the comparison is made in terms of measured ECR."

ANL and CEA data, as well as other data sets, clearly show three serious limitations in formulating post-quench-ductility criteria in terms of a fixed ECR. First, ECR is independent of hydrogen content, while embrittlement is a very strong function of hydrogen content. Second, ECR integrated over a LOCA or experimental temperature history does not distinguish time spent at high-vs.-low oxidation temperatures, while embrittlement is a strong function of oxidation temperature. Third, some alloys exhibit a low ECR rate (e.g., M5 at 1 000°C) although they embrittle at the same rate as Zry-4, even though their measured or best-estimated ECR value may be low after long times at temperature.

An embrittlement correlation, which accounts for hydrogen content and high-temperature oxidation, is proposed. There are three parts to the proposed correlation: a critical oxygen content ( $C_{crit}$  in wt %) in the prior- $\beta$  layer at the ductile-to-brittle transition; a  $\beta$ -layer oxygen solubility

limit ( $S_0$  in wt %), which is a function of temperature and hydrogen content; and a rate equation for determining the time-dependent average oxygen content ( $C_0$  in wt %) in the  $\beta$  layer, which is a function of  $S_0$ , ECR and the weight-gain rate constant  $K = K(T)$ . For non-irradiated cladding, the rate equation is expressed in terms of CP-ECR and the CP rate constant  $K$ . For irradiated cladding the correlation is based on measured ECR. Using Zry-4 data, an initial set of correlation parameters has been chosen. Also, the initial estimate for  $C_{crit}$  is 0.57 wt %. A methodology is described for refining correlation parameters and validating the correlation and  $C_{crit}$ . Following the correlation validation to prehydrated and high-burn-up Zry-4 data, prehydrated and high burn-up M5 and ZIRLO data will be used to determine alloy-dependent parameters.

Two additional limits are imposed to prohibit embrittlement at high ECR values due to excessive thinning of the  $\beta$  layer and to prohibit breakaway oxidation at lower oxidation temperatures: CP-ECR  $\leq 18\%$  and time  $\leq 1$  h at  $T > 800^\circ\text{C}$ . The 18% CP-ECR limit is needed to ensure continuity in correlation predictions for 1150-1 204°C and to prevent excessive thinning of the  $\beta$  layer for 1050-1 150°C. The time limit is needed to prevent breakaway oxidation and enhanced embrittlement for 800-1 050°C. Also, as the data base is limited to  $\leq 1$  204°C-oxidation temperatures, and the embrittlement rate is very high for  $> 1$  204°C, 1 204°C is retained as the PCT.”

#### 6.4.2.2 Vrtliková's criterion

With support from their extensive data base of post-quench ductility tests on E110, ZIRLO and standard and low tin Zircaloy-4, Vrtliková and coworkers have taken a more empirical approach to a criterion which applies to all alloys and all practical levels of pre-oxidation [124]. To understand the criterion we first note that Equation 6-3, assuming  $c = 0$ , can be written:

$$t = \frac{w^2}{2A} \exp(Q/RT) \quad (6-12)$$

or in logarithmic form

$$\log(t) = \log\left(\frac{w^2}{2A}\right) + Q/R \cdot 1/T \quad (6-13)$$

For a given value of  $w^2$ , for instance corresponding to 17% ECR we get a straight line in a diagram of  $\log(t)$  versus  $1/T$ . If we use  $Q$  and  $A$  according to the Baker-Just correlation we get the line corresponding to the current embrittlement criterion.

Vrtliková and coworkers plotted their post-quench ductility test results in a  $\log(t)$  versus  $1/T$  diagram and examined if the specimen exhibited a non-ductile behaviour or not. An example is shown in Figure 6.72. The upper yellow line is the current 17% ECR criterion calculated with the Baker-Just equation. It is clear that many of the specimens that do not violate the 17% ECR-BJ limit exhibited zero residual ductility. Therefore Vrtliková and coworkers formulated a new criterion in the form of lines which separate well their database with inadequate or adequate post-quench ductility. The lines were formulated in terms of a ductility parameter  $K$  which is calculated from:

$$K = A \exp(-B/T) \cdot \sqrt{\tau} \quad (6-14)$$

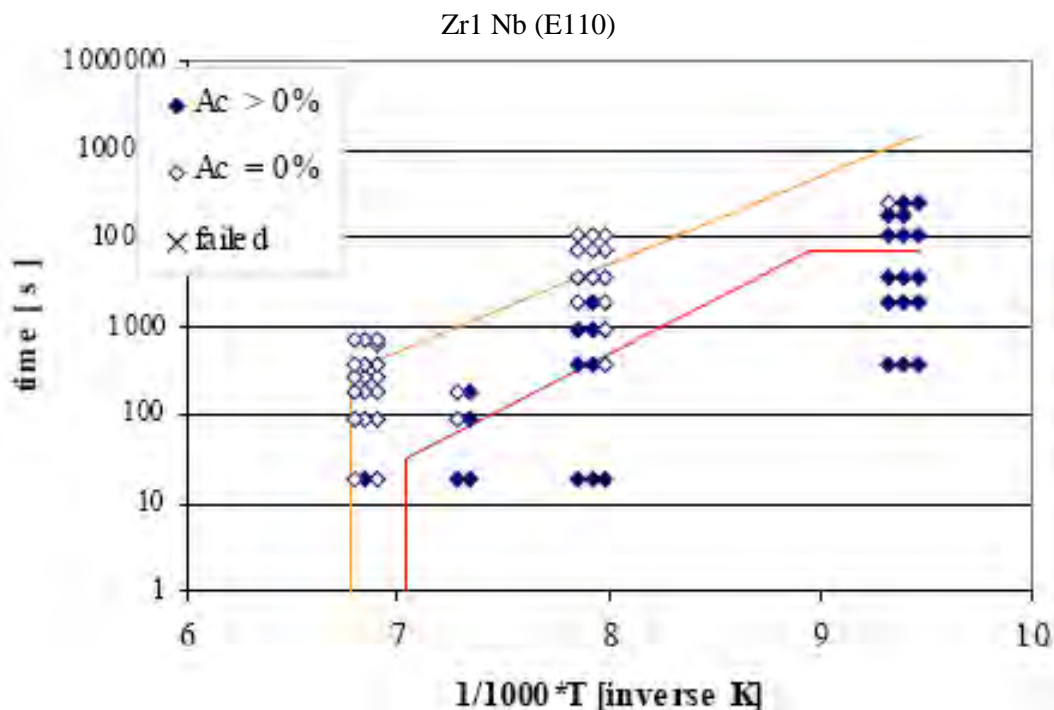
where  $T[\text{K}]$  and  $\tau[\text{s}]$ ,  $A = 3800$ ,  $B = 14170$

The significance of the ductility parameter is:

- $K < 1$ : residual ductility is preserved.
- $K = 1$ : residual ductility  $> 0$ , but does not exceed 1%.
- $K > 1$ : specimens may be brittle.

The lower red line is calculated for K=1. From actual experience this threshold limit of K can be even higher, approximately K=1.2. For non-isothermal temperature transients, K is calculated by numerical integration of the derivative of the squared version of eq. 6-14.

Figure 6.72 Post-quench ductility results at RT for isothermally exposed E110 specimens [124]  
Ac is the residual ductility.



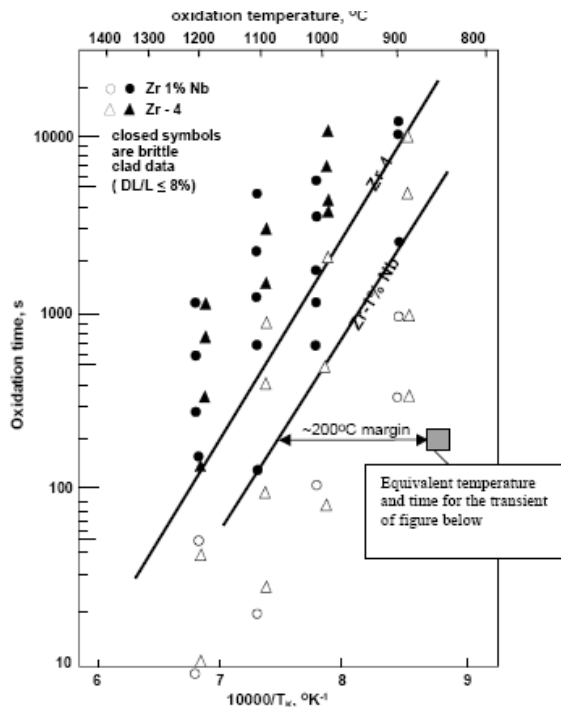
#### 6.4.2.3 The proposal by Vitanza and Hrehor

An alternative way of formulating a ductility criterion has been proposed by Vitanza and Hrehor [154]. They start by noting that the ductility data of Hobson and Rittenhouse [80] can be separated into brittle and non-brittle behaviour by the 17% ECR Baker-Just line in a log(time) versus 1/T diagram. The position of the line is dependent on the wall thickness W. For the unirradiated Zircaloy-4 used by Hobson and Rittenhouse the equation of the straight line is expressed by:

$$T_k = \frac{11500}{4.64 - 2.3\log W - 1.15\log t} \quad (6-15)$$

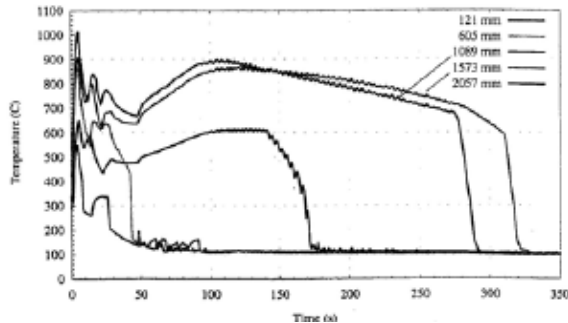
The term  $4.64 = \ln(1762) - \ln(17)$  so the 17% oxidation limit is implicitly contained in the criterion. Vitanza and Hrehor then define the temperature threshold  $T_{300s} = 1188^\circ\text{C}$  as a characteristic property of the Hobson-Rittenhouse cladding. It is anticipated that  $T_{300s}$  will depend on both alloy type and burn-up as well as on cladding thickness. The advantage with this criterion is that it is easy to express various margins. It is for instance possible to quantify the effect of cladding thickness in terms of the change in  $T_{300s}$ . It is also possible to compare two alloys or one alloy at different burn-ups in terms of the difference in  $T_{300s}$ . Figure 6.73 shows a comparison between Zircaloy-4 and E110 alloy which shows that Zircaloy-4 has ~100 K advantage over E110.

**Figure 6.73 Results of Hungarian ring compression tests of specimens subjected to isothermal high-temperature steam oxidation [155]**



For a given transient like those shown in Figure 6.74, an effective time and temperature must be calculated.

**Figure 6.74 Maximum calculated cladding temperatures in a simulated 200% cold-leg LBLOCA in the PAKS NPP**



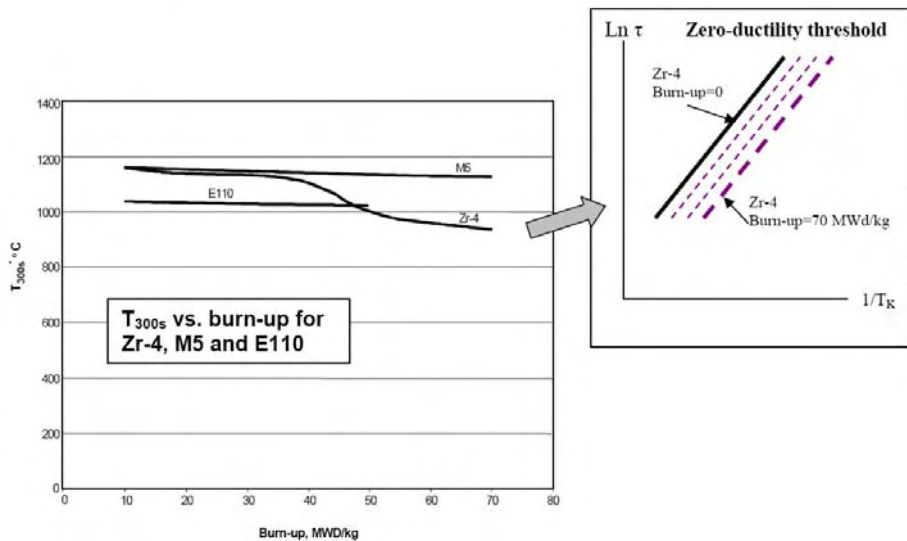
The definition of the effective temperature is somewhat arbitrary. Vitanza and Hrehor suggest the following definition of an effective temperature:

$$T_e = \frac{\int T(ECR) dECR}{ECR_F} \quad (6-16)$$

where  $ECR_F$  is the final value of ECR. For a given transient one can calculate ECR as a function of time and then perform the numerical integration necessary to calculate  $T_e$ . The effective time is then calculated as the time needed to reach  $ECR_F$  at the temperature  $T_e$ . This is the procedure used for converting the hottest transient in Figure 6.73 to the square in Figure 6.72 with the 200 K margin to the brittleness criterion for E110.

The criterion changes with burn-up due to two effects: the reduction in wall thickness due to oxidation and the hydrogen pickup caused by corrosion. The first effect is taken into account by a reduction of W and the latter by reducing the 17% limit by a factor dependent on oxide thickness before the transient on the assumption that a certain oxide thickness results in a certain hydrogen content. Figure 6.75 shows how  $T_{300s}$  changes with burn-up for the three alloys Zircaloy-4, E110 and M5.

Figure 6.75 The burn-up dependence of  $T_{300s}$  Zircaloy-4, E110 and M5 [154]



It is interesting to note that at high burn-up  $T_{300s}$  for E110 is higher than for Zircaloy-4. This is a consequence of the good long term corrosion properties of the Zr-1Nb alloys in comparison with Zircaloy-4. In a more recent paper, Vitanza has proposed a modified form of this criterion [156].

#### 6.4.2.4 Criteria proposed by Chung (contributed by Dr. H.M. Chung)

In a recent paper, Chung proposed tandem criteria, i.e., (a) calculated peak cladding temperature shall be no higher than 1 204°C (unchanged from the current limit); and (b) calculated thickness of  $\beta$  layer containing oxygen concentration of less than 0.7 wt % shall be greater than 0.3 mm (hereinafter referred to as  $L_{<0.7\text{wt}\%} > 0.3 \text{ mm}$ ) [21].

The tandem criteria, slightly modified from the two criteria proposed in [61] (i.e., a criterion for quenching thermal shock and a criterion for post-quench forces), are based on the following observations, which are documented in the reference:

1. Satisfying the  $L_{<0.7\text{wt}\%} > 0.3 \text{ mm}$  criterion was sufficient to withstand 0.3-J impact at 23°C. This limit was shown to be  $\approx 10$  times greater than the threshold impact energy required to withstand quenching thermal shock without an applied tensile load.
2.  $L_{<0.7\text{wt}\%} > 0.3 \text{ mm}$  was sufficient to avoid zero ductility at 23°C for as-received Zircaloy-4 cladding that was oxidized in steam on both sides at  $< 1 204^\circ\text{C}$ . Such samples typically contained only low contents of hydrogen of about <50 wppm. Non-zero ductility from slow ring-compression tests was confirmed in terms of non-zero plastic deformation to the first cracking, sufficient level of total deflection to fragmentation, and maximum load to the first cracking of >11 kg. The first and the second definitions of non-zero ductility are consistent with that of Hobson and Rittenhouse [80] and Hobson [81], and the third definition is consistent with that of K. Komatsu [157-158].

3. Ductility at 135°C is higher than the ductility at 23°C. Therefore, non-zero ductility threshold at 135°C has more margin than that at 23°C.  $L_{<0.7\text{wt}\%} > 0.3$  mm was sufficient to withstand three-point-fixed 0.3-J impact at 23°C for cladding tubes that were ballooned, burst, oxidized, slow-cooled, quenched, and contained hydrogen contents of 20-2230 wppm. Under the LOCA-like test conditions, virtually all hydrogen atoms are confined in the prior- $\beta$  layer.
4. The failure/survival behaviour of Zircaloy-4 fuel rods tested in PBF (failed level local oxidation temperatures  $\approx 1$  262°C,  $\approx 1$  307°C,  $\approx 1$  327°C, and  $\approx 1$  420°C; failed level local hydrogen contents 340-1 000 wppm) was consistent with the  $L_{<0.7\text{wt}\%} > 0.3$  mm criterion.
5. The  $L_{<0.7\text{wt}\%} > 0.3$  mm criterion for survival of 0.3-J impact at 23°C was valid for oxidation temperatures of 800-1400°C, hydrogen contents of 20-2230 wppm, and for various degree of wall thinning due to ballooning and burst.

At 1 204°C, the solubility limit of oxygen in  $\beta$  is 0.57 wt % at low hydrogen contents (e.g., <50 wppm). In this case,  $L_{<0.7\text{wt}\%}$  is equal to the  $\beta$ -layer thickness. Therefore, for peak oxidation temperatures  $\leq 1$  204°C, it is not necessary to calculate the distribution of oxygen in the  $\beta$  layer.

For burn-up-related higher hydrogen contents, it is necessary to calculate hydrogen-induced increase in the oxygen solubility in  $\beta$  even for  $\leq 1$  204°C. An interim method of this calculation was given in [21], which was based on: (1) temperature-dependent solubility limit of oxygen in  $\beta$  for as fabricated Zircaloy-4 (reported in [144]), (2) oxygen solubility data for Zircaloy-4 that contains high hydrogen contents of 320-730 wppm that were reported by CEA investigators, and (3) an expression developed on the basis of the CEA data by Billone which gives oxygen solubility in  $\beta$  as function of temperature and hydrogen content [109]. The CEA data indicate that at 1 200°C, the hydrogen effect saturates at a hydrogen content near  $\approx 600$  wppm.

It is desirable that more comprehensive database on the effect of hydrogen on the oxygen solubility in  $\beta$  phase will be obtained, for not only Zircaloy but also other classes of alloy, and hopefully accompanied by a calibration with independent technique(s). This could be achieved within a reasonably short period of time using unirradiated prehydrated specimens. Such database is believed to play an important role in analysing and predicting burn-up-related effects on post-quench embrittlement behaviour.

For a given burn-up level for a given class of cladding alloy, it is relatively straightforward to locate the initial oxide/ $\alpha$  phase boundary before  $\alpha$ -to- $\beta$  phase transformation starts to occur, e.g., at  $\approx 812^\circ\text{C}$  for Zircaloy-4. From thereon, it is necessary to calculate  $\alpha$ -layer growth on top of either  $\alpha + \beta$  layer up to  $\approx 975^\circ\text{C}$  or  $\beta$  layer at about  $> 975^\circ\text{C}$ . As described in Section 6.3 in this report, numerous computer codes have already been developed for this purpose for as-fabricated cladding under LOCA situations. These codes can be modified to handle the moving-boundary problem for a high-burn-up fuel.

However, the rate of  $\alpha$ -layer growth in some high-burn-up cladding, e.g., Zircaloy-4 that is covered with thick corrosion layer, could differ from that of as-fabricated material. Further metallographic analyses on some type of specimens could be very helpful for a better quantification of this difference, i.e., metallography on the high-burn-up fuel tested in ANL and the low-temperature-precorroded claddings tested in UJP.

For high-burn-up cladding, it is not clear yet if the Cathcart-Pawel correlation works well for LOCA-like transients. Therefore, it may be easier and relatively more accurate to predict the change in the thickness of  $\beta$  layer alone than to calculate all moving phase boundaries, total oxidation, and obtain a good correlation between the total oxidation and the thickness of remaining  $\beta$ .

## 6.5 Conclusions

### 6.5.1 General conclusions on oxidation and hydrogen generation

In a postulated loss of coolant accident, the zirconium-steam reaction is potentially the most significant source of hydrogen. However, if the ECCS functions according to the design basis, the hydrogen production from other sources such as radiolysis of water or containment metal corrosion reactions, generated over a longer post-LOCA time period at high temperature could predominate.

For fresh or low-burn-up cladding oxidation, hydrogen and exothermic heat generation can be adequately calculated for transients typical of hypothetical design-basis transients, using the available kinetic data on the isothermal oxidation of zirconium alloys in unlimited steam. Such data are available over a wide range of temperature, from low temperatures  $\sim 700^{\circ}\text{C}$  where oxidation rates are low, up to the melting point of zirconium. In the temperature range of  $\sim 700\text{--}1\,500^{\circ}\text{C}$  there is some scatter in the data. This is generally accepted as being due to difficulties in accurate temperature measurement combined with differences in heating technique which produce different temperature gradients across the specimen thickness. However, the Baker-Just correlation is conservative between  $\sim 1\,000\text{--}1\,500^{\circ}\text{C}$  increasingly so at higher temperatures.

The behaviour and kinetics of LOCA-like-transient oxidation in high-burn-up fuel cladding that is characterised by thick corrosion layer and a large hydrogen uptake, such as some Zircaloy-4 cladding at high burn-up, are not well understood. There are indications that such thick corrosion layer plays a significantly protective role that slows down the high-temperature oxidation. Further investigation is needed to better understand this behaviour.

Other variables having a possible influence on the zirconium alloy oxidation rate, such as steam pressure, preoxidation of cladding, deformation during oxidation, ionizing radiation and anomalous oxidation from certain two-temperature-peak-transients are not well characterised but are not thought to have significant effects on calculations of hydrogen generated from the transient Zircaloy-steam reaction in postulated design-basis loss-of-coolant accidents.

Above  $\sim 1\,500^{\circ}\text{C}$ , temperature measurement is increasingly difficult and the tendency of zirconia to transform from the tetragonal to the cubic polymorph introduces additional uncertainty in measurements of oxidation rates. For calculations in hypothetical more severe accidents in which cladding temperatures may exceed  $\sim 1\,500^{\circ}\text{C}$ , the data is sparse and scattered. Although the Baker-Just correlation is still conservative, it has been shown to be possibly less so than at lower temperatures. Above the melting point of zirconium, there is as yet, no data on oxidation in steam, although theoretical arguments suggest that the same kinetics apply as for the solid phase when the liquid is saturated with regard to oxygen.

If the availability of steam is limited, as postulated in some severe-fuel-damage accidents, the hydrogen fraction of the steam may become significant. In high hydrogen/steam ratios the oxidation rate of Zircaloy has been shown to decrease. More data are required on the effects of hydrogen in steam on the oxidation and hydrogen pick-up of Zircaloy for the accurate modelling of the core heat-up at the high temperatures and in the limited steam conditions of more severe postulated accidents.

### 6.5.2 General conclusions on embrittlement

For the prediction of intact survival or fragmentation of fuel cladding in thermal shock due to re-wetting, the embrittlement criterion based on the total oxidation (equivalent cladding reacted) has been shown to be conservative, particularly at low maximum oxidation temperatures and also if significant

wall thinning occurs. Embrittlement as defined by the total oxidation criterion can be calculated for design-basis loss-of-coolant accidents by application of the available parabolic rate constants for the zirconium alloy-steam reaction.

An embrittlement criterion based on the distribution of oxygen through the cladding wall has been proposed which adequately defines out-of-reactor and in-reactor embrittlement for thermal shock of cladding. Unless excessive, hydrogen uptake does not significantly influence the susceptibility to therma-shock failure. A similar criterion also adequately defines resistance to ambient impact of 0.3 J, thought to be a reasonable approximation to post-quench ambient impact loads. The criteria based on oxygen distribution are independent of the maximum oxidation temperature, the initial cladding thickness and the wall thinning that results from ballooning deformation. Better definition of impact forces likely to arise during quenching at the axial level of ballooned, burst, and bent claddings in fuel assembly, as well as impact forces from reflood, handling, storage, transport and seismic events would improve confidence in the above criterion. Oxidation under a realistic condition of an in-reactor transient is influenced by the mechanical restraint imposed by the fuel stack and the build up of hydrogen in the bore of the burst cladding. These effects have been shown to result in deviations of oxidation rate from those measured on small unrestrained specimens in unlimited steam in laboratory conditions [61].

The effect of hydrogen on oxygen solubility in the  $\beta$ -phase has a significant impact on the post-quench ductility of high burn-up cladding and on post-quench ductility of ballooned cladding which have absorbed hydrogen in the oxidation reaction on the inside surface of the cladding. Similar effects may also arise in long term transients at about 1 000°C when breakaway oxidation leads to significant hydrogen pickup. These effects are not addressed by the present embrittlement criteria and there is a need for new revised criteria.

## 6.6 References

1. Pettersson, K. and Haag, Y., "Deformation and failure of Zircaloy cladding in a LOCA. Effects of preoxidation and fission products on deformation and fracture behaviour. SKI project B23/78", Studsvik Energiteknik AB, STUDSVIK/K4-80/13, March 1980.
2. Baker, L. and Just, L.C., "Studies of metal-water reactions at high temperatures. III. Experimental and theoretical studies of the zirconium-water reaction", Argonne National Laboratory, ANL 6548, May 1962.
3. Parsons, P.D. and Miller, W.N., "The oxidation kinetics of zirconium alloys applicable to loss-of-coolant accidents. A review of published data", UKAEA Report ND-R-7(S), October 1977.
4. Biederman, R.R., Ballinger, R.G., and Dobson, W.G., "A study of Zircaloy-4 steam oxidation reaction kinetics", EPRI NP-225 Final Report, September 1976.
5. Biederman, R.R., *et al.*, "A study of Zircaloy-4 - steam oxidation kinetics", EPRI NP-734 Final report, April 1978.
6. Westerman, R.E. and Hesson, G.M., "Zircaloy cladding i.d./o.d. oxidation studies", EPRI NP-525 Final report, November 1977.
7. Leistikow, S., Schantz, G., and Berg, H.V., "Kinetics and morphology of isothermal steam oxidation of Zircaloy-4 at 700-1300 C", KFK 2587, March 1978.
8. Pawel, R.E., Cathcart, J.V., and McKee, R.A., "The kinetics of oxidation of Zircaloy-4 in steam at high temperatures", Journal of the Electrochemical Society, 126(1979), pp. 1105-1111.

9. Kawasaki, S., Furuta, T., and Suzuki, M., "Oxidation of Zircaloy-4 under high temperature steam atmosphere and its effect on ductility of cladding", Journal of Nuclear Science and Technology, 15(1978), pp. 589-596.
10. Brown, A.F. and Healey, T., "The kinetics of total oxygen uptake in steam-oxidized Zircaloy-2 in the range 1273-1673 K", Journal of Nuclear Materials, 88(1980), pp. 1-6.
11. Urbanic, V.F. and Heidrick, T.R., "High-temperature oxidation of Zircaloy-2 and Zircaloy-4 in steam", Journal of Nuclear Materials, 75(1978), pp. 251-261.
12. Sagat, S., "Deformation and failure of Zircaloy fuel sheath under LOCA conditions", AECL-7754, October 1982.
13. Sagat, S., Sills, H.E., and Walsworth, J.A., "Deformation and failure of Zircaloy fuel sheaths under LOCA conditions", Zirconium in the Nuclear Industry: Sixth International Symposium, 1982, Vancouver, Canada, ASTM STP 824, ASTM, pp. 709-733.
14. Pawel, R.E. and Campbell, J.J., "A comparison of the high-temperature oxidation behavior of Zircaloy-4 and pure zirconium", Zirconium in the Nuclear Industry; Fifth Conference, 1980, Boston, USA, ASTM STP 754, ASTM, pp. 370-389.
15. Aly, A.E., "Oxidation of Zircaloy-4 tubing in steam at 1350 to 1600 C", KFK 3358, May 1982.
16. Leistikow, S., *et al.*, "Comprehensive presentation of extended Zircaloy-4 steam oxidation results (600-1600 C)", OECD-NEA-CSNI/IAEA Specialists Meeting on Water Reactor Fuel Safety and Fission Product Release in Off-Normal and Accident Conditions, 1983, Risö.
17. Chung, H.M. and Thomas, G.R., "Zircaloy oxidation and hydrogen generation rates in degraded core accident conditions", International Workshop on the Impact of Hydrogen on Water Reactor Safety, 1982, Albuquerque.
18. Bibilashvili, Y.K., *et al.*, "High temperature interaction of fuel rod cladding material (Zr1%Nb alloy) with oxygen containing mediums", IAEA Technical Committee Meeting on Behaviour of LWR Core Materials under Accident Conditions, 1995, Dimitrovgrad, Russia., IAEA, pp. 117-128.
19. Urbanic, V.F., "Oxidation of zirconium alloys in steam at 1000 to 1850 C", Zirconium in the Nuclear Industry, 1976, Quebec, Canada, ASTM STP 633, ASTM, pp. 168-181.
20. Yegorova, L., *et al.*, "Experimental study of embrittlement of Zr-1%Nb VVER cladding under LOCA-relevant conditions", NUREG/IA-0211, IRSN 2005-194, NSI RRC KI 3188, March 2005.
21. Chung, H.M., "Fuel behavior under loss-of-coolant-accident situations", Nuclear Engineering and Technology, 37(2005), pp. 327.
22. Mardon, J.-P., *et al.*, "Recent data on M5 alloy under RIA and LOCA conditions", 2004 International Meeting on Light Water Reactor Fuel Performance, 2004, Orlando, Florida, American Nuclear Society, pp. 507-515.
23. Mardon, J.-P. and Waeckel, N., "Recent data on M5 alloy under LOCA conditions", 2003 Nuclear Safety Research Conference, 2003, Washington DC, Nuclear Regualtory Commission, pp. 141-160.
24. Portier, L., *et al.*, "Influence of long service exposures on the thermal-mechanical behavior of Zy-4 and M5 alloys in LOCA conditions", Zirconium in the Nuclear Industry: Fourteenth International Symposium, 2004, Stockholm, ASTM STP 1467, ASTM, pp. 896-920.
25. Bibilashvili, Y.K., *et al.*, "Thermomechanical properties of zirconium-based alloys oxidized claddings in LOCA simulating conditions", IAEA Technical Committee Meeting on Fuel behaviour under transient and LOCA conditions, 2001, Halden, Norway, IAEA, pp. 186-208.

26. Leech, W.J., "Ductility testing of Zircaloy-4 and ZIRLO cladding after high temperature oxidation in steam", Topical Meeting on LOCA Fuel Safety Criteria, 2001, Aix-en-Provence, OECD/NEA, pp. 135-143.
27. Cox, B., "Oxidation of Zirconium and its alloys. Advances in Corrosion Science and Technology", 1976: Plenum Press.
28. Schantz, G. and Leistikow, S., "ZrO<sub>2</sub>-scale degradation during Zircaloy-4 high temperature steam exposure, microstructural mechanisms and consequences for PWR safety analysis", ANS/ENS Topical Meeting on Reactor Safety Aspects of Fuel Behaviour, 1981, Sun Valley, ANS.
29. Hózer, Z., *et al.*, "Effect of hydrogen content on the embrittlement of Zr alloys", IAEA Technical Committee Meeting on Fuel behaviour under transient and LOCA conditions, 2001, Halden, Norway, IAEA, pp. 159-168.
30. Chung, H.M., "The effects of aliovalent elements on nodular oxidation of Zr-base alloys", 2003 Nuclear Safety Research Conference, 2003, Washington DC, Nuclear Regulatory Commission, pp. 283-298.
31. Cox, B., "Some thoughts on the mechanisms of in-reactor corrosion of zirconium alloys", Journal of Nuclear Materials, 336(2005), pp. 331-368.
32. Asher, R.C., "The effect of radiation on the aqueous corrosion of Zircaloy. A survey of world experience", UKAEA, UKAEA report AERE-R-7454, 1973.
33. Pawel, R.E. and Campbell, J.J., "The observation of effects of finite specimen geometry on the oxidation kinetics of Zircaloy-4", Journal of the Electrochemical Society, 127(1980), pp. 2188-2194.
34. Miquet, A. and Charquet, D., "Solid state phase equilibria of Zircaloy-4 in the temperature range 750-1050 C", Journal of Nuclear Materials, 105(1982), pp. 132-141.
35. Vandersande, J.B. and Bement, A.L., "An investigation of second phase particles in Zircaloy-4 alloys", Journal of Nuclear Materials, 52(1974), pp. 115-118.
36. Versaci, R.A. and Ipohorski, M., "Polytype structure of intermetallic precipitates in zircaloy-4 alloys", Journal of Nuclear Materials, 80(1979), pp. 180-183.
37. Parsons, P.D., Hindle, E.D., and Mann, C.A., "PWR fuel behaviour in design basis accident conditions. A State-of-the-Art Report by the Task Group on Fuel Behaviour of CSNI Principal Working Group No 2", Committee on the Safety of Nuclear Installations, OECD Nuclear Energy Agency, CSNI Report 129.
38. Jerlerud Pérez, R., *et al.*, "The Sn-Zr binary system: experiments and thermodynamic assessment", Journal of Phase Equilibria (submitted), (2006).
39. Yurek, G.J., Cathcart, J.V., and Pawel, R.E., "Microstructures of the scales formed on Zircaloy-4 in steam at elevated temperatures", Oxidation of Metals, 10(1976), pp. 225.
40. Gambini, M., *et al.*, "Behaviour of alloying elements in high temperature (1600°C-1800°C) transient oxidation of Zircaloy-4 cladding tubes", Journal of Nuclear Materials, 115(1983), pp. 343-346.
41. Brachet, J.-C., *et al.*, "Mechanical behaviour at room temperature and metallurgical study of low tin Zy-4 and M5 (Zr-Nb) alloys after oxidation at 1100 C and quenching", IAEA Technical Committee Meeting on Fuel behaviour under transient and LOCA conditions, 2001, Halden, Norway, IAEA, pp. 139-158.

42. Cheng, B., Gilmore, P.M., and Klepfer, H.H., "PWR Zircaloy fuel cladding corrosion performance, mechanisms and modelling", Zirconium in the Nuclear Industry: Eleventh International Symposium, 1995, Stockholm, ASTM ASTM STP 1295, ASTM, pp. 137-160.
43. Garzarolli, F., Stehle, H., and Steinberg, E., "Behavior and properties of Zircaloys in power reactors: A short review of pertinent aspects in LWR fuels", Zirconium in the Nuclear Industry: Eleventh International Symposium, 1995, Stockholm, ASTM ASTM STP 1295, ASTM, pp. 12-32.
44. Leistikow, S., Schantz, G., and Berg, H.V., "Investigations into the temperature transient steam oxidation of Zircaloy-4 cladding material under hypothetical PWR loss-of-coolant conditions", KFK-2810, April 1979.
45. Iglesias, F.C., Unpublished work, AECL.
46. Ozawa, M., *et al.*, "Behavior of irradiated Zircaloy-4 fuel cladding under simulated LOCA conditions", Zirconium in the Nuclear Industry: Twelfth International Symposium, 1998, Toronto, ASTM STP 1354, ASTM, pp. 279-299.
47. Kido, T., *et al.*, "PWR Zircaloy cladding corrosion behavior. Quantitative analyses", Journal of Nuclear Materials, 248(1997), pp. 281-287.
48. Nagase, F., *et al.*, "Experiments on high burn-up fuel behavior under LOCA conditions at JAERI", 2000 International Topical Meeting on Light Water Reactor Fuel Performance, 2000, Park City, Utah, American Nuclear Society.
49. Brachet, J.-C., *et al.*, "Hydrogen content, pre-oxidation and cooling scenario effects on post-quench microstructure and mechanical properties of Zircaloy-4 and M5 alloys in LOCA conditions", Zirconium in the Nuclear Industry: 15th International Symposium, Sun River, USA, Journal of ASTM International, 5(2008).
50. Cathcart, J.V., *et al.*, "Zirconium metal-water reaction kinetics. IV. Reaction rate studies", ORNL/NUREG-17.
51. Leistikow, S., Kraft, R., and Pott, E., "Is air a suitable environment for simulation of Zircaloy-steam high temperature oxidation within engineering experiments", EUR 6984.
52. Westerman, R.E., "High temperature oxidation of zirconium and Zircaloy-2 in oxygen or water vapour", HW-73511.
53. Furuta, T., *et al.*, "Deformation and inner oxidation of the fuel rod in a loss-of-coolant accident condition", JAERI-M-6339 NRC Translation NR-tr-005.
54. Furuta, T., *et al.*, "Zircaloy clad fuel rod burst behaviour under simulated loss of coolant conditions in PWRs", Journal of Nuclear Science and Technology, 15(1978), pp. 736-744.
55. Furuta, T., *et al.*, "Ductility loss of Zircaloy cladding by inner surface oxidation during high temperature transients", Journal of Nuclear Science and Technology, 18(1981), pp. 802-810.
56. Kawasaki, S., *et al.*, "Inner surface oxidation of Zircaloy cladding in a loss of coolant accident", Sixth US NRC Water Reactor Safety Research Information Meeting, 1978, Gaithersburg.
57. Uetsuka, H., *et al.*, "Zircaloy-4 cladding embrittlement due to inner surface oxidation under simulated loss of coolant conditions", Journal of Nuclear Science and Technology, 18(1981), pp. 705-717.
58. Karb, E.H., *et al.*, "LWR fuel rod behaviour in the FR2 in-pile tests simulating the heatup phase of a LOCA", KfK 3346, March 1983.
59. Furuta, T., *et al.*, "Reaction behaviour of Zircaloy-4 in steam hydrogen mixtures at high temperature", Journal of Nuclear Materials, 105(1982), pp. 1119-1131.

60. Homma, "Behaviour of the Zircaloy cladding tube in a mixed gas of hydrogen and steam", JAERI M7131. NRC translation NUREG/TR-0021.
61. Chung, H.M. and Kassner, T.F., "Embrittlement Criteria for Zircaloy Fuel Cladding Applicable to Accident Situations in Light-Water Reactors. Summary Report", NUREG/CR-1344, January 1980.
62. Chung, H.M. and Thomas, G.R., "Rate limiting effects of gaseous hydrogen on Zircaloy oxidation", NRC Workshop on the Impact of Hydrogen on Water Reactor Safety, 1981, Albuquerque, NM.
63. Chung, H.M. and Thomas, G.R., "High temperature oxidation of Zircaloy in hydrogen steam mixtures", Sixth International Symposium on Zirconium in the Nuclear Industry, 1982, Vancouver, Canada, ASTM STP 824, ASTM, pp. 793-809.
64. Chung, H.M. and Thomas, G.R., "Some new aspects of core degradation during a PWR small break LOCA", ANS Winter Meeting, 1981, San Francisco.
65. Prater, J.T. and Courtwright, E.L., "Oxidation of Zircaloy-4 in steam at 1300 to 2400 C", Zirconium in the Nuclear Industry: Seventh International Symposium, 1985, Strasbourg, France, ASTM, pp. 489-503.
66. Perez-Feró, E., *et al.*, "Experimental database of E110 cladding oxidized in hydrogen rich steam", TopFuel 2006, 2006, Salamanca, Spain, pp. 605-609.
67. Pawel, R.E., Cathcart, J.V., and Campbell, J.J., "The oxidation of Zircaloy-4 at 900 and 1100 C in high pressure steam", Journal of Nuclear Materials, 82(1982), pp. 129-139.
68. Grain, C.F. and Garvie, R.C., "Mechanism of the monoclinic to tetragonal transformation of zirconium dioxide", Bureau of Mines Report, BM-RI-6619.
69. Bramwell, I., *et al.*, "An experimental investigation into the oxidation of zircaloy-4 at elevated pressure in the temperature range 750-1000 C", UKAEA, AEA-RS-5438.
70. Vrtlikova, V., Valach, M., and Molin, L., "Oxidizing and hydriding properties of Zr-1Nb alloy cladding material in comparison with Zircaloys", Technical Committee Meeting on Influence of Water Chemistry on Fuel Cladding Behaviour, 1993, Rez, Czech Republic, IAEA, pp. 227-251.
71. Knights, C.N. and Perkins, K., "The effect of applied tensile stress on the corrosion behaviour of Zircaloy-2 in steam and oxygen", Journal of Nuclear Materials, 36(1970), pp. 180-188.
72. Bradhurst, D.H. and Heuer, P.M., "The effects of deformation on the high temperature steam oxidation of Zircaloy-2", Journal of Nuclear Materials, 55(1975), pp. 311-326.
73. Leistikow, S. and Kraft, R., "Creep rupture testing of Zircaloy-4 tubing under superimposed high temperature steam oxidation at 900°C", Sixth European Congress on Metallic Corrosion, 1977, London.
74. Furuta, T. and Kawasaki, S., "Acceleration of Zircaloy-steam reaction rate by deformation under high temperature transient", Journal of Nuclear Science and Technology, 17(1980), pp. 243-245.
75. Parsons, P.D. and Hand, K., Unpublished work.
76. Donaldson, A.T. and Evans, H.E., "Oxidation induced creep in Zircaloy-2. I, II, III", Journal of Nuclear Materials, 99(1981), pp. 38-65.
77. Hammad, F.H., Aly, A.E., and El-Raghy, S.M., "Oxidation induced dimensional changes in Zircaloy cladding tubes", 1981.

78. Leistikow, S., "Comparison of high-temperature steam oxidation kinetics under LWR accident conditions: Zircaloy-4 versus austenitic stainless steel 1.4970", Zirconium in the Nuclear Industry: Sixth International Symposium, 1982, Vancouver, Canada, ASTM STP 824, ASTM, pp. 763-779.
79. Parsons, P.D., "Zircaloy cladding embrittlement in a loss-of-coolant accident", 6<sup>th</sup> Water Reactor Safety Information Meeting, 1978, Gaithersburg, Md, USA.
80. Hobson, D.O. and Rittenhouse, P.L., "Embrittlement of Zircaloy Clad Fuel Rods by Steam During LOCA Transients", Oak Ridge National Laboratory, ORNL-4758, January 1972.
81. Hobson, D.O., "Ductile-brittle behavior of Zircaloy fuel cladding", ANS Topical Meeting on Water Reactor Safety, 1973, Salt Lake City, pp. 274-288.
82. Pawel, R.E., "Oxygen diffusion in beta Zircaloy during steam oxidation", Journal of Nuclear Materials, 50(1974), pp. 247-258.
83. Sawatsky, A., Ledoux, G.A., and Jones, S., "Oxidation of zirconium during a high-temperature transient", Zirconium in the Nuclear Industry, 1976, Quebec, Canada, ASTM STP 633, ASTM, pp. 134-149.
84. Hesson, J.C., *et al.*, "Laboratory Simulations of Cladding-Steam Reactions Following Loss-of-Coolant Accidents in Water-Cooled Power Reactors", Argonne National Laboratory, ANL-7609, January 1970.
85. Scatena, G.J., "Fuel cladding embrittlement during a loss-of-coolant accident", General Electric Company, Report NEDO-10674, October 1972.
86. Kassner, T.F. and Chung, H.M., "Clad embrittlement criteria - application to and assessment of the margin of performance of ECCS's in LWRs", 8<sup>th</sup> Water Reactor Safety Information Meeting, 1980, Gaithersburg, Md.
87. Furuta, T., Uetsuka, H., and Kawasaki, S., "Estimation of conservatism of present embrittlement criteria for Zircaloy fuel cladding under LOCA", Zirconium in the Nuclear Industry: Sixth International Symposium, 1982, Vancouver, Canada, ASTM STP 824, ASTM, pp. 734-746.
88. Haggag, F.M., "Zircaloy cladding embrittlement criteria: Comparison of in-pile and out-of-pile results", NUREG/CR-2757, July 1982.
89. Hobbins, R.R., Smolik, G., and Gibson, G., "Zircaloy cladding behaviour during irradiation tests under power-cooling-mismatch conditions", Zirconium in the Nuclear Industry, 1978, Quebec, ASTM STP 681, ASTM, pp. 586-599.
90. Hofmann, P. and Kerwin-Peck, D.K., "UO<sub>2</sub>/Zircaloy-4 chemical interactions and reaction kinetics from 1000-1700°C under isothermal conditions", KfK-3552, November 1983.
91. Seiffert, S.L., "The effect of hydrogen on the oxygen embrittlement of beta-quenched Zircaloy fuel cladding", Zirconium in the Nuclear Industry: Fifth Conference, 1982, Boston, ASTM STP 754, ASTM, pp. 302-328.
92. Chung, H.M., "Materials reactions accompanying degraded core accidents", Faculty Institute at the LWR degraded core cooling division of educational programme, 1981.
93. Katamishi, S., Sobajima, M., and Fujishoro, T., "Quenching degradation in-pile experiment on an oxidized fuel rod in the temperature range of 1000 to 1260 C", Nuclear Engineering and Design, 132(1991), pp. 239-251.

94. Nagase, F. and Fuketa, T., "Study of high burn-up fuel behaviour under a LOCA conditions at JAERI: Hydrogen effects on the failure-bearing capability of cladding tubes", 29<sup>th</sup> Nuclear Safety Research Conference, 2001, Washington, USA, NRC.
95. Nagase, F. and Fuketa, T., "Results from studies on high burn-up fuel behavior under LOCA conditions", 2004 Nuclear Safety Research Conference, 2004, Washington DC, NRC, pp. 224-230.
96. Nagase, F. and Fuketa, T., "Results from Simulated LOCA Experiments with High Burn-up PWR Fuel Claddings", 2004 International Meeting on Light Water Reactor Fuel Performance, 2004, Orlando, Florida, American Nuclear Society.
97. Nagase, F. and Fuketa, T., "Recent results from LOCA study at JAERI", 2003 Nuclear Safety Research Conference, 2003, Washington, USA, NRC.
98. Nagase, F. and Fuketa, T., "Effect of Pre-Hydrided on Thermal Shock Resistance of Zircaloy-4 Cladding under Simulated Loss-of-Coolant Accident Conditions", Journal of Nuclear Science and Technology, 41(2004), pp. 723-730.
99. Nagase, F. and Fuketa, T., "Behavior of Pre-Hydrided Zircaloy-4 Cladding under Simulated Loss-of-Coolant Accident Conditions", Journal of Nuclear Science and Technology, 42(2005), pp. 209-218.
100. Nagase, F., Otomo, T., and Uetsuka, H., "Oxidation kinetics of low-Sn Zircaloy-4 at the temperature range from 773 to 1573 K", Journal of Nuclear Science and Technology, 40(2003), pp. 213-219.
101. Nagase, F., Tanimoto, M., and Fuketa, T., "Study on high burn-up fuel behaviour under a LOCA condition at JAERI", IAEA Technical Committee Meeting on Fuel behaviour under transient and LOCA conditions, 2001, Halden, Norway, IAEA.
102. Nagase, F., Chuto, T., and Fuketa, T., "Fracture resistance of high burn-up PWR fuel cladding under simulated LOCA conditions", 2008 Water Reactor Fuel Performance Meeting, 2008, Seoul, Korea, Paper No. 8103.
103. Nagase, F., Chuto, T., and Fuketa, T., "Behavior of 66 to 77 MWd/kg fuel cladding under LOCA conditions", International Conference on the Physics of Reactors "Nuclear Power: A Sustainable Resource", 2008, Interlaken, Switzerland.
104. Nagase, F. and Fuketa, T., "Fracture behavior of irradiated Zircaloy-4 cladding under Simulated LOCA conditions", Journal of Nuclear Science and Technology, 43(2006), pp. 1114-1119.
105. Ledergerber, G., *et al.*, "Characterization of high burn-up fuel for safety related fuel testing", Journal of Nuclear Science and Technology, 43(2006), pp. 1006-1014.
106. Uetsuka, H., Furuta, T., and Kawasaki, S., "Embrittlement of Zircaloy-4 due to oxidation in environment of stagnant steam", Journal of Nuclear Science and Technology, 19(1982), pp. 158-165.
107. Kim, J.H., *et al.*, "Embrittlement behavior of Zircaloy-4 cladding during oxidation and water quench", Nuclear Engineering and Design, 235(2005), pp. 67-75.
108. Sokolov, N.B., *et al.*, "Thermomechanical behaviour of zirconium-based alloys claddings under LOCA conditions", Fontevraud 5 International Symposium, 2002, Fontevraud, France, pp. Paper 93.
109. Billone, M., "LOCA embrittlement correlation", Argonne National Laboratory, April 2005 (available at [www.nrc.gov](http://www.nrc.gov) in NRC's public document system, ADAMS, as ML051010265)
110. Billone, M., Yan, Y., and Burtseva, T.A., "Cladding embrittlement during postulated loss-of-coolant accidents", Argonne National Laboratory, NUREG/CR-XXX, 2008 (to be published - draft available at [www.nrc.gov](http://www.nrc.gov) in NRC's public document system, ADAMS, as ML070110130).

111. Meyer, R.O., Research Information Letter 080x, “Technical Basis for Revision of Embrittlement criteria in 10 CFR 50.46”, NRC memorandum from B. Sheron to J Dyer and R. Borchardt, 2008.
112. Yan, Y., Burtseva, T., and Billone, M.C., “Post-quench ductility at 135 C for 17×17 M5 cladding oxidized at 1 200 C, slow cooled to 800 C and quenched”, Argonne National Laboratory, (available at [www.nrc.gov](http://www.nrc.gov) in NRC’s public document system, ADAMS, as ML051920385)
113. Yan, Y., Burtseva, T., and Billone, M.C., “Post-quench ductility results for Zry-4 and ZIRLO oxidized at 1000 C and 1 100 C”, Argonne National Laboratory, (available at [www.nrc.gov](http://www.nrc.gov) in NRC’s public document system, ADAMS, as ML041420178).
114. Yan, Y., Burtseva, T., and Billone, M.C., “Post-quench ductility at 135 C for 17×17 Zry-4 cladding oxidized at 1 200 C, slow cooled to 800 C and quenched”, Argonne National Laboratory, (available at [www.nrc.gov](http://www.nrc.gov) in NRC’s public document system, ADAMS, as ML051920397).
115. Yan, Y., Burtseva, T., and Billone, M.C., “Post-quench ductility at 135 C for 17×17 ZIRLO cladding oxidized at 1 200 C, slow cooled to 800 C and quenched”, Argonne National Laboratory, available at [www.nrc.gov](http://www.nrc.gov) in NRC’s public document system, ADAMS, as ML051920392).
116. Yan, Y., Burtseva, T., and Billone, M.C., “Post-quench ductility results for Zry-4 and M5 oxidized at 1 000 C and 1 100 C”, Argonne National Laboratory, (available at [www.nrc.gov](http://www.nrc.gov) in NRC’s public document system, ADAMS, as ML041420185).
117. Hofmann, P. and Politis, C., “Chemical interaction between uranium oxide and Zircaloy-4 in the temperature range 900-1 500 C”, Zirconium in the Nuclear Industry: (Fourth Conference), 1978, Stratford-upon-Avon, ASTM STP 681, ASTM, pp. 537-560.
118. Mardon, J.-P. and Dunn, B., “Overview of the M5 alloy behavior under RIA and LOCA conditions”, 2007 LWR Fuel Performance Meeting/TopFuel, 2007, San Francisco, USA, American Nuclear Society, pp. 496-514.
119. Brachet, J.-C., *et al.*, “Hydrogen content, pre-oxidation and cooling scenario effects on post-quench microstructure and mechanical properties of Zircaloy-4 and M5 alloys in LOCA conditions” and “Zirconium in the Nuclear Industry: 15<sup>th</sup> International Symposium, Sun River”, USA, Journal of ASTM International, 5(2007).
120. Stern, A., *et al.*, “Investigations of the microstructure and mechanical properties of prior  $\beta$ -structure as a function of the oxygen content in two zirconium alloys”, Zirconium in the Nuclear Industry: 15<sup>th</sup> International Symposium, 2007, Sun River, USA, ASTM.
121. Sundman, B., Jansson, B., and Andersson, J.-O., “The Thermo-Calc Databank System”, Calphad, 9(1985), pp. 153–190.
122. Dupin, *et al.*, “A thermodynamic database for zirconium alloys”, Journal of Nuclear Materials, 275(1999), pp. 287-295.
123. Böhmer, J., Dietrich, M., and Linek, J., “Comparative studies on high-temperature corrosion of ZrNb1 and Zircaloy-4”, Nuclear Engineering and Design, 147(1993), pp. 53-62.
124. Vrtlikova, V., “An approach to the alternative LOCA embrittlement criterion”, SEGFSM Topical Meeting on LOCA Issues, 2004, Argonne, USA.
125. Vrtlikova, V., *et al.*, “Practical illustration of the traditional vers. alternative LOCA embrittlement criteria”, Nuclear Energy for New Europe 2005, 2005, Bled, Slovenia.
126. Vrtlikova, V., *et al.*, “Influence of preoxidation in thermomechanical properties of Zr-alloys cladding tubes after LOCA temperature transients”, Stav a perspektív palivových cyklov jadrových elektrární VVER 440, 2006, Smolenice, Slovakia.

127. Hózer, Z., *et al.*, "Experiments with VVER fuels to confirm safety criteria", ENS Top Fuel 2001, 2001, Stockholm, European Nuclear Society, pp. Paper P2-14.
128. Yegorova, L., *et al.*, "LOCA behaviour of E110 alloy", 2003 Nuclear Safety Research Conference, 2003, Washington DC, Nuclear Regualtory Commission, pp. 123-139.
129. Asmolov, V., *et al.*, "Understanding LOCA-related ductility in E110 cladding", 2002 Nuclear Safety Research Conference, 2002, Washington D.C., U.S. Nuclear Regulatory Commission, pp. 109-125.
130. Nikulin, S.A., *et al.*, "Influence of structure changes in E110 alloy claddings on ductility loss under LOCA conditions", Zirconium in the Nuclear Industry: 15<sup>th</sup> International Symposium, 2007, Sun River, USA, ASTM.
131. Holt, R.A., "The beta to alpha phase transformation in Zircaloy-4", Journal of Nuclear Materials, 35(1970), pp. 322-334.
132. Ocken, H., "An improved evaluation model for Zircaloy oxidation", Nuclear Technology, 47(1980), pp. 243.
133. ANSI/ANS-56.1-1982: Containment hydrogen control. Proposed draft standard. 1982, American Nuclear Society.
134. Courtwright, E.L., BNWL, Richland, Private communication, 1986.
135. Olander, D.R., "Oxidation of liquid Zircaloy by steam", Journal of Nuclear Materials, 119(1983), pp. 245-250.
136. Malang, S., "SIMTRAN-1L A computer code for the simultaneous calculation of oxygen distribution and temperature profiles in Zircaloy during exposure to high temperature oxidising environments", ORNL-5083, November 1975.
137. Parsons, P.D., *et al.*, "The chemical and physical degradation of PWR fuel rods in severe accident conditions", OECD-NEA-CSNI/IAEA Specialists Meeting on Water Reactor Fuel Safety and Fission Product Release in Off-Normal and Accident Conditions, 1983, Risø.
138. Malang, S. and Neitzel, H.J., "Modelling of Zircaloy-steam-oxidation under severe fuel damage conditions", OECD-NEA CSNI/IAEA Specialists meeting in water reactor fuel safety and fission product release in off-normal and accident conditions, 1983, Risø, Denmark,
139. Dobson, W.G. and Biederman, R.R., "ZORO-1: A finite difference computer code for Zircaloy-4 oxidation in steam", EPRI-NP-347, December 1976.
140. Suzuki, M. and Kawasaki, S., "Development of computer code PRECIP-II for calculation of Zr steam reaction", Journal of Nuclear Science and Technology, 17(1980), pp. 291-300.
141. Parsons, P.D., "A review of the diffusion coefficients of oxygen in a and b zirconium alloys in the temperature range 675-1800 C", UKAEA report TRG Report 2882(S), Jan. 1977
142. Pawel, R.E., "Oxygen diffusion in the oxide and alpha phases during reaction of Zircaloy-4 with steam from 1 000 C to 1 500 C", Journal of the Electrochemical Society, 126(1979), pp. 1111-1118.
143. Gebhardt, E., Seghezzi, H.D., and Duerrschnabel, W., " Research on the system zirconium-oxygen. Part 2. Research on the kinetics of the reaction between zirconium and oxygen and also the constitution of the system zirconium-oxygen", Journal of Nuclear Materials, 4(1961), pp. 225-268.
144. Chung, H.M. and Kassner, T.F., „Pseudobinary Zircaloy-oxygen phase diagram”, Journal of Nuclear Materials, 84(1979), pp. 327-339.

145. Pawel, R.E., Cathcart, J.V., and McKee, R.A., "Anomalous' oxide growth during transient temperature oxidation of Zircaloy-4", *Oxidation of Metals*, 14(1980), pp. 1-13.
146. Malang, S. and Schanz, C., "Description and verification of SIMTRAN-1 - A computer code for the calculation of high temperature steam oxidation of Zircaloy", Specialist Meeting on WR Fuel Elements under accident conditions, 1976, Spaatind, Norway, OECD/NEA.
147. Duncan, D.B., "Moving boundaries in heat conduction and mass diffusion problems", AECL 8185.
148. Iglesias, F.C., *et al.*, "Verifacation of the FROM model for Zircaloy oxidation during high temperature transients", *Journal of Nuclear Materials*, 130(1985), pp. 36-44.
149. Hofmann, P. and Neitzel, H.J., "Experimental and theoretical results of cladding oxidation under severe fuel damage conditions", *Zirconium in the Nuclear Industry: Seventh International Symposium*, 1985, Strasbourg, France, ASTM STP 939, ASTM, pp. 504-538.
150. Ignat, M., Ciocan, E., and Ion, S., "Method for describing the Zircaloy-4 oxidation using the analytical solution of the oxygen diffusion equations", *Journal of Nuclear Materials*, 240(1997), pp. 154-160.
151. Meyer, R.O., "The U.S. Nuclear Regulatory Commission's research on fuel behaviour under accident conditions", TopFuel 2006, 2006, Salamanca, Spain, pp. 284-290.
152. Billone, M., Yan, Y., and Burtseva, T.A., "Cladding embrittlement during postulated loss-of-coolant accidents", Argonne National Laboratory, NUREG/CR-6967.
153. Hache, G. and Chung, H.M., "The History of the LOCA embrittlement criteria", Topical Meeting on LOCA Fuel Safety Criteria., 2001, Aix-en-Provence, Nuclear Energy Agency, pp. 37-64.
154. Vitanza, C. and Hrehor, M., "Considerations on LOCA criteria including high burn-up effect", SEGFSM Topical Meeting on LOCA Issues, 2004, Argonne, USA.
155. Hózer, Z. and Györy, C., "Derivation of a LOCA ductility limit from AEKI ring compression tests", SEGFSM Topical Meeting on LOCA Issues, 2004, Argonne, USA,
156. Vitanza, C., "RIA failure thresholds and LOCA limits at high burn-up", *Journal of Nuclear Science and Technology*, 43(2006), pp. 1074-1079.
157. Komatsu, K., "The Effects of Oxidation Temperature and Slow Cooldown on Ductile-Brittle Behavior of Zircaloy Fuel Cladding", CSNI Specialists Meeting on the Behavior of Water Reactor Fuel Elements under Accident Conditions, 1976, Spaatind, Norway.
158. Komatsu, K., *et al.*, "Load-Bearing Capability in Deformed and Oxidized Zircaloy Cladding", CSNI Specialists Meeting on Safety Aspects of Fuel Behavior in Off-Normal and Accident Conditions, 1980, Espoo, Finland.

## 7. PLASTIC DEFORMATION OF CLADDING

### 7.1 The problem

If the external coolant pressure falls to a low value, the tensile stress which is produced in the cladding by the internal gas pressure is sufficient to cause plastic distension. The creep strength of zirconium alloys falls rapidly with temperature so that at 700°C strain rates can be up to  $1\% \text{ s}^{-1}$ . Furthermore, the ductility of the alloys is high so that strains of 50% or more are possible in principle. The spacing of PWR fuel rods is such that adjacent rods straining by 32% will touch; the key question is thus whether strains of this magnitude or greater can occur in practice in adjacent rods at the same level in the assembly. The associated question of how coolability is affected by large strain leading to progressive blockage of the coolant sub-channels is not addressed here (Section 4.2).

#### 7.1.1 Internal pressures of fuel rods

The fuel rod is internally pressurised with helium during manufacture, and this pressure is augmented during irradiation by the release of gaseous fission products. Helium is added to improve thermal conductivity at the pellet-cladding interface [1], and to reduce mechanical interaction between pellet and cladding during service [2]. A usual filling pressure for PWR fuel is of the order of 2 MPa; this is increased by the higher temperature during operation and further by fission product release. The temperature transient occurring in an accident also increases the pressure, but there should be little further release of fission products [3]. Any distension of the cladding reduces the internal pressure by increasing the free space volume.

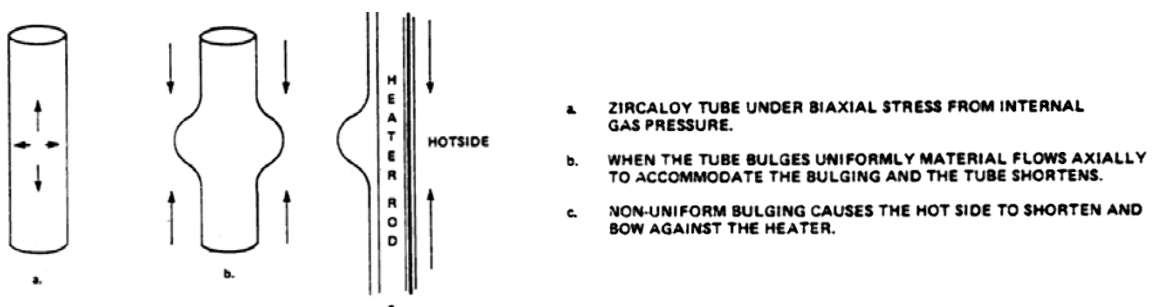
### 7.2 Factors controlling deformation and rupture of cladding

The basic parameters controlling deformation in a LOCA are stress, temperature and creep strength, the latter being affected by oxidation, grain size and anisotropy. When the temperature of a stressed tube is uniform, deformation is unstable, i.e. if the tube increases in diameter at any one axial position, the increased stress resulting from the larger diameter and reduced wall thickness will lead, by positive feedback, to a runaway deformation to rupture. In an assembly of rods at a uniform temperature, these local ruptures would occur adventitiously depending on local variations in material properties or dimensions. In this situation, a large blockage would be highly improbable. In a cooling environment, however, it is possible for a thermal stabilizing process to lead to extended deformation [4]. That is if a local region of cladding is swelling preferentially, it will be cooled to a greater extent than neighbouring regions, reducing its creep rate relative to theirs. This negative feedback effect has been found [5] to operate over a range of heat transfer conditions for tubing which is heated ohmically so that the power is generated directly in the cladding. When the heat source is internal to the cladding, as in an actual fuel rod, a further negative feedback effect is possible, from the thermal resistance interposed between pellet stack and cladding by the gas gap opened by distension. The conditions of external heat transfer obtaining in a fuel assembly following a LOCA, with a large component of convective cooling by uprising steam, will tend to produce axial temperature gradients in the fuel rods, so that distension, if it occurs, will vary along the rods. Adjacent rods, however, will tend to deform similarly though not identically.

A temperature transient which produces significant strains is quite likely to strain the cladding to rupture. This will stop distension by releasing the pressure differential stressing the cladding. Since the inherent ductility of zirconium alloys is high, early rupture, at low overall strain, will occur only when the ductility of the material is exhausted locally by non-uniform straining. A prime cause of non-uniformity is circumferential variation in temperature around the cladding [6-8], since the creep-strength of zirconium is highly temperature-sensitive, and the cladding will strain preferentially in the hottest region. Such temperature non-uniformity is caused, for example, by the fuel pellet stack not remaining co-axial with the cladding as the latter distends. The strong effect of circumferential temperature non-uniformity (or, more commonly referred to as azimuthal temperature variation) on rod deformation was investigated extensively in late 1970s [5-7]; it was found to be the key factor that controls the potential for and the degree of coplanar flow channel blockage. A good review of this topic is given in [8].

Apart from non-uniformity in heat transfer, either internally from an eccentric pellet stack or externally from, for example, inhomogeneous coolant flow, a further mechanism for introducing circumferential temperature variation in a rod follows from the anisotropic properties of the cladding. Fuel cladding manufacture imposes large reductions in wall thickness to avoid the formation of radially oriented hydride platelets [9] during service, this results in the (0001) poles being aligned close to the radial direction with a texture that resists wall thinning under the biaxial tension generated by an internal pressure. When the cladding distends, the deformation tends to be accommodated by material flowing axially into the region of distension (Appendix A). This results in axial contraction, particularly noticeable in axially unrestrained burst tests [6,10]. If wall thinning occurs preferentially at one side of a tube as a result of a local temperature increase, caused for example by contact with an internal heater rod or a fuel pellet, then only that side will shorten and the tube will bow against the heat source (Figure 7.1).

**Figure 7.1 Schematic representation of strain anisotropy in zirconium alloy tubing resulting in the “hot side straight” effect**



This ensures that deformation continues at one side – the “hot-side straight” effect. Since only a part of the circumference is thinning, the total circumferential strain potential of the tube is not achieved. Direct evidence for this has been produced at KfK by a cine-film of X-ray images from a specimen and its heater during bulging [11]. Strain anisotropy is at a maximum in the temperature range 725-775°C, but declines rapidly in the two-phase region [4]. If the combined circumferential strains of neighbouring rods exceed 65%, they will touch. After touching, the radii of curvature of the sections of cladding not in contact will decrease, reducing the hoop stresses in them. Deformation may continue above and below the contacting region if rupture did not occur; there the deformation would continue as before only if the temperature rose. Time to rupture is likely to be longer when mechanical interaction occurs.

Zircaloy-4 fuel cladding under normal service conditions is in the cold-worked and stress-relieved condition, the structure consisting of distorted lenticular grains. This structure recrystallises above 700°C in the order of 10 s [12]. Thus following a LOCA the defects introduced by irradiation

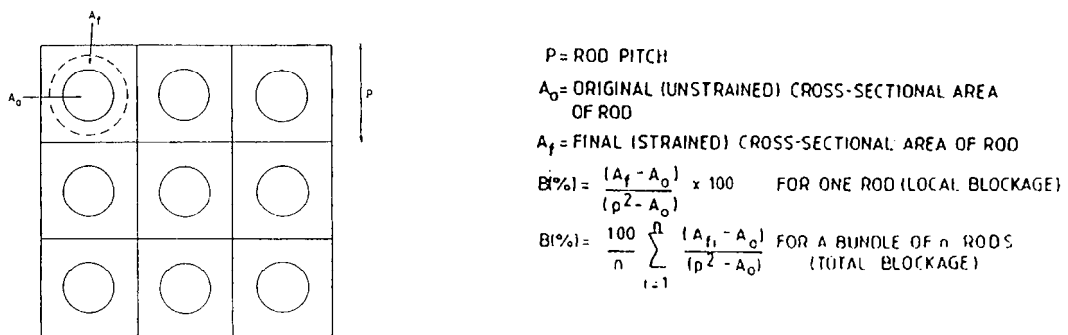
would be removed rapidly as the boundaries of the recrystallizing structure swept through the lattice. For cladding used in the recrystallized state, other annealing processes will remove radiation damage at about the same rate. The ease of plastic deformation would also prevent the build-up of internal stresses during deformation, suppressing crack formation. This effect, coupled with the fact that the texture resists wall thinning, can produce a diffuse neck, possibly leading to high circumferential strains during deformation in the range 700-800°C.

Above about 800-820°C the transformation to the  $\beta$  phase begins in Zircaloy. The presence of  $\beta$ -phase in the  $\alpha$  matrix reduces the strength considerably, while the amount of  $\beta$  is very temperature-dependent. The net effect is that in the mixed-phase region the influence of circumferential temperature variation in reducing the total strain at rupture is greater than in the single-phase region. Ductility remains high, but large strains do not usually occur unless strain rates are low.

### 7.2.1 Measurement of blockage

In the following descriptions of experimental data, the term "blockage" will appear frequently. The generally accepted definition of blockage (or coolant channel restriction) is given below and shown schematically in Figure 7.2.

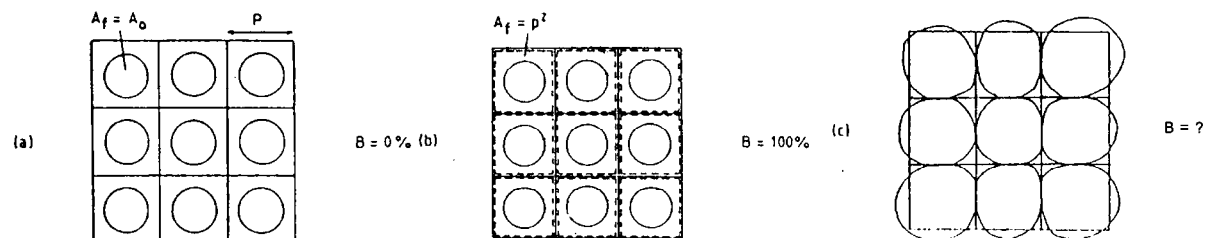
Figure 7.2 General definition of coolant channel blockage



$$B\% = 100 \times \frac{\text{difference in cross section between swollen and unswollen rod}}{\text{original coolant channel cross - sectional area}}$$

This definition gives  $B=0\%$  for no deformation and  $B=100\%$  if all the rods deform into squares of side  $p$ , where  $p$  is the rod pitch (Figure 7.3a and Figure 7.3b).

Figure 7.3 Examples of blockage

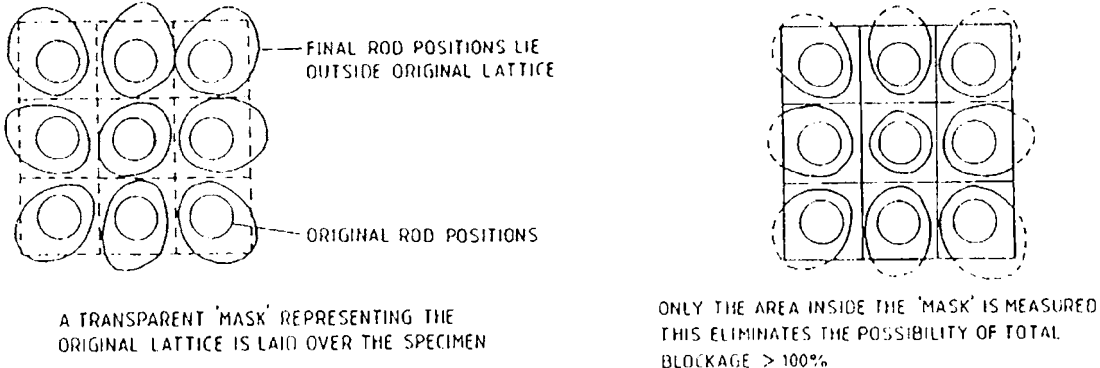


The extreme case of 100% blockage is not obtainable experimentally. However, at reasonably high rod strains the situation depicted in Figure 7.3c can be obtained, i.e. where swollen rods extend beyond the boundaries defined by the rod pitch. This situation is observed when the rods are not restrained by neighbours or a surrounding shroud and the strain is greater than 33%, or where the rod has moved from its original position in the bundle.

In this situation two options can be exercised in the evaluation of final rod area:

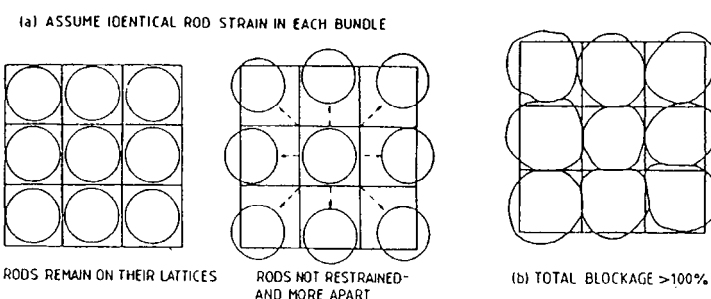
1. Total area method. Measure the area of each rod in the deformed bundle. Then use the blockage definition shown in Figure 7.2.
2. Mask method. Assume that the blockage should be evaluated only within the area defined by the original coolant channel area, see Figure 7.4. Then use the blockage definition shown in Figure 7.2

**Figure 7.4 Mask method for measurement of blockage**



The first method, “total area method”, makes no allowances for movement of the rods. Thus an array of swollen rods, each of which has moved, leaving an “open lattice”, has exactly the same numerical blockage value as an array in which the individual rods have deformed to the same extent but have not moved, when obviously there is a difference in coolant flow area (Figure 7.5a). In addition, “local” blockage values of  $>100\%$  are perfectly feasible (Figure 7.5b), if the rods swell beyond their lattice spacings. Also if the outer rods of a highly deformed bundle swell beyond the original lattice dimensions, total blockages  $>100\%$  can be obtained e.g. as reported [13] for the MT-4 bundle (Section 7.3.1.5). In both these situations, the results although mathematically correct can therefore be misleading since 100% blockage cannot be coolable and a blockage of  $>100\%$  is not physically meaningful.

**Figure 7.5 Deficiencies of the total area method**



Both give the same blockage value using total area method but flow areas are obviously different.

The second method, the “mask method” cannot produce total blockage values greater than 100%. However unless the deformation in each rod at the same plane is uniform, which in practice it is not, it does not provide an adequate description of the change in individual coolant channels e.g. the general blockage “mask” value for the cross-section shown in Figure 7.71 is about 85% (UKAEA Springfields, unpublished work [14]), whereas the individual channels are reduced by 96-98%. Similarly the PHEBUS array (Figure 7.28) has an overall blockage ratio of 48% but the area of one sub-channel has been reduced to 80% of the original (UKAEA Springfields, unpublished work [14]). What is required for heat transfer calculations is a measure of how much of the original coolant channel area remains between four

rods when they have distended to form either a closed or open sub-channel, because it is this which has a major effect on the temperature of the cladding surfaces in that sub-channel. It is also important to know the perimeter of sub-channels and the extent to which they are closed.

A mathematical description of sub-channel blockage, sub-channel perimeters and rod gaps is given in Figure 7.6. Proposals for dealing with the various types of sub-channels and burst openings are given in Figure 7.7.

Figure 7.6 Definition of sub-channel blockage (left) and sub-channel perimeters and rod gaps (right)

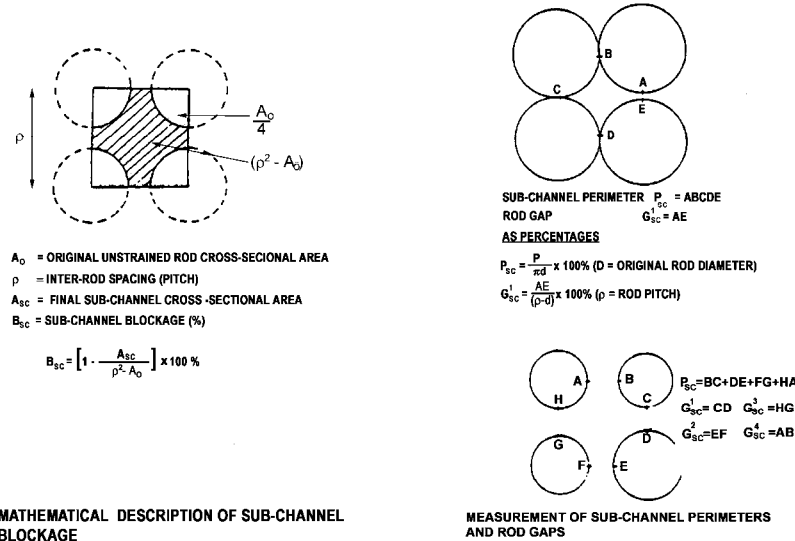
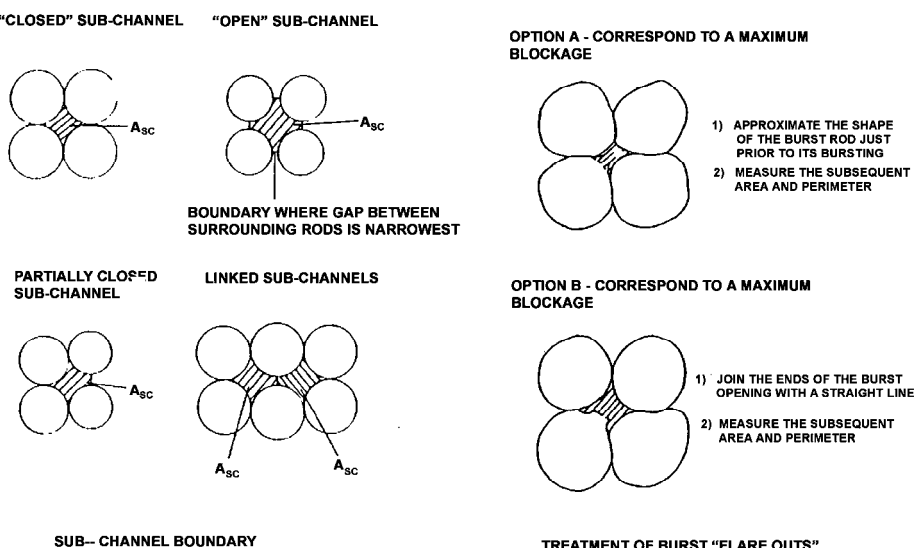


Figure 7.7 Proposals for dealing with the various types of sub-channels and burst openings



### 7.3 Experimental data

Relevant experiments may be divided into three classes:

1. Materials properties tests to determine creep strength, effects of anisotropy etc. These may or may not utilise actual cladding specimens. This type of experiment is presented in Section 5.1.1 together with relevant results.

2. Determination of oxidation and embrittlement. These have been described in a Chapter 6.
3. Determination of deformation under internal pressure.

The last class of tests may be divided into single-rod and multi-rod tests, by type of heating (ohmic, internal, furnace, or nuclear heating) and according to the degree of realistic simulation of their external heat transfer conditions. Single-rod tests performed out-of-reactor form the bulk of published results [15] and these have largely served to elucidate the controlling factors described in the preceding section. The actual strains found in single-rod tests, however, cannot be taken as representative of those occurring in an assembly, since the effects of neighbouring rods, direct or indirect, are not present.

The main series of multi-rod out-of-reactor tests have been conducted at ORNL [16], KfK [11] and JAERI [17]. The ORNL tests on 4×4 and 8×8 assemblies were performed with conservatively low steam flows, and consequently very low heat transfer coefficients, to provide data for evaluating specific requirements for the US Federal Regulation 10 CFR Part 50 Appendix K. (An analysis by the Nuclear Regulatory Commission of the cladding deformation question is presented in [18].) The test conditions were conducive to significant deformation and were selected to provide a reasonable estimate of the upper limit of the amount of deformation that could be expected under Appendix K conditions. In addition, the tests point out the differences between the behaviour of rods singly and in assemblies and between small and large assemblies. The tests cannot however be used directly to infer fuel assembly behaviour in accidents with reflood. A similar comment applies to the tests on 7×7 assemblies at JAERI. The tests in the REBEKA series at KfK have been the most realistic performed up to 1986 out-of-reactor, with simulated top or bottom reflood. Significant co-planar strains, but acceptable restriction of sub-channels, have been produced.

In-reactor tests have been performed on single rods in Germany in the FR-2 reactor and in the USA in PBF. Extended deformation occurred in both these series. The only sources of multi-rod in-reactor data are the series of experiments in the NRU reactor at AECL Chalk River [19] and the PHEBUS series at Cadarache [20-23]. A recent review of in-reactor and out-of-reactor bundle tests has been presented by Grandjean [24]. Some of his material has been included in the present review.

The experimental programmes referred to are discussed in more detail in the rest of this section.

### **7.3.1 In-reactor tests**

#### *7.3.1.1 Single rod tests in the FR2 reactor*

A series of in-reactor experiments using PWR-type single rods (active fuel length 50 cm, enrichment 4.7%) both unirradiated and irradiated (2 500-3 5000 MWd/t) and simulating the second heat-up phase of a cold leg break has been carried out in the DK loop of the FR-2 reactor at Kernforschungszentrum Karlsruhe (KfK) West Germany. Also for comparison, tests were carried out in the in-reactor loop under identical conditions except that internal electrically heated fuel rod simulators were used. The test programme is summarised in Table 7.1 [3].

The main parameter was burn-up which was achieved in the FR-2 reactor with fuel centre temperatures of 100-250 K lower than in commercial PWR fuel and a coolant pressure of only 3 bar. The rating was slightly above the peak rating of a commercial PWR. The secondary parameter was the rod internal pressure which ranged from 25-125 bar. The desired initial pressure for each test was produced by additional pressurizing with helium, just prior to the transient testing, to augment, where necessary, the fission gas generated during the previous irradiation, but there was no pressure control during testing.

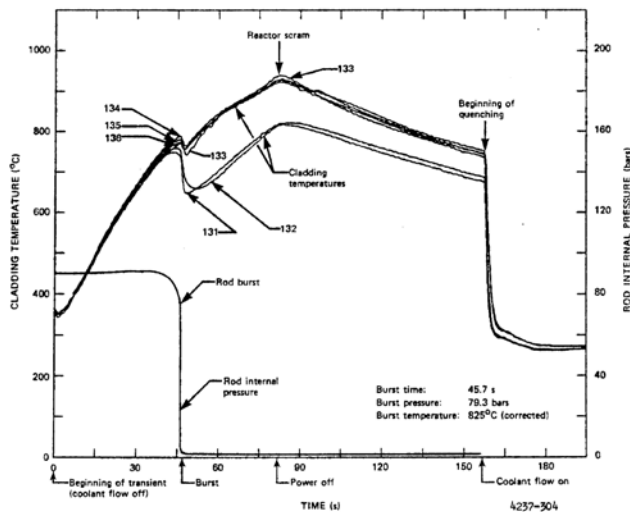
The transients which the rods experienced were initiated by interrupting the loop coolant flow of superheated steam at 300°C, 60 bar, and simultaneously depressurizing the test section of the loop. The

test rod power was kept constant at about 4 kW/m until the cladding temperature reached approximately 937°C, then reduced by reactor scram. The procedure resulted in heat-up rates in the range 6-20 K/s and rupture of all the pressurised rods during the heat-up phase. A typical transient test is shown in Figure 7.8. The effect of "cladding lift-off" can be seen in thermocouples 131 and 132 which were in the region of major deformation. These show a pronounced drop in temperature as the size of the fuel cladding gap increases as indicated by the fall in pressure.

Table 7.1 FR-2 in-pile tests on fuel behaviour, test matrix

Types of tests	Test series	Number of irradiated rods	Number of tests	Target burn-up (GWd/tU)	Range of internal pressure at steady state temperature (bar)
Calibration, scoping	A	—	5	—	25-100
Unirradiated rods (main parameter: internal pressure)	B	—	9	0	55- 90
Irradiated rods (main parameter: burn-up)	C E F G1 G2/G3	6 6 6 6 6	5 5 5 5 5	2.5 8 20 35 35	25-110 25-120 45- 85 50- 90 60-125
Electrically heated fuel rod simulators (main parameter: internal pressure)	BSS	—	8	—	20-110

Figure 7.8 Typical temperature and pressure histories for the FR-2 tests  
Measured data of test B3.1

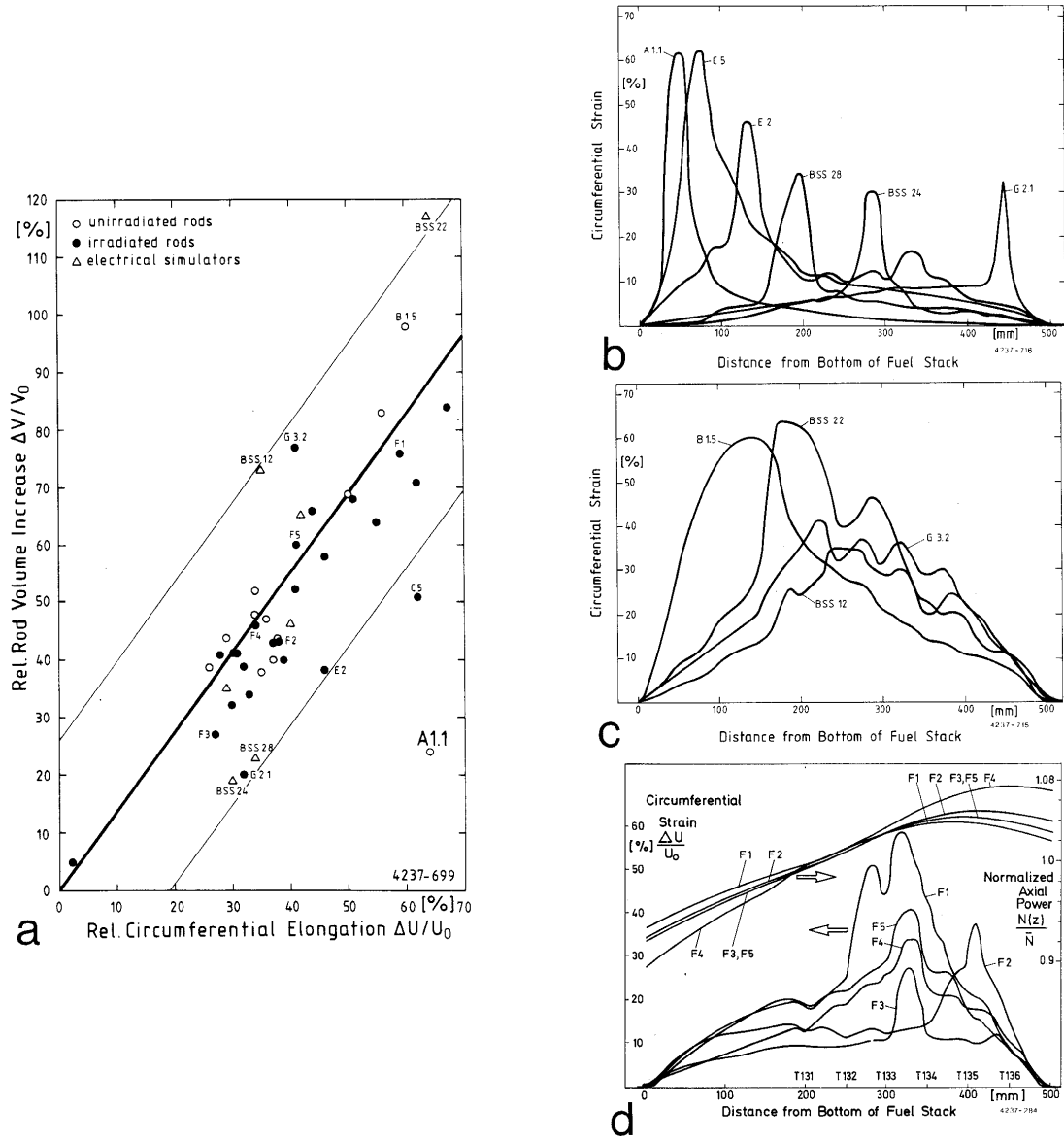


The burst temperatures quoted are considered to be those at the burst location at the time of burst and were obtained by extrapolation from the nearest cladding thermocouple reading to the burst.

The burst pressure was that measured at the start of the fast pressure drop signifying rupture. The pertinent time after initiation of the transient is called the burst time.

The pressurised rods exhibited circumferential straining over their entire heated length. The axial deformation profile was in general influenced by the power profile and locally by thermocouples, the maximum strain and burst occurring at or near the peak power position. Figure 7.9 shows the strain profiles for unirradiated rods (a, b) and for irradiated rods (c, d).

**Figure 7.9 Relative increase of total void volume**  
vs maximum circumferential elongation (a) and deformation profiles for tests below the average (b),  
above the average (c), and tests F1 through F5 representing the average (d)



In Test E5, the reactor was scrammed at the onset of ballooning in contrast with the other tests so that the cladding temperature decreased whilst the major part of the deformation was occurring. This rod deformed to the limit of 67% where it contacted the shroud over an axial length of 10 cm. Presumably ,the trapping of the bulge by the shroud caused the deformation to extend axially. The post-test neutron radiograph is shown in Figure 7.10.

The burst strains of irradiated, unirradiated and electrically heated rods are shown in Figure 7.11. There was no influence of irradiation damage, iodine or other fission products on the deformation and rupture. Low ductility failures due to iodine stress-corrosion cracking are not likely at temperatures above 700°C even if it is assumed that there is complete release of iodine from the high burn-up fuel [25]. Also the effects of irradiation damage on the cladding are annealed out when the temperature exceeds 700°C [12].

Figure 7.10 Posttest neutron radiograph of test E5 fuel rod

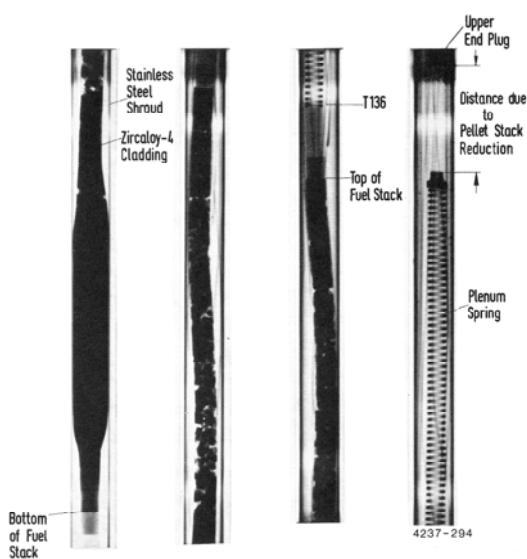
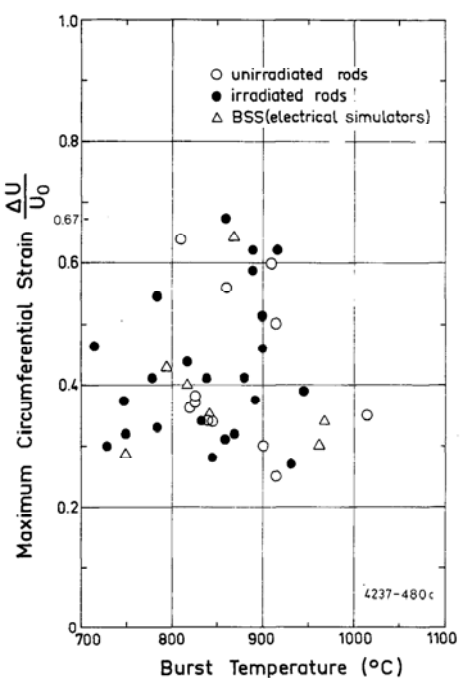


Figure 7.11 Maximum circumferential strain vs burst temperature

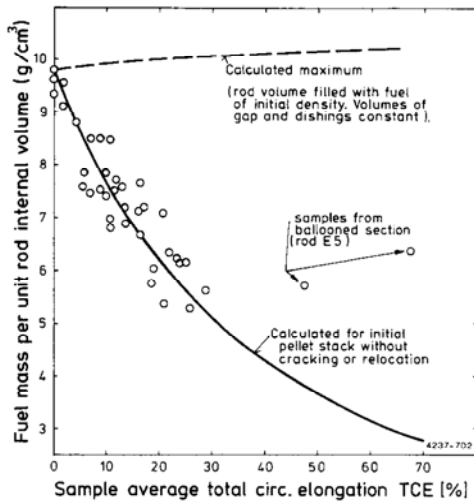


There was essentially no additional cracking of the irradiated fuel pellets during the transient tests. The mean fragment size was about 3 mm. Only a small additional amount of fission gas was released during testing.

Neutron radiographs of the rods after testing showed that in the regions of major deformation the UO<sub>2</sub> fuel pellets had completely fragmented and the fragments relocated outward and downward filling the space in the fuel rod created by the diametral expansion of the cladding. There are indications from three thermocouples placed in the upper end region of the fuel stack that collapse of the fuel column occurred at the time of burst, since the temperature monitored by these fell dramatically at burst whilst others mounted lower down the fuel rod behaved normally.

The filling ratio of the free space resulting from the clad ballooning depends on the granulometry of the fuel fragments. The analysis of the fuel particle size distribution for the rods of each test series shows very similar distributions for the burn-ups in the range 2.5 to 35 GWd/tU with 2 peaks near 2 mm and 3.15 mm in particle size; the average particle size, calculated over the whole of the irradiated rods, is 2.78 mm. The measurement of the local fuel mass per unit rod internal volume in the samples used for the particle size analysis has also provided an estimate of the filling ratio for these samples. Figure 7.12 shows, for most of the samples, a decrease in the fuel mass per unit rod volume corresponding to the increase of volume without fuel relocation; in fact, this evaluation concerns only the samples with minor circumferential elongation (<30%); the two samples that lay apart the previous trend were taken from test E5 with elongations of 48% and 67.5% respectively, where the measured fuel mass per unit volume corresponds to a filling ratio of 55.5% and 61.5% respectively.

Figure 7.12 Fuel mass per unit volume of deformed cladding tube after relocation during LOCA burst test



### 7.3.1.2 Single rod tests in the PBF

The LOC series [26] of large break LOCA simulation experiments were carried out in the Power Burst Facility (PBF) at the Idaho National Engineering Laboratory (INEL) in the United States of America.

The test programme was designed to investigate the two major parameters determining cladding circumferential strain during ballooning, i.e. cladding temperature and differential pressure, using both unirradiated and irradiated rods. In each PBF LOCA test, there were four separated 15×15 type PWR test rods 0.91 m long, two of which were internally pressurised to values representative of PWR rods at start of life and two which were pressurised to values representative of high burn-up rods. The plenum volume was scaled in proportion to the active length compared to that of a full length rod. One of each type of pressurised rod had been previously irradiated in the Saxton PWR, under conditions typical of commercial power reactors. The fuel rod and shroud design along with details of the instrumentation and test system are given in [26]. Peak cladding temperatures of 797, 917 and 1 077°C were planned to be attained in the tests by varying the rod power history and time of critical heat flux (CHF). These temperatures correspond respectively to the region where maximum ductility occurs in  $\alpha$ -phase Zircaloy, the strain-rate-dependent ductility trough in the transition region from  $\alpha$  to  $\beta$  phase, and the region of maximum ductility in the  $\beta$  phase under oxidizing conditions.

Each test with four single rods consisted of a pre-blow-down power calibration and decay heat build-up, blow-down (depressurisation of the coolant) and test termination by rapid quenching. During depressurisation, the normally sub-cooled water surrounding each test rod flashed to steam as the coolant was released through the cold leg and the cladding temperature increased.

The axial power profile along the fuel rods was shaped to flatten the power in the centre third of the active fuel length to simulate conditions typical of the central region of a PWR core. The reactor power was controlled during blow-down by the PBF transient rods and programmed to follow the power function, determined in pre-test calculations, necessary for additional heating of the test rods so that they might reach and maintain the desired test temperatures.

Out of the thirteen rods tested in the LOC series, nine ballooned and ruptured, two did not burst and two failed to achieve the planned transient owing to malfunction of the equipment. The thermal and mechanical behaviour data for the eleven rods which were satisfactorily tested are given in Table 7.2

The cladding strain was generally concentrated within the axial zone of uniform temperature, i.e. between 0.2 and 0.5 m from the bottom of the fuel stack and failure generally occurred between 0.2 and 0.4 m.

The circumferential strain at the burst elevation and over the axial zone of uniform temperature was greater in the rods previously irradiated in Saxton PWR than in the unirradiated rods for both tests which burst in the high  $\alpha$  region ( $\sim 800^\circ\text{C}$ ) and the  $\alpha+\beta$  region ( $\sim 840^\circ\text{C}$ ) (Figures 7.13 and 7.14).

Metallographic examination showed that the wall thinning was primarily concentrated in the burst region of the cladding of the unirradiated rod, whereas in the case of the previously irradiated rod the wall thinning was more uniformly distributed around the circumference.

This difference is likely to be associated with a more uniform temperature around the circumference as the cladding creep is very dependent on temperature. This encouraged uniform "lift-off" of the cladding from the fuel; thus avoiding or substantially delaying operation of the "hot-side straight" effect which limits circumferential strain. A possible cause of more uniform temperature around the circumference is more intimate contact between the cladding of the previously power-reactor-irradiated rods and the fuel compared with fresh fuel rods where the pellet-clad gap can vary around a pellet and along the rod. Further supporting evidence for this effect can be obtained by comparing the deformation of Rods 7A and 7B. Since fresh rod 7B suffered extensive cladding collapse onto the fuel stack during test LOC-5B and then was ballooned and ruptured during test LOC-5C, whilst the identical fresh rod 7A ballooned and ruptured during LOC-5A which had nearly identical thermal hydraulic conditions with test LOC-5C, the only difference should be the effect of a more circumferentially uniform gap conductance.

A comparison of the axial strain profiles of rods 7A and B is given in Figure 7.15. Rod 7A, which was undeformed prior to blow-down, burst with a circumferential strain of 19% whereas the previously collapsed cladding of Rod 7B ruptured with a strain of 48%, although the maximum strain (about 56%) was found elsewhere on the rod. It is suggested that sufficient negative feedback effects [5] halted the strain at the maximum region and that the changing thermal hydraulics then shifted the maximum temperature region above 0.2 m where failure eventually occurred.

**Figure 7.13 Comparisons of the axial profiles of cladding circumferential strain in the high pressure fresh and irradiated rods, rods 11 and 12, which burst in the  $\alpha$  phase (LOC tests in PBF, [26])**

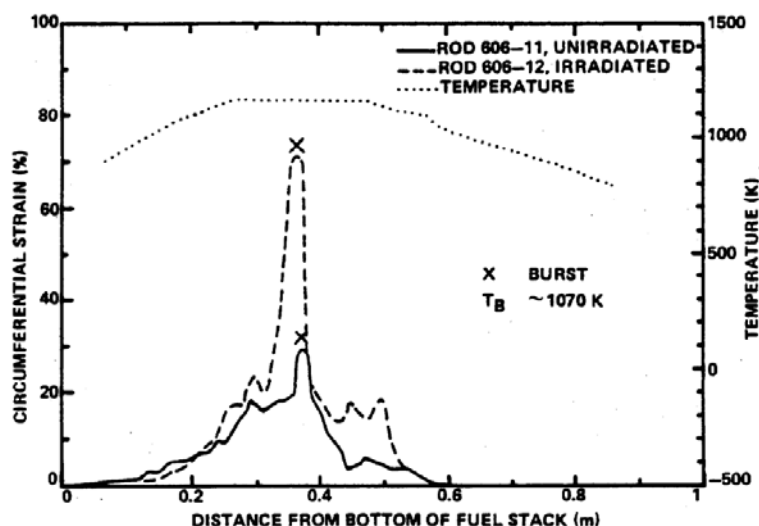


Table 7.2 Summary of cladding deformation data from Tests LOC-3, LOC-5 and LOC-6

Test	Rod Number	Initial Pressure (Mpa)	Burn-up (MWd/t)	Maximum Circumferential Elongation (%)	Axial Extent of Deformation >5% (m)
LOC-3	1	2.45	0	29	0.2 to 0.6
	2	2.38	15960	40	0.5 to 0.6
	3	4.92	0	20	0.15 to 0.6
	4	4.75	16620	41.6	0.10 to 0.65
LOC-5	6	2.41	17660	35	0.13 to 0.65
	7A	4.83	0	19	0.10 to 0.60
	7B	4.83	0	48	0.10 to 0.60
LOC-6	9	2.41	0	<1	— <sup>c</sup>
	10	2.41	10800	13.6	0.25 to 0.56
	11	4.74 <sup>d</sup>	0	31	0.25 to 0.43
	12	4.83	10800	74	0.22 to 0.52

- a. Temperature in parentheses is the best estimate within the range estimated from the cladding microstructure.
- b. This is the heating rate from the cladding surface thermocouples at 0.625 m above the bottom of the fuel.
- c. Cladding did not fail.
- d. The initial internal pressure was probably about 12 Mpa, due to a coolant leak and subsequent formation of steam.

Figure 7.14 Comparisons of the axial profiles of cladding circumferential strain in the high pressure fresh and irradiated rods, rods 3 and 4, which burst in the  $\alpha+\beta$  transition  
(LOC tests in PBF, [26])

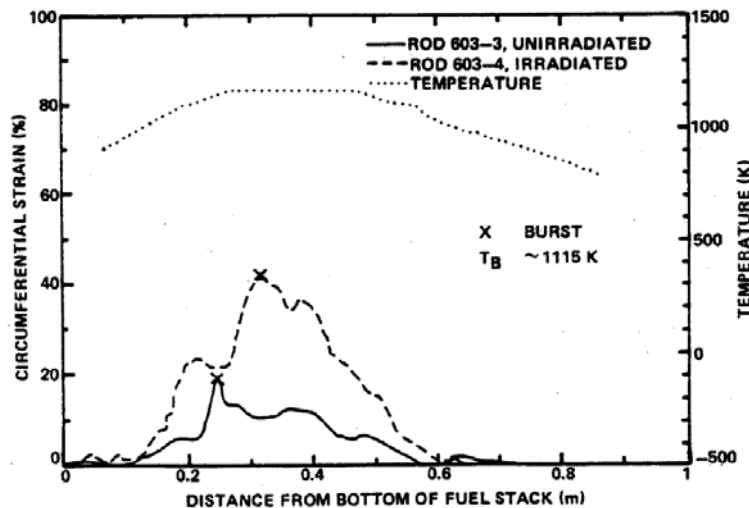
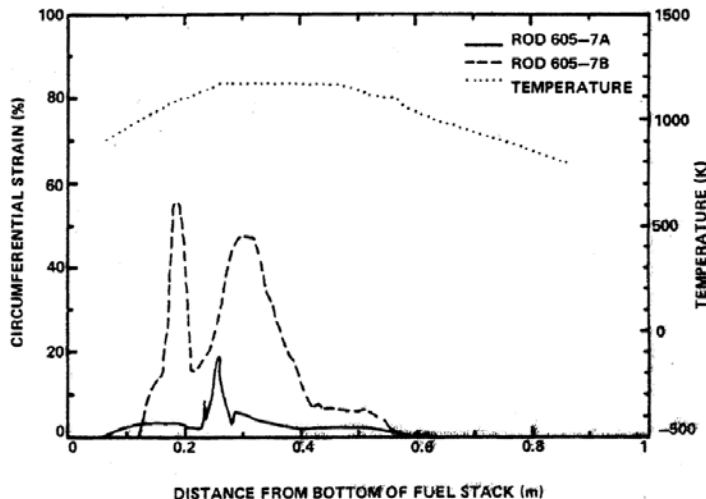


Table 7.2 Summary of cladding deformation data from Tests LOC-3, LOC-5 and LOC-6

Location of Cladding Failure (m)	Failure Time (s)	Cladding Burst Temperature <sup>a</sup> (K)	Heating Rate <sup>b</sup> (K/s)	Burst Pressure (Mpa)	Test
0.257	15.0	1 140 to 1 200 (1 190)	4.3	1.6	LOC-3
0.543	7.9	1 300 to 1 350 (1 300)	20.0	1.0	
0.244	10.1	1 105 to 1 130 (1 110)	15.0	5.1	
0.320	13.1	1 110 to 1 140 (1 120)	15.0	4.8	
0.507	10.5	1 300 to 1 400 (1 350)	0	0.6	LOC-5
0.258	2.75	1 130 to 1 230 (1 160)	100.0	3.5	
0.305	7.8	1 300 to 1 900 (1 350)	70.0	0.7	
— <sup>c</sup>	—	—	—	—	LOC-6
— <sup>c</sup>	—	—	—	—	
0.374	5.2	1 010 to 1 105 (1 098)	100.0	14.0	
0.360	18.2	1 010 to 1 105 (1 066)	0	5.3	

- a. Temperature in parentheses is the best estimate within the range estimated from the cladding microstructure.
- b. This is the heating rate from the cladding surface thermocouples at 0.625 m above the bottom of the fuel.
- c. Cladding did not fail.
- d. The initial internal pressure was probably about 12 Mpa, due to a coolant leak and subsequent formation of steam.

Figure 7.15 Comparisons of the axial profiles of cladding circumferential strain on the unirradiated high pressure rods, rods 7A and 7B with initially undeformed and collapsed cladding (LOC tests in PBF, [26])



### 7.3.1.3 Single rod tests in the ESSOR reactor

Six tests were performed in the EOLO-JR facility in the ESSOR reactor Ispra, Italy to study the ballooning behaviour of PWR-KWU type fresh fuel rods in a simulated LOCA transient [27].

The test specimens contained a 1 m long stack of natural UO<sub>2</sub> pellets 9.10 mm o.d. inside Zircaloy-4 cladding (10.75 mm o.d. 9.3 mm i.d.). They were pressurised cold to about 4.8 MPa via a gas line to the rod plenum. A pressure transducer which was outside the reactor core was connected into this line to record the change in pressure during the test and indicate rupture.

The external heat transfer medium was a helium +5% oxygen mixture [28] and simulated spacer grids were placed at 0.25 and 0.75 m elevations.

The tests were carried out by adjusting the reactor until the rod developed the prescribed power the clad temperature being controlled at 550°C by adjusting the gas circulation. This temperature was held for about two hours to allow detailed measurements of the initial state of the rod. After these had been made the coolant flow was reduced to allow the test rod to increase in temperature at about 3 K/s to the desired value in the range 700-810°C for the particular test. This temperature was maintained by control of the gas flow until the cladding had deformed and ruptured. The reactor was then scrammed to cool the specimen. This sequence is shown schematically in Figure 7.16.

The first test was devoted to calibrating the instrumentation. In the subsequent five tests, the rods bulged and ruptured at five different control temperatures in the high  $\alpha$  phase region (724-807°C).

Figure 7.16 Test procedure for EOLO tests

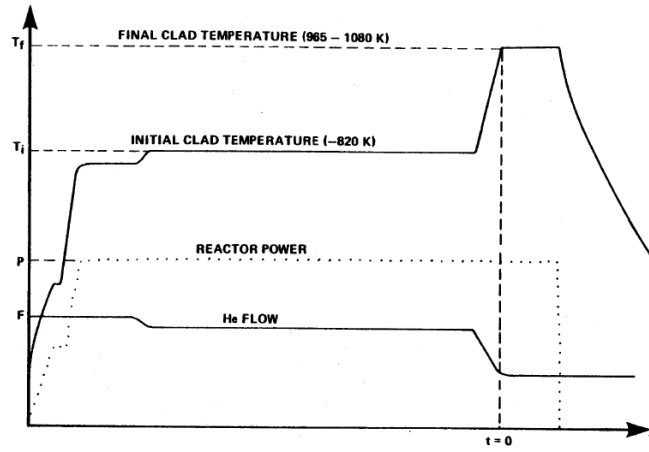


Table 7.3 Summary of the main measurements in the EOLO tests

Data	EOLO-1	EOLO-2	EOLO-3	EOLO-4	EOLO-5
Rod peak linear power (kW/m)	4.32	4.44	3.93	4.32	3.80
Fuel rod cold pressure $P_2$ (MPa)	4.82	4.79	4.9	4.9 (I) <sup>b</sup> 4.0 (II)	5.0
$P_2 - P_1$ at $t = 0$ (MPa)	6.9	5.8	6.5 max. <sup>a</sup> 6.2	6.1	6.4
$P_2 - P_1$ at burst time (MPa)	6.2	5.5	5.7	5.6	5.0
Controlled clad temperature at $t = 0$ (K)	980	1056	1080	1010	970 <sup>c</sup> 990
Peak clad temperature at burst time (K)	1075	1044	1110	1030	995
Max. $\Delta T$ during ballooning (K)	101	92	38	55	48
Burst time (s)	200	130	10	372	3460 <sup>c</sup> 540

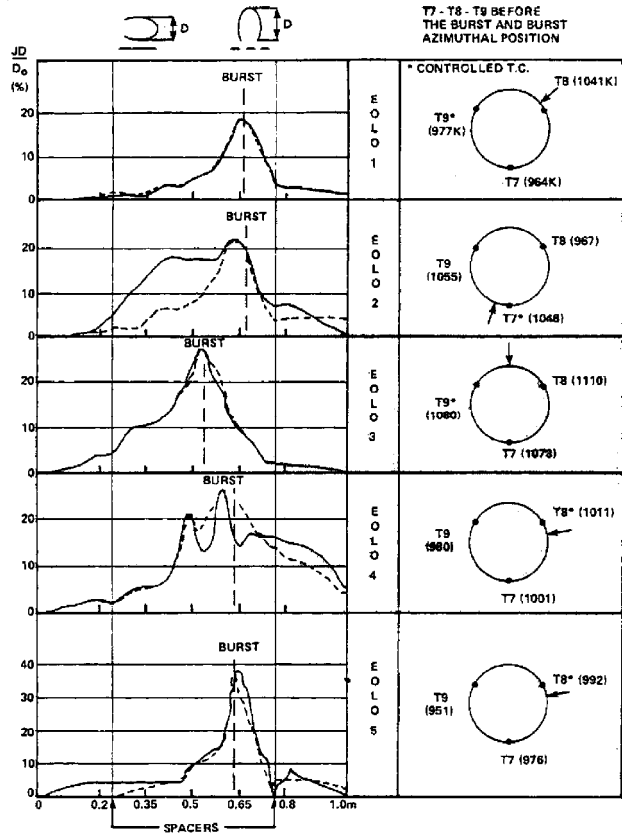
<sup>a</sup> In the test EOLO-3 the clad ballooning started during the temperature ramp ( $t = -20$  s) when the peak clad temperature was 1070 K. Thus two values of  $P_2 - P_1$  corresponding to  $t = -20$  s ( $\Delta P$  max.) and  $t = 0$  are shown.

<sup>b</sup> In the test EOLO-4 an unforeseen reactor scram occurred as soon as the required temperature was reached. The experiment was restarted but it was observed that the fuel rod cold pressure has decreased from 4.9 MPa to 4.0 MPa during the first phase, probably due to prior ballooning.

<sup>c</sup> In the test EOLO-5 the controlled PCT value  $T_f$  had been fixed at 970 K. After 2920 s without failure, the controlled clad temperature was raised to 990 K. Clad burst occurred 540 s after this change.

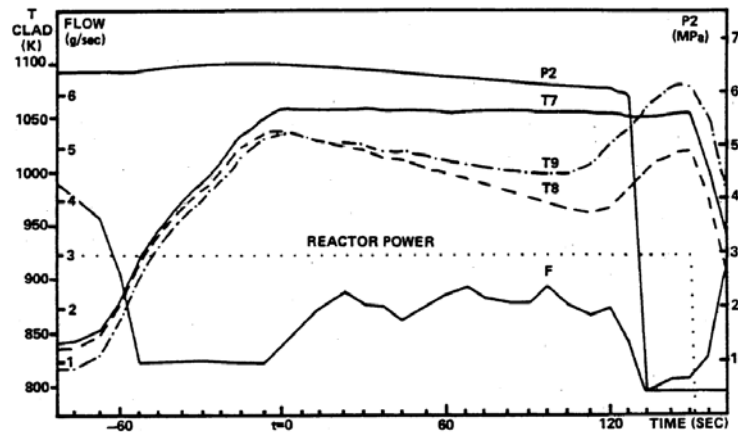
Details of the main measurements made during these tests are given in Table 7.3 and in Figure 7.17 the axial strain profiles, azimuthal temperature measurements and position of bursts are given. The latter occurred very close to the measured maximum temperature in all cases.

Figure 7.17 Post-irradiation diametral metrology of the five burst claddings in the EOLO experiments [27]



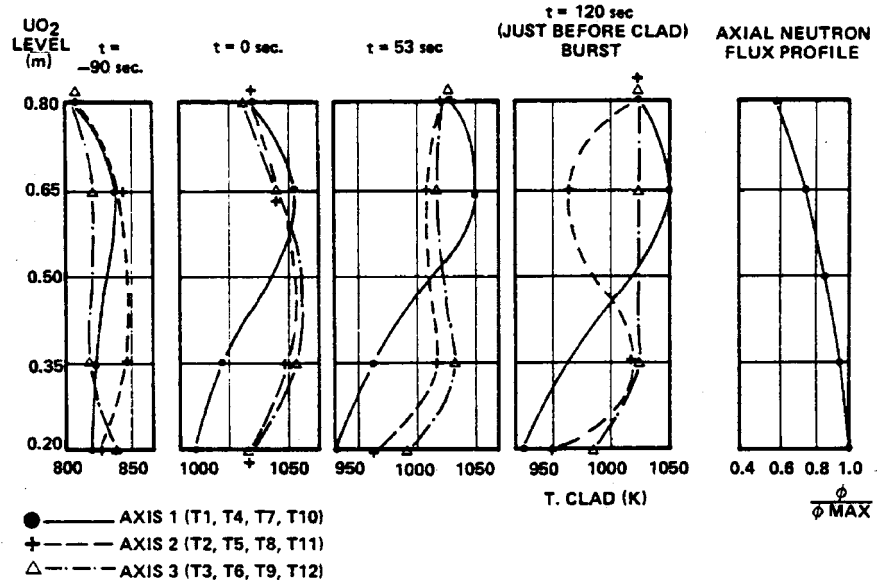
The rod pressure and clad temperature during the test EOLO 2 are shown in Figure 7.18 and the clad temperature and neutron flux profiles in Figure 7.19. In four of the tests the burst occurred at the elevation 0.65 m which is close to the estimated position of the peak clad temperature, but in EOLO 3 the burst elevation was 0.45 m. This test had the highest clad temperature and at the end of the temperature ramp, the coolant flow had to be reduced to zero to achieve this. The effect was to displace the peak temperature elevation.

Figure 7.18 EOLO 2 evolution of the cladding temperature at the level 0.65 m, coolant flow and rod fill gas pressure during the test [27]



The results showed that significant axial and circumferential temperature gradients developed during the test indicating the operation of the stabilising strain-cooling effect [5] and the “hot side straight” effect, which tends to keep clad in contact with the fuel at one side.

Figure 7.19 EOLO-2 clad temperature and neutron flux axial profiles during the test



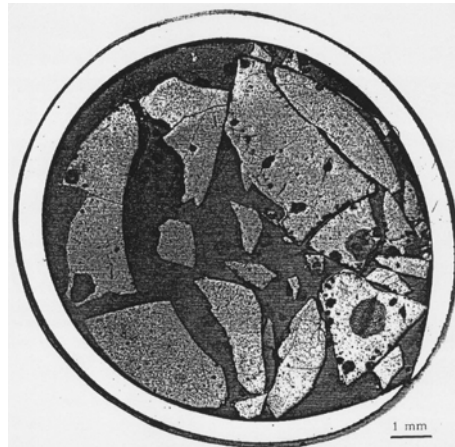
#### 7.3.1.4 Single rod tests in the SILOE reactor

Experiments have been carried out in the FLASH loop in the SILOE reactor, using single 300 mm long rods [29]. The primary aim of the programme was to study fission product release during a LOCA, but data have also been obtained on cladding deformation and oxidation and on fuel stack behaviour. The loop was blown down with residual fission power simulating decay heating, and was then reflooded. In the FLASH-1 to FLASH-4 experiments which were performed on fresh fuel rods preconditioned to low burn-ups at about 35 to 40 kW/m, peak strains of 18-62% were recorded. These data have been applied to validation of the CUPIDON code [30]. The amount of released gases corresponded roughly to the available gas inventory in the rod free volume and the fission product release to the quench water was very low.

The FLASH-5 experiment [31] was performed on a rod refabricated from a 4 cycle PWR fuel rod with a burn-up of 50.3 MWd/kgU. Before the transient it was irradiated a few weeks in the SILOE reactor in order to refresh the short-lived fission products adding 1.4 MWd/kg to the burn-up. The rod reached a temperature of 1 350°C in the transient and a strain of 16%. The low rupture strain is explained by the large azimuthal temperature differences of the rod which exceeded 110 K at the time of burst. In the FLASH-5 experiment, a fine fuel fragmentation was observed near the maximum flux level as well as a significant displacement of fuel fragments at the rupture level despite the low rupture strain (Figure 7.20).

In the FLASH-5 experiment, the amount of released gases was an order of magnitude larger than in the experiments on fresh rods and even larger for the fission product release to the water. However, this result was attributed mostly to oxidation of fuel by steam after clad rupture.

Figure 7.20 Appearance of fuel at rupture plane in the FLASH-5 experiment



#### 7.3.1.5 Multi-rod tests in the NRU reactor

Multi-rod tests in a test loop of the NRU reactor at Chalk River, Canada, have been carried out on behalf of the US NRC and the UKAEA. These tests used full length PWR fuel rods of the  $17 \times 17$  type, which are about two feet longer than the core of the reactor so that the bottom one and a half intergrid lengths and the top one half of an intergrid length are not in the neutron flux. In tests MT-1 to 4, a maximum of 12 rods were pressurised so that they could bulge and rupture. These were arranged in a cruciform shape and surrounded by guard rods which did not deform. The guard rods were spaced at the standard pitch of the pressurised rods so that the latter needed to strain over 60% before there was sufficient contact with the guard rods for the bulges to be restrained.

The tests were carried out using fresh  $\text{UO}_2$  fuel “conditioned” by briefly raising to full power three times just prior to the experiment. Post irradiation examination [32] showed that this treatment cracked the fuel pellets in a similar manner to fuel in a power reactor; however no other irradiation effects can be simulated by this treatment. In the tests proper the reactor power was raised to a level equivalent to decay heat and the assembly cooled by flowing steam. The transient was initiated by shutting off the steam flow and allowing the assembly to heat up under adiabatic conditions achieving a temperature increase of about 8 K/s.

The transient could then be terminated by tripping the reactor. Alternatively two-phase cooling conditions could be created by admitting water to the bottom of the test section. This reflooding water produced enhanced cooling which checked the temperature ramp, producing a flat-topped transient, and ultimately quenched the assembly. In three of the tests, MT-1, 2 and 4, the deformation occurred during the ramp part of the transient in steam whereas in MT-3 the major deformation occurred during the flat-topped portion of the transient under two-phase cooling conditions. The distribution of strain along the rods in the MT series is shown in Figures 7.21 to 7.24. It is evident that substantial co-planar deformations were produced and that the grids had a major influence in restraining the deformation locally. In MT-3, the grids also had a significant effect on the axial shape of the balloons. This results from de-superheating of the steam by water droplets when the two-phase coolant experiences turbulence as it encounters and passes through the grid structures. Thus the onset of significant strain occurs in the top end of the intergrid space and is terminated by the downstream grid (Figure 7.23) producing the characteristic “carrot” shaped balloon.

In MT-1, 2 and particularly MT-4, there were two peaks in the deformation in between grids. The reason for this is unknown.

Figure 7.21 Axial distribution of strain in NRU MT-1 test

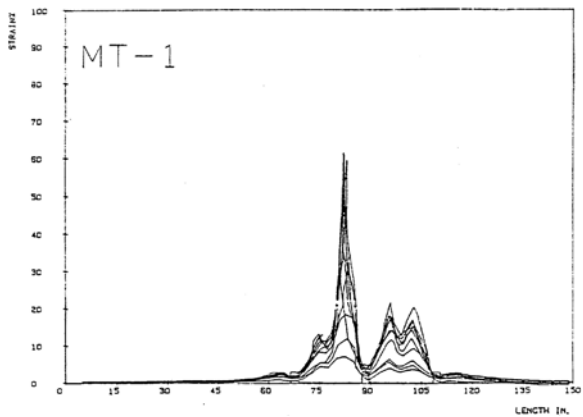


Figure 7.22 Axial distribution of strain in the NRU MT-2 test

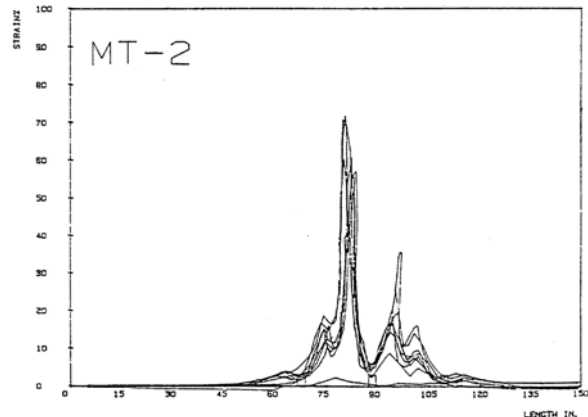


Figure 7.23 Axial distribution of strain in the NRU MT-3 test

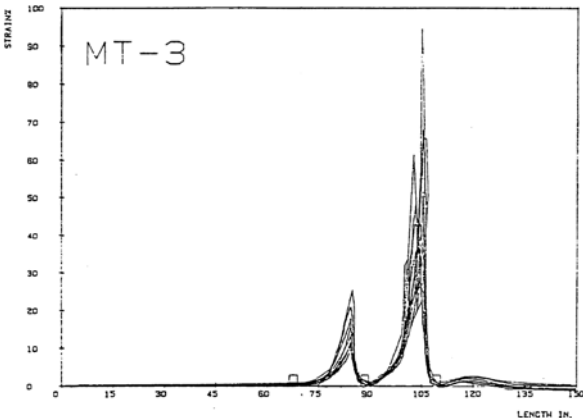
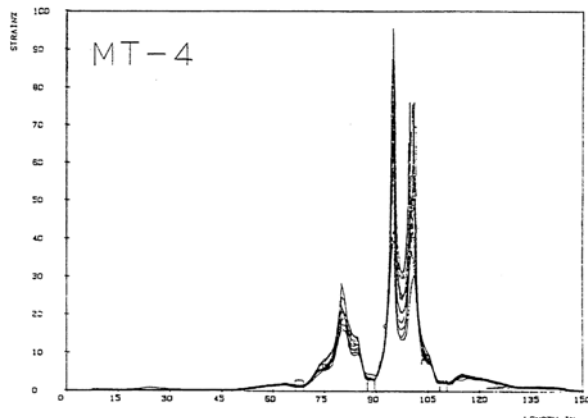


Figure 7.24 Axial distribution of strain in the NRU MT-4 test



In MT-2, the ruptures occurred early in the transient. In this test, it is likely that the fragmented fuel slumped into the bulged regions when the rods suffered the shock of bursting as in the case of the FR-2 tests described in Section 7.3.1.1. Thus, during the remainder of the transient where two-phase flow conditions existed for 80 s, whilst the ruptured regions were above 777°C [33], the conditions existed for generating local excessive cladding temperatures by increased volume of fuel in the ballooned regions as suggested in an analytical study by Bergquist [34]. This mechanism has also been reviewed by Broughton *et al.* [35]. However, there was no evidence of excessive temperatures being achieved in those regions. The surfaces of the ballooned regions appeared similar to the other parts of the rods, and no evidence of embrittlement emerged during PIE.

Post irradiation examination of the rods from the MT series 1-4 showed that except for the actual burst positions or where they were dented by the impact of adjacent bursts, the bulges remained circular [36]. This indicates that the conditions for mechanical restraint from rod to rod interaction as seen in tests with a greater number of pressurised rods (Sections 7.3.2.3, 7.3.2.4 and 7.3.2.7) were not present. Haste [37] has modelled the effect of there being more pressurised rods and deduced that their presence would result in a reduction of the “total” coolant flow area from 55% as measured to 70%. These calculations do not include any effect of clad denting owing to non-simultaneous bursts.

A further test MT-6A was carried out with all the 21 rods of a 5×5 array minus the corner rods, pressurised. All the rods ruptured during the ramp part of the transient in near adiabatic conditions.

Preliminary examination of the bundle has been carried out by cutting holes in the shroud. This showed that all the ruptures occurred in the inward looking direction and complete rod-to-rod interaction was observed at one elevation. Grandjean notes that this test is never mentioned in the PNL summary reports and speculates that the validity of this test has been deemed insufficient and the results have therefore not been retained in the data base of the experiments [24].

### 7.3.1.6 Multi-rod tests in the PHEBUS loop

The CEA has been carrying out a programme in the PHEBUS loop, which is installed in a pool type reactor, to study the behaviour of  $5 \times 5$  fuel rod bundles in a simulated PWR large break LOCA [21-23]. The rods have an active length of 800 mm and are of the  $17 \times 17$  PWR type. The first series consisting of eight thermal hydraulic experiments using unpressurised rods and one test with pressurised rods [20] was started in 1980 and completed in 1982. These experiments were carried out with the fuel rod bundle contained within an unheated shroud. In the burst test (215P), twenty-one of the rods were initially pressurised to 4 MPa to cause them to burst in the high  $\alpha$ -phase region, the remainder i.e. rods 2, 4, 6 and 16 did not deform owing to their low internal pressure. The plenum volume was  $3.2 \text{ cm}^3$ .

The pressurised rods burst within 14 s of one another at the top of the ramp position of the transient at about  $843^\circ\text{C}$  in steam, just prior to reflooding (Figure 7.25). The scatter in burst times is considered to have resulted from non-uniform rewetting which affected clad deformation by emphasising circumferential temperature gradients [20]. Examination of the bundle showed the clad deformations to be carrot shaped and co-planar (Figure 7.26) with strains greater than 33% over about 80 mm in those rods in the central  $3 \times 2$  array which had not been affected by the non-uniform rewetting i.e. rods 7, 8, 9, 12, 13 and 14.

The strains in the peripheral rods were appreciably lower, 15-35%, compared with those in the central  $3 \times 2$  array, 43-53%. This is an expected consequence arising from the steep circumferential temperature gradients induced by the unheated shroud [20]. Nine of the 21 pressurised rods had strains greater than or equal to the maximum strain of 24% seen in the three central rods 17, 18 and 19 affected by non-uniform rewetting.

Figure 7.25 PHEBUS test 215P. History of clad temperatures measured between two grid spacers

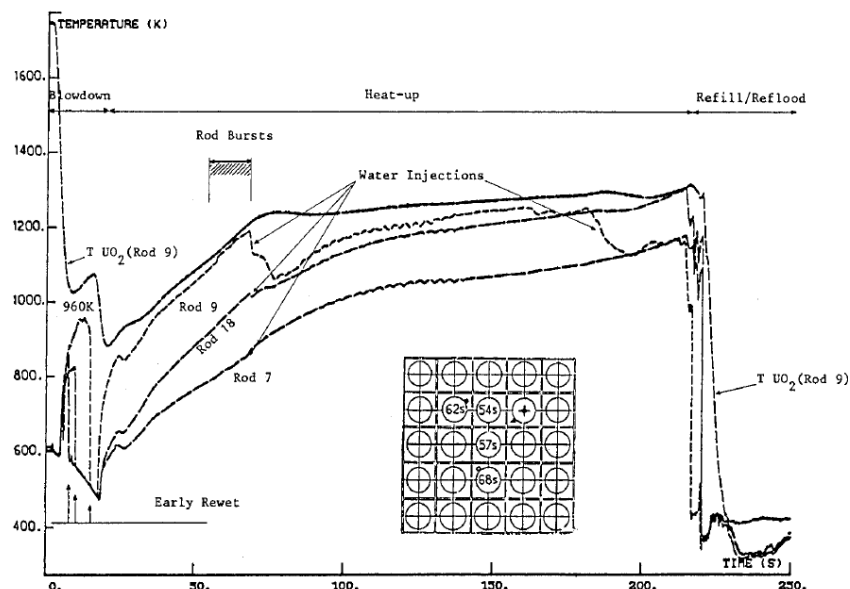
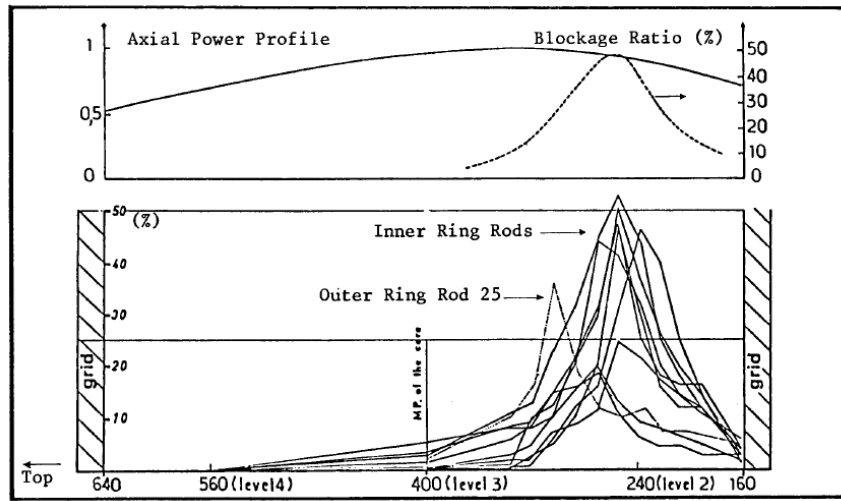


Figure 7.26 PHEBUS test 215P. Axial deformation profile between interior spacer grids and flow area restriction vs distance from bottom of fuel stack



The four tie rods (Figure 7.27) provided sufficient mechanical restraint to induce the balloons in the  $3 \times 2$  array to interact and the central rod adopted an almost square shape i.e. similar to those seen in out of reactor tests where there had been restraint [38-40] (Figure 7.28). The average flow restriction for the central  $3 \times 3$  array i.e. including the three rods with low strains was 65% [20]. However, the greatest individual flow channel reduction was approximately 80%.

Compared to the NRU-MT3 test – keeping apart the very large deformation of one rod in MT-3 – the behaviour of the central rods in PHEBUS 215-P looks similar to that of the central rods in NRU with respect to the coplanarity of the ruptures and to the corresponding flow blockage ratio.

A second test series was started in 1983 and completed in 1984 [24,41]. Ten tests were performed. Of these tests, six were performed with pressurised rods to obtain thermomechanical data. In two of the tests, no reliable data was obtained due to experimental malfunctions.

Figure 7.27 PHEBUS test 215-P. Comparison of maximum burst strains with radial position  
(Low pressure in rods 2, 4 and 6)

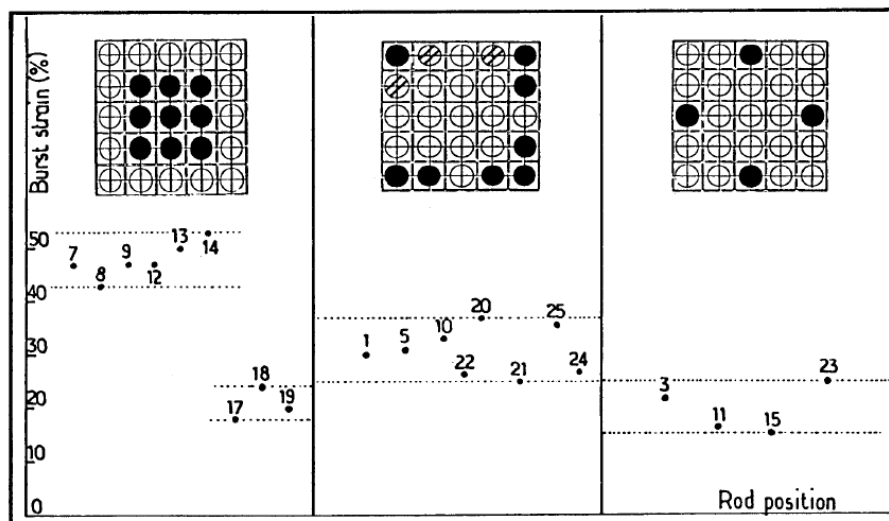
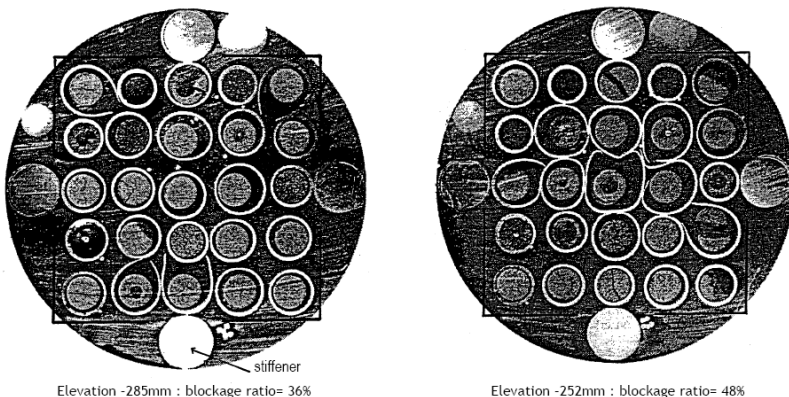


Figure 7.28 PHEBUS test 215-P. Metallographic cross sections at elevations 285 and 252 mm from fuel bottom

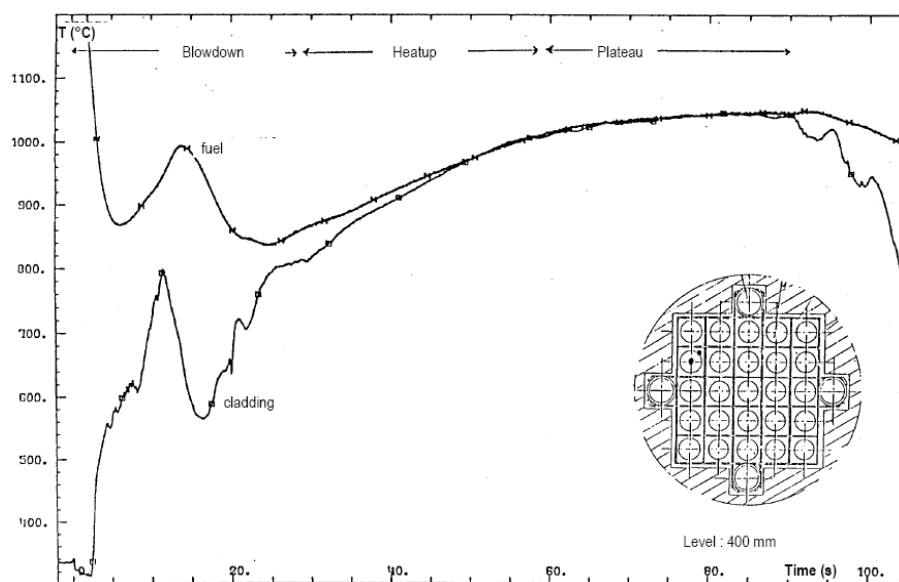


Due to the disturbances on the thermohydraulics in the 215-P test, the transient characteristics of that test have significantly deviated from those of the target transient. The 215-P test was thus followed by a series of tests that aimed at solving the encountered problems, particularly the early rewet of the bundle. This series was concluded by the performance of the 215-R test, which satisfies most of the features of the reference transient:

- First peak near 12 s, at 850-730°C on central and outer rods respectively.
- Temperature drop of 150 to 250°C after about 15 s.
- Heat-up ramp at 10°C/s towards a plateau temperature at 1050°C maintained for about 35 s.
- Progressive reflooding.

Figure 7.29 shows the temperature histories on fuel and cladding at mid-plane elevation of a non pressurised rod. It should be noted that, in test 215-R, 3 rods (nr 2, 4 and 6) were not or slightly pressurised (1 or 5 bar in cold conditions) and that the rods nr 10, 15 and 18 appeared to have lost their initial pressurisation. Finally, only 19 rods have experienced a clad ballooning and rupture during the test transient.

Figure 7.29 PHEBUS test 215-R. Histories of clad and fuel temperatures on Rod 6



All ruptures of the pressurised rods have occurred after 24 s in the adiabatic heat-up phase. For inner rods, it can be noticed that the lowest strains correspond to the earliest ruptures, which indicates that the rupture conditions have been met under high temperature ramp rate ( $\sim 25$  K/s) without leaving much time for the development of large strains. For outer rods, the lower temperature level leads to later ruptures, under a bit slower ramp rate, that should potentially lead to higher burst strains. The measured rupture strains, actually lower than on central rods, may be explained by the effect of azimuthal temperature gradients around the cladding, which appeared to be more important on outer rods, located between the hot central rods and the cold shroud and peripheral structures.

The orientation of the ruptures showed a clear trend of rupture orientations towards the hot regions which are borne on the non-pressurised rods 10 and 18. A comparison of the axial locations of ruptures and ballooned regions between 215-P and 215-R showed that these locations were below the plane of max power for 215-P and above this level for 215-R. A slightly larger extent of the ballooned regions in 215-R is the result of a flatter axial temperature profile in this test.

In consideration of the 215-P and 215-R tests results, it was chosen, for the following tests, to raise the 1st peak temperature to a higher value in order to investigate the influence of the phase transformation of Zircaloy, during that temperature excursion, on the deformation and rupture behaviour of the cladding. Thus test 216 was characterised by temperature levels higher than in the reference case: at 1<sup>st</sup> peak (920 to 1 000°C on central rods, 800 to 900°C on outer rods) as well as at plateau temperature following adiabatic heat-up (1 350°C).

The high ramp rate up to the 1st temperature peak has resulted in early ruptures with limited burst strains, ranging from 15 to 30% for all of the central or outer rods.

The high temperature at the plateau has resulted in a significant oxidation of the Zircaloy cladding (75 and 62 µm oxide thickness on outer and inner face, respectively, for Rod 9), leading to an important embrittlement of the cladding which experienced some fractures upon quenching.

The temperature transient in Test 218 followed approximately the target objectives, with:

- A first temperature peak around 14 s, reaching 930 to 980°C, thus a bit higher than the target temperature.
- A subsequent temperature drop, by 100 to 150°C, thus a bit lower than expected.
- A subsequent rise at 12 K/s up to a plateau temperature around 1 200°C, overshoot on some TC measurements.
- A final slow cooling down to 700°C followed by quenching.

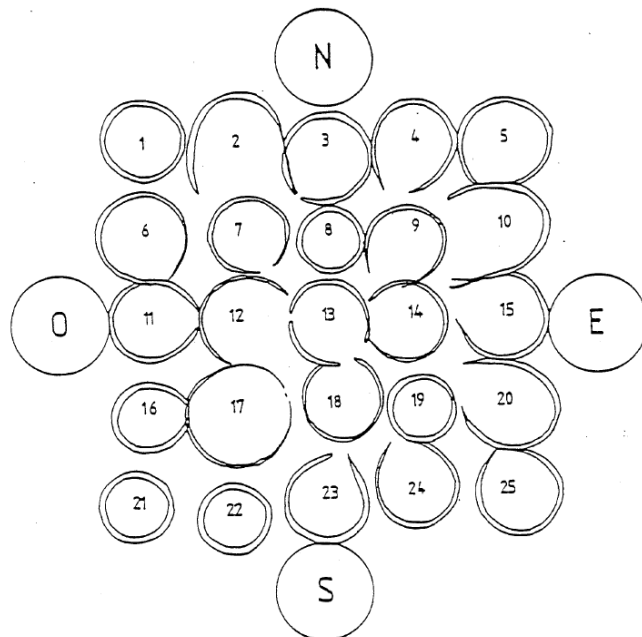
The initial internal pressure of the rods was 3.35 MPa, except for rods 16 and 21 that were initially pressurised at 0.5 MPa, and rods 8 and 19 with low initial pressure.

For the pressurised central rods, the cladding bursts occurred at the 1st temperature peak or during the subsequent drop, whereas most of outer rods burst later, around 23 s, during the so-called “adiabatic” heat-up. Thus, burst strains appeared rather low on central rods (11 to 27%), and larger on outer rods (12 to 36%), in spite of the azimuthal temperature gradients being larger on the latter. Burst elevations spread axially over 60 mm for the central rods and over 80 mm for outer rods. Metallographic examinations performed after the test have shown an average orientation of bursts towards the bundle center, as displayed on Figure 7.30. The maximum flow blockage ratio, located at the experimental level + 316 mm from bottom of fuel, reaches 24% for the central rods subgroup and 38% for the outer rods ring.

The post-test examination of the test bundle on 10 transversal cuts, concentrated over 214 mm and covering notably all the burst elevations, has allowed to determine the azimuthal distribution of

the clad oxidation at different axial levels and to observe the oxidation microstructures obtained at different temperature levels. As a function of temperature, measured by available thermocouples, a fair consistency is observed on the measurements of zirconia thickness on rods in equivalent positions. On the undeformed Rod 8, the oxide thickness measured on outer side reaches 80 µm at hot level (+314 mm), consistent with the plateau temperature having reached 1 360°C. It has also been observed on this rod, at the same level, the development of a UO<sub>2</sub>/Zr solid/solid interaction between fuel and clad, leading to the formation of an internal α-Zr layer. A spalling of the outer oxide layer has been observed on several rods at different locations, which indicates that the oxide layer formed on the central Rod 13 at the hottest level should have exceeded 90 µm since the thickness of the inner oxide layer reaches 83 µm on the measurements at this level.

Figure 7.30 PHEBUS test 218. View of burst strains of rods as projected in a same plane



The measurement of microhardness radial profiles on some rod claddings, as well as of a profile of oxygen content by microprobe analysis, have confirmed and complemented the visual microstructural observations obtained from metallographic examinations.

Test 218 has been chosen as the OECD International Standard Problem ISP-19 [42].

In order to avoid the early ruptures that occurred at 1st temperature peak in test 218, the test 219 differed from the previous test by a lower internal pressure of rods (3 MPa versus 3.35 MPa in test 218). Among 25 rods, 21 were pressurised; the 4 corner rods (Rod 1, 5, 20 and 25) were not.

The test objective was to reproduce a temperature transient consistent with the reference scenario, with the following typical periods:

- A first temperature peak around 930°C.
- A subsequent temperature drop to 800°C.
- An “adiabatic” heat-up with clad ruptures around 890°C in the α+β metallurgical state.
- A temperature plateau at 1 200°C maximum, with a duration allowing to reach 17% average oxidation on central rods.
- A prototypical reflooding phase: slow cooling down to 700°C and final quenching.

The actual scenario of the test meets correctly the target objectives, with a 1<sup>st</sup> temperature peak at  $930 \pm 20^\circ\text{C}$ , followed by a temperature drop to  $800 \pm 30^\circ\text{C}$  and a subsequent heat-up towards the temperature plateau; this plateau phase has been disturbed by an unexpected reactor scram, which induced a partial cooling; the maximum temperature during that phase reached  $1\,330^\circ\text{C}$ .

The time of rupture can have been directly determined only on rods instrumented with a pressure sensor and/or a TC in the plenum. Rupture was observed to occur between 23.8 and 25.4 s on central rods (except for Rod 19, at 35.8 s) and at 36.6 and 37.1 on outer rods number 24 and 3. No rupture was thus detected at 1<sup>st</sup> temperature peak (15 s).

The metallographic examinations that were carried out on a set of transversal cuts of the bundle show that the rupture elevations spread over 80 mm for the central rods and only over 20 mm for the outer rods. The maximum strains that were measured in these examinations range between 18.6% and 46.2% for the central rods, and between 14.5% and 26.4% for the outer rods. This confirms the observation made in tests 215-P and 215-R of an average strain lower on outer rods than on central ones, under the influence of larger azimuthal temperature gradients. The flow blockage ratio, not specified in the analysis report, should have remained limited since the maximum value of the central rods average strain does not exceed 25%.

Thanks to the high degree of available instrumentation in the test 219, it has been possible to perform a refined study linking the rupture strains on central rods with the azimuthal temperature differences as derived from different TC measurements. Over the 22-25 s time interval, corresponding to the main phase of rod deformation, an average temperature difference  $\Delta T$  has been determined for the rods number 7, 9, 12, 14 and 19, then correlated with the maximum strain measured on these rods (Figure 7.31). The resulting correlation between rupture strain and azimuthal temperature difference has then been successfully applied to different rods of tests 215-R and 218: for Rod 3 of test 218 (outer rod that ruptured during adiabatic heat-up) the calculated value of rupture strain is thus 25%, for a measured value at 27%.

The metallographic examinations performed on a set of transversal cuts of the rod bundle have revealed an unusual transversal displacement of the rods, as well as a loss of integrity on the clad of two rods (Rod 8 over about 80 mm and Rod 18 over 60 mm) which may have occurred in regions embrittled by oxidation.

The measurements of oxide and  $\alpha$  layer thickness at hot level, indicate values of the external oxide thickness ranging from 23 to 72  $\mu\text{m}$  in bounding values for the central rods, with average values per rod ranging from 31 to 55  $\mu\text{m}$ ; the alpha layer thicknesses, always a little larger than the oxide thicknesses, follow the same distribution. It is notable that the central rods 12 and 13, which remained intact, are more oxidized than Rods 8 and 18: the evaluation of the oxidation rate with the average oxide thickness alone leads indeed to values of 18 to 20% for Rods 12 and 13, and only 16 and 13% for Rods 8 and 18.

A summary of the temperature transients experienced in the five PHEBUS tests described in the previous section is shown in Figure 7.32. On each temperature curve, black dots indicate the time range during which ruptures occurred.

Table 7.4 summarises the main thermomechanical results regarding the rod ruptures and strains observed in these tests. From this table, the inner rods and outer rods exhibit a distinct overall behaviour; which is reflected by the small standard deviation on the rupture strain for each group of rods.

Figure 7.31 PHEBUS test 219. Burst strain vs average azimuthal temperature difference in the 22-25 s time interval of the transient

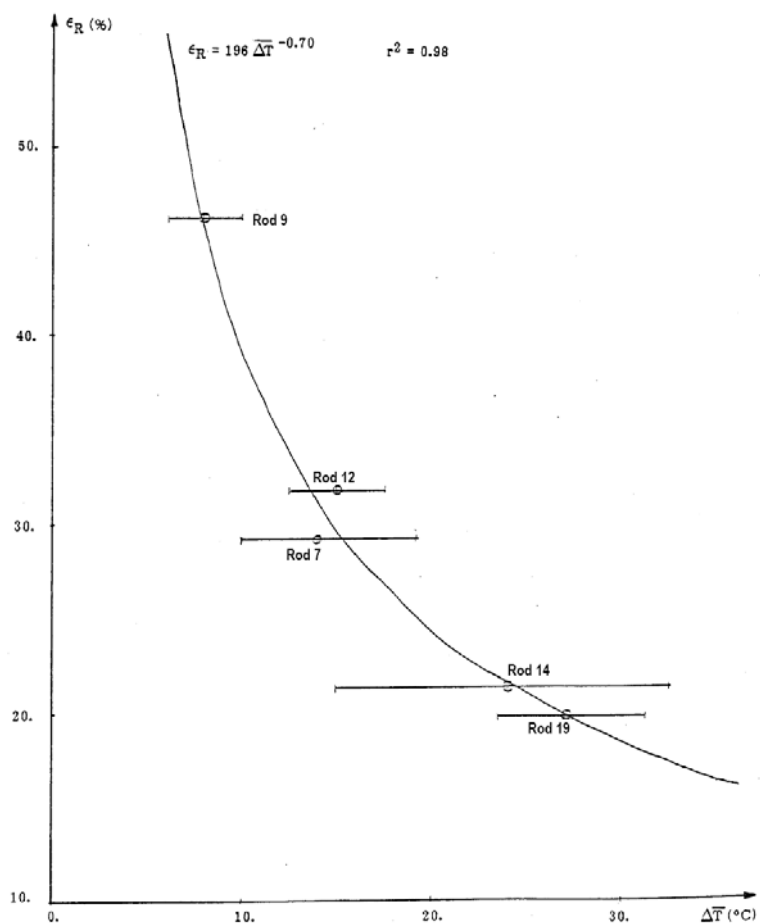


Figure 7.32 Temperature histories in the PHEBUS LOCA tests

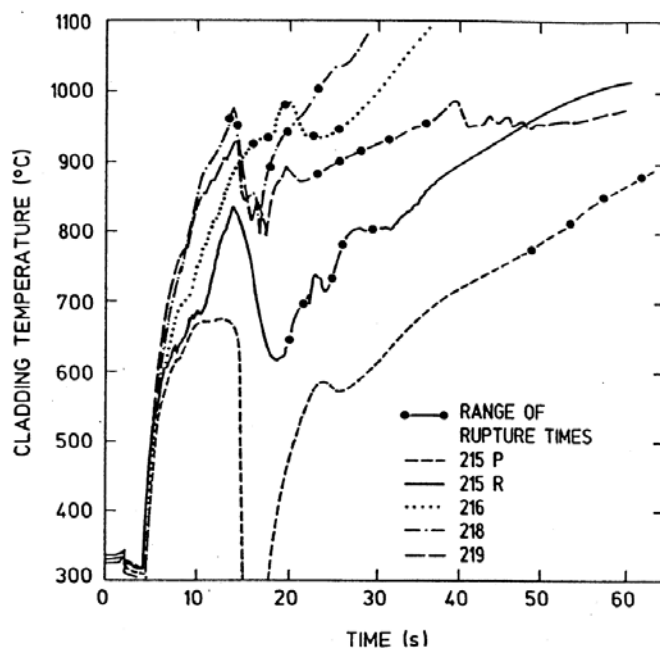


Table 7.4 Thermomechanics of the PHEBUS LOCA tests

Test number (Rod pressure)	Burst time (s)	Burst temperature (°C)	Orientation of ruptures	Burst strain			T at first peak (°C)	Mechanical interaction	
				Range	Mean (%)	Std. Dev (%)			
215-P (40 bar)	Inner outer	50 – 66 65 – 150	840 ? – 830	center center	20 – 54 15 – 38	38 26.6	13 6	No	Yes
	Outer								
215-R (40 bar)	Inner outer	20 – 25 25 – 30	800 – 860 760 – 830	center hot pins	20 – 50 15 – 35	38 29.6	9 5.5	800 – 860 760 – 830	Yes
	Outer								
216 (40 bar)	Inner outer	14.6 – 17 18.5 – 26.4	920 – 1 000 800 – 860	center center	20 ? 30 16 – 31	- 23.6	- 5	930 – 1 000 760 – 830	No
	Outer								
218 (40 bar)	Inner outer	11.5 – 13 15 – 26	900 – 1 000 820 – 900	center center	14 – 27 15 – 38	20 26	5 6	930 – 980 860 – 930	No
	Outer								
219 (40 bar)	Inner outer	21 – 34 33 ? 36	850 – 950 820 ? 880	center ?	19 – 46 14 – 27	28 20	9 4	910 – 950 850 – 910	No
	Outer								

For the inner rods, the ruptures have occurred in the  $\alpha$ -phase domain for tests 215-P and 215-R and in the mixed  $\alpha+\beta$  phase domain for tests 216, 218 and 219. The rupture strains are thus significantly higher in tests 215-P and 215-R than in the other tests. They are however very close in these two tests despite the significant difference in temperature ramp rates at the time of ballooning (7 K/s compared to 20 K/s respectively). This can be explained by the fact that strains have been limited by the large azimuthal temperature differences in test 215-P, whereas the limiting effect in 215-R was mainly the rapidity of the temperature ramp. For the three following tests, where the ruptures of central rods have occurred in the mixed phase domain, different adverse effects act simultaneously on the strain level:

- An increase in  $\beta$ -phase content limits the rupture strain.
- A rapid temperature rise also limits, by itself, the rupture strain but also delays the  $\alpha \rightarrow \beta$  phase transformation, thereby reducing the  $\beta$ -phase content which acts in opposite way.

The application of phase change kinetics models to the three Tests 216, 218 and 219 shows that significant departure from equilibrium phase fractions has been obtained in these tests, ranging from almost no  $\alpha \rightarrow \beta$  transformation at rupture in Tests 216 and 218 to a maximum of 25% phase transformation in test 219. Owing to the effect of  $\beta$  phase fraction alone, lower strains could have been expected for the test 219 rods; the observation of an opposite result leads one to conclude that the effect of the temperature ramp rate (lowest in test 219, compared to test 216 and 218) is the dominant factor.

For the outer rods, lower burst strains are generally observed with respect to that of the central rods. This result has been mainly attributed to the effect of azimuthal temperature difference, larger on outer rods owing to the influence of cold outer structures, particularly in tests 215-P and 215-R where these temperature differences were more pronounced. This effect is consistent with the orientations of the ruptures, which were found to be directed either towards the centre of the bundle (215-P, 216, and 218) or towards some hotter non-pressurised rods (215-R and 219). These orientations underline the importance of radiative transfers between rods and structures on the appearance of “hot spots” that will limit the deformation by “hot side straight effect”. In the particular case of test 218, the very rapid temperature ramp has led to rupture of the central rods at the 1<sup>st</sup> temperature peak with low burst strains, whereas the outer rods, which have ruptured later, exhibit a larger mean burst strain.

In summary, the rod thermomechanical behaviour in the PHEBUS tests appeared to be influenced by different phenomena that may be classified according to their relative order of importance:

- Kinetics of temperature transient.

- b) Azimuthal temperature differences.
- c) Kinetics of  $\alpha \rightarrow \beta$  phase change.

The efficiency of the analysis of such test results will thus highly depend on the capability of the computer codes used in these analyses to represent, more or less accurately, the above phenomena.

#### *7.3.1.7 LOCA tests in the Halden reactor*

The OECD Halden Reactor Project is a series of in-pile experiments performed in the Halden Boiling Water reactor, a heavy water cooled and moderated reactor. The project is sponsored by about twenty organisations from different countries and it is operated by the Norwegian Institutt for Energiteknikk. The experiments in the Halden reactor are assigned IFA numbers where IFA stands for Instrumented Fuel Assembly. However, IFA numbered experiments are not limited to fuel assemblies but can also be structural materials experiments.

There have been two former LOCA programmes in the Halden reactor, the IFA-511.X and IFA-54X experiments in the early 1980s and the currently running experiment IFA-650.X.

##### *7.3.1.7.1 The IFA-511.X and IFA 54X programme*

For a description of the experiments, see Section 5.3.1.4.1. The main objectives of the experiments were [43]:

1. To study the thermalhydraulics of emergency core cooling situations, in both the blowdown and reflood phases, including the rewetting of the fuel rods at various reflood rates, average linear heat generation rates, and times to reflood (i.e., the start of injection of cold liquid into the test section).
2. To compare the behaviour of nuclear fuel rods to that of electrically heated rod of different types in identical environments, also to serve as reference for laboratories that can perform experiments only with electrically heated rods.
3. To overheat nuclear and electrically heated rods to deformation and burst (ballooning) of the cladding tubes.

The results of the thermohydraulic tests will not be described in any detail in the present report. In summary and conclusion the tests showed that [43] two different temperature responses were observed: the sudden drop in temperature close to the saturation value typical of quenching by submersion and a progressive decrease in temperature that should indicate precursory cooling. This phenomenon was observed in the uppermost and sometimes in the lowest level where the thermal flux is lower. In many tests premature quenching was observed near the location of spacers.

The quenching response was very much affected by the surface conditions of the cladding tubes. The presence of a layer of oxide on the cladding surface noticeably improved the heat transfer conditions during reflooding. Quenching behaviour of the rods thus is dependent on previous test histories.

The quenching times seem not to be influenced by the time to reflood or by the peak temperatures of the rods but only by the reflood flow rate. There is no definite quenching temperature, but it follows the peak temperature. Higher peak temperatures lead to higher quenching temperatures.

In the test with electric rigs, the Semiscale heaters (solid type) show delayed quenching at any reflood rate in comparison with the nuclear rods, whereas REBEKA heaters (simulating pellet-to-clad gap) have a thermal response similar to that of nuclear rods. Quenching times can differ up to a factor of 2 between nuclear and electric rods, the boundary and initial conditions being the same.

The IFA-54X experiments have been summarised and analysed by Haste [44]. From Haste's perspective the objectives of the test series were:

- (a) To compare the behaviour of multi-rod nuclear and electrically heated assemblies in otherwise identical thermal hydraulic conditions broadly representative of blowdown and reflood in a PWR.
- (b) To undertake several experiments of each type to test the reproducibility of the results.
- (c) To aim for conditions which would promote balloons large enough to give significant interaction between neighbouring rods.

Five ballooning experiments were carried out, three being nuclear heated, IFA-543, IFA-545 and IFA-547, while the other two were electrically heated, IFA-544 and IFA-546. A further nuclear heated assembly, IFA-541 with unpressurised fuel rods, was used at the start of and during the test series in a number of tests designed to aid understanding of the thermal hydraulic performance of the assemblies and to set the conditions for the ballooning tests. The results of the tests have been summarised in Table 7.5.

Before testing the pellets in the nuclear heated tests were preconditioned by ramping to linear heat ratings of 13, 20 and 28 kW/m for IFA-543, 545 and 547 respectively. Figure 7.33 shows a typical temperature record from one of the ballooning tests.

The other two temperature transients for the nuclear heated tests were similar while the time in the electrically heated test IFA-544 was much shorter. This was caused by the attempt to match the heating rate in IFA-543. However, since the thermal capacity of the electric heaters was higher than for the UO<sub>2</sub> fuel, this led to an increased stored energy and a temperature overshoot of about 30 K at the end of the heat up phase with a consequent much shorter time to rupture. An attempt to use lower power in the second electric test, IFA-546, led to results which were judged to be unsuitable for cross comparisons and no further evaluations were done on that experiment.

**Table 7.5 Summary of rod burst strains in IFA-54X**

Rod number	Mid-rupture location above bottom of fuelled section, mm	Azimuthal orientation clockwise looking from assembly top	Rupture hoop strain, %	Fitted constant eccentricity	
				MABEL-2D	SWEM
IFA-543					
1	880	335	33	0.36	0.66
2	805	135	25	0.71	1.00
2	730	30	29	0.50	0.82
3	680	140	26	0.65	1.00
5	865	190	39	0.21	0.43
Mean( $\pm 1 \sigma$ )			$30.4 \pm 5.7$		
IFA-545					
1	1 087	~335	26	0.65	–
2	727	~13	28	0.55	–
2	820	270	27	0.60	–
3	774	20	30	0.46	–
5	1 116	95	32	0.39	–
Mean( $\pm 1 \sigma$ )			$28.6 \pm 2.4$		

Table 7.5 Summary of rod burst strains in IFA-54X (Cont'd)

Rod number	Mid-rupture location above bottom of fuelled section, mm	Azimuthal orientation clockwise looking from assembly top	Rupture hoop strain, %	Fitted constant eccentricity	
IFA-547					
1	831	~320	35	0.30	-
2	706	~350	22	0.92	-
2	757	340	34	0.33	-
3	708	10	25	0.71	-
5	789	135	31	0.42	-
Mean( $\pm 1 \sigma$ )			$29.4 \pm 5.7$		
IFA-544					
1	727	245	23	0.84	1.00
2	759	280	26	0.65	0.96
2	794	145	25	0.71	1.00 <sup>#</sup>
3	793	0	21	1.00	1.00 <sup>#</sup>
5	808	90	24	0.82	1.00 <sup>#</sup>
Mean( $\pm 1 \sigma$ )			$23.8 \pm 1.9$		

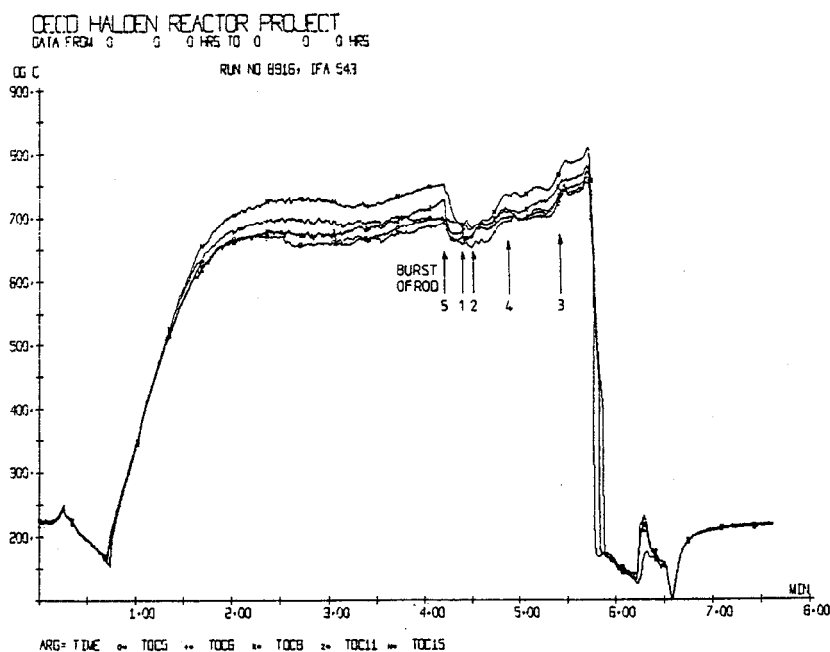
Mean rupture strain, nuclear heating =  $29.5 \pm 4.5\%$

Mean rupture strain, electric heating =  $23.8 \pm 1.9\%$

#: "Hot spot factor" invoked to indicate assumed departure from cosine azimuthal temperature distribution at low strains

The deformation times in the tests were estimated from pressure readings and confirmed in some cases by CANSWEL-2 [45] and BALLOON [46] code calculations as being 100-150 s in the nuclear test and about 30 s in the electrical test. This was in the design range for the nuclear tests whereas the electrical time was ~20 s too short. However in all tests ballooning took place under two-phase flow conditions with high heat transfer from cladding to coolant as intended in the specification.

Figure 7.33 Temperature transient a cladding level 4 in the IFA-543 ballooning test

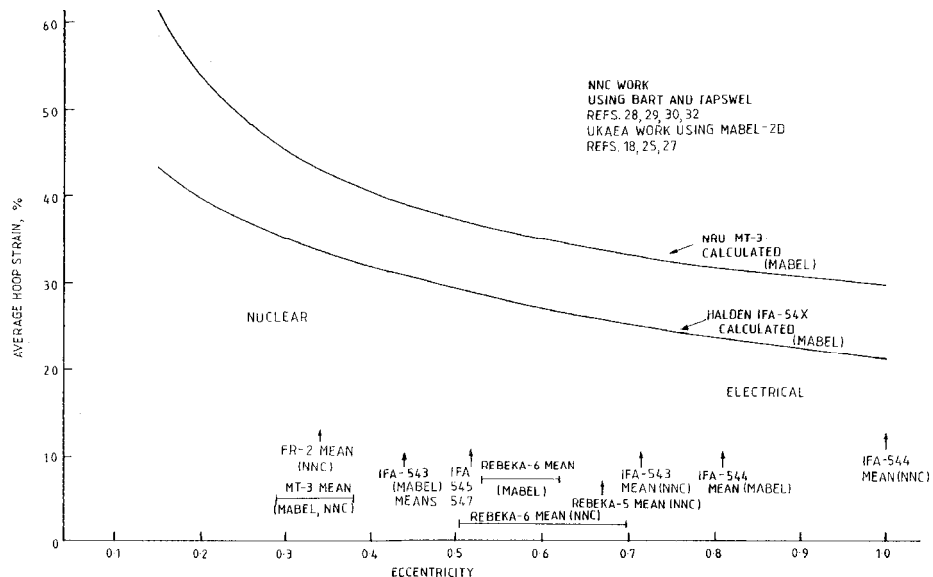


Extensive post-irradiation examinations of the ballooned bundles were carried out by CEGB staff working at AEE Winfrith including detailed mensuration,  $\gamma$  scanning and pellet fragmentation studies. Rod burst strains and rupture orientations are listed in Table 7.5. The results are mainly presented in internal CEGB documents with the exception of one conference presentation [47]. The key observations were:

- (a) The strains in the nuclear heated experiments are consistent amongst each other, despite detailed differences in the transients and in the degree of pre-conditioning experienced by the fuel pellets.
- (b) The strains in the electrical test are lower than those in the nuclear tests, the figures for mean rupture strain are  $23.8 \pm 1.9\%$  and  $29.5 \pm 4.5\%$  respectively.
- (c) The rupture sites are randomly orientated. This implies that the direction of rupture was not dominated by the surroundings i.e. by the presence of unheated outer shroud or downcomers. These structures did lead to overall lower temperatures on the outer rods, giving longer rupture times, but did not generate azimuthal temperature gradients comparable with those generated internally by the heat source/cladding asymmetry.

A notable feature of the Halden tests was that the rupture strains were low compared to all other contemporary bundle calculations. Haste discusses how this observation could be explained by calculations with the code MABEL-2D [44]. An important input parameter to the calculations is the fuel pellet eccentricity,  $e$ . It is defined as the ratio between the offset between fuel and cladding centres and the fuel cladding gap. Thus  $e=1$  implies that fuel and cladding are in contact along a generatrix of the cylindrical surfaces and  $e=0$  implies that the gap is constant around the pellet. Pellet eccentricity  $e$  need not be constant during deformation but was assumed to be so in the calculations. Table 7.5 shows the  $e$ -values needed to fit the calculations with the experimental results for MABEL-2D calculations by Haste and calculations with the code SWEM by NNC staff [44]. The effect of eccentricity on rupture strain can be seen in Figure 7.34.

**Figure 7.34 Comparison of predictions of rupture strain as a function of pellet eccentricity for MT-3 and IFA-54X**



Another possible cause of the low rupture strains could be initial wall thickness variations. Therefore the post-irradiation examination included detailed measurements of azimuthal wall thickness variations at different axial positions for rods from IFA-543, 544 and 545. The experimental

work was supported by BALLOON code calculations to show how different combinations of azimuthal temperature variations and initial wall thickness variations affect the azimuthal wall thickness variation at various strains up to rupture.

The experimental wall thickness data showed that strain localisation increases as strain increases. The azimuthal location of the wall thickness minimum varies systematically with axial location so that the locus of the minimum traces out a helix on the cladding surface. In contrast, very little rotation was observed in the electrically heated IFA-544 specimens, the minimum wall thickness is independent of axial location. The pattern of wall thickness variation in the nuclear rods is similar to that found in the NRU MT-3 experiment and suggests that the pellet stack adopts a helical configuration as clad deformation proceeds, thereby leading to azimuthal temperature and wall thickness variations resulting eventually in cladding rupture. The helical configuration can also be seen in Figure 7.10 from the FR-2 tests.

Haste notes that the KfK report [3] describing the results of the FR-2 tests argued that there were no differences in the ballooning response of nuclear and electrically heated rods (Figure 7.11). The tests were carried out by ramping single rods in an unheated shroud with the intervening space filled by flowing steam. The KfK test programme however was less sensitive to the difference between heating methods than the Halden series because: (i) there were fewer tests (only 3) in the alpha-phase region where the anisotropy of Zircaloy creep lead to relative heater/clad bowing and (ii) the heat transfer conditions were poorer so that azimuthal temperature gradients for a given eccentricity and strain were lower and burst strains were therefore higher. Differences due to the different heating methods were diluted by other strain-reducing effects such as initial non-uniformities in wall thickness, which can lead to strains down to ~60% for an initial  $\pm 2\%$  variation. The Halden tests, with their high heat fluxes across the pellet/cladding gap during ballooning, are much more sensitive to differences resulting from the heating method used.

This good heat transfer in the ballooning phase of the Halden tests led to low rod strains so that the third objective of achieving mechanical interaction between rods could not be met. However, the improved understanding of ballooning achieved from analysis of the test series and other multi-rod experiments suggests that the objective was not really achievable given the limitations imposed by the test section design.

#### 7.3.1.7.2 The IFA-650.X programme

The currently (2003-) ongoing Halden experiments numbered IFA-650.X are single pin tests and focus on effects that are different from those studied in out-of-reactor tests. A prototypical bounding LOCA transient does not exist, and Halden project participants recommended that the test conditions be selected to meet the following primary objectives:

- (a) To maximise the balloon size to promote fuel relocation, and to evaluate its possible effect on cladding temperature and oxidation.
- (b) To investigate the extent (if any) of – “secondary transient hydriding at high temperature” – on the inner side of the cladding around the burst region in presence of pellet-cladding bonding layer.

Target peak clad temperatures (PCT) for the pre-irradiated rods have been set at 800°C and 1 100°C for high and medium burn-ups. The new Halden experiments were deemed necessary because industry trends to high burn-up fuel design and introduction of new cladding materials have generated a need to re-examine and verify the validity of the safety criteria for loss of coolant accidents. High burn-up fuel rods irradiated in commercial reactors will be used in this series of tests.

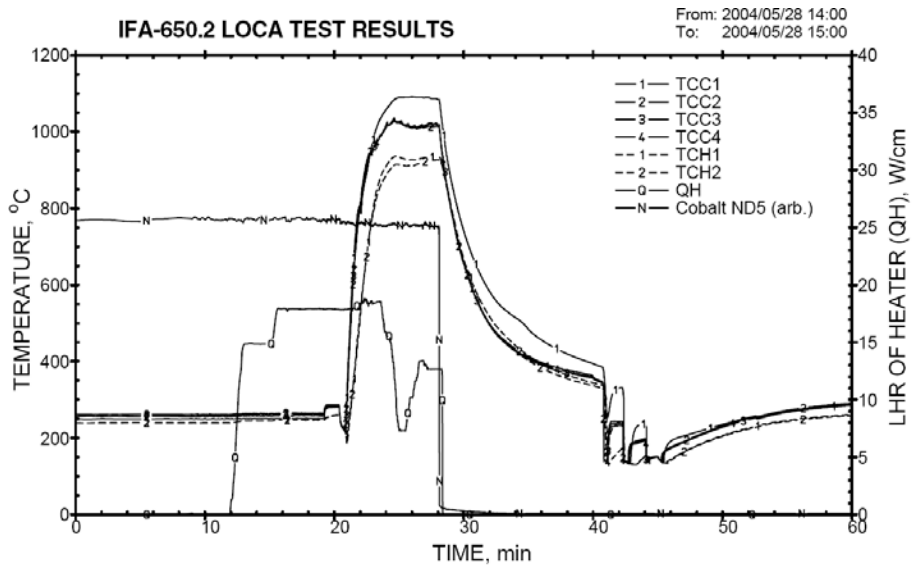
The first series of LOCA test runs of the IFA-650 test series [48] were performed in the Halden reactor using a fresh unpressurised and small-gap PWR rod with low-tin Zr-4 cladding. A total of six test runs were performed. The target PCTs of ~800 and ~1 100°C were achieved.

The cladding temperature was controlled by the power of the fuel and the outside heater. The measured temperatures reacted consistently to the power changes during the test runs. It was observed that the total LHR (fuel + heater) is the major factor that determines the clad temperature transient. The water spray was successfully tested in two test runs. The effect of the spray is local and only seen on the thermocouples located in the upper part of the fuel rod. Its main purpose is to ensure the correct conditions for oxidation. No fuel failure occurred during the test. Also technically the rig, the loop, and all the instrumentation and data collection systems worked well. The first LOCA test series provided thus a good basis for further experiments planned for pressurised and irradiated fuel rods.

Several pre-test code calculations were performed by outside laboratories as well as by the Halden Project. FRAPTRAN/GENFLO (VTT) and TRAC-BF1 (PSI) calculations were made by the outside laboratories and FTEMP3, SCTEMP and ALGOR calculations by the Halden Project. The code calculations gave good simulations of the measured clad temperatures and they will be continued in the future.

The second trial LOCA test in IFA-650.2 was carried out in May 2004. Before the LOCA test, two power ramps were performed to pre-crack the fuel pellets. The fuel rod was irradiated for 1.5 days to accumulate fission products. The test consisted of a blow down phase, heat-up, hold at PCT, and termination by a reactor scram. The target for peak cladding temperature was 1 050°C. In order to achieve this target, the heat rates of the fuel rod and heater were adjusted to 22 and 17 W/cm, respectively. These parameters were chosen on the basis of earlier experience obtained during the first trial tests in IFA-650.1.

**Figure 7.35 Measured clad (TTC1-4) and heater (TCH1-2) temperatures, linear heat rate of heater (QH) and readings of Co neutron detector (Cobalt ND5) during the LOCA test run**



Some results from the LOCA test are graphically shown in Figure 7.35. The cladding thermocouples showed that the target PCT of 1 050°C was successfully achieved. The peripheral temperature variation was negligible, i.e. within  $\pm 3^\circ\text{C}$  as measured by the upper three thermocouples. The observed average increase rate of the cladding temperature was  $7.8^\circ\text{C}/\text{s}$  up to the time of rod

failure. Failure of the fuel rod (i.e. cladding burst) was detected at a cladding temperature of ~800°C by means of cladding elongation and rod pressure measurements. The rod pressure rapidly dropped to 58 bar. This is due to the pressure monitoring technique – the bellows expansion is stopped mechanically. In reality the rod pressure will soon reach the rig pressure (2-3 bar) after ballooning and burst. The hoop stress at failure was calculated to be ~55 MPa on the basis of measured rod pressure. The rod failure was also detected, after some delay, by the  $\gamma$  monitor mounted on the blow down line. Several activity peaks of released fission products were also observed shortly after the reactor scram and use of the spray system.

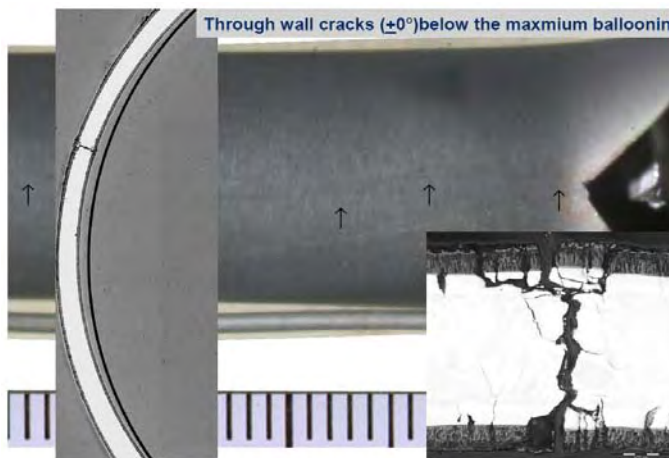
The hold time above 900°C was about 6.5 minutes. In order to provide conditions for oxidation of the cladding, the water spray was intermittently applied during the hold at PCT. Spraying was started above 900°C and the readings of the clad upper thermocouples (TCC2, TCC3 and TCC4) began to deviate from that of thermocouple TCC1 at the lower end. The duration of each spraying pulse was about 1 second and the intervals between the pulses varied from 20 to 40 s. When the spray was used, temperatures of TCC2-4 started to decrease slightly. However, at the same time the heater power was reduced from about 18 W/cm to 7-8 W/cm in order to keep its temperature below 950°C and hence this is the main contributor to the decrease in cladding temperature as recorded by TCC2-4.

An extensive post irradiation examination has been performed and presented at a LOCA workshop meeting in 2005 [49]. Figure 7.36 shows the balloon with relocated fuel pellets. However, it is thought that the relocation mainly occurred due to transport and handling since the in-pile instrumentation did not reveal any clear indications of fuel relocation. The actual burst was a totally ductile failure. However, close to the burst location a more brittle crack through the cladding was observed (Figure 7.37). Such cracks could be the result of hydriding but hydrogen analyses of the rod did not show more than about 100 ppm hydrogen near the balloon.

Figure 7.36 Ballooned region with relocated fuel in the Halden IFA-650.2 test



Figure 7.37 Through wall cracks with brittle appearance. Halden IFA-650.2 test



IFA-650.3, the first test with pre-irradiated fuel in the Halden Project LOCA test series, was conducted on April 30, 2005 [50]. The fuel was provided by Framatome ANP and had been irradiated in a commercial PWR to a high burn-up, 82 MWd/kgU. The experimental arrangements of the third test were similar to the preceding LOCA tests. The target temperature (800°C) was achieved and a rod burst occurred at ~780°C in the lower TCC weld area.

The target cladding temperature of 800°C was reached, and the hold time was ~6 min (from burst to scram). Cladding failure occurred ~266 s after blow-down at ~780°C as evidenced by rod elongation, pressure and cladding temperature measurements as well as the  $\gamma$  monitor on the blow-down line to the dump tank. The average temperature increase rate prior to the burst was 2.4 K/s.

Spraying with short pulses was applied after the burst. The cooling effect of the spray could be seen on the upper cladding thermocouples. The heater power was reduced when approaching the target temperature, which also explains the slightly decreasing temperatures after reaching the peak cladding temperature (PCT). The test was terminated by a reactor scram. At the end of the cooling, one longer spray pulse was applied to enhance the cooling. After the test was finished, the rig was filled with helium.

The first results from the PIE indicate that no large ballooning occurred and the cladding failure occurred close to the lower TCC weld. Small local ballooning had, however, started also in the middle of the rod. The rod experienced some uniform cladding deformation (7%). Bowing was also observed in the rod. However, no fuel relocation could be detected in-pile, and the PIE results also indicate that no fuel relocation occurred. The detailed results of the complete PIE of IFA 650.3 are not yet available.

IFA-650.4, a repeat of the first test with pre-irradiated fuel, IFA-650.3, was conducted on 25 April 2006 [51]. The fuel was provided by Framatome ANP and had been irradiated in a commercial PWR to a high burn-up, 92.3 MWd/kgU. The experimental arrangements of the fourth test were similar to the previous LOCA tests, especially to IFA-650.3. The target temperature (800°C) was achieved and a cladding burst with fuel relocation occurred.

In the IFA-650.4 test one pre-irradiated fuel rod was located in a standard high-pressure flask, which was connected to a heavy water loop and a blowdown system. Heating was provided from the fuel and from the heater surrounding the fuel rod. The heater was used for simulating the isothermal boundary conditions. The axial power distribution was measured with three self-powered vanadium neutron detectors (ND). Rapid power changes were monitored using two fast responding cobalt NDs. Other rig instrumentation consisted of two cladding surface thermocouples at the upper part of the fuel stack and two above the fuel stack, a cladding extensometer, a pressure sensor at the rod upper end, two heater thermocouples, and inlet and outlet coolant thermocouples. The power profile was symmetric and slightly peaked in the middle (axial peak to average power factor ~1.05).

The test was run as planned. The target cladding temperature of 800°C was reached, and the hold time was ~5 minutes (from burst to scram). Rod overpressure at hot conditions was ~65 bar. Cladding failure occurred ~336 s after the blowdown at ~785°C, as evidenced by rod elongation, pressure, neutron detector, and cladding and heater temperature measurements as well as the  $\gamma$  monitor on the blowdown line to the dump tank. The average temperature increase rate prior to the burst was 1.9 K/s.

Spraying was started 230 s after the burst. The first spray pulse was longer (12 s) than planned (0.5 s pulses every 20 s) and the cooling effect of the spray could be seen as an unfortunate temperature drop on the cladding and heater thermocouples. The heater power was kept constant throughout the test and reduced once ~150 s after the burst. The heater was switched off 35 s after starting the spray. Soon (15 s) after this, the test was terminated by a reactor scram. At the end of the cooling period, one longer spray pulse was applied to enhance the cooling. After the test was finished, the rig was filled with helium.

The results from the post-test  $\gamma$  scanning indicate that a large ballooning in the middle of the rod and burst with fuel relocation occurred. The ballooning, burst, and fuel relocation were detected in-pile and were verified by the  $\gamma$  scanning performed at Halden. The PIE of IFA-650.4 is still in progress and the detailed results are thus not yet available.

### 7.3.2 Out-of-reactor tests

#### 7.3.2.1 The REBEKA programme at Kernforschungszentrum Karlsruhe (KfK)

This programme [7] used single and multi-rod geometries to investigate the deformation of Zircaloy fuel cladding during the refilling and reflooding phases of a LOCA (Section 5.3.2.1). The REBEKA test philosophy and objectives are given in Figure 7.38 [52-53].

Many single rod tests have been carried out from which two important features of deformation have been identified. The first is the so-called “hot-side straight” effect. The second feature is direct experimental evidence of the influence of azimuthal temperature variations on the total circumferential strain (Figure 7.39). The test series has also yielded extensive knowledge of the effects of temperature and heating rate on circumferential burst strain from 970 to 1 400 K (Figure 7.40).

Four multi-rod tests R1 to R4 with hypothetical reactor LOCA conditions, have been carried out using a  $3\times 3$  array of deforming rods surrounded at the same rod pitch by an outer row of unpressurised guard heaters clad with Inconel. Thus the outer row of deforming rods has to strain about 65% before bulges can be restrained from bursting by being trapped by two or more rods. The possibility of this particular aspect of multi-rod behaviour was investigated in a materials test [54] in stagnant steam and under reflooding conditions in R5 and R6 which utilised arrays of  $7\times 7$  pressurised rods (Figure 7.38) restrained by a shroud placed at one half a rod pitch from the centres of the outer rods. The conditions for the first four tests were peak rod power 20 W/cm, internal pressure 70 bar, system pressure 4.5 bar cold flooding rate  $\sim 3$  cm/s and heat up rate during the initial temperature ramp about 7 K/s. The materials test was carried out with reduced power to the rods.

Tests R1 [11], R3 [7], R4 [52, 53], and R5 [55] represent the behaviour of medium-rated assemblies in the KWU PWR, which for a LOCA are calculated to reach 660-680°C by the time the reflooding water contacts the bottom of their heated length, whilst test R2 represents the behaviour of a highly rated assembly which is calculated to have reached 850°C at this time.

R-5 was the first test with a  $7\times 7$  array, all rods pressurised. The reflooding rate and rod powers were similar to those used in R-3 but the internal pressure was higher.

The R-6 test [56] had the objective of examining the influence of coolant flow direction on the deformation thus no reversal of flow direction occurred between the single and two-phase flow regimes, unlike the previous tests, R1 to R5. This test was selected for analysis using computer models, as a German Standard Problem (DSP7) and simultaneously as an International Standard Problem (ISP14).

In R1 [11] there was a small malfunction which caused an additional slug of cooling water to be introduced at the start of reflooding; this caused the initial temperature drop (Figure 7.41). However, the cladding which had started to deform in the steam phase at the top of the ramp continued to do so for about 100 s until rupture occurred during the period of two-phase flow. The combination of the increased surface area owing to clad deformation and the external cooling balanced the heat input so that the clad temperature remained reasonably constant for over 100 s producing a “flat-topped” transient (Figure 7.41). The maximum cladding strain was 32% and the maximum coolant channel blockage ratio 25%. The position of the maximum strain in the rods tended to be between the centre of

the inter-grid spacing and the next higher grid, i.e. shifted from the centre in the direction of coolant flow (Figure 7.42). This is a consequence of two phase flow in the presence of spacer grids. Thermodynamic non-equilibrium results in steam temperatures up to about 870 K within the two-phase mixture of superheated steam and saturated water droplets. The turbulence and the break-up of water droplets induced by the spacer grids results in desuperheating of the steam and better heat transfer which lowers the temperature of the cladding downstream of each spacer. But superheating redevelops as the mixture flows along to the next spacer producing an axial temperature gradient of up to 50 K between two spacer grids at the time of burst (Figure 7.43). This results in an axial shift of the maximum strains in the rods towards the upstream spacer and enhances the formation of co-planar deformation, while limiting its axial extent.

Figure 7.38 REBEKA test philosophy and test objectives [52-53]

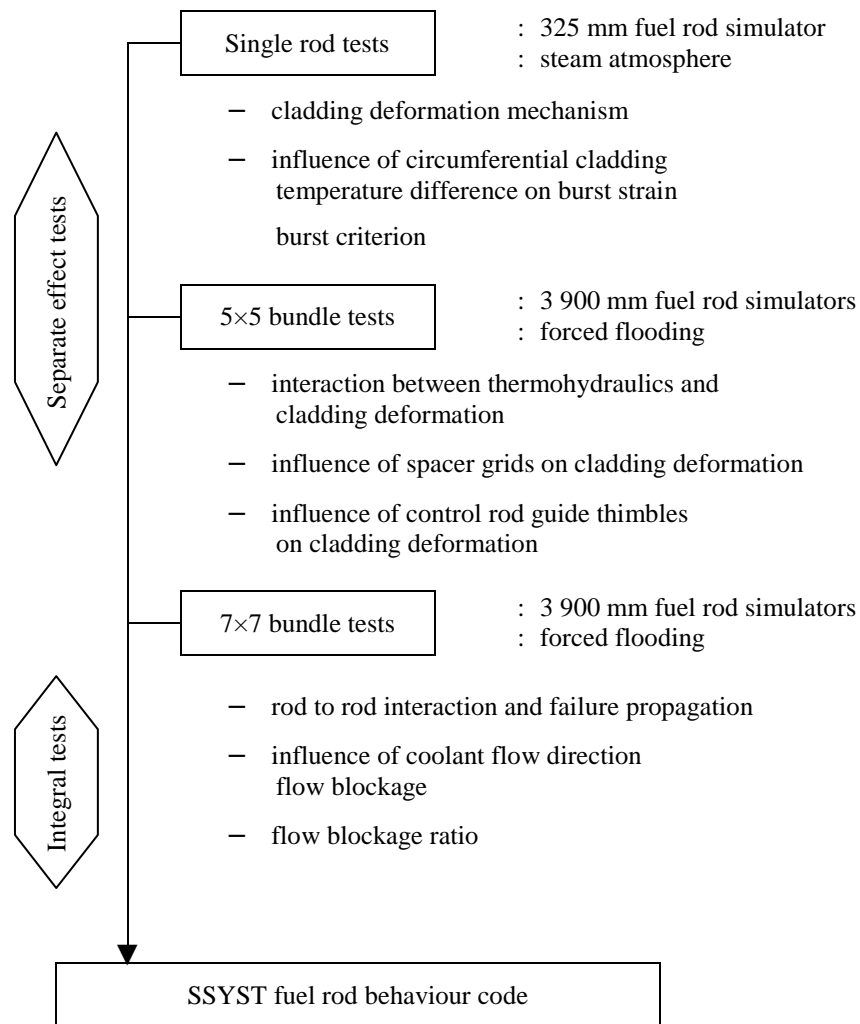


Figure 7.39 Burst strain vs azimuthal temperature difference in REBEKA out-of-pile tests

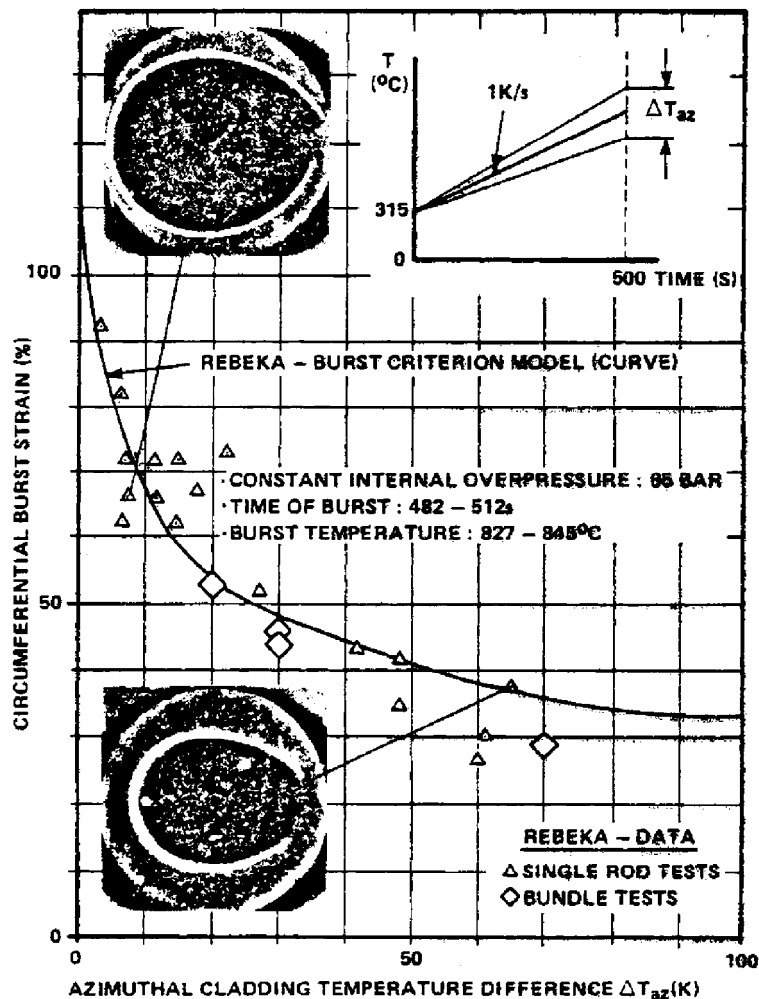


Figure 7.40 Burst strain vs burst temperature of Zircaloy claddings [7]

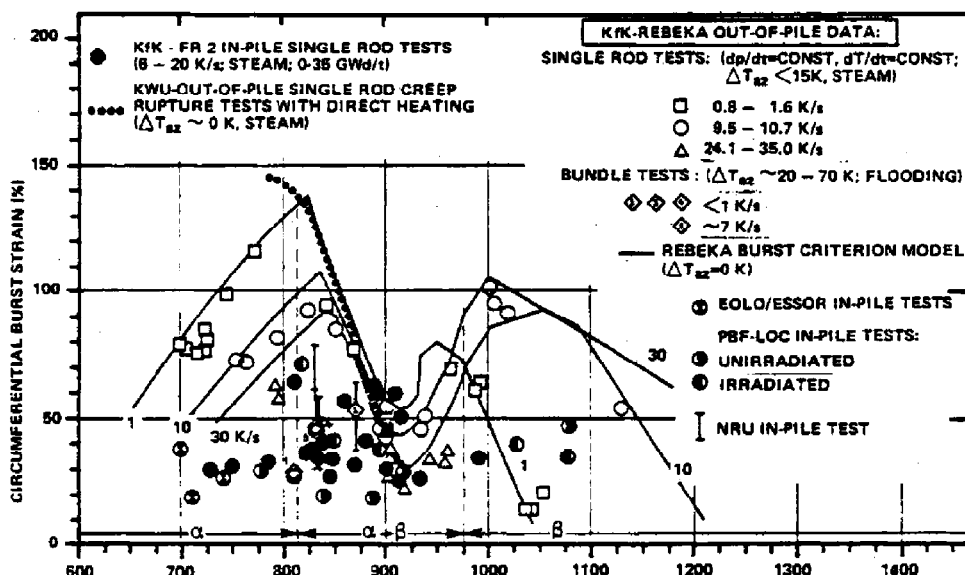


Figure 7.41 First bundle test REBEKA, Test data and test procedure  
Starting temperature was 520°C

- internal rod pressure 70 bar
- decay heat rating at midpoint 20 W/cm
- heat transfer coefficient in refill-phase  $\sim 30 \text{ W/m}^2\text{K}$
- cladding temperature at start of flooding 760-790 °C
- flooding rate, cold  $\sim 3 \text{ cm/s}$
- flood water temperature 130°C
- system pressure 4 bar

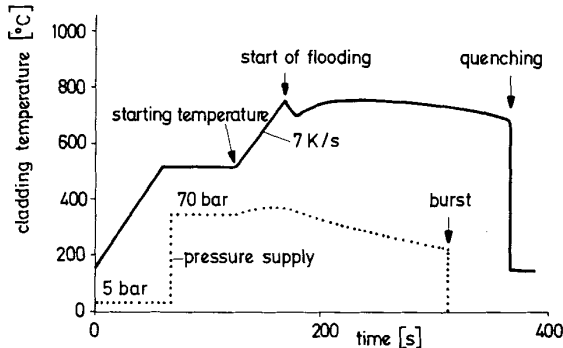
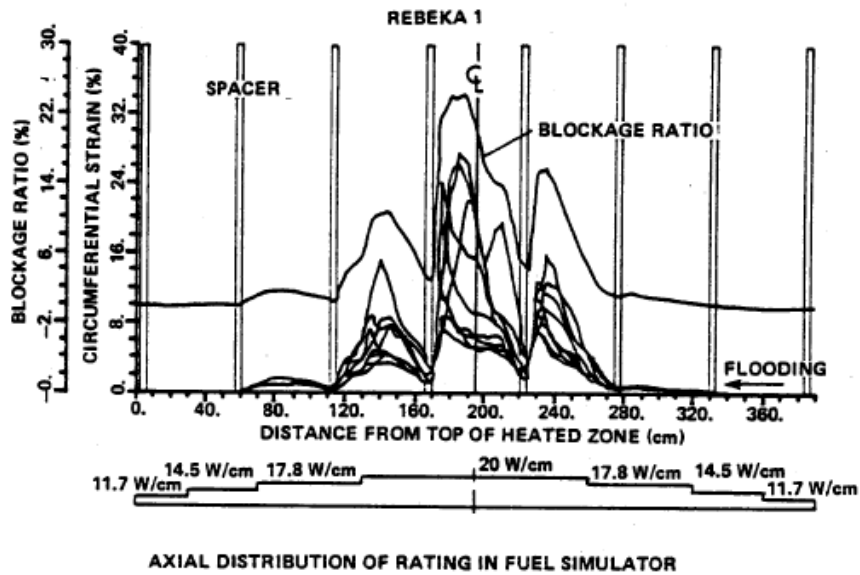


Figure 7.42 Circumferential strain of the 9 Zircaloy claddings and fuel blockage in the REBEKA 1 experiment [11]



In test R-2 [57] the reflooding was delayed to allow the rods to reach 1120 K and in this case all the deformation occurred rapidly during the heat up phase in superheated steam which was flowing down the test section simulating the effect of hot leg injection (Figure 7.43). The deformation was shifted in the direction of the steam coolant flow and large deformation occurred over two intergrid spaces (Figure 7.44). The bulges tended to be more coplanar than those produced during two-phase flow i.e. R1, R3, R4. (Compare Figures 7.42, 7.44 and 7.45). The maximum circumferential strain was 64% and the maximum flow blockage 60%.

R-3 [7] was essentially a repeat of R-1 but avoiding the malfunction which produced the additional cooling. The overall results were similar but the deformation was greater; the strains in two rods exceeded 60% and the maximum flow blockage was 52% (Table 7.6).

Figure 7.43 The temperature history at two axial locations in REBEKA 2

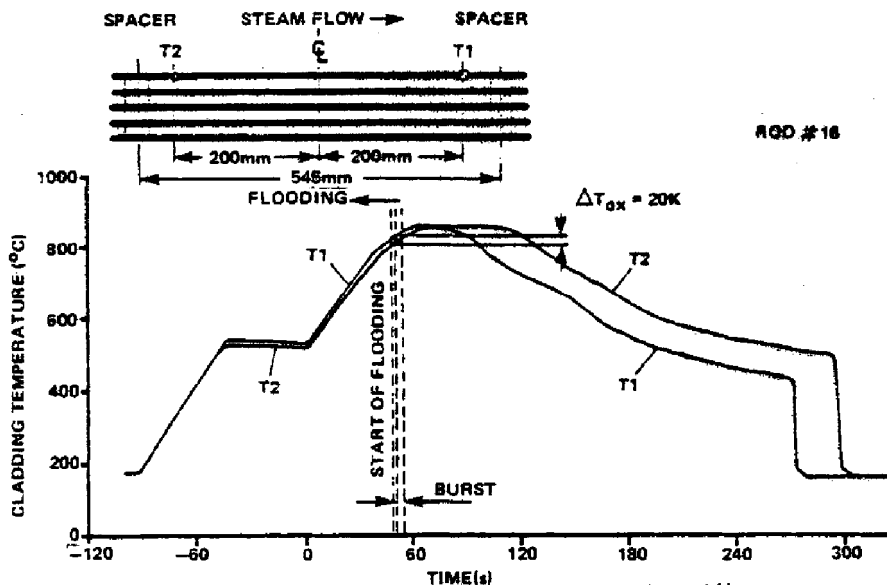
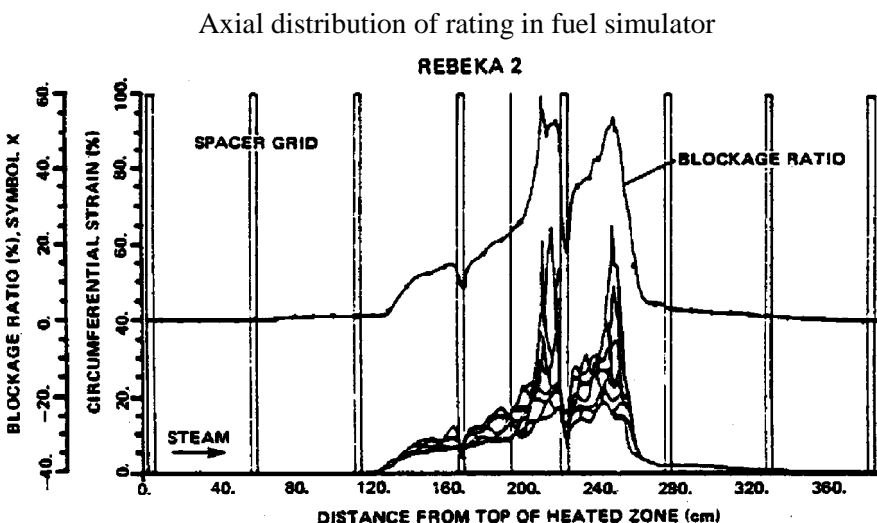


Figure 7.44 Circumferential strain of the 9 Zircaloy claddings and fuel blockage in the REBEKA 2 experiment

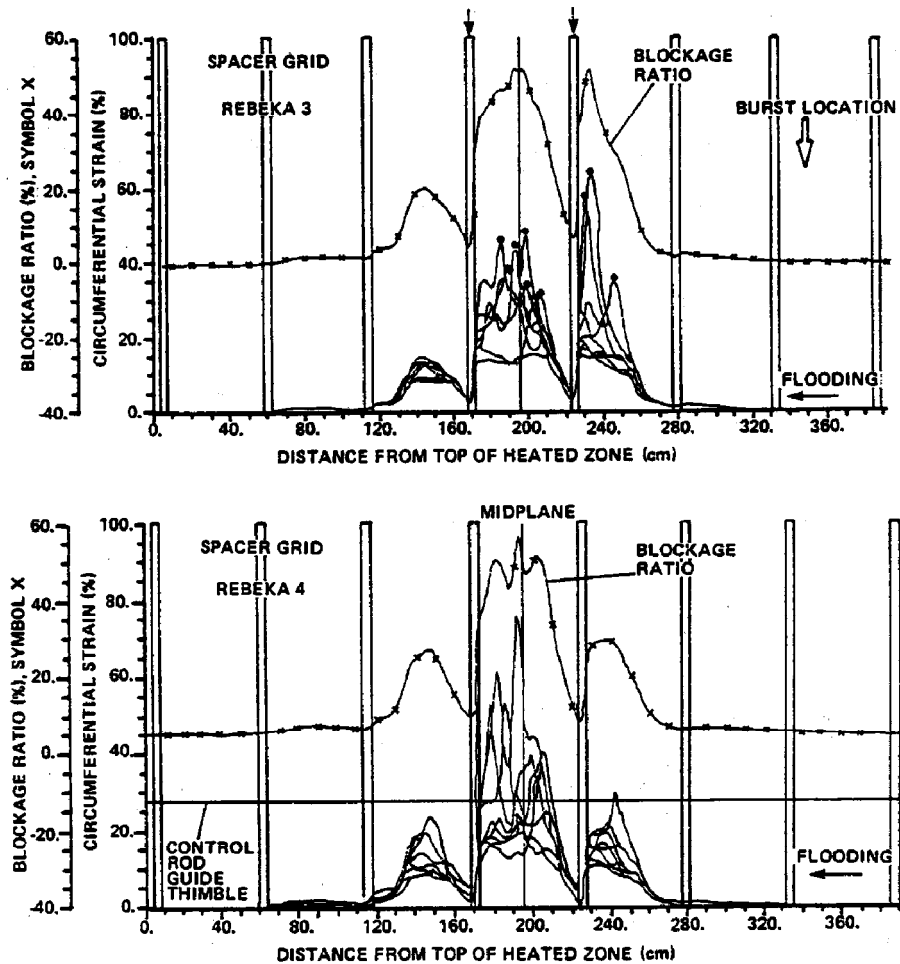


R-4 was a similar reflooding experiment to R-3 but one of the pressurised rods was replaced by a (cooled) simulated control rod guide tube to investigate if the presence of such a tube would result in lower deformation in the multi-rod array. This rod did cause pronounced azimuthal temperature differences in adjacent rods but surprisingly the deformation of the array was not only similar to that of R-3 but maximum strain was greater than in R-3, where there had been identical thermalhydraulic conditions but no "control rod guide tube". The maximum circumferential strain was 79% and the flow blockage 55%. The deformation and blockage in R-3 and R-4 are compared in Figure 7.45. The ruptures in R-3 were axially distributed (Figure 7.45) and a similar distribution was seen in R-4.

The cladding deformation characteristics in R-5 were similar to those in R-3 i.e. the regions of maximum strain were axially distributed over the intergrid region (Figure 7.46). Thus although the circumferential strains tended to be higher in R-5 the maximum blockage in both R-3 and R-5 was

52%. The axial distribution of maximum strains was sufficiently spread so that significant rod to rod interaction did not occur even though the potential for such interaction was increased by virtue of the larger number of pressurised rods.

Figure 7.45 Circumferential strain of the 9 Zircaloy claddings and fuel blockage in the REBEKA 3 and REBEKA 4 experiments [7, 52, 53]



In R-6 the rods were pressurised to 60 bar whilst steam at 150°C flowed through the rig. Then a power of about 7.8 kW was applied to each fuel rod simulator causing the bundle to ramp at about 7°C/s to 765°C. The power was reduced to 6.6 kW at this time and reflooding (3 cm/s cold reflooding rate) was initiated.

The maximum internal pressure in the inner 18 rods which behaved in a satisfactory manner was 76.6 bar. The first burst in this group of rods occurred 20.5 s after reflood was initiated and the last after 37.7 s. Their axial strain profiles (Figure 7.47) tend to be coplanar and the regions of maximum strain were shifted in the direction of two-phase coolant flow i.e. away from the downstream grid as in the MT-3 test (Figure 7.23). The burst strains ranged from about 25 to 65%. The maximum channel blockage of 60% was very localised, but 50% blockage extended for 10 cm (Figure 7.47).

The main features of the five 5×5 REBEKA tests, the 7×7 tests R-5, R7, and the Standard Problem Test R-6 are given in Table 7.6

Table 7.6 Summary of the test program in the REBEKA rig

Test number	Bundle size	Thermal-hydraulics during cladding deformation				Burst data (averaged)						Remarks	Reference <sup>(c)</sup>
		Heating rate (K/s)	Coolant flow	Flow direction	Heat transfer coeff. (W/m <sup>2</sup> /K)	Temperature measured nearest to burst at time of burst	Best-estimate burst temperature (C°)	Pressure (bar)	Circumferential strain (%)	Intergrid distribution of bursts (mm)	Max. flow blockage (%)		
1	5×5	7 <sup>a</sup> <1 <sup>b</sup>	- steam - reflood	Reversed	30... 100	685	810	60	28		25	- Inner 3×3 pressurised - Only 2 rods burst - High reflood rate at start of burst	[72]
2		7 <sup>a</sup>	steam	Uni-directional	30	870	870	55	54	95	60	- Inner 3×3 pressurised	[73]
3		7 <sup>a</sup> <1 <sup>b</sup>	- steam - reflood	Reversed	30... 100	808	830	51	44	203	52	- 3×3 pressurised	[74]
4		7 <sup>a</sup> <1 <sup>b</sup>		Reversed	30... 100	795	830	53	46	242	55	- 3×3 pressurised - Control rod guide tube in centre	[75]
M		0	Quasi stagnant steam		<10	754	754	70	63	28	84	- 1 W/cm - Inner 3×3 pressurised - 2 rods leaked	[76]
5	7×7	7 <sup>a</sup> 0 <sup>b</sup>	- steam - reflood	Reversed	30... 100	775	800	68	49	242	52	- All pressurised	[71]
6		7 <sup>a</sup> -4 <sup>b</sup>		Uni-directional	30... 100	765	790	62	42	140	60	- 2 rods unpressurised - Instrument tube in centre	[70]
7		7 <sup>a</sup> -9 <sup>b</sup>		Uni-directional	30... 100	755	790	57	55	200	66	All pressurised	

Common tests conditions:

Heated length: 3 900 mm; decay heat at midpoint: 20 W/cm; axial peaking factor: 1.19; axial power profile: 7 axial steps (5×5 tests), cosine-shaped (7×7 tests); system pressure: 4 bar; coolant flow: 2 m/s steam, ~3 cm/s forced flooding from bottom; Zircaloy-4 claddings: 10.75×0.72 mm, stress relieved.

Notes:

- a During heatup.
- b During reflood in the time period of high plastic deformation before burst.
- c in Erbacher, F.J. and Leistikow, S., "Zircaloy Fuel Cladding Behavior in a LOCA: A Review", Zirc. In the Nucl. Ind.: 7<sup>th</sup> Int. Symp; ASTM STP P39, pp. 451-488.

Figure 7.46 REBEKA-5. Circumferential cladding strain and flow blockage under reversed flow

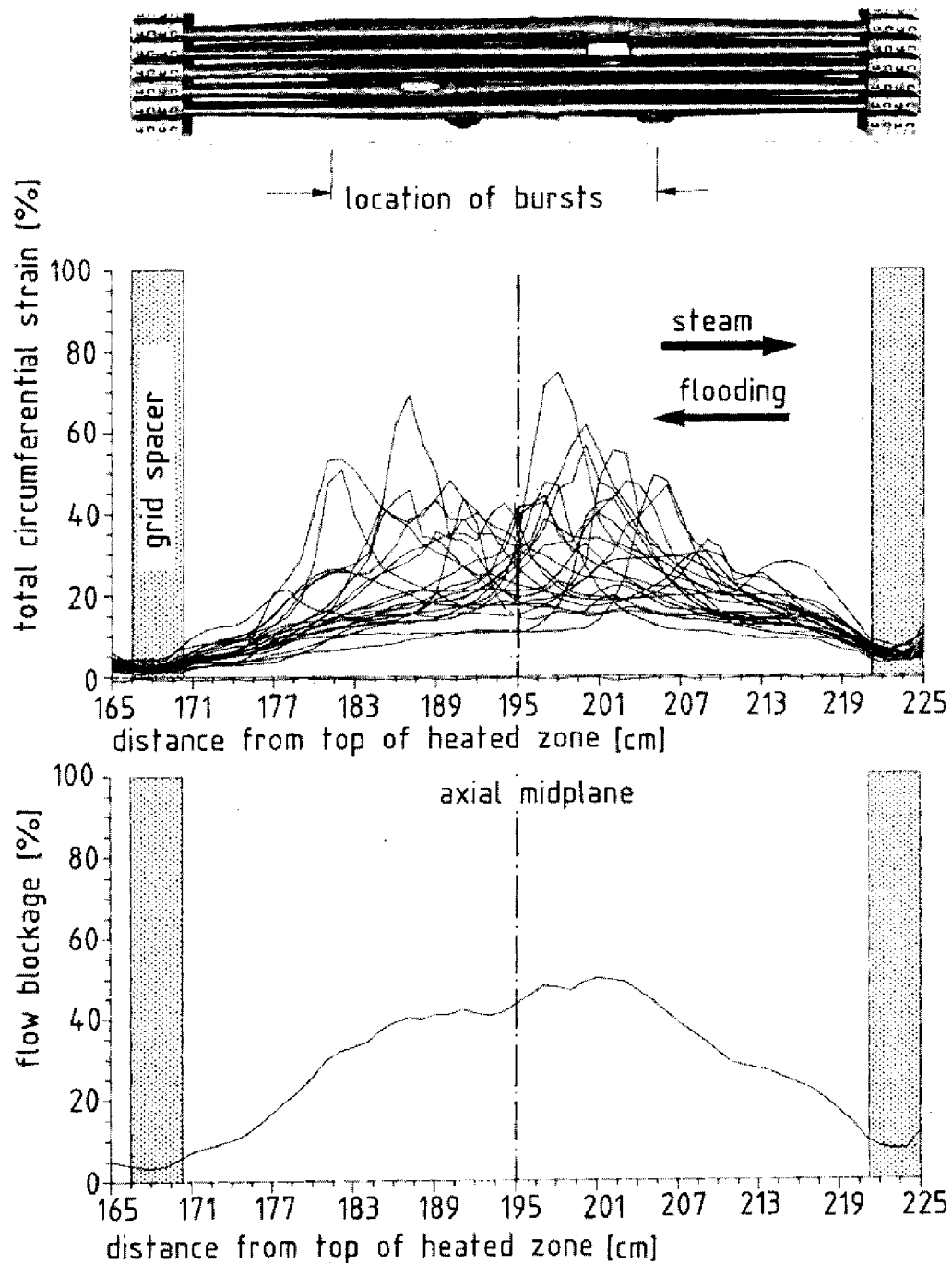
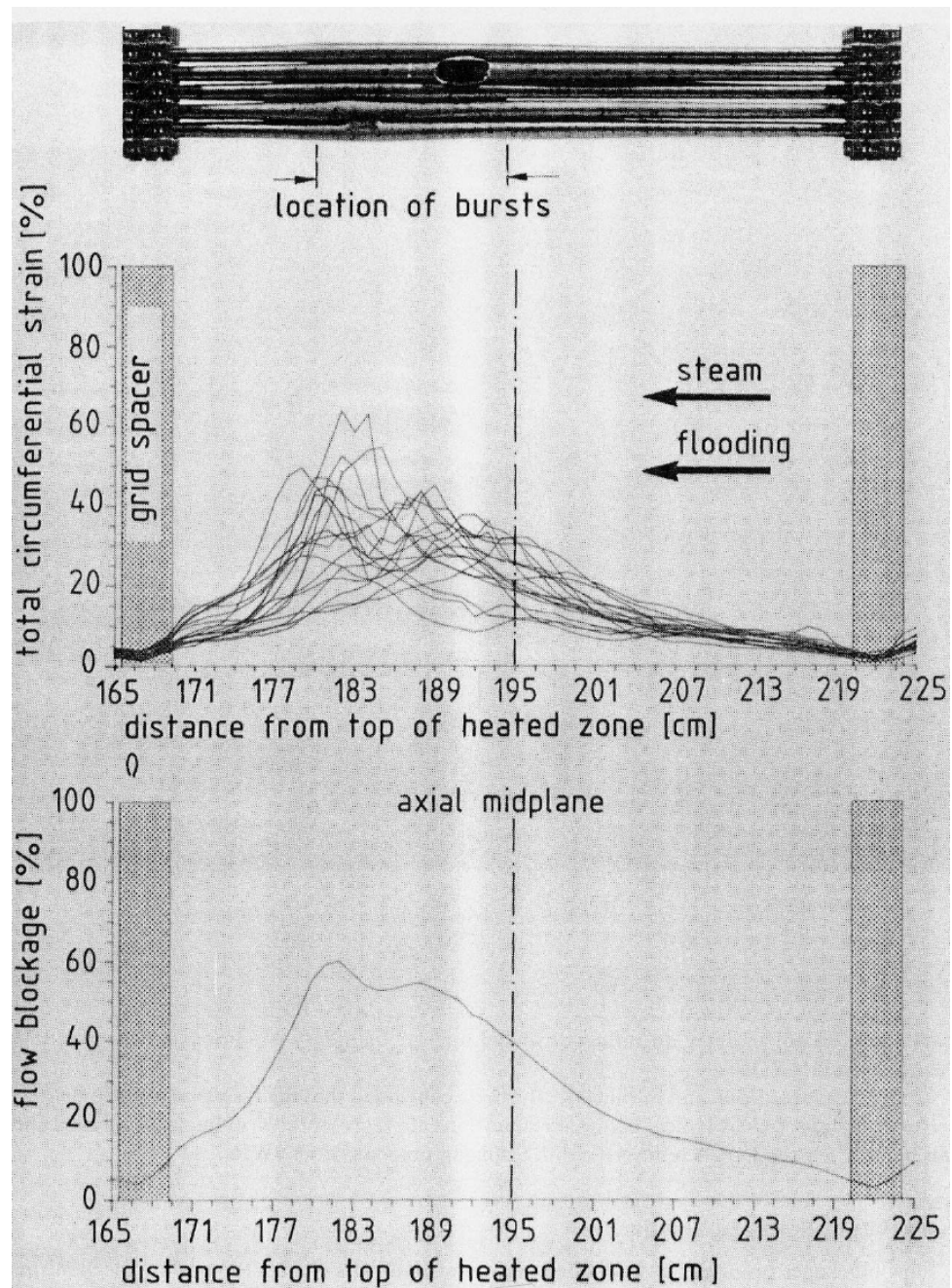


Figure 7.47 REBEKA-6. Circumferential cladding strain and flow blockage under unidirectional flow



#### 7.3.2.2 Single and multi-rod testing at KWU, Erlangen

The KWU (Kraftwerk Union) programme [58-62] consisted of three major phases:

1. Cladding tube material behaviour.
2. Fuel rod behaviour in single rod geometry.
3. Fuel rod behaviour in multi-rod geometry.

The test parameters used for studying the above are shown in Figures 7.48 and in Table 7.7

Figure 7.48 Controlled temperature transient test (left) and creep rupture test (simulation of 2<sup>nd</sup> peak, right) in the KWU programme

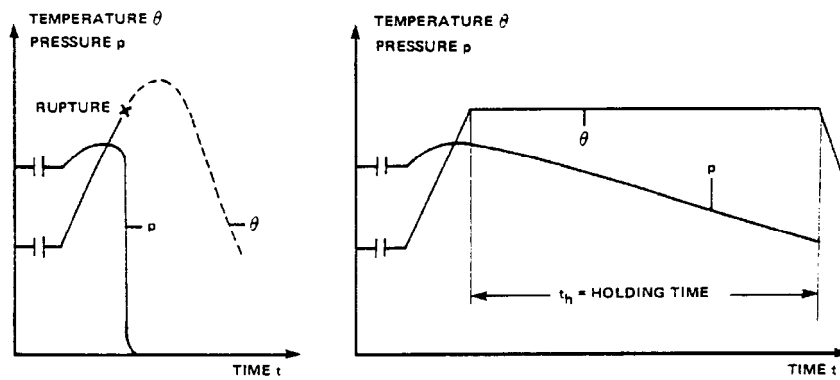


Table 7.7 Test parameters of single and multirod investigations by KWU

Test parameters	Single rod tests	Multi rod tests
Initial pressure	20-150 bar	50/65/80 bar (Constant pressure for tests with convective cooling)
Initial temperature	350°C	320°C
Initial free volume	40 cm <sup>3</sup>	40 cm <sup>3</sup> (tests with forced cooling)
Temperature range	700-1 000°C	700-900°C
Heating rate	2-28 K/s	6-25 K/s
Holding time	≤90 s	≤90 s
External atmosphere	Air/forced steam (5 kg/h)	Air/forced air 10-60 W/m <sup>2</sup> K
Pressurizing medium	Helium	Helium

1. In the material behaviour work KWU compared standard cold worked and stress relieved cladding with cladding modified as shown below:

- (a) Recrystallized: 2 h at 610°C in vacuum.
- (b) β-quenched from 1 050°C at 50-60 K/s.
- (c) Oxidized: layers up to about 40 microns produced by heating at 400-420°C for up to 9 000 h.
- (d) Varying wall thickness.

The results of the above investigation are shown in Figures 7.49, 7.50 and 7.51.

Figure 7.49 Burst temperature vs pressure from single rod tests under idealised conditions  
Comparison of different initial cladding conditions

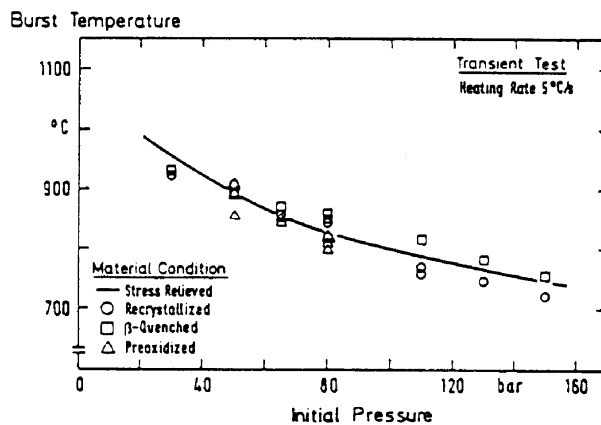


Figure 7.50 Burst strain vs burst temperature from single rod tests under idealised conditions  
Comparison of different cladding materials

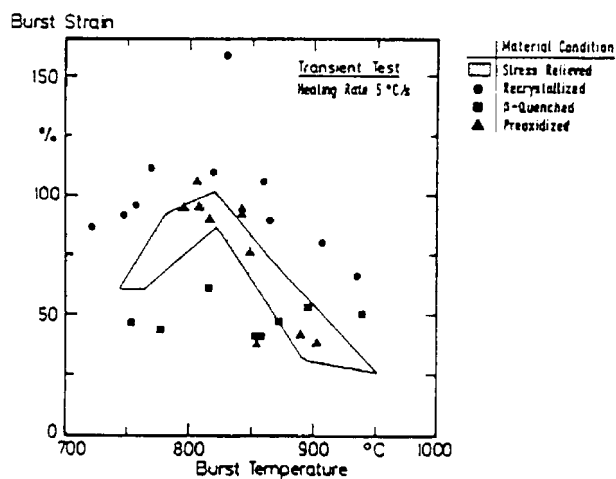
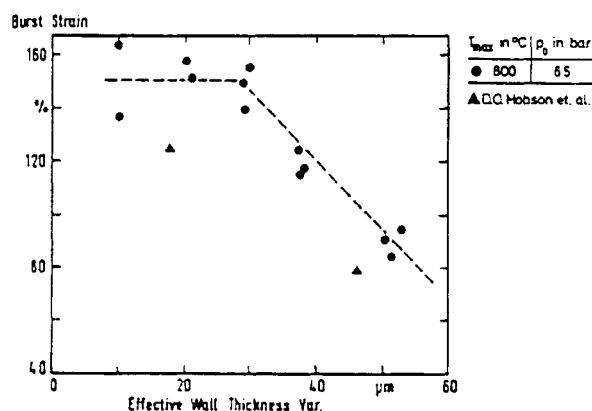


Figure 7.51 Burst strain vs wall thickness variation from single rod creep rupture tests under idealised conditions



The stress and temperature dependence of the strain rate of the cladding tube diameter was determined for the KWU cold-worked and stress-relieved cladding. Experimental values of the stress exponent n and the apparent activation energy Q in the Norton creep equation were obtained [61].

2. The aspects of fuel rod behaviour in single rod geometry which were examined were:
  - (a) Influence of azimuthal temperature variation on burst strain. Results, Figure 7.52 were similar to those of other workers, (KfK, SNL). The degree of tube bending resulting from azimuthal temperature is plotted in Figure 7.53.
  - (b) Tube bending which is a characteristic feature of Zircaloy cladding deformation in the alpha-phase region. In this study the test specimens were standard KWU cladding. They were directly heated to 800°C and caused to deform by internal gas pressure firstly without and secondly with the influence of imposed circumferential temperature differences produced by an external heating and cooling device. The upper and lower ends of the tube were restrained from moving laterally whilst the lower end was free from axial restraint.

The 1<sup>st</sup> type of experiments showed that axial contraction increased with increasing tangential strain (Figure 7.54) confirming the findings of similar studies. In the 2<sup>nd</sup> type of tests, the average axial contraction in the ballooned region was measured simultaneously on the hot and

cold side of the cladding and preferential contraction on the hot side was found (Figure 7.55). The amount of tube bending was evaluated from the ruptured samples for those tests with a non homogeneous azimuthal temperature distribution. Tube bending increases rapidly with increasing azimuthal temperature difference (Figure 7.56).

- (c) Influence of steam cooling on ductility and axial profile profile of circumferential strain. No significant deviation could be found when the results of tests in steam were compared with those produced in air. However the steam flow in the test section shifted the maximum strain region in the flow direction (Figure 7.57) as has been seen by other workers.

**Figure 7.52 Burst strain vs mean normalised azimuthal temperature difference from single rod creep rupture tests under idealised conditions**

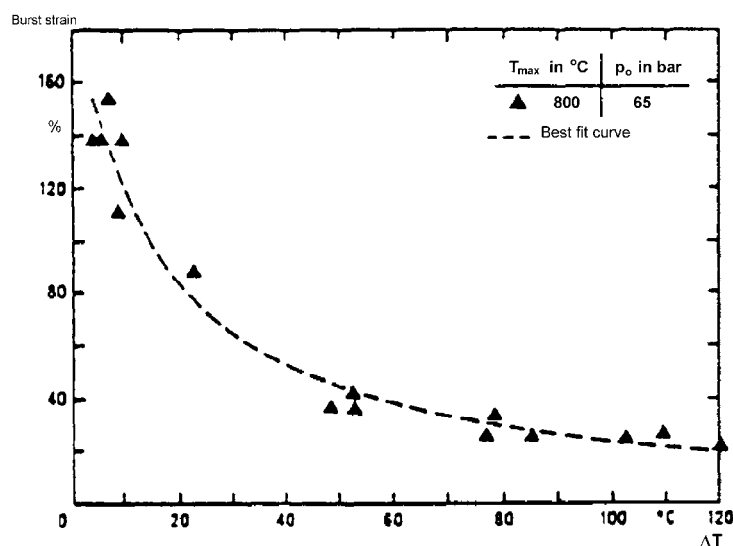


**Figure 7.53 Tube bending vs normalised azimuthal temperature difference in single rod creep rupture test in air**

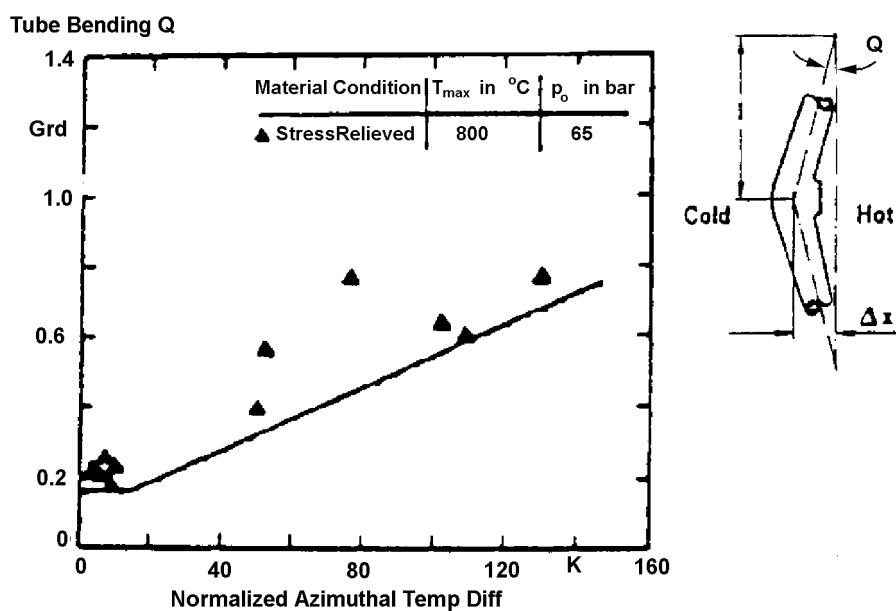


Figure 7.54 Local axial strain vs tangential strain in the plane of maximum deformation

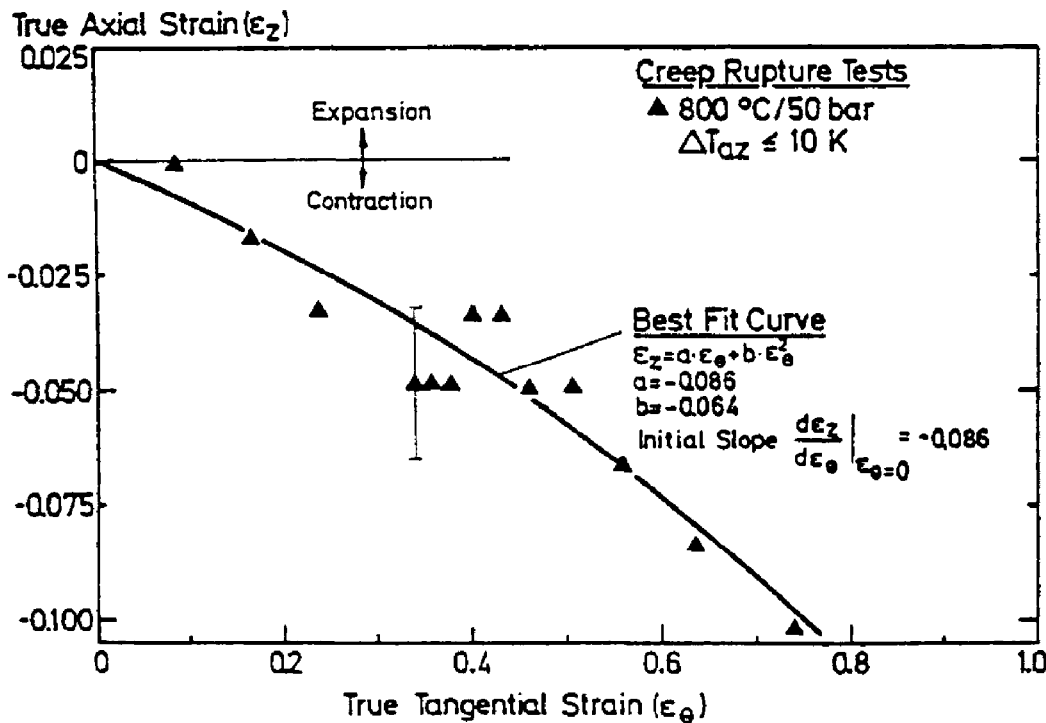


Figure 7.55 Axial strain vs tangential strain for creep rupture tests with nonhomogeneous temperature distribution on the circumference

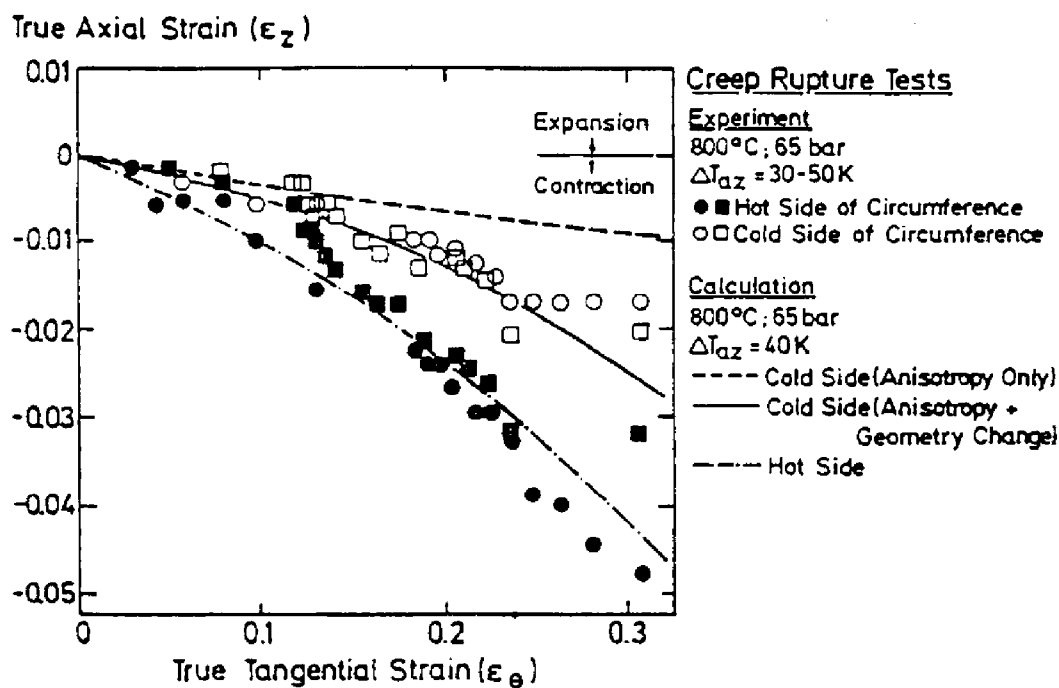


Figure 7.56 Bow vs azimuthal temperature difference

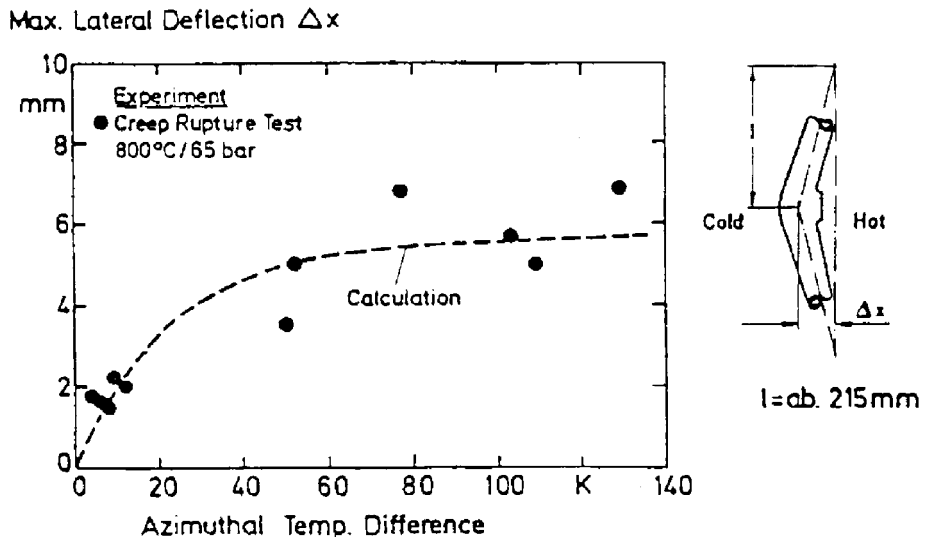
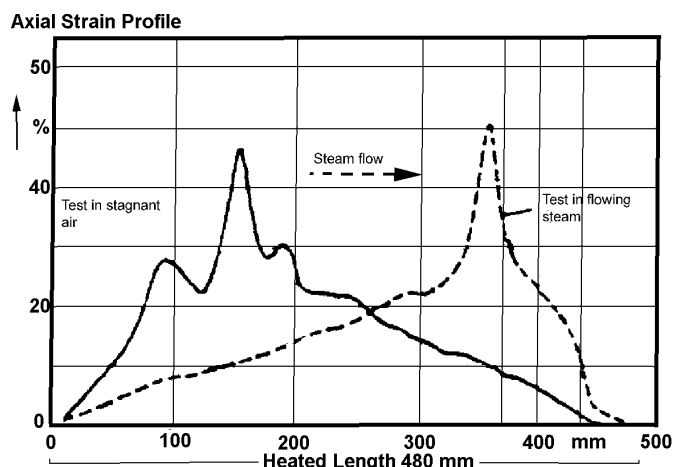


Figure 7.57 Axial profile of circumferential strain for transient test (5 K/s, 50 bar) in air and flowing steam



3. The multi-rod tests were carried out to “investigate whether the results of single rod tests are influenced by the geometrical and thermal conditions in a multi-rod geometry”, under conditions “where high circumferential strains are expected in order to reach mutual touching of rods”. However in the 3x4 array of rods only the two interior rods could be pressurised and the rod spacings were such that the deforming rods would need to strain about 65% before contacting the other rods. The tests were carried out by first heating to 350°C and pressurizing with helium, then after about 20 minutes the rods were ramped at 10-20 K/s to about 800°C and held until 90 s had elapsed or the central rod(s) burst. The temperature of the guard rods was kept constant by controlling the power to the internal heaters.

The first series had convective air cooling and the main findings were:

- From tests in which only one of the two central rods was pressurised and the temperature of the guard rods was either higher or lower it was concluded that: “At a lower temperature level of the surrounding rods the central rod shows the same burst behaviour as in a single rod test, as was expected. Burst strain and location of burst rupture are not influenced by the surrounding rods (Figure 7.58). At a higher temperature level of the surrounding rods the

burst behaviour is influenced in such a way that the burst rupture opening is directed towards the hottest rod in the neighbourhood. The locally hottest spot of the cladding determines the rupture behaviour (Figure 7.59)."

Figure 7.58 Indirectly heated multirod test (3×4)  
with one isobarically pressurised sample (65 bar) [60]

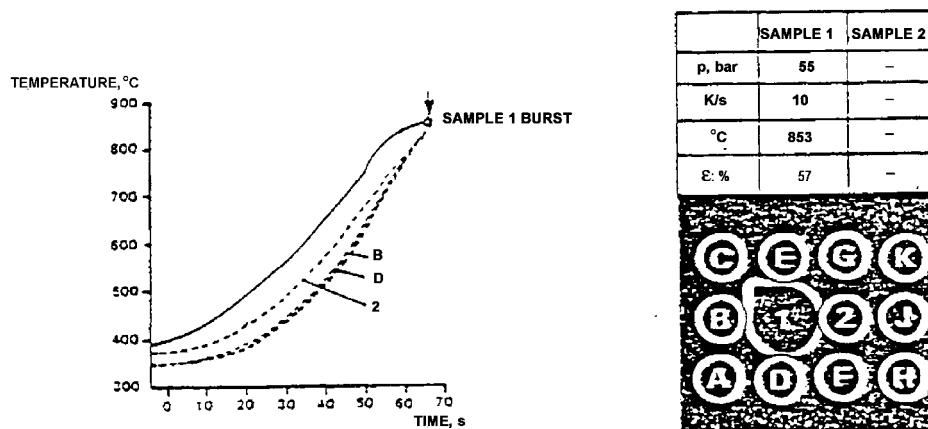
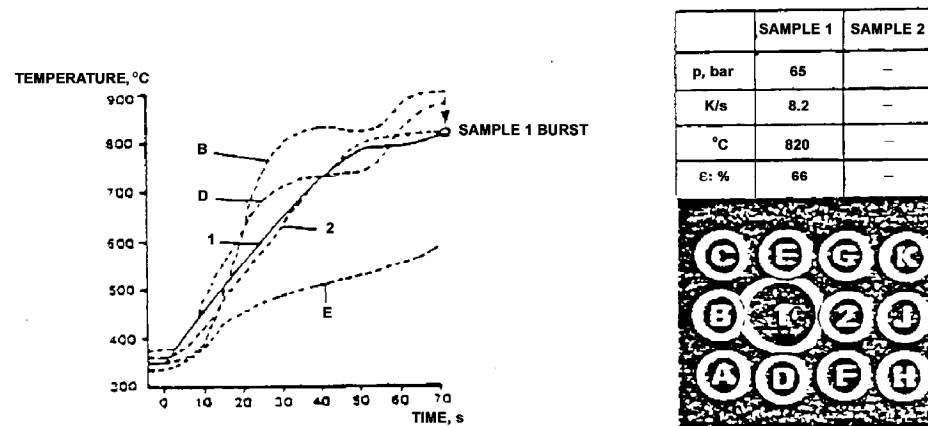


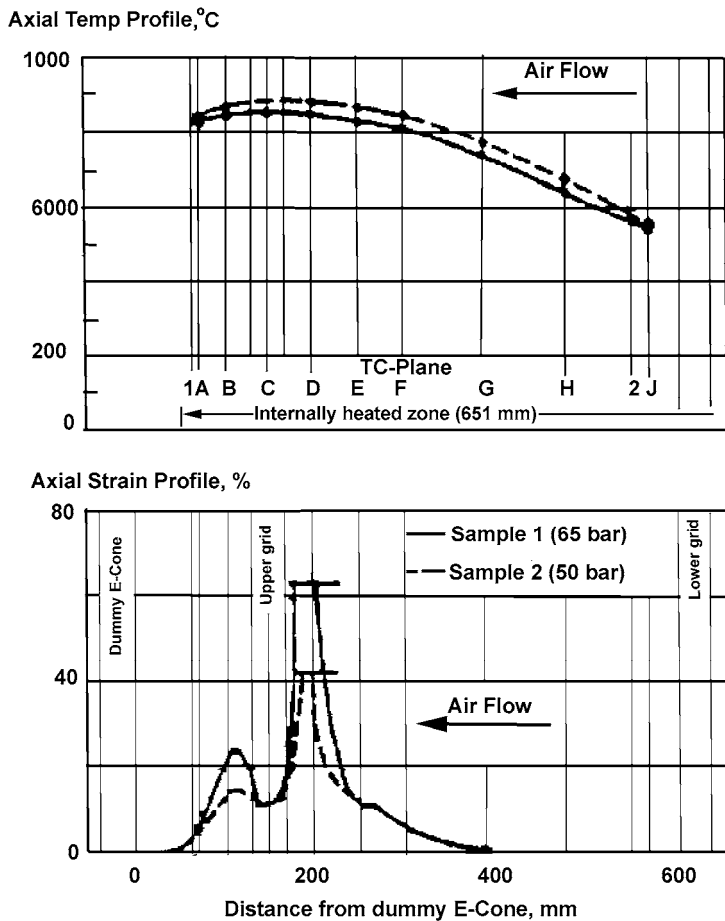
Figure 7.59 Indirectly heated multirod test (3×4)  
with one isobarically pressurised sample (65 bar) [60]



- From tests in which both central rods were pressurised and the temperature distribution in the bundle was rather homogeneous it was concluded that: "With different as well as with equal internal pressure of both central rods no mutual influence on burst behaviour history and location and size of the ballooning was observed. With different internal pressure the rods burst in temporal sequence, with equal internal pressure the rods burst nearly in the same moment."

In the second series air was forced through the test section, this caused a "downstream" shift of axial temperature and strain maxima, comparable to observations in single rod tests in flowing steam, Figure 7.60. This effect was enhanced if air velocity and thus heat transfer coefficient was increased otherwise the results were similar to those in the first series. The maximum strain achieved in the multirod tests was intermediate between that of the directly heated creep rupture tests and the fuel rod simulation tests. This can be seen from Figure 7.61 which summarises the burst strain data from the whole of the KWU investigations and includes for comparison multi-rod data from the ORNL and REBEKA tests.

Figure 7.60 Axial temperature and strain profile from KWU multirod test with forced air cooling



### 7.3.2.3 Single and multi-rod testing at the Japanese Atomic Energy Research Institute (JAERI)

The rod size used in the JAERI tests, which have  $7 \times 7$  arrays, represents those used in a  $15 \times 15$  type of PWR fuel assembly.

The first series of tests, summarised in Table 7.8, with the W-3% Re wire heaters and a close fitting unheated shroud, examined the effect of burst temperature in the high  $\alpha$  and  $\alpha+\beta$ -phase regions i.e. 740-920°C on deformation with ramp rates of about 7 K/s. A typical test history is given in Figure 7.62. There was a slight temperature gradient across the assembly presumably as a result of the unheated shroud which reduced the ramp rate in the outer rows by 1.6 K/s.

Figure 7.61 Burst strain vs burst temperature from single rod and multi rod tests (schematically)

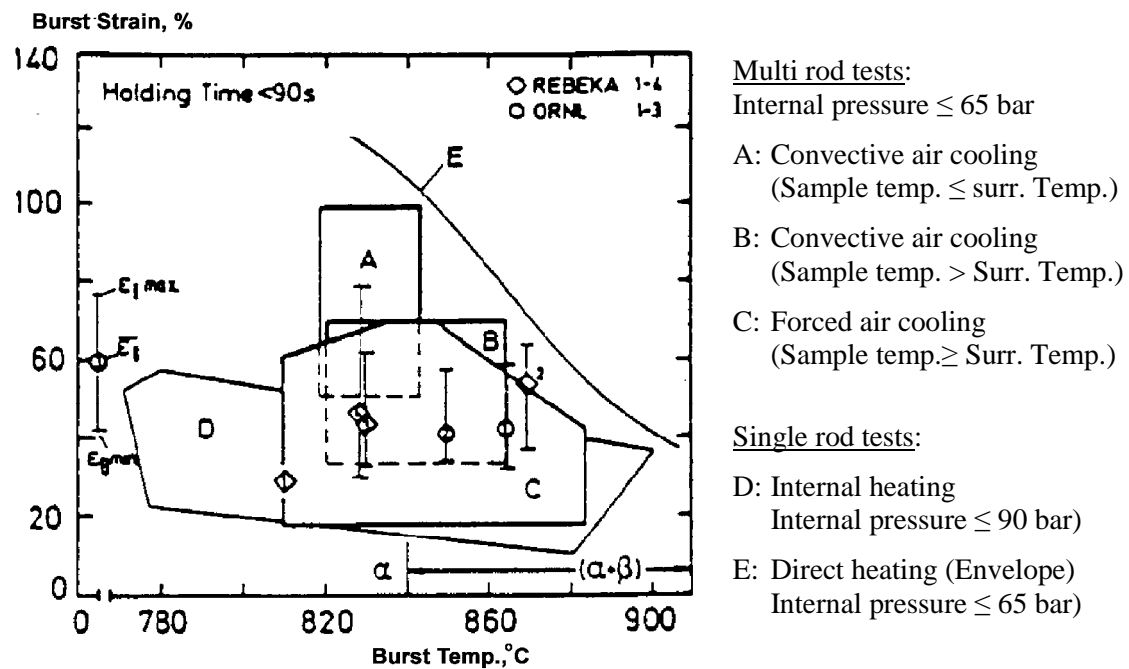


Figure 7.62 Histories of cladding temperatures and internal pressure in JAERI test 7805

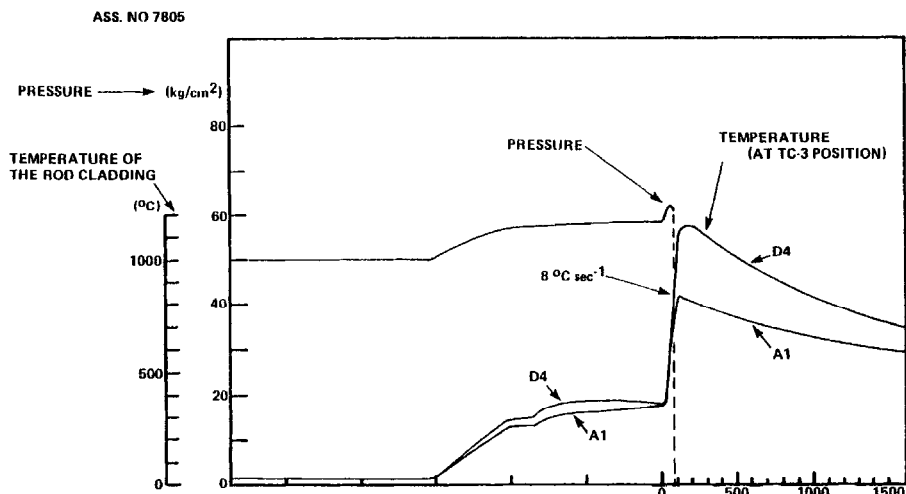


Figure 7.63 shows the axial profile of ballooning in the four tests, where one may observe, as expected, the highest burst strains for the tests that ruptured in the high  $\alpha$  region (test 7, ass. No. 7807) or in the low  $\alpha+\beta$  region (test 5, ass. No. 7805).

Table 7.8 JAERI test matrix of bundle burst tests using W-Re wire heaters and a close fitting unheated shroud

Bundle N°	Steam Flow Rate (g/cm <sup>2</sup> min)	Heating Rate (°C/s)	Initial Internal Pressure (kg/cm <sup>2</sup> )	Maximum Internal Pressure (kg/cm <sup>2</sup> )	Burst Temperature (°C)
7805	0.44	6.6-8.7 (500-860°C)	50	64-70	805-860
7806	0.40	7.3-9.0 (500-900°C)	20	26-29	870-920
7807	0.40	5.9-7.2 (430-830°C)	70	87-93	750-790
7808	0.44	5.9-7.9 (500-890°C)	35	45-48	870-880

Figure 7.63 Axial distribution of ballooning in the JAERI 7×7 multirod tests

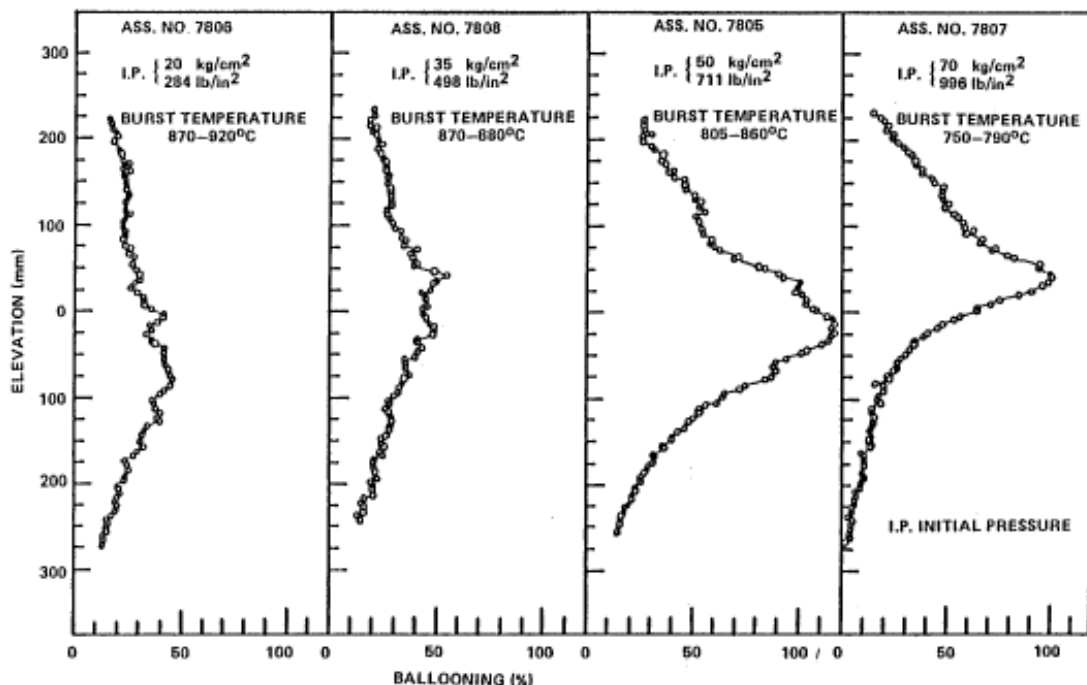


Figure 7.64 gives a failure map for test No. 5, showing the axial position of bursts in relation to the axial temperature profile and the axial extent of circumferential strains greater than 34% (value corresponding to the contact between two similarly deformed neighbour rods): there appears a clear trend for a more axially extended deformation on the interior rods than on the peripheral ones, in agreement with the MRBT B5 (Section 7.3.2.4) test results.

In the next series of Tests 9-14, the unheated shroud was replaced by an outer ring of 32 heated but unpressurised rods. In this series (9-14), the test conditions have been taken similar to those of test No. 5 which had led to highest deformations: initial internal pressure = 50 bar, temperature ramp rate = 7 K/s (except in test no. 13). The presence of an outer guard ring of heaters reduced the temperature gradient between center and periphery of the 7×7 array; this resulted in a greater axial extension of the deformations that also affects the peripheral rods (Figure 7.65).

Figure 7.64 Axial locations of burst position and ballooned region in assembly No. 7805

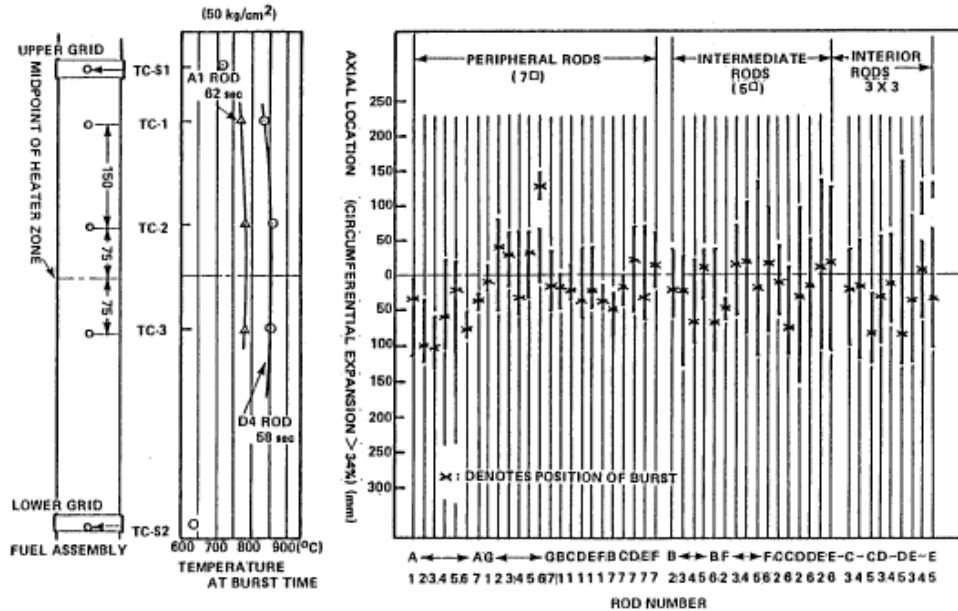
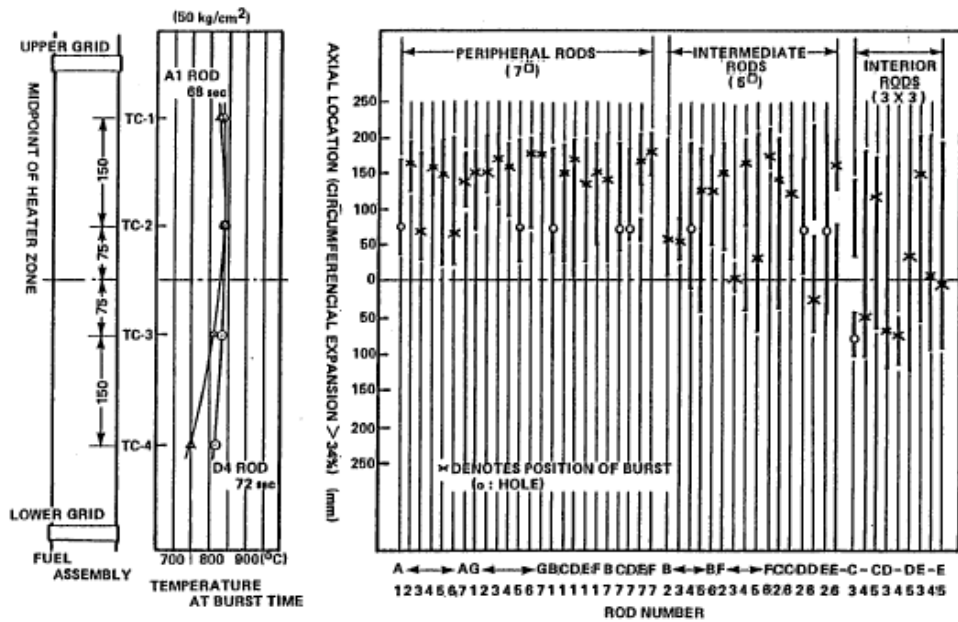


Figure 7.65 Axial locations of burst position and ballooned region in assembly No. 7910



In test No.10, all the 49 rods were heated. In test No.11, the central rod was not heated, simulating a control rod guide tube; the deformations were not as axially extended as in test no.10, but remained mostly coplanar (Figure 7.66). Test 13, as already mentioned, was run with a very low ramp rate (<1 K/s) and the rupture of rods in the range 765-800°C (high  $\alpha$  domain) have led to extensive deformations, significantly coplanar, with a maximum flow channel restriction reaching 87.6%.

In the tests 12 and 14, four rods were unheated, simulating in some extent the presence of guide tubes. Despite the azimuthal temperature differences induced by these unheated rods, significant and axially extended deformations (> 34% over more than 20 cm) were observed in some rods adjacent to

unheated rods (Figure 7.67). Although the conditions in tests 12 and 14 were quasi identical, a detailed examination of the results in Figure 7.67 reveals a different behaviour, in these two tests, of the rods adjacent to unheated rods (other than for 2 rods aligned and in between 2 unheated ones, as in positions C3, C4, D5 or E5), behaviour that resulted in longer balloons in test 14.

In a deeper analysis of these tests, Kawasaki [38] has suggested that the deformation on a heated rod adjacent to a non heated one was also highly influenced by the temperature difference with the other neighbours. This proposal was supported by a specific investigation in which analytical tests were performed on a  $3 \times 3$  heated rods array, the central rod being pressurised and surrounded by 8 unpressurised rods [63]. The results of these tests, schematised on Figure 7.68, have allowed the following understanding:

- When the central rod temperature is lower than those of adjacent rods, the deformation remains limited, the rupture occurring before or just at the instant of contact with a neighbour; a local hot spot, where the straining will initiate, will indeed become accentuated by the closeness of the hotter neighbour, and will lead to a localised burst.
- When the central rod temperature is greater than, or equal to, those of adjacent rods, a deformation starting on a local hot spot will be counteracted and stopped while the closeness and possible contact of the deforming portion with the colder neighbour, thus resulting in a radial, then axial, carry over and extension of the straining process ("long ballooning"), this as much as the temperature difference with cold neighbours is high. Ruptures are thus observed at the points of maximum stress where curvature reverses between concave portions contacting the neighbour rods and the bulging that develop in the interval between two adjacent rods. In one particular test with 2 peripheral rods unheated, it was observed that a 50 K azimuthal temperature difference was not sufficient to induce a localised straining that could lead to early rupture before contact with neighbours.

Figure 7.66 Axial locations of burst position and ballooned region in assembly No. 7911

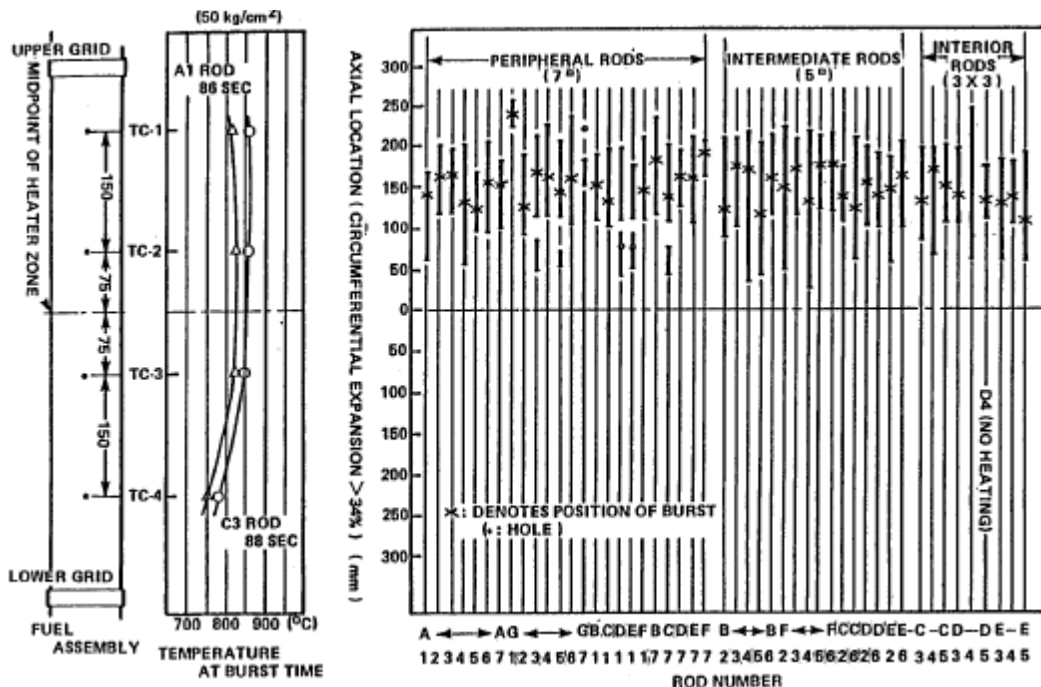
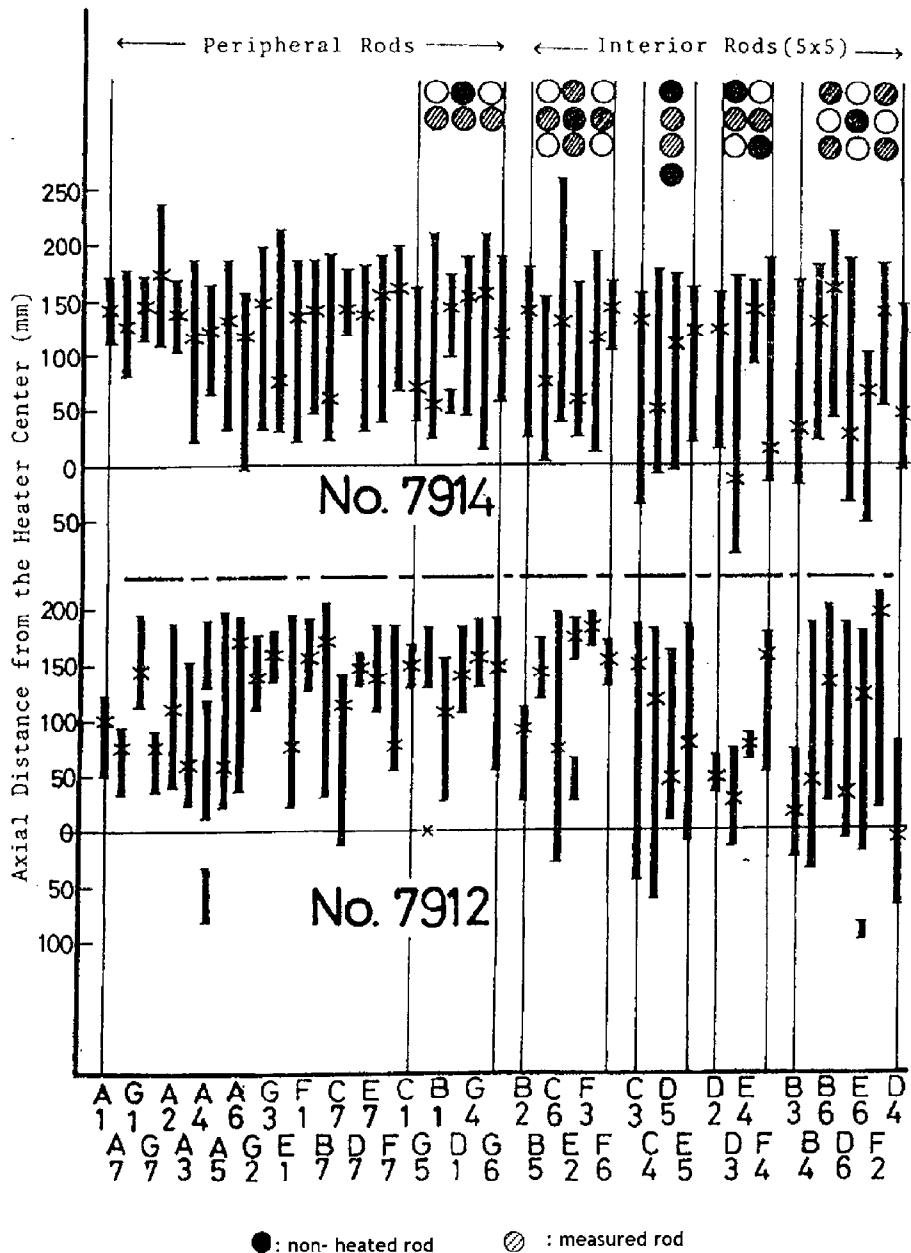
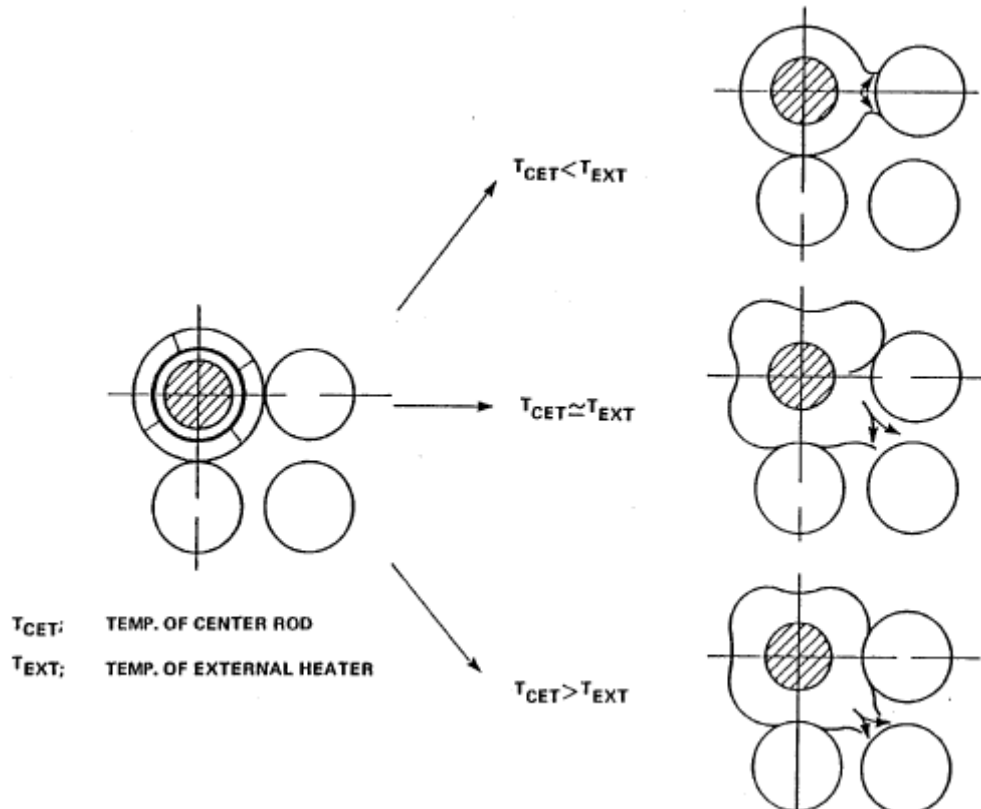


Figure 7.67 Portions of tubes with greater than 34% strain in assembly 7912



This particular investigation led to the conclusion that the deformation behaviour of a cladding in a multi-rod array is not only influenced by the temperature gradients on that cladding but also by the temperature differences with the facing areas in adjacent rods.

Figure 7.68 Illustrated deformation mechanism of a rod surrounded by external heater

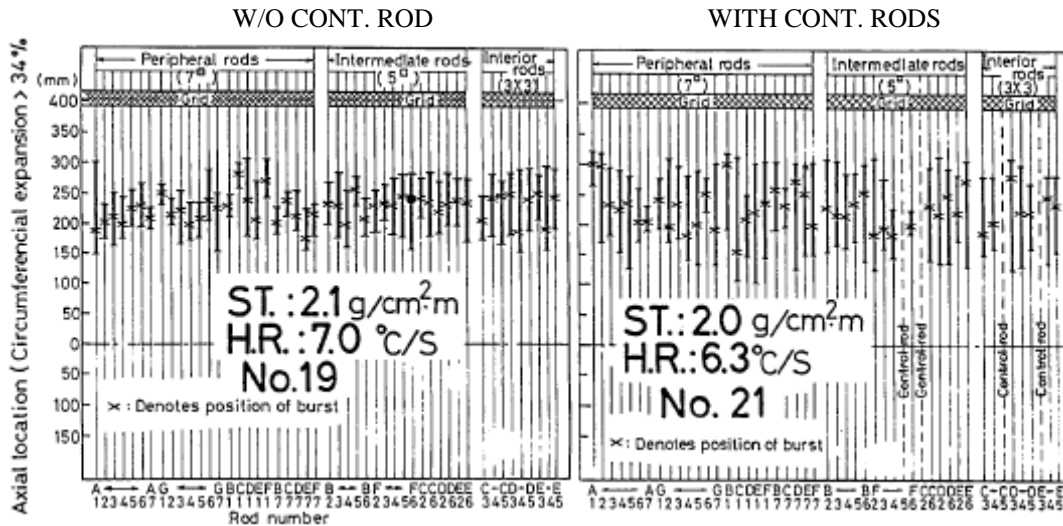


In the final test series (15-24), a shroud was introduced around the 7×7 central bundle and was backed by an outer ring of guard sub-heaters; the clearance with the bundle outer rods was 9 mm in tests 15 and 16, and at 3.7 mm thereafter. According to the shroud positioning in test 17 to 24, simulating the outer rods in a large assembly, the main objective of this part of the program was to investigate an upper bounding value of the flow restriction in the bundle with the differential impact of the presence of control rod guide tubes. To this end, in tests 21 to 24, four control rod guide tubes were substituted for pressurised rods and the test conditions are duplicated from tests 18-21. The initial pressure of heated rods was 50 bar as in previous tests and two heating rates were used, 1 K/s and 7 K/s.

The results of this test series have provided unexpected findings:

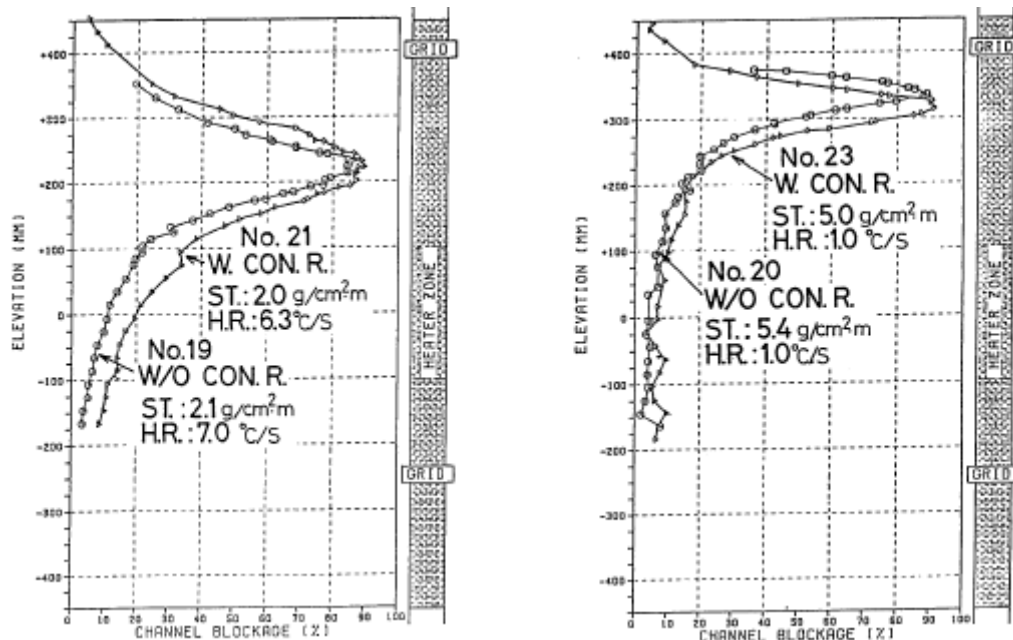
- In all tests with guide tubes, the ballooning behaviour of rods neighbouring a guide tube was not different from other rods, despite the larger azimuthal temperature gradient expected in these rods.
- The maximum flow blockage ratio in a bundle with control rod guide tubes was almost the same as that without guide tubes, and the axial extent of the highly restricted portion was even higher in tests with guide tubes (Figure 7.69) in agreement with the result of the test REBEKA-4 (Section 7.3.2.1).

Figure 7.69 Axial locations of burst position and ballooned region in tests No. 20 and 21



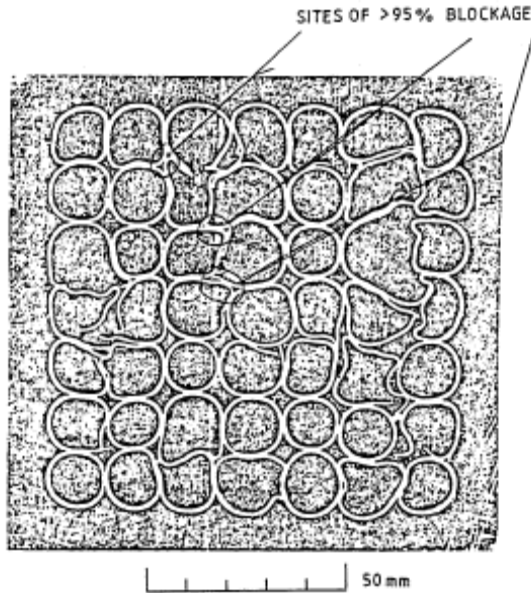
- There was little effect of the heating rate on the degree and extent of flow blockage: 91% maximum restriction for 1 K/s, and 87% for 7 K/s, see Figure 7.70.

Figure 7.70 Axial locations of channel blockage in tests No. 19 and 21, 20 and 23



In considering the 7 K/s ramp rate as more realistic and in limiting the cross-sectional area of a ruptured cladding at that of a circumference of same length as the clad length at rupture, the authors have evaluated more realistically an upper bound of flow restriction near 80% [39]. However, it should be noted that local flow blockage ratios higher than 95% have been determined in the area of maximum flow restriction in test 24 under 7 K/s heating rate (Figure 7.71).

Figure 7.71 Cross-section of maximum blockage in test No. 24 [24]



The following conclusions for the JAERI multi-rod tests are due to C. Grandjean [24]. He first notes that the tests were carried out under similar thermalhydraulic conditions to those in MRBT tests B3 and B5 and that they show results consistent with those of MRBT tests, see next section. The common feature of all these tests is the axial extension of the deformation, which develops after contact without rupture between adjacent rods.

The important result provided by JAERI multi-rod tests is related to the influence of the presence of control rod guide tubes: not only the deformation on rods adjacent to a guide tube is, in most cases, not lower than on other rods, despite the azimuthal temperature gradients induced by the cold guide tube, but the flow blockage ratio in the bundle section is even slightly increased and axially more extended. This surprising result supports the result of test REBEKA-4 (carried out however in more favourable thermal hydraulic conditions) and can be explained by the effect of the mechanical interaction between a rod and an adjacent guide tube: due to the larger diameter of the latter, the contact of a deforming neighbour rod occurs with a moderate strain (~20%) before burst. This early contact leads to a transfer of straining on other portions of the rod circumference, which homogenises the azimuthal temperature field, then to an axial extension of the deformation.

To summarise, it appears that, in a rod bundle, the mechanical interaction between rods, and more particularly with a guide tube, may lead to an increase of the burst strains and of the flow blockage:

- On one hand as a result of a mechanical interruption of the “hot side straight effect” process (the importance of which on the limitation of burst strain has been evidenced in single rod tests).
- On the other hand, as a result of the re-homogenizing of the azimuthal temperature distribution.

It may thus be concluded that, under conditions conducive to significant mechanical interactions between rods, the spatial distribution of burst strains and of the resulting flow blockage, cannot be realistically evaluated on the basis of single rod tests alone.

#### *7.3.2.4 The single and multi-rod burst test (MRBT) programme at Oak Ridge National Laboratory (ORNL)*

A series of tests at ORNL sponsored by the US NRC started in 1975 and had the following objectives: effects of rod to rod interaction on failure behaviour, magnitude and geometry of resulting blockage patterns, rupture temperature-pressure inter-relationships, flow resistance coefficients as a function of flow blockage and to provide an internally consistent data set that is amenable to statistical analysis. A description of the experimental facilities is given in Section 5.2.2.3.

The single rod test series PS (preliminary tests) were scoping and development tests for the SR series which followed [64]. These were carried out by heating the rod and test chamber, in which there was a small downward flow of super-heated steam, to 350°C using external heating only, i.e. simulator power zero. The rod helium pressure was next adjusted to the desired value and power was then applied to the simulator to initiate the transient of 28 K/s. The pressure in a rod was not controlled and rose slowly as the gas temperature increased, reached a maximum, and then decreased at an increasing rate, as the internal volume increased because of cladding strain, until rupture occurred. The rate of increase in temperature of the cladding near the rupture levelled off and in some cases diminished just prior to rupture, indicating strain cooling [65]. The variation of circumferential strain with burst temperature in the above tests is given in Figure 7.72. Also there are results from tests in argon which are similar at temperatures  $\leq 950^\circ\text{C}$  (i.e. where oxidation effects at this heating rate are minimal) but show greater strains above this level. In two tests the gas volume of the specimens was increased to 160 cm<sup>3</sup> i.e. 4 times the normal value without apparently any effect. This may have been an attempt to justify the use of 2.5 times larger volume in the standard ORNL test specimens compared to that used in American PWR fuel rods.

Figure 7.73 gives the axial length changes of the specimens as a result of testing. The effect of strain anisotropy causing the tubes to decrease in length in the alpha phase region is clearly demonstrated. In addition to the ramp tests at 28 K/s four creep rupture tests [66] were carried out in steam at about 760°C with internal gas volumes of about 51 cm<sup>3</sup>. The times to rupture at 760°C varied from 49 to 250 s and the strains from 23 to 32%. Two of these fuel simulators were then used for transient tests at 28 K/s which burst at 760-770°C, with strains of 20 and 23%. Ramp tests were also done at 5 and 10 K/s. The strains in all these tests were not significantly different from those ramped at 28 K/s, [66] (Figure 7.74) but there was a tendency for greater volume increase with decreasing ramp rate (Figure 7.75).

The first multi-rod test [67] (B-1) was carried out in 1977 using a 4×4 array of heated and pressurised rods in the test assembly shown in Figure 5.53. The two centre grids are 56 cm apart, a spacing which is similar to that in reactor fuel assemblies. The 4×4 array of rods was surrounded by a direct resistance heated shroud. To avoid electrical shorting between the test rods and the shroud there was a gap of 16 mm in between them. There was thus no restraint on the outer row of rods. The rods in B-1 were ramped, at 29.5 K/s and the shroud at 20 K/s, in flowing steam (about 4.2 kg/h, Reynolds number 250) from 350°C until the rods ruptured at about 850-880°C all within about a time span of about half a second.

Figure 7.72 Average rupture strain from single-rod tests heated at 28 K/s [64]

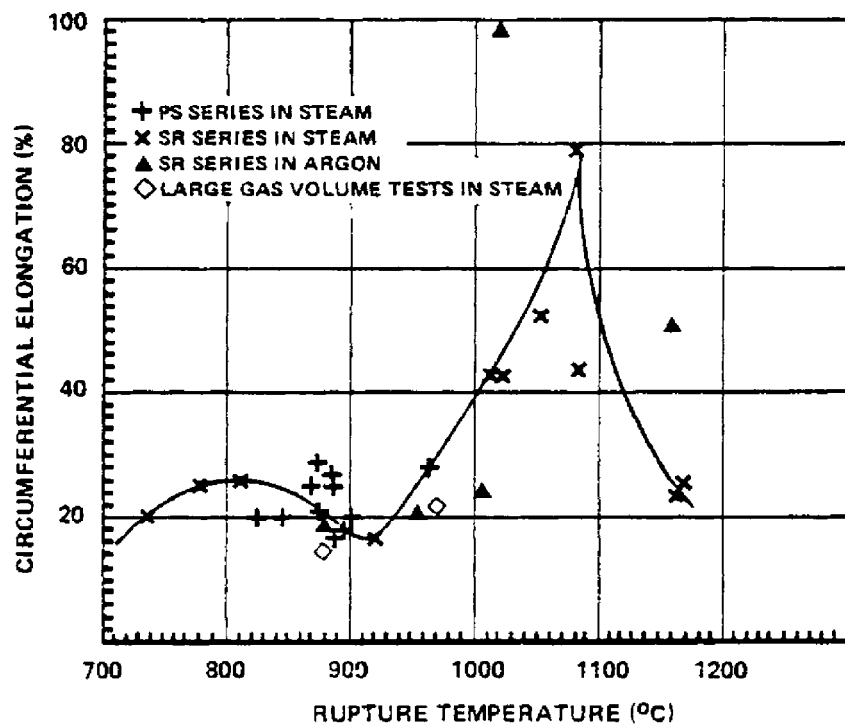


Figure 7.73 Change in Zircaloy heated length in single-rod tests [64]

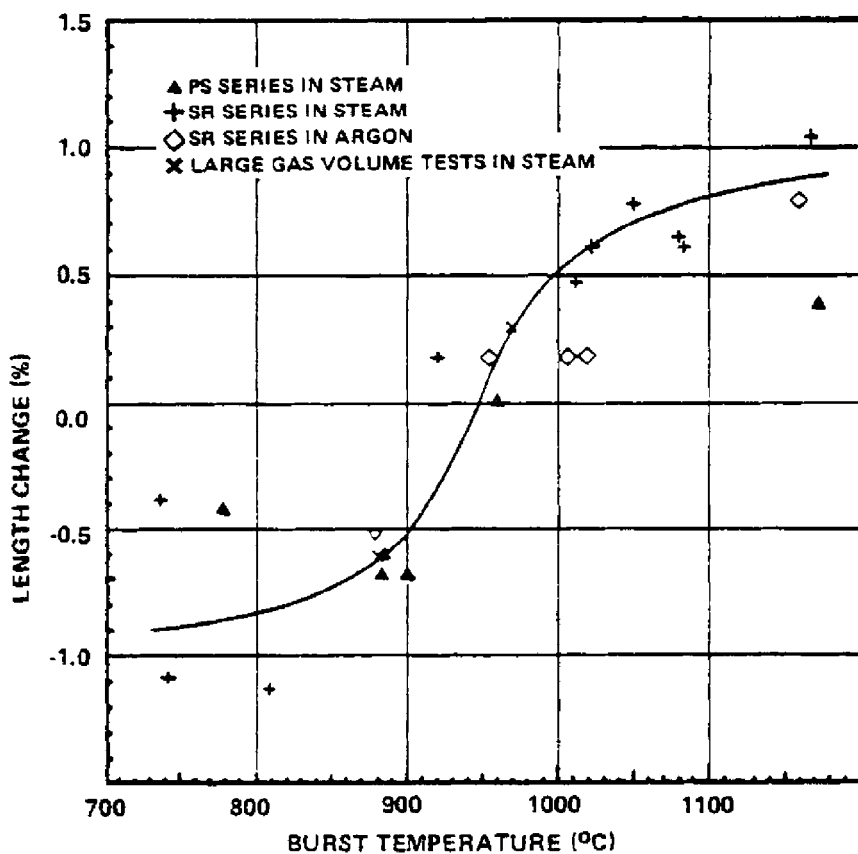


Figure 7.74 Comparison of burst strain in creep rupture and low heating rate tests with data for 28 K/s tests [66]

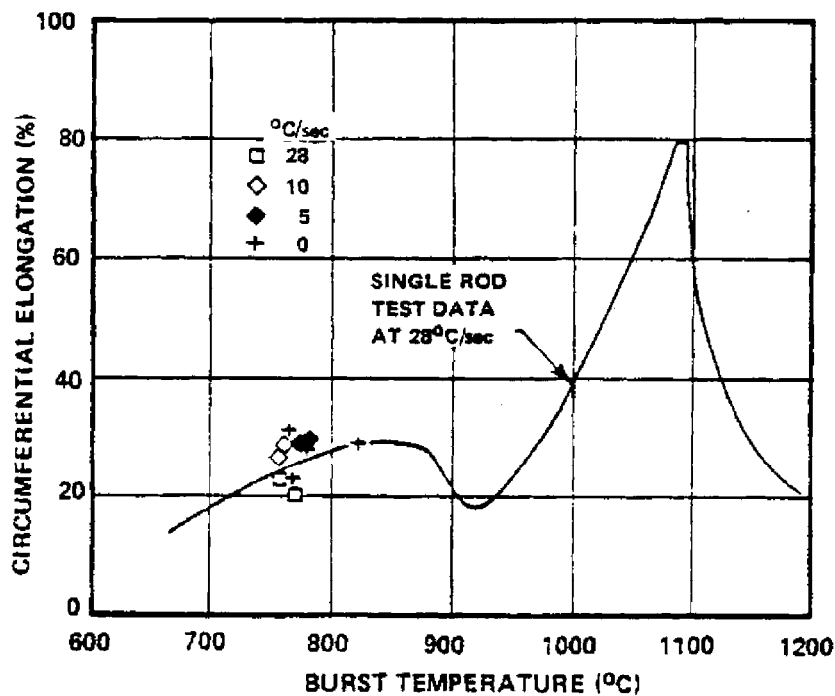
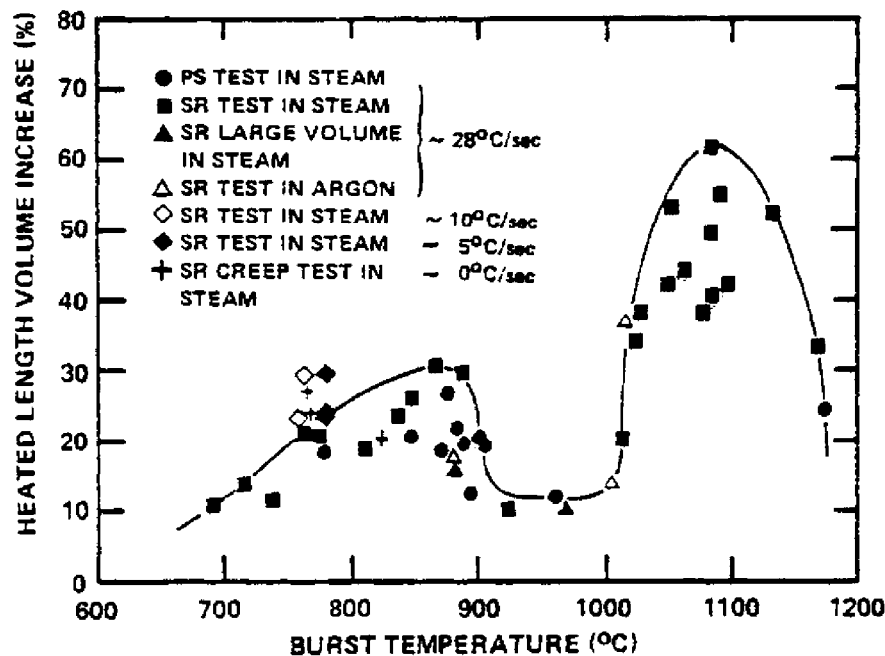
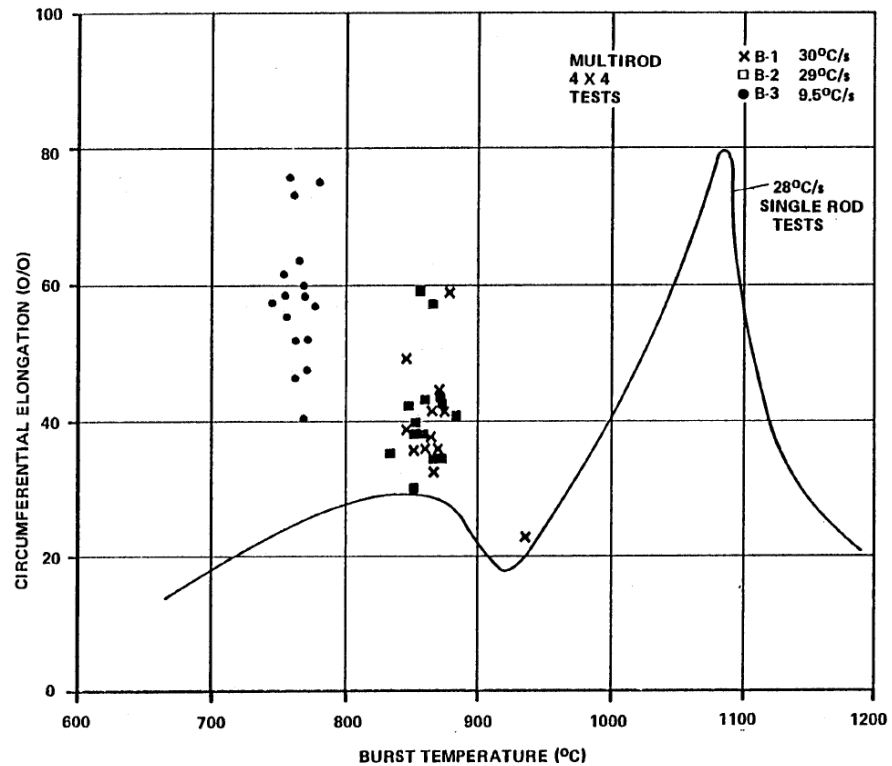


Figure 7.75 Comparison of tube volume increase (qualitatively equivalent to average tube strain) in creep rupture and low heating rate tests with data for 28 K/s tests [66]



The circumferential strains in the burst region were 32-59% which is significantly greater than achieved in the single rod tests at nominally the same conditions (Figure 7.76). The rods had moved outwards from their centre-line position, reflecting the lack of restraint. The maximum flow blockage was 49%.

Figure 7.76 Comparison of burst strains in B-1, B-2 and B-3 tests with single rod tests data



The second multi-rod test B-2 [68], ramped at 28.5 K/s, steam flow Reynolds number 290, was done with nominally the same conditions as B-1 except that the shroud was not heated. The results were similar, burst strains 34-58% [69] see Figure 7.76, flow blockage 54% except that there was greater bowing of the peripheral rods which was attributed to the larger circumferential temperature gradients resulting from the presence of an unheated shroud.

The primary objective of the next multi-rod test, B-3 [70] was to “investigate bundle deformation under test conditions believed by some to be more realistic of PWR LOCA parameters” i.e. the temperature ramp rate was reduced to about 9.5 K/s with the initial pressures adjusted to cause rupture at about 760°C. This test was done with a heated shroud (ramp rate 7.1 K/s) and the internal volumes ranged from 49-51.5 cm<sup>3</sup>. The steam flow was the same as used in B-1 i.e. about 4.5 kg/h and the Reynolds number was 263. The rods in B-3 failed at about 764°C wholly in the alpha-phase region. The maximum strain was 77% and six rods had strains greater than the maximum of either B-1 (59%) or B-2 (52%) (Figure 7.76) and much greater than single rods heated at 10 K/s (Figure 7.77). There was greater overall deformation with many portions of the assembly straining greater than 32% (Figure 7.78). The maximum flow blockage was about 77%. The ruptures all occurred within the main intergrid region [69] unlike B-1 and B-2 where bursts occurred in both intergrid regions. The same fuel simulators were used in B-1 and B-3 in exactly the same orientation and position so a direct comparison can be made between these two tests (Figure 7.79). There are known hot spots in the internal heaters and these can be correlated with burst positions, presumably in B-3. The heat transfer-strain/rate combination was such as to suppress the effects of hot spots in the upper part of the fuel simulators.

Figure 7.77 Comparison of B-3 bundle burst data with ORNL and KfK single-rod data for heating rate of ~10 K/s

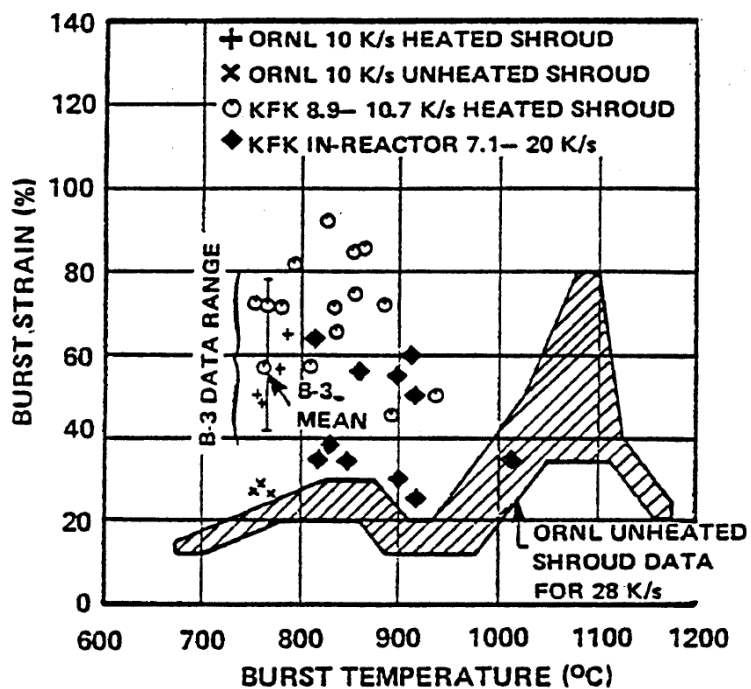
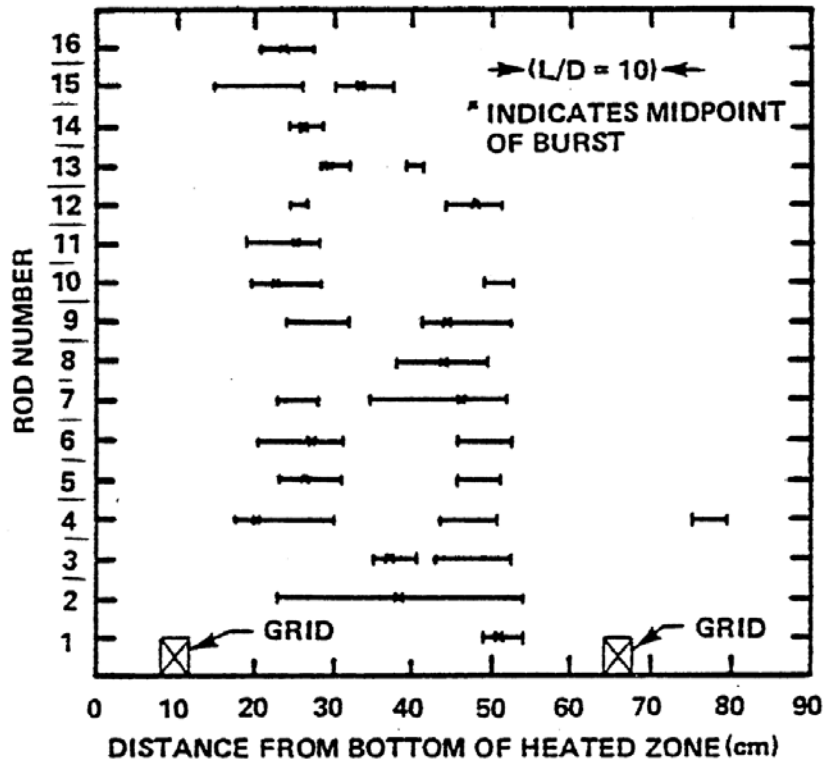


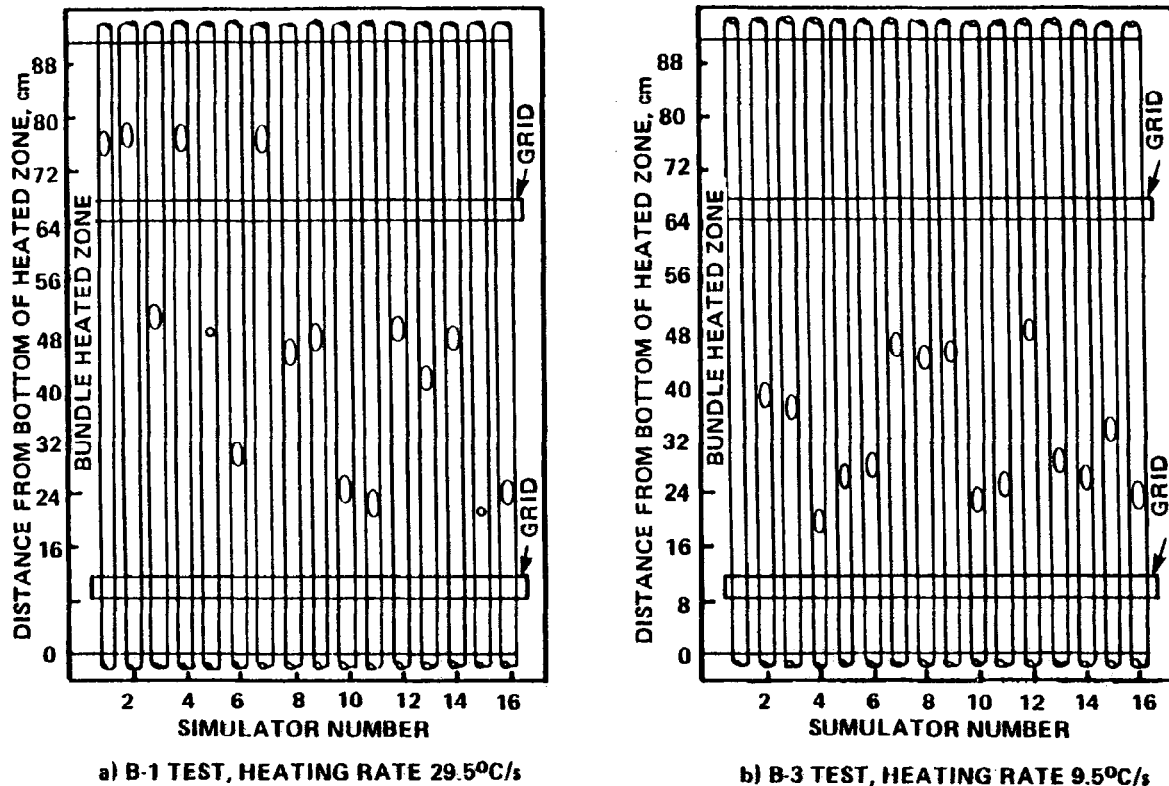
Figure 7.78 Portions of tubes with greater than 32% strain in B-3 test



The effect of steam flow was investigated further in two single rod tests [69] with grids attached, using the heater fuel rod number 4 in bundle test B-2. The first test, SR-39, had the steam flow

normally used in single-rod tests i.e. Reynolds number 800 and in the second, SR-40 the steam flow (Reynolds number 180) was lower than that used in the B-2 bundle test (Reynolds number 290). The results (Figure 7.80) showed that at the low steam flow (Reynolds 180) the fuel simulator caused the Zircaloy cladding to burst in the same position as did the cladding in the multi-rod test B-2 (Reynolds 290) whereas with the higher steam flow the position of burst was shifted along the rod in the direction of steam flow. Further evidence for this effect is shown in Figure 7.81.

Figure 7.79 Axial distribution of bursts in multi-rod burst tests B-1 and B-3 [69]



Note: The same fuel simulators were used for both tests, in the same positions and orientations.

The maximum strain produced by the same fuel simulator in the multi-rod test B-2 was about 42% whereas in the single rod test it was about 28%. This indicated that radiation from surrounding rods may be influencing the strain so a series of single rod tests using heated shrouds was carried out [16]. This showed that at ramp rates of 28 K/s, the strains were not much greater than in tests with unheated shrouds (Figure 7.82). However, heated shroud tests carried out at KfK did show greater strains at high ramp rates, 24-30 K/s, which were equivalent to those produced in the ORNL multi-rod tests B-1 and B-2 ramped at about 29 K/s (Figure 7.82).

The strains in single rods ramped at 10 K/s, at ORNL and KfK with heated shrouds were similar to those achieved in the B-3 multi-rod test with a 9.5 K/s ramp (Figure 7.77).

The target conditions for the next multi-rod test B-4 [71] with a 6×6 array were ramping at 5 K/s, i.e. to about 800°C, but malfunction of the equipment with bursting in the peak ductility region for alpha phase prevented the rods from achieving this and the maximum strain reached before the test was terminated was only about 20%.

Figure 7.80 Burst location can be displaced by change in steam flow [69]

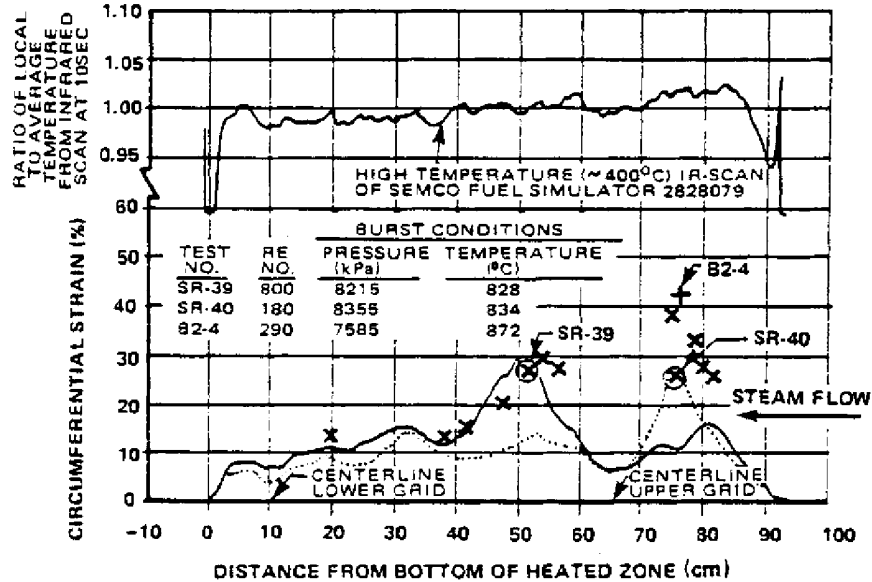
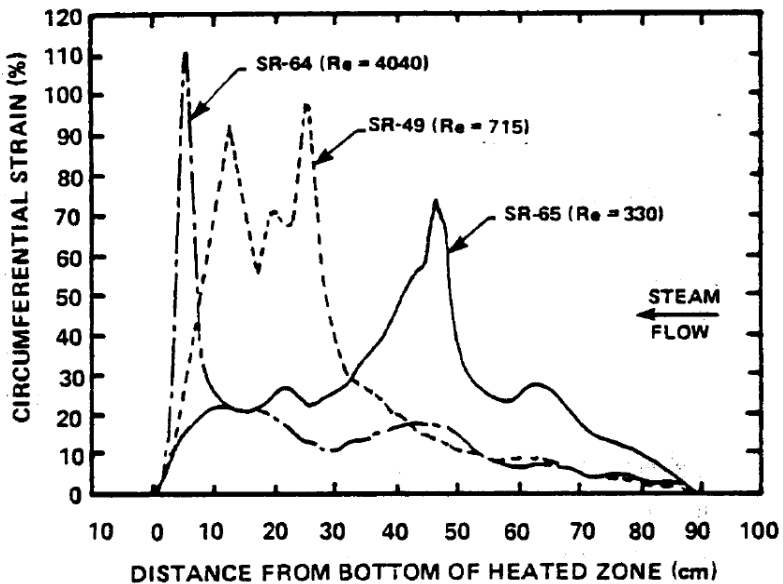
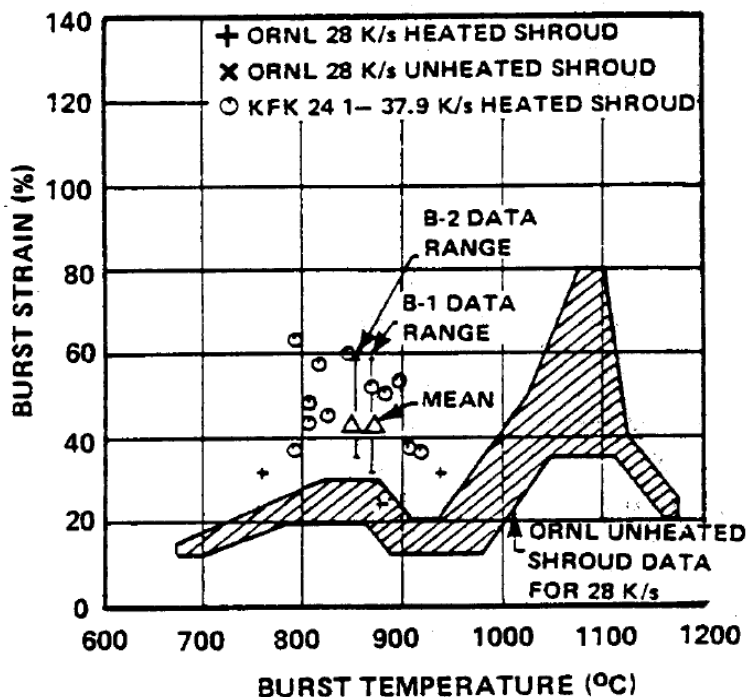


Figure 7.81 Deformation agrees with axial temperature distribution



Test B-5 [72] was conducted under conditions close to B-3 ( $4 \times 4$ ) 10 K/s, but with an  $8 \times 8$  array of heated and pressurised rods surrounded by an unheated shroud spaced at one half of the coolant channel distance from the outer rod surfaces, i.e. much closer than in previous tests, to obtain information on the effect of test array size on deformation and rod-to-rod interactions. The shroud was constructed from stainless steel (0.1 mm thick) backed by insulating material and a strong structure to withstand any radial forces from expansion of the fuel rod simulators. The shroud could not be directly electrically heated because of the close proximity of the fuel rod simulators so the inner surface was gold plated and polished to reflect radiant heat back to the test array; even so its temperature increased significantly. The rods in the  $8 \times 8$  array were pressurised after holding at  $336^\circ\text{C}$  to achieve thermal equilibrium, but one rod in the outer ring failed to hold pressure and the test was conducted with this rod heated but unpressurised. All rods except this one burst within 6 s at about  $775^\circ\text{C}$ .

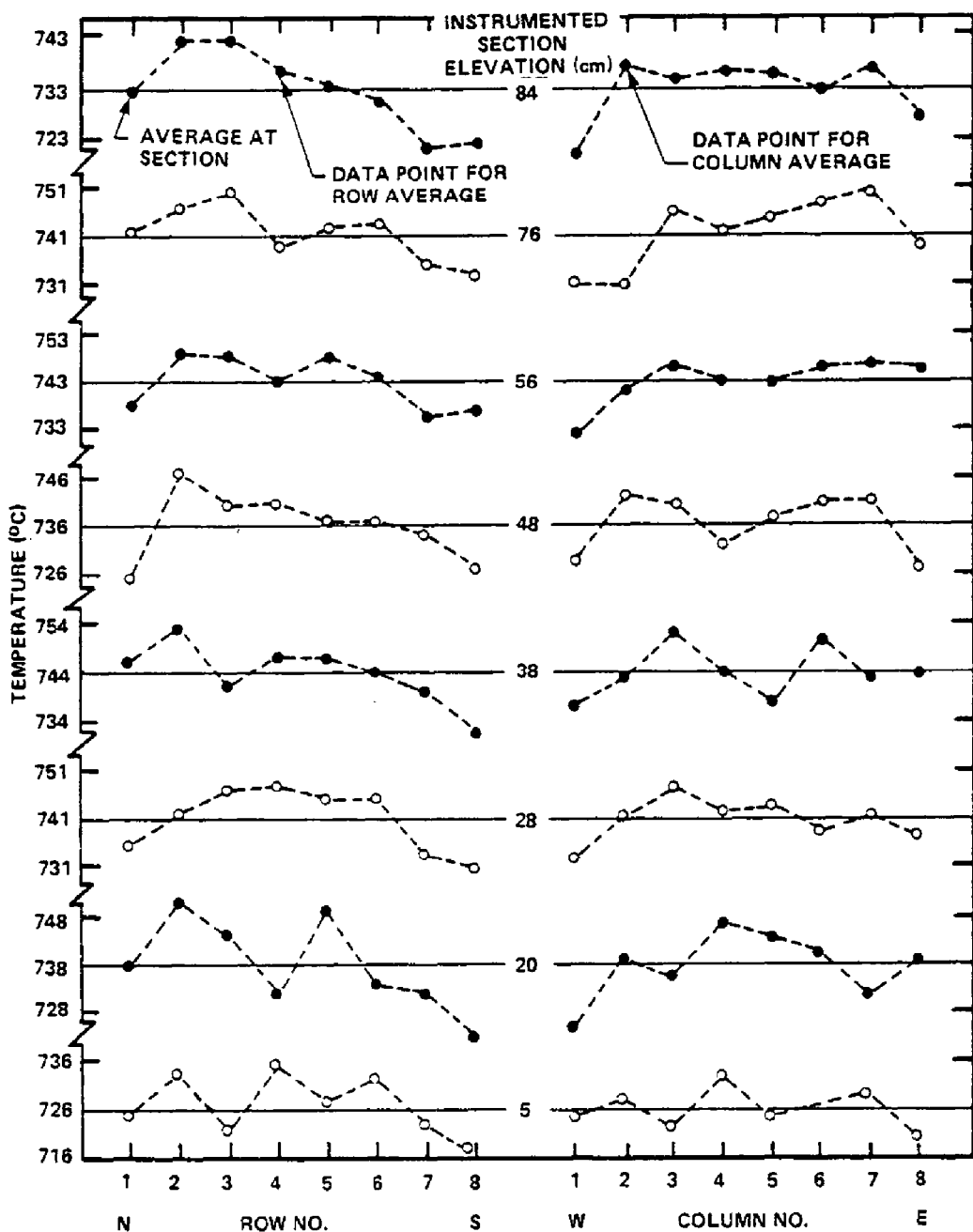
Figure 7.82 Comparison of B-1 and B-2 bundle data with ORNL and KfK single-rod data for heating rate of ~ 28 K/s



The superheated (355°C) steam flowed downwards at about the same mass flow as in B-3, about 288 g/s/m<sup>2</sup>, a Reynolds Number of 140 as it entered the test array through a single side nozzle. Unfortunately, under those conditions a uniform steam distribution could not be established, unlike previous tests with 4×4 and 6×6 arrays, resulting in a gradient across the bundle of 24°C at the top reducing to 2°C at the bottom. (Note the steam distribution system was since modified to avoid this effect.)

The non-uniformity of the steam flow had an effect on the cladding temperature during the test in that there was a 20°C gradient at the 5 cm level, also the rods on the north side had an initial average axial temperature gradient of 11°C whilst those on the south side had a gradient of 2-3°C. Figure 7.83 shows that the average temperature of the outer ring of fuel simulators was lower than those in the interior and also demonstrates the north-to-south and east-to-west gradients. Figure 7.84 shows the temperature differences between interior groups of rods.

Figure 7.83 Radial temperature distribution base on row- and column-averaged data 43 s after power-on for B-5 rods [40]



Visual examination after testing showed that cladding deformation was greater on the north face than the south face. However, the gaps between all the outer rods in both faces were completely closed in places for axial distances of 5-10 cm. None of the bursts on the exterior rods were directed towards the cooler shroud and most of the interior bursts were towards the coolant channel (Figure 7.85). Examination of the cross-section [73] from the bundle showed evidence of rod-to-rod interaction producing trapping of the bulges causing them to become square (Figure 7.86).

Some of the strains of the individual rods are given on Figure 7.86, the others can be estimated by comparing their dimensions with the outer row rod which did not strain, and the scale.

Figure 7.84 Simulator average temperature 43 s after power-on in B-5 test

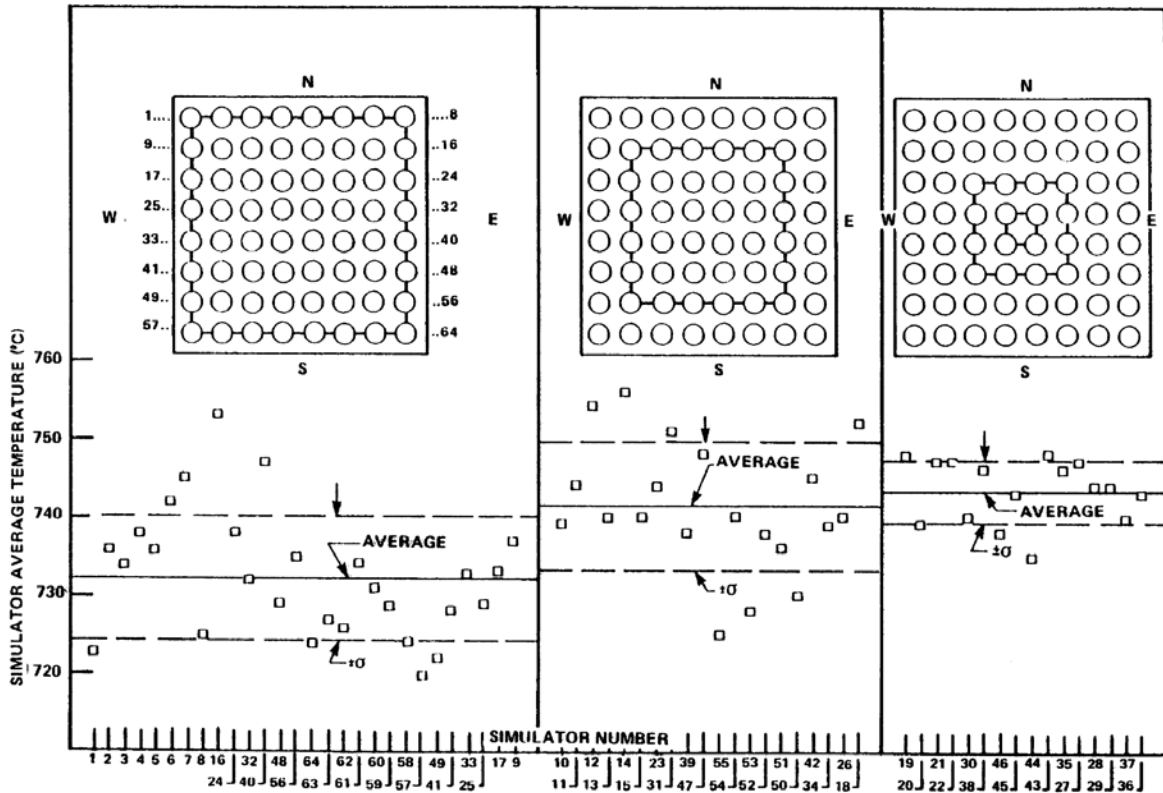
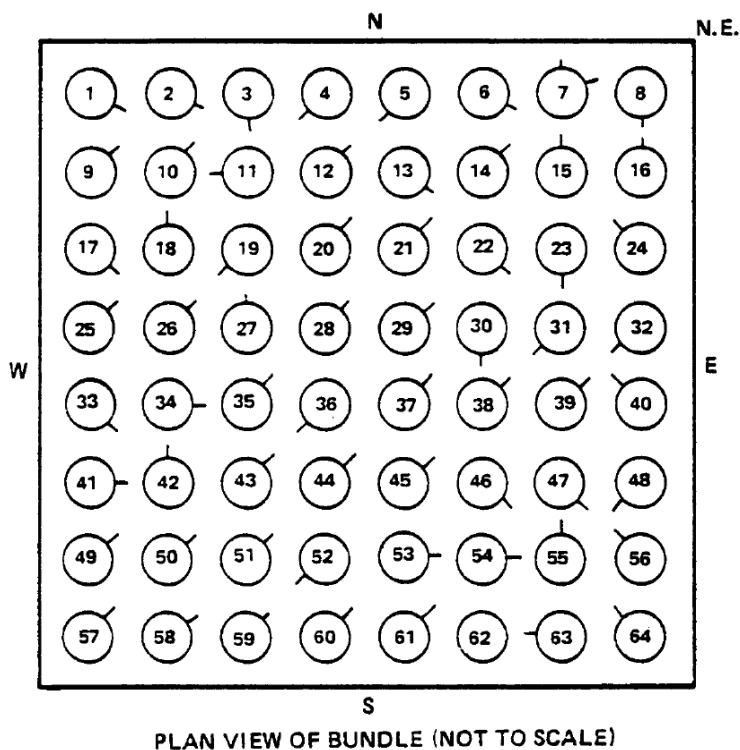


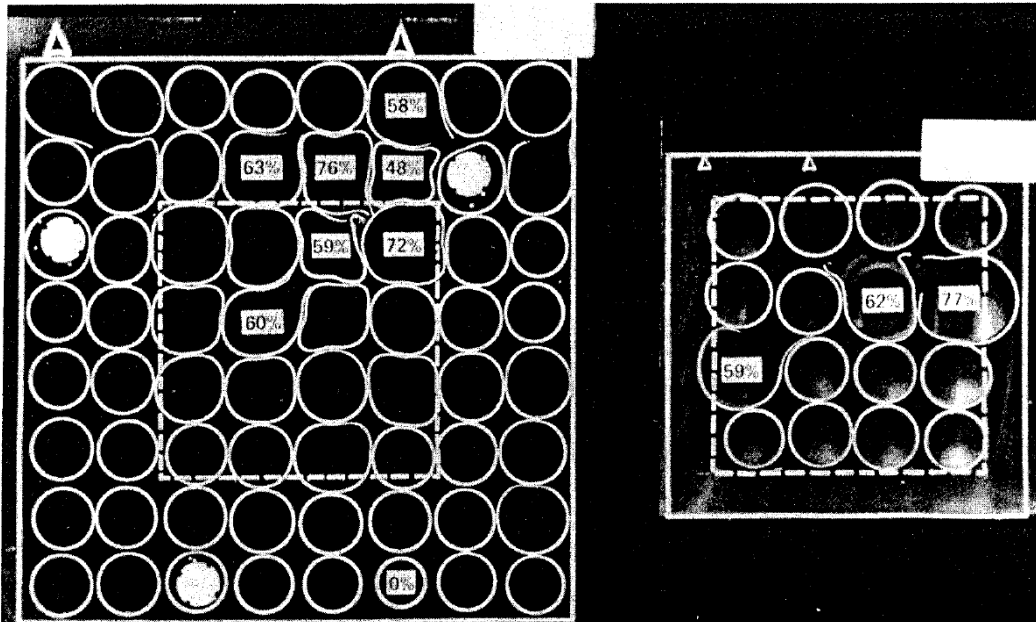
Figure 7.85 Approximate orientation of bursts in the B-5 test

The figure shows a predominance of bursts towards the flow channel and the N.E. corner [73]



**Figure 7.86 Sections from highly deformed regions of B5 and B3 bundles showing effects of confinement**

Small unconstrained bundles do not produce the same deformation pattern as large constrained bundles for same test conditions [73]



Thus the cladding strains in the rods which formed "square" cross-section are in the range of about 50-75%, whilst others which are still reasonably circular but are trapped between two or more rods have strains in the range of about 25-40%. The trapping of bulging rods appears to have caused the deformation to extend axially resulting in a greater volume increase (Figure 7.87) and greater flow restriction (Figures 7.88 and 7.89), than had been seen in the B-3 test with similar maximum strains (Figures 7.86 and 7.90). Thus the authors conclude that flow area restriction in large arrays may be underestimated by small unconstrained arrays and that two rows of deforming "guard" specimens are necessary around the deforming array under investigation to simulate the radial temperature and mechanical boundary conditions which would be present in a large array of rods such as a fuel assembly. The extent to which this applies in conditions of high heat transfer has been argued to be small, however [56].

In the concluding B-6 [72] test in the ORNL programme, carried out in December 1981, an 8x8 array with a closely fitting, unheated, shroud was ramped at 3 to 4 K/sec to fail in the region of 930°C, i.e. well into the  $\alpha+\beta$  phase region, to ascertain if the typically smaller strains seen in single rods burst under these conditions persist in large arrays. The results [72] showed this to be so, the burst strains ranging from 22 to 56% with an average of 30% consistent with an average of 36% for three single rods tested under similar conditions. The coolant channel flow area reduction was modest: 39% for the whole 8x8 array, 44% for the inner 6x6 and 46% for the central 4x4 array.

The following conclusions for the ORNL MRBT tests are due to C. Grandjean [24]. It can first be noted that the main objective of the MRBT tests was to investigate the influence of the bundle size and of the thermal and mechanical boundary conditions on the burst strain and flow blockage, under thermal heat transfer conditions that did however favour large deformations to occur.

Figure 7.87 Tube dilatation greater in B-5 interior simulators than in exterior simulators and greater than in comparable B-3 (4x4) test [73]

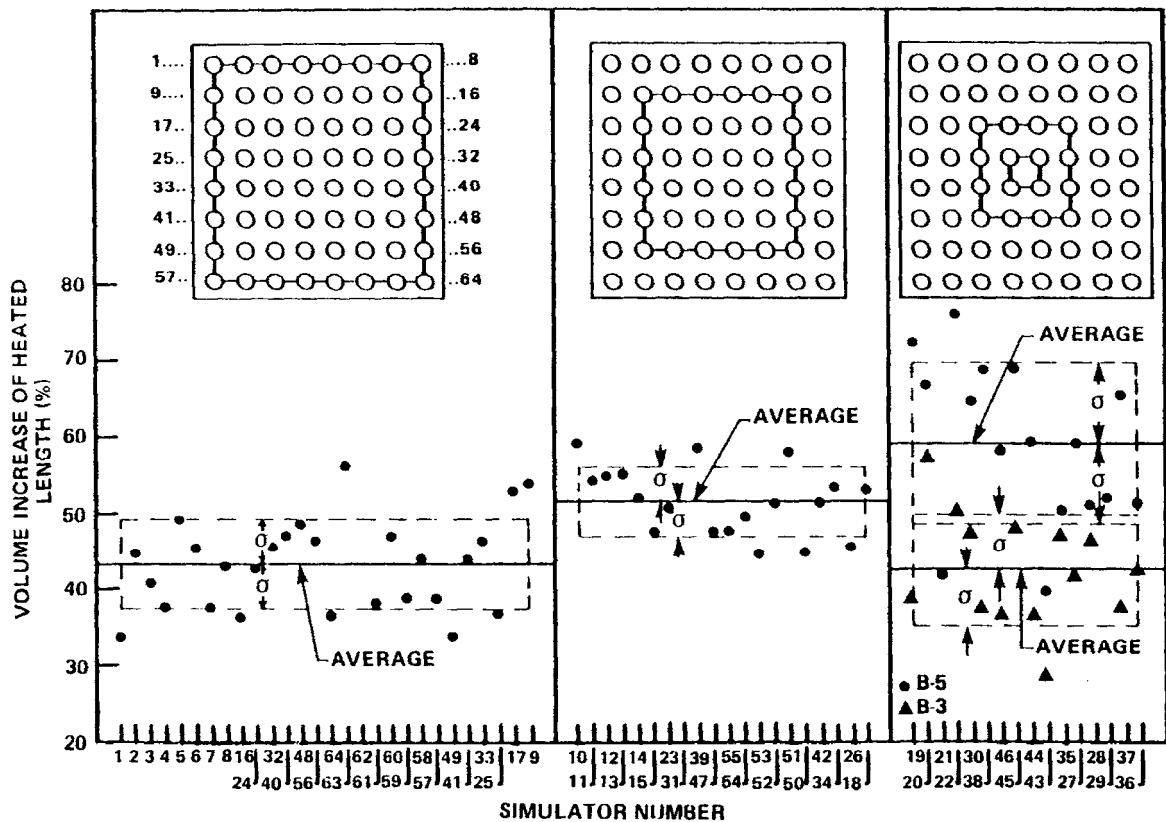


Figure 7.88 Subdivision of B-5 data show interior subarrays have greater coolant flow area restriction [40]

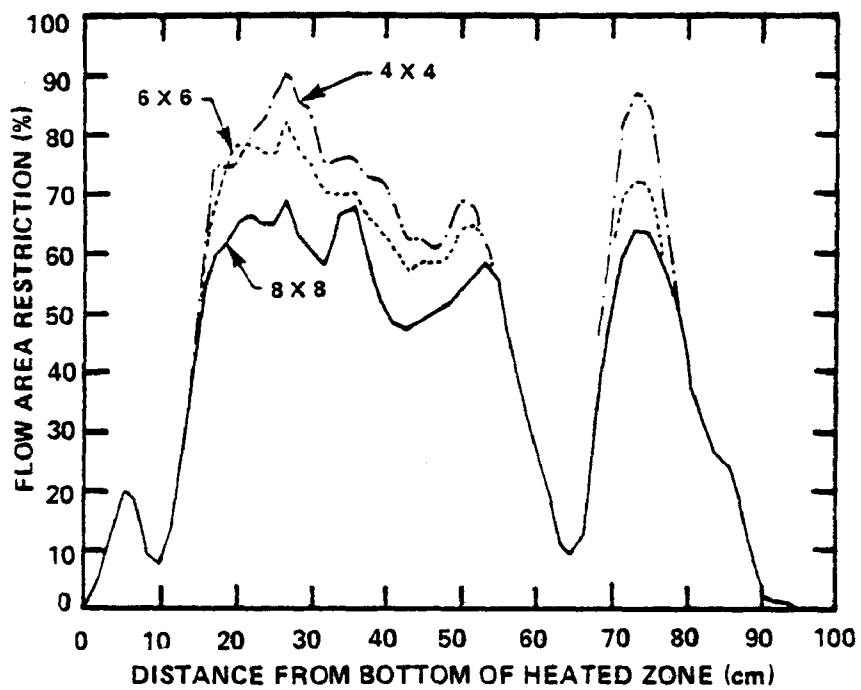


Figure 7.89 Preliminary B-5 data show inner 4×4 array has greater flow restriction than B-3 (4×4) array [40]

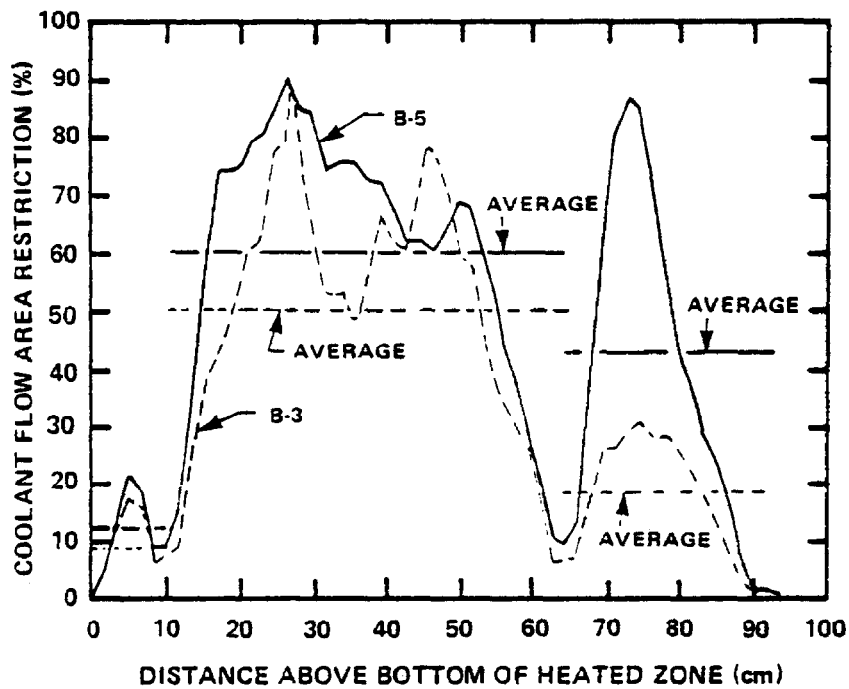
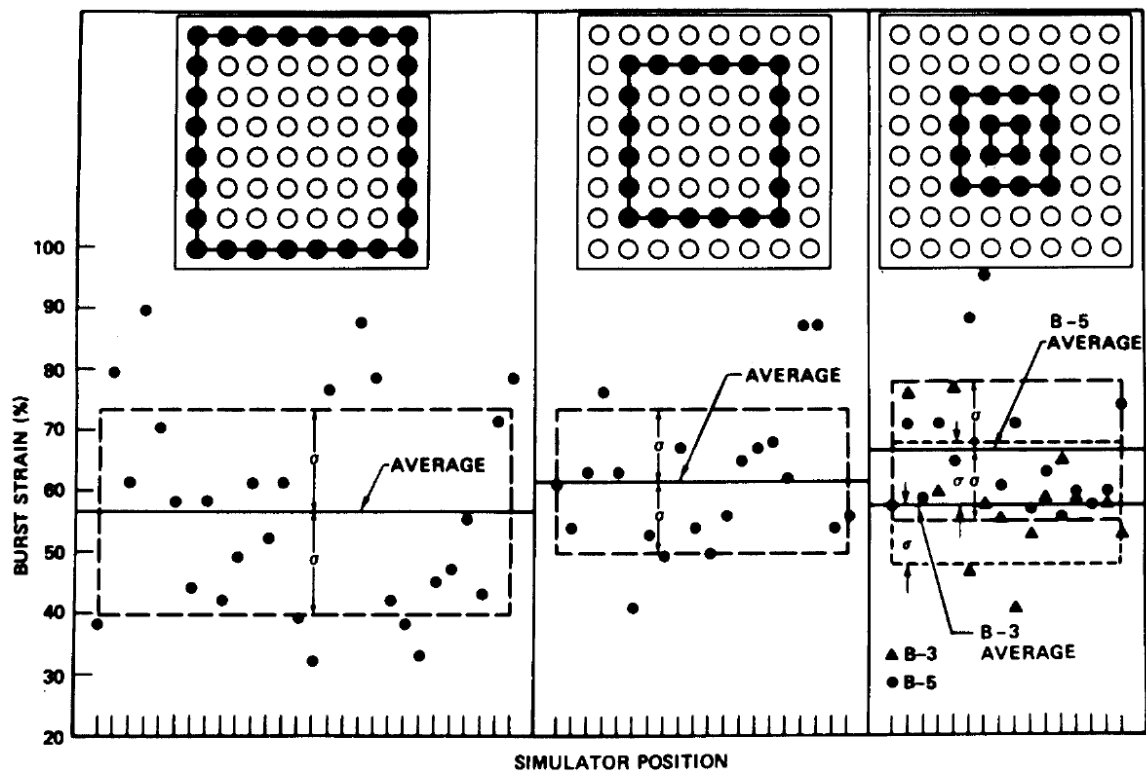


Figure 7.90 ORNL-MRBT. Burst strains of B5 tubes  
B3 (4×4) data are shown for comparison with inner 4×4 array of B-5.



The main results, as provided by the comparison of the B-3 and B-5 data, indicate that in a large array the straining of inner rods lead to mechanical interactions between neighbour rods that, although of limited impact on burst temperature and elongation, will modify significantly the spatial development of deformation until rupture. Notably, the trapping of bulging rods has appeared to cause the deformation to extend axially, resulting in a larger volume expansion and a greater axial extent of blocked regions. This also results in a deviation from the rupture temperature/pressure curve deduced from single-rod heated-shroud-tests data.

Thus the authors concluded that the flow area restriction in large arrays may be underestimated by tests results on small unconstrained arrays and that at least two rows of deforming "guard" rods are necessary around the central deforming array to properly simulate representative conditions which would be present in reactor fuel assembly.

The presentation of these results, in particular at the 6<sup>th</sup> Symposium "Zircaloy in the Nuclear Industry" by Chapman [73], has raised keen criticisms from the authors of the REBEKA program who made rather different observations. F.J. Erbacher thus claimed that the thermalhydraulic conditions in MRBT tests (slow steam cooling) are atypical of a LOCA and therefore the results are specific to these tests only. It was however replied that the two-phase cooling conditions used in REBEKA tests, under which the deformation did not appear sensitive to bundle size, were also specific of the German PWR and may not be applicable to US-designed PWRs.

It can finally be mentioned that only tests B-1 to B-3 were included in the data base that was used for the derivation of the clad swelling and rupture models described in the NUREG-630 report [18]. These three tests have in particular been used for the derivation of a coefficient relating the average burst strain to the average strain in the plane of maximum flow blockage, so as to allow the derivation of the maximum flow blockage as a function of burst temperature. It may be thought that, based on these three tests results only, the proposed correlation in the earlier year remains rather uncertain.

#### 7.3.2.5 Single and multi-rod testing at Westinghouse Electric Corporation

These tests [74] were carried out using standard Westinghouse fuel rod cladding, 15×15 size Zircaloy 4 tubing for the multi-rod tests and both 15×15 and 17×17 sizes for the single rod tests.

The single rod tests were carried out in air and flowing steam using specimens filled with alumina pellets and heated externally in a radiant heater furnace which produced a uniform hot zone at various heating rates in the range 2.8 to 111 K/s.

The results (Figure 7.91) show that the burst strains of the specimens heated at 2.8 and 14 K/s, with internal pressures typical of those "at power" in the current PWR fuel rod design, i.e. 900-1 200 lb/in<sup>2</sup> (62-80 bar) are in the range 40-110%. These heating rates are the closest in this test series to the rate of about 8.3 K/s which is calculated to occur during adiabatic heat-up following a large break LOCA.

The 4×4 multi-rod tests used direct resistance heating of the cladding which had been coated with ZrO<sub>2</sub> in an attempt to prevent electrical arcing between rods. Unfortunately, post-test examinations revealed localised cladding melting, implying that the ZrO<sub>2</sub> coatings had cracked during swelling. Only two internal pressures were used, 200 and 2 250 lb/in<sup>2</sup> (14 and 155 bar) of which the former would cause the cladding to burst in the α+β phase region and the latter would produce very high strain rates. Neither of these conditions is conducive to developing the maximum strain potential of the Zircaloy cladding as can be clearly seen from the single rod results (Figure 7.91). The maximum blockages resulting from the multi-rod (4×4) tests are about 50% (Figure 7.92).

Figure 7.91 Burst strain vs internal pressure in Westinghouse single rod burst tests [74]

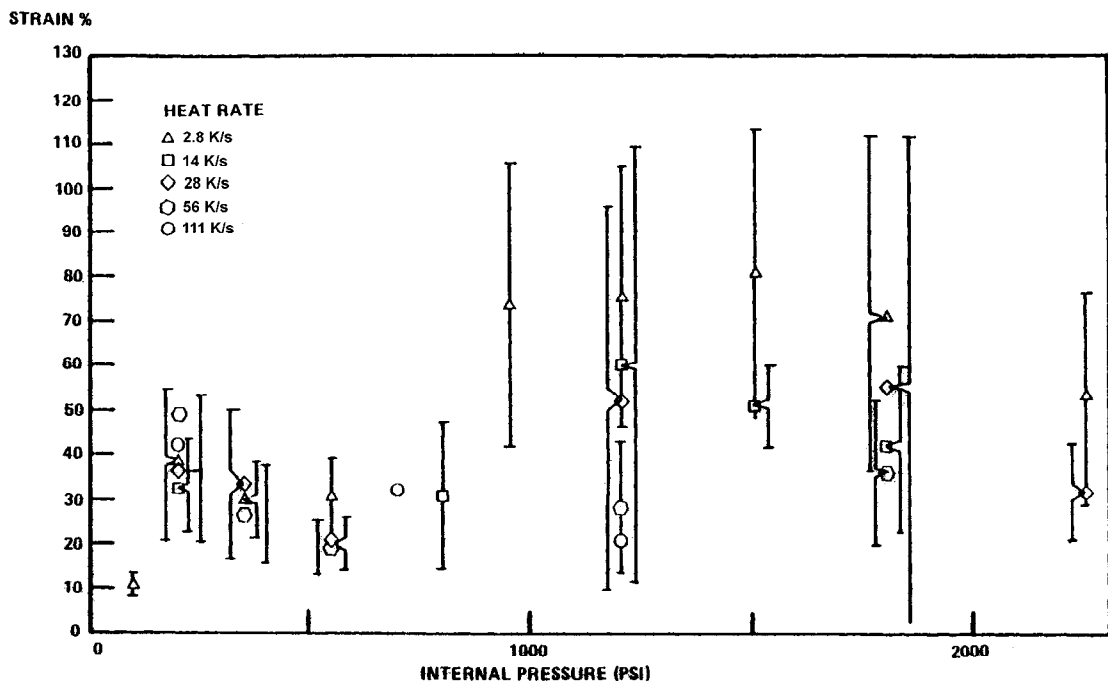
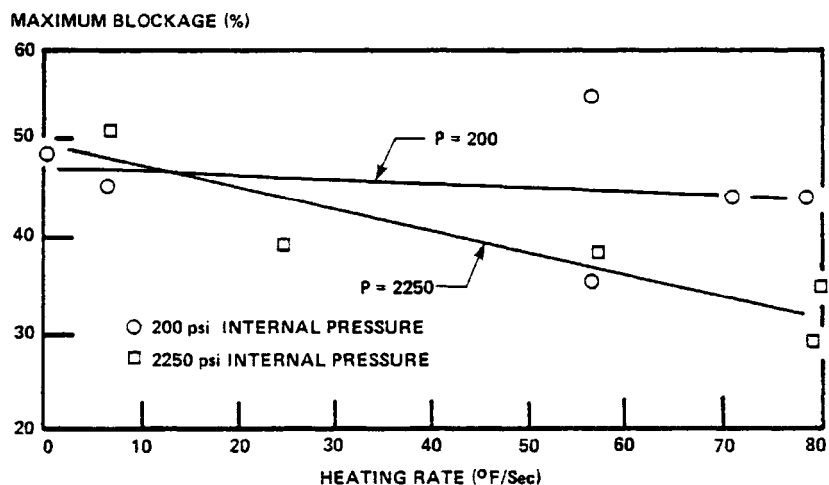


Figure 7.92 Westinghouse multi-rod burst test results [74]



### 7.3.2.6 Single rod testing at Saclay – CEA

The EDGAR experiments are separate effects tests on cladding mechanical behaviour in the stress-temperature domain of a large break LOCA. The original Zircaloy-4 base tests were performed by CEA in Saclay during the 1980s [41]. A new facility (EDGAR-2, Section 5.2.1) is still currently in use for the testing of advanced clad material and cladding properties at high burn-up [75,76].

The first objective of this programme has been to verify the actual behaviour of Zircaloy cladding under conservative calculated large break LOCA two-peak transient conditions, such as those considered in the French 900 MW(e) PWR standard safety reports. The interpretation of the Zircaloy behaviour has shown that the recrystallized material is slightly more creep resistant than the stress relieved material.

The second objective of the EDGAR programme has been to supply experimental data for the development of a deformation model and a burst criterion, which constitute a part of the data basis of the former CUPIDON code [30], and later the fuel model of CATHARE [24]. The experimental data used for this modelling are retrieved from more than 500 individual tests either with constant pressure and constant heating rate (0.2 to 100°C/s) or with constant temperature and constant pressure rate (0.01 to 0.2 MPa/s) or creep tests. Some specific tests have been added to take into account the effect of a thermal spike into the  $\alpha+\beta$  or  $\beta$  phase on the subsequent mechanical behaviour of the cladding during the two-peak transient.

The analysis of creep tests has allowed to correlate the secondary creep velocity with a Norton-type equation in each of the phase transformation domains ( $\alpha$ ,  $\alpha+\beta$ ,  $\beta$ ) of the Zircaloy material:

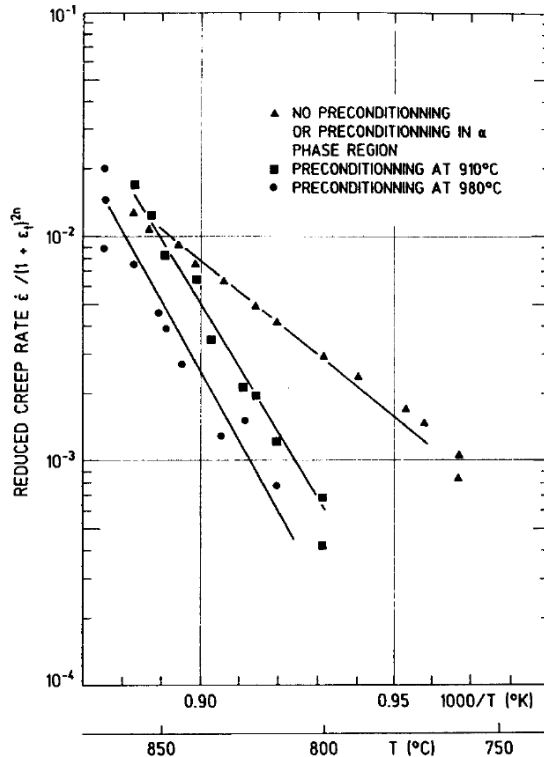
$$d\varepsilon_\theta^c / dt = A_i \exp(-Q_i / T) \sigma_\theta^{n_i} \quad (7-1)$$

where  $\varepsilon_\theta^c$  is the circumferential creep strain,  $\sigma_\theta$  the hoop stress and  $A_i, Q_i, n_i$  the coefficients of the Norton-type laws. A continuous strain homogenisation model is used to evaluate the deformation rate in the domain transition ranges.

In temperature and pressure ramp tests it has been shown that under ramp conditions the strain rate may be correctly predicted by creep test laws if a model for phase transformation kinetics has been introduced as will be shown in more detail later.

In the typical transient tests it has been observed that there is an influence on strain rate of the thermal treatment with transient temperature “first peak” within the  $\alpha+\beta$  domain (Figure 7.93). This influence can be taken into account in the modelling by evaluating the  $\alpha$ -phase fraction that results of the phase transformation during transient heat treatment.

**Figure 7.93 Effect of previous heat treatment of the cladding in the two phase domain on reduced creep rates**



As defined in Section 5.2.2, the deformation in the EDGAR tests has been characterised by two parameters: the uniform elongation  $A_r$  and the total elongation  $A_t$ . Figures 7.94 and 7.95 show the uniform and total elongations that were obtained in thermal ramp tests as function of the rupture temperature and ramp rate. The large deformations ( $> 100\%$ ) obtained in the high  $\alpha$  domain reflect the uniformity of the temperature field, in axial and azimuthal direction, as a result of the heating method, electric current through cladding, used in these tests.

Figure 7.94 Uniform elongation vs modified burst temperature in EDGAR tests

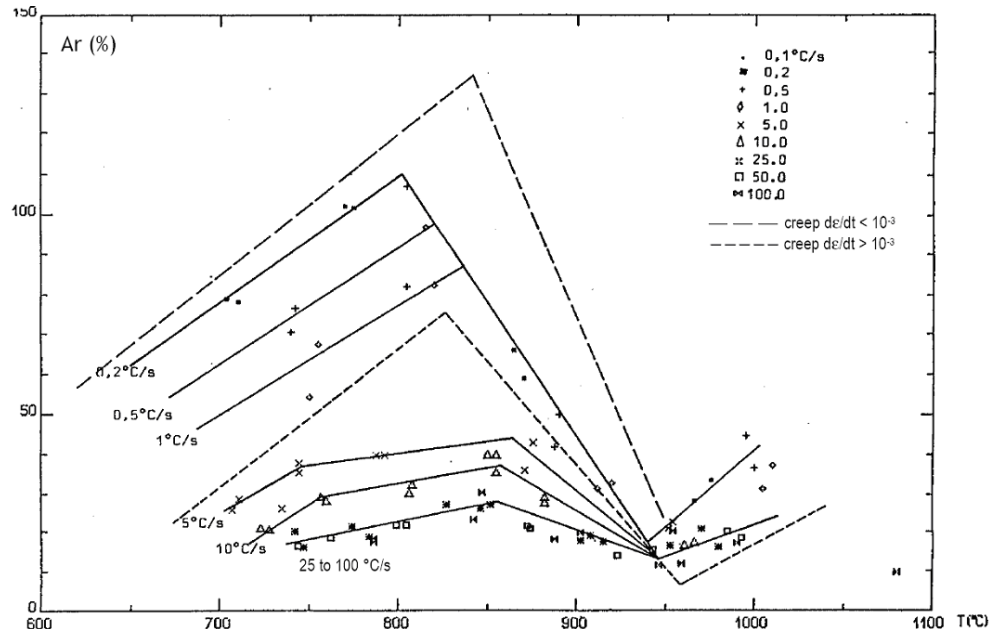
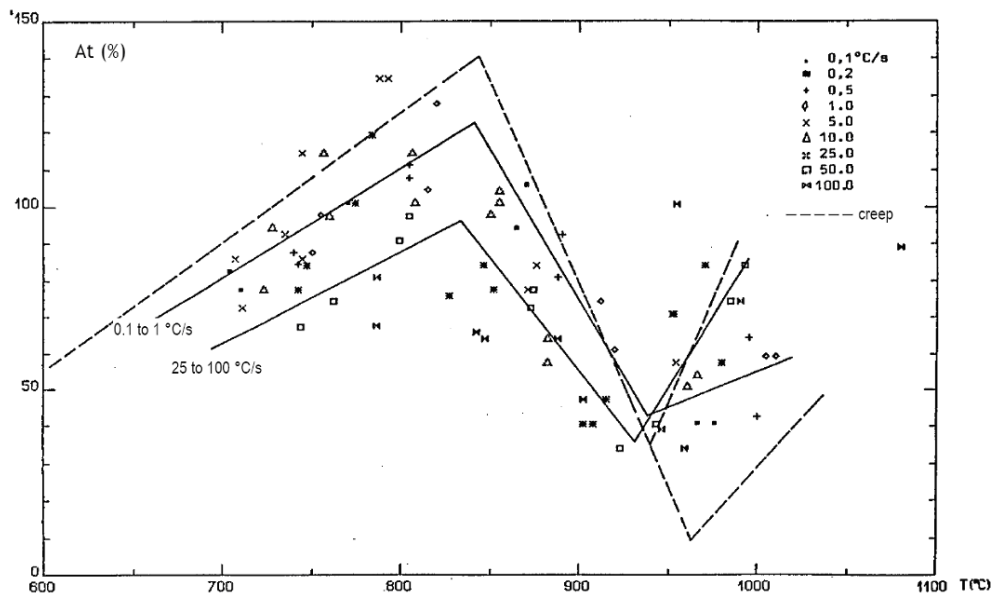


Figure 7.95 Total elongation vs modified burst temperature in EDGAR tests



One of the original objectives of the EDGAR tests was to study the influence of irradiation on the mechanical behaviour of Zircaloy. For that purpose an EDGAR rig was set up in a hot cell in Saclay.

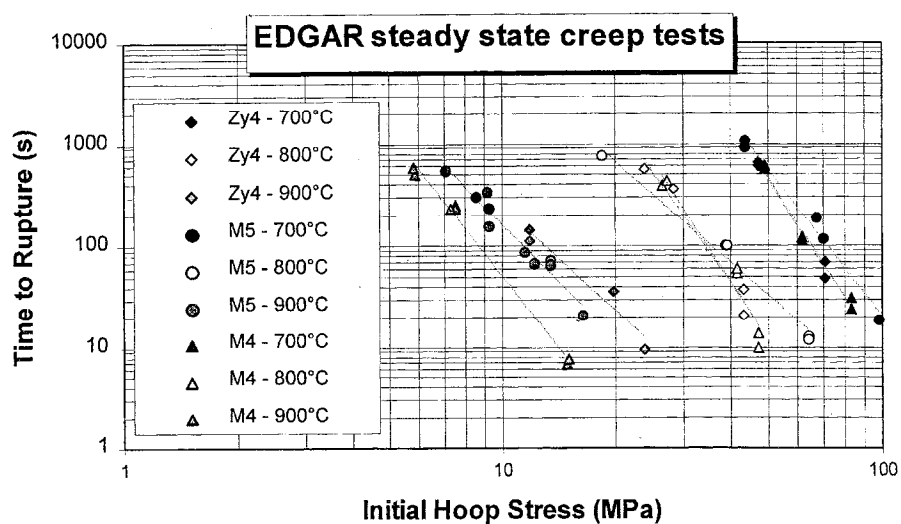
The first transient tests performed with spent fuel cladding resulted in higher creep rates in the irradiated material for the first 10 s of the two-peak transient. Moreover, the ultimate hoop stress of the irradiated cladding decreases at burst in the 800–950°C range from 15–20% compared with fresh material [30]. Réocreux and Scott de Martinville mentions that irradiation effects have been found in the EDGAR tests but that they were not well understood [41]. Grandjean also notes that experimental difficulties, mainly related to defueling of the irradiated rods, have not allowed the initially planned programme to be completed [24].

The more recent work with the EDGAR-2 facility has been performed in order to gain knowledge on the LOCA behaviour of the new alloys M4 and M5 and to determine how these alloys and Zircaloy-4 behave at high burn-ups. The basic creep properties of the M4 and M5 and the comparison with Zircaloy-4 were determined in creep tests at constant pressure and temperature [76]. A precise determination of the creep laws required about 70 to 90 EDGAR creep tests. The investigation covered temperatures between 600 and 1 000°C. Tests were performed in 50 K steps in the single phase domain and in 25 K steps in the two phase domain. The influence of stress was determined by using three different internal pressures chosen so that the rupture time would be between 10 and 1 000 s.

When the oxidation was moderate during the tests the results were easily analysed by the model for uniform expansion of a cylinder (Eq. 5-1 to 5-7). In particular, if a Norton type creep law applies, Eq. 5-7 predicts that time to rupture will be inversely proportional to  $\sigma_0^n$  where  $\sigma_0$  is the initial hoop stress and n the stress exponent in the Norton creep law. This correlation can be seen in Figure 7.96 where the results of the creep tests have been plotted as the time to rupture versus initial hoop stress.

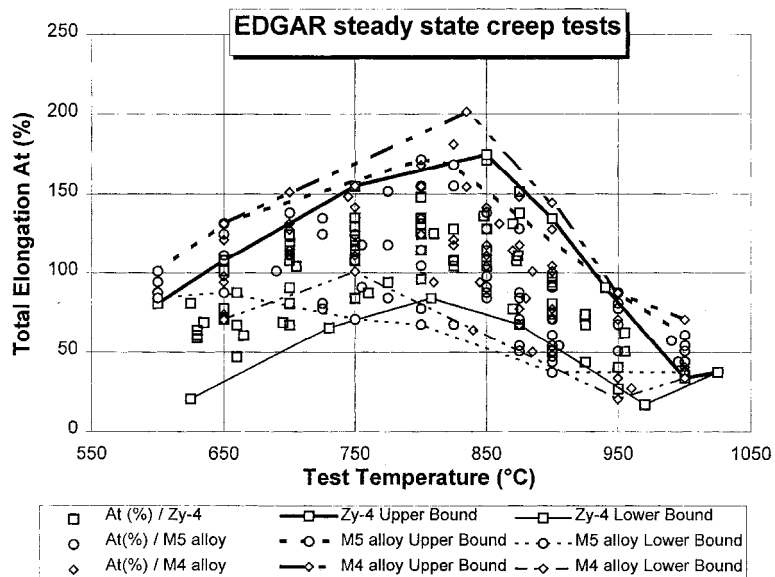
At 700°C the alloys are all in the  $\alpha$  phase. M4 and Zircaloy-4 have a similar behaviour while M5 exhibits a somewhat better creep resistance. At 800°C the slope of the  $\sigma_0$  versus  $t_R$  correlation for M5 is lower than at 700°C indicating a two-phase metallurgical state. For M4 and Zircaloy-4 the common slope, similar to that at 700°C indicates that the structure still is single phase  $\alpha$ . At 900°C the slopes indicate similar behaviour for M5 and Zircaloy-4 while phase transformation studies have shown that at this temperature M5 is almost completely transformed while the transformation of Zircaloy-4 is incomplete. The creep properties of the almost completely transformed M4 are different from the others at 900°C.

Figure 7.96 Time-to-rupture vs stress for EDGAR creep tests of Zircaloy-4, M4 and M5



The total elongations (for a definition, see Section 5.2.2), At, for the three alloys are plotted versus the test temperature in Figure 7.97.

**Figure 7.97 Total elongation as a function of test temperature for the alloys M4, M5 and Zircaloy-4**

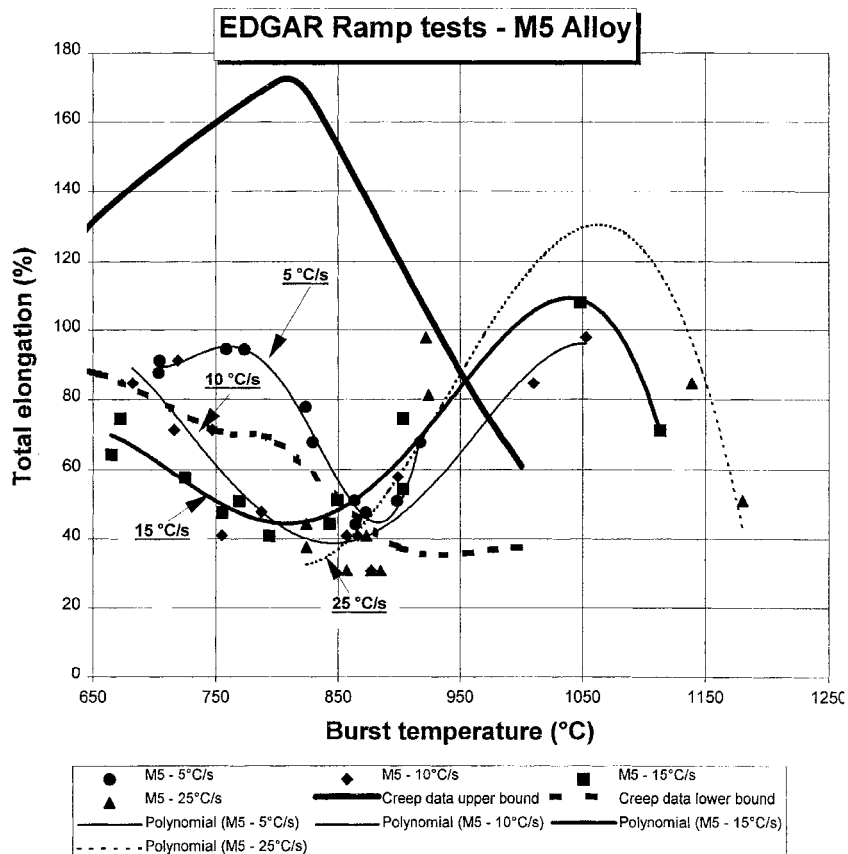


Upper and lower bounds were drawn for the three alloys. The upper bound is considered as the highest value of the ductility of the material that can be reached only in steady-state conditions with a negligible azimuthal temperature gradient and a moderate internal pressure. The lower-bound curve corresponds to short-term tests (~10 to 20 s) performed with the highest internal pressure at the test temperature. The position of the ductility peak corresponds for the three alloys to the onset of the  $\alpha \rightarrow \alpha + \beta$  transformation (about 10 to 20%  $\beta$  phase formed). A rapid decrease of the ductility was observed in the two-phase domain up to about 95%  $\beta$  formed. The increase of ductility in the  $\beta$  domain was not observed due to rapid oxidation with consequent cracking of the oxide layer and localised plastic deformation under the cracks. The second ductility peak was only observed in thermal ramp tests. As can be seen in Figure 7.97 the alloys have similar ductility boundaries.

Thermal ramp tests were performed under constant internal pressure with a constant heating rate between 350°C and the burst temperature. Tests were performed on the M4 and M5 alloys with heating rates from 2 to 100 K/s and internal gas pressures from 10 to 130 bar. Under those conditions the burst temperatures varied from 650 to 1 175°C. Results for the M5 alloy are plotted in Figure 7.98.

For each heating rate a third- or fourth-order polynomial fit has been drawn and one can see the complex influence of heating rate on the ductility. For the 5 K/s heating rate the ductility results are within the creep boundary limits but in the lower part. The maximum total elongation obtained with 75 bar internal pressure is around 90% which is half the value observed under conditions of creep. For higher heating rates and burst temperatures lower than 880°C the ductilities are observed to be below the lower creep boundary and to decrease with the burst temperature. These tests correspond to internal pressures higher than the highest pressure in the creep tests with the corresponding burst temperature. For each heating rate, a minimum ductility of about 40% is observed in the 800 to 900°C burst temperature range, possibly associated with the phase transformation. For higher burst temperatures the increase in the ductility in the  $\beta$ -phase domain is shown for burst temperatures above 900°C.

Figure 7.98 Influence of heating rate on total elongation in EDGAR thermal ramp tests for the M5 alloy



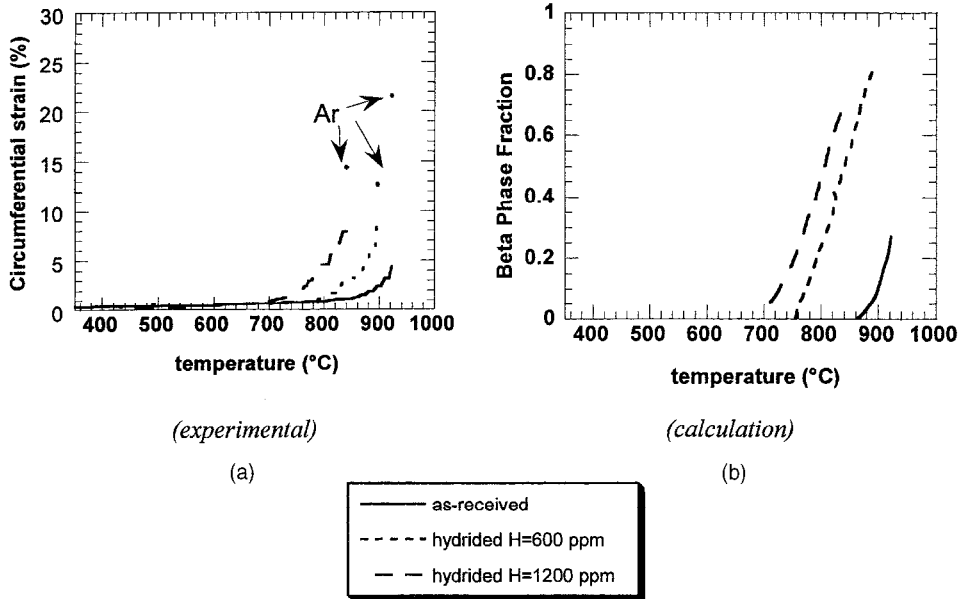
The EDGAR results indicate that the ductility in LOCA conditions also depends on the mechanical stress state. An influence of the mechanical stress on the phase equilibria and incubation kinetics cannot be excluded.

A comparison with previous results for Zircaloy-4 shows that the M5 alloy is somewhat better than Zircaloy-4 in terms of burst temperature while the M4 alloy is similar to Zircaloy-4 [76]. In terms of total elongation, the picture is quite complex but in most pressure ranges Zircaloy-4 has a better ductility than M5. However, such differences may be reduced significantly in bundle tests due to an azimuthal temperature gradient that prevents the uniform swelling up to burst characteristic of the EDGAR facility.

The main effect of a high burn-up is the hydrogen pickup caused by cladding corrosion. Figure 7.99 (a) shows the effect of hydrogen content on the thermal ramp behaviour in an EDGAR test of Zircaloy-4 cladding [75].

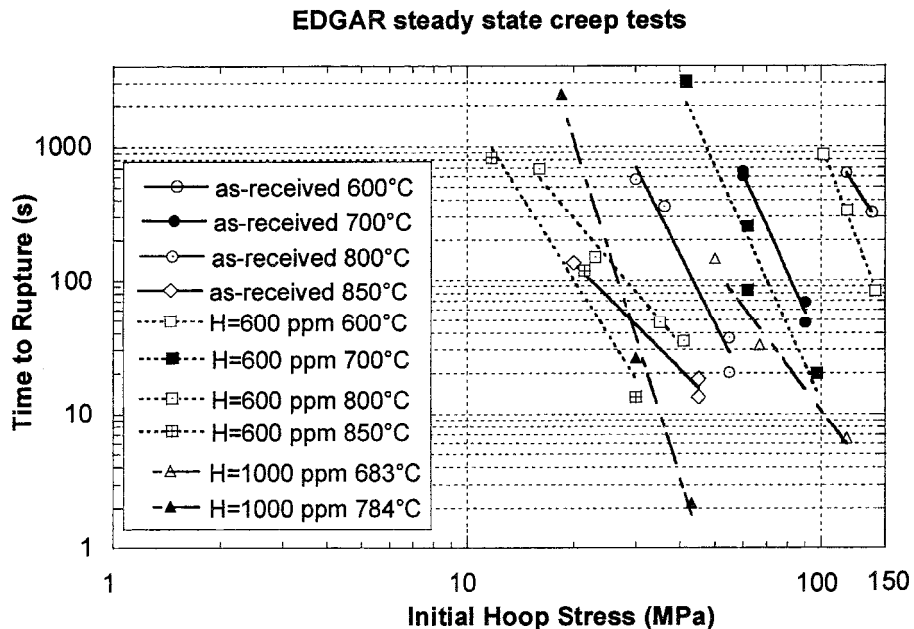
The figure clearly shows the effect of hydrogen on the mechanical behaviour. It reduces the creep resistance and the post-mortem ductility. In Figure 7.99 (b), the  $\beta$  phase fraction has been calculated according to the methods described in Section 5.1.2. As can be seen in the Figure the transformation to  $\beta$  controls much of the creep behaviour. For unhydrided Zircaloy, the maximum in ductility generally takes place at the onset of the  $\alpha \rightarrow \alpha + \beta$  transformation and rapidly drops down in the two phase domain. In hydrided samples, the deformation starts at the formation of  $\beta$  and thus rupture occurs well into the two phase domain with a consequent reduction in ductility.

Figure 7.99 (a) Deformation of as-received and hydrided Zircaloy-4 in a thermal ramp test.  
 (b) Calculated  $\beta$  phase fraction in as-received and hydrided Zircaloy-4



Hydrogen is also expected to have an intrinsic effect on the creep rates, as has been observed at lower temperatures, 350 to 400 $^{\circ}$ C [77]. Therefore, creep tests were performed under steady temperature and pressure conditions on Zircaloy-4 hydrided to 600 and 1 000 ppm and compared to results of as-received Zircaloy-4. The results are shown in Figure 7.100.

Figure 7.100 Time-to-rupture vs stress for EDGAR creep tests performed on as-received and hydrided Zircaloy-4 cladding tubes [75]



The slopes of the lines fitted to the isothermal creep results give the stress exponent,  $n$ , in the Norton type creep law, which is strongly dependent on the  $\alpha/\beta$  transformation event. The hydrided

samples exhibit lower creep resistance for all temperatures with the greatest effect at the highest hydrogen content. The sequence of slopes from the lowest temperature to the highest shows a high  $n$  in single phase  $\alpha$ , a low  $n$  in the two phase domain and again a high  $n$  for single phase  $\beta$ . The transitions are moved to lower temperature by the hydrogen. A comparison between as-received Zircaloy-4 and 600 ppm hydrided Zircaloy-4 at 700°C where both is single phase  $\alpha$  shows the intrinsic hydrogen effect as a lower creep resistance for the hydrided material but the same stress exponent. A corresponding difference at 850°C is best explained by the higher  $\beta$  phase fraction formed in the hydrided material.

The results on Zircaloy-4 can also be compared to the corresponding results on as-received and hydrided M5 shown in Figure 7.101. The sequence of slope changes in the time-to-rupture versus hoop stress lines is slightly different than for Zircaloy-4 because of the earlier transformation to  $\beta$  in the Nb-containing M5 material. Both at 600, 700 and 850°C the lower creep resistance of hydrided M5 compared to as-received M5 but with the same Norton slope indicates the intrinsic hydrogen effect on the creep resistance. A comparison between Figures 7.100 and 7.101 also shows that the hydrogen effect on creep resistance seems to be slightly higher in M5 than for Zircaloy-4.

As discussed above hydrided specimens will tend to have a lower ductility than as-received specimens because they fail well into the two phase domain. Figure 7.102 shows a summary of how hydrogen affects the ductility of Zircaloy-4 in EDGAR creep tests.

**Figure 7.101 Time-to-rupture vs stress for EDGAR creep tests performed on as-received and M5 cladding tubes [75]**

**EDGAR steady state creep tests on M5 with H=650 ppm**

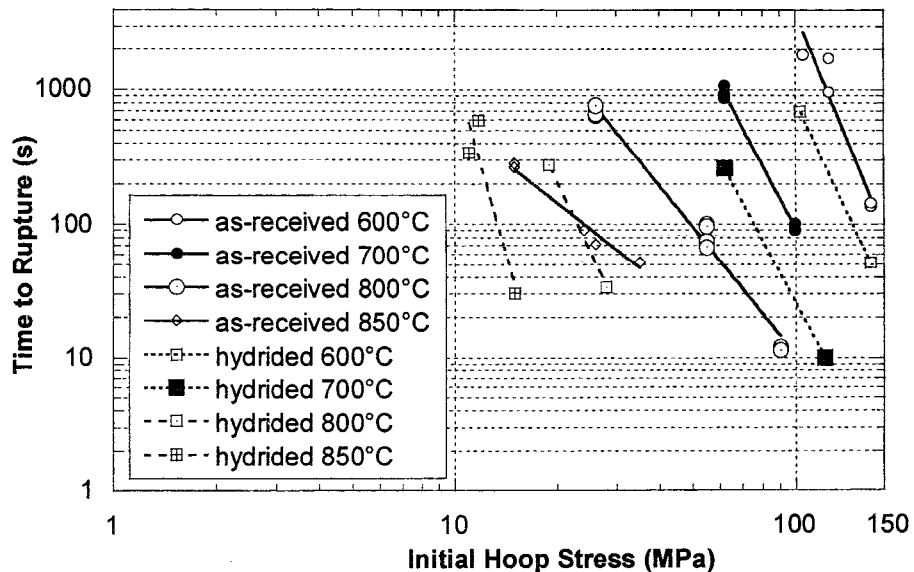
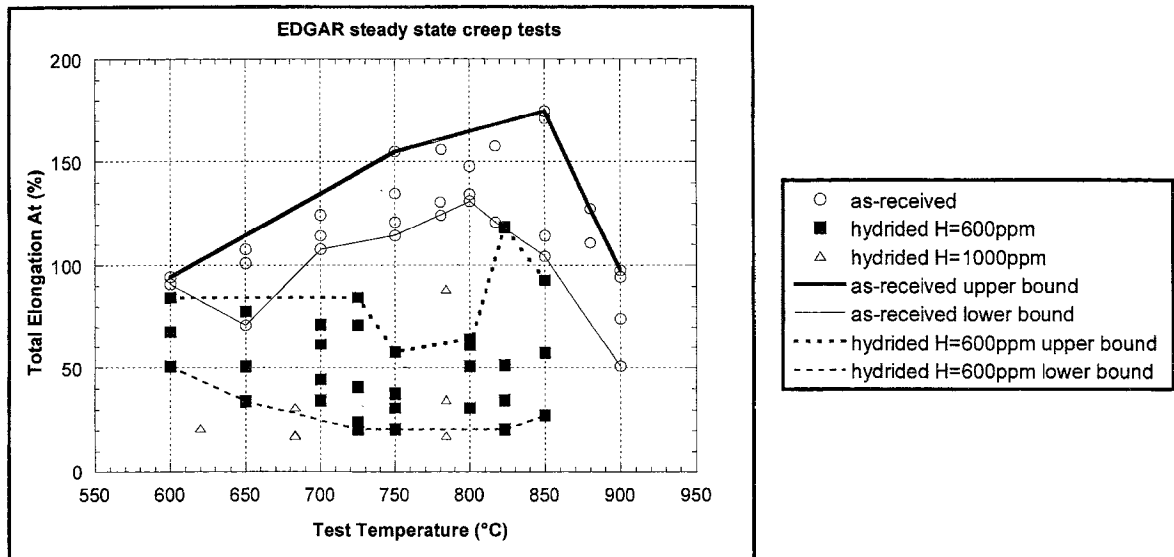


Figure 7.102 Total elongation measured after EDGAR creep tests vs test temperature for as-received and hydrided (~600 and ~1 000 ppm) Zircaloy-4 cladding tubes



Modelling of the cladding behaviour based on the EDGAR tests and accompanying tests of the  $\alpha$  to  $\beta$  phase transformation is termed the EDGAR methodology [75-76]. It is based on a set of four equations. The first equation expresses the mechanical equilibrium:

$$\sigma_\theta = \sigma_\theta^0 (1 + \varepsilon_\theta)^2 \quad (7-2)$$

where  $\sigma_\theta^0 = p(D_0 - h)/2h$  the initial hoop stress

$\varepsilon_\theta$  = the circumferential strain

$p$  = the internal pressure.

$D_0$  = initial external diameter.

$h$  = the initial wall thickness.

The second equation is a phase transformation model:

$$df_\alpha / dt = \text{function}[(f_\alpha, T, T_{eq}(f_\alpha))] \quad (7-3)$$

where  $f_\alpha$  = the  $\alpha$ -phase volume fraction.

The third equation is the Norton type creep law:

$$d\varepsilon_\theta / dt = A_i \exp(-Q_i / T) \sigma_\theta^{n_i} \quad (7-4)$$

where subscript  $i$  represents the current phase transformation domain defined as follows: ( $i = \alpha$  if  $f_\alpha = 1$ ,  $i = \alpha + \beta$  if  $0.9 > f_\alpha > 0.1$ ,  $i = \beta$  if  $f_\alpha \leq 0.01$ ) and  $T$  = cladding temperature.

$A_i$ ,  $Q_i$ ,  $n_i$  = material parameters.

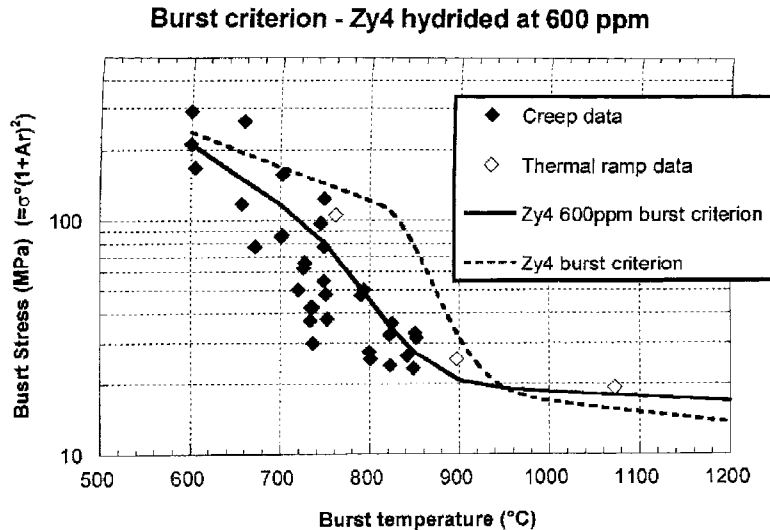
The fourth relation needed to model cladding behaviour is a burst criterion:

$$\begin{aligned} \sigma_\theta &= \sigma_B(f_\alpha, T) = \sigma_{B_\alpha}^{f_\alpha} \cdot \sigma_{B_\alpha}^{1-f_\alpha} \\ \sigma_\theta &= \sigma_\theta^0 (1 + A_r)^2 \\ \sigma_{B_i} &= k_i \exp(-q_i T) \end{aligned} \quad (7-5)$$

Where  $A_r$  = the uniform elongation and  $k_i$ ,  $q_i$  constants characteristic of the  $\alpha$  or  $\beta$  phase.

The constants  $k_i$  and  $q_i$  must be determined from the results of the EDGAR experiments. Figure 7.103 shows a comparison between the burst criterion for as-received and hydrided to 600 ppm Zircaloy-4 cladding tubes [75].

**Figure 7.103 Comparison between the burst criterion for as-received and hydride (at 600 ppm) Zircaloy-4 cladding tubes [75]**

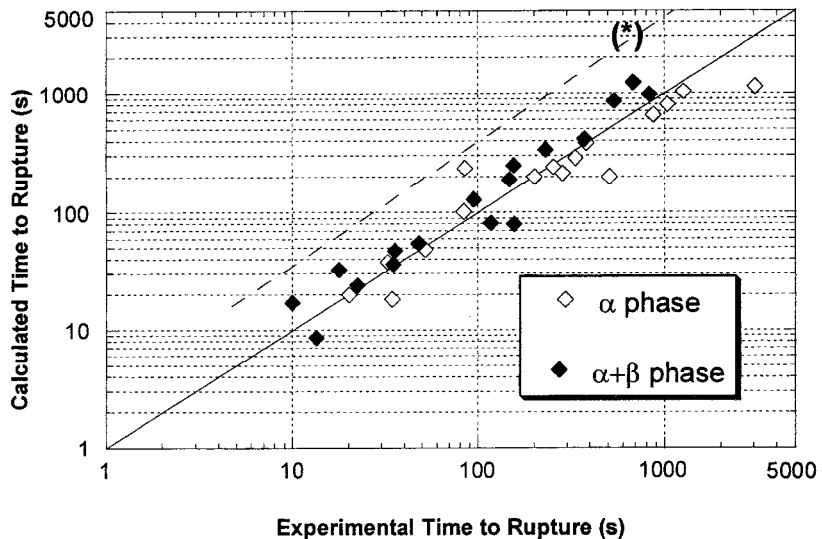


Ideally the constants should be determined from creep tests. However in the case of hydrided Zircaloy-4 no creep test data was available in the  $\beta$  domain and results of thermal ramp tests were used to determine the burst criterion [75].

The success and development of the EDGAR methodology is illustrated in Figure 7.104. It shows a comparison between calculated and experimental time to rupture for EDGAR experiments.

**Figure 7.104 Comparison between experimental and simulated time to rupture of Zircaloy-4 hydrided to 600 ppm using two different models**

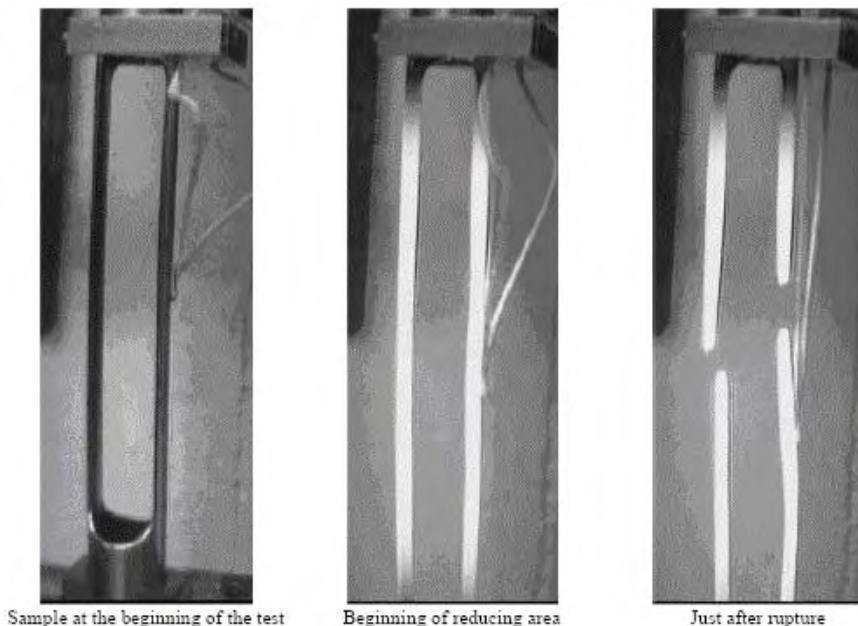
(a) a model based on experiments with as-received Zircaloy-4 [76], dashed line, and (b) a new model based on experiments with hydrided Zircaloy-4 and taking into account the effect of hydrogen on the  $\alpha/\beta$  phase transformation [75]



The dashed line shows the results of using a previous model based on creep laws determined on as-received Zircaloy-4 and without taking into account the effect of hydrogen on the  $\alpha \rightarrow \beta$  phase transformation. The more recent model uses creep laws based on experiments with hydrided Zircaloy-4 and also takes into account the effect of hydrogen on the phase transformation temperatures.

For determination of the creep properties of irradiated cladding under LOCA conditions a uniaxial tensile test method has been used [78]. For comparison tests with the same method have also been performed on as-received and hydrided cladding. The tests are carried out on a dynamic tensile device. Specific double-leg tensile samples have been designed in order to minimise the temperature gradient along the sample (Figure 7.105).

**Figure 7.105 Evolution of a sample during a thermal ramp test under uniaxial stress loading [78]**



The samples are 90 mm long and have 2 legs of 48 mm in gauge length. The specimens were machined by spark erosion (after mechanical abrading of the outer zirconia layer of irradiated samples). The width (~4 mm) and thickness of each leg is measured to calculate the axial stress applied during a test.

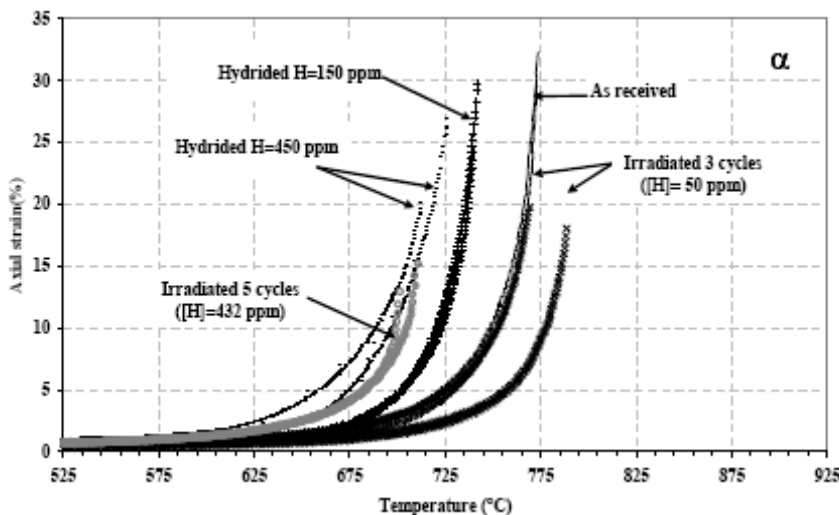
To obtain rapid heating rates, direct Joule effect heating was adopted. During the test, the axial load is first applied and then the temperature transient starts. The temperature is increased up to 350°C, stabilised during 2 minutes and then starts the heating ramp up to rupture. On-line monitoring of the following parameters is carried out during the test:

- The sample axial elongation by a LVDT captor.
- The axial load.
- The sample temperature, with a K-type thermocouple spot-welded on the middle of one leg of the sample.

Taking into account the rapid temperature increase (25 and 100 K/s) and the thermal inertia of the thermocouple, the temperature measured by the thermocouple is under-estimated and systematic corrections based on pyrometer measurements have to be applied after the tests. Post mortem measurements are conducted in order to evaluate the total axial elongation that cannot be directly deduced from the on-line axial measurements.

The experiments have demonstrated fairly conclusively that the main effect of irradiation is the hydrogen pickup due to corrosion during reactor operation. Figure 7.106 shows a typical result for as-received, hydrided and irradiated Zircaloy-4. The behaviour of unirradiated cladding hydrided to 450 ppm is very similar to the behaviour of irradiated Zircaloy-4 with a measured hydrogen content of about 430 ppm.

**Figure 7.106 Influence of irradiation and hydrogen content on the axial strain of Zircaloy-4 samples during a thermal ramp test under uniaxial loading (80 MPa) upon heating with 100 K/s [78]**



Similar tests on irradiated M5 showed that they behave in a manner similar to that of as-received M5 as a result of the low corrosion and hydrogen pickup of M5 during irradiation [78].

#### 7.3.2.7 Single and multiple rod testing in the United Kingdom

A test series [79] was carried out at the Springfields Nuclear Laboratories on short internally pressurised Zircaloy tube specimens heated by direct resistance heating to investigate deformation behaviour in steam and inert atmospheres. This work showed the dramatic effect of oxygen pick-up on mechanical behaviour above about 1150 K with oxide and stabilised  $\alpha$ -phase layers contributing mainly to the increased strength and resulting in reduced circumferential strain owing to localised straining at cracks in these layers. Very small amounts of oxidation were also found to influence the character and extent of deformation at about 1020 K. Following on from this work, tests on larger specimens showed up the phenomenon of axially extended deformation under both mainly radiative cooling conditions [65] and mainly convective cooling [80] (see Figure 7.107). This was investigated in depth and supported by similar studies at Berkeley Nuclear Laboratories [81]. The basic process responsible is that of local cooling of the straining region combined with the high temperature-dependence of secondary creep in Zircaloy; however, other factors can come into play as shown in Figure 7.108.

Figure 7.107 Results of stylised transient testing of Zircaloy-4 PWR cladding with mainly convective cooling [4]

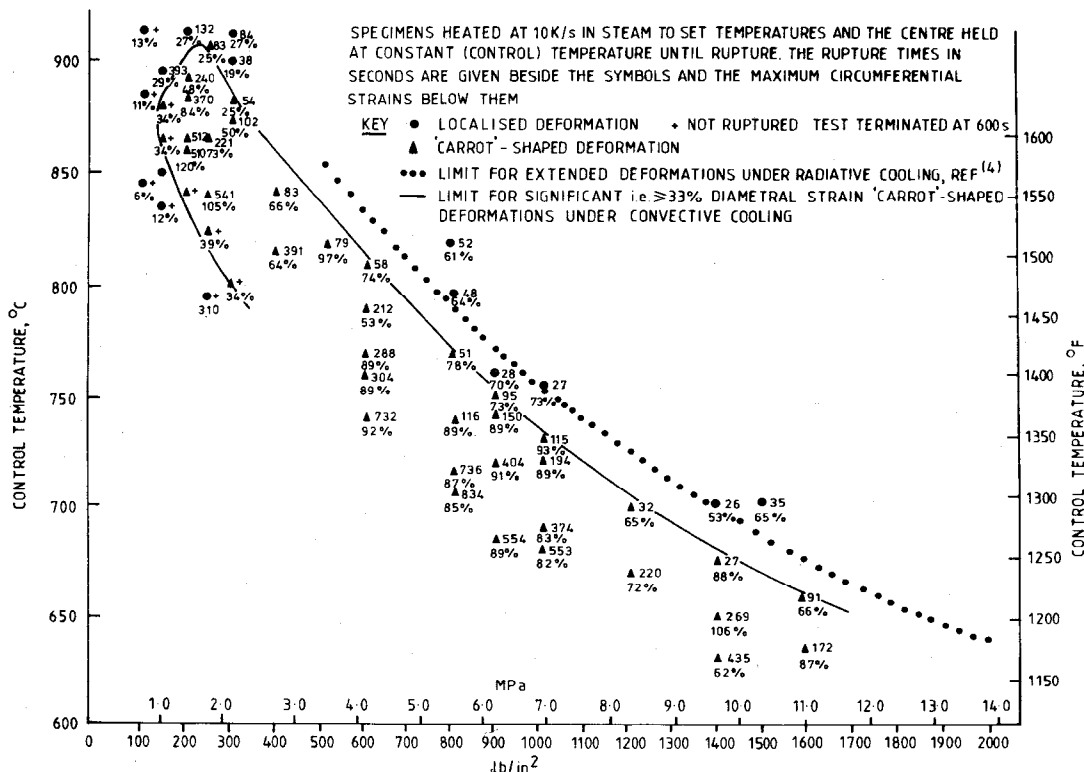
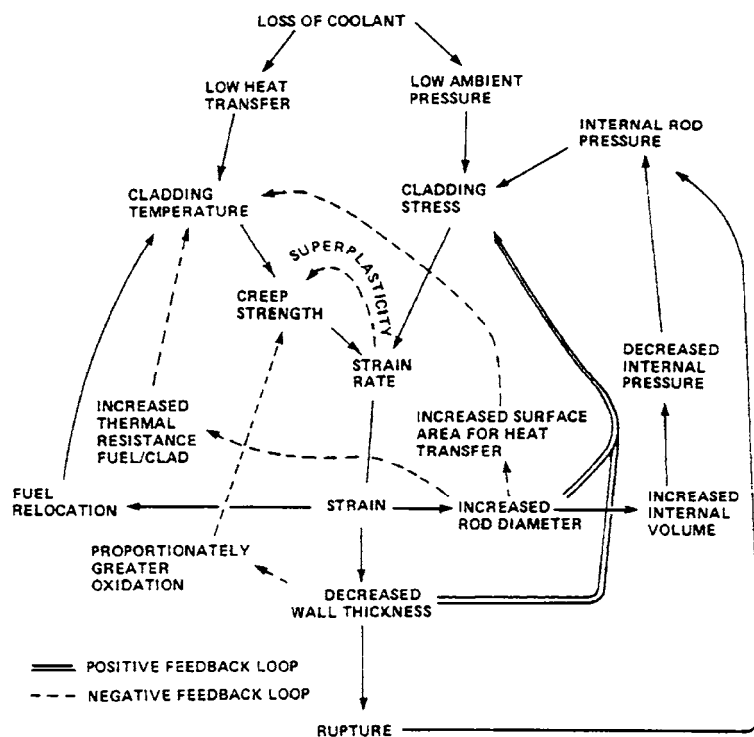


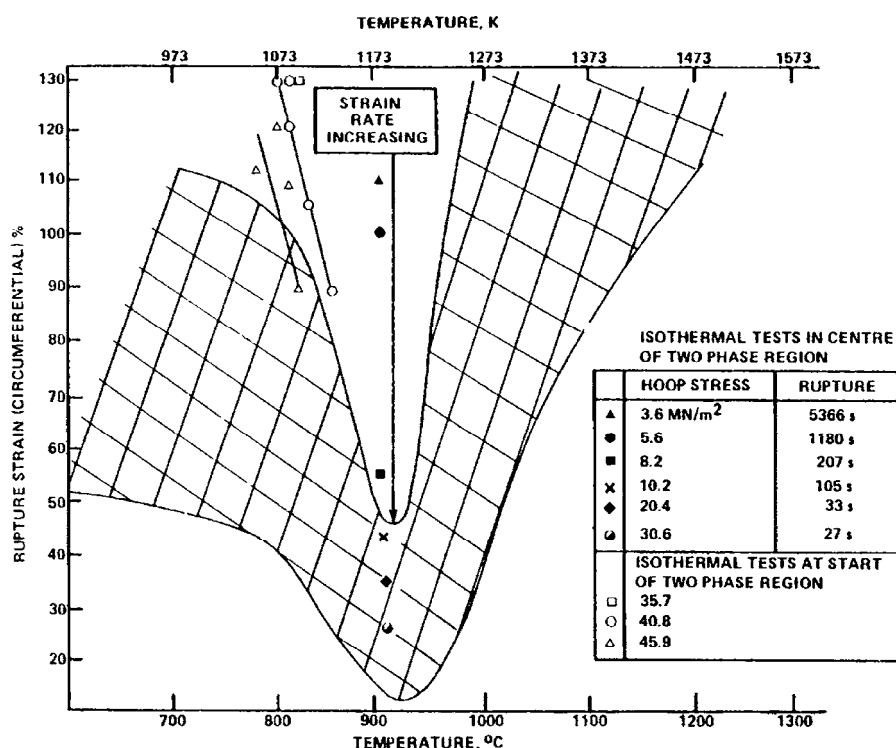
Figure 7.108 Processes controlling strain and its stabilisation [14]



Tests were carried out using internal heaters with a reflective but unheated shroud and similar results have been obtained except that the circumferential strains tend to be lower [14]. However, when heated shrouds are used, the strains are equivalent [82].

The full range of internal pressures which could be used in PWR fuel rods has been investigated and, depending upon the temperatures reached, extended deformation occurs over the whole pressure range. A tendency for super-plastic deformation in the two-phase region has also been observed with pressures of about 2 MPa (300 lb/in<sup>2</sup>). Cladding strained in this region, under fast heating (and hence strain) rates greater than 5-10 K/s, exhibits a ductility trough; however this is a strain-rate-dependent phenomenon (Figure 7.109) and strains of 200% have been produced in this region in a test lasting 200 s [83].

**Figure 7.109 Variation of tube rupture strain with rupture temperature during isothermal tests at Springfields Nuclear Laboratories [83]**



Stainless steel cladding as used in PWRs i.e. Type 304 has also been investigated [14]. This material is strong enough to resist the internal pressure at temperatures up to about 950°C so that deformation is negligible. Ultimately at higher temperatures it will deform but the inherent ductility is such that the maximum strains are 25-30%, insufficient to allow mutual support of columnar bulges, so that coolant flow channel restriction would be very limited.

At the Windscale Nuclear Laboratories, 450 mm lengths cut from commercial PWR fuel rods irradiated to 20 GWd/tU (rod average) have been internally pressurised and subjected to temperature transients to simulate LOCA conditions [84]. The primary purpose of the work was to examine the mechanical stability of the fuel column when the cladding has bulged away from it under internal pressurisation and to evaluate the extent of fuel fragmentation and re-location that occurs. However, data on the ductility of cladding which has experienced actual reactor service has also been produced.

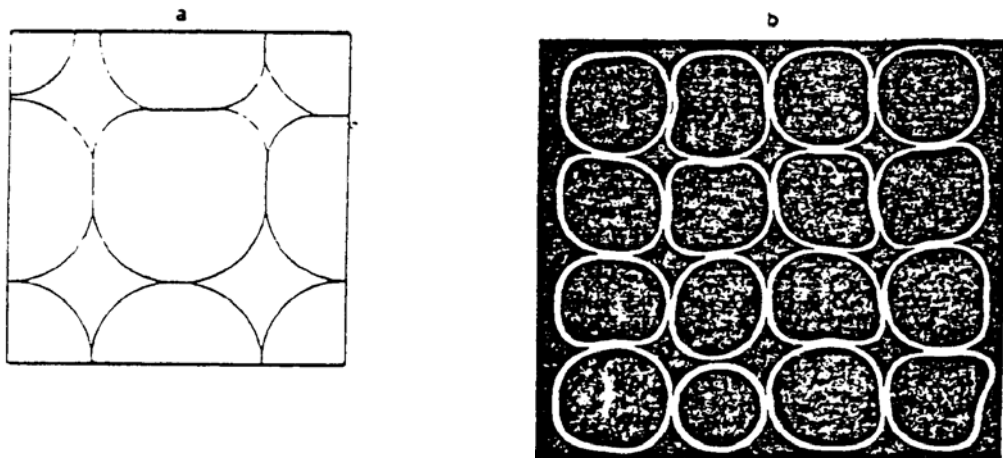
In the fuel re-location tests, carried out at 973 to 1 073 K, the cladding deformation was stopped upon reaching approximately 40% diametral strain by a reduction in temperature and, after cooling, the fuel was fixed in position by introduction of epoxy resin through a spark-machined hole in the cladding [84]. The spatial distribution of fuel was then determined by X-radiography,  $\gamma$  scanning and optical examination of sections.

The lower section approximately 100 mm below the section of cracked fuel stack, was shown to have remained in the form of intact pellets, although the fuel column had moved laterally to touch the cladding. Above this region, the pellet fragments had separated, often quite considerably, but in general, only a relatively small amount (less than 5%) of fuel axial relocation had taken place. Thus, the positions of pellet-pellet interfaces were still visible on axial sections.

The deformation of the cladding in these tests was quite comparable the behaviour of axially extended bulging that was observed during direct electrical heating tests on unirradiated Zircaloy tubing at the Springfields Laboratories [65,83]. The results confirmed that no significant difference in strain behaviour exists between unirradiated and low burn-up irradiated cladding, even though the latter presumably has an additional thin oxide layer resulting from reactor exposure.

The multi-rod test programme at the Springfields Nuclear Laboratories included a materials test in which a  $4 \times 4$  array contained in a shroud was heated to about 700°C in argon in a muffle furnace. Steam was then introduced and the rods pressurised to 7.9 MPa. Examination showed that they had bulged and tended to adopt a square cross-section as a result of rod-to-rod interaction (Figure 7.110). The object of this test was to study mechanical interaction of balloons to assist code development [85-88].

**Figure 7.110 Mechanical restraint by deformable neighbours. CANSWEL-2 idealisation (a) compared with (b) Springfields  $4 \times 4$  cladding deformation rig cross sections**



The use of high and low helium filling pressures in alternate fuel rods in an assembly has been proposed as a means of reducing the probability of a high degree of co-planar blockage [89]. Computer modelling [90] of the deformation of such an assembly has shown that for this concept not to be effective, 80% overall strain would be required in the straining rods. This requires the individual cladding temperatures all to be uniform to within 4°C. The evidence from the MT-3 test [32] and analysis [91] of irradiated PWR fuel rod ballooning tests indicate that such temperature uniformity is unattainable in nuclear heated rods ballooned under reflood conditions.

### 7.3.2.8 Experiments in PARAMETR-M and TEFSAI-19 facilities in Russia

A description of the PARAMETR-M and TEFSAI-19 facilities can be found in Section 5.3.2.4. Variables studied in the experiments are heating rate, max fuel rod cladding temperature, steam flow rate, quench conditions and fuel rod cladding material [92].

The objectives of the experiments and post-test examinations were to investigate:

- Temperature-force loading parameters, corresponding to various thermohydraulic LB-LOCA scenarios, influence on the assemblies damage characteristics.
- Deformation behaviour of the fuel rod simulator claddings gathered in an assembly and their depressurisation parameters (temperature, pressure, deformations and coordinates of places of rupture).
- Distribution of assembly flow channel blockage and cladding ballooning along the assembly height.

The results reported by Bibilashvili *et al.* in 2001 [92] are summarised in Table 7.9.

The temperature conditions of tests with the assemblies No. 1, 2, 4, and 6 exceed the conditions of the second LOCA stage for fuel rods with maximum calculated linear heat rating, while the tests No. 3, 5, and 7 (maximum cladding temperature about 900°C) correspond to an accident scenario for a group of fuel rods with linear heat rating above the average.

A typical example of temperature and pressure records is shown in Figure 7.111. The temperature and pressure records allow an estimate of the time for cladding depressurisation. By taking into account the delay in thermocouple indications (up to 50 K, depending on the heating rate) and lack of coincidence in the axial locations of ruptures and thermocouples rupture temperatures were estimated to lie in the interval of 800-900°C.

The steam flow and mass flow rate through the assembly cross section influences the extension of the ballooning area (Figure 7.112 for tests No. 1, 2 and 3). At greater mass flow rates the balloonings are more likely to be found in the upper part of the assembly.

Cladding heating rate has a significant influence on the cladding rupture strain. In Figure 7.112, test No. 1 with a heating rate of 2 K/s can be compared to test No. 3 with a heating rate of 0.2 K/s. The expected cladding heating rate in a LOCA transient is about 2-4 K/s due to residual heat release in the fuel. The maximum cross section blockage for the 7 inner simulators in test No. 3 was 70% (Table 7.9) compared to 27% for test No. 1. All tubes ruptured.

Tests on two 19-element assemblies with Zr1%Nb and E635 claddings (No.2 and No. 4) in similar conditions revealed higher ductility of E635 claddings (Table 7.9). Maximum cross-section blockage for the bundle of the 7 inner simulators of E635 assembly No. 4 did not exceed 69%. In test on assembly No. 6 with E635 claddings with excess inner pressure (simulation of burn-up effects) lower rupture deformation and cross-section blockage values were observed than in case of assembly No. 4 (Table 7.9).

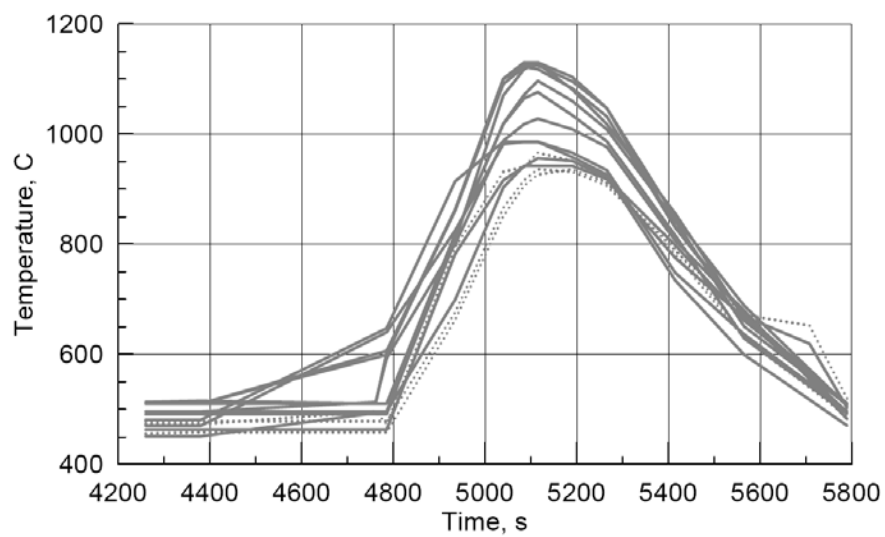
In the tests No. 1, 2, 4, and 6 with the highest cladding temperatures, 1 100 to 1 150°C all rods ruptured.

Tests on two 37-element assemblies with Zr1%Nb and E635 claddings (No. 5 and No. 7) were carried out under conditions typical of the second stage of the accident (heating due to residual heat

release in fuel) for the representative group of heat-stressed fuel rods. The distinctive feature of these assemblies construction is the presence of passive fuel rods (1 central + 12 fuel rods of the third row). The cladding temperature of the passive simulators in the hot area was substantially lower (approximately 100 K), than that of the electro-heated fuel rods. In the experiment with assembly No. 7 (Zr1%Nb) all, but three claddings ruptured. In the experiment with assembly No.5 (E635) none of the passive fuel rods lost tightness.

**Figure 7.111 Cladding temperature (A) and pressure records (B) for test No. 1 (Zr1%Nb alloy) [92]**

A) Claddings' thermocouple indications in hot zone.



B) Simulators' pressure transducer indications.

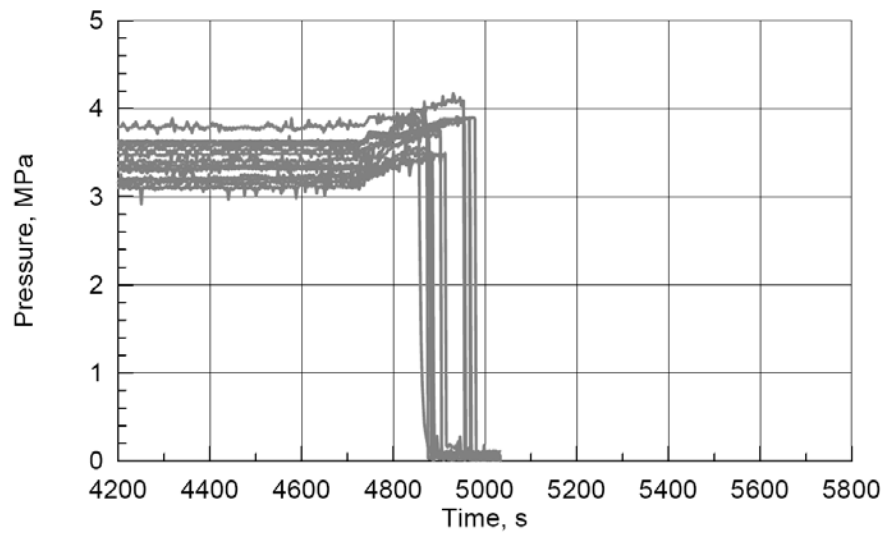
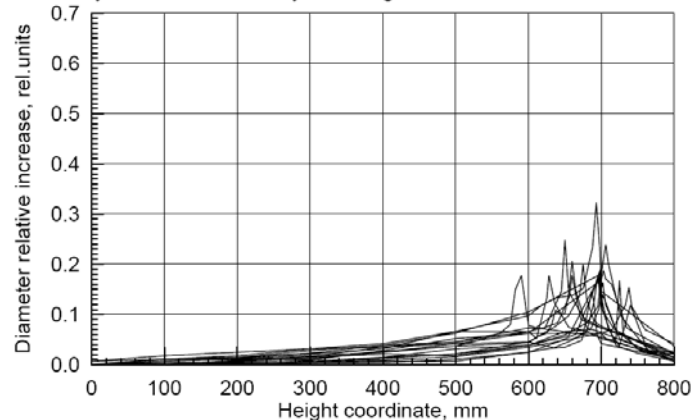


**Table 7.9 The main test parameters and results of VVER type assemblies under LOCA conditions in electroheated facility**

Characteristics	Assembly No. 1	Assembly No. 2	Assembly No. 3	Assembly No. 4	Assembly No. 5	Assembly No. 6	Assembly No. 7
Facility	PARAMETR	TEFSAI-19	PARAMETR	TEFSAI-19	PARAMETR-M	TEFSAI-19	PARAMETR-M
Test time	1999	1999	1999	2000	2001	2001	2001
Cladding material	ZR1%NB	ZR1%NB	ZR1%NB	E635	E635	E635	ZR1%NB
Simulators quantity	19	19	19	19	37	19	37
Active part height,	800 mm	1 000 mm	800 mm	1 000 mm	1 250 mm	1 000 mm	1 250 mm
Simulators free vol.	26 cm <sup>3</sup>	21 cm <sup>3</sup>	26 cm <sup>3</sup>	25 cm <sup>3</sup>	33 cm <sup>3</sup>	25 cm <sup>3</sup>	33 cm <sup>3</sup>
Initial He pressure	2 MPa	4 MPa	2 MPa				
Initial temperature	450°C						
Steam flow rate per FA	4 g/s	2 g/s	4 g/s	2 g/s	6 g/s	3 g/s	6 g/s
Heating rate up to claddings rupture	2 K/s	1 K/s	0.2 K/s	1 K/s	2.5 K/s	1 K/s	2.5 K/s
Maximum temperature	1 150°C	1 150°C	900°C	1 100°C	900°C	1 100°C	900°C
Ballooning height coordinates	590-740 mm	520-840 mm	700-800 mm	550-850 mm	1 000-1 200 mm	550-850 mm	Research is continued.
Hoop strain in places of rupture, (average/max)	19.2%/32.2%	24.1%/40%	40%/70%	41%/77%	15.3%/48.6%	20%/32%	
Downsizing of the assemblies' cross section (19 element/7 central fuel rods)	22%/27%	27%/39%	50%/70%	42%/69%	31%/52%	-/35%	

**Figure 7.112 Axial cladding strain distributions in tests No. 1, 2 and 3**

A) Assembly №1. Zr1%Nb alloy. Heating rate 2 K/s. Steam flow rate 4 g/s.



B) Assembly №2. Zr1%Nb alloy. Heating rate 1 K/s. Steam flow rate 2 g/s.

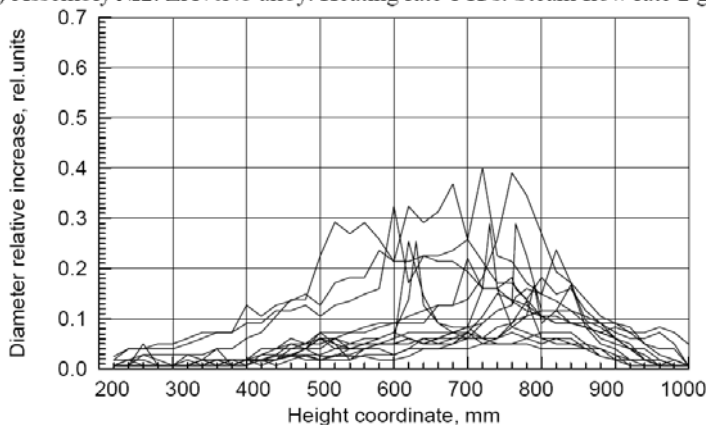
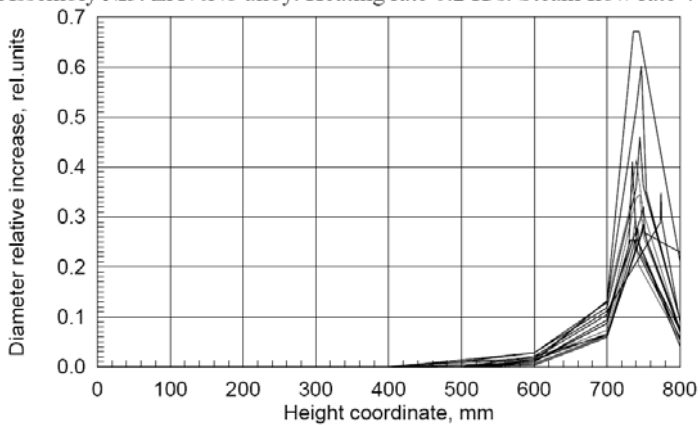


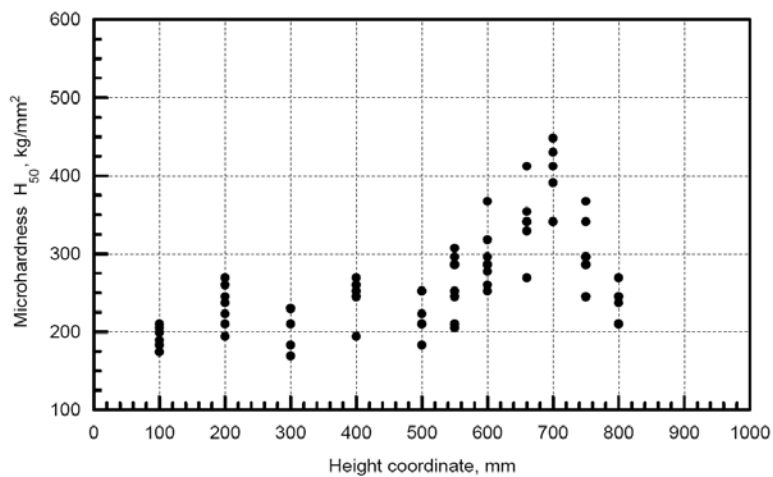
Figure 7.112 Axial cladding strain distributions in tests No. 1, 2 and 3 (Cont'd)

C) Assembly №3. Zr1%Nb alloy. Heating rate 0.2 K/s. Steam flow rate 4 g/s.



All the assemblies kept the integrity after the tests, despite that in the test they were quenched with cold water (except assembly No. 1). The simulator claddings survived disassembly and kept the integrity. The microhardness axial distribution along the simulator 2.1 of assembly No. 1 is shown in Figure 7.113. This assembly was tested at maximum temperature of 1 150°C.

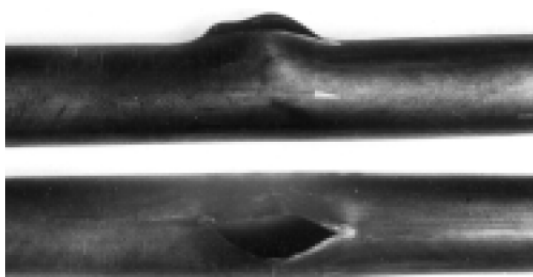
Figure 7.113 Microhardness distribution along the simulator 2.1 of test No. 1



The appearances of fuel rod simulators claddings of E635 and Zr1%Nb alloys, assemblies No. 5 and No. 7, tested at maximum temperature of 900°C, are presented in Figure 7.114.

Figure 7.114 Post-test appearance of E635 and Zr1%Nb alloy

A) Assembly No. 5, E635 alloy



B) Assembly No. 7, Zr1%Nb alloy



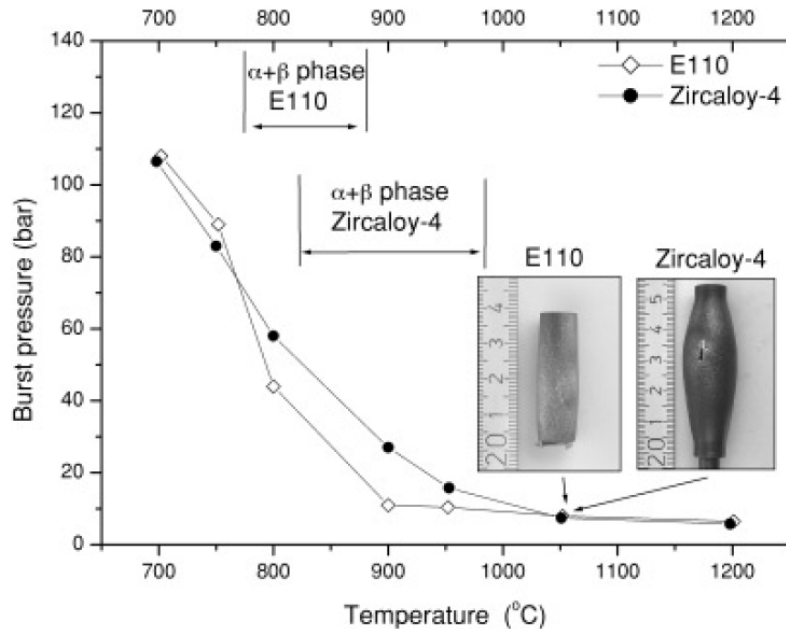
### 7.3.2.9 Ballooning of E110 cladding in comparison with Zircaloy-4

Hózer *et al.* have performed extensive ballooning experiments on the E110 alloy [93]. They performed isothermal experiments on short lengths, 50 mm, of E110 and Zircaloy-4 cladding with different pressurisation rates. The experiments were performed in an Ar atmosphere but in order to determine the influence of oxidation, some of the E110 specimens had been pre-oxidized at 900°C to oxide thicknesses up to 56 µm. A few specimen had also been pre-exposed to iodine but no effect of the iodine was observed. In a second test series longer specimens of E110 were tested, three of them in a steam atmosphere. These experiments used either constant temperature with different pressurisation rate or constant initial pressure with different heating rates. In a third test series, they studied ballooning in a 7 rods array with the VVER hexagonal geometry. The tests were carried out both in an inert atmosphere and in steam.

In general, they observed a relatively large scatter in burst pressure and in maximum circumferential burst strain. However, the main trends followed the behaviour of Zircaloy-4 with an important exception. As shown in Figure 7.115, there is a clear effect of the earlier start of transformation to  $\beta$  phase for the Nb alloyed E110 which leads to a reduction of burst pressure in the temperature interval 800–1 000°C.

The inserted pictures in Figure 7.115 illustrate the general difference in burst strains between E110 and Zircaloy-4.

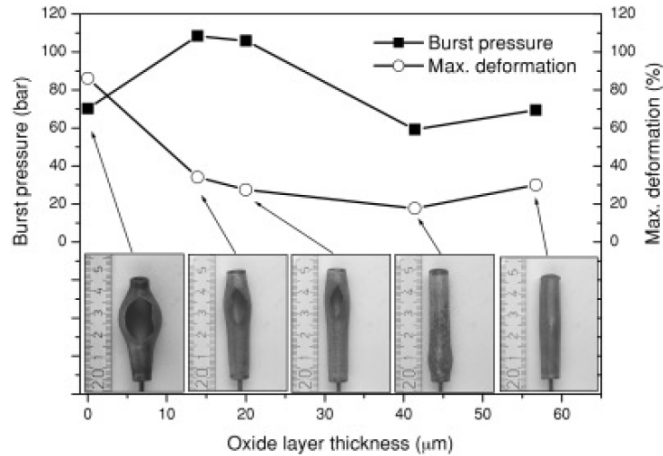
**Figure 7.115 Burst pressure vs burst temperature of E110 and Zircaloy-4 claddings tested under similar conditions**



The influence of pre-oxidation on burst pressure and deformation is shown in Figure 7.116. It shows that the burst pressure first increases up to a maximum and then decreases with increasing oxide thickness. The decrease in burst pressure with increasing oxide thickness is probably because of the effect of increasing hydrogen content which decreases the  $\alpha \rightarrow \beta$  transformation temperature. The reduction in ductility can be due to cracking in the  $\alpha$  layer which grows under the pre-oxide similar to effects observed in slow LOCA transient tests on fresh cladding.

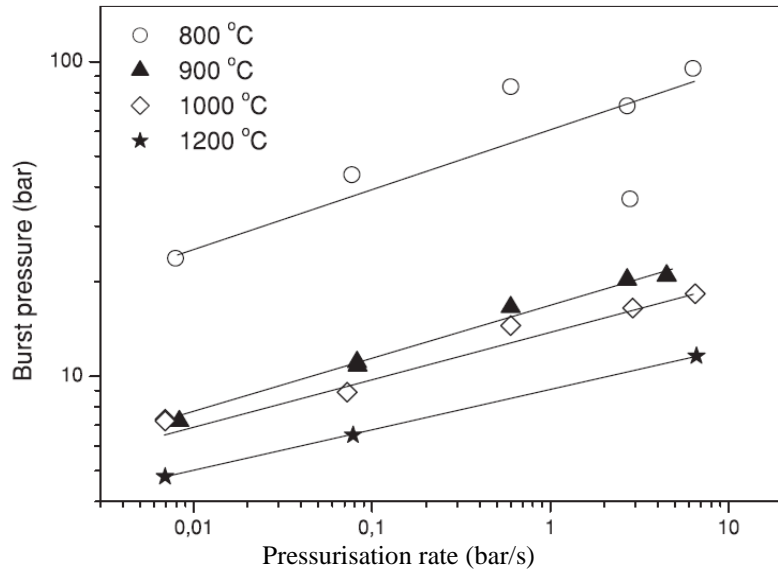
Similar effects were also observed in the tests in steam compared to the tests in an inert environment. In particular, the multi-rod tests showed clearly that failure strains were lower in the steam environment and the flow blockage was reduced from 57-76% in argon to 33-57% in steam.

Figure 7.116 Burst pressure an maximum deformation vs oxide layer thickness of E110 cladding



In the isothermal ballooning tests, there was a significant effect of the pressurisation rate on burst pressure, as can be seen in Figure 7.117.

Figure 7.117 Burst pressure vs pressurisation rate for E110 alloy



This effect can actually be derived from equations 5-1 to 5-4. If the pressurisation rate is  $dp/dt$ , the burst pressure  $p_f$  is approximately given by:

$$p_f = C \left( \frac{dp}{dt} \right)^{1/n+1} \quad (7-6)$$

where  $n$  is the exponent in the Norton creep law. The slopes in Figure 7.117 indicate an  $n$ -value of about 6-7.5. No effect of heating rate at constant initial pressure was observed.

## 7.4 References

1. Ferrari, H.M., "Pressurisation improves fuel rod reliability", Nuclear Engineering International, 15(1970), pp. 623-625.
2. Brzoska, B., *et al.*, "Parameter study in the influence of prepressurisation on PWR fuel rod behaviour during normal operating and hypothetical LOCA", Nuclear Technology, 46(1979), pp. 205-212.
3. Karb, E.H., *et al.*, "LWR fuel rod behaviour in the FR2 in-pile tests simulating the heatup phase of a LOCA", KfK 3346, March 1983.
4. Hindle, E.D. and Mann, C.A., "An experimental study of the deformation of Zircaloy PWR fuel rod cladding under mainly convective cooling", Zirconium in the Nuclear Industry; Fifth Conference, 1980, Boston, USA, ASTM STP 754, ASTM, pp. 284-302.
5. Rose, K.M., Mann, C.A., and Hindle, E.D., "The axial distribution of deformation in the cladding of pressurized water reactor fuel rods in a loss-of-coolant accident", Nuclear Technology, 46(1979), pp. 220-227.
6. Chung, H.M. and Kassner, T.F., "Embrittlement Criteria for Zircaloy Fuel Cladding Applicable to Accident Situations in Light-Water Reactors. Summary Report", NUREG/CR-1344, Jan. 1980.
7. Erbacher, F.J., "LWR fuel cladding deformation in a LOCA and its interaction with the emergency core cooling", ANS/ENS Topical Meeting on Reactor Safety Aspects of Fuel Behaviour, 1981, Sun Valley, USA.
8. Parsons, P.D., Hindle, E.D., and Mann, C.A., "The deformation, oxidation and embrittlement of PWR fuel cladding in a loss-of-coolant accident", UKAEA Springfield Nuclear Power Development Laboratories, ND-R-1351, September 1986.
9. Hindle, E.D. and Slattery, G.F., "The influence of processing variables on the grain structure and hydride orientations in Zircaloy-2 tubing", Journal of the Institute of Metals, 94(1966), pp. 245-249.
10. Hardy, D.G., "High temperature expansion and rupture behaviour of Zircaloy tubing", Topical Meeting on Water Reactor Safety, 1973, Salt Lake City, USA, pp. 254-273.
11. Erbacher, F.J., Neitzel, H.J., and Wiehr, K., "Studies of Zircaloy clad ballooning in a loss-of-coolant accident – results of burst tests with indirectly heated fuel rod simulators", Zirconium in the Nuclear Industry (Fourth Conference), 1978, Stratford-on-Avon, United Kingdom, ASTM STP 681, ASTM, pp. 429-446.
12. Hindle, E.D., "Annealing studies of Zircaloy cladding at 580-850 C", UKAEA report ND-R38(S), May 1978.
13. Mohr, C.L. and Hesson, G.M., "LOCA rupture strains and coolability of full length PWR fuel bundles", 7<sup>th</sup> SMIRT Conference, 1983, Chicago, United States of America.
14. Parsons, P.D., Hindle, E.D., and Mann, C.A., "PWR fuel behaviour in design basis accident conditions. A State-of-the-Art Report by the Task Group on Fuel Behaviour of CSNI Principal Working Group No 2", Committee on the Safety of Nuclear Installations, OECD Nuclear Energy Agency, CSNI Report 129.
15. Hindle, E.D. and Mann, C.A., "Deformation of PWR cladding following a loss-of-coolant accident", UKAEA report ND-R-362(S), July 1979.
16. Chapman, R.H., *et al.*, "Multi-rod burst test program. Progress report for July-Dec 1979", NUREG/CR-1450, Aug. 1980.

17. Kawasaki, S., "Transient burst tests of multi-rod", 6<sup>th</sup> Water Reactor Safety Information Meeting, 1978, Gaithersburg, USA.
18. Powers, D.A. and Meyer, R.O., "Cladding swelling and rupture models for LOCA analysis", NUREG-0630, April 1980.
19. Russcher, G.E., *et al.*, "Experiment operations plan for a loss-of-coolant accident simulation in the NRU reactor", NUREG/CR 1735, April 1981.
20. Adroguer, B., Hueber, C., and Trotabas, M., "Behavior of PWR fuel in LOCA conditions – PHEBUS Test 215P", OECD/NEA CSNI/IAEA Specialists meeting in water reactor fuel safety and fission product release in off-normal and accident conditions., 1983, Risø, Denmark.
21. Del Negro, R., *et al.*, "Phebus program – First results", International Meeting on Thermal Reactor Safety, 1982, Chicago, USA.
22. Hueber, C., *et al.*, "Le programme experimental PHEBUS", International Colloquium on Irradiation Tests for Reactor Safety Programs, 1979, Petten, Netherlands.
23. Manin, A., Del Negro, R., and Reocreux, M., Specialist Meeting on Safety Aspects of Fuel Behaviour in Off Normal and Accident Conditions, 1980, Espoo, Finland.
24. Grandjean, C., "A state-of-the-art review of past programs devoted to fuel behaviour under LOCA conditions: 1<sup>st</sup> Part: Clad swelling and rupture, assembly flow blockage", IRSN, Technical Report DPAM/SEMCA 2005/313, December 2005.
25. Hofmann, P. and Spino, J., "Can we expect a low ductility failure of Zircaloy tubing due to iodine-induced stress corrosion cracking in a LOCA transient", ANS/ENS Topical Meeting on Reactor Safety Aspects of Fuel Behaviour, 1981, Sun Valley, USA.
26. Broughton, J.M., *et al.*, "PBF LOCA test LOC-6 fuel behavior report", NUREG/CR-3184, April 1983.
27. Jones, P., *et al.*, "EOLO-JR: A single rod burst test programme in the ESSOR reactor", IAEA Specialists meeting on water reactor fuel element performance computer modelling, 1982, Preston, United Kingdom.
28. Jones, P.M. and Crichton, D., "Creep-rupture tests on Zircaloy-4 tubes in various atmospheres", UKAEA Report ND-R-376(S), 1980.
29. Bruet, M. and Janvier, J.C., "FLASH experiments in SILOE reactor; fuel rod behaviour during LOCA tests", OECD/NEA CSNI/IAEA Specialists meeting in water reactor fuel safety and fission product release in off-normal and accident conditions., 1983, Risø, Denmark.
30. Houdaille, B., Fillatre, A., and Morize, P., "Development and qualification of the LOCA analysis system CUPIDON-DEMETER", OECD/NEA CSNI/IAEA Specialists meeting in water reactor fuel safety and fission product release in off-normal and accident conditions., 1983, Risø, Denmark.
31. Bruet, M., *et al.*, "High burn-up fuel behaviour during a LOCA type accident: the FLASH 5 experiment", IAEA Technical Committee Meeting on Behavior of Core Materials and Fission Product Release in Accident Conditions in LWR's, 1992, Cadarache, France.
32. Mohr, C.L., *et al.*, "LOCA simulation in the National Research Universal Reactor Program: Data report MT-3", NUREG/CR-2528, PNL-4166, April 1983.
33. Wilson, C.L., *et al.*, "LOCA simulation in the NRU program: Data Report MT-4", NUREG/CR-3272 PNL 4669, July 1983.
34. Bergquist, P., *et al.*, "Impact of the calculated peak clad temperature of a redistribution of the fuel after fuel swelling and rupture", AB Fjärrvärme, FV-78-0010/01.

35. Broughton, J.M., *et al.*, "Effect of fuel re-distribution on cladding temperatures during a large break LOCA and impact on NRC licensing requirements", CSNI Meeting, 1982, Tokai Mura.
36. Mohr, C.L. and Hesson, G.M., "Ballooning and flow blockage for high  $\alpha$  LOCA conditions. Paper 19", IAEA Specialists meeting on water reactor fuel element performance computer modelling, 1982, Preston, United Kingdom.
37. Haste, T.J., "Modelling the effect of different mechanical restraint conditions on PWR fuel rod deformation under conditions relevant to the NRU MT-3 experiment, using the MABEL 2-D code", UKAEA Report ND-R-988(S).
38. Kawasaki, S., *et al.*, "Effect of non-heated rods on the ballooning behaviour in a fuel assembly under a loss-of-coolant condition", ANS/ENS Topical Meeting on Reactor Safety Aspects of Fuel Behaviour, 1981, Sun Valley, USA.
39. Kawasaki, S., Vetsuka, H., and Furuta, T., "Mulit-rod burst tests under loss of coolant conditions", OECD-NEA CSNI/IAEA Specialists meeting in water reactor fuel safety and fission product release in off-normal and accident conditions., 1983, Risø, Denmark.
40. Longest, A.W., "Multi-rod burst test program. Progress report Jan-June 1981", NUREG/CR-2366 Vol. 1 ORNL/NUREG/TM-8058, Dec. 1981.
41. Réocreux, M. and Scott de Martinville, E.F., "A study of fuel behavior in PWR design basis accident: an analysis of results from the PHEBUS and EDGAR experiments", Nuclear Engineering and Design, 124(1990), pp. 363-378.
42. Scott de Martinville, E.F. and Pignard, M., "International standard problem ISP-19 - Behaviour of a fuel rod bundle during a large break LOCA transient with a two peak temperature history (PHEBUS experiment)", OECD Nuclear Energy Agency, CSNI Report 131, 1987.
43. Svanholm, K., *et al.*, "Halden Reactors IFA-511.2 and IFA-54X: Experimental series under adverse cooling conditions", Experimental Thermal and Fluid Science, 11(1995).
44. Haste, T.J., "Conclusions from the IFA-54X series to compare the ballooning response of nuclear and electrically heated PWR fuel rods in the Halden reactor", Halden Project Seminar on High Burn-up Fuel Performance Topics, 1987, Fredrikstad, Norway, Halden Reactor Project.
45. Haste, T.J., "CANSWEL-2: A computer model of the creep deformation of Zircaloy cladding under loss-of-coolant accident conditions; Part 1, Model description", ND-R-814(S), July 1982.
46. Donaldson, A.T., Horwood, R.A., and Healey, T., "Pre-test prediction and post-test analysis of PWR fuel rod ballooning in the MT-3 in-pile LOCA simulation experiment in the NRU reactor", IAEA Specialists meeting on water reactor fuel element performance computer modelling., 1982, Preston, UK, Applied Science Publishers, pp. 367-391.
47. Healey, T., *et al.*, "Ballooning response of nuclear and electrically heated PWR fuel rods tested in the Halden reactor and under laboratory simulation conditions", Conference of Nuclear Fuel Performance., 1985, Stratford-on-Avon, UK, British Nuclear Energy Society.
48. Lestinen, V., Kolstad, E., and Wiesenack, W., "LOCA testing at Halden, trial runs in IFA-650", 2003 Nuclear Safety Research Conference, 2003, Washington, DC, USA, NRC, pp. 299-309.
49. Ek, M., "Minutes of the LOCA Workshop Meeting", LOCA Workshop Meeting, 2005, Halden, Norway.
50. Ek, M., "LOCA testing at Halden, the third experiment IFA-650.3", OECD Halden Reactor Project, HWR-785, October 2005.

51. Kekkonen, L., "LOCA testing at Halden, the fourth experiment IFA-650.4", OECD Halden Reactor Project, HWR-838, November 2005.
52. Wiehr, K., Erbacher, F.J., and Neitzel, H.J., "Influence of cold control rod guide thimble on the ballooning behaviour of Zircaloy claddings in a LOCA", CSNI Specialist Meeting on Safety Aspects of Fuel Behaviour in Off-Normal and Accident Conditions, 1980, Espoo, Finland, OECD, pp. 141-154.
53. Wiehr, K., Erbacher, F.J., and Neitzel, H.J., "Influence of thermohydraulics on fuel rod behaviour in a LOCA", CSNI Specialist Meeting on Safety Aspects of Fuel Behaviour in Off-Normal and Accident Conditions, 1980, Espoo, Finland, OECD, pp. 59-73.
54. Erbacher, F.J., "REBEKA test results", 9<sup>th</sup> Water Reactor Safety Information Meeting, 1981, Gaithersburg, USA, NRC.
55. Rininsland, H., *et al.*, "Stand der Reaktorsicherheitsforschung in Projekt Nukleare Sicherheit", KfK Jahreskolloquium, 1982.
56. Erbacher, F.J., Neitzel, H.J., and Wiehr, K., "Effects of thermohydraulics on clad ballooning, flow blockage and coolability in a LOCA", OECD-NEA-CSNI/IAEA Specialists' Meeting on Water Reactor Fuel Safety and Fission Product Release in Off-Normal and Accident Conditions., 1983, Risø, Denmark.
57. Erbacher, F.J., Neitzel, H.J., and Wiehr, K., "Interactions between thermohydraulics and fuel clad ballooning in a LOCA - results of REBEKA multi-rod burst tests with flooding", 6<sup>th</sup> Water Reactor Safety Information Meeting, 1978, Gaithersburg, USA, NRC.
58. Weidinger, H.W., *et al.*, "LOCA - fuel rod behaviour of KWU-pressurized water reactors", CSNI Specialist Meeting on the Behaviour of Water Reactor Fuel Elements under Accident Conditions, 1976, Spaatind, Norway, OECD.
59. Ortlieb, E., Cheliotis, G., and Weidinger, H.W., "Influence of mechanical anisotropy on the LOCA deformation behaviour of Zircaloy cladding"International Meeting on Thermal Nuclear Reactor Safety, 1982, Chicago, USA.
60. Cheliotis, G., Romeiser, H., J., and Weidinger, H.W., "Multi-rod burst tests - investigations of LOCA behaviour of PWR fuel assemblies", Atomkernenergi Kerntechnik, 34(1979), pp. 255-257.
61. Cheliotis, G., Ortlieb, E., and Weidinger, H.W., "Single and multi rod investigations for the experimental and theoretical verification of LOCA fuel behaviour", ANS/ENS Topical Meeting on Reactor Safety Aspects of Fuel Behaviour, 1981, Sun Valley, USA.
62. Cheliotis, G., *et al.*, "Verification of LOCA clad ballooning behaviour in mulit rod tests by means of single rod investigations", CSNI Specialist Meeting on Safety Aspects of Fuel Behaviour in Off-Normal and Accident Conditions, 1980, Espoo, Finland, OECD.
63. Suzuki, M., "Simulation test on interactions of Zircaloy claddings deforming in fuel assembly under LOCA conditions", Journal of Nuclear Science and Technology, 20(1983), pp. 475-490.
64. Chapman, R.H., *et al.*, "Status of Zircaloy deformation and oxidation research at Oak Ridge National Laboratory", Specialist Meeting on WR Fuel Elements under accident conditions, 1976, Spaatind, Norway, OECD/NEA.
65. Hindle, E.D., "Zircaloy fuel clad ballooning tests ar 900-1070 K in steam", UKAEA Report ND-R-6(S), June 1977.
66. Chapman, R.H., *et al.*, "Effect of creep time and heating rate on deformation of Zircaloy-4 tubes tested in steam with internal heaters", NUREG/CR-0343, ORNL/NUREG/TM-245, Oct. 1978.

67. Chapman, R.H., *et al.*, "Bundle B-1 test data", ORNL/NUREG/TM-322, June 1979.
68. Chapman, R.H., *et al.*, "Bundle B-2 test data", ORNL/NUREG/TM-337, August 1979.
69. Chapman, R.H., "Preliminary multi-rod burst test program results and implications of interest to reactor safety evaluations", 6<sup>th</sup> Water Reactor Safety Information Meeting, 1978, Gaithersburg, USA, NRC.
70. Chapman, R.H., *et al.*, "Multi-rod burst test program. Bundle B-3 test data", ORNL/NUREG/TM-360, Jan. 1980.
71. Longest, A.W., Crowley, J.L., and Chapman, R.H., "Experiment data report for multirod burst test (MRBT) bundle B-4", NUREG/CR-2968, Dec. 1982.
72. Chapman, R.H., Longest, A.W., and Crowley, J.L., "Experiment data report for multirod burst test (MRBT) B-6", NUREG/CR-3460, July 1984.
73. Chapman, R.H., Crowley, J.L., and Longest, A.W., "Effect of bundle size on cladding deformation in LOCA simulation tests", Zirconium in the Nuclear Industry: Sixth International Symposium, 1982, Vancouver, Canada, ASTM STP 824, ASTM, pp. 693-708.
74. Burman, D.L., *et al.*, "Comparison of Westinghouse LOCA burst test results with ORNL and other program results", CSNI Specialist Meeting on Safety Aspects of Fuel Behaviour in Off-Normal and Accident Conditions, 1980, Espoo, Finland, OECD, pp. 251-284.
75. Brachet, J.-C., *et al.*, "Influence of hydrogen content on the alpha/beta phase transformation temperatures and the thermal-mechanical behavior of Zy-4, M4 (ZrSnFeV), and M5 (ZrNbO) alloys during the first phase of a LOCA transient", Zirconium in the Nuclear Industry: Thirteenth International Symposium, 2001, Annecy, ASTM STP 1423, ASTM, pp. 673-701.
76. Forgeron, T., *et al.*, "Experiment and modeling of advanced fuel rod cladding behavior under LOCA conditions: Alpha-Beta phase transformation kinetics and EDGAR methodology", Zirconium in the Nuclear Industry: Twelfth International Symposium, 1998, Toronto, ASTM STP 1354, ASTM, pp. 256-278.
77. Bouffoux, P. and Rupa, N., "Impact of hydrogen on plasticity and creep of unirradiated Zircaloy-4 cladding tubes", Zirconium in the Nuclear Industry: Twelfth International Symposium, 1998, Toronto, ASTM STP 1354, ASTM, pp. 399-422.
78. Portier, L., *et al.*, "Influence of long service exposures on the thermal-mechanical behavior of Zy-4 and M5 alloys in LOCA conditions", Zirconium in the Nuclear Industry: Fourteenth International Symposium, 2004, Stockholm, ASTM STP 1467, ASTM, pp. 896-920.
79. Hindle, E.D. and Mowat, J.A.S., "Swelling behaviour of SGHWR fuel cladding in steam in laboratory tests simulating LOCA involving temperatures above 900 C", Specialist Meeting on WR Fuel Elements under accident conditions, 1976, Spaatind, Norway, OECD/NEA.
80. Hindle, E.D. and Mann, C.A., "Zircaloy PWR fuel cladding deformation tests under mainly convective cooling conditions", UKAEA report ND-R-364(S), Jan. 1980.
81. Healey, T., Clay, B.D., and Duffey, R.B., "Analysis of the axial ballooning behaviour of directly heated Zircaloy tubes", CEGB RD/B/N4145, Sept. 1977.
82. Hindle, E.D., Mann, C.A., and Reynolds, A.E., "Simulation of Zircaloy cladding deformation under accident conditions derived from analysis of data from Three Mile Island-2", CSNI Specialist Meeting on Safety Aspects of Fuel Behaviour in Off-Normal and Accident Conditions, 1980, Espoo, Finland, OECD, pp. 155-157.

83. Hindle, E.D., "Zircaloy fuel clad ballooning tests at 900-1070K in steam. Further results at 890-1150K", UKAEA report ND-R-6(S) 1st supplement, Oct. 1977.
84. Garlick, A. and Hindmarch, P., "Cladding elongation and fuel stack mechanical stability during internal pressurization tests on irradiated PWR fuel", UKAEA Report ND-R628(W), March 1983.
85. Bowring, R.W., *et al.*, "MABEL-2: A code to analyse cladding deformation in a loss-of-coolant accident. Part 4", UKAEA Report AEEW-R-1532.
86. Bowring, R.W., *et al.*, "MABEL-2: A code to analyse cladding deformation in a loss-of-coolant accident. Part 3", UKAEA Report AEEW-R-1531.
87. Bowring, R.W., *et al.*, "MABEL-2: A code to analyse cladding deformation in a loss-of-coolant accident. Part 2", UKAEA Report AEEW-R-1530.
88. Bowring, R.W., *et al.*, "MABEL-2: A code to analyse cladding deformation in a loss-of-coolant accident. Part 1", UKAEA Report AEEW-R-1529.
89. Hindle, E.D., European patent application No. 81 302280.3, 1981.
90. Haste, T.J., "Modelling the mechanical constraint of the deformation of Zircaloy cladding in a non-uniform environment, using the CANSWEL-2 code", IAEA Specialists meeting on water reactor fuel element performance computer modelling, 1982, Preston, United Kingdom.
91. Jackson, P.A. and Palmer, I.D., "The influence of fuel pellet fragmentation on predicted azimuthal temperature variations in ballooning cladding", OECD/NEA/CSNI-IAEA Specialists Meeting on Water Reactor Fuel Safety and Fission Product Release in Off-Normal and Accident Conditions, 1983, Risø.
92. Bibilashvili, Y.K., *et al.*, "WWER-1000 type fuel assembly tests on electroheated facilities in LOCA simulating conditions", IAEA Technical Committee Meeting on Fuel behaviour under transient and LOCA conditions., 2001, Halden, Norway, IAEA, pp. 169-185.
93. Hózer, Z., *et al.*, "Ballooning experiments with VVER cladding", Nuclear Technology, 152(2005), pp. 273-285.

## 8. PREDICTIVE COMPUTER CODES

### 8.1 Some general comments on computer codes

Workers in several countries have developed codes aimed at predicting the behaviour of a fuel assembly in a LOCA. In general, these codes attempt to predict the deformation of a fuel rod, the termination of deformation by rupture, the temperature reached by the cladding, oxidation of cladding, and in some codes, the interaction between neighbouring rods. A code typically draws input information on coolant condition from a thermal-hydraulic code, and data on fuel from a steady-state code, while a range of sub-codes calculate fission gas release, deformation etc. Leading examples are considered below.

As will be seen later many of the computer codes used today are the same as or developments of codes that were used at the time of writing of the previous LOCA state-of-the-art report in 1986 [1]. However, there has been a dramatic change in the computing environment. In 1986, one of the fastest computers, Cray X-MP, had a computing power of 500-1 000 MFlops<sup>1</sup> depending on configuration. Normally, however, computer codes for LOCA analysis would be run on a less powerful mainframe computer. In 2007, a computer code would typically be run on a desktop PC with one or more microprocessors each with a computing power of perhaps 30 GFlops assisted by a graphics processor operating with perhaps 500 GFlops. The cost of computing power has been reduced accordingly, from several 100 000 USD/GFlops to a few USD/GFlops. Many of the computer codes are not adjusted to this new environment, input and output procedures are frequently similar to the procedures used for batch processing in mainframe computers. However, there exist a number of new codes which take full account of a modern computer environment with an advanced graphics based user interface.

#### 8.1.1 Types of computer codes

In order to model a LOCA or an experiment simulating a LOCA or a subset of a LOCA event three categories of codes are needed:

- Reactor physics codes.
- Fuel behaviour codes.
- Thermohydraulics codes.

The reactor physics codes provide the starting condition for a LOCA event. Recent developments have included a more advanced graphics user-interface and the merger of reactor physics codes with system thermohydraulics codes [2].

The fuel behaviour codes can be separated into steady state codes and transient codes. The steady-state codes describe the normal operation of the fuel and may contain submodels which calculate fission gas release, restructuring of fuel with burn-up, any deformation occurring etc. The steady-state code then provides the starting conditions for the transient code which calculates cladding deformation and

---

1. Flops = floating point operations per second.

fracture during the transient. Fuel behaviour codes tend to be design specific and are typically used by regulatory and industry groups in the country of origin. The transient codes used for accident conditions may contain modelling options for both conservative and best estimate calculations [2].

System thermohydraulic codes are typically less design specific and are applied to a wider variety of designs and conditions. A limited number of these codes are widely used around the world by regulatory, research and industry organisations. The codes developed by regulatory bodies are typically used as best estimate codes and do not contain specific models for conservative analysis. However, many of the industry supported codes contain models for conservative and best estimate analyses. These thermohydraulic codes are characterised by mechanistic models for two fluid, non-equilibrium hydrodynamics, point and multi-dimensional reactor kinetics, control systems and other system components such as pumps, valves and accumulators. These codes can typically be used to model a wide range of configurations for single pipes, experimental facilities and full plants and, in many cases, have been applied to most reactor designs around the world.

In later sections, we shall use the categorisation, single rod codes, assembly/channel codes, and system codes. The latter are of course more or less synonymous with thermohydraulics codes.

### **8.1.2 Documentation**

The following text is a direct quote from Reference 1.

“Each computer code needs to be adequately documented to facilitate review of the models and correlations employed, and to ensure that the models for important phenomena are appropriate and are not applied outside their range of validity. The documentation would also provide a description of the uncertainties of important models and the overall code for typical applications. The code documentation would also include user guidelines and input descriptions to ensure that the user can use the software properly. Although the guidance may vary depending on the complexity of the codes and the modelling parameters available to the user, the user guidelines or validation documentation need to give the user some guidance on the influence of important modelling parameters, recommendations for typical applications of the code, the type of nodalization to be used and the important trends to be expected.

Typically, a complete set of documentation would include:

- An abstract of the programme.
- A theory manual.
- A user’s manual and description of the inputs.
- A programmer’s manual.
- A validation report.

The scope of documentation may vary depending on the complexity of the code and on the applications to which it is applied. In the most comprehensive examples, multiple volumes may be necessary to describe the design and implementation of code models and correlations. In some cases, separate manuals may be provided in which the models and correlations used in individual codes are discussed. For example, the models and correlations document for each code:

- (a) May provide information on its original source and its database.
- (b) May describe how it is implemented in the code.
- (c) May describe the expected accuracy of the models, including an assessment of any effects were the code to be used outside its basis of data, the effects of the specific manner in which the model is implemented in the code and the effects of any unique numerical features necessary to overcome computational difficulties.
- (d) May provide information on the applicability of the model to the analysis of reactor systems.

In general terms, the documentation for internationally recognised codes is quite extensive and in most cases includes descriptions of the key phenomenological models, user's manuals and results of assessment calculations. The system thermohydraulic codes typically have the most comprehensive documentation since these codes have extensive manuals prepared by the code developers in addition to a number of contributors of different nationalities who have provided independent reports on the results of the code assessment and validation. The documentation for the codes for accident conditions beyond the design basis is more diverse, with nearly all codes having some form of user's manual and manuals describing the theory of the model. Some of the codes also include manuals for material properties, code developer's assessment and validation, and user guidelines. Some codes also have manuals available in electronic form or through the Internet."

### **8.1.3 Code verification**

Code verification can be defined as a comparison of the source coding with its description in the documentation. It has not been applied consistently to many of the codes used around the world. Since line by line verification of these large codes is a time consuming and expensive process, this process is limited to those codes which are relatively static and not subject to continual change. In particular, many industry sponsored codes have been subjected to stringent verification procedures as a consequence of the regulatory licensing process.

### **8.1.4 Code validation**

There is normally [2] a regulatory requirement that codes be assessed (validated) in relation to relevant experimental data for the major phenomena expected to occur. The validation relates to the confidence that can be placed on the accuracy of the values predicted by the code. Three sources of data are generally used to validate these codes: phenomenological data, data on separate effects (component data), and integral data.

For validation, certain quantities are selected for the comparison of calculations with experimental data. These quantities serve as "indicators" for determining whether or not a code provides satisfactory results; i.e. indicators that can be used to measure the "level of validation" of a code. The identification or choice of indicators is, therefore, a crucial step in the validation. The quantification of the validation can be expressed in terms of the accuracy with which a code predicts an indicator, and it must relate to the agreement between the values of the indicators as predicted and as measured experimentally. The indicators are directly related to the physical driving phenomena of the response to the accident and are usually those code output quantities which are compared with acceptance criteria in accident analysis.

Historically, the validation of many codes has included the formulation of a model (or hypothesis), design of validation experiments, collection of experimental data, analysis of these data, comparison of experimental data with code predictions and reformulation (if necessary) of the model. The need for the reformulation of the model and reiteration depends on whether or not the code is judged to have met the validation goals or criteria. Currently, since many experimental programmes are run independently of the activities for code development and validation, the design of experiments, collection of data and analysis of the data may be performed separately. In addition, since many of the experimental programmes have been completed, validation of new models and codes may rely very heavily on archival data sources. However, it remains important to validate the code against at least some of the experiments which have not been used directly to support the models in individual codes. A code can sometimes predict a set of data with a high degree of accuracy and still be extremely inaccurate for other data sets. This has led to the need to develop a "validation matrix" for each code through which different types of experimental facilities and different sets of conditions in the same facility are used for code validation [2-4].

Most internationally recognised codes have been subjected to systematic validation procedures through a number of international programmes, with system thermohydraulic codes receiving the most attention. Other types of codes have also been systematically validated, but to a lesser extent. The system thermohydraulic codes maintained by regulatory and research organisations are still the subject of a high level of effort in this area as a result of the work of the code developers and of other international activities. Under these programmes, which include those of the IAEA, the OECD/CSNI, extensive experimental matrices for code validation have been established and the codes have been assessed in relation to many of the experiments that are included in those matrices. The validation exercises have also included comparisons with relevant data from plant operations and participation in international standard problems [5-6].

### ***8.1.5 The accuracy of codes***

The following text is an edited version of a corresponding section in Reference 1.

“Although the primary objective of the code validation process is to help define the accuracy of codes, such accuracy may be defined in qualitative rather than quantitative terms owing to the time and expense associated with estimation of the uncertainties in predicted behaviour for wide ranges of LOCA conditions and designs. The assessment of the accuracy of individual codes typically includes a series of steps:

- (a) Identifying the important trends in the supporting experimental data and expected fuel behaviour.
- (b) Estimating the uncertainties in the overall code results associated with the fundamental numerical approaches used.
- (c) Estimating uncertainties in key models and overall code results.
- (d) Establishing sensitivities in important processes.

A number of different techniques are used with code to data comparisons, the preferred technique when an adequate basis of data exists. Code to code comparisons, model to model comparisons and engineering judgement are also important techniques. The identification of important trends in the supporting experimental data and in the expected fuel behaviour is an important step for several reasons. It allows analysts to select the proper models and codes to be used for a particular analysis and to evaluate the overall performance of the computer codes being used.

Although the documentation of the codes needs to provide some description of the limits of applicability of the codes, such descriptions provide only rough guidelines to the analyst. The estimation of the uncertainties arising from the numerical approaches used in each code serves a number of primary needs. The uncertainties associated with the numerics of individual codes or models can arise from several sources. First, since many of the processes being modelled are non-linear, uncertainties can arise from the discretization of the equations used. Sensitivities to time step and nodalization are prime examples. Second, uncertainties can arise from differences in computer architecture, operating systems and compilers due to differences in machine accuracy, errors introduced by optimisation of the compiler and installation errors. Although many code developers assess the numerical accuracy of their codes for different machines, and provide guidelines on time step and nodalization, it is impossible for developers to evaluate all possible computer configurations for a complete range of code applications. From the perspective of code developers, the estimation of these uncertainties is important to ensure that the contributions from the numerical approaches used are negligibly small compared with the overall modelling uncertainties, and that convergence in terms of time steps and nodalization can be obtained. From the perspective of analysts, this estimation is important to ensure that the proper user guidelines for such parameters as time step control and nodalization are followed and are appropriate to the problems being analysed. It is also important to ensure that the codes have been installed properly and that the

influence of operating system errors and compiler errors on their computers has been minimised. As a consequence, it is important that analysts evaluate the impact of these uncertainties through convergence studies and comparison with developer supplied test problems.

The estimation of model uncertainties and code uncertainties has been formalised using a range of methods. Fundamental to all methods is the adequacy of the supporting experimental data and the scalability of that basis of data to full plant conditions. The experimental data can be used in a variety of ways, with direct comparisons between the results of measurements and those of calculations being one of the most common approaches. Code to code comparisons, particularly the benchmarking of parametric codes and models against more mechanistic codes, are also important checks on the overall uncertainties in the codes. Assessment of codes with respect to fundamental problems, for which analytical solutions or other independent sources of results are available, is also valuable.

The estimation of uncertainties in the model or the code needs also to include the effects of important model input parameters. Although defaults for model input parameters have to be set by code developers to reflect the central or best estimate value of the uncertainty bands, this is not always done. In particular, in some parametric codes the model input parameters can be varied for each code to data or code to code comparison to minimise the variations in such comparisons. In this case analysts need to be aware of the influence of these parameters and to set them to reflect best estimate values on the basis of their own code to data or code to code comparisons appropriate to their applications. Recent efforts to automate the generation of uncertainty estimates through options such as the propagation of errors in the calculated results may help analysts. Sensitivity studies can also be useful in gaining an understanding of the influence of important modelling parameters. Code developers need to provide users with some guidance on usage, including nodalization guidelines, recommended modelling parameters, and estimates of the overall trends and uncertainties in typical code calculations. However, it is also important for analysts to assess the applicability of the codes for their particular application, to establish an adequate level of nodalization, to determine the impact of important modelling parameters, and to assess the trends and accuracy of the calculations in relation to their applications.”

## 8.2 Single rod codes

### 8.2.1 Steady-state codes

For the purpose of LOCA analysis it is necessary to first use a computer code which defines the state of the fuel rod at the start of the transient. This type of code is usually called steady-state codes in contrast to the codes used for the transient behaviour of the fuel rods. However, the steady-state codes can normally handle power transients within normal operating conditions of power reactor fuel so the term steady-state is slightly misleading.

There are a large number of steady-state codes. As with most codes, they are named with some acronym with the addition of a number which defines the version of the code. A typical example is the FRAP family of programs where FRAP simply means “fuel rod analysis package”. By adding a suffix S or T as in FRAP-TX, it is specified that the code calculates steady state or transient behaviour and that it is version X of the code.

The following list of steady-state codes has been compiled from different sources but the main source is a recent code survey performed by the CSNI Special Expert Group on Fuel Safety Margins.

It is not within the scope of the present report to discuss in detail what the different codes can accomplish. In general, many of them produce relatively accurate results for instance in regard to fission gas release.

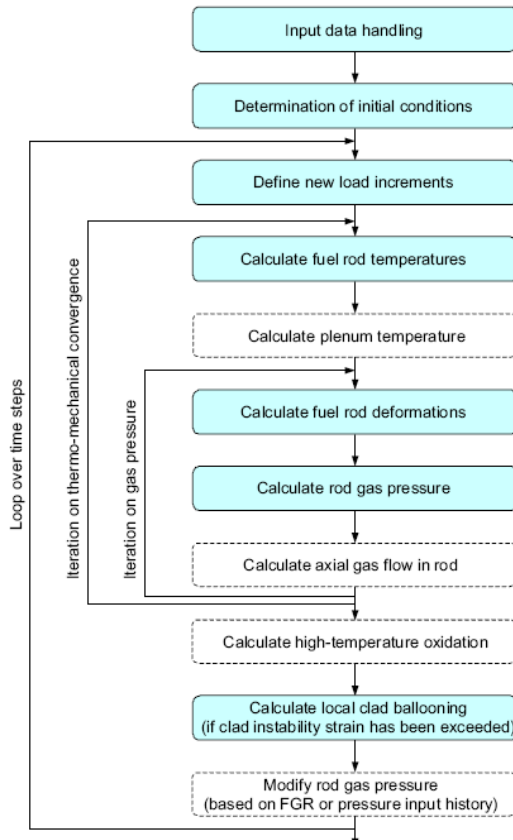
Code	User/Owner	Code	User/Owner
FRAPCON	NRC	ENIGMA	Westinghouse (BNFL)
TRANSURANUS	FZK Karlsruhe	FEMAXI-X	JAEA
RAPTA-5	VNIM	ELESTRES	AECL/COG
COPERNIC3	AREVA	TOUTATIS	CEA
FALCON	EPRI	ALCYONE	CEA
METEOR	CEA	STAV-X	Westinghouse (Sweden)
CARO	Siemens	FOXFIRE	Westinghouse

While many of the codes are relatively old a few modern codes like COPERNIC3 [7-8] and FOXFIRE [9] fully utilise a modern graphics user interface and hierarchical data structures. Since both are developed within organisations created by company mergers they contain models from many of the older codes listed above. The objective of COPERNIC3 is said to be to accurately predict fuel behaviour under steady-state, transient and storage conditions. However, the descriptions available do not mention any modelling of LOCA transients.

### 8.2.2 Transient codes

As an example of a transient codes, we can take FRAPTRAN-1.3, a descendent of the previous FRAP-TX codes. The code calculates the transient response of a single fuel rod under a range of accidents ranging from operational transients to LOCA and reactivity insertion accidents. It is a modular code comprising several sub-codes which interactively calculate the effects of fuel, cladding and plenum temperatures, fuel and cladding deformation and rod internal pressure, including fission gas release. A flowchart of the code is shown in Figure 8.1.

Figure 8.1 Flowchart for the code FRAPTRAN-1.3 [10]



FRAPTRAN-1.3 is basically a one-dimensional code but a submodel of the code, BALON2, can calculate the shape of the balloon after that the code has established that plastic instability has been reached.

As for steady-state codes there exists a large number of codes which handles transient behaviour of fuel. The following list shows codes used for LOCA analysis.

<b>Code</b>	<b>User/Owner</b>	<b>Code</b>	<b>User/Owner</b>
FRAP-TX	NRC	MABEL	UK
FRAPTRAN	NRC	CUPIDON	CEA
FRAS-LOCA	NRI	CARATE	Siemens
ELOCA	AECL	BETHY	Siemens
TRACE	PSI	BART-A1	NNC
FREY	EPRI	TESPA	GRS
RANNS	JAEA	CATHACOMB	CEA

There are several more codes, some of them obsolete, some of them incorporated into new codes under another name to some extent due to the restructuring of the nuclear industry in the last few years.

In a recent publication van Uffelen *et al.* present how the steady state code TRANSURANUS has been extended to use under design basis accident conditions [11].

### 8.3 Assembly/channel codes

The purpose of an assembly/channel code is to describe what happens to a fuel assembly during a LOCA event, how the different fuel rods interact and to get an idea of how the channel may be blocked by ballooned fuel rods. For determination of the temperature transient, most thermohydraulic codes can be used since they are easily adapted to small systems as well as complete reactor systems.

Codes which calculate fuel rod behaviour in whole assemblies including rod-to-rod interactions are relatively rare. One such code is the Japanese FRETA-B code [12]. FRETA-B is described as being specialised in two-dimensional analysis in the transverse direction [13]. Axially the rods are divided into essentially independent segments. For modelling of a fuel bundle, each fuel rod is divided into four azimuthal sectors for the thermal calculation. One coolant subchannel with four surrounding fuel rod sectors constitutes the basic unit of geometry. For the ballooning calculation, a cladding circumference is represented by 20 nodes, and local cladding temperature is derived by cosine interpolation from the four sector temperatures.

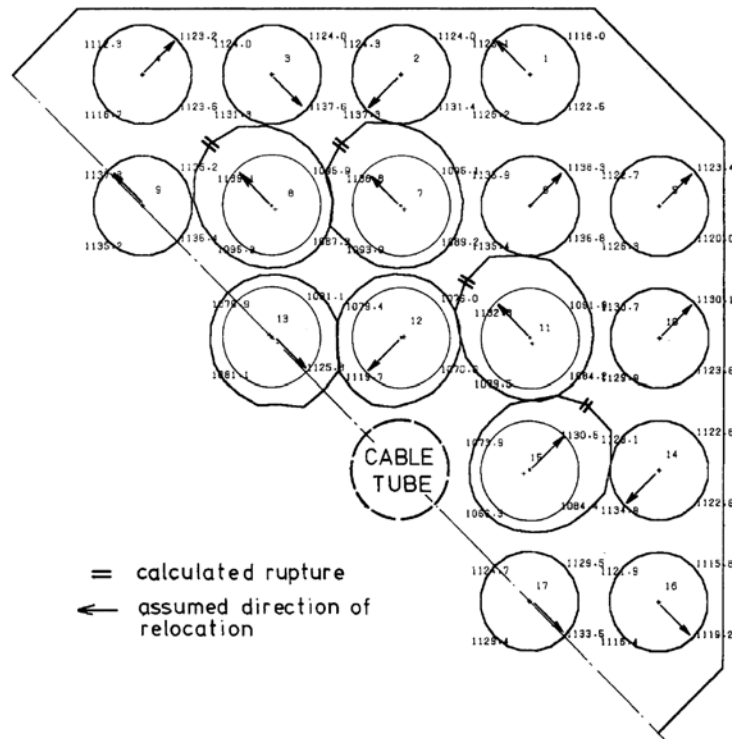
The ballooning model takes anisotropy into account. Rod-rod contact is monitored at every node, and when a node is found to be covered by another rod the strain increment there is set to zero. A rod is determined to have ruptured when a local hoop strain has exceeded a threshold value. This is slightly unrealistic because fracture strains are often very high, but the shell model for ballooning cannot follow such extreme strain localisations. Figure 8.2 shows the result of calculations of deformations in the MT-1 experiment (Section 7.3.1.5) with FRETA-B [13].

S. Sunder has contributed the following brief description of ELOCA 2.2, a CANDU safety analysis code which calculates the thermo-mechanical response of a CANDU fuel element (including fuel failure) under the high temperature transient conditions representative of CANDU reactor loss-of-coolant accident (LOCA) scenarios.

Understanding the behaviour of nuclear fuel pins under accident conditions is a key facet of CANDU safety analysis. A change in fuel element power output, or a change in heat transfer characteristics, will cause an immediate change in the temperature distribution in a fuel element. The temperature distribution change will be accompanied by concomitant changes in fuel and fuel sheath

material properties and the internal gas pressure within the element. In turn, the contact pressure between the fuel and the sheath may be affected, causing a further change in the fuel temperatures. Because of this potentially large feedback mechanism, CANDU fuel codes, such as ELOCA, must not only be capable of modelling the heat generation and thermal conductance within the fuel, but also the complex mechanical interactions between the fuel and the fuel sheath during LOCA.

Figure 8.2 Deformation pattern at level 15 of the MT-1 experiment as calculated by FRETA-B



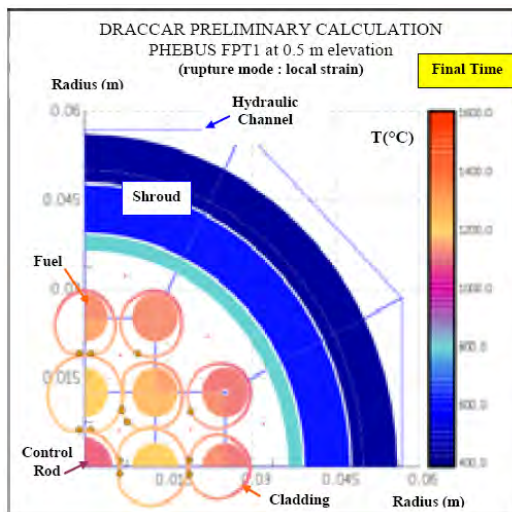
Under the extremes of temperature, typical of an accident, sheath failure may occur due to internal pressurization of the fuel pin, by oxidation from the external environment, or by a combination of the two. ELOCA-IST 2.2 code contains the following six mechanisms to determine sheath failure in a CANDU fuel element during LOCA:

- *Sheath failure due to overstrain:* The sheath is typically assumed to fail when the sheath strain, averaged along the length of the fuel pin reaches 5%.
- *Low ductility sheath failure:* At low temperature and high stress, cold-worked Zircaloy tubes have large strain-rate sensitivity with a small temperature dependency leading to potential sheath failure at low strains (<0.5%).
- *Sheath failure by beryllium-assisted crack penetration:* At the elevated temperatures of an accident transient (>1 000 K) and under large hoop stresses, the Zircaloy pads and spacers (beryllium-brazed onto the sheath surface) can assist in crack penetration of the sheath through liquid metal embrittlement.
- *Sheath failure by oxygen embrittlement:* The presence of dissolved oxygen in the Zircaloy sheath, at concentrations between 0.5 and 1.0 wt %, sufficiently embrittles the sheath at low temperatures (<600 K) that it can no longer withstand the hydraulic forces and thermal shock associated with rapid quenching; the sheath may fail on re-wet following a loss-of-coolant accident.

- *Sheath failure by overstrain under oxide cracks:* The oxide formed on the outside of a Zircaloy fuel sheath is brittle, and cracks may form in the oxide at low strains. Once a crack has started, the stress concentration at the crack tip can lead to propagation of the crack into the sheath wall. The reduced sheath thickness under the crack tip results in localised strains that are higher than the average values for the sheath and may result in sheath failure.
- *Sheath failure due to high strain rate:* At high strain rates, the fuel sheath can fail before the local sheath failure criterion has been reached. The high strain rate criterion determines sheath failure based on the current sheath strain rate.

A code currently under development at IRSN is called DRACCAR. The purpose of the code is to simulate the thermo-mechanical behaviour of a rod bundle under LOCA with a 3D multi-rod description as illustrated in Figure 8.3.

**Figure 8.3 Example of DRACCAR calculation in a bundle geometry with rod deformation as the result of a LOCA type transient [14]**



It is anticipated that this tool will allow a consistent analysis of the existing experimental data base both for single rod and bundle tests. It will also be used to evaluate complementary research needs for the behaviour of reactor assemblies and to perform reference calculations on well defined configurations with evaluation of related uncertainties.

#### 8.4 System codes

System thermohydraulic codes describe the behaviour of the reactor systems, including hydrodynamics, heat transfer, reactor kinetics, control systems and other system components. Examples of codes in this category include RELAPX [15], TRAC-P/B (PWR/BWR)[15] and COBRA-TRAC [15] (United States of America), CATHARE [16] (France), ATHLET [17] (Germany), DINAMIKA [18] (Russian Federation), SMABRE [19] and APROS [20] (Finland), and CATHENA [21] (Canada).

#### 8.5 References

1. Parsons, P.D., Hindle, E.D., and Mann, C.A., “PWR fuel behaviour in design basis accident conditions. A State-of-the-Art Report by the Task Group on Fuel Behaviour of CSNI Principal Working Group No 2”, Committee on the Safety of Nuclear Installations, OECD Nuclear Energy Agency, CSNI Report 129.

2. Accident analysis for nuclear power plants, International Atomic Energy Agency, Safety Report Series No. 23, 2002.
3. CSNI integral test facility validation matrix for the assessment of thermal-hydraulic codes for LWR LOCA and transients, Committee on the Safety of Nuclear Installations, OECD Nuclear Energy Agency, OCDE/GD(97)12, July 1996.
4. Aksan, N., *et al.*, “Separate effects tests matrix for thermal-hydraulic code validation”, Vol. I: Phenomena characterization and selection of facilities and tests, Vol. II: Facility and experiment characteristics, Committee on the Safety of Nuclear Installations, OECD Nuclear Energy Agency, CSNI Report, OECD/NEA/GD (94)/82, 1994.
5. CSNI International Standard Problems (ISP), brief descriptions (1975-1999), Committee on the Safety of Nuclear Installations, OECD Nuclear Energy Agency, NEA/CSNI/R(2000)S, Feb. 2000.
6. Contribution from twenty-two years of CSNI International Standard Problems, Committee on the Safety of Nuclear Installations, OECD Nuclear Energy Agency, NEA/CSNI/R(97)29, March 1998.
7. Garnier, C., *et al.*, “Recent modelling features in the COPERNIC3 AREVA NP fuel rod performance code”, TopFuel 2006, 2006, Salamanca, Spain, pp. 538-542.
8. Garnier, C., *et al.*, “The COPERNIC3 project: How AREVA is successfully developing an advanced global fuel rod performance code”, 2007 LWR Fuel Performance Meeting/TopFuel, 2007, San Francisco, USA, American Nuclear Society, pp. 603-612.
9. Sutharshan, B., *et al.*, “New developments in fuel performance modelling”, TopFuel 2006, 2006, Salamanca, Spain, pp. 112-116.
10. Manngård, T., “Evaluation of the FRAPTRAN-1.3 computer code”, SKI, SKI Report 2007:15, March 2007.
11. Van Uffelen, P., *et al.*, “Extending the application range of a fuel performance code from normal operating to design basis accident conditions”, Journal of Nuclear Materials (in press), (2008).
12. Uchida, M., Nakamura, J., and Otsuba, N., “FRETA-B: a computer code for the analysis of fuel rod bundle behaviors under accident conditions”, Japan Atomic Energy Research Institute, JAERI-M 9485, 1981.
13. Uchida, M., “Application of a two-dimensional ballooning model to out-pile and in-pile simulation experiments”, Nuclear Engineering and Design, 77(1984), pp. 37-47.
14. Papin, J., *et al.*, “IRSN R&D studies on high burn-up fuel behaviour under RIA and LOCA conditions”, TopFuel 2006, 2006, Salamanca, Spain, pp. 274-278.
15. Compendium of ECCS research for realistic LOCA analysis, NRC, NUREG-1230, Dec. 1988.
16. Fasrvacque, M., “Users’ manual of CATHARE 2 V1.3 E.”, STR/LML/EM/91-61.
17. Lerchl, G. and Austregesilo, O.H., “ATHLET MOD 1.1, Cycle C, Users’ Manual”, Gesellschaft fuer Anlagen- und Reaktorsicherheit, 1995.
18. Computer code: Calculation of transient regimes of power plants with VVER reactors: DINAMIKA 5M, Technical Specifications No. 8624606.00311-019101-LU, GKAE-OKB. 1987, Moscow, Russia: Gidropress.
19. Miettinen, J. and Hämäläinen, A., “Development and validation of the fast running thermohydraulic model SMABRE for simulator purposes”, 8<sup>th</sup> International Conference on Nuclear Engineering (ICON-E-8), 2000, Baltimore, Maryland, ASME, pp. ICONE-8188.
20. Puska, E.K., *et al.*, “APROS simulation system for nuclear power plant analysis”, 3<sup>rd</sup> JSME/ASME Joint International Conference on Nuclear Engineering., 1995, Phoenix, USA.
21. Hanna, B.N., “CATHENA: A thermohydraulic code for CANDU analysis”, Nuclear Engineering and Design, 180(1997), pp. 113-131.

## **9. ENERGY AND CORE DAMAGE DISTRIBUTION ASSESSMENT: METHODOLOGIES AND RESULTS**

Energy and damage distribution calculations of reactor core damage in a LOCA are necessary in order to assess the radiological consequences of a LOCA as discussed to some extent in Section 4.3 of the present report. The extent of fuel cladding rupture during a large break LOCA is dependent on a number of factors. Foremost is the number of rods in the core that achieve high cladding temperatures during the transient. This is a function of the rod power census and the ECCS design capability. Another important factor is the cladding pressure differential for the various rods, which is affected by the initial helium fill pressure, the fission gas generation and fission gas release from the fuel with burn-up, the fuel rod power and the coolant pressure.

### **9.1 A review of core damage assessment practices in Europe**

In 2000, the European Commission issued a report with the slightly misleading title “Fuel cladding failure criteria” [1-2]. The report presents the results of a collaborative exercise concerned with the calculation of the extent of fuel clad failure following a large loss-of-coolant accident (LOCA) in light water reactors. The partners in the collaborative study were Tractebel (Belgium), IPSN and EdF (France), Siemens and GRS (Germany), NRG (Netherlands), IBERDROLA (Spain), ERI (Switzerland) and NNC (UK). The objectives of the exercise were to:

- Review the existing clad failure criteria and licensing approaches in each participant’s country.
- Form a consensus view on clad failure criteria.
- Determine the effect of the clad failure criteria on the extent of clad failure for a reference design in each participant’s country.

The report describes in great detail the methodologies used by the different organisations of how fuel rods are calculated to fail. There are basically two types of failure criteria: the empirical failure criterion based on NUREG-0630 [3] or a more mechanistic failure criterion based on knowledge of creep properties and expected azimuthal temperature differences for the rods in a fuel assembly.

The mechanistic model applies best-estimate creep models for each specific cladding material under consideration. The knowledge of rod power, burn-up and the thermo-hydraulic events during the LOCA is taken as a basis for the failure calculation. All these calculations rely on computer codes as described in Chapter 8. A typical flow chart for a deterministic calculation of fuel failure rates is shown in Figure 9.1.

In contrast to that, the empirical NUREG-0630 model ignores the cladding creep. It provides a simple relation between the mechanical load on the undeformed cladding and the rupture temperature of the cladding.

The NUREG-0630 correlation is:

$$T_R = 3960 - \frac{20.4\sigma}{1+H} - \frac{8.51 \times 10^6 \times \sigma}{100(1+H) + 2790\sigma} \quad (9-1)$$

where       $T_R$  =    rupture temperature ( $^{\circ}\text{C}$ )  
                $\sigma$  =    hoop stress (kpsi)  
                $H$  =    ramp rate ratio ( $^{\circ}\text{C}/\text{s}$  to  $28\ ^{\circ}\text{C}/\text{s}$ )

$$\sigma = \frac{d\Delta P}{2t}$$

where       $d$  =    undeformed cladding mid-wall diameter (inches)  
                $t$  =    undeformed cladding thickness (inches)  
                $\Delta P$  =    differential pressure across the cladding wall at the time of  
                         rupture (kpsi)

As an alternative to the deterministic analysis, probabilistic analyses are made. These analyses also use the deterministic codes for the production of statistical data based on statistical distributions of the input data. However, it may be quite cumbersome to run through a code for each randomly selected set of input parameters. Therefore, a subset of the input data is run with the code to produce a so called response surface which establishes a regressive relationship between the input and output data sets. This response surface is subsequently used for calculating the output data from random input data. Figure 9.2 shows the probability of fuel rod failure as a function of rod power for different burn-ups. It is clear that the failure probability increases steeply with burn-up. With the knowledge of the failure probabilities or alternatively a deterministically established failure threshold as a function of burn-up overviews of core damage due to a LOCA can be constructed as can be seen in Figure 9.3. For the particular case calculated in Figure 9.3 only a few rods at a burn-up of 10-15 MWd/kg exceeds the failure threshold.

A comparison of the results of the different participants led to the following conclusions:

- Mechanistic and the non-mechanistic NUREG-0630 fuel failure models can be used to evaluate best estimate fuel failure fraction because they are in good agreement with experimental data. The NUREG-0630 model provides a conservative approximation of the fuel rod burst compared to the mechanistic model, because the mechanistic model allows the consideration of the fuel rod ballooning which is a consequence of the cladding creep under stress and temperature.
- Of the parameters that cause fuel clad failures, the clad temperature is certainly one of the most important. It is thus not surprising that failures happen primarily in the hot rods.
- The other important parameter is the rod internal pressure. The lower value of internal pressure in BWR rods causes fewer fuel failures in comparison with a PWR. The internal rod pressure can also be influenced by modifying the volume of the gas plenum of the fuel rods. As a consequence, the fuel design is of importance. For a given design, the internal pressure increases with the burn-up. In contrast, the expected peak linear power decreases with burn-up much faster than the threshold value of fuel failure.
- The performed calculations show that the combination of both effects causes rods to fail at a burn-up lower than 35 GWd/te, except for MOX rods, which could fail at higher burn-ups.

Figure 9.1 Determination of fuel failure rate after LOCA with deterministic method (Siemens)

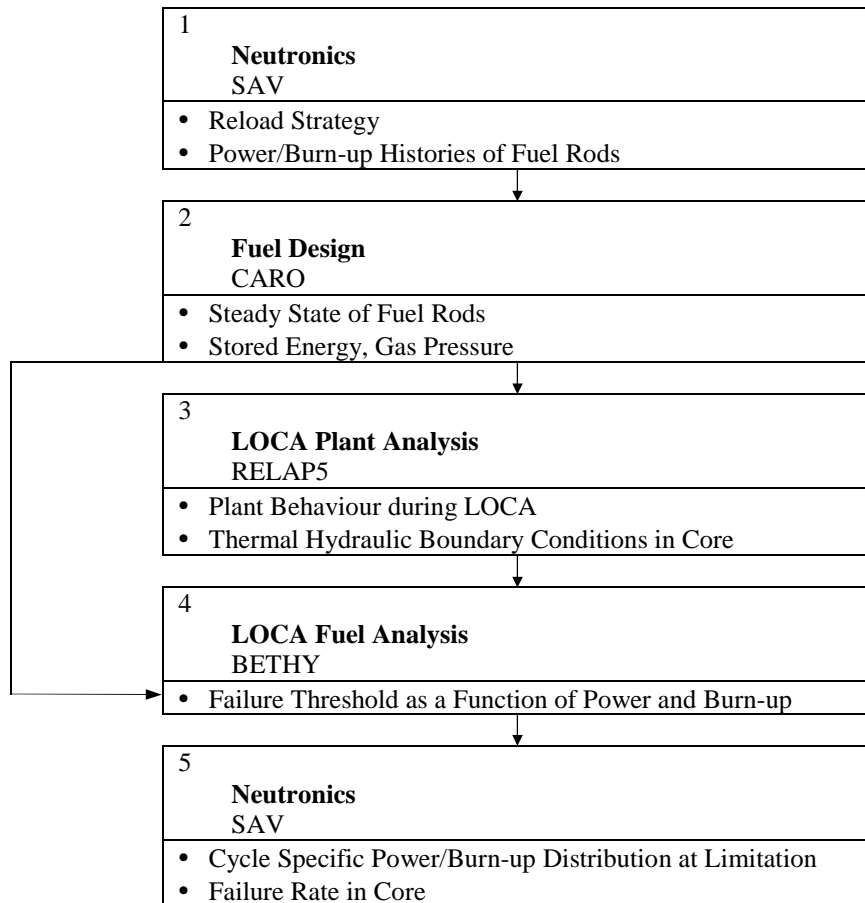
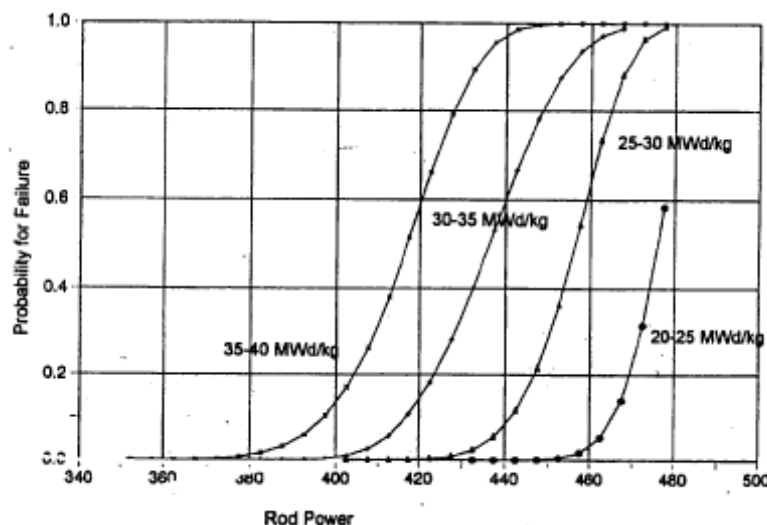


Figure 9.2 Probability for fuel rod failure as a function of rod power at different burn-ups (Siemens)



Despite the fact that all participants used different models and codes, there was agreement with regard to the best-estimate result of the number of failed rods, no failures at all as can be seen in Table 9.1.

**Figure 9.3 Power and burn-up distribution in a core with failure threshold**  
 Each number gives the number of fuel rods at the particular power-burn-up combination (Siemens)

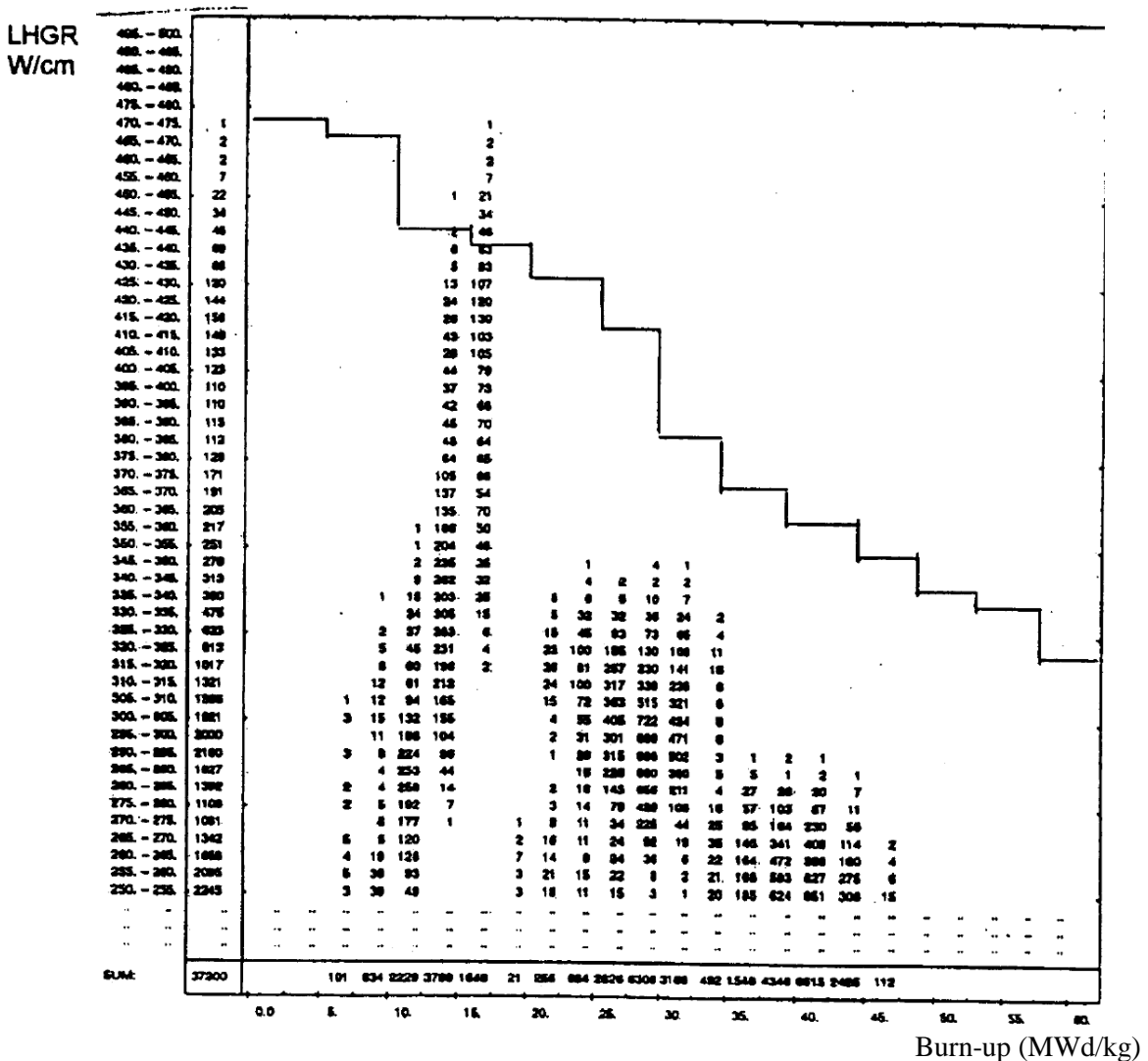


Table 9.1 Best estimate analyses of percentage of fuel rod failures [1]

<b>Participants</b>	<b>Boundary conditions</b>	<b>Rupture criterion</b>	<b>Failed fuel fraction (%)</b>
NNC	Best Estimate	NUREG-0630 B.E.	0
EdF	Cons./B.E.	NUREG-0630 B.E.	0
EdF	Cons./B.E.	EDGAR bundle	0
IBERINCO	Conservative	NUREG-0630 B.E.	0
GRS ( $\text{UO}_2$ )	Conservative	NUREG-0630 B.E.	3.2
Siemens	Best Estimate	Mechanistic B.E.	0
Siemens	Best Estimate	NUREG-0630 B.E.	0
NRG	Best Estimate	NUREG-0630 B.E.	0

When judging the results mentioned above one should keep in mind that the results reported in [1] and [2] have generic character only. That is, the underlying thermal hydraulic transient, the cladding material investigated (fresh Zry-4, no hydrogen up-take in cladding, etc.) and the fuel rod design are arbitrarily chosen.

From the common licensing practice in Germany, it is known that the failed fuel fraction sometimes reaches values close to the licensing limit of 10%. This is the case if conservative thermal-hydraulic boundary conditions and conservative assumptions for the operation mode of the reactor are combined with realistic power histories of the fuel rods in the normal operation phase before the LOCA event.

The latest trend in proofing the licensing limit in Germany is to account for the power history of each fuel rod in the core in order to keep closest track on the best-estimate fuel rod internal pressure. This development of the licensing procedure is the consequence of the enhanced utilisation of MOX fuel, of cores loaded with power up-rated fuel rods and the permanent increase of the discharge fuel burn-up. An example of such a calculation is given in Section 9.3.

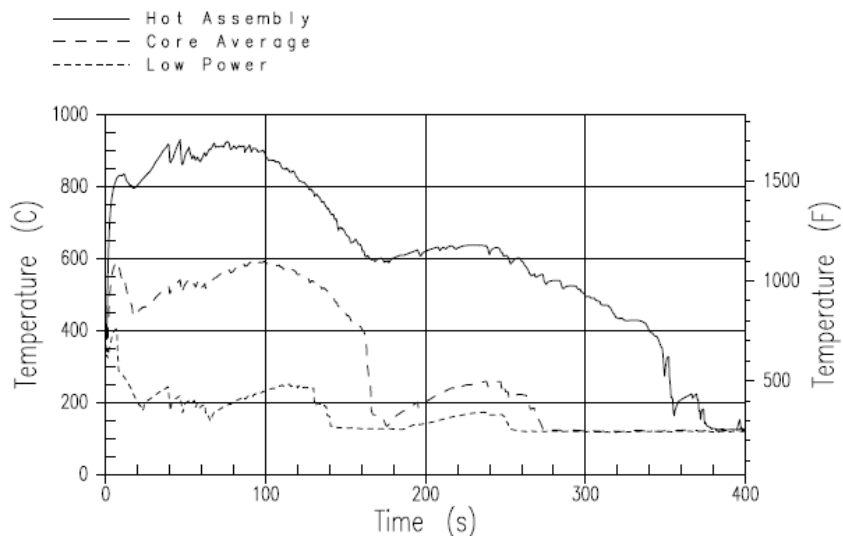
## 9.2 Damage assessments for a Westinghouse PWR

A common practice in USA for assessment of the radiological consequences of a LOCA is to assume that 100% of the rods in the core fail. On the other hand it may be instructive to consider what a realistic failure fraction might be under more representative conditions. One such study has been reported by Nissley *et al.* for a 4-loop Westinghouse PWR [4]. The study was done in two parts. The first part dealt with a 3 600 MWt reactor with  $17 \times 17$  fuel assemblies and used deterministic calculations. The other part concerned a 3 216 MWt reactor with  $15 \times 15$  fuel assemblies and used a statistical analysis.

In the first analysis, it was assumed that a full train of ECCS was lost in order to ensure some cladding rupture. It was also assumed that peaking factors were 15% higher than the maximum expected values. On this basis, cladding temperature response was calculated with the code WCOPRA/TRAC. A few examples are shown in Figure 9.4. On the basis of cladding temperature distributions, the internal pressure was calculated and compared to an empirically determined burst temperature versus hoop stress curve for the Zirlo cladding used. With the core loading assumed, the fraction of assemblies with ruptured rods was about 10%.

This assessment of a conservatively assumed base load power distribution was compared to design basis results using an NRC-approved uncertainty methodology. The comparison showed that the realistic assessment resulted in a peak cladding temperature of 944°C compared to 1 140°C for the design basis calculations. The ECRs at burst locations were 1.4% and 12% respectively and in non-burst rods 0.8% and 6%.

**Figure 9.4 Peak cladding temperature response for deterministic assessment of extent of rupture**



The statistical study used a sampling of 59 separate large break LOCA transients, each with its own combination of randomly sampled uncertainty parameters. According to the statistical theory, the most limiting of the 59 cases will bound at least 95% of the actual PCT distribution, with 95% confidence. The goal of the assessment was to examine the extent of local oxidation within and away from the ballooned region for the most limiting cases, and assess to what degree the limiting PCT elevation and the cladding rupture elevation were coincidental. Table 9.2 shows the results for all of the cases above 925°C.

**Table 9.2 Cases of peak clad temperature (PCT) above 925°C**

Case	1	2	3	4	5	6	7	8	9
PCT (°C)	1 037	1 035	995	973	964	959	933	928	925
ECR (Burst), %	2.1	1.6	1.0	1.4	1.2	1.3	1.4	1.0	1.0
ECR (Non Burst)	1.0	1.0	1.7	0.7	0.6	1.2	1.3	0.5	0.6
PCT @ Burst?	No	No	No	No	No	No	No	No	No
Burst Strain (%)	40	44	47	44	38	48	60	39	24
Packing Fraction*	0.66	0.78	0.65	0.75	0.62	0.67	0.71	0.69	0.67

\* Fraction of the available volume at the rupture elevation that contains pellet fragments following relocation.

Below this threshold, oxidation levels are very low. The most limiting PCT case (1 037°C) is seen to also correspond to the maximum local oxidation case (2.1%). The maximum local oxidation occurred at the rupture elevation in this case, but the PCT did not.

Nissley *et al.* summarise with the following observations and conclusions:

- The extent of core-wide fuel cladding rupture which would actually be expected in a large break LOCA is far less than the 100% assumed by many US licensees in their radiological dose calculations. Even assuming the worst single failure and a conservative normal operating power shape with linear heat rates 15% higher than predicted, less than 10% of the rods in the core were estimated to have cladding failures.
- Significant margins exist between realistic estimates of PCT and ECR, and those resulting from design basis analyses. Even assuming the worst single failure and a conservative normal operating power shape with linear heat rates 15% higher than predicted, the PCT was reduced by ~200°C, and the ECR was reduced to negligible amounts compared to the design basis analysis results.
- The rupture location tends to have the maximum ECR, due to thinning of the cladding and double-sided oxidation.
- PCT frequently occurs away from the rupture location, for plants that have a certain LOCA transient response (e.g., 4-loop plants with large dry containment designs).

Finally Nissley *et al.* notes that the information presented in these large break LOCA assessments should be interpreted as illustrative and representative. Extent of rupture and degree of oxidation are highly dependent on the transient conditions, which are highly dependent on plant-specific parameters such as core power, nuclear peaking factors, ECCS capacity and other factors.

### 9.3 A German example of core damage extent analysis

In a recent presentation Heins has outlined the current procedure to calculate core damage extent in German reactors [5]. The German requirements for LOCA analyses differ from most other countries. In addition to the common LOCA criteria it is also necessary to show that less than 10% of the fuel rods rupture during a LOCA in order to secure that the radiological consequences will be limited. For each PWR, this requirement must be met in each fuel cycle. The analysis must be

performed both at the beginning and end of the fuel cycle. According to Heins, future analyses will be performed with a statistical approach as shown in Figure 9.5. This can be compared to the flow chart shown in Figure 9.1. The result of a core damage extent analysis is shown in Figure 9.6.

Figure 9.5 Flow chart over statistical damage assessment for German PWRs

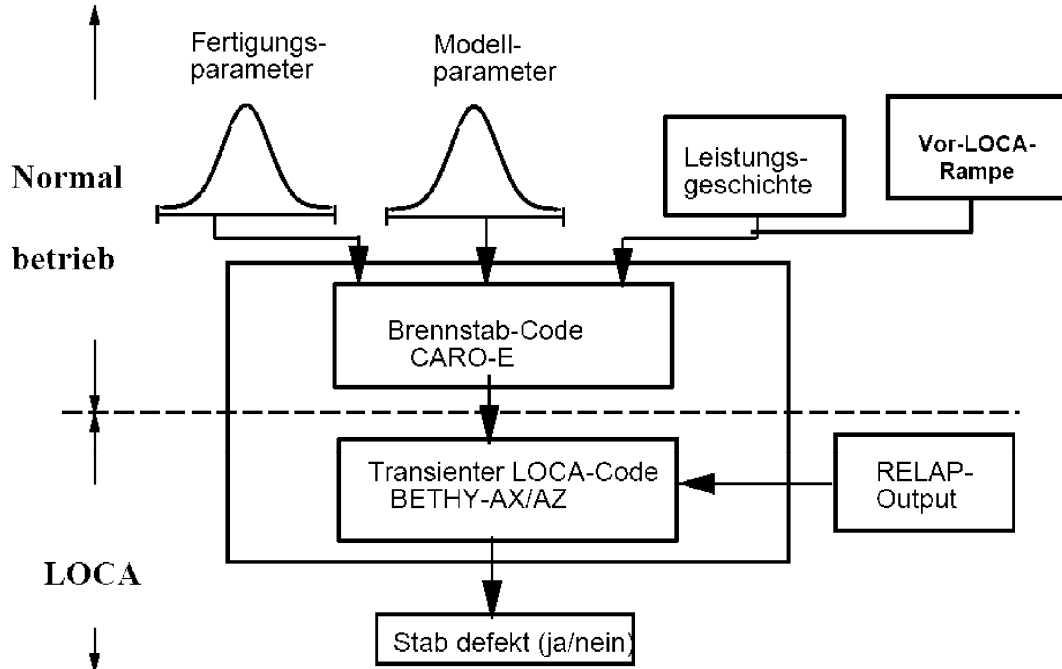
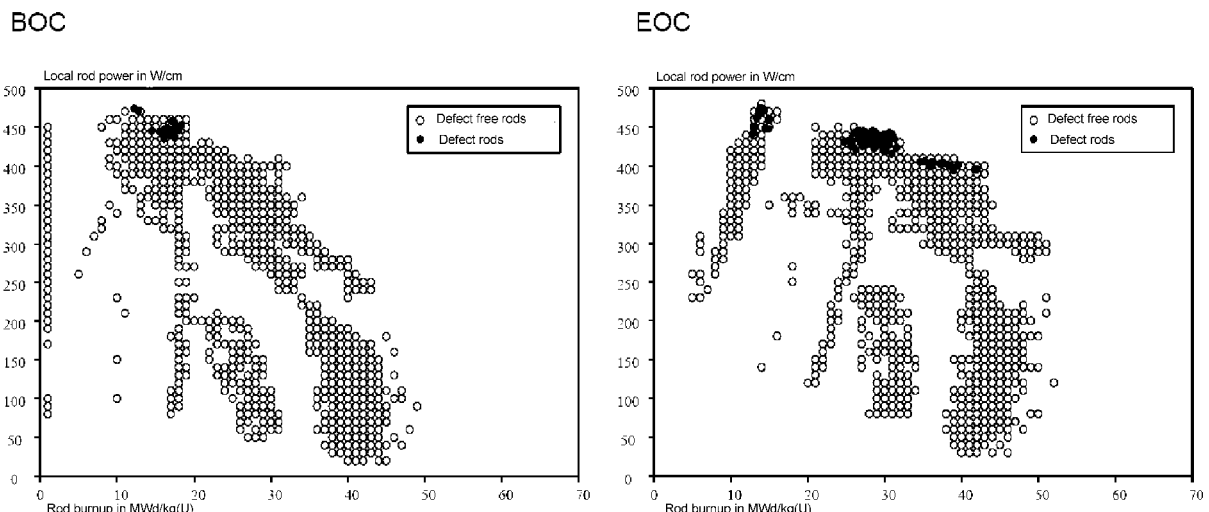


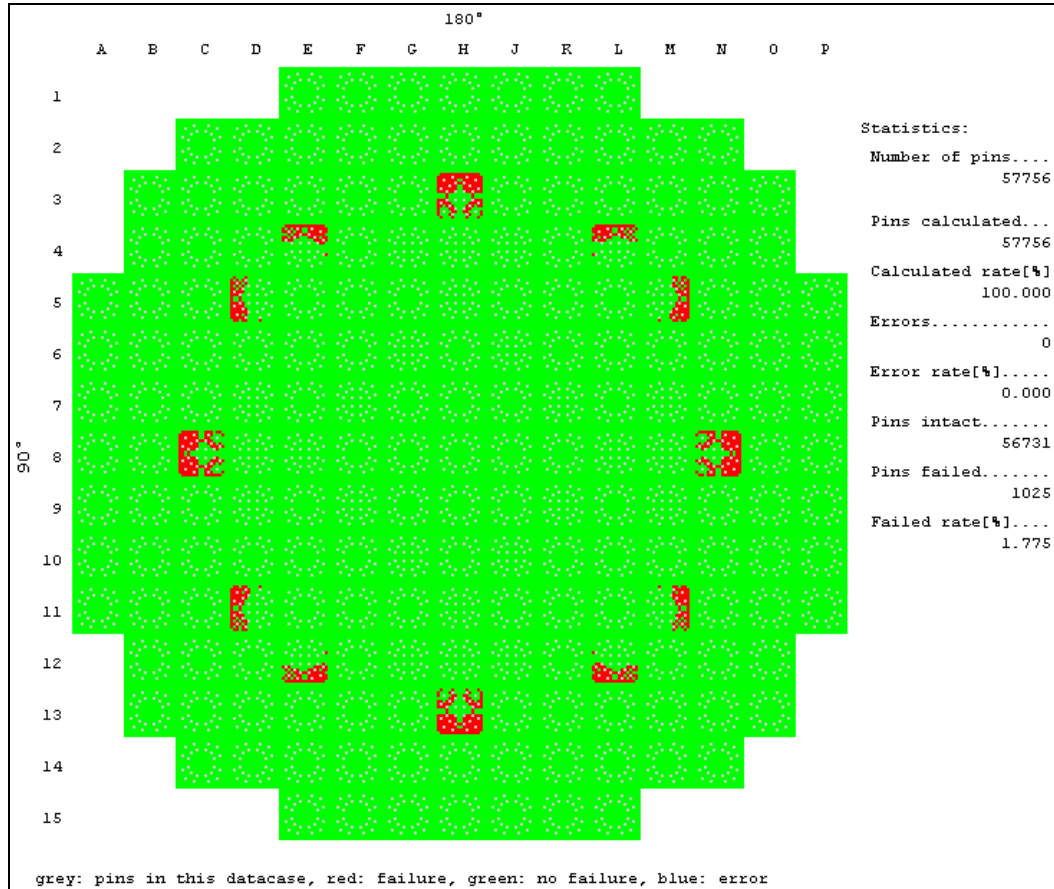
Figure 9.6 Map over core damage extent in German PWR after a large break LOCA



A further alternative, recently introduced in Germany, is a deterministic calculation of the lifetime of each individual fuel rod of the core and a subsequent LOCA-transient. Such calculations use the material and geometrical data and the power history of the individual fuel rods. Based on the calculated actual strain and stress values, the failure/non failure is derived according to the mechanistic failure criterion implemented in the code. Performed for all fuel rods of the core of a specific reload

this procedure provides the number of failed fuel rods (respective failure rate) in a core through a LOCA transient (Figure 9.7).

Figure 9.7 Number of failed fuel rods/failure rate during LOCA



#### 9.4 References

1. Fuel cladding failure criteria, European Commission, EUR 19256EN, September 1999.
2. Bratby, P.A.W., Dutton, L.M.C., and Sutherland, L., "Fuel cladding failures following a large LOCA", NNC Report C5665/TR/006, Issue 01, May 1999.
3. Powers, D.A. and Meyer, R.O., "Cladding swelling and rupture models for LOCA analysis", NUREG-0630, April 1980.
4. Nissley, M.E., Frepoli, C., and Ohkawa, K., "Realistic assessment of fuel rod behavior under large-break LOCA conditions", 2004 Nuclear Safety Research Conference, 2004, Washington DC, NRC, pp. 258-273.
5. Heins, L., "Core damage extent analysis to fulfil an additional LOCA criterion", SEGFSM Topical Meeting on LOCA Issues, 2004, Argonne, USA.

## **10. CONCLUSIONS**

In 1986, a Working Group of the Committee on the Safety of Nuclear Installations (CSNI) issued a state-of-the-art report (SOAR) on water reactor fuel behaviour in design basis accident (DBA) conditions. The 1986 report was limited to the oxidation, embrittlement and deformation of PWR fuel in a loss of coolant accident. The current state-of-the-art report on fuel behaviour in LOCA conditions is an updated version that describes phenomena of importance in the loss-of-coolant-accident (LOCA). New information has been produced concerning these phenomena. Older cladding materials have been replaced by newer alloys that may behave differently under postulated accident conditions. There is also a clear need to include discussions on accident issues for other water cooled reactor types. This is especially important now when the Eastern European countries have joined the discussion on nuclear safety issues.

### **LOCA methodology and criteria**

In the design of nuclear power plants, the consequences of hypothetical accidents are analysed so that suitable mitigating systems can be devised. For design basis accidents, a fundamental acceptance criterion is that there should be no or very limited radiological consequences to the public. In order to fulfil this criterion, derivative acceptance criteria have been formulated for the safety systems of the reactor.

For the pressurised water reactor, a design basis loss-of-coolant-accident involves the break of one of the large coolant pipes between the reactor vessel and the main circulation pump. In order to mitigate the consequences of this break, it is necessary to design the emergency core cooling systems so that the fuel is cooled efficiently during all phases of the accident. This requirement naturally leads to a criterion that the fuel must maintain its coolable geometry throughout the whole LOCA sequence and that the structural integrity of the fuel rods is maintained.

The requirement of coolable geometry and structural integrity has turned out to be a very complex issue due to the particular properties of the zirconium alloys used as cladding for the fuel. During the event, the cladding heats up to temperatures over 1 000°C. When the temperature reaches about 800°C, zirconium starts to transform from  $\alpha$  to the  $\beta$  phase. Oxygen dissolves in the metal and embrittles the  $\alpha$  phase. Therefore, there must be a limit on the oxygen-stabilised  $\alpha$  phase, since the load bearing prior  $\beta$  layer must not be too thin in order to ensure structural integrity of the fuel during the quench phase of the LOCA.

There are many other issues which also must be taken into account. When the fuel rods heat up during the LOCA and the external pressure is lost, the rod internal pressure is large enough to cause plastic deformation of the cladding which leads to ballooning and burst. The ballooning can potentially be detrimental to cooling of the fuel assemblies and the burst of a rod also leads to cladding oxidation from the inside. In addition, a significant amount of hydrogen is picked up by the cladding. Hydrogen pickup significantly exacerbates cladding embrittlement, especially after the quenching phase. Finally, at elevated temperatures, the rate of steam-cladding oxidation may become so high that the heat can no longer be adequately dissipated by cooling, and eventually lead to autocatalytic oxidation. If not arrested, cladding metal and reactor core can melt.

Most fuel safety criteria are based on the criteria applied by the United States Nuclear Regulatory Commission (USNRC). These are found in Title 10 of the United States Code of Federal Regulations, Part 50 (10 CFR 50).

There are three specific points that are the focus of the current NRC criteria:

- The calculated maximum fuel element cladding temperature shall not exceed 2 200°F (1 204°C).
- The calculated total oxidation of the cladding shall nowhere exceed 0.17 times the total cladding thickness before oxidation.
- The rate of energy release, hydrogen generation, and cladding oxidation from the metal/water reaction shall be calculated using the Baker-Just equation.

The purpose of the first two criteria, regarding maximum cladding temperature and total oxidation, was to ensure that the cladding shall remain sufficiently ductile so that it does not break up and fragment during and after the quench phase of the LOCA transient. Another important purpose of the 2 200°F limit was to ensure that fuel cladding does not enter the regime of runaway oxidation and uncontrollable heat-up.

These criteria require a thorough understanding of zirconium properties and behaviour. Beginning only in the early 1970s, it was understood that embrittlement of zirconium-based cladding is caused by the diffusion of oxygen into the metal underneath the surface oxide rather than by the surface oxide itself. That is, cladding structural integrity is really controlled by the small fraction of oxygen atoms that are dissolved in the remaining metallic zirconium layer. In calculating oxygen distribution in the metallic layers, the NRC regulations used the time required to accumulate 17% oxidation as a surrogate measure of the time required to diffuse enough oxygen into the underlying metal to embrittle it.

Many countries have adopted the US NRC criteria. The exceptions include Japan, which has adopted a maximum oxidation value of 15% instead of the usual 17%. The Japanese criteria on cladding embrittlement, 15% and 1 200°C, are not based on the concept of zero ductility of cladding, but on the failure threshold value determined in the integral thermal shock tests under restrained conditions.

The Czech Republic uses a value of 18% for VVER 440 reactors but retains the 17% value for VVER 1000 reactors. The 18% ECR-value is also applied in Russia. However, this value is based on quench test results rather than on ring compression tests, which are judged to be more restrictive. Most countries have adopted the US NRC peak cladding temperature limit of 2 200°F (~1 200°C).

In Canada, there is no formalised cladding oxidation or peak cladding temperature limits. In Germany, in addition to the maximum temperature and oxidation limits, an additional requirement is imposed that the fraction of burst fuel rods shall not exceed 10% of the total rods in the core. The purpose of this requirement is to limit fission gas release due to cladding burst.

A comprehensive description of loss-of-coolant accident scenarios begins with the pressurised water reactor (PWR). The design basis accident in the PWR is a double-ended guillotine break in a cold leg between the reactor coolant pump and the reactor vessel.

In this event, a short blow-down period occurs as a result of the break through which the primary coolant is rapidly expelled. The core voids and negative void reactivity rapidly shuts down the reactor. The primary system pressure decreases and the high-pressure safety and accumulator injection begin,

but most of this flow is lost out of the break. As the blowdown progresses, the lower plenum begins to fill with accumulator water. While the lower plenum is refilling, the core heats up due to decay heat. Some fuel rods balloon and burst.

When the lower plenum has filled, core refill begins. The lower elevations quench first as the quench front moves upward through the core. As the front advances, the fuel rod upper elevations are cooled by a two-phase mixture of superheated steam and entrained droplets. Eventually, there is sufficient cooling to terminate the increase in cladding temperature.

For smaller breaks, the primary system depressurises to the high-pressure safety injection set point and high pressure safety injection begins. Smaller breaks do not depressurise the reactor coolant system because the reactor charging flow can replace the lost inventory. The limiting small-break LOCA is one that is large enough that the high-pressure safety injection system cannot make-up the mass loss from the reactor system but small enough that the reactor system does not quickly depressurise to the accumulator set point.

In the BWR/6 boiling water reactor, the design basis accident is a double-ended break in the suction-side of the recirculation line. Shortly after the break, the reactor scrams, typically on drive flow pressure. Because of the large flow reductions caused by this event, there is a large increase in the core average void fraction. The negative void reactivity rapidly shuts down the reactor.

With the loss of core flow, cladding temperatures rapidly increase. Blow-down peak cladding temperature is dominated by the stored energy in the fuel. As depressurisation continues, there is a large amount of flashing of the fluid in the lower plenum. This causes an increase in the coolant flow through the core, quenching the fuel, and temporarily returning the core to saturation temperature.

Depressurisation continues, and the level inside the core region decreases. The flow into the core is limited and the core uncover leads to a second boiling transition. High pressure core spray system begins to deliver coolant to the top of the core. The low-pressure injection begins when the system pressure drops below the shutoff head for the pumps. The core refills before the lower plenum. The refilling and reflooding processes restore the liquid inventory in the core and quench the core.

The BWR/4 is similar, but core reflood takes somewhat longer than in a BWR/6. The BWR/2 is the older-generation BWR without jet pumps. The core cannot be reflooded. The peak cladding temperature is controlled by a balance between decay heat and the core spray heat transfer. Typically, the peak cladding temperature occurs late in the transient and quenching of the fuel rods is very slow.

In 2004, the Nuclear Regulatory Commission stated that the NRC staff should determine an appropriate risk-informed alternative break size and that breaks larger than this size should be removed from the design basis event category.

Based on the above Commission guidance, the staff prepared a proposed rule that contained alternative evaluation requirements. The proposed rule would divide the current spectrum of LOCA break sizes into two regions. The division between the two regions is determined by a “transition break size” (TBS). The first region includes small breaks up to and including the TBS. The second region includes breaks larger than the TBS up to and including the double-ended guillotine break of the largest reactor coolant system pipe.

Pipe breaks in the smaller break size region are considered much more likely than pipe breaks in the larger region. Consequently, each region would be subject to requirements commensurate with the relative likelihood of breaks in that region. LOCAs in the smaller region would continue to be “design basis accidents” and would continue to be analysed by current methods, assumptions, and criteria.

LOCAs in the larger region, up to and including a break of the largest reactor coolant system pipe, must be mitigated but the analysis may be more realistic. This rule remains under consideration.

In a CANDU reactor, the fuel is loaded into horizontal pressure tubes, and is cooled by the flow of pressurised heavy water. The moderator is heavy water contained in a calandria vessel. The pressure tubes pass through the calandria vessel and are separated from the moderator by a calandria tube and a CO<sub>2</sub> filled annulus. Coolant is supplied to the pressure tubes via a system of large headers and smaller feeder pipes.

In broad terms, a LOCA in a CANDU follows a similar sequence to that described for a PWR. A break in the heat transport system initiates reactor shut down. There is an initial period of blowdown as the pressurised coolant vents from the system. As the coolant pressure drops, cooling is degraded and the fuel undergoes a temperature transient. Initiation of emergency core cooling system re-floods the reactor core, cooling the fuel and terminating the accident.

Despite these similarities with the PWR LOCA sequence, the horizontal pressure tube design and heavy water moderator mean that the details of the accident progression are quite different. The presence of the moderator around the fuel channels also plays an important role as a heat sink during the accident. Hence the determination of the pressure tube behaviour plays an important role in CANDU safety analysis.

The VVER is a pressurised water reactor, and the VVER-1000 design is equipped with emergency core cooling and containment spray systems with similar design basis and basic configuration. These systems are redundant with the exception of the ECCS water storage tank, which is common to all subsystems.

### **Phenomena that need to be addressed by experiments and modeling**

The extended operational exposure that accompanies high burn-up causes changes to the fuel and cladding that may affect the fuel rod's ability to withstand the accident without losing its integrity. These changes, which occur gradually over the life of the fuel rod, can be considered as initial conditions for the accident.

There are many changes that occur to the fuel and cladding as a result of prolonged exposure to the irradiation field present in a reactor core, and to the corroding environment and to high temperature. The combination of high temperature, radiation damage, transmutations, mechanical stresses and chemical reactions causes the microstructure of cladding and fuel to evolve considerably during reactor exposure. These changes in microstructure, microchemistry, and macroscopic characteristics of pellet and cladding are responsible for the changes in material behaviour observed at high burn-up. These changes are very complex and difficult to predict in a mechanistic fashion. Of the many changes to the fuel and cladding, it is important to discern which are of greatest importance to determining fuel rod behaviour during LOCA. Some of the more important material degradation phenomena are listed below.

**Fission products.** During normal operation, solid and gaseous fission products are generated within the UO<sub>2</sub> fuel pellet. Whereas the solid fission products generally remain at the birth site, the gaseous fission products are more mobile and distribute widely.

**Rim formation.** Because of <sup>238</sup>U resonance neutron capture near the UO<sub>2</sub> pellet surface, the amount of Pu formed in the fuel is greater at the edge of the pellet than in the centre. This causes the fission rate near the pellet surface to slowly increase with burn-up while the fission rate in the bulk of the pellet decreases.

**Fuel restructuring and macrocracking.** During the initial rise to power, the thermal stresses caused by the pellet radial temperature gradient cause the pellet to crack. Cracked pellet segments relocate outwards toward the cladding. The combined effects of pellet relocation, fuel irradiation swelling, and cladding creepdown result in a closed pellet-cladding gap.

**Pellet-cladding interface.** With the onset of pellet-cladding contact, a bond layer develops between the fuel pellet and the cladding. Pellet-cladding bonding is thought to progress as oxygen atoms diffuse between  $\text{UO}_2$  or  $(\text{U},\text{Pu})\text{O}_2$  and  $\text{ZrO}_2$ , which is formed under irradiation.

A significant increase of the gas volume inside pores and bubbles at the grain boundaries occurs in the rim zone of high burn-up  $\text{UO}_2$  fuel and in the  $(\text{U},\text{Pu})\text{O}_2$  clusters of some mixed-oxide (MOX) fuels. The grain boundary gas inventory is probably one of the more relevant parameters to predict the high burn-up fuel behaviour during accidental events, since it may contribute significantly to transient fuel swelling and gas release.

The difference in operating temperature between reactor types has a significant effect on the state of cladding. The main degradation mechanisms to PWR cladding include uniform waterside corrosion, hydriding and radiation damage.

The main concerns associated with excessive corrosion in PWR cladding are: potential for oxide spalling, degradation of heat transfer, non-uniform or overall wall thinning, and excessive hydrogen uptake and hydriding.

The primary effects of BWR operation on cladding are also waterside corrosion, hydriding, and radiation damage. BWR cladding corrosion thicknesses (as opposed to build-up of other cladding surface deposits) may be significantly less than observed in the PWR. For modern BWR cladding, the primary corrosion-related effects are wall thinning, decreased heat transfer, and hydrogen pickup. Generally, lower hydrogen concentration is observed in BWR fuel cladding than PWR.

For light water reactors, the primary considerations relative to cladding radiation damage are radiation hardening and the corresponding impact on mechanical properties, and deformation caused by irradiation-induced growth and creep.

Although normal nominal burn-up in CANDU reactors is lower than that in light water reactors considerable work has been carried out to study the behaviour of CANDU fuel at higher burn-ups. Fission-gas release is a key performance parameter at extended burn-up. Fuel microstructural changes follow a similar trend.

The different phenomena involved in the heat-up, cool down and quench during a LOCA are more complex than one might think. This complexity results from the changes of properties of the zirconium cladding alloys that occur during the transient. These changes in the fuel and cladding are most easily identified by the sequence in which they occur during the transient.

Typically a LOCA will start with the fuel under normal operating conditions. The cladding then has a temperature slightly above  $300^\circ\text{C}$ . At the pellet cladding interface, the temperature is about  $400^\circ\text{C}$  with higher temperatures within the pellet. At the centre of the pellet, the temperature is perhaps  $1200\text{--}2000^\circ\text{C}$  depending on the local power level. At the start of the LOCA, the fission process ceases due to the loss of moderator and insertion of control rods. With the loss of coolant, the cladding will start to heat-up. The stored energy in the pellet redistributes towards a flatter radial temperature profile but heat-up still will occur due the decay heat. The initial heat-up of the cladding is mainly due to the stored energy of the pellet, but in the longer term, it is the decay heat which is responsible for the heating of the cladding.

During the transient, pressure inside the cladding will increase due to heat-up of the mixture of the fill gas and released fission gases. At the same time, the strength of the cladding is reduced and it will eventually start to deform plastically. It is thus necessary to know the properties of zirconium alloys, which may be very anisotropic, and how they depend on alloy composition.

Another complication is the phase transformation which takes place at temperatures around 800°C and above. Pure zirconium transforms from the hexagonal closed packed phase alpha to the body centred cubic  $\beta$  phase at  $\sim 860^\circ\text{C}$ . Quite clearly a number of different phenomena must be mastered in order to predict the instance of rupture.

The basic parameters controlling deformation in a LOCA are stress, temperature and creep strength, the latter being affected by oxidation, grain size and anisotropy. A temperature transient which produces significant strains is quite likely to strain the cladding to rupture. Since the inherent ductility of zirconium alloys is high, early rupture, at low overall strain, will occur only when the ductility of the material is exhausted locally by non-uniform straining. A prime cause of non-uniformity is circumferential variation in temperature around the cladding, which is the key factor that controls the potential for and the degree of coplanar flow channel blockage.

Deformation under internal pressure was studied in single-rod and multi-rod tests. The main series of multi-rod out-of-reactor tests have been conducted at ORNL, KfK and JAERI. In-reactor tests have been performed on single rods in Germany in the FR-2, Italy in EOLO-JR facility in the ESSOR reactor, France in the FLASH loop in the SILOE reactor and in the United States of America in PBF. The only sources of multi-rod in-reactor data are the series of experiments in the NRU reactor at AECL Chalk River and the PHEBUS series at Cadarache.

The main source of embrittlement, which follows rupture, is the absorption of oxygen into the cladding. The dissolved oxygen embrittles the alpha phase. In addition, significant heat is released when the zirconium oxidizes. At high temperatures, oxidation may be rapid, and the heat from this oxidation can be significant.

Following a LOCA, impaired coolability could result from plastic deformation of the cladding, leading to constriction of the sub-channels between rods, or from fragmentation of the cladding through oxidation and embrittlement. The coolability of a deformed assembly is a key question following the event and has thus been subject to extensive research.

If the external coolant pressure falls to a low value the tensile stress which is produced in the cladding by the internal gas pressure is sufficient to cause plastic distension. The creep strength of zirconium alloys falls rapidly with temperature so that at 700°C and since the ductility of the alloys is high, strains of 50% or more are possible. The spacing (pitch/diameter) of PWR fuel rods is such that adjacent rods straining by 32% will be in contact each to other, and a key question is whether strains of this magnitude or greater can occur in practice in adjacent rods at the same level in the assembly, thus causing water flow blockage.

The cladding plastic straining on the consequent ballooning may also favour the relocation of fuel fragments from above into the ballooning region. This may in turn cause a greater heat generation locally, and thus higher cladding temperature.

The FEBA (Flooding Experiments with Blocked Arrays) program involved performing separate effects tests under different reflood conditions. The main FEBA test result was that temperature in the blockage generally was lower than in the by-pass even with 90% blockage. In cases without by-pass, the coolability was significantly increased.

The SEFLEX (Fuel Rod Simulator Effects in Flooding Experiments) program was designed to evaluate the sensitivity of FEBA-type reflood test results on fuel rod and blockage simulation technologies. The SEFLEX programme results illustrate that better cooldown and significantly earlier cladding rewetting occur within and downstream from the blockage in comparison to the by-pass or during a blockage-free test.

The THETIS program, carried out by the United Kingdom Atomic Energy Authority, involved a set of thermo-hydraulic tests on an assembly containing 49 full-length fuel rod simulators with a severe blockage of 80 or 90% over a length of 20 cm. Results of these tests indicated that with a 3 cm/s reflood rate, the blockage was found to be coolable. The THETIS test results seem to imply that a long 90 percent blockage may no longer be coolable at a constant reflood rate below 2 to 3 cm/s.

The FLECHT SEASET program (Full Length Emergency Cooling Heat Transfer – Separate Effects and System Effects Tests) was an extensive programme that was launched in 1977 in cooperation between USNRC, EPRI and Westinghouse. For the non-coplanar blockages, the temperatures were generally lower in the blocked region compared to the unblocked configuration, with the exception of the short balloons for which there was little difference between the temperatures.

In conclusion, blockages of significant ratios (90 percent) but of moderate lengths (<10 cm) do not create any particular problems in terms of coolability. However, it should not be assumed, that a 90% blockage is always coolable. It has also been demonstrated that the maximum blockage ratio of 90% does not necessarily represent the most penalising case in terms of coolability for axially extended deformations. Furthermore, the significant difference between comparable test results seems to indicate that significant thermal coupling between the heat source and the ballooned cladding – as may exist in a clad balloon full of relocated fuel fragments – is susceptible of significantly hindering the coolability of a blockage with such balloons, in comparison to a case where fuel relocation does not occur.

The OECD Halden Reactor Project is a series of in-pile experiments performed in the Halden Boiling Water reactor, a heavy water cooled and moderated reactor. The goals were:

- (a) To maximise the balloon size to promote fuel relocation, and to evaluate its possible effect on cladding temperature and oxidation.
- (b) To investigate the extent (if any) of – “secondary transient hydriding at high temperature” – on the inner side of the cladding around the burst region in presence of pellet-cladding bonding layer.

In the frame of those tests the first test with pre-irradiated fuel in the Halden Project LOCA test series, was conducted. The results indicate that a large ballooning in the middle of the rod and burst with fuel relocation occurred in one case. However, more experimental evidence and analyses are needed in order to assess the applicability of the results of this particular test to actual power plant situations.

The test with the Russian cladding alloys were performed in PARAMETR-M and TEFSAI-19 facilities in Russia. The test on ballooning carried out in KFKI found the general difference in burst strains between E110 and Zircaloy-4.

Following a successfully terminated large break LOCA, a number of fuel rods will have failed. Large amounts of radioactivity will have reached the containment in the form of gases or particulate aerosols. From a regulatory point of view some of this radioactivity will leak out of the containment and reach the environment outside the nuclear plant where it will cause a dose burden to the public.

The inventory of fission products is distributed unevenly in the fuel rods and not all of them are available for release. The distribution is also strongly burn-up dependent. The part of the inventory

most readily released is the gap inventory consisting noble gases and volatile iodine compounds. In the gap there may also be water soluble fission products like cesium species. The fission products less readily available for release can be slowly leached out from the fuel matrix. The rates of release will depend on the fragmentation of the fuel which may be highly burn-up dependent. With knowledge of fission product distributions and reliable estimates of the number of failed fuel rods, it would (in principle) be possible to reach reasonably realistic numbers for the in-containment source term.

The most complex part of the containment source term problem is the retention in the containment since it also determines the time dependence of the source term. The retention of iodine in the containment and the effect of pH in the sump water may be considered. Other phenomena that should be considered include aerosol CsI removal, radiolysis in the water phase, other reactions in the water phase, reactions in the gas phase, mass transfer from sump to the gas phase, deposition on wall surfaces in the gas phase and formation of organic iodine.

### **Overview of LOCA testing methodology and the tests results**

LOCA testing methodology comprises different techniques. The methodology is classified into the following three groups; separate effects tests aimed at elucidating specific phenomena, tests with moderate integration in which the interaction between two or more phenomena is studied, and integrated tests on rod or fuel bundles in or out of reactor.

The creep properties of cladding alloys are central for modelling the deformation and failure of cladding tubes during a LOCA. Therefore, separate tests for the creep properties have been performed for Zircaloy and Zr-Nb cladding tubes. As a result, information regarding creep equations has been obtained experimentally. However, it is noted that deformation behaviour of the cladding during a LOCA is very complex, and caution is needed in the interpretation of the simulation tests performed under simplified conditions.

High temperature oxidation tests have been conducted to determine oxidation kinetics of the cladding since early 1970s. Temperature measurement technique has been improved and many investigations have been made with different heating methods using resistance furnace, radiant infrared heater, induction heating and internal heating element.

Modelling of the growth of the oxide layer and the oxygen stabilised  $\alpha$  layer requires knowledge on the diffusion coefficients of oxygen in the two phases. In addition, the diffusion coefficient in the  $\beta$  layer is necessary for calculating how fast the  $\alpha$  grows into the  $\beta$  phase. To fulfil this requirement, a few experiments have been conducted to determine appropriate diffusion constants.

In zirconium cladding alloys, the  $\alpha$  phase transforms to the  $\alpha + \beta$  and  $\beta$  phases as temperature increases during a LOCA. The resulting cladding behaviour depends strongly on the phase structure. Therefore, tests have been performed for the basic Zr-O binary system and the Zircaloy-O pseudo-binary system. Tests have additionally been performed because of the recent interest in the  $\alpha$  to  $\beta$  transformation due to the increased use of Nb containing alloys and the expected high hydrogen concentration in high burn-up fuel.

Ductility tests are necessary for determining cladding embrittlement after a LOCA simulation, which is very important to safety. The ring compression test technique has been the most widely used ductility test because it is very straightforward to perform, requires a minimum of specimen preparation and is appropriate when there is a limited amount of material to be tested. However, there seems to be no common definition of an acceptable level of ductility in ring compression tests, though some definitions, based on offset displacement and strain energy, have been proposed and adopted.

Tests with moderate integration have been performed in Canada, France, Japan, Korea, Russia, and the United Kingdom to examine steam oxidation, cladding deformation or ballooning in steam, and constrained deformation or ballooning in steam with or without quench. Some of the tests are still used to investigate high burn-up effect on the cladding deformation and fracture during a LOCA.

Fully integrated tests were performed at FR-2 (Germany), PBF (United States of America), PHEBUS (France). Those tests provided valuable data base for understanding fuel behaviour in the bundle geometry under more realistic LOCA conditions and validation of computer codes in this category. The test series recently performed at the Halden reactor is a very unique program, where the primary objective is to assess the extent and effect of axial relocation of fuel fragments into the ballooning volume. These tests were performed with high burn-up fuels, taking advantage of various in-pile measurement techniques at the Halden reactor.

Zirconium alloy fuel cladding is reactive in steam. The reaction is generally believed to be controlled by the rate of diffusion of oxygen anions in the anion deficient zirconia film. Diffusion controlled solid state processes are characterised by a parabolic rate law. Extensive investigations have been performed mainly with Zircaloy to obtain the parabolic rate law constants for weight gain and oxide layer growth. The oxidation kinetics data of the Zircaloy are available over a wide temperature range from 700 to 1 500°C. Some scatter in the data can be attributed to difficulties in accurate temperature measurement combined with differences in heating technique which produce different temperature gradients across the specimen thickness. The Baker-Just correlation is found to be conservative between ~1 000-1 500°C increasingly so at higher temperatures. Oxidation tests have been also performed with the E110 alloy for VVER and advanced cladding alloys including M5 and ZIRLO for PWR. The results show that E110 oxidizes slightly slower than Zircaloy-4 under conditions of steady scale growth. However, E110 is prone to oxide spalling and may exhibit transition to linear growth kinetics. The oxidation kinetics of M5 appears to be generally very similar or slightly smaller than the kinetics of the Zircaloy-4.

The oxidation of the zirconium alloy cladding changes to linear kinetics with time. The "breakaway" occurs in specific temperature ranges, for example, 850-950 and 1 000-1 050°C in Zircaloy. The breakaway oxidation has been identified as a major problem for the cladding LOCA performance since it is associated with a significant hydrogen pickup which degrades post-quench properties. Therefore, careful examinations are required also for advanced high corrosion-resistance cladding alloys to examine the temperature-time range where the breakaway oxidation occurs.

Virgin cladding was used in most performed oxidation tests. Data have been accumulated to a certain extent on effects of irradiation, alloying elements, pre-oxidizing and pre-hydriding of the cladding, steam purity (addition of nitrogen or air), and high atmospheric pressure. However, more investigations may be required to better understand the oxidation behaviour of the high burn-up fuel cladding.

Current embrittlement criteria limit the maximum cladding temperature and maximum cladding oxidation (fractional cladding thickness which would be converted to zirconia). The criteria were established long ago based on the experimental data that were available at that time mostly on as-fabricated Zircaloy.

In the recent years, there has been considerable testing of the post-quench ductility of current cladding alloys in the United States of America, France, Russia, and Hungary. In the case of Zircaloy, the objective has been to determine the effects of the changes in fuel rods associated with high-burn-up operation, such as due to thick corrosion layer, high hydrogen concentration in the cladding, and pellet-cladding bonding. M5 and ZIRLO are relatively new alloys and data on their LOCA behaviour at all levels of burn-up are needed for safety assessment of fuel fabricated from this new class of cladding. Results show that the embrittlement threshold for, e.g. unirradiated Zircaloy (Zr-Sn) or for

cladding types like M5 and E110 exhibit different embrittlement thresholds. The variations in embrittlement threshold appear to result mainly from manufacturing differences rather than from specific alloy composition. Tests with the so-called pre-hydrided specimens showed a strong effect of hydrogen concentration for Zircaloy-4 cladding. A cooling-rate effect was also seen that was absent in fresh cladding that contained no hydrogen.

Similar tests were then performed on irradiated cladding taken from high burn-up fuel rods with Zircaloy-4, ZIRLO, and M5 cladding. As expected, the embrittlement thresholds in the irradiated materials were found at substantially lower oxidation levels as compared with as fabricated materials. The effect of hydrogen on oxygen solubility in the  $\beta$ -phase has a significant impact on the post-quench ductility of high burn-up cladding and on post-quench ductility of ballooned cladding which have absorbed hydrogen in the oxidation reaction on the inside surface of the cladding. Similar effects may also arise in long-term transients at about 1 000°C when breakaway oxidation leads to significant hydrogen pickup. These effects are not addressed by the present regulatory criteria and hence there is a need to revise criteria.

As discussed in the section on regulatory analysis, recent results on (mostly simulated) high burn-up cladding, new zirconium alloys, and an increased awareness of the consequences of breakaway oxidation in both pre-LOCA and during a LOCA transient has led to the conclusion that current regulation concerning LOCA is somewhat inadequate. As a consequence, a number of workers in the field have proposed changes in the LOCA criteria. Four examples of these proposals are given in the present report.

Oxidation and quenching after rod burst experiments have been performed in Japan to investigate cladding embrittlement and fracture during the quench. The test rods are cooled and quenched under restrained conditions, considering possible loading in the bundle geometry. Data are currently accumulated on the fracture conditions of the high burn-up fuel cladding including M5 and ZIRLO. Although some moderate burn-up effect can be discerned, there is no evidence that the current (15% or 17% ECR) limit need to be lowered at high burn-up, based on the outcome obtained so far by these Japanese tests.

### **Additional remarks**

Codes aimed at predicting the behaviour of a fuel assembly in a LOCA have been developed in several countries. Many of the computer codes used today are the same as or developments of codes that were used at the time of writing of the previous LOCA State-of-the-Art Report in 1986. However there has been a dramatic change in the computing environment. In order to model a LOCA or an experiment simulating a LOCA or a subset of a LOCA event three categories of codes are needed:

- Reactor physics codes.
- Fuel behaviour codes.
- Thermohydraulics codes.

The reactor physics codes provide the starting condition for a LOCA event. Recent developments have included a more advanced graphics user-interface and the merge of reactor physics codes with system thermohydraulics codes.

The fuel behaviour codes can be separated into steady state codes and transient codes. System thermohydraulic codes are typically less design specific and are applied to a wider variety of designs and conditions. A limited number of these codes are widely used around the world by regulatory, research and industry organisations. These codes can typically be used to model a wide range of configurations for single pipes, experimental facilities and full plants and, in many cases, have been applied to most reactor designs around the world.

The documentation requirements on the codes did not change substantially during the last 20 years. Code verification and validation are part of those documents. There is normally a regulatory requirement that codes are validated in relation to relevant experimental data for the major phenomena expected to occur. Three sources of data are generally used to validate these codes: phenomenological data, data on separate effects, and integral data. As a code can sometimes predict a set of data with a high degree of accuracy and still be extremely inaccurate for other data sets a “validation matrix” has been developed for each code through which different types of experimental facilities and different sets of conditions in the same facility are used for code validation. The validation exercises have also included comparisons with relevant data from plant operations and participation in international standard problems.

The uncertainties associated with the algorithms of individual codes or models can arise from several sources, as discretisation, nodalisation, differences in computer architecture, operating systems and numerical accuracy. The estimation of model uncertainties and code uncertainties has been formalised using a range of methods. Fundamental to all methods is the adequacy of the supporting experimental data and the scalability of that basis of data to full plant conditions. Sensitivity studies can also be useful in gaining an understanding of the influence of important modelling parameters.

Representatives of the single rod codes for steady state condition and transients, assembly/channel codes and system hydraulic codes are listed in the report.

Energy and damage distribution calculations of reactor core damage in a LOCA are necessary in order to assess the radiological consequences of a LOCA. The extent of fuel cladding rupture during a large break LOCA is dependent on a number of factors. Foremost is the number of rods in the core that achieve high cladding temperatures during the transient.

The report of EU with title “Fuel cladding failure criteria” [EUR 19256EN] describes in great detail the methodologies used by the different organisations of how fuel rods are calculated to fail.

A common practice in USA for assessment of the radiological consequences of a LOCA is to assume that 100% of the rods in the core fail but a study taking into account more representative condition shows that it is an overly conservative assumption.

In comparison to others the German requirements for LOCA analyses differ from most other countries. In addition to the common LOCA criteria it is also necessary to show that less than 10% of the fuel rods rupture during a LOCA in order to secure that the radiological consequences will be limited. In the future will be this analysis performed with a statistical approach.

## **Recommendations**

WGFS concludes that CSNI and CNRA should consider the following future activities to further refine the nuclear community’s understanding of the key aspects of the water reactor fuel behaviour in LOCA conditions:

- To update the CSNI State-of-the-Art Report on water reactor fuel behaviour in LOCA conditions in suitable intervals, to provide a useful reference for workers in this area.
- Ductility-based LOCA criteria derived from ring compression tests of double-side oxidized specimens, and fracture-based LOCA criteria derived from integral rod testing result in quite different burn-up effect on the derived safety limit. There are thus a number of open questions about the different results and the two different methodologies, which have to be further discussed and assessed.

- The breakaway oxidation, which occurs in specific temperature ranges, has been identified as a major problem for the cladding LOCA performance since it is associated with a significant hydrogen pickup which degrades post-quench properties. Therefore, careful examinations are required also for advanced high corrosion-resistance cladding alloys to examine the temperature-time range where the breakaway oxidation occurs.
- As-fabricated cladding was used in the most performed oxidation tests. Data have been accumulated to a certain extent on effects of irradiation, alloying elements, pre-oxidizing and pre-hydriding of the cladding, steam purity (addition of nitrogen or air), and high atmospheric pressure. However, more investigations may be required to better understand the oxidation behaviour of the high burn-up fuel cladding.

## Appendix A

### TAKING ACCOUNT OF ANISOTROPY IN CREEP CALCULATIONS

#### A1.1 Introduction

In the following a cylindrical coordinate system will be used with axes  $r$ ,  $\theta$ , and  $z$  corresponding respectively to the through thickness (radial), circumferential and axial directions of a cladding tube. For a multiaxial state of stress where the principal stress axes coincide with the coordinate axes yielding or creep is controlled by an effective stress which can be written:

$$\begin{aligned}\sigma_e &= \frac{1}{\sqrt{2}} \left( (\sigma_\theta - \sigma_z)^2 + (\sigma_z - \sigma_r)^2 + (\sigma_r - \sigma_\theta)^2 \right)^{1/2} = \\ &= \left( 0.5(\sigma_\theta - \sigma_z)^2 + 0.5(\sigma_z - \sigma_r)^2 + 0.5(\sigma_r - \sigma_\theta)^2 \right)^{1/2}\end{aligned}\quad (A-1)$$

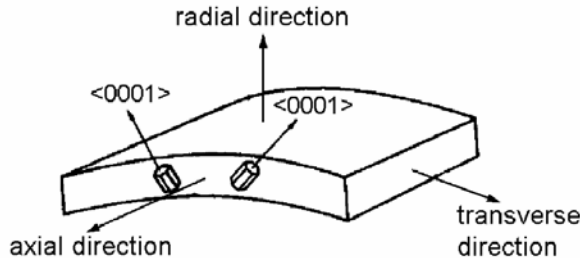
for an isotropic material. For an anisotropic material like Zircaloy the effective stress can be modified according to the following equation proposed by Hill [1]:

$$\sigma_e = \left( F(\sigma_\theta - \sigma_z)^2 + G(\sigma_z - \sigma_r)^2 + H(\sigma_r - \sigma_\theta)^2 \right)^{1/2} \quad (A-2)$$

Many studies of the anisotropy of zirconium alloys have shown that it is actually more complex than the simple ellipsoid yield surface defined by eq. A-2 [2]. However eq. A-2 and its associated flow rule have been widely used for treating the anisotropy of zirconium alloys and it takes the main features of the anisotropy into account much better than the effective stress for an isotropic material.

Figure A-1 shows a schematic picture of the main grain orientations in a zirconium alloy cladding tube.

**Figure A-1 A schematic picture of the main grain orientations in a zirconium alloy cladding tube**



The hexagonal zirconium crystal can deform by many deformation systems, both slip systems and twinning systems [2]. However the by far lowest critical shear stress applies to slip in the  $<1\bar{1}\bar{2}0>$  direction on the  $\{1\bar{1}00\}$  prism planes. Therefore for the texture shown in Figure A-1 we would expect the yield strength to be lowest in the  $z$ -direction, higher in the  $\theta$ -direction and highest in

the r-direction. Normally it is very difficult to test for the yield strength in the radial directions. However the high yield strength is manifested by small reductions in wall thickness when the cladding tube material is subjected to uniaxial tension tests in either of the circumferential or axial directions.

### A1.2 The strain increments for the anisotropic material

The requirement that the strain vector is perpendicular to the yield surface leads to the following equations for the plastic strain increments for a state of stress where the principal stress axes coincide with the coordinate axes which are also axes of the anisotropy:

$$\begin{aligned}\frac{d\epsilon_r}{d\lambda} &= (G + H)\sigma_r - G\sigma_z - H\sigma_\theta \\ \frac{d\epsilon_\theta}{d\lambda} &= (F + H)\sigma_\theta - F\sigma_z - H\sigma_r \\ \frac{d\epsilon_z}{d\lambda} &= (F + G)\sigma_z - F\sigma_\theta - G\sigma_r\end{aligned}\tag{A-3}$$

$d\lambda$  is a common factor which contains the ratio  $d\sigma_e/\sigma_e$ .

### A1.3 Determination of the anisotropy constants

The simplest way to determine the anisotropy constants F, G, and H is to perform uniaxial tensile tests in the circumferential and axial directions and determine the ratios between the strains in the directions perpendicular to the tensile direction. For a test in the circumferential direction we get:

$$R_{zx} = \frac{\epsilon_z}{\epsilon_r} = \frac{F}{H}\tag{A-4}$$

and for a test in the axial direction we get

$$R_{\theta z} = \frac{\epsilon_\theta}{\epsilon_r} = \frac{F}{G}\tag{A-5}$$

Let us as an example assume that we have determined  $R_{zx} = 5$  and  $R_{\theta z} = 4$ . Then  $G = 0.25$  F and  $H = 0.2$  F. If these values are inserted in A-2 we can note that  $\sigma_e$  is proportional to  $F^{1/2}$ . This means that the magnitude of F is arbitrary since it will work as a scale factor for the yield strength we use for comparison with a calculated effective stress. In a case of creep deformation a change of F will give a corresponding change in the proportionality factor in the creep law.

One way to remove the arbitrariness of one of the anisotropy constants is to look at the second formulation of the isotropic yield criterion A-1. We can then note that the sum of the coefficients on the squared differences between the principal stresses is 1.5. It is then some logic in prescribing that:

$$F + G + H = 1.5\tag{A-6}$$

With our previous example we then get  $F = 1.034$ ,  $G = 0.259$ , and  $H = 0.207$ . For an applied uniaxial stress of 100 MPa the corresponding effective stresses for the different directions are for the r direction  $\sigma_e = 69$  MPa, for the  $\theta$  direction 111 MPa and for the z direction 114 MPa. Thus the yield strength in the r direction will be more than 60 % higher than in the other two directions.

#### A 1.4 Application to a case of creep

As an example of how the anisotropy model of Hill is applied to creep we can take a modelling effort by Rosinger who started with uniaxial creep data in the axial direction which was then applied to the diametral creep of cladding stressed by an internal pressure [3]. For the creep in the axial direction, Rosinger found that:

$$\dot{\epsilon}_z = A_z \exp(-Q/RT) \sigma_z^n \quad (\text{A-7})$$

This implies that the effective creep rate as a function of effective stress can be written

$$\dot{\epsilon}_e = A_e \exp(-Q/RT) \sigma_e^n \quad (\text{A-8})$$

The energy expended in the creep process per unit of volume can be written:

$$\dot{W} = \sigma_r \dot{\epsilon}_r + \sigma_\theta \dot{\epsilon}_\theta + \sigma_z \dot{\epsilon}_z = \sigma_e \dot{\epsilon}_e \quad (\text{A-9})$$

where the right hand side constitutes the definition of an effective creep rate. For the case of uniaxial creep in the z direction (A-9) reduces to:

$$\sigma_z \dot{\epsilon}_z = (F + G)^{1/2} \sigma_z \dot{\epsilon}_e \quad (\text{A-10})$$

If (A-10) is combined with (A-8) and (A-9) we find that:

$$A_e = A_z (F + G)^{-(n+1)/2} \quad (\text{A-11})$$

For the case of creep with an internal pressure we have  $\sigma_z = 1/2\sigma_\theta$  and the creep law we want to use is:

$$\dot{\epsilon}_\theta = A_\theta \exp(-Q/RT) \sigma_\theta^n \quad (\text{A-12})$$

A relationship between  $A_\theta$  and  $A_e$  can be found by using (A-8) and (A-9). The latter equation get the following form for diametral expansion with an internal pressure:

$$\begin{aligned} \dot{W} &= \sigma_\theta \dot{\epsilon}_\theta + \sigma_z \dot{\epsilon}_z = \sigma_\theta \dot{\epsilon}_\theta + 0.5 \frac{G - F}{F + 2H} \sigma_\theta \dot{\epsilon}_\theta = \\ &= \frac{2H + 0.5(F + G)}{F + 2H} \sigma_\theta \dot{\epsilon}_\theta = \sigma_e \dot{\epsilon}_e = (H + 1/4(F + G))^{1/2} \sigma_\theta \dot{\epsilon}_e \end{aligned} \quad (\text{A-13})$$

Combining this result with (A-8) and (A-12) gives:

$$A_e = \frac{1}{(H + 0.25(F + G))^{\frac{n-1}{2}} (H + 0.5F)} A_\theta \quad (\text{A-14})$$

(A-14) combined with (A-11) give us as a final result that:

$$A_\theta = \frac{(H + 0.5F)(H + 0.25(F + G))^{\frac{n-1}{2}}}{(F + G)^{\frac{n+1}{2}}} A_z \quad (\text{A-15})$$

For the anisotropy constants used before and an n-value of 5 we get  $A_0 = 0.094A_z$ . Thus the creep in the hoop direction is only one tenth of the creep rate in the axial direction at the same applied stress. For an isotropic material we would get  $A_0 = 0.49 A_z$  since the effective stress is lower than  $\sigma_0$  in the case of expansion with internal pressure.

### A1.5 The true stress in a constant pressure creep test of tubing

If the tube is expanded with an internal pressure  $p$  the axial and circumferential stresses are:

$$\begin{aligned}\sigma_z &= \frac{pD_i}{4h} \\ \sigma_\theta &= \frac{pD_i}{2h}\end{aligned}\quad (\text{A-16})$$

where  $D_i$  and  $h$  are current values of inner diameter and wall thickness respectively. These parameters can be related through equations A-3:

$$\begin{aligned}\frac{d\epsilon_r}{d\lambda} &= -\left(\frac{G}{2} + H\right) \frac{pD_i}{2h} \\ \frac{d\epsilon_\theta}{d\lambda} &= \left(\frac{F}{2} + H\right) \frac{pD_i}{2h}\end{aligned}\quad (\text{A-17})$$

Noting that  $dh/h = d\epsilon_r$  and  $dD_i/D_i = d\epsilon_\theta$  we get:

$$\frac{dh}{h} = -\frac{G/2 + H}{F/2 + H} \frac{dD_i}{D_i} = -A \frac{dD_i}{D_i} \quad . \quad (\text{A-18})$$

which can be integrated to:

$$\frac{h}{h_0} = \left( \frac{D_i}{D_{i0}} \right)^{-A} \quad (\text{A-19})$$

where  $h_0$  and  $D_{i0}$  are the initial values for wall thickness and diameter. If we use these values in the equation for  $\sigma_\theta$  we get:

$$\sigma_\theta = \frac{pD_{i0}}{h_0} \left( \frac{D_i}{D_{i0}} \right)^{A+1} \quad (\text{A-20})$$

This relation can be expressed in terms of initial stress and engineering strain  $e$  in the circumferential direction:

$$\sigma_\theta = \sigma_{\theta0}(1+e)^{A+1} = \sigma_{\theta0} \exp((A+1)\epsilon_\theta) \quad (\text{A-21})$$

This relation can be compared to equations 5-4 and 5-5. With the anisotropy constants used as an example above,  $A = 0.46$ . Thus the true stress in a zirconium alloy tube will increase significantly slower with strain than in an isotropic material. This is an effect in addition to the relative strengthening expressed by equation A-15.

## A1.6 References

1. Hill, R., Plasticity. 1950, Oxford: Oxford University Press.
2. Tenckhoff, E., "Review of deformation mechanisms, texture, and mechanical anisotropy in zirconium and zirconium base alloys", Zirconium in the Nuclear Industry: Fourteenth International Symposium, 2004, Stockholm, ASTM STP 1467, ASTM, pp. 25-50.
3. Rosinger, H. E., "A model to predict the failure of Zircaloy-4 fuel sheathing during postulated LOCA conditions", Journal of Nuclear Materials, 120(1984), pp. 41-54.

## *Appendix B*

### **LIST OF ABBREVIATIONS**

The list below does not contain acronyms of computer codes.

ACR	Advanced CANDU Reactor
ADS	Automatic depressurization system
AEC	U.S. Atomic Energy Commission
AECL	Atomic Energy of Canada Limited
ANL	Argonne National Laboratory
ANS	American Nuclear Society
AOO	Anticipated operational occurrences
AVN	Association Vinçotte-Nucléaire,
BOC	Beginning-of-cycle
BOL	Beginning-of-life
BSE	Back scattered electron
BTF	Blowdown Test Facility
BWR	Boiling Water Reactor
CANDU	Canadian deuterium uranium (reactor)
CE	Combustion Engineering
CEA	Commissariat à l'énergie atomique
CEGB	Central Electricity Generating Board
CFR	Code of Federal Regulations
CHF	Critical heat flux
CNRA	Committee on Nuclear Regulatory Activities
COG	CANDU Owners Group
CP-ECR	Equivalent cladding reacted calculated with the Cathcart-Pawel correlation
CSNI	Committee on the Safety on Nuclear Installations
DBA	Design basis accident
DSP	German Standard Problem
ECCS	Emergency core cooling system
ECR	Equivalent cladding reacted
ECR-BJ	Equivalent cladding reacted calculated with the Baker-Just correlation
EdF	Electricité de France
EOC	End-of-cycle
EPMA	Electron probe microanalysis
EPRI	Electric Power Research Institute
FEBA	Flooding experiments with blocked arrays
FGR	Fission gas release
FLECHT	Full length emergency cooling heat transfer
Flops	Floating point operations per second
GB	Grain boundary
GDC	General Design Criterion
GRS	Gesellschaft für Reaktorsicherheit

Gwd/MTU	Gigawattdays per metric ton uranium
GWd/t	Gigawattdays per ton
HBS	High burn-up structure
HPSI	High-pressure safety injection
IAEA	International Atomic Energy Agency
IE	Irradiation Experiments
IFA	Instrumented fuel assembly
INEL	Idaho National Engineering Laboratory (now Idaho National Laboratory)
IPSN	Institut de protection et de sûreté nucléaire
ISP	International Standard Problem
JAERI	Japanese Atomic Energy Research Institute (now Japan Atomic Energy Agency)
KfK	Kernforschungszentrum Karlsruhe (now Forschungszentrum Karlsruhe)
KWU	Kraftwerk Union
LB	Large break
LHGR	Linear heat generation rate
LHR	Linear heat rate
LOCA	Loss-of-coolant-accident
LOM	Light optical microscopy (microscope)
LPCI	Low-pressure coolant injection
LVDT	Linear variable differential transformer
LWR	Light water reactor
MDA	Mitsubishi Developed Alloy
MOX	Mixed oxide
MRBT	Multi-rod burst test
MWd/kg	Megawattdays per kilogram
MWd/t	Megawattdays per ton
MWh/kg HE	Megawatthours per kilogram heavy element
ND	Neutron detector
NDA	New Developed corrosion resistance Alloy
NEI	Nuclear Energy Institute
NNC	National Nuclear Corporation
NRC	Nuclear Regulatory Commission
NRU	National Research Universal reactor
OD	Outer diameter
OECD	Organization for Economic Co-operation and Development
OM	Optical microscopy
OPG	Ontario Power Generation
ORNL	Oak Ridge National Laboratory
PBF	Power Burst Facility
PCM	Power Coolant Mismatch
PCT	Peak cladding temperature
PIE	Post-irradiation-examination
PIRT	Phenomenon Identification and Ranking Tables
PQD	Post-quench-ductility
PWR	Pressurized water reactor
RBMK	High power boiling reactor with pressurized channels (Russian design)
RCS	Reactor coolant system
RIA	Reactivity initiated accident
RRS	Reactor regulating system
RT	Room temperature

SB	Small break
SEASET	Separate effects and system effects tests
SEFLEX	Fuel rod simulator effects in flooding experiments
SEM	Scanning electron microscopy (microscope)
SGHWR	Steam Generating Heavy Water Reactor
SNL	Springfields Nuclear Laboratories
SOAR	State-of-the-art-report
SPERT-CDC	Special Power Excursion Reactor Tests-Capsule Driver Core
STP	Standard temperature and pressure
TBS	Transition break size
TEM	Transmission electron microscopy (microscope)
TGA	Thermogravimetric analysis (analyzer)
TREAT	Transient test reactor
UKAEA	United Kingdom Atomic Energy Authority
USD	United States dollar
USNRC	United States Nuclear Regulatory Commission
VVER	Water moderated, water cooled power reactor (Russian design)
WWER	Water moderated, water cooled power reactor (Russian design)
ZDT	Zero-ductility temperature
Zr	Zirconium
Zr-4	Zircaloy-4
Zy-4	Zircaloy-4

OECD PUBLICATIONS, 2 rue André-Pascal, 75775 PARIS CEDEX 16  
Printed in France.